

The University of Nottingham

UNITED KINGDOM • CHINA • MALAYSIA

Transition Metal Diphenolate and Dithiophenolate Complexes as Synthetic Analogues of the Active Sites of Nickel Superoxide Dismutase and Galactose Oxidase

George Marshall, MSci

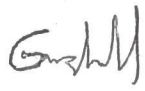
Thesis submitted to the University of Nottingham

for the degree of Doctor of Philosophy

June 2016

Declaration

Except where specific reference is made to other sources, the work presented in this thesis is the original work of the author. It has not been submitted in whole, or in part, for any other degree.

Signed:  George Marshall

Date: 05/09/2016

Acknowledgements

I would like to thank to University of Nottingham and the School of Chemistry for the many opportunities and challenges that they have provided me with over my time here. I would particularly like to thank my supervisors, Dr Jonathan McMaster and Prof. Martin Schröder for their assistance and guidance throughout my PhD.

I would like to extend special thanks to Dr Stephen Davies for his tireless assistance with electrochemical and spectroscopic experiments, as well as for many insightful discussions, and to Prof. Sandy Blake and Dr William Lewis for their assistance with the crystallographic aspects of this work, in addition to thanking Will for taking over as my second supervisor following Martin's departure from Nottingham. I would also like to acknowledge the contributions of 4th year MSci students Joe Jones, Megan Thomsett and David Edwards for their initial work on the synthesis and characterisation of some of the compounds discussed in Chapter Two. I would also like to thank Dr Amgalanbaatar Baldansuren and the EPSRC National EPR Service at the University of Manchester for carrying out the ESEEM and HYSCORE measurements presented in Chapter Four.

I have been privileged to work with a huge number of special people throughout my PhD. I would particularly like to thank the group of Post-Docs - Joe, Ben, Emma, Tom, and Carlo - who were instrumental in training me as a new PhD student, together with all of the people who have been a part of C41 and the group during my time here: Fran, Bahar, Ana, Adam, Jess, Charlene, Ogu, Maggie, Louisa, Pete, Stephen, Jack and Nick, together with countless project students and others associated with the wider Schörder group. I would particularly like to thank Gemma, Joe and Jere who have been a great help as we finished our PhD's together in Nottingham. Finally I would like to thank Eve, without whom nothing would be the same.

Table of Contents

Abstract IX

Abbreviations XI

Complex Abbreviations XIII

Chapter One – Introduction **1**

1.1 Bioinorganic Chemistry and Metalloenzymes 2

1.1.1 Metalloenzymes 2

1.2 Nickel Superoxide Dismutase 4

1.3 Analogues of the Active Site of Nickel Superoxide Dismutase 8

1.4 Galactose Oxidase 20

1.5 Synthetic Analogues of the Active Site of Galactose Oxidase 22

1.5.1 1,4,7-Triazacyclononane (TACN) Based Models of GO 22

1.5.2 Tripodal bis(pyridyl) alkylamine Models of GO 23

1.5.3 Analogues of GO Incorporating Salen-type Ligands 25

1.6 Aims 29

1.7 References 31

Chapter Two - The Syntheses of Pentacoordinate Diphenolate Zinc(II), Nickel(II) and Copper(II) complexes **37**

2.1 Introduction 38

2.1.1 Pentacoordinate Schiffs Base Compounds 38

2.1.2 Variation of Diphenolate Substituents 40

2.1.3 Aims new page 41

2.2 Synthesis of 3,5 Disubstituted Salicylaldehydes 43

2.3 Synthesis and Characterisation of Proligands $^{R}L_{O}^{NMe}$, and their Zinc, Nickel and Copper Complexes $M^{R}L_{o}^{NMe}$ (M= Zn, Ni, Cu; R = Cl, Br, Nap, Ph, PhMe, PhOMe, ^{t}Bu/Br, ^{t}Bu/Ph, ^{t}Bu/PhMe, ^{t}Bu/PhOMe) 45

2.4 The Structural Characterisations of $M^{R}L_{o}^{NMe}$ by Single Crystal X-ray Diffraction Studies. (R = Cl, Br, Nap, Ph, PhMe, PhOMe, ^{t}Bu/Br, ^{t}Bu/Ph, ^{t}Bu/PhMe, ^{t}Bu/PhOMe; M= Zn, Ni, Cu) 47

2.4.1 Introduction 47

2.4.2 Structures of $M^{R}L_{o}^{NMe}$ (R = Cl, Br, Nap, Ph, PhMe, PhOMe, ^{t}Bu/Br, ^{t}Bu/Ph, ^{t}Bu/PhMe, ^{t}Bu/PhOMe; M= Zn, Ni, Cu) 49

2.4.3 Discussion 66

2.4 EPR Spectroscopy 71

2.5 Density Functional Theory (DFT) Calculations 76

2.5.1 Geometry Optimisations 77

2.5.2 Spectroscopic Calculations 81

2.5.3 Dichloromethane Solvates and Frontier Orbitals 82

2.6 Conclusions 85

2.7 Experimental 87

2.8 References 102

Chapter Three - The Oxidation of Pentacoordinate Diphenolate Zinc(II), Nickel(II) and Copper(II) complexes 105

3.1 Introduction 106

3.1.1 Previous Work 106

3.1.2 Aims 107

3.2 Electrochemistry of $M^{R}L_{O}^{NMe}$ (R = Cl, Br, Nap, ^{t}Bu/Br; M = Zn, Ni, Cu) 109

3.2.1 Cyclic Voltammetry of $M^{R}L_{O}^{NMe}$ (M = Zn, Ni, Cu; R = Cl, Br, Nap) 109

3.2.2 UV/Vis Spectroelectrochemistry of $Ni^{Cl}L_{o}^{NMe}$, $Ni^{Br}L_{o}^{NMe}$, and $Ni^{Nap}L_{o}^{NMe}$ 112

3.2.3 Discussion 115

3.3 Electrochemistry of $M^{R}L_{o}^{NMe}$, (M = Zn, Ni, Cu;R = Ph, PhMe, PhOMe) 117

3.3.1 Cyclic voltammetry of $Zn^{R}L_{o}^{NMe}$, (R = Ph, PhMe, PhOMe) 117

3.3.2 Cyclic voltammetry of $M^{R}L_{o}^{NMe}$, (M = Ni, Cu; R = Ph, PhMe, PhOMe) 119

3.3.3 Discussion 124

3.4 UV/vis and EPR spectroscopic studies of $Zn^{R}L_{o}^{NMe}$, (R = Ph, PhMe, PhOMe) and their oxidation products 127

3.4.1 Spectroelectrochemistry of $Zn^{R}L_{o}^{NMe}$ (R = Ph, PhMe, PhOMe) 127

3.4.1.1 Spectroelectrochemistry of $Zn^{Ph}L_{o}^{NMe}$ 127

3.4.1.2 Spectroelectrochemistry of $Zn^{PhMe}L_{o}^{NMe}$ 128

3.4.1.3 Spectroelectrochemistry of $Zn^{PhOMe}L_{o}^{NMe}$ 129

3.4.2 Controlled Potential Electrolysis and EPR spectroscopy of the oxidation product of $Zn^{PhOMe}L_o^{NMe}$ 131

3.4.3 Discussion 133

3.5 UV/vis and EPR spectroscopic studies of $Ni^{R}L_o^{NMe}$, (R = Ph, PhMe, PhOMe) and their oxidation products 136

3.5.1 Spectroelectrochemistry of $Ni^{R}L_o^{NMe}$ (R = Ph, PhMe, PhOMe) 136

3.5.1.1 Spectroelecrochemistry of $Ni^{Ph}L_o^{NMe}$ 136

3.5.1.2 Spectroelecrochemistry of $Ni^{PhMe}L_o^{NMe}$ 138

3.5.1.3 Spectroelecrochemistry of $Ni^{PhOMe}L_o^{NMe}$ 140

3.5.2 Controlled Potential Electrolysis and EPR spectroscopy of the oxidation products of $Ni^{R}L_o^{NMe}$ (R = Ph, PhMe, PhOMe) 143

3.5.3 Discussion 146

3.6 UV/vis and EPR spectroscopic studies of $Cu^{R}L_o^{NMe}$, (R = Ph, PhMe, PhOMe) and their oxidation products 150

3.6.1 Spectroelectrochemistry of $Cu^{R}L_o^{NMe}$ (R = Ph, PhMe, PhOMe) 150

3.6.1.1 Spectroelectrochemistry of $Cu^{Ph}L_o^{NMe}$ 150

3.6.1.2 Spectroelectrochemistry of $Cu^{PhMe}L_o^{NMe}$ 152

3.6.1.3 Spectroelectrochemistry of $Cu^{PhOMe}L_o^{NMe}$ 153

3.6.2 Controlled Potential Electrolysis and EPR spectroscopy of the oxidation product of $Cu^{Ph}L_o^{NMe}$ 155

3.6.3 Discussion 156

3.7 Electrochemistry of $M^{R}L_o^{NMe}$ (R = ^{t}Bu/Br, ^{t}Bu/Ph, ^{t}Bu/PhMe, ^{t}Bu/PhOMe; M = Zn, Ni, Cu) 160

3.7.1 Electrochemistry of $M^{tBu/Br}L_o^{NMe}$ (M = Zn, Ni, Cu) 160

3.7.2 Electrochemistry of $M^{R}L_o^{NMe}$ (R = ^{t}Bu/Ph, ^{t}Bu/PhMe, ^{t}Bu/PhOMe; M = Zn, Ni, Cu) 164

3.7.2.1 Cyclic Voltammetry of $Zn^{R}L_o^{NMe}$ (R = ^{t}Bu/Ph, ^{t}Bu/PhMe, ^{t}Bu/PhOMe) 164

3.7.2.2 Cyclic Voltammetry of $Ni^{R}L_o^{NMe}$ (R = ^{t}Bu/Ph, ^{t}Bu/PhMe, ^{t}Bu/PhOMe) 166

3.7.2.3 Cyclic Voltammetry of $Cu^{R}L_o^{NMe}$ (R = ^{t}Bu/Ph, ^{t}Bu/PhMe, ^{t}Bu/PhOMe) 168

3.7.2.4 Discussion 170

3.7.3 UV/vis and EPR spectroscopy of the Oxidation Products of $Ni^{R}L_O^{NMe}$ (R = ^{t}Bu/Ph, ^{t}Bu/PhMe, ^{t}Bu/PhOMe) 172

3.7.3.1 Spectroelectrochemistry of $Ni^{R}L_o^{NMe}$ (R = ^{t}Bu/Ph, ^{t}Bu/PhMe, ^{t}Bu/PhOMe) 172

3.7.3.1.1 Spectroelectrochemistry of $^{tBu/Ph}NiL_o^{NMe}$ 172
3.7.3.1.2 Spectroelectrochemistry of $Ni^{tBu/PhMe}L_o^{NMe}$ 174
3.7.3.1.3 Spectroelectrochemistry of $Ni^{tBu/PhOMe}L_o^{NMe}$ 175
3.7.3.2 Controlled Potential Electrolysis and EPR spectroscopy of the oxidation products of $^{tBu/Ph}NiL_o^{NMe}$ 177
3.7.3.2.1 Discussion 180
3.7.3.3 Spectroelectrochemistry of $Cu^RL_o^{NMe}$ (R = ^{t}Bu/Ph, ^{t}Bu/PhMe, ^{t}Bu/PhOMe) 181
3.7.3.3.1 Spectroelectrochemistry of $Cu^{tBu/Ph}L_o^{NMe}$ 181
3.7.3.3.2 Spectroelectrochemistry of $Cu^{tBu/PhMe}L_o^{NMe}$ 183
3.7.3.3.3 Spectroelectrochemistry of $Cu^{tBu/PhOMe}L_o^{NMe}$ 185
3.7.3.3.4 Discussion 186
3.7.3.4 Controlled Potential Electrolysis and EPR spectroscopy of the oxidation products of $Cu^{tBu/Ph}L_o^{NMe}$ and $Cu^{tBu/PhOMe}L_o^{NMe}$ 177
3.7.4 Discussion 190
3.8 Conclusions 191
3.9 References 195
Chapter Four - Diphenolate and Dithiophenolate Transition Metal Complexes as Analogues of the Active Site of Nickel Superoxide Dismutase 197
4.1 Introduction 198
4.1.2 Aims 199
4.2 Investigations into the Role of Pendant Pyridine Donors in Controlling the Properties of Ni-containing Diphenolate Complexes 200
4.2.1 The Syntheses and Characterisation of Ni^{II} Complexes with Ligands Incorporating Diphenolate Donors 200
4.2.1.1 Introduction 200
4.2.2 Electrochemistry of $M^{tBu}L_O^R$ (M = Zn, Ni, Cu; R = Py, Ph, PyOMe) 208
4.2.2.1 Introduction 208
4.2.2.2 Cyclic Voltammetry of $M^{tBu}L_O^R$ (M = Zn, Ni, Cu; R = Py, Ph, PyOMe) 209
4.2.2.3 Spectroelectrochemistry of $Ni^{tBu}L_O^{Ph}$ 212
4.2.2.4 Controlled Potential Electrolysis of $Ni^{tBu}L_O^{Ph}$ 213
4.2.2.5 Spectroelectrochemistry of $Cu^{tBu}L_O^{Ph}$ 214
4.2.2.6 Spectroelectrochemistry of $Ni^{tBu}L_O^{PyOMe}$ 215

4.2.2.7 Controlled Potential Electrolysis of $Ni^{tBu}L_O^{PyOMe}$ 216
4.2.2.8 Spectroelectrochemistry of $Cu^{tBu}L_O^{PyOMe}$ 212

4.2.3 Discussion 219

4.3 Preparation and Characterisation of $Ni^{tBu}L_s^{Py}$ and $Ni^{tBu}L_s^{PyOMe}$ 225

4.3.1 Synthesis of the Ni^{II}-dithiophenolate Complexes $Ni^{tBu}L_s^{Py}$ and $Ni^{tBu}L_s^{PyOMe}$ 225

4.3.2 Synthesis of $Ni^{tBu}L_s^{PyOMe}$ 226

4.3.3 Electrochemistry of $Ni^{tBu}L_s^{Py}$ and $Ni^{tBu}L_s^{PyOMe}$ 226

4.2.2 Electrochemical studies of NiL_s^{Py} 226

4.4 EPR Spectroscopy of $Ni^{tBu}L_S^{Py}$ 229

4.4.1 Continuous Wave (CW) EPR Spectroscopy $Ni^{tBu}L_S^{Py}$ 229

4.4.2 ESEEM and HYSCORE EPR Spectroscopy and DFT Calculations on $Ni^{tBu}L_S^{Py}$ 229
4.4.2.1 Introduction 229
4.5.2.2 ESEEM and HYSCORE of $[Ni^{tBu}L_S^{Py}]^+$ 231
4.5.2.3 DFT Calculations on $[Ni^{tBu}L_S^{Py}]^+$ 234

4.6 Conclusions 238

4.7 Experimental 239

4.8 References 254

Chapter Five – Conclusions **257**

Appendices **A1**

Appendix 1 – General Synthetic Experimental Procedures and Physical Measurements A2

Appendix 2 - X-ray Crystallographic Experimental Details and Additional Information and Figures A5

Appendix 3 - Computational Methods A26

Appendices References A27

Abstract

This thesis describes the synthesis of diphenolate and dithiophenolate complexes of Zn^{II}, Ni^{II} and Cu^{II} that derive inspiration from the natures of the active sites of the nickel-containing superoxide dismutase (NiSOD) and the copper-containing galactose oxidase (GO).

Chapter One introduces the roles of transition metals in biology. The structures of the active sites of NiSOD and GO are described, together with a discussion of the proposed mechanisms of their action. A brief review of the coordination chemistry relevant to the chemistry of the actives sites of NiSOD and GO is presented and the aims of the research described in this thesis are set out.

Chapter Two describes the syntheses and structural characterisations of a series of pentacoordinate Zn^{II}, Ni^{II} and Cu^{II} diphenolate complexes $M^{R}L_{o}^{NMe}$ (M= Zn, Ni, Cu; R = Cl, Br, Nap, Ph, PhMe, PhOMe, ^{t}Bu/Br, ^{t}Bu/Ph, ^{t}Bu/PhMe, ^{t}Bu/PhOMe; page xiii) that differ in the natures of the substituents at the 3- and 5-positions of the phenolate rings within the ligand backbone. X-ray crystallographic studies on the Zn^{II}, Ni^{II} and Cu^{II} complexes, and room temperature and frozen solution EPR spectroscopic experiments on the Cu^{II} complexes provide insight into the influence of the 3- and 5- substitution on the coordination geometries. The changes in substitution at the 3 position of the phenolate rings in $M^{R}L_{o}^{NMe}$ (M= Zn, Ni, Cu; R = ^{t}Bu/Ph, ^{t}Bu/PhMe, ^{t}Bu/PhOMe) have significantly less influence on the geometry about the metal centre when compared to complexes that have substitutions that vary at the 3 and 5 positions in $M^{R}L_{o}^{NMe}$ (M= Zn, Ni, Cu; R = Ph, PhMe, PhOMe). DFT calculations provide a qualitative description of the electronic structures of these complexes, suggesting an increase in the metal character within the HOMOs for the Ni^{II} complexes relative to those of their Zn^{II} and Cu^{II} counterparts.

Chapter Three describes the electrochemical characterisations of the complexes synthesised in Chapter Two [$M^{R}L_{o}^{NMe}$ (M= Zn, Ni, Cu; R = Cl, Br, Nap, Ph, PhMe, PhOMe, ^{t}Bu/Br, ^{t}Bu/Ph, ^{t}Bu/PhMe, ^{t}Bu/PhOMe)]. Cyclic voltammetry demonstrates that $M^{R}L_{o}^{NMe}$ (M= Zn, Cu; R = Cl, Br, Nap, ^{t}Bu/Br) possess oxidation processes that are not reversible. $M^{R}L_{o}^{NMe}$ (M= Ni; R = Cl, Br, Nap, ^{t}Bu/Br) possess a reversible oxidation process assigned to the Ni^{III}/Ni^{II} redox couple. $M^{R}L_{o}^{NMe}$ (M= Zn, Ni, Cu; R = Ph, PhMe, PhOMe, ^{t}Bu/Ph, ^{t}Bu/PhMe, ^{t}Bu/PhOMe) display multiple oxidation processes, some of

which demonstrate electrochemical reversibility, particularly when M = Ni or Cu. UV/Vis and EPR spectroscopic studies on the oxidised species $[M^{R}L_{o}^{NMe}]^{+}$ (M= Zn, Ni, Cu; R = Ph, PhMe, PhOMe, ^{t}Bu/Ph, ^{t}Bu/PhMe, ^{t}Bu/PhOMe), supported by DFT calculations, suggest that the first oxidation process is significantly more metal based when M = Ni than for M = Cu or Zn and for the generation of $[Ni^{R}L_{o}^{NMe}]^{+}$ is associated with the formation of formal Ni^{III} species. The UV/vis and EPR spectroscopic results also suggest that $[Ni^{PhOMe}L_{o}^{NMe}]^{+}$ exhibits temperature-dependent Ni^{III}-phenolate ↔ Ni^{II}-phenoxyl redox tautomerism. The variation of the aromatic substituents systematically decreases the redox potential in the order R = Ph > PhMe > PhOMe, consistent with the relative electron donor properties of each group.

Chapter Four examines complexes that incorporate an aromatic, N-donor group pendant to the ligand background. These complexes serve as analogues of the active site of NiSOD. The dithiophenolate and diphenolate complexes $Ni^{tBu}L_{S}^{Py}$, $Ni^{tBu}L_{S}^{PyOMe}$, $Ni^{tBu}L_{O}^{Py}$, $Ni^{tBu}L_{O}^{PyOMe,}$ and $Ni^{tBu}L_{O}^{Ph}$ are prepared and characterised to examine the effect of different N-donor groups as potential axial donors to the metal centre on the redox properties of each complex. Advanced pulsed ESSEM and HYSCORE EPR spectroscopic studies probe the weak superhyperfine couplings involving the ^{14}N imine donors in $[Ni^{tBu}L_{S}^{Py}]^{+}$, and benchmark the spin densities associated with these donors calculated by DFT. These spectroscopically validated DFT calculations show how the distribution of spin density varies between complexes incorporating an N-donor pendant to the ligand backbone and those that do not. Thus, those incorporating an additional N-donor possess spin density that is considerably more localised at the formal Ni^{III} centre than those that do not.

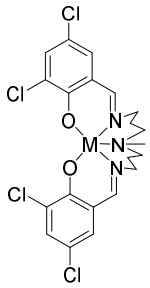
Chapter Five discusses the key conclusions of the research described in this thesis and compares and contrasts the chemistry exhibited by Zn^{II}, Ni^{II} and Cu^{II} diphenolate and dithiophenolate complexes. The structural and electrochemical differences observed upon the introduction of alternative diphenolate substituents in $M^{R}L_{o}^{NMe}$ (M= Zn, Ni, Cu; R = Cl, Br, Nap, Ph, PhMe, PhOMe, ^{t}Bu/Br, ^{t}Bu/Ph, ^{t}Bu/PhMe, ^{t}Bu/PhOMe) are summarised, together with the importance of the geometric structure of $Ni^{tBu}L_{S}^{Py}$ in controlling the redox chemistry of this centre. Finally, implications for the chemistry of the active sites of GO and NiSOD are discussed.

Abbreviations

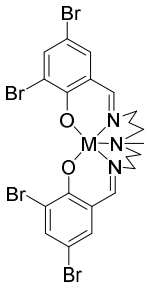
Å	Angstroms: 1 Å=0.1 nm
a_{iso}^{N}	Isotropic hyperfine coupling constant for nitrogen
Ar	Aromatic
br	Broad
CHN	Carbon, Hydrogen, Nitrogen
Δ	Chemical shift
CV	Cyclic Voltammetry
Cys	Cystine
dmFc	Decamethyl Ferrocene, $Fe(C_5Me_5)_2$
°	Degrees
DFT	Density functional theory
DMSO	Dimethylsulfoxide
d	Doublet
dd	Doublet of doublets
EI	Electron Ionisation
ENDOR	Electron-nuclear double resonance
EPR	Electron Paramagnetic Resonance
ESEEM	Envelope spin echo envelope modulation
esd	Estimated standard deviation
ESI	Electrospray Ionisation
ε	Extinction coefficient
$E_{1/2}$	Half wave potential
E_p^a	Anodic peak potential
E_p^c	Cathodic peak potential
Et_2O	Diethyl ether
EtOAc	Ethyl acetate
Fc	Ferrocene
Fc^+	Ferrocenium ion
G	Gauss
g_{iso}	Isotropic g value
g_{av}	Average g value
GO	Galactose oxidase
His	Histidine
HOMO	Highest occupied molecular orbital
HYSCORE	Hyperfine sub-level correlation spectroscopy
i_p^a	Anodic peak current
i_p^c	Cathodic peak current
^{i}Pr	Isopropyl
IR	Infrared
K	Kelvin
LMCT	Ligand to metal charge transfer
LUMO	Lowest unoccupied molecular orbital
MALDI	Matrix Assisted Laser Desorption Ionisation
m	Multiplet, medium
Me	Methyl
mg	Milligram
MHz	Megahertz
MLCT	Metal to ligand charge transfer
MS	Mass spectrometry

m/z	Mass/Charge
Nap	Napthyl
NiSOD	Nickel Superoxide Dismutase
NMR	Nuclear Magnetic Resonance
Ph	Phenyl
PhMe	4-methylphenyl
PhOMe	4-methoxyphenyl
Py	Pyridine
q	Quartet
quin	Quintet
RT	Room temperature
s	Singlet, strong
SCE	Saturated Calomel Electrode
sh	Shoulder
τ	Pentacoordinate structural parameter where 0 = square based pyramidal and 1 = trigonal bipyramidal
t	Triplet
TACN	1,4,7-triazacyclononane
^{t}Bu	Tertiary butyl
THF	Tetrahydrofuran
TMEDA	N,N,N',N'-Tetra-methylethylenediamine
Tyr	Tyrosine
UV/Vis	Ultraviolet/visible
w	Weak
XRD	X-ray Diffraction
Z	Number of empirical formula in unit cell
Z'	Number of empirical formula in asymmetric unit

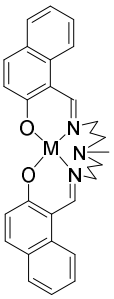
Complex Abbreviations



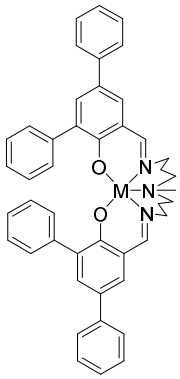
$M^{Cl}L_o^{NMe}$



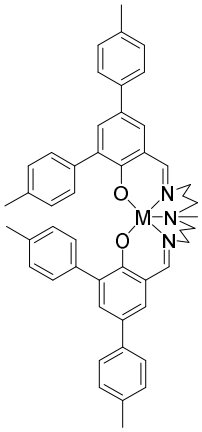
$M^{Br}L_o^{NMe}$



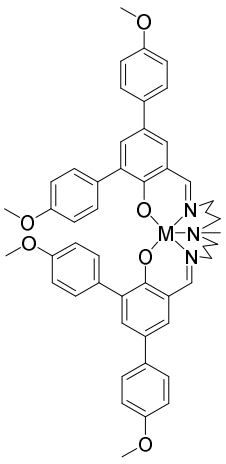
$M^{Nap}L_o^{NMe}$



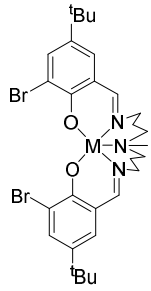
$M^{Ph}L_o^{NMe}$



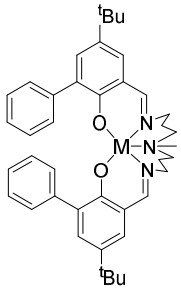
$M^{PhMe}L_o^{NMe}$



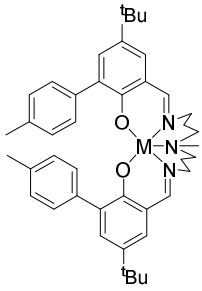
$M^{PhOMe}L_o^{NMe}$



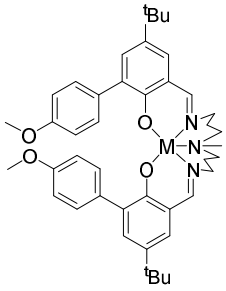
$M^{tBu/Br}L_o^{NMe}$



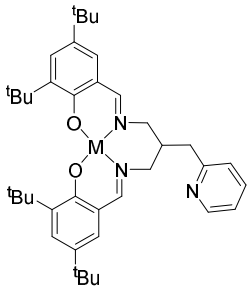
$M^{tBu/Ph}L_o^{NMe}$



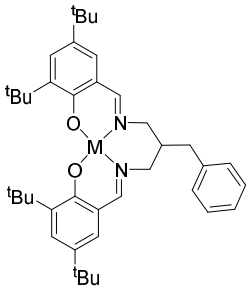
$M^{tBu/PhMe}L_o^{NMe}$



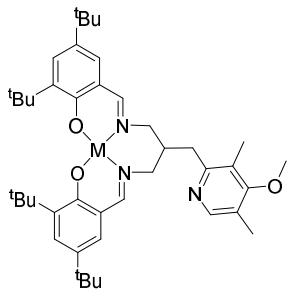
$M^{tBu/PhOMe}L_o^{NMe}$



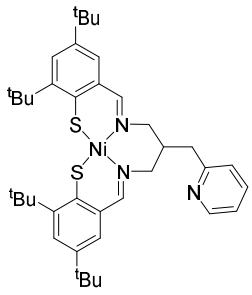
$M^{tBu}L_o^{Py}$



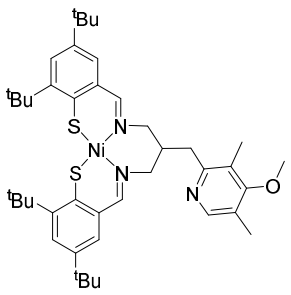
$M^{tBu}L_o^{Ph}$



$M^{tBu}L_o^{PyOMe}$



$Ni^{tBu}L_S^{Py}$



$Ni^{tBu}L_S^{PyOMe}$

M = Zn, Ni, Cu

Chapter 1

Introduction

1.1 Bioinorganic Chemistry and Metalloenzymes

Bioinorganic chemistry includes the study of the roles of metals in biology, and is an interdisciplinary field which continues to attract interest.[1] Twenty eight elements, including 10 transition metals and 4 s-block metals are known, or presumed, to be essential for human life, with many more used as diagnostic[2] and therapeutic agents.[3] Metals play a key role in a wide variety of biological systems[4] including biominerals such as bones teeth and shells,[5] vitamins such as vitamin B_{12}[6] and in drug molecules[3] including antimicrobials,[7, 8] anti-cancer[9, 10] and anti-arthritic drugs.[11] One of their key roles, however, is at the active sites of enzymes, with *ca*. 40% of know enzymes incorporating one or more metal atoms at their active site,[4] and it is the study of these species that has attracted particular interest among bioinorganic chemists.[12-15]

1.1.1 Metalloenzymes

Enzymes are proteins that act as catalysts for biochemical processes in living organisms. Chemical change occurs at the active site of an enzyme, which may only consist of a very small portion of the overall enzymatic structure. Enzymes are highly selective catalysts, and this selectivity is driven by the nature of the active site and the wider geometric structure of the enzyme, promoting geometric and electronic selectivity.

Metalloenzymes employ a metal centre at their active site. Many enzymes are structured in this way in order to exploit the redox active nature of metal ions in order to catalyse chemical transformations. A wide range of metal centres are employed at the active sites of metalloenzymes including the hydrogenases (Ni, Fe),[16, 17] ureases (Ni),[18] ribonucleotide reductases (Fe, Mn),[19, 20] cytochromes (Fe),[21] xanthine oxidase (Mo),[22] superoxide dismutases (Ni, Fe, Mn, Cu, Zn)[23-34] and galactose oxidase (Cu)[35, 36] among many other examples.

The nature of the redox chemistry carried out by many metalloenzymes may be associated with the redox chemistry of coordinated amino acid side-chains. The reactivity and stability of these enzymes therefore often relies not just on the properties of the redox active metal centre itself, but on the nature of the surrounding atoms which coordinate to it. The ability of the coordination sphere of the metal centre to delocalise radical character – so called ‘redox non-innocence’ - is therefore

key to the function of many metalloenzymes. The choice of metals employed by metalloenzymes can also often be surprising, and starkly different from that which might be chosen from chemical first principles for the catalysis of the same process.[20] The complex and unusual structures surrounding the redox active metal centres in metalloenzymes are therefore key to understanding their reactivity.

With the complex structures and redox active metal centres found in metalloenzymes, bioinorganic chemistry provides an ideal opportunity to explore the structure and function of these often unusual species. Consequently the syntheses of small molecule analogues of the active sites of metalloenzymes has become a well-developed field.

In this work a variety of transition metal complexes of zinc, nickel and copper are presented. These all employ either diphenolate or dithiophenolate donors and we investigate the influence on the geometric and electronic structure of introducing additional nitrogen donor atoms to give pentacoordinate species. These complexes can be considered relevant to the active sites of two enzymes, nickel superoxide dismutase (NiSOD) and galactose oxidase (GO), both of which continue to attract attention from bioinorganic chemists. The active sites of these enzymes exhibit interesting features including formal Ni^{III}/Ni^{II} and Cu^{II}/Cu^{I} redox couples and redox non-innocent thiolate and phenolate coordinating ligands, respectively.

1.2 Nickel Superoxide Dismutase

Superoxide is an unavoidable by-product of aerobic respiration, with 3-10 % of dioxygen used by tissues being converted into reactive intermediates such as superoxide.[37] Such species have been implicated in a number of diseases, particularly degenerative conditions[37-39] including amyotrophic lateral sclerosis (ALS),[24, 40] Parkinson's disease[41] and Alzheimer's disease.[42] More recently it has been shown that superoxide is also generated as part of the immune response,[43, 44] and consequently it has attracted attention in relation to a number of autoimmune disorders including type 1 diabetes,[45, 46] encephalomyelitis[47] and inflammatory bowel disease.[48, 49]

Superoxide dismutases exploit redox active metal centres in order to catalyse the disproportionation of superoxide to hydrogen peroxide and molecular dioxygen.[50] Extensive characterisation of two distinct classes of SODs has taken place: CuZnSOD, with a binuclear core and 3 histidine ligands surrounding the Zn atom and 4 histidine donors around the Cu;[24-26] and Mn or Fe SOD[27-29] which consist of a Mn or Fe mononuclear active site coordinated by three histidine residues, one aspartic acid and one solvent molecule. More recently, a third class of SODs, named NiSOD, has been identified and isolated from several *Streptomyces* species[30, 31] and cyanobacteria.[32] The active site of the enzyme has been elucidated by X-ray crystallography,[33, 34] with the Ni-containing active site located within a nine residue hook motif at the N-terminus of the hexameric protein which consists of four helix bundles. The Ni centre is ligated by the amine of His-1, the amide of Cys-2 and the thiolate donors of Cys-2 and Cys-6 in the reduced Ni^{II} state, with the imidazolate of His-1 also binding in the axial position in the oxidised Ni^{III} form (Figure 1.2.1).[34]

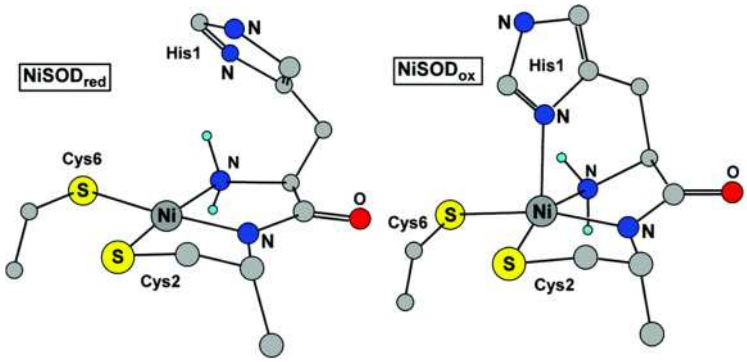


Figure 1.2.1: The active site of NiSOD in its reduced and oxidised states[51]

Extensive studies on the native enzyme have been undertaken in order to characterise its structure and function. Further analyses of X-ray crystallographic studies,[52] together with EPR measurements[34, 53, 54] X-Ray absorption spectroscopic[52, 53, 55] and computational studies[56, 57] have highlighted the importance of the immediate thiolate coordination around the nickel centre,[55] the axial coordination of His-1 in the oxidised form[52] and the wider hydrogen-bonding network about the active site.[52]

SODs catalyse the disproportionation of superoxide *via* a ping-pong mechanism, shuttling between the oxidised and reduced forms of the enzyme, with the oxidation of superoxide accompanied by reduction of the metal site and production of O_2, and the reduction of the substrate accompanied by the oxidation of the metal site and production of H_2O_2. (Figure 1.2.2).[58] Getzoff *et al.* originally proposed such a mechanism for the NiSOD enzyme based on a cycling between the formal Ni^{II} and Ni^{III} states with the accompanying disproportionation of superoxide to O_2 and H_2O_2, and the binding of His-1 in an axial position that may stabilise the Ni^{III} state (Figure 1.2.3).[33]

$$Ni^{II} + O_2^{\cdot -} \longrightarrow Ni^{III} + H_2O_2$$

$$Ni^{III} + O_2^{\cdot -} \longrightarrow Ni^{II} + O_2$$

Figure 1.2.2: Redox reactions of NiSOD

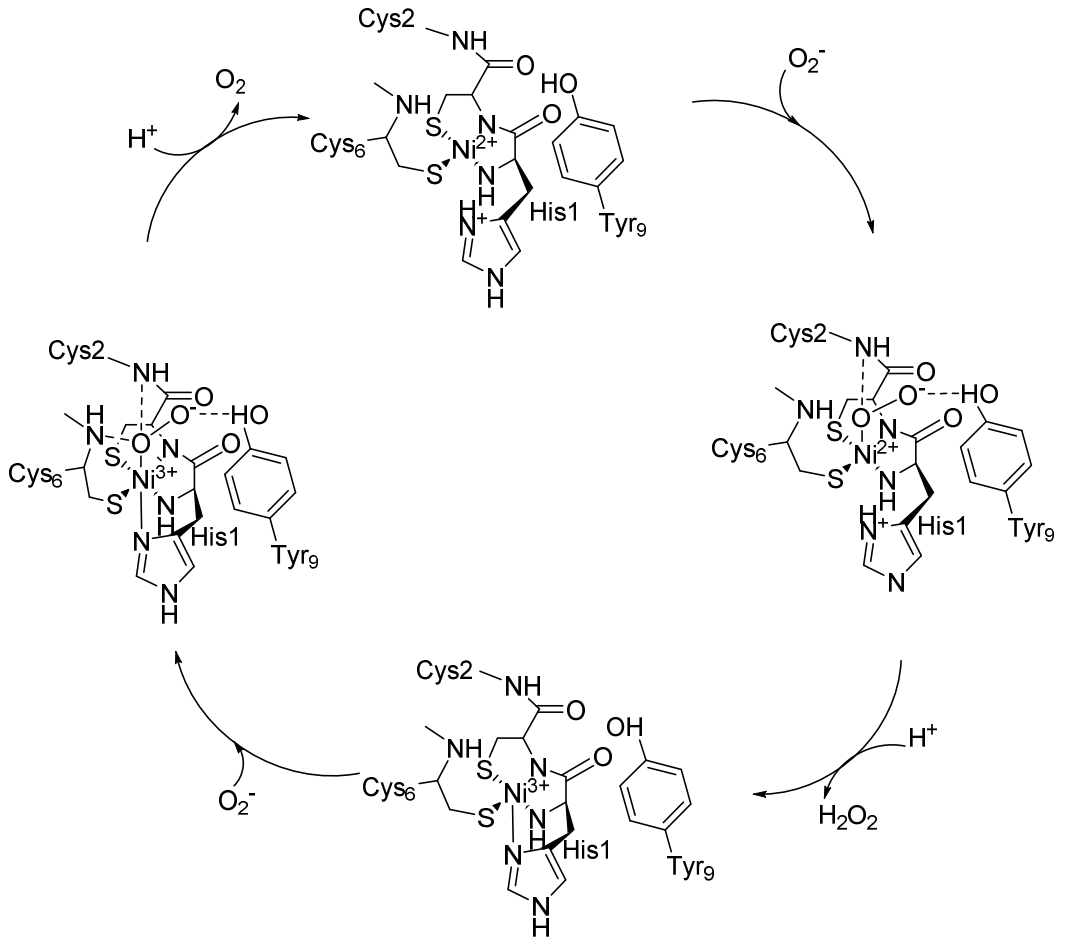


Figure 1.2.3: Summary of the proposed mechanism of the active site of NiSOD[59]

Detailed EPR spectroscopic studies have been undertaken to probe the electronic structure of the oxidised form of the active site of NiSOD;[34] this oxidised form possesses a rhombic EPR signal, which has been simulated with g values g_{11} = 2.306, g_{22} = 2.232 and g_{33} = 2.016 and A values A_{11} = 16.2 G, A_{22} = 17.7 G and A_{33} = 24.6 G (Figure 1.2.4a). The rhombic signal has been attributed to unpaired spin density associated with the Ni centre *via* ^{61}Ni isotopic labelling studies (Figure 1.2.4b), with the influence of nitrogen and sulfur coordination confirmed *via* ^{15}N and ^{33}S isotopic labelling studies, respectively (Figure 1.2.4c and d).[34] ^{15}N studies also reveal previously unresolved hyperfine splitting arising from N in the g = 2.23 region,[34] which has also been confirmed using pulsed EPR techniques.[54] The ^{33}S superhyperfine splitting is small (3.6 G) and is consistent with spin density largely associated with the Ni centre.[34] Electronic absorption spectra have also revealed an intense absorption band at ~380 nm (ε = 6800 Mol^{-1} cm^{-1}), which is assigned to

S(Cys) → Ni^{III} LMCT by resonance Raman spectroscopic studies and theoretical calculations.[51] These computational models reproduce the experimentally determined g values and hyperfine splittings, which are consistent with a $(d_z^2)^1$ ground state.[51] Further computational work has revealed the importance of the ligand arrangement around the Ni centre and its effect on the electronic structure. The equatorial anionic thiolate and amidate donors lower the reduction potential of the active site through filled/filled π orbital interactions with the Ni centre, and the loss of the axial nitrogen coordination from His-1 is key to the stabilisation of the dz^2 orbital in its reduced form. This leads to a HOMO composed principally of Ni^{II} and anionic equatorial ligand filled π orbitals for the reduced form of the enzyme that results in a lower reduction potential.[51]

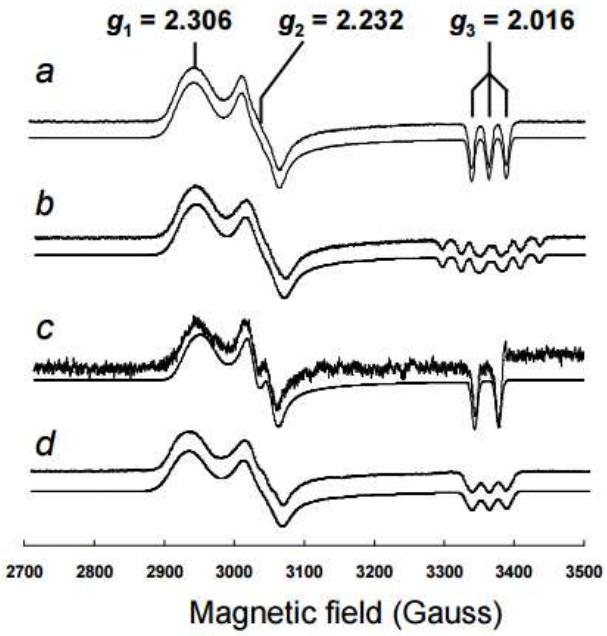


Figure 1.2.4: Frozen solution X-band EPR of the oxidised form of NiSOD. A: Native enzyme with naturally abundant isotopes, B: ^{61}Ni enriched material, C: ^{15}N enriched material, D: ^{33}S enriched material. [34]

1.3 Analogues of the Active Site of Nickel Superoxide Dismutase

The structure and function of the active site of NiSOD has attracted much interest among bioinorganic chemists and over the past decade an increasing number of peptide-based and low molecular weight analogues of the active site of NiSOD have been prepared in order to investigate the properties and mode of action of the metalloenzyme.[60]

Metallopeptide-based analogues of the active site of NiSOD are readily prepared as all of the Ni ligating residues are within six residues of the N-terminus.[61] Shearer *et al.* have prepared a number of metallopeptide based models[62-65] and have used these to investigate the influence of axial coordination in these systems,[65] and to elucidate mechanistic information.[63, 64] These, and similar studies,[66] have reinforced the importance of the N donors at the active site of NiSOD that help to avoid oxidative damage at the cysteinates, and have further highlighted the important role of the axial histidine residue.[63] Whilst several such protein-based models catalyse the disproportionation of the superoxide anion, O_2^-,[62, 67, 68] further mechanistic and spectroscopic insights can be gained through the detailed study of low molecular weight coordination compounds.

An extensive range of Ni- centred coordination compounds have been synthesised and studied as models for the active site of NiSOD. Initial work focussed on the syntheses of [Ni(N_2S_2)] square planar systems, originally developed as models for the active site of the nickel iron hydrogenases.[69, 70] $[Ni(emb)]^{2-}$ (emb = N,N'-ethylenebis(*o*-mercaptobenzamide),[69, 71] $[Ni(ema)]^{2-}$ (ema = *N,N'*-ethylenebis(2-(acetylthio)acetamide)),[70] $[Ni(phma)]^{2}$ (phma = *N,N'*-phenylenebis(2-(acetylthio)acetamide)),[70] and [Ni(phmi)]$(NEt_4)_2$, (phmi = *N,N'*-1,2phenylenebis(2-sulfanyl-2-methyl)propionamide))[70] (Figure 1.3.1) have been prepared and studied by Holm and Krüger, and possess electrochemically reversible redox processes at $E_{1/2}$ = -0.04, -0.34, -0.24 and -0.42 V *vs.* SCE respectively. EPR spectroscopic studies of electrochemically generated $[Ni(ema)]^-$ and $[Ni(phma)]^-$ reveal near axial spectra with large g-anisotropies, consistent with the formation of formally Ni^{III} species, whilst the products of oxidation of $[Ni(ema)]^{2-}$ and $[Ni(phma)]^{2-}$ to $[Ni(ema)]^-$ and $[Ni(phma)]^-$ at -30 °C are EPR silent, consistent with the formation of sulfur bridged dimers at low temperature.[69, 70]

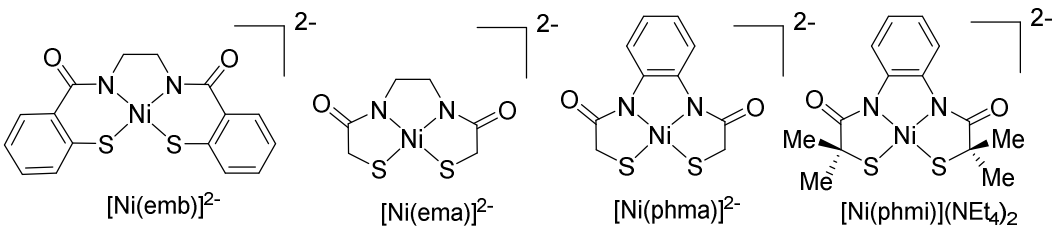


Figure 1.3.1: Ni thiolate complexes reported by Holm and Krüger[69, 70]

Masuda *et al.* have prepared a Ni(N_2S_2) square planar complex (Figure 1.3.2 top) which displays reactivity towards the superoxide anion. This complex possesses two redox processes at -0.68 and 1.71 V *vs.* NHE, assigned to $Ni^{II/I}$ and $Ni^{III/II}$ couples respectively. A mechanism is proposed in which the Ni^{II} form of the complex is reduced to Ni^{I} before it reacts with O_2 to give the same product as when the Ni^{II} species is directly reacted with KO_2 (Figure 1.3.2).[72]

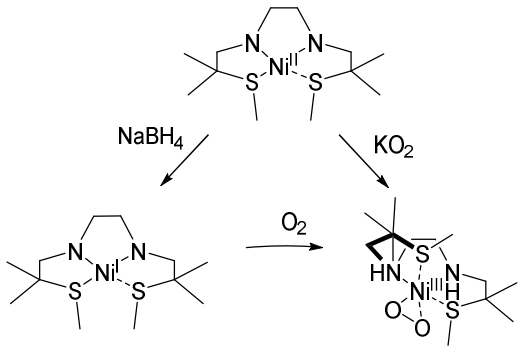


Figure 1.3.2: Ni(N_2S_2) *complex synthesised by Masuda et al. and proposed reactivity with* KO_2.[72]

Other research groups have focussed on probing the influence of the mixed amine/amide coordination supporting the thiolate donors around the Ni centre. Density functional theoretical (DFT) calculations based on metallopeptide maquettes show a decrease in S character (~8 %) and an increase in Ni character (~13 %) in the HOMO of the bis-amide ligand *vs.* the amine/amide mixed model, which is proposed to result from the activation of the Ni-S(π)* orbital.[73] Grapperhaus *et al.* have also shown through calculations on a series of bis-amine, bis-amide and amine/amide complexes and their oxygenated analogues, that mixed amine/amide complexes are less susceptible to oxygenation than their bis-amide counterparts.[74]

Shearer *et al.* have synthesised $[Ni(BEAAM)]^-$ (BEAAM = N-{2-[benzyl(2-mercapto -2- methylpropyl) amino] ethyl} -2- mercapto -2- methylpropionamide) (Figure 1.3.3) that incorporates a mixed amine/amide N_2S_2 coordination sphere. $[Ni(BEAAM)]^-$ exhibits a quasireversible redox process at $E_{1/2}$ = 0.12 V *vs.* Ag/AgCl, which is shown by DFT to be mostly Ni based.[75] This reduction potential is intermediate between the couples observed for the bis-amine complex [Ni(bmmp-dmed)] (bmmp-dmed = N,N'-bis-2-methyl-mercaptopropyl-N,N'-dimethylethylenediamine) (0.41 V *vs.* Ag/AgCl) and the bis-amide complex $[NEt_4]$ [Ni(emi)] (-0.34 V *vs.* Ag/AgCl).[75]

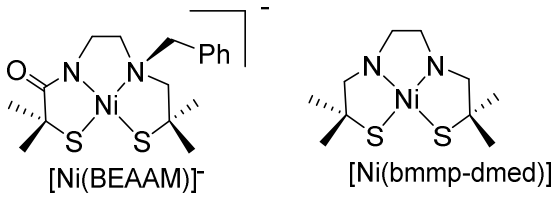


Figure 1.3.3: $[Ni(BEAAM)]^-$ and [Ni(bmmp-dmed)] complexes reported by Shearer et al.[75]

This work, when examined in combination with previous computational studies, demonstrates a potential role for the mixed amine/amide coordination at the active site of NiSOD. Thus, a bis-amine coordination is electrochemically incompatible with SOD activity, and a bis-amide is potentially unstable to oxygenation. Subsequent work, using X-ray absorption spectroscopy, has shown an increased metal-ligand covalency for $[Ni(BEAAM)]^-$ compared to the bis-immine or bis-amine analogues, and a reduction of the Ni(3d)/S(π)* HOMO energy with increasing amine ligand character that potentially deactivates the complex towards oxygenation.[76] While $[Ni(BEAAM)]^-$ possesses a quasireversible redox couple at 0.12 V (*vs.* Ag/AgCl), which is an appropriate potential for SOD activity, none was observed and this was attributed to either potential thiolate oxidation, the instability of the formally Ni^{III} species, or the absence of a suitable axial donor to the Ni-centre.[75]

The presence and importance of an axial N donor to the Ni centre in the oxidised form of NiSOD has been investigated extensively. Holm and Krüger first reported the binding of exogeneous pyridine to the oxidised Ni-containing thiolate complex $[Ni(emb)]^-$ resulting in EPR spectra consistent with a metal centred oxidation and the binding of pyridine in an axial position.[71] They subsequently extended this work

to a wider range of complexes[70] before reporting the first aliphatic thiolate Ni^{III} complex $(NEt_4)_2$[Ni(phmi)] and demonstrating, through EPR spectroscopic studies, the metal centred nature of the oxidation upon the coordination of exogenous pyridine.[77]

The effect of coordinating solvent molecules upon the oxidation processes of Ni-containing thiolate complexes has subsequently attracted much interest.[78-80] Duboc *et al.* used imidazole to more closely replicate the coordination at the active site of the native enzyme and showed by EPR spectroscopy and DFT calculations a shift to a significantly more metal centred oxidation for a nickel bisamine aliphatic dithiolate complex. Upon oxidation nickel(2,2'-(2,2'-bipyridine-6,6'-diyl) bis (1,1-diphenylethane thiol)) possesses a DFT-calculated Ni spin population of 49 %, but this spin population increases to 82 % upon imidazole coordination in an axial position.[78]

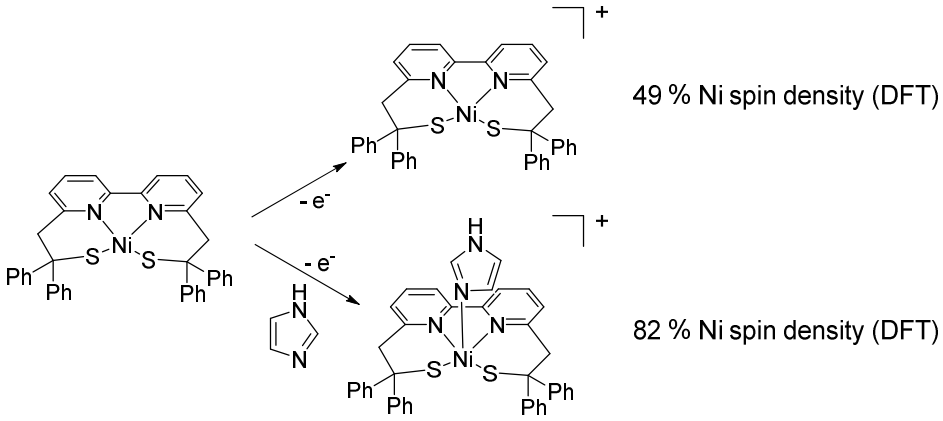


Figure 1.3.4: Nickel(2,2'-(2,2'-bipyridine-6,6'-diyl) bis (1,1-diphenylethane thiol)) and its oxidation product in the presence and absence of exogenous imidazole.

Previous work within the McMaster group has led to the synthesis of several Schiff base N_2S_2 square planar complexes as analogues for the active site of NiSOD (Figure 1.3.5).[79]

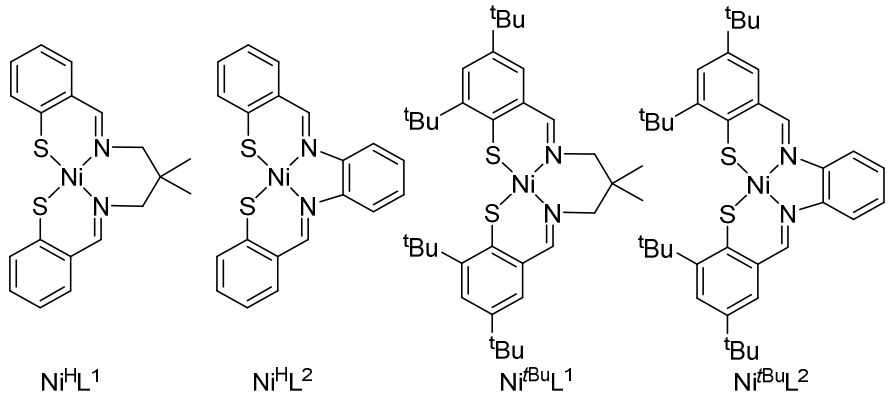


Figure 1.3.5: Ni thiosalen complexes previously prepared by the McMaster group.[79]

Complexes $Ni^{H}L^{1}$ and $Ni^{H}L^{2}$ exhibit a series of oxidative redox processes which do not display any reversibility at E_p^a = 0.29, 0.60 and 0.88 V (*vs.* Fc^+/Fc) for $Ni^{H}L^{1}$ and E_p^a = 0.41 V (*vs.* Fc+/Fc) for $Ni^{H}L^{2}$. The addition of ^{t}Bu substituents in $Ni^{tBu}L^{1}$ and $Ni^{tBu}L^{2}$ results in reversible oxidations which are observed at $E_{1/2}$ = 0.16 V and 0.10 V (*vs.* Fc^+/Fc) for $Ni^{tBu}L^{1}$ and $Ni^{tBu}L^{2}$ respectively, accompanied by a further oxidation process at E_p^a = 0.82 and 0.93 V (*vs.* Fc+/Fc) respectively. This shift to less positive redox potentials and increase in electrochemical reversibility following the incorporation of ^{t}Bu substituents on the phenyl rings is consistent with previous results for diphenolate ligands in which the ^{t}Bu groups limit decomposition *via* proton abstraction that could result from the delocalisation of the radical character around the phenyl ring system (Figure 1.3.6).[81] This approach is particularly important for dithiophenolate species due to the lower stability of the thiophenoxyl radical compared to its phenoxyl equivalent.[82]

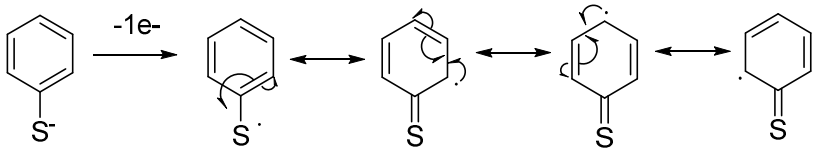


Figure 1.3.6: Radical delocalisation within thiophenoxyl radical species

The reversible oxidation of $Ni^{tBu}L^{2}$ at $E_{1/2}$ = 0.10 V (*vs.* Fc^+/Fc) loses its reversibility below 253 K. This loss of reversibility at low temperature is likely due to the formation of sulfur bridged dimers.[70] EPR studies of the oxidised species $[Ni^{tBu}L^{1}]^+$ and $[Ni^{tBu}L^{2}]^+$ at room temperature reveal a radical EPR signal with narrow linewidth consistent with the formation of a ligand-based radical. $[Ni^{tBu}L^{1}]^+$ and $[Ni^{tBu}L^{2}]^+$ are EPR silent upon cooling, consistent with dimer formation which was

confirmed by crystallographic characterisation of the disulfide dimer $[Ni^{tBu}L^2](ClO_4)_2 \cdot 2CH_2Cl_2$, with the two nickel units joined by a single sulfur-sulfur bond (3.185(2) Å). The EPR spectra of $[Ni^{tBu}L^1]^+$ and $[Ni^{tBu}L^2]^+$ exhibit significant changes on the addition of pyridine at room temperature,[77] with the oxidised species generating a spectrum with high g-anisotropy and a five-line ^{14}N superhyperfine splitting consistent with the binding of two pyridine molecules (Figure 1.3.7).[79] DFT studies have been carried out which support these conclusions showing a ligand-based SOMO for the complex which shifts to a more metal-based SOMO upon the coordination of pyridine ligands at the axial positions (Figure 1.3.7).

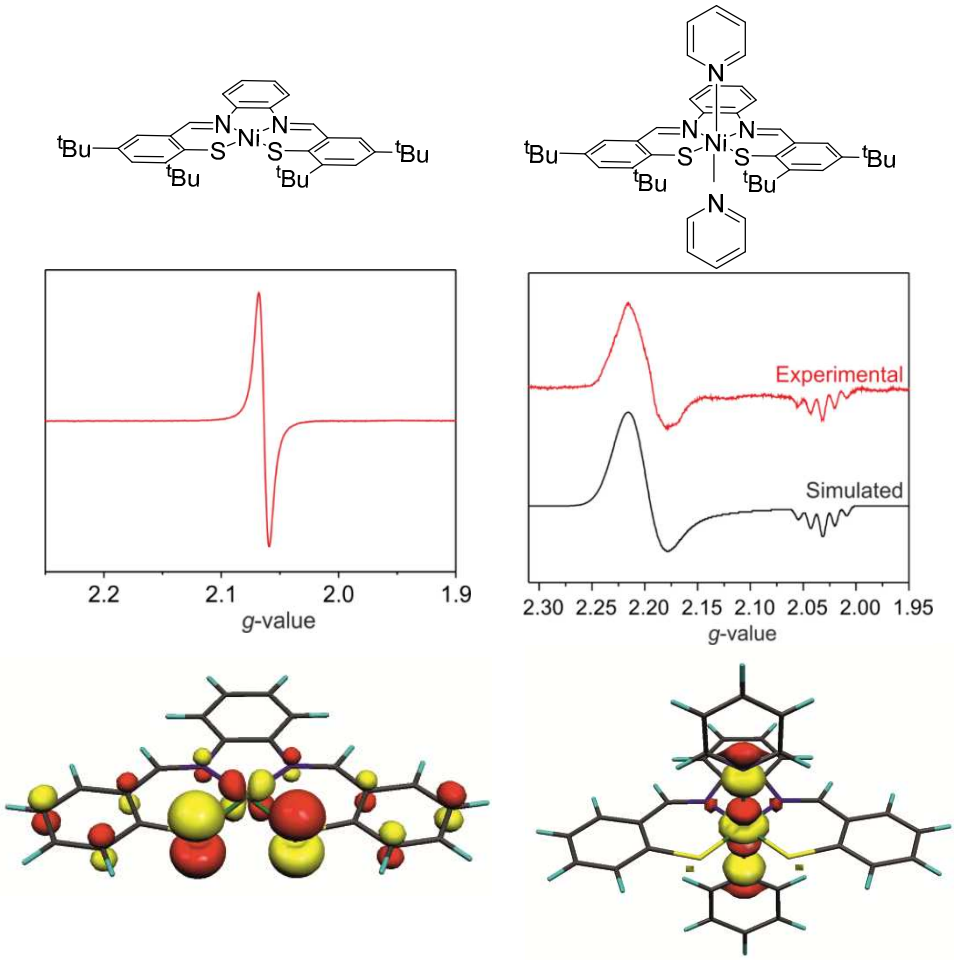


Figure 1.3.7: $[Ni^{tBu}L^2]^+$ (left) and $[Ni^{tBu}L^2]^+$ with excess exogenous pyridine (right)-X-band EPR spectrum at 77 K and SOMO calculated by DFT.[79]

Masuda *et al.* have combined a mixed amine/amide coordination sphere in a square planar nickel complex NiL^3 (Figure 1.3.8). Studies using exogenous methylimidazole supports a proposed mechanism for the superoxide reducing and

oxidising steps (Figure 1.3.9).[80] This work also examined the influence of the second coordination sphere, with electronic absorption bands, C=O stretching vibrations and redox potentials all shown to be solvent dependant. These data suggest a potential role for hydrogen bonding interactions between the solvent and C=O groups about the active site in tuning the reduction potential of the Ni centre for the disproportionation of superoxide. The addition of methylimidazole and ^{15}N-labeled methylimidazole to $[NiL^3]^+$ has been followed by EPR spectroscopy and indicates an axial binding of imidazole similar to that observed for the native NiSOD enzyme. The reactivity of the Ni^{II} complex NiL^3 with superoxide has been monitored by UV/Vis and EPR spectroscopies with results consistent with the formation of an end-on Ni^{II} superoxo bound species following the addition of potassium superoxide to a solution of the Ni^{II} complex NiL^3.[83] The addition of a proton source to this superoxo species led to the formation of an EPR silent species, whilst the same experiment in the presence of imidazole gave similar spectra to those obtained previously for $[NiL^3]^+$ in the presence of imidazole. These observations reinforce the importance of the coordination of N donors in the axial position and the presence of a proton source. The superoxide oxidising step accomplished by NiSOD has also been investigated by the addition of superoxide to a solution of $[NiL^3]^+$ with imidazole bound in the axial position. This results in a decrease in the intensity of the EPR signal, corresponding to reduction to the Ni^{II} species.

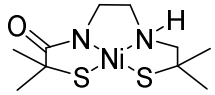


Figure 1.3.8: NiL^3 synthesised by Masuda at al.[80]

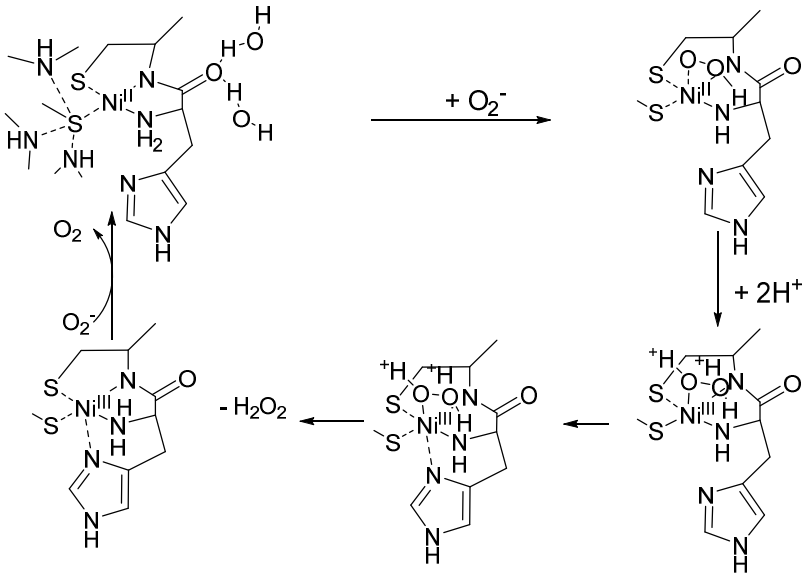


Figure 1.3.9: Proposed mechanism of NiSOD based on modelling studies on NiL[3] by Masuda et al. [80]

Recent work has also focussed on incorporation of a tethered N-containing donor to replicate the His-1 residue at the active site of the native enzyme and to remove the requirement for the addition of exogenous N-donors. N_3O_2 type systems can often provide useful models for their N_3S_2 analogues and are less susceptible to oxidative stress. A limited number of these pentacoordinate systems as models for metalloenzymes have been synthesised.[84, 85] Kuo *et al.* reported the five coordinate system, [Ni(BDPP)] (DBPP = 2,6-bis(((S)-2-(diphenyl-hydroxymethyl)-1-pyrrolidinyl)methyl)pyridine), incorporating a tethered pyridyl group, as an analogue for the active site of NiSOD.[85]

[Ni(BDPP)] possesses a quasi-reversible redox process at 0.31 V (*vs.* Ag/AgCl), and the oxidised species $[Ni(BDPP)]^+$ exhibits an axial EPR spectrum with three line ^{14}N superhyperfine coupling, similar to that observed for the oxidised form of NiSOD.[33] The X-ray crystal structure of $[Ni(BDPP)]^+$ reveals a distorted square based pyramidal geometry ($\tau = 0.24$) similar to that of the active site of NiSOD ($\tau = 0.20$). In addition, on exposure of $[Ni(BDPP)]^+$ to potassium superoxide, a quantitative amount of O_2 gas was collected and its identity confirmed by gas chromatography. This, along with simultaneous reduction of $[Ni(BDPP)]^+$ to [Ni(BDPP)], demonstrated that $[Ni(BDPP)]^+$ is capable of reproducing the superoxide oxidising step proposed for NiSOD.

Efforts have also focussed on the syntheses of thiolate complexes incorporating axial N-donors. $NiN_2S_2^{Py}$ incorporates a pendant pyridine capable of acting as an axial donor in a mixed amine/amide N_2S_2 complex (Figure 1.3.10 left).[86] Unfortunately, despite this ligand set representing the first isolated synthetic model of reduced NiSOD, upon oxidation no binding of the axial pyridine was evident; a disulfide linked species was identified crystallographically (Figure 1.3.10 bottom). Nevertheless, the oxidation process is chemically reversible with the regeneration of $NiN_2S_2^{Py}$ following the reduction of the disulfide species with $[Co(Cp^*)_2]$.[86]

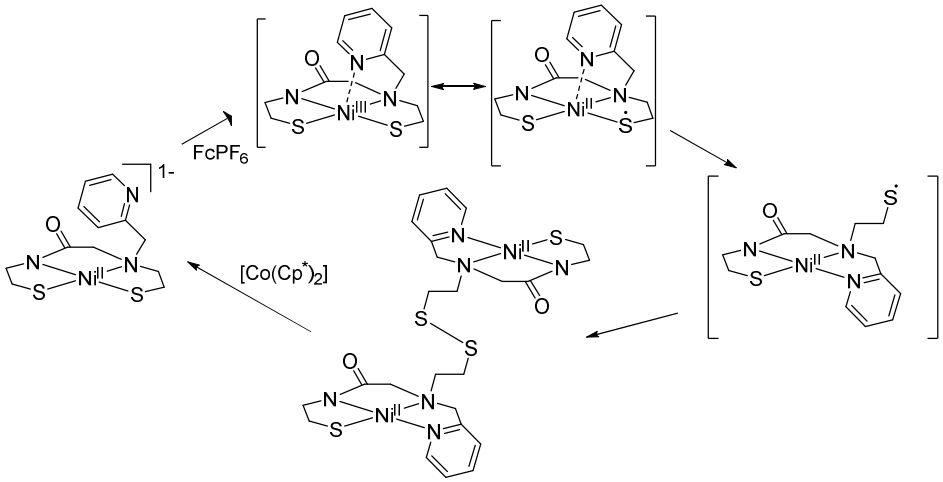


Figure 1.3.10: Mechanism of interconversion between $NiN_2S_2^{Py}$ complex (top) and the related disulfide bridged species (bottom). [86]

$[Ni(N_2S)(SR)]$ (R = $PhNH_2$), incorporating aniline based axial N-donor substituents (Figure 1.3.11),[87] demonstrate that positioning an NH_2 group at the ortho position of the aryl (SR) group allows access to oxidised species which are spectroscopically characterised as a combination of the resonance hybrids Ni^{III}-SR and Ni^{II}-·SR.

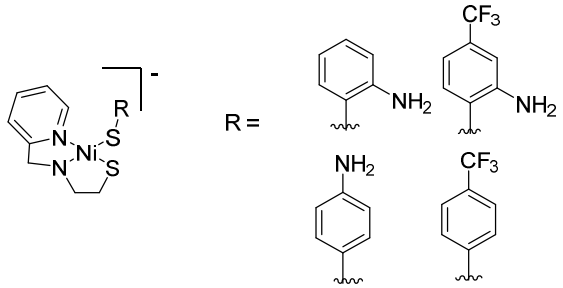


Figure 1.3.11: Series of complexes synthesised by Harrop et al.

$[Ni(H_2BA^RTPP)](ClO_4)_2$ (R = Ph, ^{i}Pr)[88] ($H_2BA^{Ph}TPP$ = 2,6-bis((2-(N-anilinylthiocarbonyl)pyrrolidin-1-yl)methyl)pyridine and $H_2BA^{Pr}TPP$ = 2,6-bis((2-(N-isopropylaminothiocarbonyl)pyrrolidin-1-yl)methyl)pyridine) contain an

additional pyridyl N-donor in an axial position and both exhibit oxidation processes around $E_{1/2}$ = 0.84 V (*vs.* Fc^+/Fc). Oxidation gives a Ni^{III} species in a pentacoordinate S_2N_3 environment, which exhibits a rhombic EPR signal with high g-anisotropy consistent with a formal Ni^{III} centre.

$Ni^{tBu}L_S^{Py}$, containing a pendant pyridine donor,[89] possesses an oxidation process at $E_{1/2}$ = 0.05 V (*vs.* Fc^+/Fc) with an unusually large ΔE_p of 100 mV, [89] which is assigned to a structural rearrangement upon oxidation with the pyridine binding to the Ni centre, as previously observed by Shearer *et al.* in NiSOD metalloprotein maquettes.[62, 65]

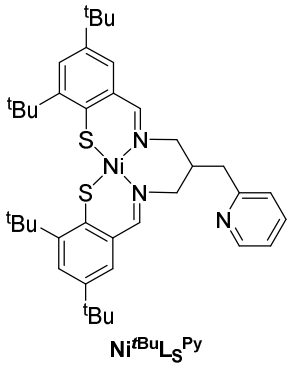


Figure 1.3.12: Nickel dithiophenolate complex with incorporated pendant bridge $Ni^{tBu}L_S^{Py}$ 89

The phenyl and pyridyl analogues, $Ni^{tBu}L_S^{Ph}$ and $Ni^{tBu}L_S^{Py2}$ (Figure 1.3.13), possess oxidation processes at more positive potentials and with a smaller peak separation (ΔE_p = 70 mV), suggesting that the pyridyl functionality stabilises the oxidation product for $Ni^{tBu}L_S^{Py}$ relative to those for $Ni^{tBu}L_S^{Ph}$ and $Ni^{tBu}L_S^{Py2}$. A proposed structural rearrangement that occurs on the oxidation of $Ni^{tBu}L_S^{Py}$ in which the pendant pyridyl ligand binds to the metal centre leads to an increased ΔE_p. This rearrangement does not occur for $Ni^{tBu}L_S^{Ph}$ and $Ni^{tBu}L_S^{Py2}$ and suggests that the pyridyl group in $Ni^{tBu}L_S^{Py2}$ is located further from the Ni centre than the equivalent group in $Ni^{tBu}L_S^{Py}$.

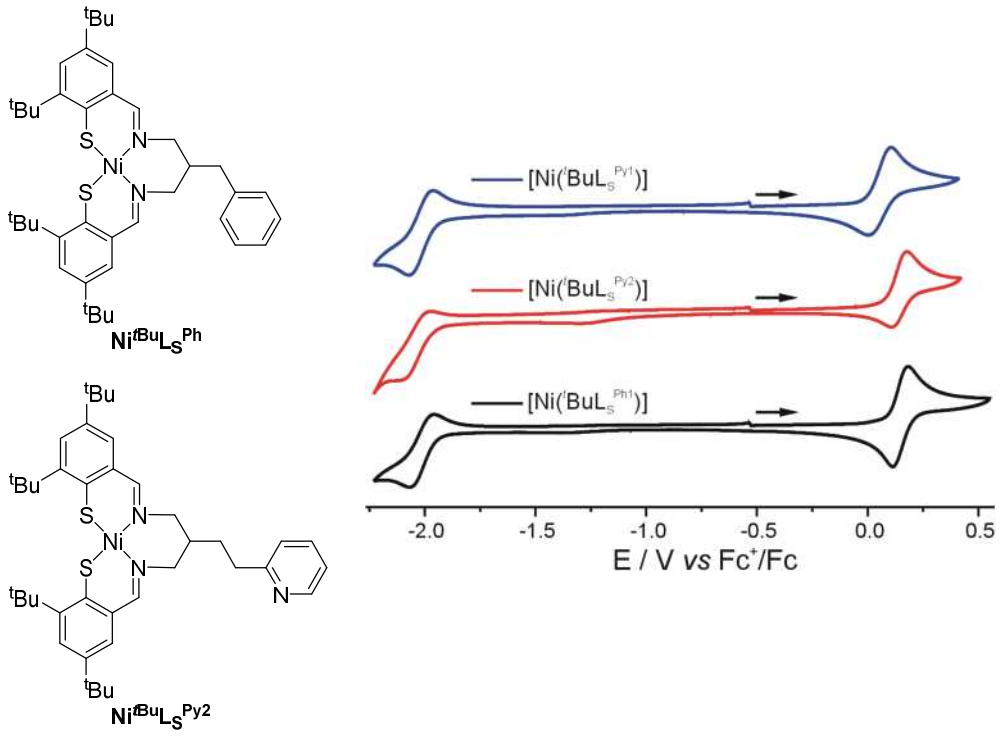


Figure 1.3.13: Left: Phenyl Ni^{tBu}L$_S$^{Ph} and extended pyridyl Ni^{tBu}L$_S$^{Py2} functionalised dithiophenolate complexes; Right: Comparison of cyclic voltammograms of Ni^{tBu}L$_S$^{Py} (top, blue), Ni^{tBu}L$_S$^{Py2}(centre, red) and Ni^{tBu}L$_S$^{Ph} (bottom, black).[89]

Further investigations of the oxidation products [Ni^{tBu}L$_S$^{Py}]$^{+}$ [Ni^{tBu}L$_S$^{Ph}]$^{+}$ and [Ni^{tBu}L$_S$^{Py2}]$^{+}$ have been carried out by EPR spectroscopy. The oxidation of the phenyl analogue Ni^{tBu}L$_S$^{Ph} to [Ni^{tBu}L$_S$^{Ph}]$^{+}$ results in a fluid EPR spectrum with a feature at g_{iso} = 2.072 and a linewidth of 16 G. The oxidised, extended pyridyl functionalised complex [Ni^{tBu}L$_S$^{Py2}]$^{+}$ exhibits very similar features (g_{iso} = 2.071 and 18 G), consistent with the pyridyl group remaining unbound upon the oxidation of Ni^{tBu}L$_S$^{Py2}. These EPR spectra are consistent with previously reported results[79] indicating predominantly ligand based oxidation for Ni^{tBu}L^{1} and Ni^{tBu}L^{2}.[79] In addition, frozen solutions of [Ni^{tBu}L$_S$^{Ph}]$^{+}$ and [Ni^{tBu}L$_S$^{Py2}]$^{+}$ are EPR silent suggesting the formation of sulfur bridged dimers upon cooling.[79] The addition of exogenous pyridine prior to the oxidation of Ni^{tBu}L$_S$^{Ph} results in an EPR spectrum exhibiting five lines, consistent with the spectra of Ni^{tBu}L$_1$ and Ni^{tBu}L$_2$ (see above) indicating the binding of two exogenous pyridine molecules.[71, 79] In contrast, the oxidised pyridyl analogue [Ni^{tBu}L$_S$^{Py}]$^{+}$ gives very different results, with a rhombic EPR spectrum in frozen solution (g_{11} = 2.282, g_{22} = 2.200 g_{33} = 2.016, a_{33} = 24.9 G) consistent with a metal centred SOMO and a well-defined three line ^{14}N

superhyperfine coupling in the g_{33} region. This is consistent with binding of a single N-donor in the axial position, resulting in an EPR spectrum similar to that observed for the oxidised form of NiSOD and suggesting the binding of the pendant pyridine donor in the axial position in $[Ni^{tBu}L_S^{Py}]^+$ (Figure 1.3.14).[89]

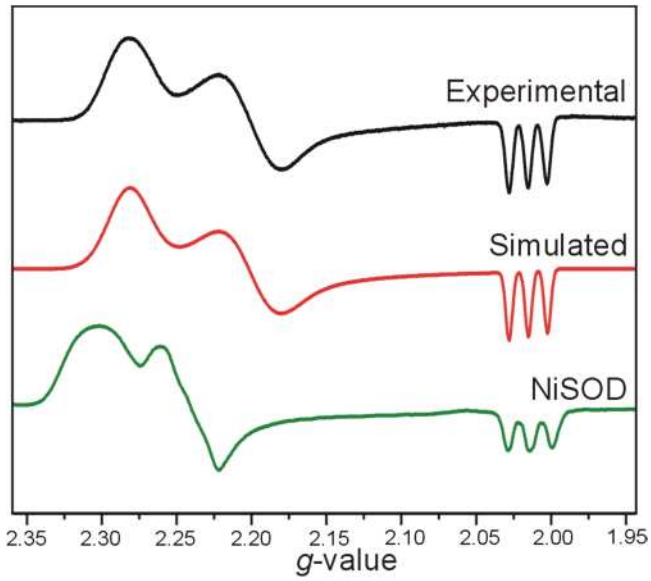


*Figure 1.3.14: X-band EPR spectrum at 77 K of **5** in frozen CH_2Cl_2 solution (black), simulation (red), spin Hamiltonian parameters g_{11} = 2.282, g_{22} = 2.200 g_{33} = 2.016, a_{33} = 24.9 G. X-band EPR spectrum at 77 K of native oxidised S. seoulensis NiSOD (green).*[89]

1.4 Galactose Oxidase

Galactose oxidase (GO) is an 68.5 kDa extracellular enzyme secreted by *Fusarium spp*.[90] which catalyses the two electron oxidation of primary alcohols to their corresponding aldehydes,[91, 92] together with the oxidation of aldehydes to carboxylic acids at a significantly slower rate.[93] The nature of the active site of GO has been determined crystallographically and contains a Cu centre ligated by two tyrosine and two histidine residues (Figure 1.4.1).[36, 94] GO is regioselective, and whilst it has been shown to oxidise a wide range of primary alcohols beyond its natural substrate of D-galactose, it does not oxidise secondary alcohols to ketones.[91, 95, 96]

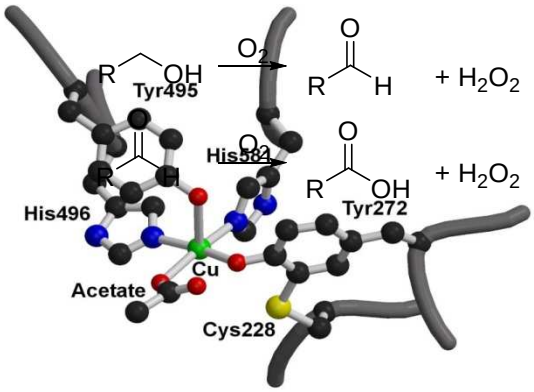


Figure 1.4.1: Left: Crystal structure of the active site of GO. Right: Reactions catalysed by GO.

The catalysis of a two electron reaction using only a $Cu^{II/I}$ redox active metal centre is supported by the redox chemistry associated with the phenolate motif of Tyr272, which has undergone a post translational modification in the ortho position resulting in a thioether linkage to Cys228.[94] In addition to increasing the rigidity of the active site, this modification has been shown to significantly shift the reduction potential of the post translationally modified tyrosine residue relative to tyrosine from 0.95 to 0.45 V (*vs.* NHE).[97] This modification occurs *via* a so called 'self-processing' reaction requiring only the apo-protein and dioxygen, and no other external enzymes or proteins.[98-100] The existence of this redox active cofactor in addition to the Cu centre is essential in order to facilitate the two electron oxidative chemistry catalysed by GO.[96, 101]

The catalytic cycle of GO has been widely studied and consists of distinct oxidation and reduction steps in a ping-pong mechanism.[91, 102] GO can exist in three well defined oxidation states: a Cu^{II}-tyrosyl radical oxidised species; an intermediate Cu^{II}-tyrosinate species; and a reduced Cu^{I}-tyrosine species. The $Cu^{II/I}$ and tyrosyl/tyrosinate redox couples have been estimated as -0.24 V and 0.01 V *vs.* Fc^{+}/Fc respectively.[97]

A proposed mechanism for the mode of action of GO is presented in Figure 1.4.2. The cycle involves the displacement of a water molecule by the substrate alcohol, which is deprotonated by the basic axial tyrosine residue. This is followed by the rate determining step of proton abstraction by the thioether-modified tyrosyl radical cofactor, with the radical species transferred to the substrate molecule. The key step then involves the release of the aldehyde, with the concomitant reduction of the Cu^{II} centre to Cu^{I}. Subsequent reoxidation to the resting Cu^{II} state, is then accompanied by the reduction of O_2 to H_2O_2.[91, 96, 103-105]

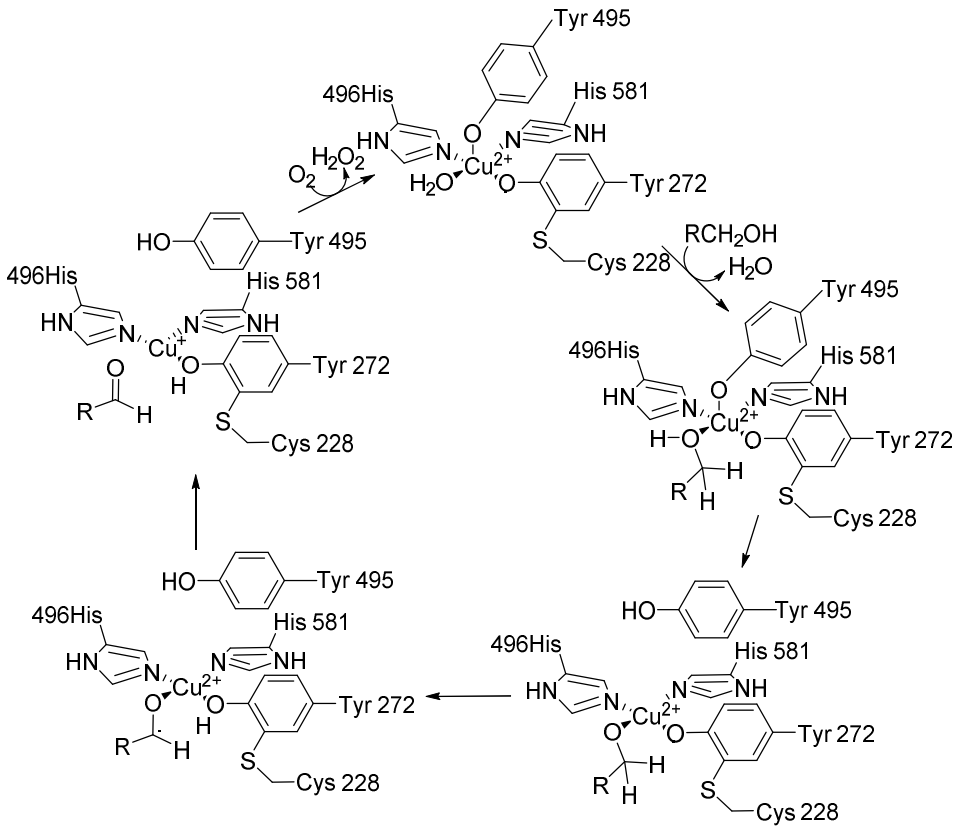


Figure 1.4.2: Proposed mechanism of GO.[91]

1.5 Synthetic Analogues of the Active Site of Galactose Oxidase

The unusual Cu^{II}-phenoxyl radical containing active site of GO has generated significant interest from bioinorganic chemists, and has driven the syntheses of a range of complexes containing metal centres coordinated by phenoxyl radical species.[96, 106-109] Herein we will discuss some of the more significant contributions to this extensive body of work which contain pro-phenoxyl radical ligation. Three categories of ligand set have been studied extensively: 1,4,7-triazacyclononane (TACN) based systems; tripodal ligands; and salen based ligands. In all of these cases the presence of bulky substituents in the ortho and para positions of the phenolate groups is important in order to limit radical decomposition by proton abstraction upon the formation and subsequent delocalisation of phenoxyl radicals.[110]

1.5.1 1,4,7-Triazacyclononane (TACN) Based Models of GO

The nine-membered TACN macrocycle can bind to a single metal ion through its three amine groups. Additional groups pendant to the ring, such as phenols and pyridines, can bind to the metal centre to give coordination numbers of four, five or six; a number of mono and bis-phenolate TACN complexes have been prepared.[111-114] The monophenolate Cu^{II} TACN complex Cu(1 - (3, 5 - di^{t}butyl – 2 – hydroxylbenzyl) - 4, 7 – diisopropyl - 1, 4, 7 - triazacyclononane)(Cl) (Figure 1.5.1.1) exhibits an EPR signal consistent with a Cu^{II} d^9 centre, a UV/Vis transition at 526 nm (ε = 1200 M^{-1} cm^{-1}), which is assigned to a phenolate to Cu^{II} LMCT, and an electrochemically reversible oxidation process at 0.31 V (*vs.* Fc^+/Fc) assigned to the phenoxyl radical/phenolate redox couple.[111, 114]

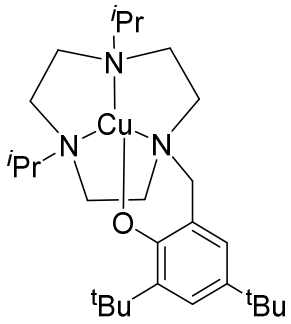


Figure 1.5.1.1 Cu(Cl)(1 - (3, 5 - di^{t}butyl – 2 - hydroxybenzyl) - 4, 7 – diisopropyl - 1, 4, 7 - triazacyclononane) [111, 114]

TACN systems containing two or three pendant phenolate units have also been developed for incorporation into models for the active site of GO (Figure 1.5.1.2).[112, 113] Cu^{II} complexes of such ligands including 1-ethyl-4,7-bis(3-*tert*-butyl-5-methoxy-2-hydroxybenzyl)-1,4,7-triazacyclononane (Figure 1.5.2 left), 1,4,7-tris(3,5-di-*tert*-butyl-2-hydroxy-benzyl)-1,4,7-triazacyclononane (Figure 1.5.2 right) or 1,4,7-tris(3-*tert*-butyl-5-methoxy-2-hydroxy-benzyl)-1,4,7-triazacyclononane (Figure 1.5.2 right) form pentacoordinate species with an additional uncoordinated phenol unit present in the latter two cases. These complexes typically possess two oxidation processes, with the single electron oxidised species being EPR silent, presumably due to magnetic coupling between a generated phenoxyl radical and the Cu^{II} centre resulting in a S= 0 or S = 1 ground state. This formulation is reinforced by UV/Vis and resonance Raman studies that show the presence of a Cu^{II}-phenoxyl radical species with similar spectroscopic properties to GO.[112, 113]

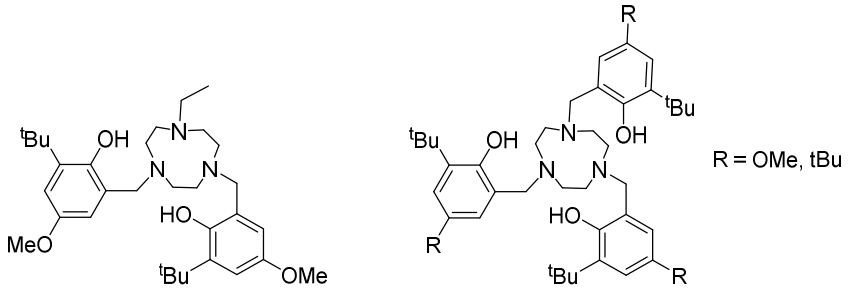


Figure 1.5.2: Examples of reported TACN complexes by Wieghardt[112, 113]

1.5.2 Tripodal bis(pyridyl) alkylamine Models of GO

Tripodal bis(pyridyl) alkylamine ligand frameworks incorporating one or two phenol units to provide N_3O_2 or N_2O_2 donor sets have been used in the development of analogues of the active site of GO.[115-128] A range of aromatic groups have been employed including substituted and unsubstituted pyridine, substituted phenol and imidazole units (Figure 1.5.2.1). Two main groups of tripodal ligands have been used as models for GO, N_2O_2 mono(pyridyl) alkylamines[115-119] with two phenol groups and N_3O bis(pyridyl) alkylamines[119, 123-129] bound to a single phenol unit.

The key requirements for the formation of mononuclear Cu^{II} complexes of N_3O ligands (Figure 1.5.2.1A-C) are substitution in the ortho position of the phenol with a sterically bulky group, and the presence of a base such as triethylamine.[126-128] X-ray crystallography has shown such complexes (Figure 1.5.2.1A-C) to be

pentacoordinate, with the coordination sphere completed by a solvent molecule.[119, 120, 126-130] These complexes typically have a structural parameter τ value of < 0.35, indicating a predominantly square based pyramidal geometry.[131] N_3O systems containing pyridine groups typically exhibit phenolate to Cu LMCT absorption bands around 400 nm and lower energy d-d transitions around 600 nm, together with rhombic EPR spectra that are typical of Cu^{II} d^9 monomeric systems.[126-128] Cu(2-hydroxy-3,5-di^{t}butylbenzyl)bis(2-pyridylmethyl)amine) (Figure 1.5.2.1A) exhibits such absorption bands at ~410 nm (ε ~ 8000 cm^{-1} dm^{-3} mol^{-1}) and ~ 550 nm (ε ~ 1000 cm^{-1} dm^{-3} mol^{-1}) while the related Cu(2-hydroxy-3,5-di^{t}butylbenzyl)bis(2-pyridylethyl)amine) complex (Figure 1.5.2.1B) exhibits similar absorptions at slightly lower energies at ~522 nm (ε ~ 6000 cm^{-1} dm^{-3} mol^{-1}). The introduction of pyridyl substituents such as in Cu(2-hydroxy-3,5-di^{t}butylbenzyl)bis(6-methyl-2-pyridylethyl)amine) (Figure 1.5.2.1C) results in a shift in the absorption bands to ~544 nm (ε ~ 800 cm^{-1} dm^{-3} mol^{-1}). In contrast to N_3O complexes, N_2O_2 systems form dimeric copper species, even in the presence of bulky phenolate ortho substituents,[120] and can only be isolated as monomers in the presence of coordinating solvents.[115, 116]

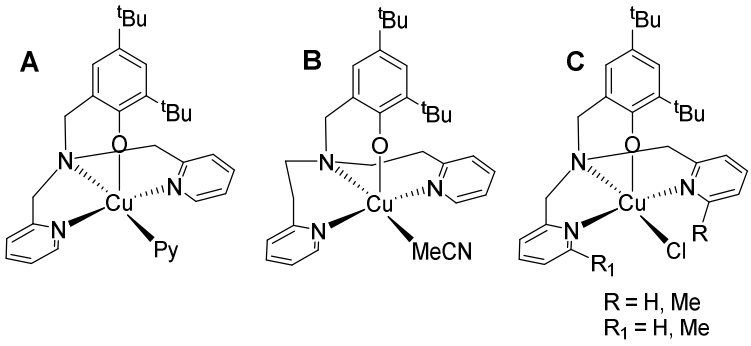


Figure 1.5.2.1:Mononuclear Cu^{II} phenolate complexes employing bis(pyridyl)alkylamine ligands reported by Philibert et al. (A)[126] Itoh et al. (B),[128] and Shimazaki et al. (C).[127]

In addition to introducing substituents on the pyridyl rings, the use of a tripodal ligand framework has facilitated the examination of the impact of substitution of the phenolate ring.[120, 125] Thioether[120, 125] and methoxy[120] substitutions stabilise the oxidised form of the complex in copper 2-(methylthio)-4-methyl-6-[[bis[2-(2-pyridyl)ethyl]amino]methyl]-phenolate[125] (Figure 1.5.2.2A) and Cu_2(N-(1 -methyl-2-imidazolyl methyl) -N- (2'-hydroxy-3',5'-di^{t}butylbenzyl) -N- (2''- hydroxy-3''-methoxy benzyl) amine)$_2$ $(ClO_2)_2$ (Figure 1.5.2.2B).[120] This is particularly relevant

to exploring the chemistry of GO given the post translational thioether modification observed at its active site.[94]

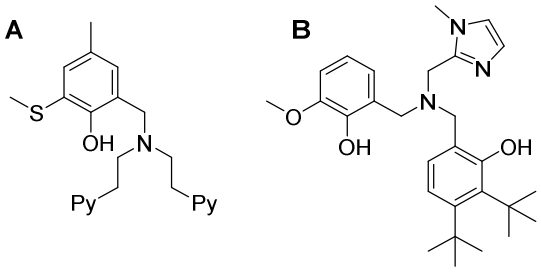


Figure 1.5.2.2: Ligands used in tripodal models of the active site of GO incorporating alternative phenolate substituents.

1.5.3 Analogues of GO Incorporating Salen-type Ligands

The chemistry of salen-based complexes is well developed.[132] The presence of bulky ortho and para substituents on the phenolate groups supports the formation of phenoxyl radicals bound to a metal centre.[110, 133] Salen ligands typically provide a N_2O_2 donor set in a square planar or distorted tetrahedral arrangement, with the nature of the different linking groups between the two nitrogen donors driving the degree of distortion between square planar and tetrahedral geometries, as determined by X-ray crystallography.[134-136]

The first salen-type ligand employed in the synthesis of analogues of the active site of galactose oxidase was the coper complex of an OH functionalised, unsubstituted phenolate, N,N'- (2-hydroxy-propane-l,3-diyl) bis(salicylaldiminato)copper(II) reported by Katajiama in 1986 (Figure 1.5.3.1 left).[137] Whilst reaction of this complex with alcohols showed no evidence for the formation of a phenoxyl radical, salen complexes of ligands incorporating additional phenolate ring substituents, $^{t\mathrm{Bu}\mathrm{R}}\mathrm{Lo}^{\mathrm{NAP2}}$ (R = S^{i}Pr, SPh, ^{t}Bu) (Figure 1.5.3.1 centre) were subsequently shown to exhibit two successive oxidation processes corresponding to the formation of phenoxyl and bis-phenoxyl species.[110, 133] The formation of these radical species has been probed using UV/Vis and NIR spectroscopies with characteristic bands observed for phenoxyl $\pi \rightarrow \pi^*$ transitions (400-450 and 600-700 nm; ε = 18,000 and 1,000 M^{-1} cm^{-1}, respectively) and phenolate-phenoxyl charge transfer was also observed by Stack *et al.* for the mono-phenoxyl species (Figure 1.5.3.1, centre).[138, 139] Further development of these systems by Thomas *et al.* gave the reduced amine forms $^{t\mathrm{Bu}}\mathrm{Lo}_{\mathrm{AM}}{}^{\mathrm{RR}}$ (Figure 1.5.5 right). $\mathrm{Cu}^{t\mathrm{Bu}}\mathrm{Lo}_{\mathrm{AM}}{}^{\mathrm{RR}}$ is much more readily oxidised

to the phenoxyl and bis-phenoxyl species than its imine based counterpart, exhibiting redox potentials *ca.* 0.5 V less positive.[140]

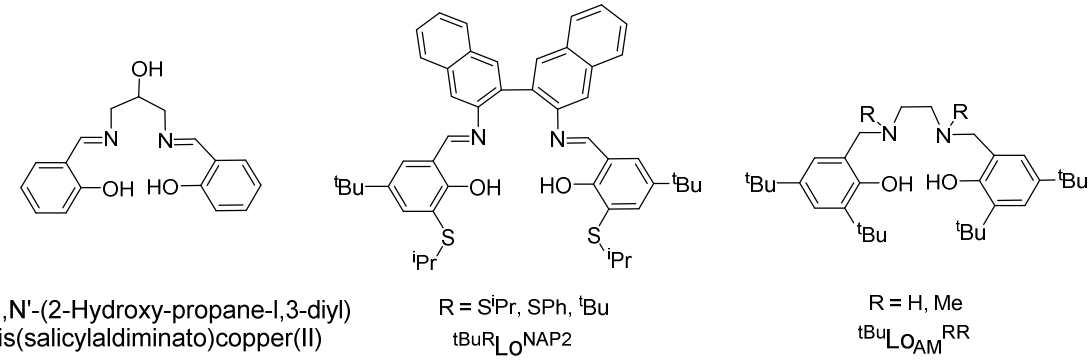


Figure 1.5.3.1: Salen type models for galactose oxidase reported by Katajiama (left),[137] Stack (centre)[110, 133] and Thomas (right).[140]

Stack *et al.* carried out mechanistic studies on Cu$^{t\mathrm{Bu}}$L$_{\mathrm{OAM}}$$^{\mathrm{ch}}$ and its imine analogue Cu$^{t\mathrm{Bu}}$L$_{\mathrm{O}}$$^{\mathrm{ch}}$ (Figure 1.5.7).[138, 139] Whilst the one electron oxidised forms of [Cu$^{t\mathrm{Bu}}$L$_{\mathrm{OAM}}$$^{\mathrm{ch}}$]$^{+}$ and [Cu$^{t\mathrm{Bu}}$L$_{\mathrm{O}}$$^{\mathrm{ch}}$]$^{+}$ demonstrated reactivity towards the oxidation of benzyl alcohol, the amine complex [Cu$^{t\mathrm{Bu}}$L$_{\mathrm{OAM}}$$^{\mathrm{ch}}$]$^{+}$ showed a much faster rate of reaction than its imine counterpart [Cu$^{t\mathrm{Bu}}$L$_{\mathrm{O}}$$^{\mathrm{ch}}$]$^{+}$, despite being a poorer oxidant. This is attributed to [Cu$^{t\mathrm{Bu}}$L$_{\mathrm{O}}$$^{\mathrm{ch}}$]$^{+}$ undergoing a simple bimolecular reaction, whilst [Cu$^{t\mathrm{Bu}}$L$_{\mathrm{OAM}}$$^{\mathrm{ch}}$]$^{+}$ undergoes substrate binding prior to the key reaction step in a manner more akin to that seen in the native GO enzyme.

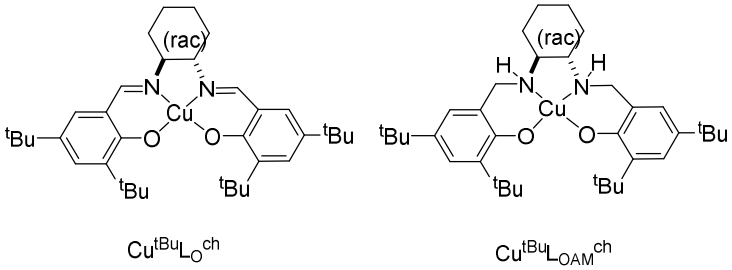


Figure 1.5.7: Imine and reduced amine complexes directly compared by Stack et al.[138, 139]

Further synthetic developments in salen based model complexes followed a report by Campbell and Nguyen describing the syntheses of unsymmetrical mixed diphenolate complexes *via* the synthesis of the hydrochloride salt of cyclohexane-1,2-diamine as a protection strategy, allowing the sequential reaction with two different salicyaldehydes.[141] This approach has permitted the unsymmetric introduction of thioether substituents using two different phenolate groups as a model for the post translational thioether modification observed at the active site of

GO (Figure 1.5.9).[142] Electrochemical studies of $Cu^{tBuR1tBuR2}L_{OAM}{}^{ch}$ (R1 = ^{t}Bu, OMe, S^{i}Pr; R2 = ^{t}Bu OMe, S^{i}PR) (Figure 1.5.9) demonstrated a thermodynamic preference for the oxidation of phenolates with electron donating substituents, with the first redox potential of an OMe- substituted phenolate shown to be relatively independent of the nature of the second phenolate group.[142]

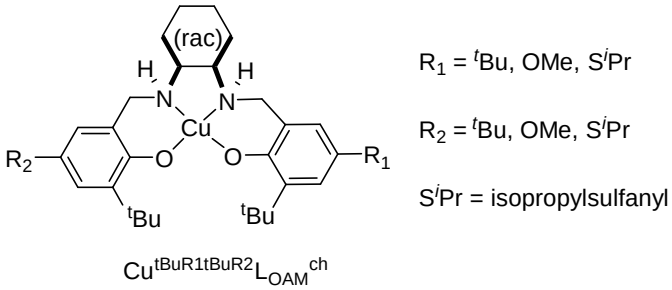


Figure 1.5.9 : Unsymmetrical models reported by Stack et al. [142]

Recent work within the McMaster group on analogues of the active site of GO has focussed on a salen type system which incorporate an additional nitrogen donor in the linker group, providing a N_3O_2 coordination sphere in a pentacoordinate, distorted trigonal bipyramidal arrangement (Figure 1.5.8).[84]

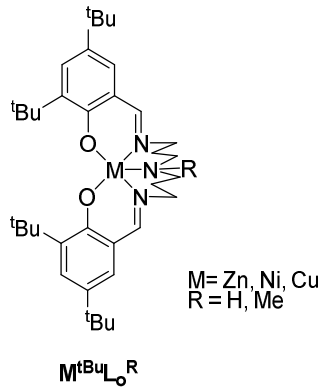


Figure 1.5.8: Pentacoordinate Schiff base complexes reported by McMaster et al. with N_3O_2 donor set. [84]

The complexes $M^{tBu}L_o{}^R$ (M = Zn, Ni, Cu; R = NMe, NH) are comprised of two phenol, two imine and one amine donors and have been characterised crystallographically. EPR spectroscopic studies have confirmed that this coordination sphere is maintained in solution. Electrochemical studies have shown two reversible oxidation processes for $M^{tBu}L_o{}^R$ (M = Zn, Cu; R = NMe, NH) that are associated with the sequential formation of mono and bis-phenoxyl species, whilst

the presence of the additional N donor allows a metal based first oxidation process to occur for the Ni$^{t\text{Bu}}$L$_o^{R}$ (R = NMe, NH) analogues.[84]

1.6 Aims

In this work, a series of Ni^{II}, Cu^{II} and Zn^{II} diphenolate and dithiophenolate complexes are described that significantly extend the range of redox active salen-type complexes. These complexes may find use as new redox active catalysts for oxidation reactions and/or provide further insight into the interplay of the metal centres and their immediate coordination environments at the active sites of NiSOD and GO (Figure 1.6.1).

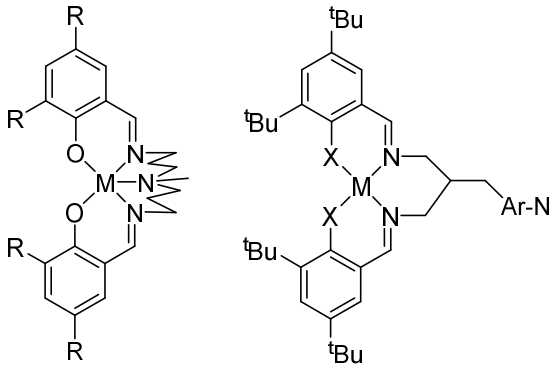


Figure 1.6.1: Schematic representation of the complexes examined in this thesis where: M = Zn, Ni, Cu; R = Halogen, substituted aromatic group; X = O, S; Ar-N = aromatic group containing a nitrogen donor (pyridine, imidazole) atom.

The research described in this thesis significantly extends previous work within the group on redox-active pentacoordinate Schiff base diphenolate complexes $M^{tBu}L_O^R$ (M = Zn, Ni, Cu; R = NMe, NH) (Section 1.5).[84] The development of a versatile synthetic methodology provides a route to a range of functionalised salicyaldehydes that allow access to a wide range of Ni^{II}, Cu^{II} and Zn^{II} complexes. Our studies allow for a comprehensive assessment of how the geometric and electronic structure of these complexes vary with the nature of the phenolate ligand substituents, and provide insights into the effects of substitution in the ortho *vs.* para positions of the diphenolate rings on these properties. This chemistry has particular relevance to the chemistry of active site of GO.

Our examination of $Ni^{tBu}L_S^{Py}$ [89] by advanced pulsed ESEEM and HYSCORE EPR spectroscopic techniques, supported by DFT calculations, provides further insight into the electronic structure of the Ni-centre at the active site of NiSOD. This centre possesses a N_2S_2/N_3S_2 coordination sphere, both of which are closely replicated by

the $^{tBu}L_S^{Py}$ ligand. We also examine Ni^{II} diphenolate metal complexes incorporating similar pendant pyridine N-donors to that employed in $Ni^{tBu}L_S^{Py}$ in order to investigate the relative effects of phenolate *vs*. thiophenolate coordination on the electronic properties of the Ni centre. We also attempt to vary the nature of the N-donor pendant to the salen-type ligand backbone to probe the role of this N-donor in controlling the chemistry of potentially pentacoordinate diphenolate and dithiophenolate species.

The research described provides some insight into the interplay between the coordination sphere and the nature of the redox chemistry exhibited by diphenolate and dithiophenolate coordination complexes.

References

1. R. J. P. Williams, *Coord. Chem. Rev.*, 1990, **100**, 573-610.
2. C. F. G. C. Geraldes and S. Laurent, *Contrast Media. Mol. I.*, 2009, **4**, 1-23.
3. Z. Guo and P. J. Sadler, *Angew. Chem. Int. Ed.*, 1999, **38**, 1512-1531.
4. W. Kaim, B. Schwederski and A. Klein, *Bioinorganic Chemistry: Inorganic Elements in the Chemistry of Life*, Wiley, Chichester, West Sussex, UK, 2nd Edition edn., 2013.
5. S. Mann, in *Biological Inorganic Chemistry*, Eds. I. Bertini, H. Gray, E. Stiefel and J. Valentine, University Science Books, Sausalito, California, 2007, ch. VI, pp. 79-94.
6. D. C. Hodgkin, J. Kamper, M. Mackay, J. Pickworth, K. N. Trueblood and J. G. White, *Nature*, 1956, **178**, 64-66.
7. J. A. Lemire, J. J. Harrison and R. J. Turner, *Nat Rev Micro*, 2013, **11**, 371-384.
8. Z. H. Chohan, A. Munawar and C. T. Supuran, *Metal-Based Drugs*, 2001, **8**, 137-143.
9. B. Rosenberg, L. Vancamp, J. E. Trosko and V. H. Mansour, *Nature*, 1969, **222**, 385-386.
10. A. D. Richards and A. Rodger, *Chem. Soc. Rev.*, 2007, **36**, 471-483.
11. W. F. Kean, L. Hart and W. W. Buchanan, *Br. J. Rheumatol.*, 1997, **36**, 560-572.
12. C. D. Garner, *J. Chem. Soc., Dalton Trans.*, 1997, 3903-3908.
13. J. R. Morrow, *Inorg. Chem.*, 2015, **54**, 11039-11042.
14. A. J. Thomson and H. B. Gray, *Curr. Opin. Chem. Biol.*, 1998, **2**, 155-158.
15. M. H. Lim and Y. Lu, *Curr. Opin. Chem. Biol.*, 2015, **25**, vii-viii.
16. C. Tard and C. J. Pickett, *Chem. Rev.*, 2009, **109**, 2245-2274.
17. S. P. J. Albracht, E. G. Graf and R. K. Thauer, *FEBS Lett.*, 1982, **140**, 311-313.
18. P. A. Karplus, M. A. Pearson and R. P. Hausinger, *Acc. Chem. Res.*, 1997, **30**, 330-337.
19. E. Mulliez and M. Fontecave, *Coord. Chem. Rev.*, 1999, **185–186**, 775-793.
20. C. E. Valdez, Q. A. Smith, M. R. Nechay and A. N. Alexandrova, *Acc. Chem. Res.*, 2014, **47**, 3110-3117.
21. C. J. Reedy and B. R. Gibney, *Chem. Rev.*, 2004, **104**, 617-650.
22. C. Enroth, B. T. Eger, K. Okamoto, T. Nishino, T. Nishino and E. F. Pai, *P. Nat. Acad. Sci. USA*, 2000, **97**, 10723-10728.
23. D. Ferro, N. Franchi, V. Mangano, R. Bakiu, M. Cammarata, N. Parrinello, G. Santovito and L. Ballarin, *Aquat. Toxicol.*, 2013, **140–141**, 369-379.
24. D. R. Rosen, T. Siddique, D. Patterson, D. A. Figlewicz, P. Sapp, A. Hentati, D. Donaldson, J. Goto, J. P. O'Regan, H.-X. Deng, Z. Rahmani, A. Krizus, D. McKenna-Yasek, A. Cayabyab, S. M. Gaston, R. Berger, R. E. Tanzi, J. J. Halperin, B. Herzfeldt, R. Van den Bergh, W.-Y. Hung, T. Bird, G. Deng, D. W. Mulder, C. Smyth, N. G. Laing, E. Soriano, M. A. Pericak-Vance, J. Haines, G. A. Rouleau, J. S. Gusella, H. R. Horvitz and R. H. Brown, *Nature*, 1993, **362**, 59-62.
25. Y. Abe, G. Ishikawa, H. Satoh, K. Azumi and H. Yokosawa, *Comp. Biochem. Physio. B*, 1999, **122**, 321-326.
26. J. Richardson, K. A. Thomas, B. H. Rubin and D. C. Richardson, *P. Nat. Acad. Sci. USA*, 1975, **72**, 1349-1353.
27. G. E. O. Borgstahl, H. E. Parge, M. J. Hickey, W. F. Beyer, Jr., R. A. Hallewell and J. A. Tainer, *Cell*, **71**, 107-118.
28. W. C. Stallings, T. B. Powers, K. A. Pattridge, J. A. Fee and M. L. Ludwig, *P. Nat. Acad. Sci. USA*, 1983, **80**, 3884-3888.

29. D. Ringe, G. A. Petsko, F. Yamakura, K. Suzuki and D. Ohmori, *P. Nat. Acad. Sci. USA*, 1983, **80**, 3879-3883.
30. H.-D. Youn, E.-J. Kim, J.-H. Roe, Y. C. Hah and S.-O. Kang, *Biochem. J*, 1996, **318**, 889-896.
31. H.-D. Youn, H. Youn, J.-W. Lee, Y.-I. Yim, J. K. Lee, Y. C. Hah and S.-O. Kang, *Arch. Biochem. Biophys.*, 1996, **334**, 341-348.
32. B. Palenik, B. Brahamsha, F. W. Larimer, M. Land, L. Hauser, P. Chain, J. Lamerdin, W. Regala, E. E. Allen, J. McCarren, I. Paulsen, A. Dufresne, F. Partensky, E. A. Webb and J. Waterbury, *Nature*, 2003, **424**, 1037-1042.
33. D. P. Barondeau, C. J. Kassmann, C. K. Bruns, J. A. Tainer and E. D. Getzoff, *Biochem.*, 2004, **43**, 8038-8047.
34. J. Wuerges, J.-W. Lee, Y.-I. Yim, H.-S. Yim, S.-O. Kang and K. D. Carugo, *P. Nat. Acad. Sci. USA*, 2004, **101**, 8569-8574.
35. A. J. Baron, C. Stevens, C. Wilmot, K. D. Seneviratne, V. Blakeley, D. M. Dooley, S. E. Phillips, P. F. Knowles and M. J. McPherson, *J. Biolo. Chem.*, 1994, **269**, 25095-25105.
36. N. Ito, S. E. V. Phillips, K. D. S. Yadav and P. F. Knowles, *J. Mol. Biol.*, 1994, **238**, 704-814.
37. R. Noor, S. Mittal and J. Iqbal, *Med. Sci. Monit.*, 2002, **8**, Ra210-215.
38. H. R. Warner, *Free Radical Biol. Med.*, 1994, **17**, 249-258.
39. W.Z. Lee, G.J. Lee, H.M, Hsieh, C.W. Chiang, B. Huang, Y.S. Fu, Y.M. Wang, US201514605968, 2015.
40. H. X. Deng, A. Hentati, J. A. Tainer, Z. Iqbal, A. Cayabyab, W. Y. Hung, E. D. Getzoff, P. Hu, B. Herzfeldt, and R. P. Roos, *Science*, 1993, **261**, 1047-1051.
41. S. Bostantjopoulou, G. Kyriazis, Z. Katsarou, G. Kiosseoglou, A. Kazis and G. Mentenopoulos, *Funct. Neurol.*, 1997, **12**, 63-68.
42. F. P. Zemlan, O. J. Thienhaus and H. B. Bosmann, *Brain Res.*, 1989, **476**, 160-162.
43. M. Marikovsky, V. Ziv, N. Nevo, C. Harris-Cerruti and O. Mahler, *J. Immunol.*, 2003, **170**, 2993-3001.
44. T. J. Guzik, R. Korbut and T. Adamek-Guzik, *J Physiol. Pharmacol.*, 2003, **54**, 469-487.
45. J. D. Piganelli, S. C. Flores, C. Cruz, J. Koepp, I. Batinic-Haberle, J. Crapo, B. Day, R. Kachadourian, R. Young, B. Bradley and K. Haskins, *Diabetes*, 2002, **51**, 347-355.
46. L. Padgett, A. Burg, W. Lei and H. Tse, *J. Immunol.*, 2014, **192**, 176.176-176.176.
47. C. Massilamany, A. Gangaplara, H. Kim, C. Stanford, G. Rathnaiah, D. Steffen, J. Lee and J. Reddy, *J. Neuroimmunol.*, 2013, **256**, 19-27.
48. L. Kruidenier, I. Kuiper, W. van Duijn, S. L. Marklund, R. A. van Hogezand, C. B. Lamers and H. W. Verspaget, *J. Pathol.*, 2003, **201**, 7-16.
49. A. D. Millar, D. S. Rampton, C. L. Chander, A. W. Claxson, S. Blades, A. Coumbe, J. Panetta, C. J. Morris and D. R. Blake, *Gut*, 1996, **39**, 407-415.
50. Y. Sheng, I. A. Abreu, D. E. Cabelli, M. J. Maroney, A.-F. Miller, M. Teixeira and J. S. Valentine, *Chem. Rev.*, 2014, **114**, 3854-3918.
51. A. T. Fiedler, P. A. Bryngelson, M. J. Maroney and T. C. Brunold, *J. Am. Chem. Soc.*, 2005, **127**, 5449-5462.
52. K. C. Ryan, A. I. Guce, O. E. Johnson, T. C. Brunold, D. E. Cabelli, S. C. Garman and M. J. Maroney, *Biochem.*, 2015, **54**, 1016-1027.
53. S. B. Choudhury, J.-W. Lee, G. Davidson, Y.-I. Yim, K. Bose, M. L. Sharma, S.-O. Kang, D. E. Cabelli and M. J. Maroney, *Biochem.*, 1999, **38**, 3744-3752.
54. H.-I. Lee, J.-W. Lee, T.-C. Yang, S.-O. Kang and B. Hoffman, *J. Biolo. Inorg. Chem.*, 2010, **15**, 175-182.

55. K. Ryan, O. Johnson, D. Cabelli, T. Brunold and M. Maroney, *J. Biolo. Inorg. Chem.*, 2010, **15**, 795-807.
56. V. Pelmenschikov and P. E. M. Siegbahn, *J. Am. Chem. Soc.*, 2006, **128**, 7466-7475.
57. R. Prabhakar, K. Morokuma and D. G. Musaev, *J. Comput. Chem.*, 2006, **27**, 1438-1445.
58. I. A. Abreu and D. E. Cabelli, *B.B.A.- Proteins and Proteom.,* 2010, **1804**, 263-274.
59. D. P. Barondeau, C. J. Kassmann, C. K. Bruns, J. A. Tainer and E. D. Getzoff, *Biochem.*, 2004, **43**, 8038-8047.
60. E. P. Broering, P. T. Truong, E. M. Gale and T. C. Harrop, *Biochem.*, 2012, **52**, 4-18.
61. C. L. Dupont, K. Neupane, J. Shearer and B. Palenik, *Environ. Microbiol.*, 2008, **10**, 1831-1843.
62. J. Shearer and L. M. Long, *Inorg. Chem.*, 2006, **45**, 2358-2360.
63. J. Shearer, *Acc. Chem. Res.*, 2014, **47**, 2332-2341.
64. J. Shearer, K. L. Peck, J. C. Schmitt and K. P. Neupane, *J. Am. Chem. Soc.*, 2014, **136**, 16009-16022.
65. K. P. Neupane, K. Gearty, A. Francis and J. Shearer, *J. Am. Chem. Soc.*, 2007, **129**, 14605-14618.
66. J. O. Campeciño, L. W. Dudycz, D. Tumelty, V. Berg, D. E. Cabelli and M. J. Maroney, *J. Am. Chem. Soc.*, 2015, **137**, 9044-9052.
67. M. E. Krause, A. M. Glass, T. A. Jackson and J. S. Laurence, *Inorg. Chem.*, 2010, **49**, 362-364.
68. D. Tietze, M. Tischler, S. Voigt, D. Imhof, O. Ohlenschläger, M. Görlach and G. Buntkowsky, *Chem. Eur. J.*, 2010, **16**, 7572-7578.
69. H. J. Kruger and R. H. Holm, *J. Am. Chem. Soc.*, 1990, **112**, 2955-2963.
70. H. J. Kruger, G. Peng and R. H. Holm, *Inorg. Chem.*, 1991, **30**, 734-742.
71. H. J. Krueger and R. H. Holm, *Inorg. Chem.*, 1987, **26**, 3645-3647.
72. D. Nakane, S.-i. Kuwasako, M. Tsuge, M. Kubo, Y. Funahashi, T. Ozawa, T. Ogura and H. Masuda, *Chem. Commun.*, 2010, **46**, 2142-2144.
73. K. P. Neupane and J. Shearer, *Inorg. Chem.*, 2006, **45**, 10552-10566.
74. C. S. Mullins, C. A. Grapperhaus and P. M. Kozlowski, *J. Biolo. Inorg. Chem.*, 2006, **11**, 617-625.
75. J. Shearer and N. Zhao, *Inorg. Chem.*, 2006, **45**, 9637-9639.
76. J. Shearer, A. Dehestani and F. Abanda, *Inorg. Chem.*, 2008, **47**, 2649-2660.
77. J. Hanss and H.-J. Krüger, *Angew. Chem. Int. Ed.*, 1998, **37**, 360-363.
78. M. Gennari, M. Orio, J. Pécaut, F. Neese, M.-N. Collomb and C. Duboc, *Inorg. Chem.*, 2010, **49**, 6399-6401.
79. P. A. Stenson, A. Board, A. Marin-Becerra, A. J. Blake, E. S. Davies, C. Wilson, J. McMaster and M. Schröder, *Chem. Eur. J.*, 2008, **14**, 2564-2576.
80. D. Nakane, Y. Wasada-Tsutsui, Y. Funahashi, T. Hatanaka, T. Ozawa and H. Masuda, *Inorg. Chem.*, 2014, **53**, 6512-6523.
81. O. Rotthaus, F. Thomas, O. Jarjayes, C. Philouze, E. Saint-Aman and J.-L. Pierre, *Chem. Eur. J.*, 2006, **12**, 6953-6962.
82. J. Hioe and H. Zipse, *Org. Biomol. Chem.*, 2010, **8**, 3609-3617.
83. M. T. Kieber-Emmons, J. Annaraj, M. S. Seo, K. M. Van Heuvelen, T. Tosha, T. Kitagawa, T. C. Brunold, W. Nam and C. G. Riordan, *J. Am. Chem. Soc.*, 2006, **128**, 14230-14231.
84. M. Franks, A. Gadzhieva, L. Ghandhi, D. Murrell, A. J. Blake, E. S. Davies, W. Lewis, F. Moro, J. McMaster and M. Schröder, *Inorg. Chem.*, 2013, **52**, 660-670.
85. W.-Z. Lee, C.-W. Chiang, T.-H. Lin and T.-S. Kuo, *Chem. Eur. J.*, 2012, **18**, 50-53.

86. E. M. Gale, A. C. Simmonett, J. Telser, H. F. Schaefer and T. C. Harrop, *Inorg. Chem.*, 2011, **50**, 9216-9218.
87. E. P. Broering, S. Dillon, E. M. Gale, R. A. Steiner, J. Telser, T. C. Brunold and T. C. Harrop, *Inorg. Chem.*, 2015, **54**, 3815-3828.
88. C.-W. Chiang, Y.-L. Chu, H.-L. Chen, T.-S. Kuo and W.-Z. Lee, *Chem. Eur. J.*, 2014, **20**, 6283-6286.
89. M. Franks, PhD, The University of Nottingham, 2011.
90. Z. B. Ögel, D. Brayford and M. J. McPherson, *Mycol. Res.*, 1994, **98**, 474-480.
91. J. W. Whittaker, *Chem. Rev.*, 2003, **103**, 2347-2364.
92. G. Avigad, D. Amaral, C. Asensio and B. L. Horecker, *J. Biol. Chem.*, 1962, **237**, 2736-2743.
93. F. M. Kelleher and V. P. Bhavanandan, *J. Biol. Chem.*, 1986, **261**, 11045-11048.
94. N. Ito, S. E. V. Phillips, C. Stevens, Z. B. Ogel, M. J. McPherson, J. N. Keen, K. D. S. Yadav and P. F. Knowles, *Nature*, 1991, **350**, 87-90.
95. C. D. Borman, C. G. Saysell, A. Sokolowski, M. B. Twitchett, C. Wright and A. G. Sykes, *Coord. Chem. Rev.*, 1999, **190–192**, 771-779.
96. B. A. Jazdzewski and W. B. Tolman, *Coord. Chem. Rev.*, 2000, **200–202**, 633-685.
97. C. Wright and A. G. Sykes, *J. Inorg. Biochem.*, 2001, **85**, 237-243.
98. M. S. Rogers, A. J. Baron, M. J. McPherson, P. F. Knowles and D. M. Dooley, *J. Am. Chem. Soc.*, 2000, **122**, 990-991.
99. M. M. Whittaker and J. W. Whittaker, *J. Biol. Chem.*, 2003, **278**, 22090-22101.
100. S. J. Firbank, M. S. Rogers, C. M. Wilmot, D. M. Dooley, M. A. Halcrow, P. F. Knowles, M. J. McPherson and S. E. V. Phillips, *Proc. Nat. Acad. Sci. USA*, 2001, **98**, 12932-12937.
101. A. K. Nairn, S. J. Archibald, R. Bhalla, B. C. Gilbert, E. J. MacLean, S. J. Teat and P. H. Walton, *Dalton Trans.*, 2006, DOI: 10.1039/B512296C, 172-176.
102. M. M. Whittaker and J. W. Whittaker, *J. Biol. Chem.*, 1988, **263**, 6074-6080.
103. H.-J. Krüger, *Angew. Chem. Int. Ed.*, 1999, **38**, 627-631.
104. E. Zueva, P. H. Walton and J. E. McGrady, *Dalton Trans.*, 2006, 159-167.
105. Y. Lee and K. D. Karlin, in *Concepts and Models in Bioinorganic Chemistry*, Eds. H. Kraatz and N. Metzler-Nolte, Wiley-VCH, Weinheim, 1st edn., 2006, ch. 16, pp. 363-396.
106. F. Thomas, *Eur. J. Inorg. Chem.*, 2007, **2007**, 2379-2404.
107. C. T. Lyons and T. D. P. Stack, *Coord. Chem. Rev.*, 2013, **257**, 528-540.
108. S. Itoh, M. Taki and S. Fukuzumi, *Coord. Chem. Rev.*, 2000, **198**, 3-20.
109. V. Mahadevan, R. J. M. K. Gebbink and T. D. P. Stack, *Curr. Opin. Chem. Biol.*, 2000, **4**, 228-234.
110. Y. Wang and T. D. P. Stack, *J. Am. Chem. Soc.*, 1996, **118**, 13097-13098.
111. J. A. Halfen, B. A. Jazdzewski, S. Mahapatra, L. M. Berreau, E. C. Wilkinson, L. Que and W. B. Tolman, *J. Am. Chem. Soc.*, 1997, **119**, 8217-8227.
112. A. Sokolowski, H. Leutbecher, T. Weyhermüller, R. Schnepf, E. Bothe, E. Bill, P. Hildebrandt and K. Wieghardt, *J. Biolo. Inorg. Chem.*, 1997, **2**, 444-453.
113. E. Bill, J. Müller, T. Weyhermüller and K. Wieghardt, *Inorg. Chem.*, 1999, **38**, 5795-5802.
114. J. A. Halfen, V. G. Young and W. B. Tolman, *Angew. Chem. Int. Ed.*, 1996, **35**, 1687-1690.
115. F. Thomas, G. Gellon, I. Gautier-Luneau, E. Saint-Aman and J.-L. Pierre, *Angew. Chem. Int. Ed.*, 2002, **41**, 3047-3050.
116. D. Zurita, I. Gautier-Luneau, S. Ménage, J. L. Pierre and E. Saint-Aman, *J. Biolo. Inorg. Chem.*, **2**, 46-55.

117. Y. Shimazaki, S. Huth, A. Odani and O. Yamauchi, *Angew. Chem. Int. Ed.*, 2000, **39**, 1666-1669.
118. M. Taki, H. Kumei, S. Nagatomo, T. Kitagawa, S. Itoh and S. Fukuzumi, *Inorg. Chim. Acta*, 2000, **300–302**, 622-632.
119. H. Adams, N. A. Bailey, I. K. Campbell, D. E. Fenton and Q.-Y. He, *J. Chem. Soc., Dalton Trans.*, 1996, 2233-2237.
120. Y. Shimazaki, S. Huth, S. Hirota and O. Yamauchi, *Inorg. Chim. Acta*, 2002, **331**, 168-177.
121. D. Zurita, C. Scheer, J.-L. Pierre and E. Saint-Aman, *J. Chem. Soc., Dalton Trans.*, 1996, 4331-4336.
122. F. Michel, F. Thomas, S. Hamman, E. Saint-Aman, C. Bucher and J.-L. Pierre, *Chem. Eur. J.*, 2004, **10**, 4115-4125.
123. F. Michel, S. Torelli, F. Thomas, C. Duboc, C. Philouze, C. Belle, S. Hamman, E. Saint-Aman and J.-L. Pierre, *Angew. Chem. Int. Ed.*, 2005, **44**, 438-441.
124. M. Taki, H. Hattori, T. Osako, S. Nagatomo, M. Shiro, T. Kitagawa and S. Itoh, *Inorg. Chim. Acta*, 2004, **357**, 3369-3381.
125. S. Itoh, S. Takayama, R. Arakawa, A. Furuta, M. Komatsu, A. Ishida, S. Takamuku and S. Fukuzumi, *Inorg. Chem.*, 1997, **36**, 1407-1416.
126. A. Philibert, F. Thomas, C. Philouze, S. Hamman, E. Saint-Aman and J.-L. Pierre, *Chem. Eur. J.*, 2003, **9**, 3803-3812.
127. Y. Shimazaki, S. Huth, S. Hirota and O. Yamauchi, *Bull. Chem. Soc. Jpn.*, 2000, **73**, 1187-1195.
128. S. Itoh, M. Taki, H. Kumei, S. Takayama, S. Nagatomo, T. Kitagawa, N. Sakurada, R. Arakawa and S. Fukuzumi, *Inorg. Chem.*, 2000, **39**, 3708-3711.
129. M. Vaidyanathan, R. Viswanathan, M. Palaniandavar, T. Balasubramanian, P. Prabhaharan and P. Muthiah, *Inorg. Chem.*, 1998, **37**, 6418-6427.
130. F. Michel, S. Hamman, F. Thomas, C. Philouze, I. Gautier-Luneau and J.-L. Pierre, *Chem. Commun.*, 2006, 4122-4124.
131. A. W. Addison, T. N. Rao, J. Reedijk, J. van Rijn and G. C. Verschoor, *J. Chem. Soc. Dalton Trans.*, 1984, **0**, 1349-1356.
132. T. Tsumaki, *Bull. Chem. Soc. Jpn.*, 1938, **13**, 252-260.
133. Y. Wang, J. L. DuBois, B. Hedman, K. O. Hodgson and T. D. P. Stack, *Science*, 1998, **279**, 537-540.
134. H. H. Yao, J. M. Lo, B. H. Chen and T. H. Lu, *Acta Crystallogr. C*, 1997, **53**, 1012-1013.
135. E. N. Baker, D. Hall and T. N. Waters, *J. Chem. Soc. A*, 1970, 400-405.
136. T. P. Cheeseman, D. Hall and T. N. Waters, *J. Chem. Soc. A*, 1966, 1396-1406.
137. N. Kitajima, K. Whang, Y. Moro-oka, A. Uchida and Y. Sasada, *J. Chem. Soc., Chem. Commun.*, 1986, **0**, 1504-1505.
138. R. C. Pratt and T. D. P. Stack, *Journal of the American Chemical Society*, 2003, **125**, 8716-8717.
139. R. C. Pratt and T. D. P. Stack, *Inorg. Chem.*, 2005, **44**, 2367-2375.
140. F. Thomas, O. Jarjayes, C. Duboc, C. Philouze, E. Saint-Aman and J.-L. Pierre, *Dalton Trans.*, 2004, **0**, 2662-2669.
141. E. J. Campbell and S. T. Nguyen, *Tetrahedron Lett.*, 2001, **42**, 1221-1225.
142. R. C. Pratt, C. T. Lyons, E. C. Wasinger and T. D. P. Stack, *J. Am. Chem. Soc.*, 2012, **134**, 7367-7377.

Chapter 2

The Syntheses of Pentacoordinate Diphenolate $Zinc^{II}$, $Nickel^{II}$ and $Copper^{II}$ complexes

2.1 Introduction

2.1.1 Pentacoordinate Schiffs Base Compounds

Schiff base compounds, discovered by Hugo Schiff in the middle of the 19th century,[1-3] have been widely synthesised and have attracted much interest in inorganic chemistry. They possess a wide range of properties[4] and have been employed as antimicrobial agents[5] against organisms such as *Mycobacterium tuberculosis*[6, 7] and as catalysts for a variety of chemical processes including polymerisation,[8] and epoxidation.[9-11]

Four and six coordinate Schiff base compounds have been extensively studied as analogues of the active site of galactose oxidase,[12-14] and recent work within the McMaster group has extended this to examine pentacoordinate species.[15] These species are particularly interesting as they possess a coordination sphere that is coordinatively unsaturated as well as possessing a coordination number more aligned to that found at the active site in the native enzyme.[16, 17] Pentacoordinate species also permit the incorporation of an additional donor atom into the coordination sphere of the metal centre, thereby potentially promoting the formation of metal based oxidation products, particularly Ni^{III}, as has been observed upon the addition of pyridine as a coordinating solvent during the oxidation of four coordinate Ni^{II} complexes including $[Ni(emb)]^{2-}$ (emb = *N,N'*-ethylenebis(*o*-mercaptobenzamide), and $[Ni(phmi)](NEt_4)_2$, (phmi = *N,N'*-1,2phenylenebis(2-sulfanyl-2-methyl)propionamide)) (Chapter One).[18-20] Six pentacoordinate species, $M^{tBu}L_O^R$ (M = Zn, Ni, Cu; R = NH, NMe), which possess an amine donor in addition to the two phenolate and two imine donors to complete the coordination sphere of the metal centre, have been synthesised previously within the group (Figure 2.1.1.1).

Each of $M^{tBu}L_O^R$ (M = Zn, Ni, Cu; R = NH, NMe) possess two oxidation processes that exhibit some chemical reversibility, and the products of these oxidation processes have been examined using a combination of spectroelectrochemical and EPR spectroscopic methods. These studies have demonstrated that the first and second electron oxidation processes for $M^{tBu}L_o^R$ (M = Zn, Cu; R = NMe, NH) are ligand based, leading to the formation of phenoxyl radicals bound to a metal

centre. In contrast, the one electron oxidation of Ni$^{t\mathrm{Bu}}$L$_o^{\mathrm{NMe}}$ and Ni$^{t\mathrm{Bu}}$L$_o^{\mathrm{NH}}$ leads to the formation of Ni$^{\mathrm{III}}$ products that can be probed by EPR spectroscopy (Figure 2.1.1.2 left). A single crystal X-ray structure of [Ni$^{t\mathrm{Bu}}$L$_o^{\mathrm{NMe}}$][BF$_4$] supports a Ni$^{\mathrm{III}}$ formulation (Figure 2.1.1.2 right).[15]

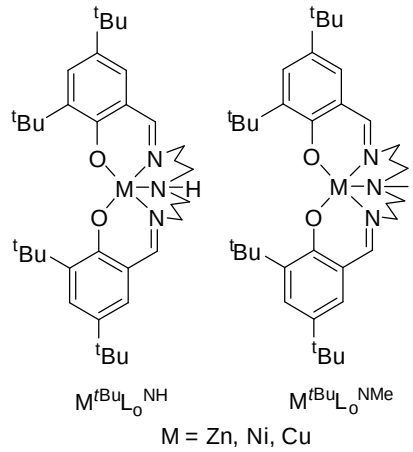


Figure 2.1.1.1: Previously reported pentacoordinate diphenolates M^{tBu}L$_O^R$ (M = Zn, Ni, Cu; R = NH, NMe).[15]

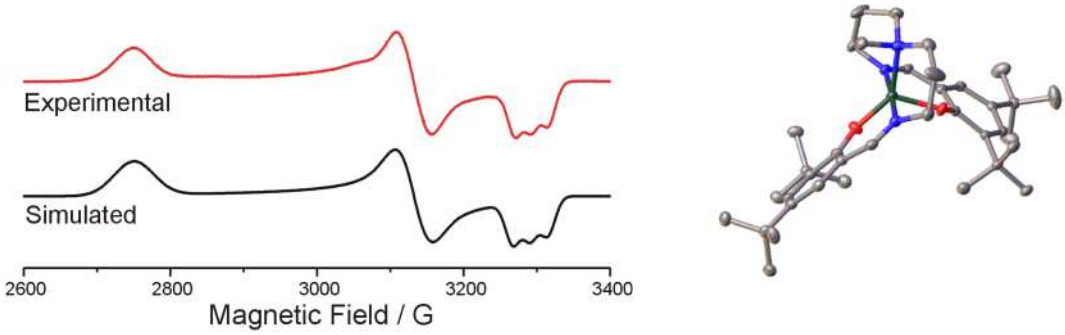


Figure 2.1.1.2: Left: EPR of [^{tBu}NiL$_o^{NMe}$]$^+$ - Right: Molecular structure of [^{tBu}NiL$_o^{NMe}$]$^+$ - H atoms and [BF$_4$]$^-$ counterion omitted for clarity.

The influence of the additional amine donor on the properties of the complexes has also been investigated through the comparison of complexes containing NH and NMe groups. M$^{t\mathrm{Bu}}$L$_O^{\mathrm{R}}$ with R = NH possess a shorter M-N(amine) bond than their counterparts with R = NMe, which could lead to an increased electron density at the metal centre, together with a less positive first redox potential, particularly for the Cu$^{\mathrm{II}}$ and Ni$^{\mathrm{II}}$ analogues. This is suggestive of a correlation between the electron density at the metal centre and the redox potential of the oxidation processes of these complexes.[15]

This study shows significant promise for pentacoordinate diphenolate complexes, particularly as the presence of the additional amine donor is shown to support metal-based redox chemistry for Ni$^{t\text{Bu}}$L$_o^{\text{NMe}}$ and Ni$^{t\text{Bu}}$L$_o^{\text{NH}}$. This, coupled with the well-defined redox processes exhibited by these systems, and the unsaturated coordination sphere make pentacoordinated complexes containing phenolate ligands interesting targets for further study.

2.1.2 Variation of Diphenolate Substituents

There has been a wide range of studies carried out on salen containing complexes as models for galactose oxidase (Chapter One), however the majority of this work uses the well-known 3,5-di^{t}butylsalicyaldehyde as a precursor to the diphenolate donor set.[14, 21] The disubstitution in the 3 and 5 positions of the phenolate ring with substituents which do not contain α protons limits decomposition by proton abstraction. In the absence of this substitution the delocalisation of radical character around the phenyl ring that places unpaired electron spin adjacent to a C-H bond, which provides a decomposition pathway.[22] 3,5-Di^{t}butylsalicyaldehyde is widely used as a precursor to substituted phenolate-containing ligands because of its availability and favourable crystallisation properties that assist purification and structural studies.[14, 23-25]

Recent investigations have considered alternative aldehydes as precursors to 4-coordinate salen-based ligands.[26-30] Many of these ligands have incorporated thioether substituents (SMe, S^{i}Pr, S^{t}Bu) to replicate the post translational modification involving Tyr272 and Cys228 at the active site of the native galactose oxidase.[26, 27] While limited studies have also been undertaken to incorporate Me,[30] OMe,[30, 31] amine[29] and halide[30] substituents in the 3 and 5 positions of the phenolate ring of transition metal diphenolate complexes (Chapter One), no detailed, systematic study has been undertaken with the aim of controlling the structural, spectroscopic and electrochemical properties of diphenolate-containing complexes through appropriate substitution of the phenyl rings.

2.1.3 Aims

Given our recent studies on the pentacoordinate species $M^{tBu}L_o^{NMe}$ (M = Zn, Ni, Cu),[15] and the use of alternative diphenolate substituents to tune the electrochemical properties of Schiff base compounds,[26-30] our aim was to synthesise a wide range of pentacoordinate complexes containing diphenolate donors to assess the factors that influence their structural, spectroscopic and electrochemical properties, and their reactivity. In this chapter we demonstrate the syntheses of a range of pentacoordinate complexes containing diphenolate donors through adaptable synthetic routes. We focus on the introduction of a variety of substituents at the 3 and 5 positions of the diphenolate ring systems in order to assess the effect of substitution at these different positions on the structural, spectroscopic and electrochemical properties of the complexes. We exploit the synthetic methodology employed previously for the syntheses of $M^{tBu}L_o^{x}$ (x = NMe, NH, M = Zn, Ni, Cu)[15] to synthesise a range of Zn, Ni and Cu compounds (Figure 2.1.3.1). This work focuses on the incorporation of a methyl substituted tertiary amine bridge as this is more effective in stabilising the oxidation processes exhibited by the complexes than for complexes incorporating the corresponding secondary amine bridge.[15] The compounds are characterised by X-ray crystallography and by a range of solution-phase spectroscopic and electrochemical techniques. Density functional theory (DFT) calculations provide a framework within which to aid our interpretation of the electronic structure of the complexes and to guide our future electrochemical investigations.

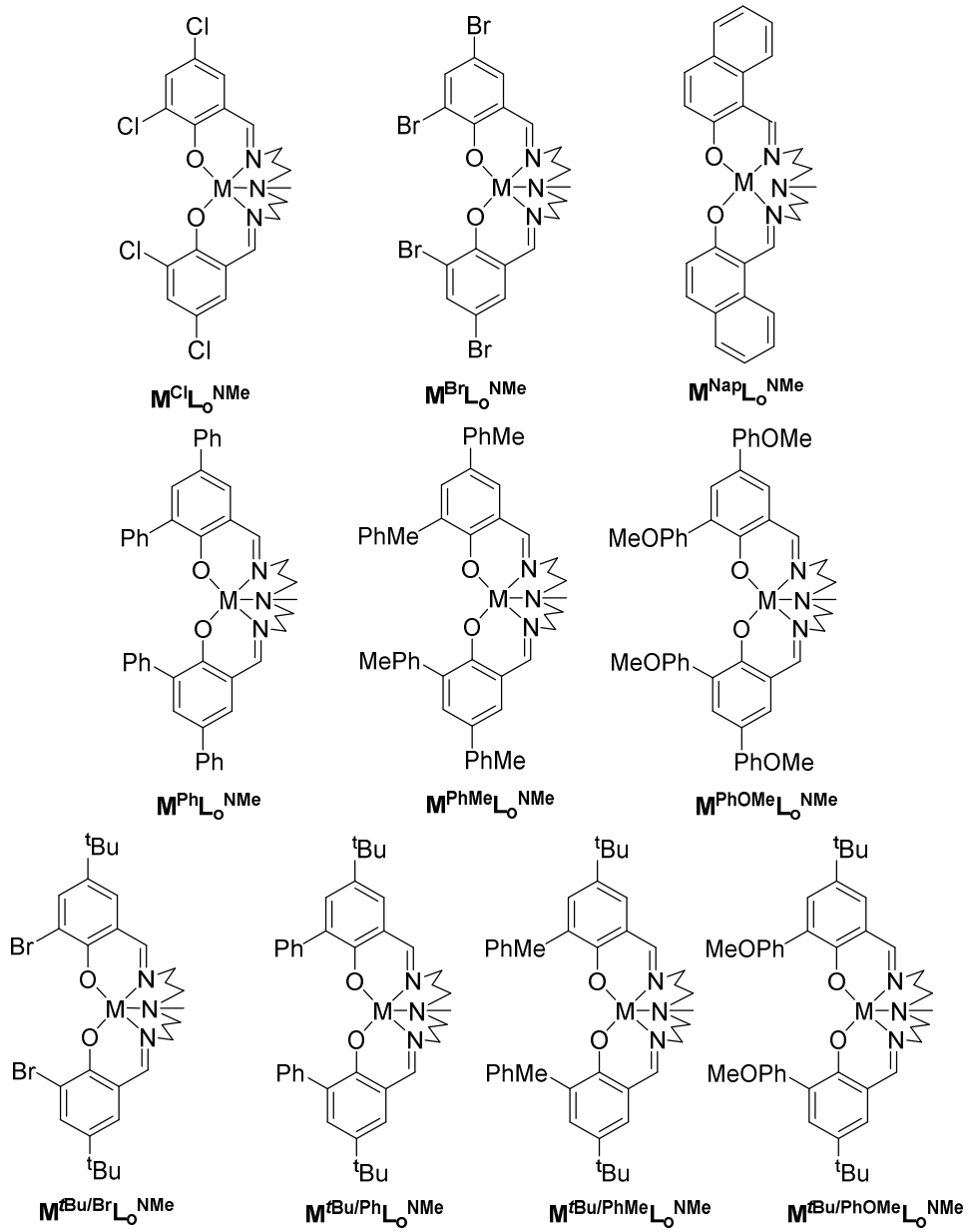
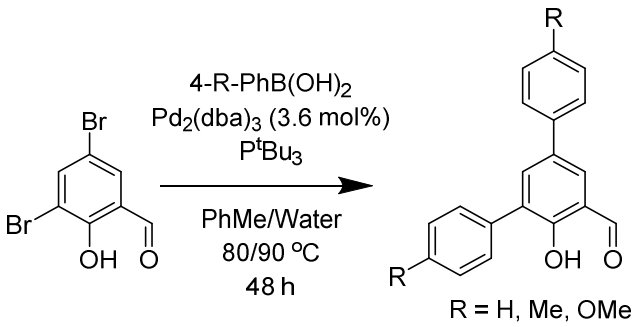


Figure 2.1.3.1: Summary of the complexes synthesised in this chapter $M^RL_o^{NMe}$ (M = Zn, Ni, Cu): Top- Compounds with halide substituents and a napthyl system (R = Cl, Br, Nap); Middle- Compounds with substituted aromatic substituents in the 3 and 5 positions (R = Ph, PhMe, PhOMe); Bottom-Compounds with ^{t}butyl substituents in the 5 position and aromatic substituents in the 3 position (R = ^{t}Bu/Ph, ^{t}Bu/PhMe, ^{t}Bu/PhOMe).

2.2 Synthesis of 3,5 Disubstituted Salicylaldehydes

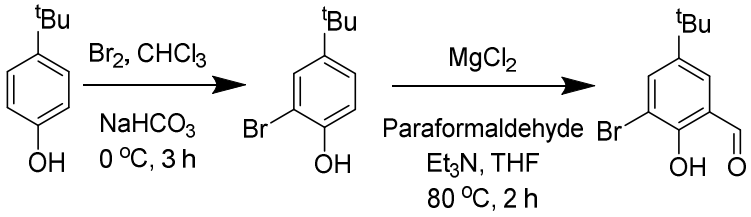
The proligands and their complexes are synthesised from 3,3'-diamino-N-methyldipropylamine and a 3,5-disubstituted salicylaldehyde, or a napthyl-based salicyaldehyde. 3,5-Dibromo- and 3,5-dichloro- salicylaldehyde are commercially available and 2-hydroxynapthaldehyde can be readily prepared from naphthalene-2-ol.[32] The availability of the dibromo substituted species allowed us to investigate Suzuki coupling as a route to extend our range of available aldehydes with identical extended aromatic substituents at the 3 and 5 positions of the salicylaldehyde.

Early attempts to prepare 3,5-diphenylsalicyladehyde from 3,5-dibromosalicyaldehyde and phenyl boronic acid using $Pd(PPh_3)_4$ were unsuccessful, however the use of the more active palladium catalyst derived from $Pd_2(dba)_3$ (dba = dibenzylideneacetone) with $P(^tBu)_3$ and K_2CO_3 gave 3,5 diphenylsalicyladehyde in 90% yield after 48 hours at 80 °C. This methodology was subsequently adopted for the syntheses of 3,5-di(4-methyl)phenylsalicylaldehyde (90 °C, 48 h, 73 %) and 3,5-di(4-methoxy)phenylsalicylaldehyde (90 °C, 48 h, 89 %) from para-methylphenyl boronic acid and para-methoxyphenyl boronic acid, respectively (Scheme 2.2.1). This approach enabled us to isolate 3,5-diphenylsalicyladehyde, 3,5-di(4-methyl)phenylsalicylaldehyde, and 3,5-di(4-methoxy)phenylsalicylaldehyde for incorporation into Schiff base complexes with progressively more electron donating substituents in the 3 and 5 positions of the phenolate ring of the salicylaldehyde.



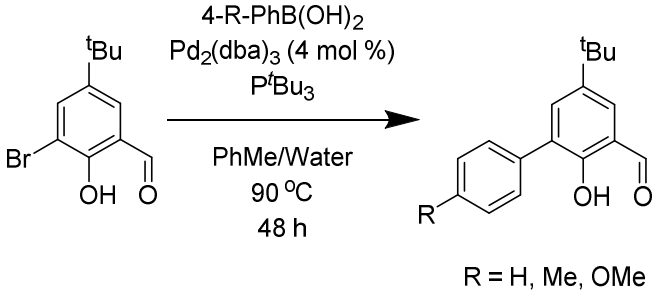
Scheme 2.2.1: Syntheses of 3,5-di(4-substituted)phenylsalicyaldehydes.

In addition, different substituents at the 3 positions of the salicyaldehyde ring may also be incorporated to facilitate investigations into their relative influences on the properties of the resultant transition metal complexes. This was accomplished *via* the preparation of 3-bromo-5-^{t}butyl salicylaldehyde from 4-^{t}butylphenol (Scheme 2.2.2),[33, 34] to give a salicyaldehyde with one ^{t}butyl group and one bromo position available for further functionalisation.



Scheme 2.2.2: Preparation of 3-bromo-5-^{t}butyl-salicylaldehyde.[33, 34]

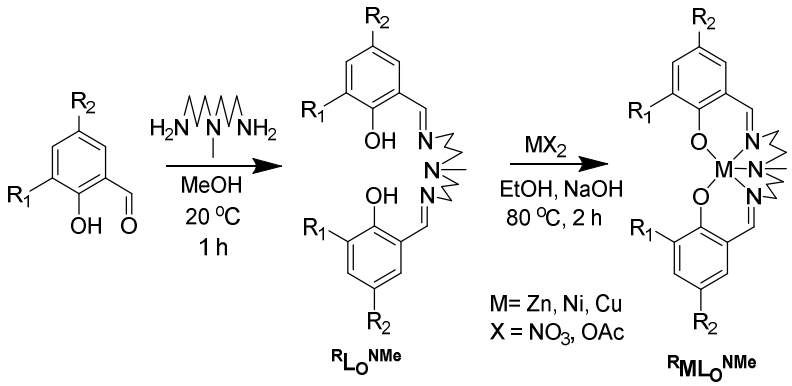
Subsequent reaction of 3-bromo-2-^{t}butyl-salicylaldehyde with a diamine gives a ^{t}butyl/bromo substituted ligand. Similar Suzuki coupling methodologies can be applied to synthesise other substituted salicylaldehydes using one equivalent of phenyl, 4-methylphenyl or 4-methoxyphenyl boronic acid under the same conditions as described previously (Scheme 2.2.1) to give an extended range of salicylaldehydes (Scheme 2.2.3). Thus, a wide range of salicylaldehydes can be readily prepared as precursors for proligand syntheses using a Schiff base methodology.



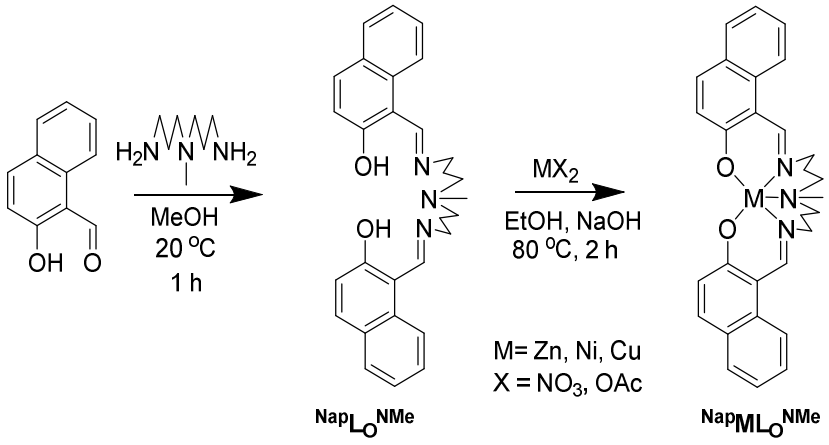
Scheme 2.2.3: Preparation of 3-(4-substituted)phenyl-5-^{t}butyl-salicylaldehydes.

2.3 Synthesis and Characterisation of Proligands $^{R}L_{O}^{NMe}$, and their Zinc, Nickel and Copper Complexes $M^{R}L_{o}^{NMe}$ (M= Zn, Ni, Cu; R = Cl, Br, Nap, Ph, PhMe, PhOMe, ^{t}Bu/Br, ^{t}Bu/Ph, ^{t}Bu/PhMe, ^{t}Bu/PhOMe)

The proligands $^{R}L_{O}^{NMe}$, (R = Cl, Br, Nap, Ph, PhMe, PhOMe, ^{t}Bu/Br, ^{t}Bu/Ph, ^{t}Bu/PhMe, ^{t}Bu/PhOMe) were synthesised using the methodology employed previously for the analogous ^{t}butyl substituted species[15] by the addition of two equivalents of the appropriate aldehyde to 3,3'-diamino-N-methyldipropylamine in methanol. The products are isolated as crude yellow oils and used without further purification in reactions with one equivalent of the metal salts [$Zn(OAc)_2 \cdot 2H_2O$/$Ni(NO_3)_2 \cdot 6H_2O$/ $Cu(OAc)_2 \cdot H_2O$] in ethanol in the presence of 2.2 equivalents of sodium hydroxide for two hours (Schemes 2.3.1 and 2.3.2) to give the transition metal complexes $M^{R}L_{o}^{NMe}$ (R = Cl, Br, Nap, Ph, PhMe, PhOMe, ^{t}Bu/Br, ^{t}Bu/Ph, ^{t}Bu/PhMe, ^{t}Bu/PhOMe; M= Zn, Ni, Cu). We have successfully prepared the Zn^{II}, Ni^{II} and Cu^{II} complexes using a direct metalation strategy with the appropriate metal salt. This is in contrast to the preparation of $Ni^{tBu}L_{o}^{NMe}$ and $Cu^{tBu}L_{o}^{NMe}$ *via* transmetallation from $Zn^{tBu}L_{o}^{NMe}$ reported previously;[15] we have found that this direct approach is equally successful and eliminates an additional synthetic step and the potential for contamination of the Ni^{II} and Cu^{II} complexes with residual Zn^{II}.



Scheme 2.3.1: Syntheses of the NMe bridged phenolate complexes $M^{R}L_{o}^{NMe}$: $M^{Cl}L_{o}^{NMe}$ $R_1 = R_2 = Cl$, $M^{Br}L_{o}^{NMe}$ $R_1 = R_2 = Br$, $M^{Ph}L_{o}^{NMe}$ $R_1 = R_2 = Ph$, $M^{PhMe}L_{o}^{NMe}$ $R_1 = R_2 = Ph\text{-}4\text{-}Me$, $M^{PhOMe}L_{o}^{NMe}$ $R_1 = R_2 = Ph\text{-}4\text{-}OMe$, $M^{tBu/Br}L_{o}^{NMe}$ $R_1 = Br$ $R_2 = {}^{t}Bu$, $M^{tBu/Ph}L_{o}^{NMe}$ $R_1 = Ph$ $R_2 = {}^{t}Bu$, $M^{tBu/Me}L_{o}^{NMe}$ $R_1 = Ph\text{-}4\text{-}Me$ $R_2 = {}^{t}Bu$, $M^{tBu/OMe}L_{o}^{NMe}$ $R_1 = Ph\text{-}4\text{-}OMe$ $R_2 = {}^{t}Bu$.



Scheme 2.3.2: Synthesis of NMe bridged phenolate complexes $M^{Nap}L_o^{NMe}$ $R_1 = R_2 = Nap$.

Each complex was purified by recrystallisation from a saturated solution of dichloromethane using methanol as an antisolvent and the purity of each complex was confirmed by CHN analyses. ^{1}H NMR studies of the diamagnetic Zn(II) complexes at ambient temperature show broadening of the peaks in the aliphatic region for all of the species synthesised. This suggests some degree of fluxionality of the CH_2 groups in a disordered diamine bridge. ^{1}H NMR spectroscopic studies of $^{Cl}ZnL_o^{NMe}$ and $^{Br}ZnL_o^{NMe}$ at low temperature (233 K - 298 K) show that this effect is significantly reduced such that the resonances in this aliphatic region are clearly resolved (Figure 2.3.2).

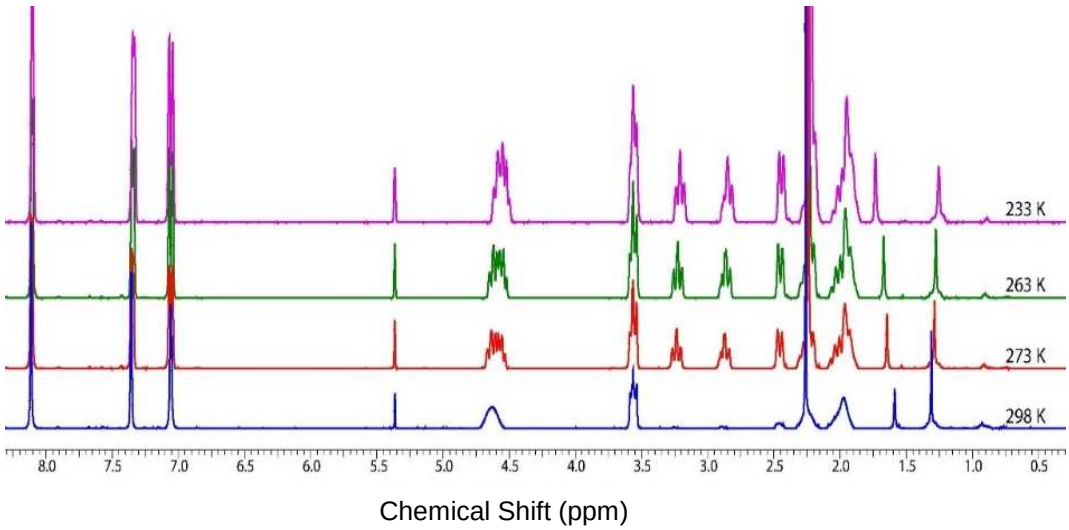


Figure 2.3.2 Variable temperature ^{1}*H NMR spectra of* $Zn^{Cl}L_O^{NMe}$ *at 298-233 K.*

2.4 The Structural Characterisations of $M^{R}L_{o}^{NMe}$ by Single Crystal X-ray Diffraction Studies. (M= Zn, Ni, Cu; R = Cl, Br, Nap, Ph, PhMe, PhOMe, ^{t}Bu/Br, ^{t}Bu/Ph, ^{t}Bu/PhMe, ^{t}Bu/PhOMe)

2.4.1 Introduction

Single crystals suitable for X-ray diffraction studies for all of the complexes $M^{R}L_{o}^{NMe}$ (M= Zn, Ni, Cu; R = Cl, Br, Nap, Ph, PhMe, PhOMe, ^{t}Bu/Br, ^{t}Bu/Ph, ^{t}Bu/PhMe, ^{t}Bu/PhOMe) except $Cu^{tBu/PhMe}L_{O}^{NMe}$ were grown variously by slow diffusion of pentane, methanol or diethyl ether into a CH_2Cl_2 solution of the complex, or by vapour diffusion of diethyl ether into a CH_2Cl_2 solution of the complex.

All of the structures examined (except $Ni^{PhMe}L_{O}^{NMe}$ and $Ni^{tBu/Br}L_{O}^{NMe}$) show disorder within the dipropylamine bridge over two orientations in at least one of the molecules in the asymmetric unit (Figure 2.4.1). This is consistent with the flexible nature of this bridge as revealed by low temperature ^{1}H NMR spectroscopy for $Zn^{Cl}L_{o}^{NMe}$ and $Zn^{Br}L_{o}^{NMe}$ (Section 2.3). The occupancies of the two orientations were refined competitively converging at a variety of ratios from 0.51:0.49 to 0.92:0.08. For $Ni^{tBu/PhMe}L_{O}^{NMe}$, $Zn^{tBu/PhOMe}L_{O}^{NMe}$, and $Ni^{tBu/PhOMe}L_{O}^{NMe}$, where Z' = 0.5, this bridge was disordered across a special position. This required the occupancies of the two components of this disordered bridge to be fixed at 0.5. In these cases a riding model could not be used for the protons of the CH_2 unit closest to the imine nitrogen as, owing to a combination of the site symmetry and disorder of the bridge, the use of negative parts is required to prevent erroneous bonding. A limitation of this refinement method is that the final carbon in this group is not considered by SHELXTL[35] as a secondary carbon, even in the event that a BOND instruction is employed to obtain correct bonding at this carbon. Consequently, the program will not assign the correct HFIX code to the site and it is not possible to refine the hydrogens at this site as riding on the parent carbon. Therefore the hydrogen atoms were refined from the electron density map and CH and HCH distances restrained in order to give an appropriate geometry for these groups.

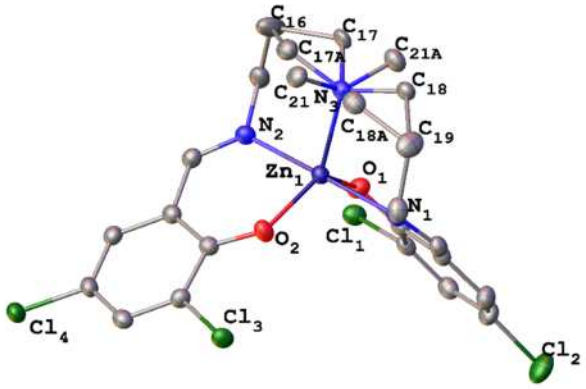


Figure 2.4.1: Molecular structure of $Zn^{Cl}L_O^{NMe}$ showing a typical example of the disordered diproylamine bridge (C17, C18, C21/C17A, C18A, C21A). H atoms and lattice solvent molecules are omitted for clarity.

A variety of other disordered components were observed for some of the structures: a disordered PhMe group (C72-C78/C27A-C78A) in the structure of $Ni^{PhMe}L_O^{NMe}$, disordered PhMe (C69-C75/C69A-C75A) and ^{t}butyl groups (C60-C62/C60A-C62A) in the structure of $Zn^{tBu/PhMe}L_O^{NMe}$, a disordered ^{t}butyl group (C20-C22/C20A-C22A) in the structure of $Ni^{tBu/Br}L_O^{NMe}$, and a disordered PhOMe group (C9-C15, O3/C9A-C15A, O3A) in the structure of $Cu^{PhOMe}L_O^{NMe}$. In this final case the intermolecular H-H distance between CH_3 protons of the neighbouring PhOMe groups (H22D-H71A_$1 and H22E-H71A_$1, symmetry operator 3/2-x, ½+y, ½-z) were restrained to be approximately equal to 2.4 Å in order to prevent the formation of H-H close contacts due to non-ideal placement of these atoms when using a riding model. The application of such restraints did not result in the movement of the parent carbon atom with only rotation of the protons around this carbon observed.

Many of the structures also exhibited disorder within the solvent molecules, principally CH_2Cl_2, which is incorporated into the crystalline lattice. The solvent molecules were refined using a variety of strategies including the competitive refinement of disordered occupancies, the use of fixed occupancies and the use of rigid fragments by restraining 1,2-Cl-C and 1,3-Cl-Cl distances in the CH_2Cl_2 molecules. In extreme cases the Platon SQUEEZE procedure was used in order to remove the scattering contribution from highly disordered solvent molecules.[36] A range of thermal parameter and similarity restraints were used throughout the refinements; further crystallographic experimental and refinement details are given

in Appendix 2. The figures below present only one of the molecules in the asymmetric unit with disordered components, lattice solvent molecules and hydrogen atoms are omitted for clarity. Figures of the full content of the asymmetric units are contained in Appendix 2, and .cif files containing full structural information are attached to this thesis.

The degree of distortion within pentacoordinate structures from an ideal trigonal bipyramid towards a square pyramidal geometry may be assessed quantitatively by considering the structural index parameter $\tau = (\beta-\alpha)/60$ where β is the largest basal angle, N1-M-N2 for the complexes described below, and α = O1-M-O2 for the complexes described below (Figure 2.4.2).[37] This parameter is calculated for each of the structures presented in this chapter and can be compared to τ for other pentacoordinate complexes.[15, 38]

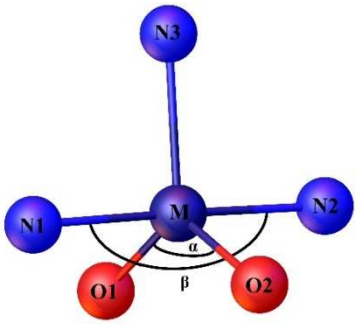
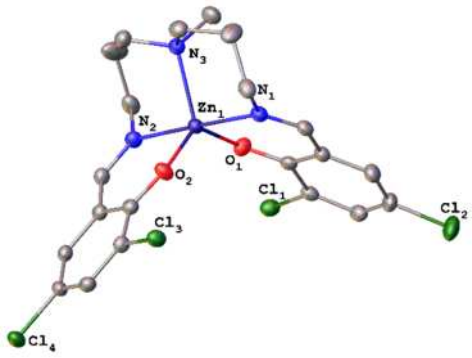


Figure 2.4.2: α and β values used for calculation of structural index parameter τ.

2.4.2 Structures of $M^{R}L_{o}^{NMe}$ (R = Cl, Br, Nap, Ph, PhMe, PhOMe, ^{t}Bu/Br, ^{t}Bu/Ph, ^{t}Bu/PhMe, ^{t}Bu/PhOMe; M= Zn, Ni, Cu)

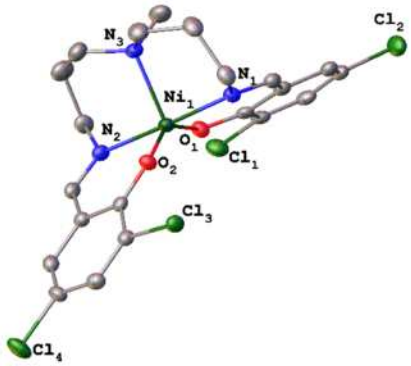
The chloro and bromo substituted complexes $^{R}ML_{o}^{NMe}$ (M = Zn, Ni, Cu; R = Cl, Br) all crystallise in the monoclinic space group P21/c. $M^{Br}L_{O}^{NMe}$ (M = Zn, Ni, Cu) are isomorphous and isostructural (Z' = 2), whilst $Ni^{Cl}L_{O}^{NMe}$ and $Cu^{Br}L_{O}^{NMe}$ crystallise in different unit cells, with Z' = 2, and $Zn^{Cl}L_{O}^{NMe}$ crystallises in a unit cell containing one molecule and one CH_2Cl_2 solvent molecule. When Z' = 2, whilst the bond lengths are essentially indistinguishable between the two molecules in the unit cell, there is significant deviation in bond angles and consequently in the structural parameter τ. This suggests a significant influence of packing effects on the coordination geometries adopted by these complexes in the solid state. π-π interactions are observed between the phenolate rings of the two molecules in the asymmetric unit of $M^{Br}L_{O}^{NMe}$ (M = Zn, Ni, Cu) and $M^{Cl}L_{O}^{NMe}$ (M

= Ni, Cu), with a centroid-centroid separation of *ca*. 3.6 Å for face to face interactions, accompanied by weaker edge-face interactions with a centroid-centroid separation of ca. 5.5 Å. Neither of these interactions are observed in the solvated structure of $Zn^{Cl}L_O^{NMe}$.



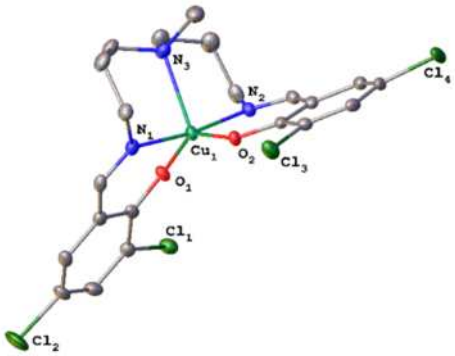
Zn_1-N_1	2.0699(15)	Zn_1-O_1	1.9856(12)
Zn_1-N_2	2.0633(15)	Zn_1-O_2	1.9879(13)
Zn_1-N_3	2.1433(15)		
O_1-Zn_1-O_2	126.93(5)	O_2-Zn_1-N_2	88.69(6)
O_1-Zn_1-N_1	87.93(5)	O_2-Zn_1-N_3	116.92(5)
O_1-Zn_1-N_2	90.31(5)	N_1-Zn_1-N_3	90.73(6)
O_1-Zn_1-N_3	116.15(5)	N_2-Zn_1-N_1	178.16(6)
O_2-Zn_1-N_1	91.94(5)	N_2-Zn_1-N_3	90.53(6)

Figure 2.4.2.1: Molecular structure of $Zn^{Cl}L_O^{NMe}$. H atoms, disordered CH_2 groups and lattice solvent molecules are omitted for clarity; Table 2.4.2.1: Selected bond lengths (Å) and angles (º) for $Zn^{Cl}L_O^{NMe}$. Z' = 1, τ = 0.85.



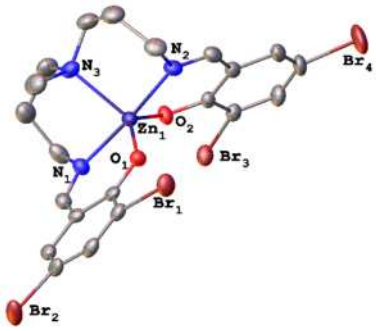
	Molecule 1	Molecule 2		Molecule 1	Molecule 2
Ni_1-N_1	2.0144(16)	2.0160 (16)	Ni_1-O_1	1.9663(14)	1.9792 (13)
Ni_1-N_2	2.0159(16)	2.0144 (16)	Ni_1-O_2	1.9792(13)	1.9661 (13)
Ni_1-N_3	2.0703(17)	2.0703 (17)			
O_1-Ni_1-O_2	148.87(6)	148.87 (6)	O_2-Ni_1-N_2	89.28(6)	89.24 (6)
O_1-Ni_1-N_1	89.23(6)	89.28 (6)	O_2-Ni_1-N_3	104.07(7)	107.03 (7)
O_1-Ni_1-N_2	89.14(6)	91.36 (6)	N_1-Ni_1-N_2	177.83(7)	177.84 (6)
O_1-Ni_1-N_3	107.03(7)	104.07 (7)	N_1-Ni_1-N_3	91.38(7)	90.47 (7)
O_2-Ni_1-N_1	91.36(6)	89.14 (6)	N_2-Ni_1-N_3	90.47(7)	91.38 (7)

Figure 2.4.2.2: Molecular structure of $Ni^{Cl}L_O^{NMe}$. H atoms are omitted for clarity; Table 2.4.2.2: Selected bond lengths (Å) and angles (º) for $Ni^{Cl}L_O^{NMe}$. Z' = 2, τ = 0.48 and 0.48.



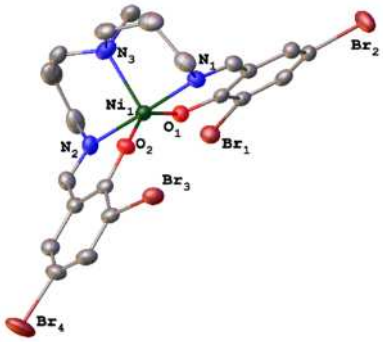
	Molecule 1	Molecule 2		Molecule 1	Molecule 2
Cu_1-N_1	1.9586(17)	1.9651 (17)	Cu_1-O_1	1.9652(14)	1.9935 (15)
Cu_1-N_2	1.9625(17)	1.9519 (17)	Cu_1-O_2	1.9746(14)	1.9561 (14)
Cu_1-N_3	2.3125(18)	2.2393 (18)			
O_1-Cu_1-O_2	142.32(6)	135.72 (6)	O_2-Cu_1-N_2	91.79(6)	92.27 (7)
O_1-Cu_1-N_1	90.49(6)	90.18 (7)	O_2-Cu_1-N_3	109.20(6)	116.78 (7)
O_1-Cu_1-N_2	93.35(6)	90.59 (7)	N_1-Cu_1-N_3	88.39(7)	88.27 (7)
O_1-Cu_1-N_3	108.45(6)	107.47 (7)	N_1-Cu_1-N_2	172.57(7)	176.47 (7)
O_2-Cu_1-N_1	89.04(6)	89.58 (6)	N_2-Cu_1-N_3	84.37(7)	88.22 (7)

Figure 2.4.2.3: Molecular structure of $Cu^{Cl}{}_{O}{}^{NMe}$. H atoms are omitted for clarity; Table 2.4.2.3: Selected bond lengths (Å) and angles (º) for $Cu^{Cl}L_{O}{}^{NMe}$. Z' = 2, τ = 0.50 and 0.68.



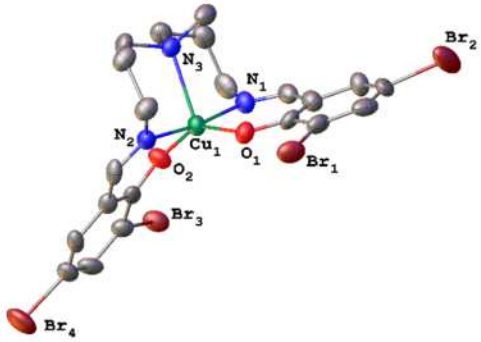
	Molecule 1	Molecule 2		Molecule 1	Molecule 2
Zn_1-N_1	2.056(3)	2.089(3)	Zn_1-O_1	1.999(2)	1.983(3)
Zn_1-N_2	2.060(3)	2.063(3)	Zn_1-O_2	1.981(2)	1.961(2)
Zn_1-N_3	2.193(3)	2.140(3)			
O_1-Zn_1-O_2	132.12(10)	129.31(12)	O_2-Zn_1-N_2	88.70(11)	90.13(11)
O_1-Zn_1-N_1	89.85(11)	87.60(11)	O_2-Zn_1-N_3	113.57(11)	119.16(12)
O_1-Zn_1-N_2	90.61(11)	91.73(11)	N_1-Zn_1-N_3	85.85(12)	89.51(12)
O_1-Zn_1-N_3	114.29(10)	111.50(13)	N_2-Zn_1-N_1	175.02(12)	178.63(11)
O_2-Zn_1-N_1	94.67(11)	91.22(10)	N_2-Zn_1-N_3	89.44(12)	89.62(12)

Figure 2.4.2.4: Molecular structure of $Zn^{Br}L_{O}{}^{NMe}$. H atoms are omitted for clarity; Table 2.4.2.4: Selected bond lengths (Å) and angles (º) for $Zn^{Br}L_{O}{}^{NMe}$. Z' = 2, τ = 0.72 and 0.82.



	Molecule	Molecule 2		Molecule 1	Molecule 2
Ni_1-N_1	2.011(3)	2.009(3)	Ni_1-O_1	2.007(2)	1.946(2)
Ni_1-N_2	2.012(3)	2.027(3)	Ni_1-O_2	1.986(2)	1.973(2)
Ni_1-N_3	2.097(3)	2.085(3)			
O_1-Ni_1-O_2	147.22(9)	139.54(12)	O_2-Ni_1-N_2	88.98(10)	88.51(10)
O_1-Ni_1-N_1	89.88(10)	90.47(11)	O_2-Ni_1-N_3	104.93(11)	102.16(12)
O_1-Ni_1-N_2	89.81(10)	88.58(10)	N_1-Ni_1-N_3	87.52(12)	91.50(12)
O_1-Ni_1-N_3	107.84(10)	118.20(12)	N_1-Ni_1-N_2	178.42(12)	178.16(11)
O_2-Ni_1-N_1	92.12(10)	91.19(11)	N_2-Ni_1-N_3	91.10(12)	90.34(11)

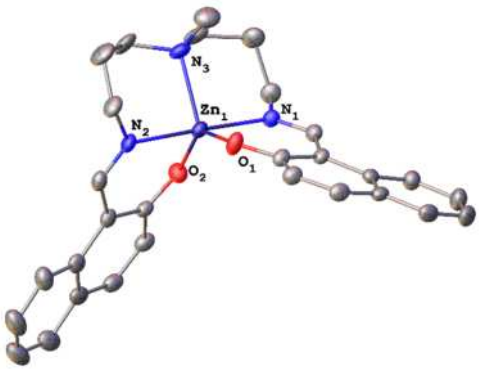
Figure 2.4.2.5: Molecular structure of $Ni^{Br}L_O^{NMe}$. H atoms are omitted for clarity; Table 2.4.2.5: Selected bond lengths (Å) and angles (º) for $Ni^{Br}L_O^{NMe}$. Z' = 2, τ = 0.61 and 0.64.



	Molecule 1	Molecule 2		Molecule 1	Molecule 2
Cu_1-N_1	1.966(13)	1.960 (10)	Cu_1-O_1	1.966(11)	1.948 (9)
Cu_1-N_2	1.979(13)	1.973 (10)	Cu_1-O_2	1.967(12)	1.972 (9)
Cu_1-N_3	2.300(12)	2.233 (10)			
O_1-Cu_1-O_2	143.8(5)	139.1 (4)	O_2-Cu_1-N_2	91.0(5)	89.0 (4)
O_1-Cu_1-N_1	89.6(5)	92.2 (4)	O_2-Cu_1-N_3	109.5(5)	115.8 (4)
O_1-Cu_1-N_2	93.0(5)	89.0 (4)	N_1-Cu_1-N_3	88.1(5)	89.2 (4)
O_1-Cu_1-N_3	106.6(5)	115.8 (4)	N_1-Cu_1-N_2	173.6(5)	177.4 (4)
O_2-Cu_1-N_1	90.3(5)	91.2 (4)	N_2-Cu_1-N_3	85.5(5)	88.2 (4)

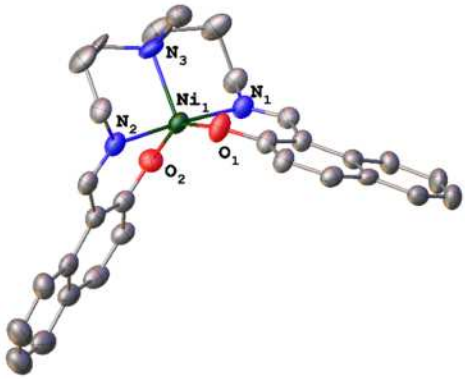
Figure 2.4.2.6: Molecular structure of $Cu^{Br}L_O^{NMe}$. H atoms are omitted for clarity; Table 2.4.2.6: Selected bond lengths (Å) and angles (º) for $Cu^{Br}L_O^{NMe}$. Z' = 2, τ = 0.50 and 0.63.

$Zn^{Nap}L_O{}^{NMe}$, $Ni^{Nap}L_O{}^{NMe}$, and $Cu^{Nap}L_O{}^{NMe}$ also crystallise in the monoclinic space group P21/c, and are isomorphous and isostructural to one another with Z' = 1 (Figures 2.4.9-2.4.11). One CH_2Cl_2 solvent molecule is observed in the asymmetric unit and no π-π interactions are observed in any of these structures (Figure 2.4.10).



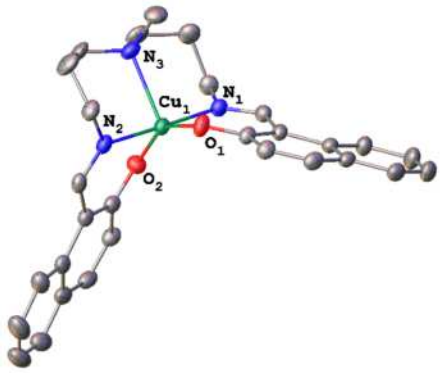
Zn_1-N_1	2.071(3)	Zn_1-O_1	1.984(3)
Zn_1-N_2	2.065(3)	Zn_1-O_2	1.991(2)
Zn_1-N_3	2.155(3)		
O_1-Zn_1-O_2	134.08(11)	O_2-Zn_1-N_2	86.84(11)
O_1-Zn_1-N_1	86.81(11)	O_2-Zn_1-N_3	110.83(11)
O_1-Zn_1-N_2	92.88(11)	N_1-Zn_1-N_3	91.17(12)
O_1-Zn_1-N_3	115.08(12)	N_2-Zn_1-N_1	178.32(12)
O_2-Zn_1-N_1	92.18(11)	N_2-Zn_1-N_3	90.46(12)

Figure 2.4.2.7: Molecular structure of $Zn^{Nap}L_O{}^{NMe}$. H atoms, disordered CH_2 groups and lattice solvent molecules are omitted for clarity; Table 2.4.2.7: Selected bond lengths (Å) and angles (º) for $Zn^{Nap}L_O{}^{NMe}$. Z' = 1, τ = 0.74.



Ni_1-N_1	2.008(4)	Ni_1-O_1	1.982(3)
Ni_1-N_2	2.011(4)	Ni_1-O_2	1.987(3)
Ni_1-N_3	2.095(4)		
O_1-Ni_1-O_2	145.51(16)	O_2-Ni_1-N_2	87.28(15)
O_1-Ni_1-N_1	87.18(15)	O_2-Ni_1-N_3	105.16(16)
O_1-Ni_1-N_2	91.39(15)	N_1-Ni_1-N_2	175.76(16)
O_1-Ni_1-N_3	109.33(17)	N_1-Ni_1-N_3	92.34(17)
O_2-Ni_1-N_1	91.63(15)	N_2-Ni_1-N_3	91.90(17)

Figure 2.4.2.8: Molecular structure of $Ni^{Nap}L_O{}^{NMe}$. H atoms, disordered CH_2 groups and lattice solvent molecules are omitted for clarity. Table 2.4.2.8: Selected bond lengths (Å) and angles (º) for $Ni^{Nap}L_O{}^{NMe}$. Z' = 1, τ = 0.50.



Cu_1-N_1	1.959(2)	Cu_1-O_1	1.9566(19)
Cu_1-N_2	1.957(2)	Cu_1-O_2	1.9601(19)
Cu_1-N_3	2.285(2)		
O_1-Cu_1-O_2	147.51(9)	O_2-Cu_1-N_2	88.77(9)
O_1-Cu_1-N_1	89.11(9)	O_2-Cu_1-N_3	104.81(9)
O_1-Cu_1-N_2	91.23(9)	N_1-Cu_1-N_3	89.65(9)
O_1-Cu_1-N_3	107.68(9)	N_1-Cu_1-N_2	179.03(9)
O_2-Cu_1-N_1	91.43(9)	N_2-Cu_1-N_3	89.38(9)

Figure 2.4.2.9: Molecular structure of $Cu^{Nap}L_O^{NMe}$. H atoms, disordered CH_2 groups and lattice solvent molecules are omitted for clarity; Table 2.4.2.9: Selected bond lengths (Å) and angles (°) for $Cu^{Nap}L_O^{NMe}$. Z' = 1, τ = 0.53.

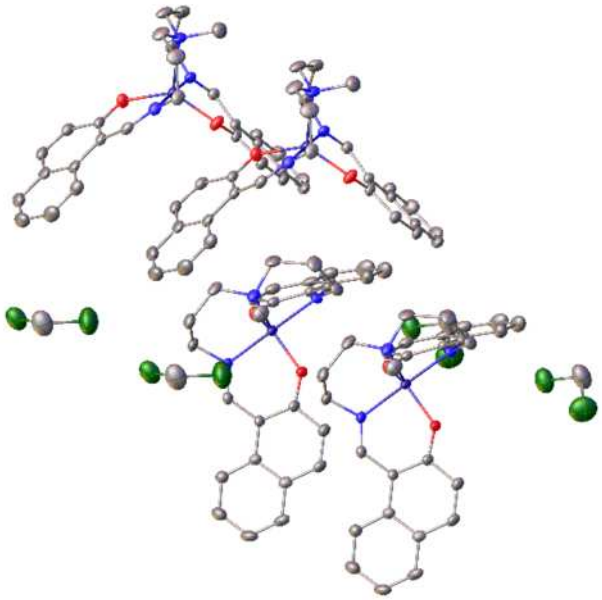
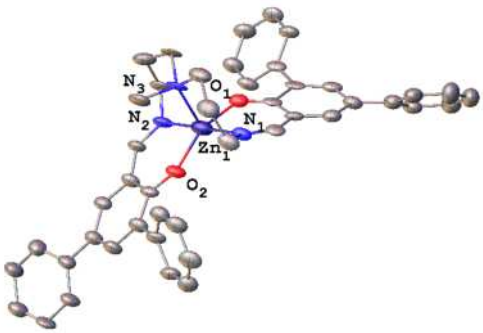


Figure 2.4.2.10: Extended structure of napthyl based complexes shown using $Zn^{Nap}L_O^{NMe}$ as a typical example.

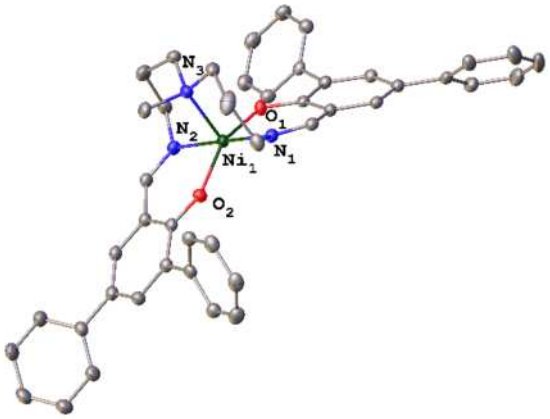
The doubly aromatic substituted complexes $M^RL_O^{NMe}$ (M = Zn, Ni, Cu; R = Ph, PhMe, PhOMe) crystallise in a diverse range of space groups, with $Zn^{Ph}L_O^{NMe}$ crystallising in the orthorhombic space group Fdd2 to give a solvated structure with Z' = 1, whilst $Ni^{Ph}L_O^{NMe}$ and $Cu^{Ph}L_O^{NMe}$ both crystallise in the monoclinic C2/c space group to give solvated structures with Z' = 1. $^{Ph}ML_o^{NMe}$ (M = Zn, Ni, Cu) all display face to face π-π stacking interactions between the phenolate rings of neighbouring molecules (centroid-centroid separation 4.351(11) Å, 4.4104(18) Å, and 4.18696(10) Å, plane-plane angle 17.1(6) °, 17.35(10) °, and 16.9011(6) °, and plane-plane shift 1.76(2) Å, 1.971(4) Å and 1.33142(14) Å for $Zn^{Ph}L_O^{NMe}$,

$Ni^{Ph}L_O^{NMe}$ and $Cu^{Ph}L_O^{NMe}$, respectively) however these interactions are significantly less than those observed for the halogen substituted complexes $M^{Cl}L_O^{NMe}$ (M = Ni, Cu) and $Ni^{Br}L_O^{NMe}$ (M = Zn, Ni, Cu). Long range edge-to-face interactions are also observed in all three complexes between neighbouring phenolate rings with centroid-centroid separations of *ca.* 5.7 Å.



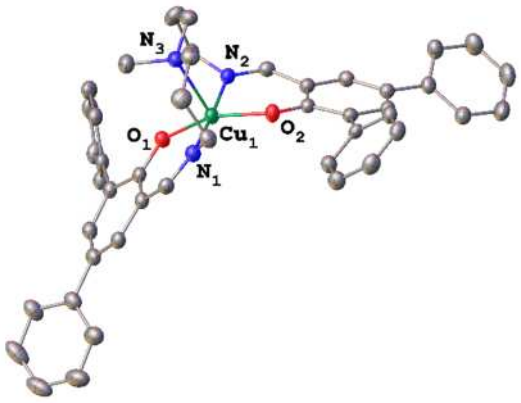
Zn_1-N_1	2.014(12)	Zn_1-O_1	2.044(10)
Zn_1-N_2	2.013(12)	Zn_1-O_2	1.973(10)
Zn_1-N_3	2.095(12)		
O_1-Zn_1-O_2	155.1(4)	O_2-Zn_1-N_2	88.6(4)
O_1-Zn_1-N_1	88.7(4)	O_2-Zn_1-N_3	100.8(4)
O_1-Zn_1-N_2	90.8(4)	N_1-Zn_1-N_3	91.7(5)
O_1-Zn_1-N_3	104.0(4)	N_2-Zn_1-N_1	179.2(5)
O_2-Zn_1-N_1	91.6(4)	N_2-Zn_1-N_3	89.1(5)

Figure 2.4.2.11: Molecular structure of $Zn^{Ph}L_O^{NMe}$. H atoms, disordered CH_2 groups and lattice solvent molecules are omitted for clarity; Table 2.4.2.10: Selected bond lengths (Å) and angles (º) for $Zn^{Ph}L_O^{NMe}$. Z' = 1, τ = 0.40.



Ni_1-N_1	2.0128(17)	Ni_1-O_1	1.9988(14)
Ni_1-N_2	2.0239(17)	Ni_1-O_2	2.0036(15)
Ni_1-N_3	2.0950(18)		
O_1-Ni_1-O_2	154.93(6)	O_2-Ni_1-N_2	88.24(7)
O_1-Ni_1-N_1	88.75(6)	O_2-Ni_1-N_3	101.38(7)
O_1-Ni_1-N_2	91.83(7)	N_1-Ni_1-N_3	90.69(7)
O_1-Ni_1-N_3	103.70(7)	N_1-Ni_1-N_2	179.08(7)
O_2-Ni_1-N_1	90.93(7)	N_2-Ni_1-N_3	89.86(7)

Figure 2.4.2.12: Molecular structure of $Ni^{Ph}L_O^{NMe}$. H atoms, disordered CH_2 groups and lattice solvent molecules are omitted for clarity; Table 2.4.2.11: Selected bond lengths (Å) and angles (º) for $Ni^{Ph}L_O^{NMe}$. Z' = 1, τ = 0.40.



Cu_1-N_1	1.971(2)	Cu_1-O_1	1.9776(1
Cu_1-N_2	1.955(2)	Cu_1-O_2	1.9732(1
Cu_1-N_3	2.293(2)		
O_1-Cu_1-O_2	156.38(8	O_2-Cu_1-N_2	89.90(8)
O_1-Cu_1-N_1	89.43(8)	O_2-Cu_1-N_3	104.62(8
O_1-Cu_1-N_2	90.47(8)	N_1-Cu_1-N_3	87.01(9)
O_1-Cu_1-N_3	99.00(8)	N_1-Cu_1-N_2	176.52(9
O_2-Cu_1-N_1	91.58(8)	N_2-Cu_1-N_3	89.57(9)

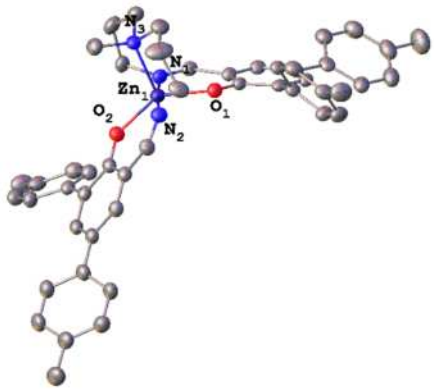
Figure 2.4.2.13: Molecular structure of $Cu^{Ph}L_O^{NMe}$. H atoms, disordered CH_2 and CH_3 groups and lattice solvent molecules are omitted for clarity; Table 2.4.2.12: Selected bond lengths (Å) and angles (º) for $Cu^{Ph}L_O^{NMe}$. Z' = 1, τ = 0.34. F-F

The methylphenyl and methoxyphenyl substituted complexes $M^RL_O^{NMe}$ (R = PhMe, PhOMe; M = Zn, Ni, Cu) crystallise in a range of monoclinic and triclinic space groups with Z' = 1, 2 or 3. The PhMe substituted complexes $M^{PhMe}L_O^{NMe}$ (M = Zn, Ni, Cu) do not exhibit face-to-face π-π stacking interactions, but all three exhibit edge-to-face interactions between the phenolate rings of neighbouring molecules and the phenolate ring of one molecule and the 5-methylphenyl substituent of another.

The methoxyphenyl substituted complexes $M^{PhOMe}L_O^{NMe}$ (M = Zn, Ni, Cu) exhibit a diverse range of stacking effects, with $Zn^{PhOMe}L_O^{NMe}$ exhibiting only edge-face interactions between the phenolate ring and neighbouring methoxyphenyl substituents, and between neighbouring methoxy phenyl substituents. $Ni^{PhOMe}L_O^{NMe}$ exhibits no such interactions and $Cu^{PhOMe}L_O^{NMe}$ shows face-to-face interactions involving neighbouring phenolate rings accompanied by edge-to-face interactions between phenolate rings and neighbouring methoxyphenyl substituents.

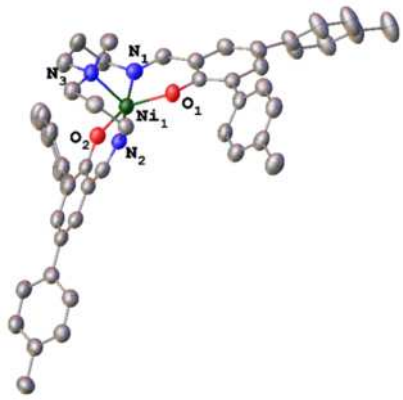
The diverse range of π-π stacking effects observed in the aromatic substituted complexes $M^RL_O^{NMe}$ (R = Ph, PhMe, PhOMe; M = Zn, Ni, Cu) can be attributed to the bulky and extended nature of the substituents. These groups appear to have a significant effect on the crystallisation of these species; good quality crystals of these more extended systems are significantly more troublesome to obtain than their ^{t}butyl- or halogen-substituted counterparts. The deviation observed in τ values

for chemically equivalent molecules in the asymmetric unit when Z'>1 can be attributed to solid state effects on the coordination spheres of these complexes in the solid state structures, which appear to be greater in these extended aromatic structures compared to those of their more compact halogen and ^{t}butyl substituted counterparts.



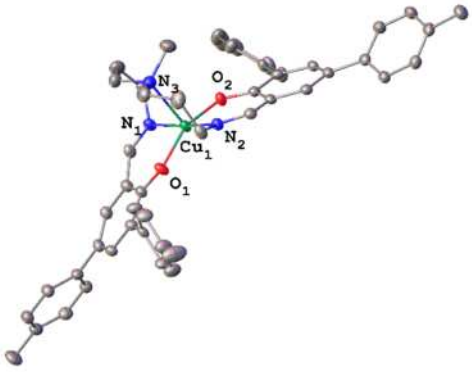
	Molecule 1	Molecule 2		Molecule 1	Molecule 2
Zn_1-N_1	2.067(3)	2.050(3)	Zn_1-O_1	2.003(2)	2.007(2)
Zn_1-N_2	2.070(3)	2.052(3)	Zn_1-O_2	1.990(2)	1.997(2)
Zn_1-N_3	2.131(3)	2.153(3)			
O_1-Zn_1-O_2	141.16(10)	139.32(10)	O_2-Zn_1-N_2	87.71(10)	88.44(10)
O_1-Zn_1-N_1	87.67(10)	88.16(10)	O_2-Zn_1-N_3	110.87(10)	110.04(10)
O_1-Zn_1-N_2	88.98(11)	92.07(10)	N_1-Zn_1-N_3	90.23(11)	89.91(11)
O_1-Zn_1-N_3	107.87(10)	110.62(10)	N_2-Zn_1-N_1	176.64(11)	179.12(11)
O_2-Zn_1-N_1	94.67(10)	90.82(10)	N_2-Zn_1-N_3	91.14(11)	90.81(11)

Figure 2.4.2.14: Molecular structure of $Zn^{PhMe}L_O^{NMe}$. H atoms, disordered CH_2 and CH_3 groups and lattice solvent molecules are omitted for clarity; Table 2.4.2.13: Selected bond lengths (Å) and angles (°) for $Zn^{PhMe}L_O^{NMe}$. Z' = 2. τ = 0.59 and 0.66.



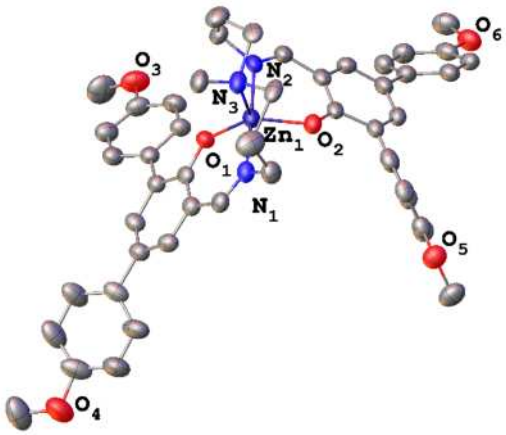
	Molecule 1	Molecule 2		Molecule 1	Molecule 2
Ni_1-N_1	2.008(5)	2.013(5)	Ni_1-O_1	1.997(4)	1.976(4)
Ni_1-N_2	2.000(4)	2.012(4)	Ni_1-O_2	1.996(4)	1.992(4)
Ni_1-N_3	2.091(5)	2.090(5)			
O_1-Ni_1-O_2	150.31(16)	151.76(16)	O_2-Ni_1-N_2	88.69(16)	87.80(18)
O_1-Ni_1-N_1	88.18(17)	88.25(17)	O_2-Ni_1-N_3	104.76(17)	106.50(17)
O_1-Ni_1-N_2	91.31(16)	90.47(17)	N_1-Ni_1-N_3	90.44(19)	91.48(18)
O_1-Ni_1-N_3	104.93(17)	101.74(17)	N_1-Ni_1-N_2	179.3(2)	176.08(18)
O_2-Ni_1-N_1	91.49(16)	91.57(18)	N_2-Ni_1-N_3	90.19(18)	92.41(18)

Figure 2.4.2.15: Molecular structure of $Ni^{PhMe}L_O{}^{NMe}$. H atoms and disordered methyl substituted phenyl ring are omitted for clarity; Table 2.4.2.14: Selected bond lengths (Å) and angles (º) for $Ni^{PhMe}L_O{}^{NMe}$. Z' = 2. τ = 0.48 and 0.41.



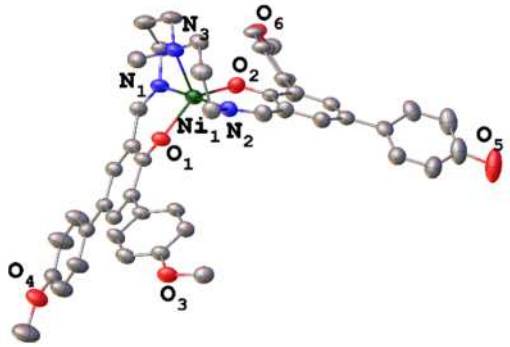
Cu_1-N_1	1.966(2)	Cu_1-O_1	1.9517(17)
Cu_1-N_2	1.968(2)	Cu_1-O_2	1.9698(17)
Cu_1-N_3	2.363(2)		
O_1-Cu_1-O_2	156.28(8)	O_2-Cu_1-N_2	91.46(8)
O_1-Cu_1-N_1	89.46(8)	O_2-Cu_1-N_3	106.37(8)
O_1-Cu_1-N_2	90.50(8)	N_1-Cu_1-N_3	87.10(9)
O_1-Cu_1-N_3	97.34(8)	N_1-Cu_1-N_2	173.51(10)
O_2-Cu_1-N_1	91.19(8)	N_2-Cu_1-N_3	86.46(9)

Figure 2.4.2.16: Molecular structure of $Cu^{PhMe}L_O{}^{NMe}$. H atoms, disordered CH_2 and CH_3 groups and lattice solvent molecules are omitted for clarity; Table 2.4.2.15: Selected bond lengths (Å) and angles (º) for $Cu^{PhMe}L_O{}^{NMe}$. Z' = 1, τ = 0.29.



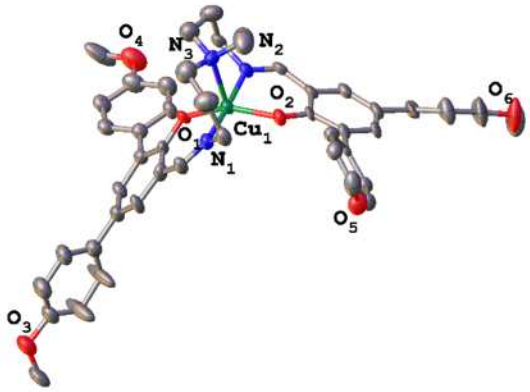
Zn_1-N_1	2.063(5)	Zn_1-O_1	1.990(3)
Zn_1-N_2	2.065(5)	Zn_1-O_2	1.987(3)
Zn_1-N_3	2.164(5)		
O_1-Zn_1-O_2	88.31(16)	O_2-Zn_1-N_2	88.38(15)
O_1-Zn_1-N_1	94.18(16)	O_2-Zn_1-N_3	120.90(16)
O_1-Zn_1-N_2	110.33(16)	N_1-Zn_1-N_3	90.10(19)
O_1-Zn_1-N_3	128.76(15)	N_2-Zn_1-N_1	177.42(17)
O_2-Zn_1-N_1	90.58(16)	N_2-Zn_1-N_3	88.40(18)

Figure 2.4.2.17: Molecular structure of $Zn^{PhOMe}L_O{}^{NMe}$. H atoms, disordered CH_2 and CH_3 groups and lattice solvent molecules are omitted for clarity; Table 2.4.2.16: Selected bond lengths (Å) and angles (º) for $Zn^{PhOMe}L_O{}^{NMe}$. Z' = 1, τ = 0.81.



	Molecule 1	Molecule 2	Molecule 3		Molecule 1	Molecule 2	Molecule 3
Ni_1-N_1	2.007(6)	2.010(6)	2.030(6)	Ni_1-O_1	2.010(5)	1.973(6)	1.986(5)
Ni_1-N_2	2.001(6)	2.004(6)	2.023(6)	Ni_1-O_2	1.987(5)	1.997(5)	1.975(5)
Ni_1-N_3	2.130(6)	2.072(8)	2.104(6)				
O_1-Ni_1-O_2	140.5(2)	157.2(3)	148.0(2)	O_2-Ni_1-N_2	89.0(2)	88.3(2)	89.3(2)
O_1-Ni_1-N_1	88.3(2)	87.9(2)	87.6(2)	O_2-Ni_1-N_3	112.2(2)	100.2(3)	109.9(2)
O_1-Ni_1-N_2	91.9(2)	90.5(2)	91.7(2)	N_1-Ni_1-N_3	90.3(2)	93.3(3)	91.4(2)
O_1-Ni_1-N_3	107.2(2)	102.5(3)	102.1(2)	N_1-Ni_1-N_2	178.0(3)	176.4(3)	178.0(2)
O_2-Ni_1-N_1	89.7(2)	92.0(2)	90.3(2)	N_2-Ni_1-N_3	91.5(2)	90.2(3)	90.6(2)

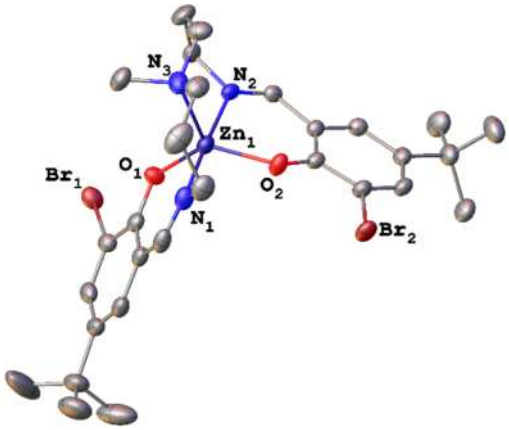
Figure 2.4.2.18: Molecular structure of $Ni^{PhOMe}L_O{}^{NMe}$. H atoms, disordered CH_2 and CH_3 groups and lattice solvent molecules are omitted for clarity; Table 2.4.2.17: Selected bond lengths (Å) and angles (º) for $Ni^{PhOMe}L_O{}^{NMe}$. Z' = 3. τ = 0.63, 0.32 and 0.50).



	Molecule 1	Molecule 2	Molecule 3		Molecule 1	Molecule 2	Molecule 3
Cu_1-N_1	1.997(8)	1.960(8)	1.972(8)	Cu_1-O_1	1.921(9)	1.972(7)	1.961(6)
Cu_1-N_2	1.975(8)	1.952(8)	1.974(8)	Cu_1-O_2	1.960(8)	1.995(7)	1.963(6)
Cu_1-N_3	2.289(12)	2.327(8)	2.295(8)				
O_1-Cu_1-O_2	160.6(4)	143.3(3)	151.4(3)	O_2-Cu_1-N_2	89.9(3)	89.7(3)	89.2(3)
O_1-Cu_1-N_1	88.9(4)	90.8(3)	90.4(3)	O_2-Cu_1-N_3	98.4(4)	106.1(3)	101.1(3)
O_1-Cu_1-N_2	90.2(4)	90.2(3)	90.2(3)	N_1-Cu_1-N_3	90.1(4)	88.4(3)	87.2(3)
O_1-Cu_1-N_3	101.0(4)	110.6(3)	107.5(3)	N_1-Cu_1-N_2	178.1(4)	176.9(3)	176.3(4)
O_2-Cu_1-N_1	91.5(3)	91.3(3)	92.0(3)	N_2-Cu_1-N_3	88.4(4)	88.5(3)	89.2(3)

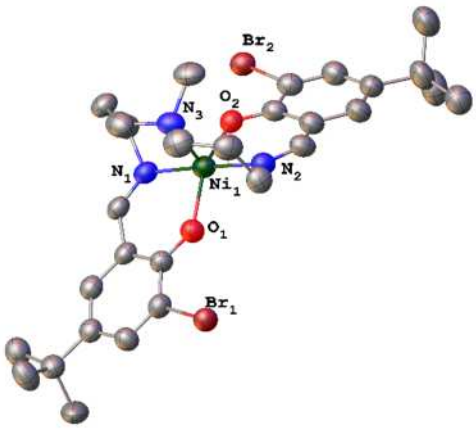
Figure 2.4.2.19: Molecular structure of $Cu^{PhOMe}L_O^{NMe}$. H atoms, disordered CH_2 and CH_3 groups and lattice solvent molecules are omitted for clarity; Table 2.4.2.18.: Selected bond lengths (Å) and angles (°) for $Cu^{PhOMe}L_O^{NMe}$. Z' = 3, τ = 0.29, 0.56, 0.42.

The least bulky complexes with different substituents in the 3 and 5 positions $M^{tBu/Br}L_O^{NMe}$ (M = Zn, Ni, Cu) crystallise in a range of monoclinic and triclinic space groups to give solvated structures with Z' = 1 for $Zn^{tBu/Br}L_O^{NMe}$ and $Ni^{tBu/Br}L_O^{NMe}$ and Z' = 2 for the analogous $Cu^{tBu/Br}L_O^{NMe}$. $Zn^{tBu/Br}L_O^{NMe}$ and $Cu^{tBu/Br}L_O^{NMe}$ exhibit face to face π-π stacking interactions, with no such interactions observed for the $Ni^{tBu/Br}L_O^{NMe}$. No significant edge-to-face π-π interactions are observed with centroid-centroid separations exceeding 5.5 Å in all three cases



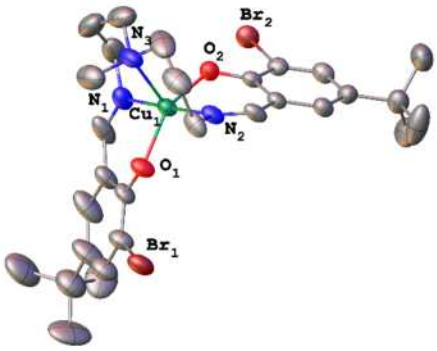
Zn_1-N_1	2.068(2)	Zn_1-O_1	1.9965(18)
Zn_1-N_2	2.054(2)	Zn_1-O_2	1.9788(18)
Zn_1-N_3	2.156(2)		
O_1-Zn_1-O_2	128.54(8)	O_2-Zn_1-N_2	88.50(8)
O_1-Zn_1-N_1	89.24(8)	O_2-Zn_1-N_3	114.76(9)
O_1-Zn_1-N_2	92.73(8)	N_1-Zn_1-N_3	90.38(10)
O_1-Zn_1-N_3	116.67(8)	N_2-Zn_1-N_1	177.43(9)
O_2-Zn_1-N_1	88.98(8)	N_2-Zn_1-N_3	90.22(9)

Figure 2.4.2.20: Molecular structure of $Zn^{tBu/Br}L_O^{NMe}$. H atoms, disordered CH_2 and CH_3 groups and lattice solvent molecules are omitted for clarity; Table 2.4.2.19: Selected bond lengths (Å) and angles (º) for $Zn^{tBu/Br}L_O^{NMe}$. Z' = 1, τ = 0.81.



Ni_1-N_1	2.004(8)	Ni_1-O_1	1.997(6)
Ni_1-N_2	2.015(8)	Ni_1-O_2	1.997(6)
Ni_1-N_3	2.090(8)		
O_1-Ni_1-O_2	153.8(3)	O_2-Ni_1-N_2	89.3(3)
O_1-Ni_1-N_1	88.8(3)	O_2-Ni_1-N_3	102.6(3)
O_1-Ni_1-N_2	89.5(3)	N_1-Ni_1-N_3	91.5(3)
O_1-Ni_1-N_3	103.6(3)	N_1-Ni_1-N_2	177.9(3)
O_2-Ni_1-N_1	91.6(3)	N_2-Ni_1-N_3	90.2(3)

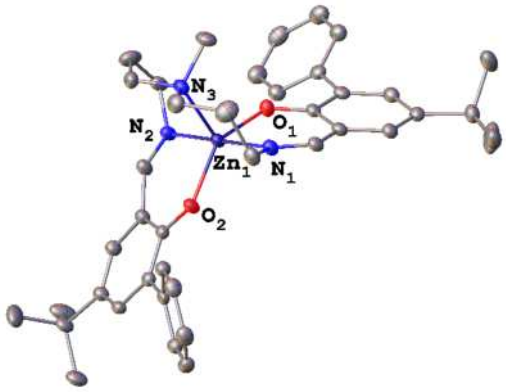
Figure 2.4.2.21: Molecular structure of $Ni^{tBu/Br}L_O^{NMe}$. H atoms, disordered CH_2 and CH_3 groups and lattice solvent molecules are omitted for clarity; Table 2.4.2.20: Selected bond lengths (Å) and angles (º) for $Ni^{tBu/Br}L_O^{NMe}$. Z' = 1, τ = 0.40.



	Molecule 1	Molecule 2		Molecule 1	Molecule 2
Cu_1-N_1	1.942(7)	1.941(6)	Cu_1-O_1	1.936(6)	1.973(5)
Cu_1-N_2	1.959(8)	1.960(6)	Cu_1-O_2	1.965(6)	1.964(4)
Cu_1-N_3	2.306(8)	2.308(7)			
O_1-Cu_1-O_2	150.0(3)	147.5(2)	O_2-Cu_1-N_2	90.6(3)	89.8(2)
O_1-Cu_1-N_1	89.9(3)	91.2(2)	O_2-Cu_1-N_3	107.5(3)	105.4(2)
O_1-Cu_1-N_2	88.5(3)	90.7(2)	N_1-Cu_1-N_3	90.1(3)	91.1(3)
O_1-Cu_1-N_3	102.4(3)	107.1(2)	N_1-Cu_1-N_2	177.9(3)	178.0(2)
O_2-Cu_1-N_1	91.5(3)	88.3(2)	N_2-Cu_1-N_3	89.1(3)	89.1(3)

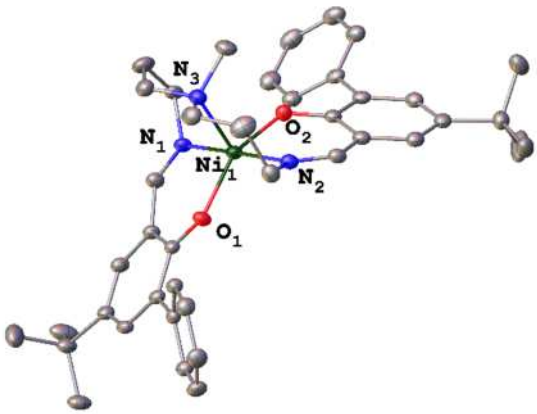
Figure 2.4.2.22: Molecular structure of $Cu^{tBu/Br}L_O^{NMe}$. H atoms, disordered CH_2 and CH_3 groups and lattice solvent molecules are omitted for clarity; Table 2.4.2.21: Selected bond lengths (Å) and angles (º) for $Cu^{tBu/Br}L_O^{NMe}$. Z' = 2. τ = 0.47 and 0.51.

$Zn^{tBu/Ph}L_O^{NMe}$ and $Ni^{tBu/Ph}L_O^{NMe}$ are isomorphous and isostructural, and crystallise in the monoclinic space group $P2^1/c$ with Z' = 1; $Cu^{tBu/Ph}L_O^{NMe}$ also crystallises in $P2^1/c$. The introduction of aromatic substituents at the ortho position of the phenolate rings prevents face-to-face π-π interactions with only very weak edge-face π-π interactions observed between the phenolate ring of one molecule and the ortho-phenyl ring of its neighbour in all three complexes.



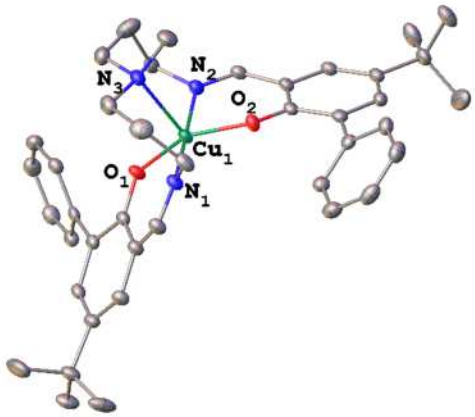
Zn_1-N_1	2.061(2)	Zn_1-O_1	2.0049(15)
Zn_1-N_2	2.045(2)	Zn_1-O_2	1.9980(17)
Zn_1-N_3	2.158(2)		
O_1-Zn_1-O_2	140.27(7)	O_2-Zn_1-N_2	88.87(7)
O_1-Zn_1-N_1	87.16(7)	O_2-Zn_1-N_3	110.49(7)
O_1-Zn_1-N_2	90.19(8)	N_1-Zn_1-N_3	91.08(8)
O_1-Zn_1-N_3	109.24(7)	N_2-Zn_1-N_1	176.92(8)
O_2-Zn_1-N_1	92.17(7)	N_2-Zn_1-N_3	91.27(8)

Figure 2.4.2.23: Molecular structure of $Zn^{tBu/Ph}L_O^{NMe}$. H atoms, disordered CH_2 and CH_3 groups and lattice solvent molecules are omitted for clarity; Table 2.4.2.22: Selected bond lengths (Å) and angles (º) for $Zn^{tBu/Ph}L_O^{NMe}$. Z' = 1. τ = 0.61.



Ni_1-N_1	2.0087(11)	Ni_1-O_1	1.9872(10)
Ni_1-N_2	1.9977(12)	Ni_1-O_2	2.0003(10)
Ni_1-N_3	2.0973(12		
O_1-Ni_1-O_2	150.49(4)	O_2-Ni_1-N_2	89.10(4)
O_1-Ni_1-N_1	88.11(4)	O_2-Ni_1-N_3	105.36(4)
O_1-Ni_1-N_2	89.51(4)	N_1-Ni_1-N_3	91.87(5)
O_1-Ni_1-N_3	104.14(4)	N_1-Ni_1-N_2	176.02(5)
O_2-Ni_1-N_1	91.40(4)	N_2-Ni_1-N_3	91.89(5)

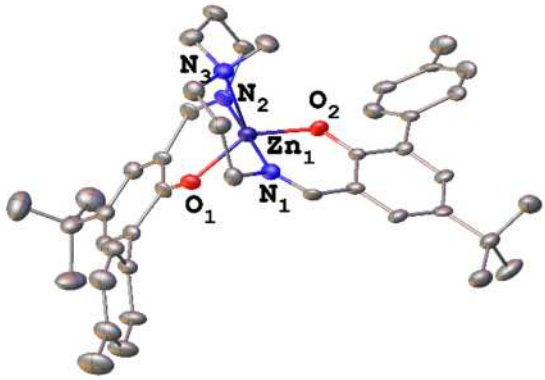
Figure 2.4.2.24: Molecular structure of $Ni^{tBu/Ph}L_O^{NMe}$. H atoms, disordered CH_2 and CH_3 groups and lattice solvent molecules are omitted for clarity; Table 2.4.2.23: Selected bond lengths (Å) and angles (º) for $Ni^{tBu/Ph}L_O^{NMe}$. Z' = 1. τ = 0.43.



Cu_1-N_1	1.9536(13)	Cu_1-O_1	1.9704(11)
Cu_1-N_2	1.9628(13)	Cu_1-O_2	1.9599(11)
Cu_1-N_3	2.3208(13)		
O_1-Cu_1-O_2	153.42(5)	O_2-Cu_1-N_2	89.70(5)
O_1-Cu_1-N_1	90.58(5)	O_2-Cu_1-N_3	102.91(5)
O_1-Cu_1-N_2	91.13(5)	N_1-Cu_1-N_3	88.88(5)
O_1-Cu_1-N_3	103.66(5)	N_1-Cu_1-N_2	177.59(5)
O_2-Cu_1-N_1	89.55(5)	N_2-Cu_1-N_3	89.05(5)

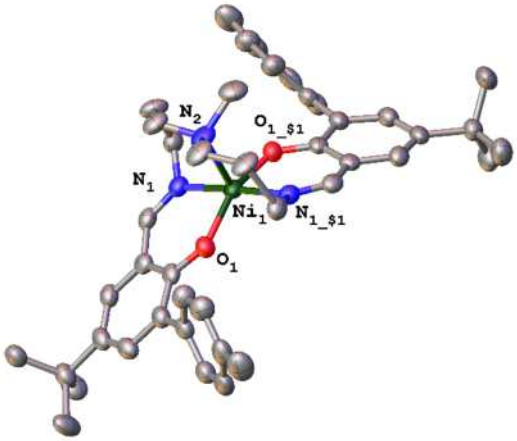
Figure 2.4.2.25: Molecular structure of $Cu^{tBu/Ph}L_O^{NMe}$. H atoms, disordered CH_2 and CH_3 groups and lattice solvent molecules are omitted for clarity; Table 2.4.2.24: Selected bond lengths (Å) and angles (º) for $Cu^{tBu/Ph}L_O^{NMe}$. Z' = 1. τ = 0.40.

$Zn^{tBu/PhMe}L_o^{NMe}$ and $Ni^{tBu/PhMe}L_o^{NMe}$ crystallise in the orthorhombic space groups Pbca and Pcca with Z' = 2 and 0.5 respectively. $Zn^{tBu/PhMe}L_o^{NMe}$ exhibits edge-to-face π-π interactions between both the phenolate ring and the pendant methylphenyl group of the neighbouring molecule, and between two methylphenyl substituents of neighbouring molecules, but no such interactions are observed for $Ni^{tBu/PhMe}L_o^{NMe}$. Suitable crystals of the copper analogue $Cu^{tBu/PhMe}L_O^{NMe}$ could not be obtained despite a range of crystallisation conditions being investigated.



	Molecule 1	Molecule 2		Molecule 1	Molecule 2
Zn_1-N_1	2.052(8)	2.067(9)	Zn_1-O_1	2.009(7)	1.959(8)
Zn_1-N_2	2.043(8)	2.093(9)	Zn_1-O_2	2.005(6)	1.965(8)
Zn_1-N_3	2.191(8)	2.212(11)			
O_1-Zn_1-O_2	138.8(3)	130.6(4)	O_2-Zn_1-N_2	92.2(3)	89.7(4)
O_1-Zn_1-N_1	90.5(3)	89.2(3)	O_2-Zn_1-N_3	111.8(3)	112.3(4)
O_1-Zn_1-N_2	88.5(3)	93.4(3)	N_1-Zn_1-N_3	90.9(3)	88.5(4)
O_1-Zn_1-N_3	109.3(3)	117.1(4)	N_2-Zn_1-N_1	179.0(3)	175.6(4)
O_2-Zn_1-N_1	88.5(3)	91.3(4)	N_2-Zn_1-N_3	89.6(3)	87.2(4)

Figure 2.4.2.26: Molecular structure of $Zn^{tBu/PhMe}L_O{}^{NMe}$. H atoms, disordered CH_2 groups and lattice solvent molecules are omitted for clarity; Table 2.4.2.25: Selected bond lengths (Å) and angles (º) for $Zn^{tBu/PhMe}L_O{}^{NMe}$. Z' = 2, τ = 0.67 and 0.75.

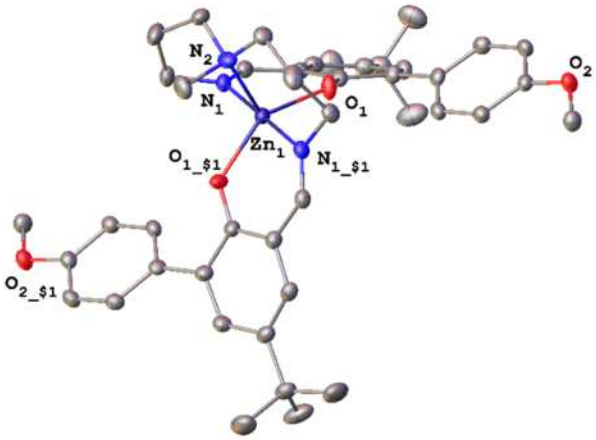


Ni_1-N_1	2.009(3)	Ni_1-O_1	1.972(2)
Ni_1-N_2	2.065(4)		
O_1-Ni_1-$O_{1_\$1}$	156.34(13)	$O_{1_\$1}$-$Ni_1$-$N_{1_\$1}$	88.71(11)
O_1-Ni_1-N_1	88.71(11)	$O_{1_\$1}$-$Ni_1$-$N_2$	101.83(7)
O_1-Ni_1-$N_{1_\$1}$	90.61(10)	N_1-Ni_1-N_2	91.65(8)
O_1-Ni_1-N_2	101.83(7)	N_1-Ni_1-$N_{1_\$1}$	176.70(15)
$O_{1_\$1}$-$Ni_1$-$N_1$	90.61(11)	$N_{1_\$1}$-$Ni_1$-$N_2$	91.65(8)

Figure 2.4.2.27: Molecular structure of $Ni^{tBu/PhMe}L_O{}^{NMe}$. H atoms, disordered CH_2 and CH_3 groups are omitted for clarity; Table 2.4.2.26: Selected bond lengths (Å) and angles (º) for $Ni^{tBu/PhMe}L_O{}^{NMe}$. Z' = 0.5, τ = 0.34. Symmetry operator $1 = 3/2 –x, 1-y, +z

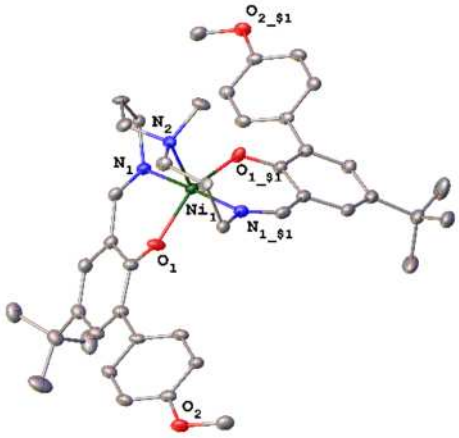
$M^{tBu/PhMe}L_O{}^{NMe}$ (M = Zn, Ni, Cu) crystallise in a range of orthorhombic, monoclinic and triclinic space groups, and none of these three complexes exhibit any formal π-π interactions. $Zn^{tBu/PhMe}L_O{}^{NMe}$ and $Cu^{tBu/PhMe}L_O{}^{NMe}$ both exhibit a

stacking of the methoxy phenyl rings, although the separation of these rings is greater than that which would normally be considered a formal face-to-face π-π interaction (>4.8 Å) (Figure 2.4.33). This stacking is not seen in the structure of $Ni^{tBu/PhMe}L_O^{NMe}$ which exhibits a more close packed structure.



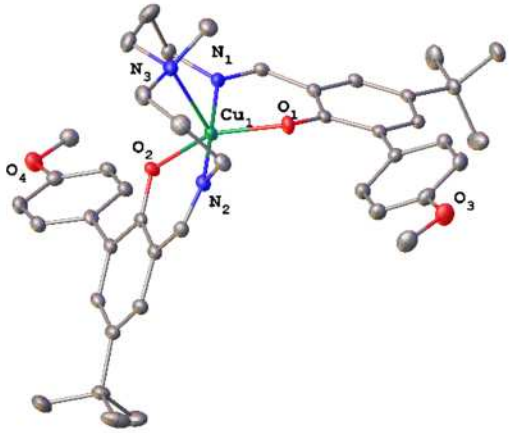
Zn_1-N_1	2.0667(17)	Zn_1-O_1	2.0078(15)
Zn_1-N_2	2.124(3)		
O_1-Zn_1-$O_{1_\$1}$	138.45(11)	$O_{1_\$1}$-$Zn_1$-$N_{1_\$1}$	87.22(7)
O_1-Zn_1-N_1	87.22(7)	$O_{1_\$1}$-$Zn_1$-$N_2$	110.77(5)
O_1-Zn_1-$N_{1_\$1}$	92.37(6)	N_1-Zn_1-N_2	90.57(6)
O_1-Zn_1-N_2	110.77(5)	N_1-Zn_1-$N_{1_\$1}$	178.86(12)
$O_{1_\$1}$-$Zn_1$-$N_1$	92.37(6)	$N_{1_\$1}$-$Zn_1$-$N_2$	90.57(6)

Figure 2.4.2.28: Molecular structure of $Zn^{tBu/PhOMe}L_O^{NMe}$. H atoms and disordered CH_2 and CH_3 groups are omitted for clarity; Table 2.4.2.27: Selected bond lengths (Å) and angles (°) for $Zn^{tBu/PhOMe}L_O^{NMe}$. Z' = 0.5, τ = 0.67. Symmetry operator \$1 = 1-x, 1-y, +



Ni_1-N_1	2.0126(12)	Ni_1-O_1	1.9964(10)
Ni_1-N_2	2.082(2)		
O_1-Ni_1-$O_{1_\$1}$	150.07(7)	$O_{1_\$1}$-$Ni_1$-$N_{1_\$1}$	88.13(5)
O_1-Ni_1-N_1	88.13(5)	$O_{1_\$1}$-$Ni_1$-$N_2$	103.1(8)
O_1-Ni_1-$N_{1_\$1}$	90.98(5)	N_1-Ni_1-N_2	90.5(10)
O_1-Ni_1-N_2	106.8(8)	N_1-Ni_1-$N_{1_\$1}$	176.54(7)
$O_{1_\$1}$-$Ni_1$-$N_1$	90.98(5)	$N_{1_\$1}$-$Ni_1$-$N_2$	93.0(10)

Figure 2.4.2.29: Molecular structure of $Ni^{tBu/PhOMe}L_O^{NMe}$. H atoms and disordered CH_2 and CH_3 groups are omitted for clarity; Table 2.4.2.28: Selected bond lengths (Å) and angles (°) for $Ni^{tBu/PhOMe}L_O^{NMe}$. Z' = 0.5, τ = 0.44. Symmetry operator \$1 = 1-x, +y, 3/2-z



Cu_1-N_1	1.9692(12)	Cu_1-O_1	1.9684(10)
Cu_1-N_2	1.9595(13)	Cu_1-O_2	1.9603(10)
Cu_1-N_3	2.3299(13)		
O_1-Cu_1-O_2	150.89(5)	O_2-Cu_1-N_2	90.83(5)
O_1-Cu_1-N_1	89.56(5)	O_2-Cu_1-N_3	105.61(5)
O_1-Cu_1-N_2	90.47(5)	N_1-Cu_1-N_3	89.04(5)
O_1-Cu_1-N_3	103.50(5)	N_1-Cu_1-N_2	176.81(5)
O_2-Cu_1-N_1	90.47(5)	N_2-Cu_1-N_3	87.85(5)

Figure 2.4.2.30: Molecular structure of $Cu^{tBu/PhOMe}L_O^{NMe}$. H atoms and disordered CH_2 and CH_3 groups are omitted for clarity; Table 2.4.29: Selected bond lengths (Å) and angles (°) for $Cu^{tBu/PhOMe}L_O^{NMe}$. Z' = 1, τ = 0.43.

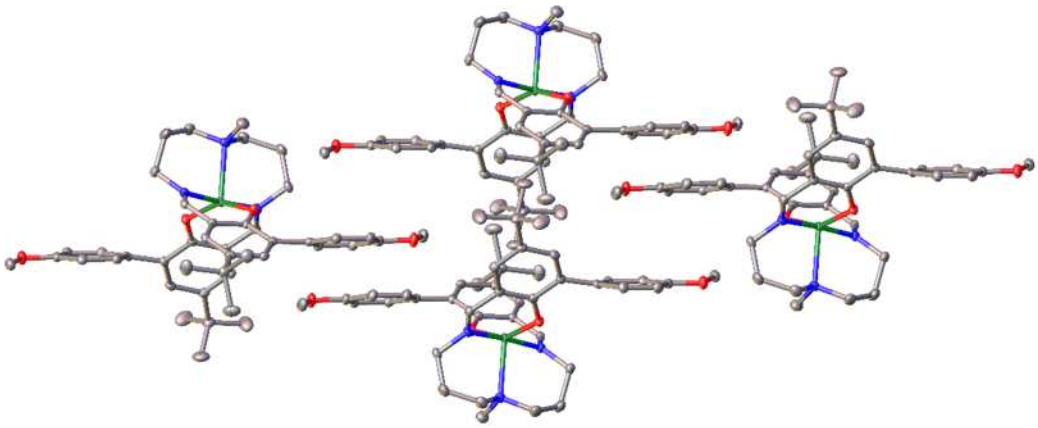
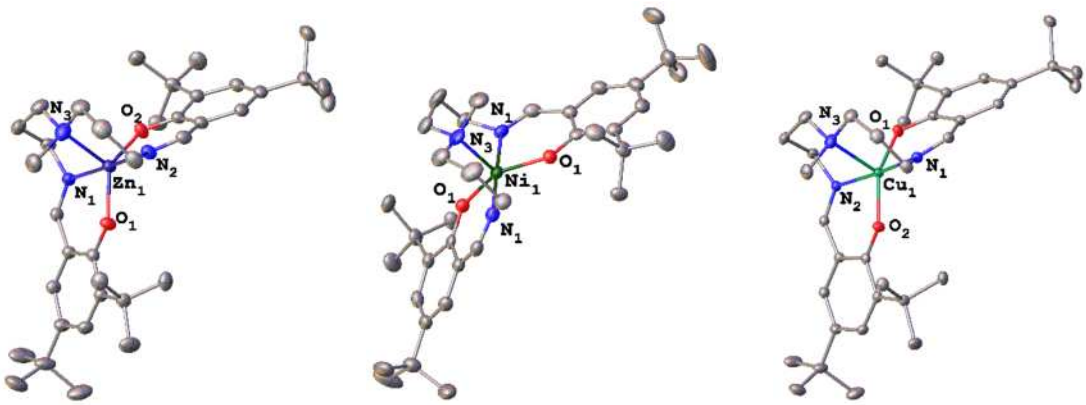


Figure 2.4.31: Extended network of $Cu^{tBu/PhOMe}L_O^{NMe}$ H atoms and disordered CH_2 and CH_3 groups are omitted for clarity

2.4.3 Discussion

$M^RL_O^{NMe}$ (M = Zn, Ni; R = Cl, Br, Nap, Ph, PhMe, PhOMe, ^{t}Bu/Br, ^{t}Bu/Ph, ^{t}Bu/PhMe, ^{t}Bu/PhOMe) and $Cu^RL_O^{NMe}$ (R = Cl, Br, Nap, Ph, PhMe, PhOMe, ^{t}Bu/Br, ^{t}Bu/Ph, ^{t}Bu/PhMe, ^{t}Bu/PhOMe) all exhibit structures which are broadly similar to those observed for the doubly ^{t}butyl substituted analogues $M^{IBu}L_O^{NMe}$ (M = Zn, Ni, Cu) (Figure 2.4.3.1, Table 2.4.3.1)[15] and are similar to other pentacoordinate complexes, including the Ni salicyladehyde dipropylmethylamine complex $Ni^HL_O^{NMe}$ (Ni-O 1.955(10) Å, Ni-$N_{(im)}$ 2.009(11) Å, Ni-$N_{(am)}$ 2.086(8) Å, τ = 0.61).[38] The coordination spheres of all 29 complexes studied also exhibit bond lengths commensurate with those seen in structurally related hexacoordinated complexes including the dioxane coordinated structure of the dichloro species $C_4H_8O_2 \cdot Ni^{Cl}L_O^{NMe}$ (Ni-O 2.014(3) Å, Ni-$N_{(im)}$ 2.024(4) Å, Ni-$N_{(am)}$ 2.147(3) Å) [39]



	$Zn^{tBu}L_O^{NMe}$	$Ni^{tBu}L_O^{NMe}$	$Cu^{tBu}L_O^{NMe}$		$Zn^{tBu}L_O^{NMe}$	$Ni^{tBu}L_O^{NMe}$	$Cu^{tBu}L_O^{NMe}$
M-N_1	2.0535(11)	2.009(3)	1.9668(10)	M-O_1	1.9814(9)	1.996(2)	1.9670(8)
M-N_2	2.0702(11)	2.009(3)	1.9602(10)	M-O_2	1.9907(9)	1.996(2)	1.9573(9)
M-N_3	2.1781(12)	2.099(4)	2.3401(11)				
O_1-M-O_2	137.89(4)	150.66(13)	152.58(4)	O_2-M-N_2	87.65(4)	88.56(10)	90.80(4)
O_1-M-N_1	88.83(4)	88.56(10)	89.60(4)	O_2-M-N_3	110.58(5)	104.67(7)	103.80(4)
O_1-M-N_2	91.78(4)	91.21(10)	91.83(4)	N_1-M-N_3	89.39(5)	90.46(8)	87.23(4)
O_1-M-N_3	111.51(5)	104.67(7)	103.58(4)	N_1-M-N_2	178.54(4)	179.09(15)	174.75(4)
O_2-M-N_1	92.79(4)	91.21(10)	90.26(4)	N_2-M-N_3	89.15(5)	90.46(8)	87.53(4)

Figure 2.4.3.1: Previously reported molecular structures of $Zn^{tBu}L_O^{NMe}$ (Left), $Ni^{tBu}L_O^{NMe}$ (Centre) and $Cu^{tBu}L_O^{NMe}$ (Right).[15] Disordered components and H atoms are omitted for clarity. Table 2.4.3.1: Bond lengths and angles for $Zn^{tBu}L_O^{NMe}$, $Ni^{tBu}L_O^{NMe}$ and $Cu^{tBu}L_O^{NMe}$.[15]

The metal heteroatom bond lengths between different ligand systems and metal centres are compared in Figure 2.4.32. The Zn complexes $Zn^RL_O^{NMe}$ (R = Cl, Br, Nap, Ph, PhMe, PhOMe, ^{t}Bu/Br, ^{t}Bu/Ph, ^{t}Bu/PhMe, ^{t}Bu/PhOMe) exhibit the greatest deviation in bond length between the M-O and M-N(imine) bonds, with the average Zn-O bonds *ca.* 0.07 Å shorter than the Zn-N(imine) average bond length. This difference is significantly smaller for $Ni^RL_O^{NMe}$ (*ca.* 0.02 Å) and is negligible across the $Cu^RL_O^{NMe}$ series. The M-N(amine) bond however is significantly longer than the other metal-heteroatom bonds in all cases, with the longest M-N(amine) bonds observed in $Cu^RL_O^{NMe}$ (R = Cl, Br, Nap, Ph, PhMe, PhOMe, ^{t}Bu/Br, ^{t}Bu/Ph, ^{t}Bu/PhMe, ^{t}Bu/PhOMe) (*ca.* 2.3 Å) and the shortest in $Ni^RL_O^{NMe}$ (*ca.* 2.1 Å).

Some trends in metal-heteroatom bond length may be discerned as the ligand system is varied, particularly across the $Zn^RL_O^{NMe}$ series (R = Cl, Br, Nap, Ph,

PhMe, PhOMe, ^{t}Bu/Br, ^{t}Bu/Ph, ^{t}Bu/PhMe, ^{t}Bu/PhOMe). Whilst the magnitude of the ESD's for the bond lengths in the phenyl substituted complex $Zn^{Ph}L_o{}^{NMe}$ preclude definitive conclusions being drawn, the data suggests that the Zn-N(amine) and Zn-N(imine) bonds elongate with the introduction of more electron donating substituents with the Zn-N(amine) bond length increasing from Ph (2.095(12) Å) < PhMe (2.142(4) Å), to PhOMe (2.164(5) Å) and the Zn-Imine N-donor bond length also increasing to a smaller degree from Ph (2.014(17) Å) to PhMe (2.060(6) Å) ≈ PhOMe (2.064(7) Å). These increases are accompanied by a decrease in the Zn-O bond length from Ph (2.009(14) Å) > PhMe (2.000(4) Å) ≈ PhOMe (1.989(4) Å). Such a trend is not observed where only one substituent of the phenolate ring is varied; few changes in the coordination spheres of $Zn^{tBu/Ph}L_o{}^{NMe}$, $Zn^{tBu/PhMe}L_o{}^{NMe}$ and $Zn^{tBu/PhOMe}L_o{}^{NMe}$ are resolved in the X-ray crystal structures of these compounds.

The structural parameter τ for the complexes studied can also be a useful comparative tool, and τ for all 29 complexes described in this Chapter, together with those of the analogous ^{t}butyl substituted system,[15] are shown in Table 2.3.31. The variations in τ for each ligand set follows the trend Zn^{II}>Ni^{II}~Cu^{II}, with values of τ indicating that in general the Zn^{II} complexes are primarily trigonal bipyramidal, whereas the Ni^{II} and Cu^{II} complexes possess geometries that are intermediate between trigonal bipyramidal and square based pyramidal.[37] No consistent trend is observed for complexes possessing different ligand substituents and this suggests that substitution at the 3 and 5 positions of the phenolate rings does not significantly perturb the geometry of the coordination sphere of the metal centre. The effects of crystal packing must also be considered, as demonstrated by the change in τ value between different molecules in the asymmetric unit for complexes where Z' >1.

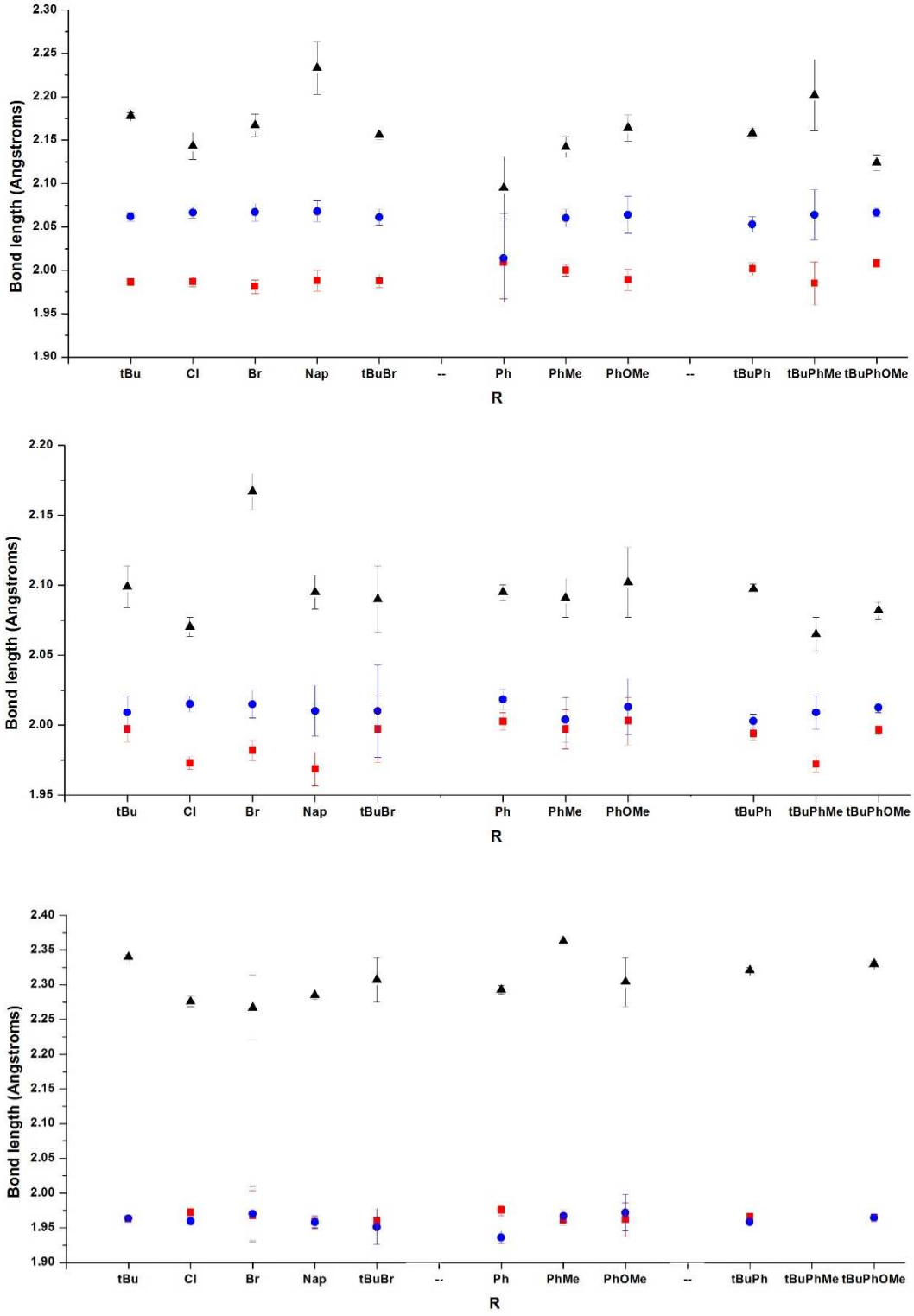


Figure 2.4.3.2: Trends in bond lengths upon changing phenolate ligand substituents for zinc (top) nickel (middle) and copper (bottom) complexes, (M-O (red), M-N_{imine} (blue) M-N_{amine} (black)). Error bars represent 3σ.

Complex	Zn	Ni	Cu
$M^{tBu}L_O^{NMe}$ [15]	0.68	0.47	0.37
$M^{Cl}L_O^{NMe}$	0.85	0.48 (Molecule 1) 0.48 (Molecule 2)	0.50 (Molecule 1) 0.68 (Molecule 2)
$M^{Br}L_O^{NMe}$	0.69 (Molecule 1) 0.82 (Molecule 2)	0.61 (Molecule 1) 0.64 (Molecule 2)	0.50 (Molecule 1) 0.63 (Molecule 2)
$M^{Nap}L_O^{NMe}$	0.74	0.50	0.53
$M^{tBu/Br}L_O^{NMe}$	0.81	0.40	0.47 (Molecule 1) 0.51
$M^{Ph}L_O^{NMe}$	0.40	0.40	0.34
$M^{PhMe}L_O^{NMe}$	0.59 (Molecule 1) 0.66 (Molecule 2)	0.48 (Molecule 1) 0.41 (Molecule 2)	0.29
$M^{PhOMe}L_O^{NMe}$	0.81	0.63 (Molecule 1) 0.50 (Molecule 2) 0.32 (Molecule 3)	0.29 (Molecule 1) 0.56 (Molecule 2) 0.42 (Molecule 3)
$M^{tBu/Ph}L_O^{NMe}$	0.61	0.43	0.40
$M^{tBu/PhMe}L_O^{NMe}$	0.67 (Molecule 1) 0.75 (Molecule 2)	0.34	
$M^{tBu/PhOMe}L_O^{NMe}$	0.67	0.44	0.43

Table 2.4.3.2: Structural parameter τ values for complexes $M^RL_O^{NMe}$.

Whilst some general conclusions can be drawn from these results, the differences in τ value for different molecules of the same complex where Z'>1 demonstrate that it is difficult to fully determine the effect of solid state packing and π-π stacking effects in the structures $M^RL_O^{NMe}$ series (M = Zn, Ni, Cu; R = Cl, Br, Nap, Ph, PhMe, PhOMe, ^{t}Bu/Br, ^{t}Bu/Ph, ^{t}Bu/PhMe, ^{t}Bu/PhOMe). Solution techniques and computational studies may provide more insight as to the effect of changing substitution on the geometry around the metal centre when these solid-state effects are absent.

Taken together our results indicate that the coordination geometry about the metal centre in $M^RL_O^{NMe}$ series (M = Zn, Ni, Cu; R = Cl, Br, Nap, Ph, PhMe, PhOMe, ^{t}Bu/Br, ^{t}Bu/Ph, ^{t}Bu/PhMe, ^{t}Bu/PhOMe) is not significantly perturbed by the introduction of increasingly larger aromatic groups at the 3 and 5 positions of the phenolate rings. However, further study of these species in solution is required in order to eliminate solid state packing effects as a significant factor in these results.

2.4 EPR Spectroscopy

Electron paramagnetic resonance (EPR) spectroscopy has been employed to examine the coordination environment of the metal centre in solution for paramagnetic $Cu^{R}L_{O}^{NMe}$ (R = Cl, Br, Nap, Ph, PhMe, PhOMe, ^{t}Bu/Br, ^{t}Bu/Ph, ^{t}Bu/PhMe, ^{t}Bu/PhOMe). $Ni^{R}L_{O}^{NMe}$ are EPR silent at 77 K in the X band EPR spectrum, due to the presence of multiple unpaired electrons and large zero-field splitting parameters.[40-42] $Cu^{R}L_{O}^{NMe}$ are Cu^{II} d^{9} systems and are EPR active.

X-band EPR spectra of dichloromethane/toluene (10:1) solutions of $Cu^{R}L_{O}^{NMe}$ (R = Cl, Br, Nap, Ph, PhMe, PhOMe, ^{t}Bu/Br, ^{t}Bu/Ph, ^{t}Bu/PhMe, ^{t}Bu/PhOMe) were recorded at 77 K. The complexes exhibit S = ½ rhombic signals with 4 line hyperfine couplings resulting from the coupling of the unpaired electron with ^{63,65}Cu (I = 3/2). Re-recording the spectra after rotation of the sample showed no change in each spectrum demonstrating that each solution formed an amorphous glass.

Simulation of each EPR spectrum was carried out using the Simfonia software package and the experimental and simulated spectra, together with their spin Hamiltonian parameters are shown in Figures 2.4.1-2.4.5. The calculated parameters are consistent with other five coordinate Cu^{II} complexes including $Cu^{tBu}L_{O}^{NMe}$ (g_{xx} = 2.025, g_{yy} = 2.112, g_{zz} = 2.255; A_{xx} = 1 G, A_{yy} = 5 G, A_{zz} = 147 G) and [Cu(L^{2}H)]$CH_{3}OH$ [L^{2}H = 1,4,7-tris(3-^{t}butyl-5-methoxy-2-hydroxy-benzyl) 1,4,7-triazacyclononane] (g_{xx} = 2.06, g_{yy} = 2.05, g_{zz} = 2.25; A_{xx} = A_{yy} = 10.7 G, A_{zz} = 192.8 G),[43] and demonstrate that the ligands provide a similar coordination environment around the Cu^{II} centre to $Cu^{tBu}L_{O}^{NMe}$ in solution.[15] Thus, the EPR spectra of $Cu^{R}L_{O}^{NMe}$ (R = Cl, Br, Nap, Ph, PhMe, PhOMe, ^{t}Bu/Br, ^{t}Bu/Ph, ^{t}Bu/PhMe, ^{t}Bu/PhOMe) are consistent with a pentacoordinate coordination sphere being retained in solution.

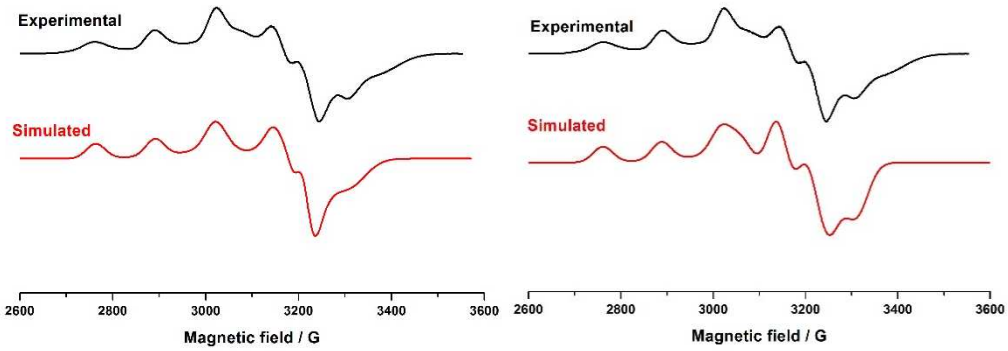


Figure 2.4.1: Left $Cu^{Cl}L_O^{NMe}$*:* g_{xx} *= 2.0850,* g_{yy} *= 2.0800,* g_{zz} *= 2.2425,* A_{xx} *= 7.5 G,* A_{yy} *= 85 G,* A_{zz} *= 129 G Gaussian linewidths* W_{xx} *= 27.0 G,* W_{yy} *= 70.0 G,* W_{zz} *= 40.0 G. ; Right* $Cu^{Br}L_O^{NMe}$*:* g_{xx} *= 2.0790,* g_{yy} *= 2.0730,* g_{zz} *= 2.2455,* A_{xx} *= 20 G,* A_{yy} *= 77 G,* A_{zz} *= 128 G, Gaussian linewidths* W_{xx} *= 40.0 G,* W_{yy} *= 55.0 G,* W_{zz} *= 42.5 G.*

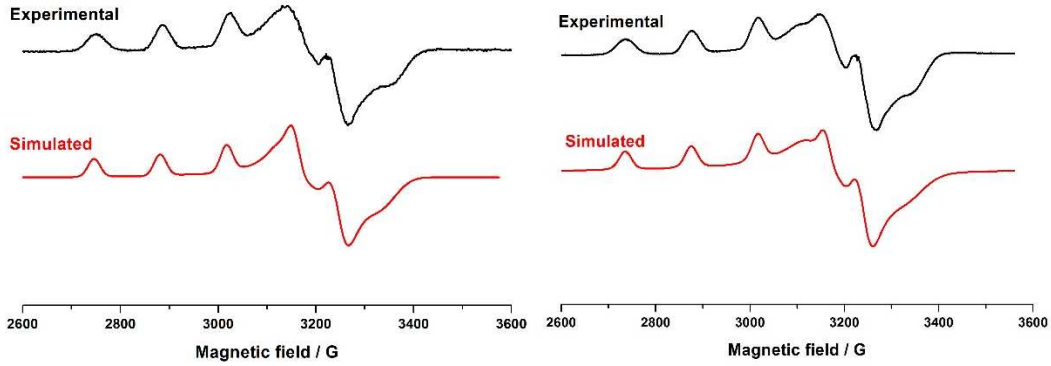


Figure 2.4.2: Left $Cu^{Nap}L_O^{NMe}$*:* g_{xx} *= 2.0510,* g_{yy} *= 2.0720,* g_{zz} *= 2.2510,* A_{xx} *= 50 G,* A_{yy} *= 20 G,* A_{zz} *= 141 G, Gaussian linewidths* W_{xx} *= 37.0 G,* W_{yy} *= 62.0 G,* W_{zz} *= 25.0 G; Right* $Cu^{Ph}L_O^{NMe}$*:* g_{xx} *= 2.0450,* g_{yy} *= 2.0760,* g_{zz} *= 2.2500,* A_{xx} *= 67 G,* A_{yy} *= 25 G,* A_{zz} *= 141 G, Gaussian linewidths* W_{xx} *= 65.0 G,* W_{yy} *= 37.5 G,* W_{zz} *= 28.0 G.*

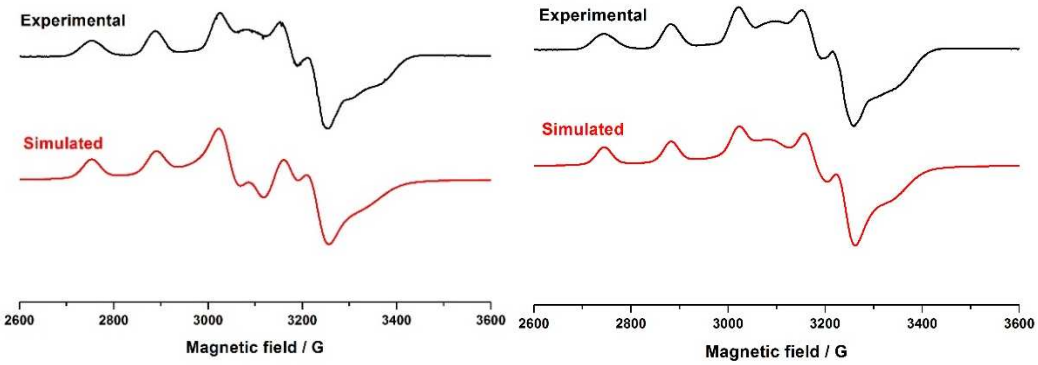


Figure 2.4.3: Left $Cu^{PhMe}L_O^{NMe}$*:* g_{xx} *= 2.0383,* g_{yy} *= 2.0940,* g_{zz} *= 2.2420,* A_{xx} *= 76 G,* A_{yy} *= 40 G,* A_{zz} *= 136.5 G Gaussian linewidths* W_{xx} *= 80.0 G,* W_{yy} *= 40.0 G,* W_{zz} *= 35.0 G.; Right* $Cu^{PhOMe}L_O^{NMe}$*:* g_{xx} *= 2.0540,* g_{yy} *= 2.0760,* g_{zz} *= 2.2450,* A_{xx} *= 77 G,* A_{yy} *= 25 G,* A_{zz} *= 139 G, Gaussian linewidths* W_{xx} *= 65.0 G,* W_{yy} *= 35.0 G,* W_{zz} *= 30.0 G.*

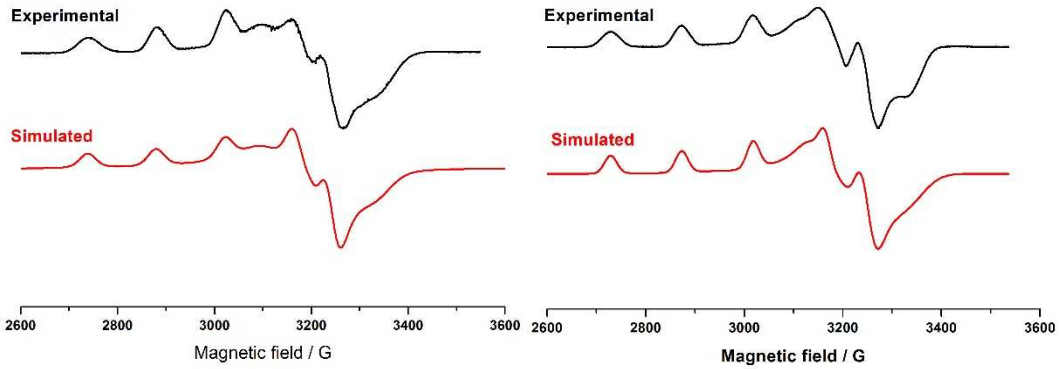


Figure 2.4.4: Left $Cu^{tBu/Br}L_O^{NMe}$*:* g_{xx} *= 2.0540,* g_{yy} *= 2.0720,* g_{zz} *= 2.2465,* A_{xx} *= 72 G,* A_{yy} *= 15 G,* A_{zz} *= 142 G, Gaussian linewidths* W_{xx} *= 65.0 G,* W_{yy} *= 30.0 G,* W_{zz} *= 32.0 G; Right* $Cu^{tBu/Ph}L_O^{NMe}$*:* g_{xx} *= 2.0720,* g_{yy} *= 2.0380,* g_{zz} *= 2.2500,* A_{xx} *= 28 G,* A_{yy} *= 55 G,* A_{zz} *= 145 G, Gaussian linewidths* W_{xx} *= 30.0 G,* W_{yy} *= 70.0 G,* W_{zz} *= 25.0 G.*

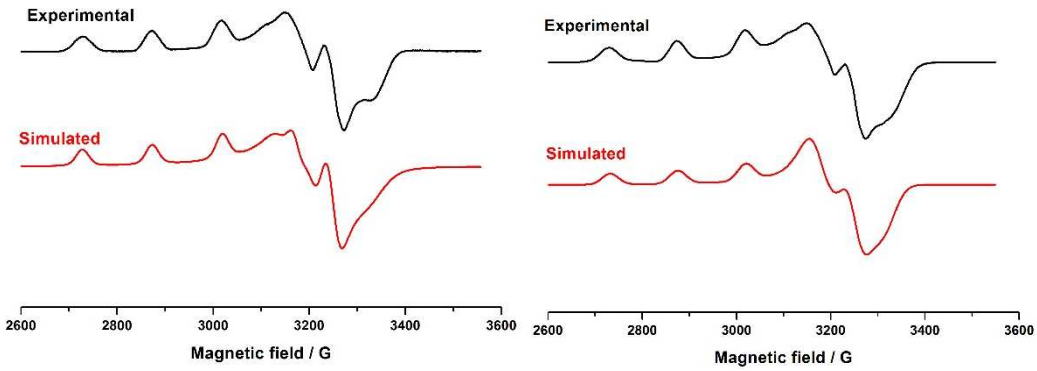


Figure 2.4.5: Left $Cu^{tBu/PhMe}L_O^{NMe}$*:* g_{xx} *= 2.0730,* g_{yy} *= 2.0450,* g_{zz} *= 2.2500,* A_{xx} *= 28 G,* A_{yy} *= 55 G,* A_{zz} *= 146 G, Gaussian linewidths* W_{xx} *= 30.0 G,* W_{yy} *= 65.0 G,* W_{zz} *= 25.0 G; Right* $Cu^{tBu/PhOMe}L_O^{NMe}$*:* g_{xx} *= 2.0740,* g_{yy} *= 2.0400,* g_{zz} *= 2.2500,* A_{xx} *= 28 G,* A_{yy} *= 55 G,* A_{zz} *= 146 G, Gaussian linewidths* W_{xx} *= 40.0 G,* W_{yy} *= 50.0 G,* W_{zz} *= 35.0 G.*

Whilst no large ligand dependent changes are observed in the EPR spectra of $Cu^{R}L_O^{NMe}$ (R = Cl, Br, Nap, Ph, PhMe, PhOMe, ^{t}Bu/Br, ^{t}Bu/Ph, ^{t}Bu/PhMe, ^{t}Bu/PhOMe), analysis of the g values and hyperfine coupling constants in the g_{zz} direction shows some subtle trends. Substitution of the 3, 5 positions with halogens in $Cu^{Cl}L_O^{NMe}$ and $Cu^{Br}L_O^{NMe}$ results in a decrease in g_{zz} and A_{zz} which can potentially be attributed to contributions arising from the larger spin-orbit coupling constant from the heavier halogen atoms in these complexes. The doubly aromatic substituted species $Cu^{Ph}L_O^{NMe}$, $Cu^{PhMe}L_O^{NMe}$ and $Cu^{PhOMe}L_O^{NMe}$ show more variation in g_{zz} and A_{zz} from one another (2.242-2.250 and 136.5-141.0 G) than the singly aromatic substituted compounds $Cu^{tBu/PhMe}L_O^{NMe}$, $Cu^{tBu/PhMe}L_O^{NMe}$ and

$Cu^{tBu/PhMe}L_O^{NMe}$ which all exhibit identical g_{zz} and A_{zz} values (2.25, 146 G) to one another and very similar values to $Cu^{tBu}L_O^{NMe}$ (2.255, 147 G). This reduced change for complexes with identical substituents in the 5 position is consistent with the structural changes in metal-heteroatom bond lengths and τ values that have been observed crystallographically (Section 2.4) with more significant changes observed between complexes with aromatic substituents in the 3 and 5 positions compared to the complexes maintaining a ^{t}butyl substituent in the 5 position. These comparisons are shown in Figure 2.4.6.

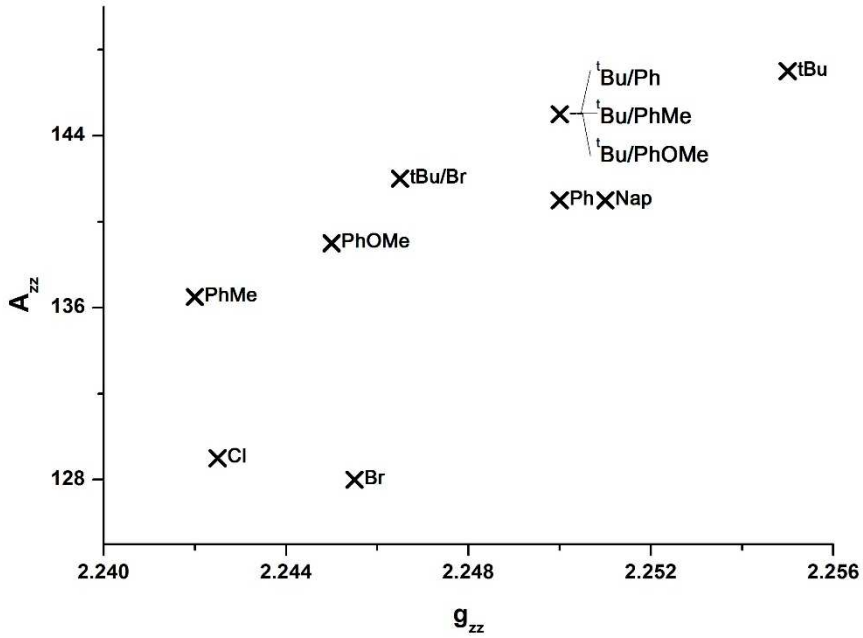


Figure 2.4.6: Plot of g_{zz} vs. A_{zz} for all 10 Cu^{II} complexes $Cu^RL_O^{NMe}$ (R = Cl, Br, Nap, Ph, PhMe, PhOMe, ^{t}BuBr, ^{t}BuPh, ^{t}BuPhMe ^{t}BuPhOMe) studied by EPR spectroscopy, values of $Cu^{tBu}L_O^{NMe}$ included for reference.[15]

These results show that the greatest perturbations in spin Hamiltonian parameters for $Cu^RL_O^{NMe}$ occur when both substituents in the 3 and 5-positions ($Cu^RL_O^{NMe}$ R = Cl, Br, Ph, PhMe, PhOMe) are varied relative to when only the substituent in the 3-position is varied ($Cu^RL_O^{NMe}$; R = ^{t}Bu/Br, ^{t}Bu/Ph, ^{t}Bu/PhMe, ^{t}Bu/PhOMe). This appears to be consistent with the crystallographic results that show smaller changes in the Cu-ligand bond distances as only the substituent in the 3-position is varied relative to those where substituents in both the 3- and 5-postions are varied (Section 2.3). This is potentially interesting when considering the impact of ortho substitution of the tyrosine residue in GO, which is essential in order to modify the redox potential of the tyrosine/tyrosinate radical cofactor.[16, 17] Limited studies have

previously been undertaken examining both tripodal[44] and salen based[27] complexes incorporating phenolate groups with varying substituents in the ortho position (see Chapter 1 Sections 1.5.2 and 1.5.3) which demonstrate an impact of such substitution on redox potential. Our crystallographic and EPR studies show that such substitution has a limited effect on the geometry of the metal centre in $M^{R}L_{O}^{NMe}$ (M = Zn, Ni, Cu; R = ^{t}Bu/Ph, ^{t}Bu/PhMe, ^{t}Bu/PhOMe).

2.5 Density Functional Theory (DFT) Calculations

Density functional theory (DFT) calculations were carried out for models of $M^{R}L_{o}^{NMe}$ (M = Zn, Ni, Cu; R = Ph, PhMe, PhOMe, ^{t}Bu/Ph, ^{t}Bu/PhMe, ^{t}Bu/PhOMe) to provide insight into the potential electronic structures of the complexes described in this Chapter, We have used these calculations to provide a qualitative description of the structure and bonding of the complexes and to provide a framework to interpret the spectroscopic and electrochemical results (Chapter 3). Details of the computational methods used in these calculations are presented in Appendix 3.

Models derived from the X-ray crystal structures of $M^{R}L_{o}^{NMe}$ were used in the gas phase geometry optimisations. Where disordered components are present in the structures, the major component was used to provide a model structure for the calculations. Where Z'<1 a model of the entire molecular structure of one molecule was generated by symmetry. Where Z'>1 ($Zn^{PhMe}L_{o}^{NMe}$, $Ni^{PhMe}L_{o}^{NMe}$, $Ni^{PhOMe}L_{o}^{NMe}$, $Cu^{PhOMe}L_{o}^{NMe}$, $Zn^{tBu/PhMe}L_{o}^{NMe}$) geometry optimisations using coordinates for each molecule were undertaken in order to probe the implications of solid state packing effects upon these structures. For these cases ($Zn^{PhMe}L_{o}^{NMe}$, $Ni^{PhMe}L_{o}^{NMe}$, $Ni^{PhOMe}L_{o}^{NMe}$, $Cu^{PhOMe}L_{o}^{NMe}$, $Zn^{tBu/PhMe}L_{o}^{NMe}$) the gas phase calculations converge to essentially indistinguishable optimised geometries regardless of the starting geometry employed. These results suggest that the difference observed in the crystallographic structures are most likely due to solid state packing effects.

The gas phase geometry optimised structures are compared with the experimental X-ray crystal structures (Tables 2.5.1.1-2.5.1.3). The gas-phase geometry optimised structures were then used as models in single point calculations where the effects of solvation were modelled using COSMO (Conductor-like screening model).[45] Given that our subsequent electrochemical analyses will be carried out in CH_2Cl_2 solution, these calculations provide a framework to interpret the electrochemical results for each complex $M^{R}L_{o}^{NMe}$ (M = Zn, Ni, Cu; R = Ph, PhMe, PhOMe, ^{t}Bu/Ph, ^{t}Bu/PhMe, ^{t}Bu/PhOMe) (Chapter 3).

2.5.1 Geometry Optimisations

The geometry optimised structures were calculated for $M^{R}L_{o}^{NMe}$ (M = Zn, Ni, Cu; R = Ph, PhMe, PhOMe, ^{t}Bu/Ph, ^{t}Bu/PhMe, ^{t}Bu/PhOMe). We also undertook DFT calculations on $M^{tBu}L_{o}^{NMe}$ (M = Zn, Ni, Cu) for comparison.[15] The average metal-heteroatom bond lengths and angles within the coordination sphere, and τ values for the gas phase geometry optimised structures are compared to the experimental values in Tables 2.5.1.1-2.5.1.3 and in Figures 2.5.1.1-2.5.1.3.

The DFT geometry optimised structures generally provide a good model of the crystallographically obtained parameters, with the M-N(imine) bond lengths generally well estimated (largest Δ = 0.064 Å for $Zn^{Ph}L_{o}^{NMe}$, generally < 0.02 Å – Tables 2.5.1.1-2.5.1.2), although they consistently overestimate the M-O and M-N(amine) bond lengths by *ca.* 0.03 and 0.05 Å respectively. The degree of distortion between trigonal bipyramidal and square based pyramidal geometry is well reproduced for each complex with the difference in τ between the experimental and calculated structures (Δτ) generally <0.1. These small deviations in the arrangement of the immediate coordination sphere of the metal centre relative to the crystallographically obtained structures, together with the differences seen in the crystallographic structures where Z'>1 which converge to the same geometry in our DFT calculations indicate that the ligands employed in these complexes are capable of supporting a range of geometries. This may have important implications for the electrochemical properties of the complexes.

	$Zn^{Ph}L_o^{NMe}$	$Zn^{PhMe}L_o^{NMe}$	$Zn^{PhOMe}L_o^{NMe}$	$Zn^{tBu/Ph}L_o^{NMe}$	$Zn^{tBu/PhMe}L_o^{NMe}$	$Zn^{tBu/PhOMe}L_o^{NMe}$	$Zn^{tBu}L_o^{NMe}$
M-O av. X-Ray	2.009(14)	2.000(3)	1.989(4)	2.001(23)	1.985(8)	2.0078(15)	1.9862(13)[15]
M-O av. BP	2.054	2.021	2.017	2.019	2.023	2.047	2.017
M-N(im) av. X-Ray	2.014(17)	2.060(4)	2.064(7)	2.053(3)	2.064(10)	2.0667(17)	2.0618(16)[15]
M-N(im) av. BP	2.078	2.055	2.057	2.05	2.05	2.032	2.043
M-N(amine) X-Ray	2.095(12)	2.142(4)	2.164(5)	2.158(2)	2.202(12)	2.124(3)	2.1781(12)[15]
M-N(amine) BP	2.25	2.274	2.274	2.29	2.285	2.271	2.337
τ av. X-Ray	0.40	0.63	0.81	0.61	0.71	0.67	0.68[15]
τ BP	0.49	0.78	0.76	0.70	0.71	0.61	0.67

Table 2.5.1.1: Comparison of crystallographic and DFT-derived geometric parameters for $Zn^{R}L_o^{NMe}$ (R = Ph, PhMe, PhOMe, ^{t}Bu/Ph, ^{t}Bu/PhMe, ^{t}BuPhOMe and ^{t}Bu).

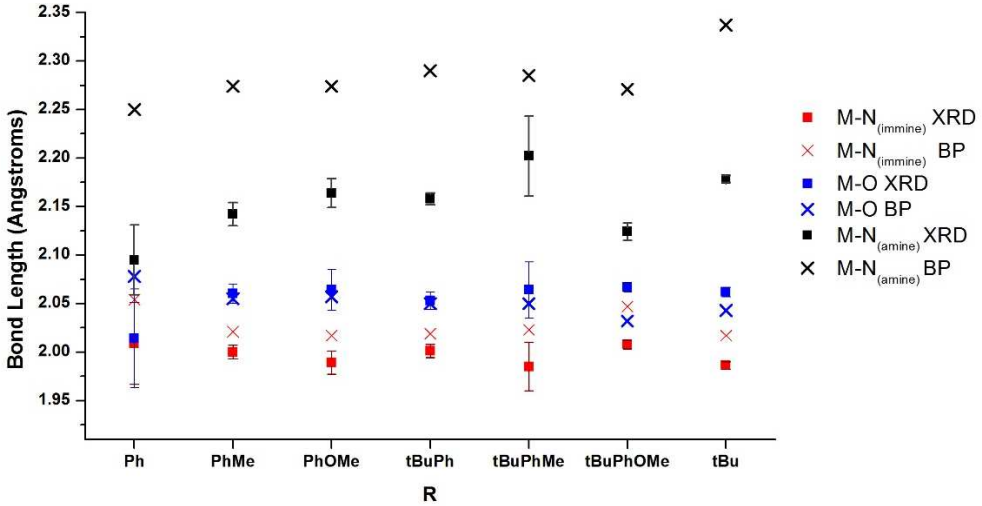


Figure 2.5.1.2: Comparison of crystallographic and DFT-derived geometric parameters for $Zn^{R}L_o^{NMe}$ (R = Ph, PhMe, PhOMe, ^{t}BuPh, ^{t}BuPhMe, ^{t}BuPhOMe, ^{t}Bu). Error bars represent 3σ for crystallographic data.

	$Ni^{Ph}L_o^{NMe}$	$Ni^{PhMe}L_o^{NMe}$	$Ni^{PhOMe}L_o^{NMe}$	$Ni^{tBu/Ph}L_o^{NMe}$	$Ni^{tBu/PhMe}L_o^{NMe}$	$Ni^{tBu/PhOMe}L_o^{NMe}$	$Ni^{tBu}L_o^{NMe}$
M-O av. X-Ray	2.0026(21)	1.997(5)	2.003(6)	1.9938(14)	1.972(3)	1.996(14)	1.997(3)[15]
M-O av. BP	2.019	2.015	2.015	2.020	2.025	2.036	2.030
M-N(im) av. X-Ray	2.01835(24)	2.004(5)	2.013(7)	2.0030(16)	2.01(4)	2.0126(17)	2.009(4)[15]
M-N(im) av. BP	1.989	1.988	1.988	1.987	1.985	1.980	1.986
M-N(amine) X-Ray	2.0950(18)	2.091(7)	2.102(8)	2.0973(12)	2.065(4)	2.082(2)	2.099(4)[15]
M-N(amine) BP	2.126	2.138	2.135	2.130	2.119	2.118	2.143
τ X-Ray	0.40	0.45	0.48	0.49	0.31	0.44	0.47[15]
τ BP	0.46	0.53	0.48	0.43	0.36	0.38	0.57

Table 2.5.1.2: Crystallographic and computational geometric parameters for nickel complexes $Ni^RL_o^{NMe}$

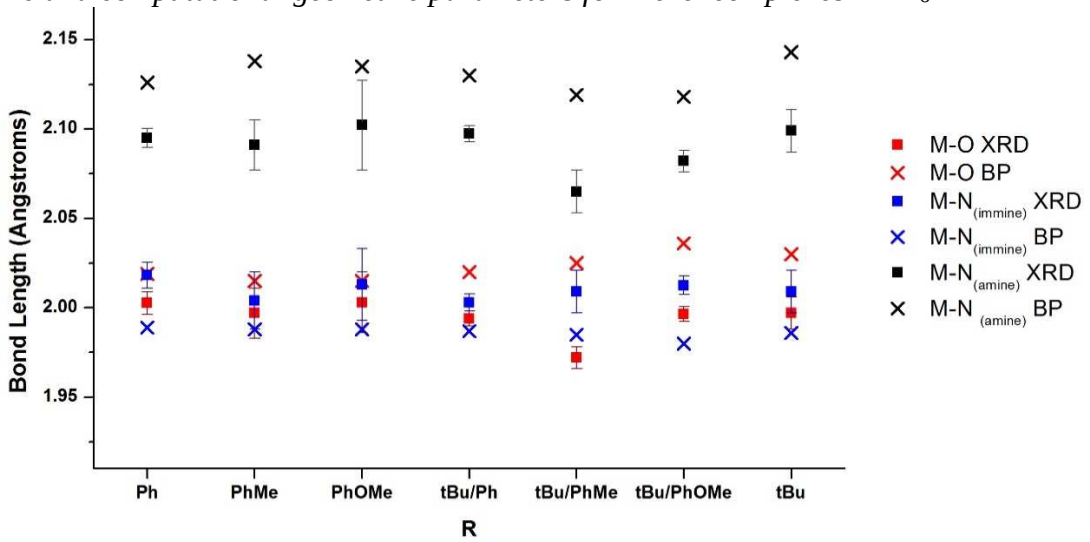


Figure 2.5.1.2: Comparison of crystallographic and DFT-derived geometric parameters for $Ni^RL_o^{NMe}$ *(R = Ph, PhMe, PhOMe,* ^{t}*BuPh,* ^{t}*BuPhMe,* ^{t}*BuPhOMe,* ^{t}*Bu). Error bars represent 3σ for crystallographic data.*

	$Cu^{Ph}L_o^{NMe}$	$Cu^{PhMe}L_o^{NMe}$	$Cu^{PhOMe}L_o^{NMe}$	$Cu^{tBu/Ph}L_o^{NMe}$	$Cu^{tBu/PhMe}L_o^{NMe}$	$Cu^{tBu/PhOMe}L_o^{NMe}$	$Cu^{tBu}L_o^{NMe}$
M-O av. X-Ray	1.9754(25)	1.9608(24)	1.962(8)	1.9652(16)	-	1.9644(14)	1.9622(12)[15]
M-O av. BP	2.018	2.006	2.003	1.974	2.006	2.032	2.011
M-N(im) av. X-Ray	1.936(3)	1.967(3)	1.972(9)	1.9582(18)	-	1.9644(18)	1.9635(14)[15]
M-N(im) av. BP	1.947	1.949	1.952	1.945	1.95	1.956	1.944
M-N(amine) X-Ray	2.293(2)	2.363(2)	2.304(12)	2.3208(13)	-	2.3299(13)	2.3401(11)[15]
M-N(amine) BP	2.385	2.454	2.440	2.462	2.448	2.407	2.520
τ X-Ray	0.34	0.29	0.42	0.40	-	0.43	0.37[15]
τ BP	0.48	0.39	0.40	0.38	0.32	0.43	0.38

Table 2.5.1.3: Comparison of crystallographic and DFT-derived geometric parameters for $Cu^{R}L_o^{NMe}$ *(R = Ph, PhMe, PhOMe, ^{t}Bu/Ph, ^{t}Bu/PhMe, ^{t}BuPhOMe and ^{t}Bu).*

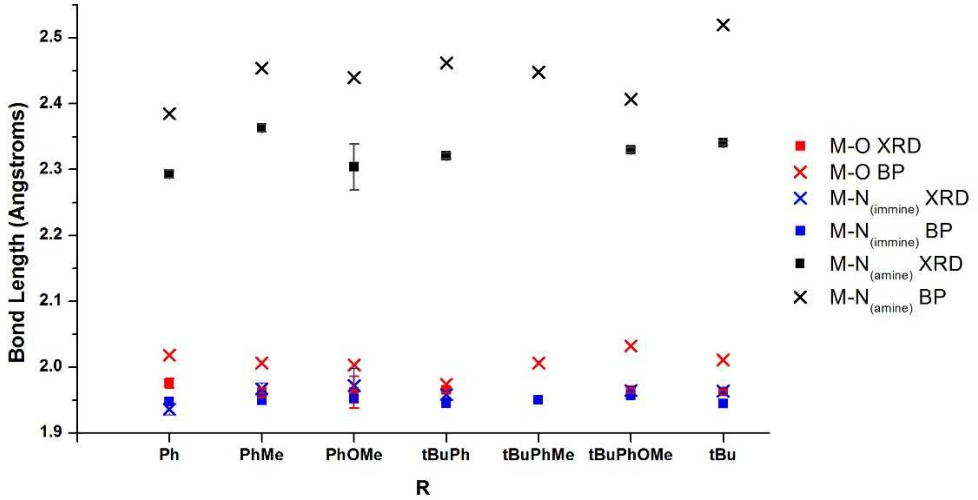
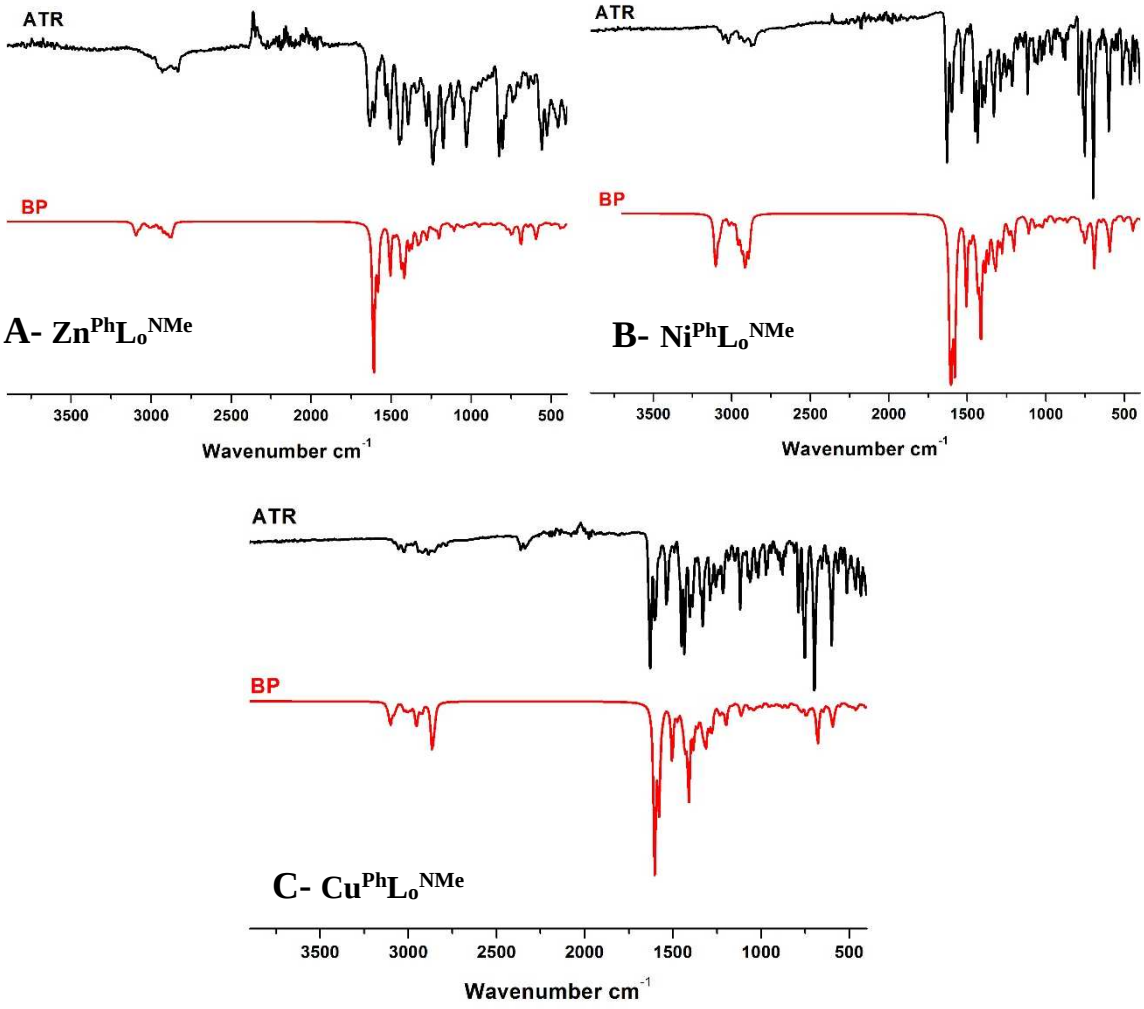


Figure 2.5.1.2: Comparison of crystallographic and DFT-derived geometric parameters for $Cu^{R}L_o^{NMe}$ *(R = Ph, PhMe, PhOMe, ^{t}BuPh, ^{t}BuPhMe, ^{t}BuPhOMe, ^{t}Bu). Error bars represent 3σ for crystallographic data.*

2.5.2 Spectroscopic Calculations

The calculation of vibrational frequencies following DFT geometry optimisations is a useful tool to verify that an energy minimum has been reached in the geometry optimisation calculation. This is assessed *via* the verification of the absence of imaginary frequencies. In addition frequency calculations may be used to help to assign experimental IR spectra. Calculated IR spectra have been compared to the IR spectra recorded for each complex using an IR spectrometer equipped with a ATR cell with good agreement observed in each case. The calculated and experimental spectra of $Zn^{Ph}L_o^{NMe}$, $Ni^{Ph}L_o^{NMe}$ and $Cu^{Ph}L_o^{NMe}$ are shown below as typical examples.



Comparison of experimental (ATR; Black) and computationally calculated (BP; Red) IR spectra for: $Zn^{Ph}L_o^{NMe}$ (A), $Ni^{Ph}L_o^{NMe}$ (B), $Cu^{Ph}L_o^{NMe}$ (C).

In each case the computed and experimental IR spectra of $Zn^{Ph}L_o^{NMe}$, $Ni^{Ph}L_o^{NMe}$ and $Cu^{Ph}L_o^{NMe}$ are similar to one another. Key vibrational bands corresponding to C=N and C-O stretches are well simulated and appear around 1610 and 1415 cm^{-1}, respectively, in both the experimental and calculated spectra. Weak bands around 3100 and 2900 cm^{-1} are assigned to C-H stretches associated with sp^2 and sp^3 hybridised C centres respectively, and also show good agreement with the experimental spectra. These are accompanied by intense bands around 1550 and 1420 cm^{-1} which are assigned to a sp^2 and sp^3 C-H bend respectively. Whilst the full detail of the experimental spectra is not reproduced by the computational simulation, a further increase in spectral intensity is observed in the 700 cm^{-1} region of the calculated spectra corresponding to stronger experimentally observed bands in this region assigned to further C-H bends and C=C bends.

2.5.3 Dichloromethane Solvates and Frontier Orbitals

Single point solvated models in CH_2Cl_2 were calculated using COSMO (Conductor-like screening model)[45] in order to take into account solvent effects that may be important in influencing solution properties. The energies and the metal contributions to the frontier orbitals of these complexes are shown in Tables 2.5.3.1 - 2.5.3.3.

	HOMO		
	Orbital	Energy	% Zn
$Zn^{tBu}L_o^{NMe}$	173A	-0.170179	0
$Zn^{Ph}L_o^{NMe}$	189A	-0.178330	0
$Zn^{PhMe}L_o^{NMe}$	205A	-0.173744	0
$Zn^{PhOMe}L_o^{NMe}$	221A	-0.170396	0
$Zn^{tBu/Ph}L_o^{NMe}$	181A	-0.174306	0
$Zn^{tBu/PhMe}L_o^{NMe}$	189A	-0.171050	0
$Zn^{tBu/PhOMe}L_o^{NMe}$	197A	-0.171874	0

Table 2.5.3.1: HOMO orbital energies for $Zn^{R}L_o^{NMe}$ (R = Ph, PhMe, PhOMe ^{t}Bu/Ph, ^{t}Bu/PhMe, ^{t}Bu/PhOMe)

	HOMO			HOMO-1		
	Orbital	Energy	% Ni	Orbital	Energy	% Ni
$Ni^{tBu}L_o^{NMe}$	173A_A	-0.141536	42.68	171A_B	-0.153217	35.72
$Ni^{Ph}L_o^{NMe}$	189A_A	-0.148281	44.84	187A_B	-0.163488	36.55
$Ni^{PhMe}L_o^{NMe}$	205A_A	-0.146222	44.68	203A_B	-0.160817	36.59
$Ni^{PhOMe}L_o^{NMe}$	219A_B	-0.153578	46.43	221A_A	-0.154123	42.42
$Ni^{tBu/Ph}L_o^{NMe}$	181A_A	-0.148251	41.17	179A_B	-0.159627	36.75
$Ni^{tBu/PhMe}L_o^{NMe}$	189A_A	-0.141899	41.93	187A_B	-0.158606	34.33
$Ni^{tBu/PhOMe}L_o^{NMe}$	197A_A	-0.143311	45.67	195A_B	-0.158669	33.33

Table 2.5.3.1: HOMO and HOMO-1 orbital energies for $Ni^{R}L_o^{NMe}$ (R = Ph, PhMe, PhOMe ^{t}Bu/Ph, ^{t}Bu/PhMe, ^{t}Bu/PhOMe)

	HOMO			HOMO-1		
	Orbital	Energy	% Cu	Orbital	Energy	% Cu
$Cu^{tBu}L_o^{NMe}$	173A_A	-0.159705	33.26	172A_B	-0.165206	12.64
$Cu^{Ph}L_o^{NMe}$	189A_A	-0.165561	32.27	188A_B	-0.172040	11.29
$Cu^{PhMe}L_o^{NMe}$	205A_A	-0.165793	33.36	204A_B	-0.170568	12.22
$Cu^{PhOMe}L_o^{NMe}$	221A_A	-0.164196	31.45	220A_B	-0.167594	9.45
$Cu^{tBu/Ph}L_o^{NMe}$	181A_A	-0.162352	33.26	180A_B	-0.169175	15.50
$Cu^{tBu/PhMe}L_o^{NMe}$	189A_A	-0.160829	33.75	188A_B	-0.169294	12.25
$Cu^{tBu/PhOMe}L_o^{NMe}$	197A_A	-0.165117	34.55	196A_B	-0.169366	9.4

Table 2.5.3.1: HOMO and HOMO-1 orbital energies for $Cu^{R}L_o^{NMe}$ (R = Ph, PhMe, PhOMe ^{t}Bu/Ph, ^{t}Bu/PhMe, ^{t}Bu/PhOMe)

The energies and compositions of these frontier orbitals will aid our future interpretation of our electrochemical results (Chapter Three). The clear differences in orbital composition upon coordination to Zn^{II}, Ni^{II} and Cu^{II} respectively are shown graphically below using the ligand system $^{Ph}L_o^{NMe}$ as an example (Figure 2.3.5.1).

A principally phenolate based HOMO is found for $Zn^{Ph}L_o^{NMe}$, while the HOMO in each of $Ni^{Ph}L_o^{NMe}$ and $Cu^{Ph}L_o^{NMe}$ possesses substantial metal character, 45 and 32 % respectively, with small phenolate ring contributions to the HOMO (<2%).

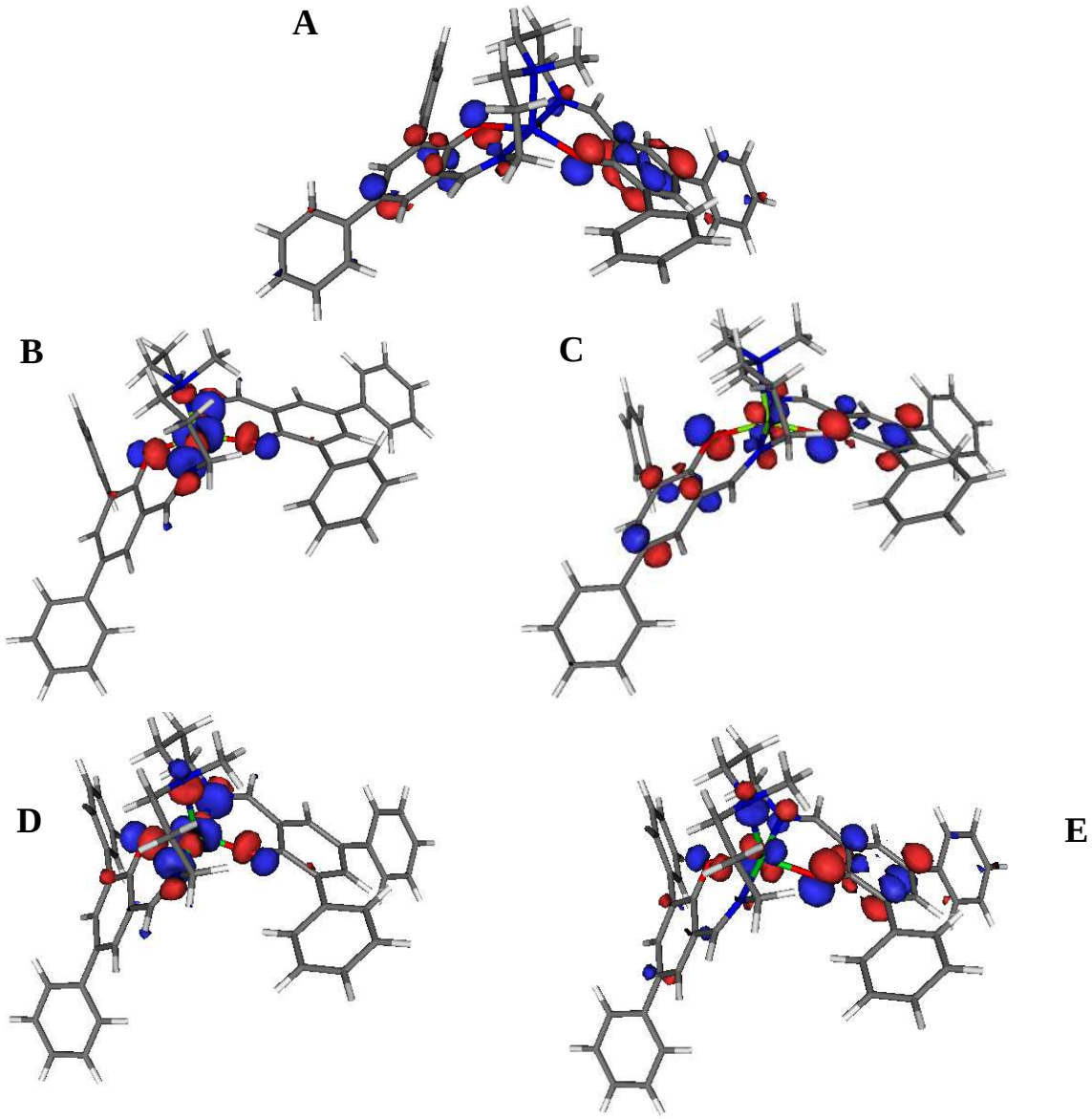


Figure 2.3.5.1: Frontier orbitals of $M^{Ph}L_o^{NMe}$, Isosurface level 0.05 eÅ^{-3} ***A*** *- $Zn^{Ph}L_o^{NMe}$ HOMO,* ***B*** *- $Ni^{Ph}L_o^{NMe}$ HOMO,* ***C*** *- $Ni^{Ph}L_o^{NMe}$ HOMO-1,* ***D*** *- $Cu^{Ph}L_o^{NMe}$ HOMO,* ***E*** *- $Cu^{Ph}L_o^{NMe}$ HOMO-1.*

These calculations do not generally show significant changes between different ligand systems, and further computational work considering the oxidised species will be required in order to draw further conclusions about the effect of ligand substituents upon the electronic structure of the complexes (see Chapter Three).

2.6 Conclusions

An extended range of pentacoordinate diphenolate complexes have been synthesised. We incorporated an extended napthyl system into the ligand framework and used the halogen substituted salicylaldehydes 3,5-dichlorosalicyladehyde and 3,5-dibromosalicyladehyde as precursors to the pentadentate diphenolate-containing ligands $^{Cl}L_O{}^{NMe}$, $^{Br}L_O{}^{NMe}$ and $^{Nap}L_O{}^{NMe}$ in our initial investigations. Suzuki coupling between 3,5-dibromosalicyladehyde and phenylboronic acid, 4-methylphenylboronic acid and 4-methoxyphenylboronic acid allows access to 3,5-diphenylsalicyladehyde, 3,5-di(4-methylphenyl)salicylaldehyde and 3,5-di(4-methoxyphenyl)salicylaldehyde and facilitates the systematic variation of substituents in the 3 and 5 positions of the proligands $^{Ph}L_O{}^{NMe}$, $^{PhMe}L_O{}^{NMe}$ and $^{PhOMe}L_O{}^{NMe}$. The synthesis of 3-bromo-5-^{t}butylsalicyaldehyde allowed the application of a similar Suzuki coupling with phenylboronic acid, 4-methylphenylboronic acid and 4-methoxyphenylboronic acid to give access to 3-phenyl-5-^{t}butylsalicyladehyde, 3-(4-methylphenyl)- 5-^{t}butylsalicylaldehyde and 3-(4-methoxyphenyl) 5-^{t}butylsalicylaldehyde which can be used to extend the range of ligands to include $^{t\text{Bu/Ph}}L_O{}^{NMe}$, $^{t\text{Bu/PhMe}}L_O{}^{NMe}$ and $^{t\text{Bu/PhOMe}}L_O{}^{NMe}$. The incorporation of $^{R}L_O{}^{NMe}$ (R = Ph, PhMe, PhOMe, ^{t}Bu/Br, ^{t}Bu/Ph, ^{t}Bu/PhMe, ^{t}Bu/PhOMe) into Zn^{II}, Ni^{II} and Cu^{II} complexes enables a comprehensive, systematic study of the effects of these substitutions on the spectroscopic and electrochemical properties of these compounds.

$M^RL_O{}^{NMe}$ (M = Zn^{II}, Ni^{II} and Cu^{II}; R = Cl, Br, Nap, Ph, PhMe, PhOMe, ^{t}Bu/Br, ^{t}Bu/Ph, ^{t}Bu/PhMe, ^{t}Bu/PhOMe) have been structurally characterised by single crystal X-ray crystallography, and $Cu^RL_O{}^{NMe}$ have been studied in solution by EPR spectroscopy. $M^RL_O{}^{NMe}$ possess similar coordination spheres and do not show large deviations in their structural characteristics as the 3, 5 diphenolate substituents are varied. The most significant changes in the geometric structures of the complexes observed crystallographically are found in $M^RL_O{}^{NMe}$ (R = Ph, PhMe, PhOMe) as the substituents in the 3 and 5 positions are varied, compared to smaller changes in $M^RL_O{}^{NMe}$ (R = ^{t}Bu/Ph, ^{t}Bu/PhMe, ^{t}Bu/PhOMe) where the 5 substituent is maintained as ^{t}butyl and only the 3 position is modified. Similarly, EPR spectroscopic studies show more variation in g_{zz} from 2.250 to 2.242 and A_{zz}

from 141.0 G to 136.5 G for $M^{R}L_{O}^{NMe}$ (R = Ph, PhMe, PhOMe) than for $M^{R}L_{O}^{NMe}$ (R = ^{t}Bu/Ph, ^{t}Bu/PhMe, ^{t}Bu/PhOMe) where g_{zz} and A_{zz} remain unchanged at 2.250 and 146 G respectively. The observation that substitution at the ortho position appears to have less effect on the geometry of the coordination sphere of the metal centre could have potential relevance to GO and the thioether post translational modification seen in the native enzyme, where the ortho position of the tyrosine residue contains a thioether linkage which is essential in order to modulate the redox potential of the tyrosine/tyrosinate radical co-factor (Chapter 1).[16]

DFT calculations have been used in order to examine the electronic structure of these systems and to inform our spectroscopic assignments and future electrochemical analyses. Differences are seen in the metal contribution to the frontier orbitals, with the largest contribution to the HOMO seen in the Ni^{II} complexes $Ni^{R}L_{O}^{NMe}$ (41-47 %), with their Cu^{II} analogues $Cu^{R}L_{O}^{NMe}$ exhibiting a smaller contribution (31 – 35 %), and the smallest contribution seen in $Zn^{R}L_{O}^{NMe}$ (0 %). This information will be used to aid our future assignment of the redox chemistry of these systems.

2.7 Experimental

2-hydroxy-1-napthaldehyde was prepared from napthalen-2-ol according to literature procedures.[32] 3,3'-diamino-N-methyldiproplamine, 3,5-dichlorosalicyaldehyde, 3,5-dibromosalicyaldehyde, and 4-^{t}butylphenol were obtained from commercial suppliers and used as received. General experimental procedures and details of spectroscopic measurements are given in Appendix 1. Crystallographic methods and experimental data is given in Appendix 2.

Synthesis of 3,5-diphenylsalicyladehyde

A solution of phenylboronic acid (0.87 g, 7.25 mmol), K_2CO_3 (2.00 g, 14.5 mmol), and 3,5-dibromosalicyaldehyde (0.87 g, 3.10 mmol) in a mixture of water (25.0 cm^3) and toluene (100 cm^3) was thoroughly degassed under argon and heated to 50 ºC. P(^{t}Bu)$_3$ (1.50 cm^3, 1.00 mmol solution in toluene, 1.50 mmol) and $Pd_2(dba)_3$ (0.10 g, 0.11 mmol) were added and the solution heated to 80 ºC for 48 hours. The organic layer was extracted with ethyl acetate (3 x 100 cm^3), washed with brine (100 cm^3), dried over Na_2SO_4 and the solvent removed *in vacuo* to give a yellow oil which was purified by column chromatography (petroleum ether: ethyl acetate; 19:1) to give a bright yellow crystalline solid (1.79 g, 90 %).

Elemental Anal.: (calc for $C_{19}H_{14}O_2$); C, 83.19; H, 5.14. Found: C, 82.23; H, 5.16. ^{1}H NMR (400 MHz, $CHCl_3$); 11.65 (1H, s, O*H*), 10.02 (1H, s, CO*H*), 7.93 (1H, d, *J* 2.4, Ar*H*), 7.78 (1H, d, *J* 2.4, Ar*H*), 7.74 (2H, d, *J* 7.0, Ar*H*), 7.66 (2H, d, *J* 7.3, Ar*H*), 7.55 (4H, q, *J* 7.1, Ar*H*), 7.49-7.43 (2H, m, Ar*H*). ^{13}C (100 MHz) $CDCl_3$; 197.0 (*C*H), 158.3 (*C*), 139.3 (*C*), 136.5 (*C*H), 136.4 (*C*), 133.2 (*C*), 131.3 (*C*H), 130.9 (*C*), 129.4 (*C*H), 129.1 (*C*H), 128.4 (*C*H), 127.9 (*C*H), 127.6 (*C*H), 126.7 (*C*H), 121.1 (*C*). FTIR ν/cm^{-1} (ATR): 3060 (w), 2878 (w), 1652 (m), 1602 (w), 1459 (m), 1437 (m), 1405 (w), 1337 (w), 1280 (m), 1204 (m), 1111 (w), 1066 (w), 1028 (w), 764 (m), 744 (m), 630 (s), 597 (m). MS (ESI^+, m/z): 297.0880 $(M + Na)^+$.

Synthesis of 3,5-di (4-methylphenyl)salicylaldehyde

Prepared as 3,5-diphenylsalicylaldehyde using 3,5-dibromosalicylaldehyde (1.00 g, 3.57 mmol), potassium carbonate (1.93 g, 13.9 mmol), 4-methylbenzeneboronic

acid (0.95 g, 6.99 mmol), $Pd_2(dba)_3$ (0.14 g, 0.24 mmol) and $P(^tBu)_3$ (1.75 cm^3, 1.00 mmol solution in toluene, 1.75 mmol) in a mixture of toluene (100 cm^3) and water (27.0 cm^3). (0.79 g, 73 %).

^{1}H NMR (270 MHz, $CDCl_3$); 11.45 (1H, s, O*H*), 10.01 (1H, s, CO*H*), 7.82 (1H, d, *J* 2.2, Ar*H*), 7.72 (1H, d, *J* 2.5, Ar*H*), 7.50 (4H, dd, *J* 11.8 3.7, Ar*H*), 7.28-7.24 (4H, m, Ar*H*), 2.54 (3H, s, CH_3) 2.53 (3H, s, CH_3). ^{13}C (100 MHz, $CDCl_3$); 197.1 (CH), 158.2 (C), 137.7 (C), 137.3 (C), 136.5 (C), 136.2 (CH), 133.5 (C), 133.2 (C), 130.9 (C), 130.8 (CH), 129.8 (CH), 129.3 (CH), 129.2 (CH), 126.6 (CH), 121.1 (C), 21.4 (CH_3), 21.2 (CH_3). FTIR ν/cm^{-1} (ATR): 3025 (w, br), 2970 (w), 1738 (m), 1650 (s), 1516 (w), 1450 (s), 1385 (m), 1276 (m), 1217 (m), 1205 (m), 1111 (m), 812 (s), 771 (s), 729 (s), 587 (m). MS (ESI^+, m/z): 303.1380 $(M + H)^+$, 325.1200 $(M + Na)^+$.

Synthesis of 3,5-di(4-methoxyphenyl)salicylaldehyde

Prepared as 3,5-diphenylsalicylaldehy1de using 3,5-dibromosalicylaldehyde (0.45 g, 1.61 mmol), potassium carbonate (0.88 g, 6.40 mmol), 4-methoxybenzeneboronic acid (0.50 g, 3.29 mmol), $Pd_2(dba)_3$ (0.05 g, 0.06 mmol) and $P(^tBu)_3$ (0.75 cm^3, 1.00 mmol solution in toluene, 0.75 mmol) in toluene (58.0 cm^3) and water (15.0 cm^3). (0.48 g, 89 %).

Elemental Anal.: (calc for $C_{19}H_{14}O_2$); C, 75.43; H, 5.43. Found: C, 73.25; H, 5.46. ^{1}H NMR (270 MHz, $CDCl_3$); 11.45 (1H, s, O*H*), 10.00 (1H, s, CO*H*), 7.78 (1H, d, *J* 2.1, Ar*H*), 7.66 (1H, d, *J* 2.3, Ar*H*), 7.59-7.49 (4H, m, Ar*H*), 7.01-6.96 (4H, m, Ar*H*), 3.89 (3H, s, CH_3), 3.88 (3H, s, CH_3). ^{13}C (100 MHz, $CDCl_3$); 197.1 (CH), 159.4 (C), 159.3 (C), 157.8 (C), 135.9 (CH), 133.0 (C), 131.9 (C), 130.5 (CH), 130.4 (C), 130.3 (CH), 128.7 (C), 127.7 (CH), 121.0 (C), 114.5 (CH), 113.9 (CH), 55.5 (CH_3), 55.4 (CH_3). FTIR ν/cm^{-1} (ATR): 2969 (w, Br), 1738 (m), 1648 (m), 1607 (m), 1512 (m), 1452 (m), 1393 (w), 1284 (m), 1243 (m), 1114 (w), 1026 (m), 928 (w), 831 (s), 734 (m), 701 (m). MS (ESI^+, m/z): 335.1278 $(M + H)^+$.

Synthesis of 2-bromo-4-^{t}butylphenol

A solution of ^{t}butyl phenol (5.00 g, 33.3 mmol) and $NaHCO_3$ (3.60 g, 42.9 mmol) in chloroform (40.0 cm^3) was cooled to 0 ºC and a solution of bromine (5.46 g,

1.76 cm^3, 34.2 mmol) in chloroform (9.00 cm^3) was added dropwise. The solution was stirred at 0 ºC for 3 hours before being quenched by the addition of saturated sodium sulfite solution (20.0 cm^3) and stirred for a further 15 minutes. The organic layer was separated, washed with water (20.0 cm^3), brine (20.0 cm^3) and dried over Na_2SO_4 to give 2-bromo-4-*t*butylphenol as a colourless oil (5.90 g, 78 %).

^{1}H NMR (400 MHz, $CHCl_3$); 7.47 (1H, d, *J* 2.4, Ar*H*), 7.27 (1H, dd, *J* 2.3 8.7, Ar*H*), 6.98 (1H, d, *J* 8.5, Ar*H*), 1.31 (9H, s, CH_3); ^{13}C NMR (100 MHz, $CHCl_3$); 149.9 (*C*), 145.1 (*C*), 128.8 (*C*H), 126.3 (*C*H), 115.5 (*C*H), 109.9 (*C*), 34.2 (*C*), 31.4 (*C*H_3). FTIR ν/cm^{-1} (Thin Film): 3513 (br), 2963 (s), 2867 (m), 1604 (w), 1577 (w), 1499 (s), 1480 (m), 1404 (w), 1364 (w), 1332 (w), 1286 (m), 1268 (m), 1210 (m), 1183 (m), 1039 (m), 875 (m), 820 (s), 759 (m), 737 (m). MS(EI$^+$, m/z): 228.0150 $(M)^+$.

Synthesis of 3-bromo-4-*t*butylsalicylaldehyde

Triethylamine (1.50 g, 15.0 mmol) was added to a solution of magnesium dichloride (0.95 g, 10 mmol) and paraformaldehyde (0.45 g, 15.0 mmol) in THF (20.0 cm^3) and stirred for 10 minutes at room temperature. 2-bromo-4-tbutylphenol (1.15 g, 5.00 mmol) was added and the solution heated to reflux for 2 hours. The reaction mixture was cooled to room temperature, diluted with ether (10.0 cm^3) and quenched with hydrochloric acid (20.0 cm^3, 1.00 M) to give a colourless solution. The organic layer was separated, washed with further hydrochloric acid (20.0 cm^3, 1.00 M), and water (20.0 cm^3) and dried over $MgSO_4$ to give 3-bromo-4-*t*butylsalicyaldehyde as a pale yellow solid (0.60 g, 47 %).

Elemental Anal.: (calc for $C_{19}H_{14}O_2$); C, 51.38; H, 5.10. Found: C, 50.58; H, 5.07. ^{1}H NMR (400 MHz, $CHCl_3$); 11.44 (1H, s, O*H*), 9.88 (1H, s, CO*H*), 7.84 (1H, d, *J* 2.1, Ar*H*), 7.54 (1H, d, *J* 2.4, Ar*H*), 1.36 (9H, s, CH_3). ^{13}C NMR (100 MHz, $CHCl_3$); 196.2 (*C*H), 155.9 (*C*), 144.2 (*C*), 137.7 (*C*H), 129.4 (*C*H), 120.7 (*C*), 110.9 (*C*), 34.3 (*C*), 31.2 (*C*H_3). FTIR ν/cm^{-1} (ATR): 2959 (m), 2872 (w), 1654 (m), 1456 (m), 1417 (m), 1380 (m), 1263 (s), 1217 (m), 1160 (s), 1120 (m), 1042 (w), 891 (m), 821 (m), 735 (s), 693 (s), 630 (m).

Synthesis of 3-phenyl-4-^{t}butylsalicyaldehyde

Prepared as 3,5-diphenylsalicyladehyde, using 3-bromo-4-tbutylsalicyaldehyde (0.50 g, 2.00 mmol), phenylboronic acid (0.27 g, 2.25 mmol), K_2CO_3 (0.63 g, 4.60 mmol), $Pd_2(dba)_3$ (0.03 g, 0.03 mmol) and P(^{t}butyl)$_3$ (0.47 cm^3, 1.00 mol solution in toluene, 0.47 mmol), in water (12.5 cm^3) and toluene (50.0 cm^3) at 80 ºC for 48 hours to give a yellow oil which was purified by column chromatography (petroleum ether: ethyl acetate 19:1) to give 3-phenyl-4-^{t}butylsalicyaldehyde as a yellow crystalline solid (0.27 g, 53 %).

Elemental Anal.: (calc for $C_{17}H_{18}O_2$); C, 80.28; H, 7.13. Found: C, 79.75; H, 7.23. ^{1}H NMR (400 MHz, $CHCl_3$); 11.39 (1H, s, O*H*), 9.99 (1H, s, C=O*H*), 7.69 (1H, d, J 2.5, Ar*H*), 7.64 (1H, t, J 1.6, Ar*H*), 7.62 (1H, s, Ar*H*), 7.56 (1H, d, J 2.5, Ar*H*), 7.49 (2H, t, J 7.5, Ar*H*), 7.44-7.39 (1H, m, Ar*H*), 1.41 (9H, s, CH_3). ^{13}C NMR (100 MHz, $CHCl_3$); 197.0 (*C*), 156.8 (*C*), 142.8 (*C*), 136.9 (*C*), 135.7 (*C*H), 130.0 (*C*), 129.4 (*C*H), 128.8 (*C*H), 128.3 (*C*H), 127.6 (*C*H), 120.3 (*C*), 34.2 (*C*), 31.3 (*C*H$_3$). FTIR ν/cm^{-1} (ATR): 3054 (m), 2863 (w), 1639 (s), 1614 (m), 1460 (s), 1439 (m), 1410 (m), 1384 (m), 1292 (m), 1280 (m), 1216 (s), 1129 (m), 955 (m), 887 (m), 768 (s), 736 (m), 717 (m), 695 (s), 637 (s), 546 (s), 518 (m). MS (ESI$^+$, m/z): 255.1382 (M + H)$^+$

Synthesis of 3-(4-methylphenyl)-5-^{t}butylsalicyaldehyde

Prepared as 3,5-diphenylsalicyladehyde, using 3-bromo-5-^{t}butyl-2-hydroxybenzaldehyde (2.50 g, 8.14 mmol), potassium carbonate (2.50 g, 18.0 mmol) 4-methylphenylboronic acid (1.53 g, 11.2 mmol), $Pd_2(dba)_3$ (0.15 g, 0.25 mmol) and P(^{t}Bu)$_3$ (2.00 cm^3, 1.00 mmol solution in toluene, 2.00 mmol) in a mixture of toluene (250 cm^3) and water (62.5 cm^3) at 90 ºC for 48 hours to give a yellow oil which was purified by column chromatography (petroleum ether: ethyl acetate 19:1) to give 3-(4-methylphenyl)-5-^{t}butylsalicyaldehyde as a yellow crystalline solid. (2.10 g, 96 %)

Elemental Anal.: (calc for $C_{18}H_{20}O_2$); C, 80.56; H, 7.51. Found: C, 80.32; H, 7.61. ^{1}H NMR (400 MHz, $CHCl_3$); 11.37 (1H, s, OH), 9.97 (1H, s, CO*H*), 7.68 (1H, dd, *J* 2.3, 0.8, Ar*H*), 7.54-7.52 (3H, m, Ar*H*), 7.31-7.28 (2H, m, Ar*H*), 2.44 (3H, s,

C*H*$_3$), 1.40 (9H, s, C*H*$_3$). ^{13}C (100 MHz, $CDCl_3$); 197.1 (*C*H), 156.8 (*C*), 142.7 (*C*), 137.4 (*C*), 135.6 (*C*H), 133.9 (*C*), 130.0 (*C*), 129.2 (*C*H), 129.1 (*C*H), 129.0 (*C*H), 120.3 (*C*), 34.2 (*C*), 31.3 (*C*H_3), 21.3 (*C*H_3). FTIR ν/cm^{-1} (ATR): 2965 (m), 2868 (w), 1636 (s), 1450 (m), 1326 (s), 1282 (s), 1249 (s), 1211 (s), 1113 (s), 1020 (m), 955 (m), 888 (w), 820 (s), 771 (s), 738 (s), 702 (s), 646 (m), 634 (w), 585 (w). MS (ESI$^+$, m/z): 269.1528 $(M + H)^+$.

Synthesis of 3-(4-methoxyphenyl)-5-^{t}butylsalicyaldehyde

Prepared as 3,5-diphenylsalicyladehyde, using 3-bromo-5-^{t}butyl-2-hydroxybenzaldehyde (2.50 g, 8.14 mmol), potassium carbonate (2.21 g, 16.0 mmol) 4-methoxyphenylboronic acid (1.29 g, 8.50 mmol), $Pd_2(dba)_3$ (0.07 g, 0.12 mmol) and P(^{t}Bu)$_3$ (1.88 cm^3, 1.00 mmol solution in toluene, 1.88 mmol) in a mixture of toluene (200 cm^3) and water (50.0 cm^3) at 90 ^{o}C for 48 hours to give a yellow oil which was purified by column chromatography (petroleum ether: ethyl acetate 19:1) to give 3-(4-methoxyphenyl)-5-^{t}butylsalicyaldehyde as a yellow crystalline solid. (1.37 g, 59 %).

Elemental Anal.: (calc for $C_{18}H_{20}O_3$); C, 76.03; H, 7.09. Found: C, 75.49; H, 7.21. ^{1}H NMR (270 MHz, $CDCl_3$); 11.37 (1H, s, O*H*), 9.93 (1H, s, CO*H*), 7.64 (1H, d, *J* 2.5, Ar*H*), 7.54 (2H, dt, *J* 8.8, 2.1, Ar*H*), 7.49 (1H, d, *J* 2.6, Ar*H*), 6.99 (2H, dt, *J* 8.8, 2.1, Ar*H*), 3.85 (3H, s, C*H*$_3$), 1.36 (9H, s, C*H*$_3$). ^{13}C (100 MHz, $CDCl_3$); 197.2 (*C*H), 159.2 (*C*), 156.8 (*C*), 142.8 (*C*), 135.5 (*C*H), 130.5 (*C*H), 129.7 (*C*), 129.2 (*C*), 129.0 (*C*H), 120.3 (*C*), 113.8 (*C*H), 55.4 (*C*H_3), 34.3 (*C*), 31.4 (*C*H_3). FTIR ν/cm^{-1} (ATR): 2960 (m), 1738 (w), 1635 (s), 1608 (s), 1513 (m), 1327 (m), 1244 (s), 1181 (m), 1067 (m), 955 (w), 832 (m), 788 (m), 703 (m), 593 (w). MS (ESI$^+$, m/z): 285.1492 $(M + H)^+$.

Typical Procedure for the Synthesis of Proligands

Proligands were prepared according to a modified literature procedure.[10] 3,3'-diamino-N-methyldipropylamine (0.56 g, 3.90 mmol) was added dropwise to a solution of 3,5-disubstituted salicyladehyde (7.80 mmol) in methanol (50.0 cm^3) and stirred at room temperature for 1 hour. The solvent was removed *in vacuo* to give the proligand as a yellow oil which was used immediately without further purification.

$^{Cl}L_O^{NMe}$:

(98 %). ^{1}H NMR (270 MHz, $CDCl_3$): 8.22 (2H, s, N=C*H*), 7.38 (2H, d, J 2.6, Ar*H*), 7.09 (2H, d, J 2.5, Ar*H*), 3.67 (4H, t, J 6.6, CH_2), 2.47-2.35 (4H, m, CH_2), 2.20 (3H, s, NCH_3), 1.85 (4H, quin, J 6.78, CH_2); δ ^{13}C NMR (100 MHz, $CDCl_3$): 163.6 (*C*H), 159.4 (*C*), 132.3 (*C*H), 129.0 (*C*H), 123.5 (*C*), 120.7 (*C*), 118.3 (*C*), 55.0 (*C*H_2), 54.8 (*C*H_2), 41.7 (*C*H_3), 27.9 (*C*H_2). MS(ESI$^+$, m/z): 492.0584 (M + H)$^+$

$^{Br}L_O^{NMe}$:

(97 %). ^{1}H NMR (270 MHz, $CDCl_3$); 8.17 (2H, s, N=C*H*), 7.67 (2H, t, J 2.3, Ar*H*), 7.30-7.25 (2H, m, Ar*H*), 3.67 (4H, t, J 6.5, C*H*2), 2.46-2.36 (4H, m, CH_2), 2.19 (3H, d, J 3.9, NCH_3), 1.85 (4H, quin, J 6.75, CH_2); ^{13}C NMR (100 MHz, $CDCl_3$): 163.6 (*C*H), 161.2 (*C*), 137.9 (*C*H), 132.8 (*C*H), 118.7 (*C*), 113.9 (*C*), 107.5 (*C*), 54.8 (*C*H_2), 54.7 (*C*H_2), 41.8 (*C*H_3), 27.9 (*C*H_2). MS(ESI$^+$, m/z): 669.8475 (M + H)$^+$

$^{Nap}L_O^{NMe}$:

(98 %). ^{1}H NMR (400 MHz, $CDCl_3$); 8.65 (1H, d, J 12.3, N=C*H*), 7.81-7.74 (1H, m, Ar*H*), 7.62 (1H, t, J 7.9, Ar*H*), 7.53 (1H, t, J 8.8, Ar-*H*), 7.40-7.30 (1H, m, Ar*H*), 7.19-7.13 (1H, m, Ar*H*), 6.87 (1H, d, J 9.4, Ar*H*), 3.62-3.56 (2H, m, CH_2), 3.41-3.39 (2H, m, CH_2), 2.68 (1H, q, J 6.9, CH_2), 2.44-2.32 (4H, m, CH_2), 2.19-2.16 (3H, m, NCH_3), 1.86-1.80 (2H, m, CH_2), 1.58 (1H, quint., J 6.7, CH_2); ^{13}C (100 MHz) $CDCl_3$; 177.5 (*C*), 157.9 (*C*H), 137.4 (*C*H), 134.0 (*C*), 129.2 (*C*H), 127.9 (*C*H), 126.1 (*C*), 125.5 (*C*H), 122.6 (*C*H), 117.7 (*C*H), 106.3 (*C*), 55.0 (*C*H_2), 50.8 (*C*H_2), 41.6 (*C*H_3), 28.1 (*C*H_2). MS(ESI$^+$, m/z): 454.2492 (M + H)$^+$

$^{Ph}L_o^{NMe}$

(98 %). ^{1}H NMR (270 MHz, $CHCl_3$); 8.49 (2H, s, C=N*H*), 7.68-7.64 (5H, m, Ar*H*), 7.59-7.51 (4H, m, Ar*H*), 7.49-7.31 (15H, m, Ar*H*), 3.72 (4H, t, *J* 6.5, CH_2), 2.58 (4H, s br, CH_2), 2.34 (3H, s, NCH_3), 1.99 (4H, s br, CH_2). ^{13}C (100 MHz) $CDCl_3$; 165.2 (*C*H), 158.7 (*C*), 140.3 (*C*), 137.8 (*C*), 132.0 (*C*H), 131.5 (*C*), 130.3 (*C*), 129.4 (*C*H), 129.0 (*C*H), 128.9 (*C*H), 128.2 (*C*H), 127.3 (*C*H), 126.9 (*C*H), 126.6 (*C*H), 119.0 (*C*), 57.2 (*C*H_2), 55.2 (*C*H_2), 42.0 (*C*H_3), 28.5 (*C*H_2). MS(ESI$^+$, m/z): 658.3403 (M + H)$^+$

PhMeL^{Me}

(91 %). ^{1}H NMR (400 MHz, $CDCl_3$); 8.44 (2H, d, *J* 7.4, C=N*H*), 7.61-7.58 (2H, m, Ar*H*), 7.57-7.52 (4H, m, Ar*H*), 7.48-7.38 (7H, m, Ar*H*), 7.27-7.19 (7H, m, Ar*H*), 3.66 (4H, t, *J* 5.9, CH_2), 3.46 (3H, s, NCH_3), 2.77-2.70 (4H, m, CH_2), 2.44-2.35 (16H, m, *Ph*-CH_3/CH_2), ^{13}C (100 MHz, $CDCl_3$); 165.2 (*C*H), 158.3 (*C*), 137.54 (*C*), 136.9 (*C*), 136.5 (*C*), 134.9 (*C*), 131.7 (*C*H), 131.4 (*C*), 130.2 (*C*), 129.5 (*C*H), 129.2 (*C*H), 128.9 (*C*H), 128.5 (*C*), 126.4 (*C*H), 118.9 (*C*), 57.2 (*C*H_2), 55.7 (*C*H_2), 55.2 (*C*H_2), 42.1 (*C*H_3), 28.5 (*C*H_2), 21.2 (*C*H_3), 21.1 (*C*H_3). MS (ESI$^+$, m/z): 714.4054 $(M + H)^+$

PhOMeL^{NMe}

(88 %). ^{1}H NMR (270 MHz, $CDCl_3$); 8.42 (2H, d, *J* 8.4, C=N*H*), 7.65-7.57 (8H, m, Ar*H*), 7.54-7.47 (4H, m, Ar*H*), 7.40 (1H, d, J 2.4, Ar*H*), 7.36 (1H, d, *J* 2.4, Ar*H*), 7.03-6.94 (8H, m, Ar*H*), 3.88-3.84 (12H, m, OCH_3), 3.70-3.67 (4H, m, CH_2), 3.47 (3H, s, NCH_3), 2.78-2.73 (4H, m, CH_2), 2.47-2.43 (4H, m, CH_2). ^{13}C (100 MHz, $CDCl_3$); 207.0 (*C*), 165.3 (*C*H), 158.9 (*C*), 158.8 (*C*), 158.8 (*C*), 158.0 (*C*), 133.1 (*C*), 131.4 (*C*H), 130.5 (*C*H), 130.2 (*C*), 128.1 (*C*H), 127.6 (*C*H), 118.9 (*C*), 114.3 (*C*H), 113.7 (*C*H), 57.2 (*C*H_2), 55.7 (*C*H_2), 55.3 (*C*H_3), 50.5 (*C*H_3), 42.13 (*C*H_3), 28.5 (*C*H_2). MS (ESI$^+$, m/z): 778.3870 $(M + H)^+$

***t*Bu/BrL_o^{NMe}**

(94 %). ^{1}H NMR (400 MHz, $CHCl_3$); 8.29 (2H, s, C=N*H*), 7.62 (2H, d, *J* 2.4, Ar*H*), 7.19 (2H, t, *J* 2.4, Ar*H*), 3.67 (4H, t, *J* 6.5, CH_2), 2.48-2.41 (4H, m, CH_2), 2.03 (3H, s, NCH_3), 1.91-1.85 (4H, m, CH_2), 1.32 (9H, s, C(CH_3)$_3$). ^{13}C (100 MHz, $CDCl_3$); 164.8 (*C*H), 157.8 (*C*), 141.5 (*C*), 133.3 (*C*H), 127.2 (*C*H), 117.0 (*C*), 111.5 (*C*), 55.8 (*C*H_2), 49.8 (*C*H_3), 40.3 (*C*H_2), 34.0 (*C*), 31.3 (*C*H_3), 28.1 (*C*H_2). MS(ESI$^+$, m/z): 624.1591 $(M + H)^+$

***t*Bu/PhL_o^{NMe}**

(98 %). ^{1}H NMR (400 MHz, $CHCl_3$); 8.42 (2H, s, C=N*H*), 7.66 (2H, s, Ar*H*), 7.64 (2H, s, Ar*H*), 7.48-7.42 (4H, m, Ar*H*), 7.36 (2H, d, *J* 7.1, Ar*H*), 7.25 (2H, d, *J* 2.4, Ar*H*), 3.65 (4H, t, *J* 6.7, CH_2), 2.44 (4H, t, J 7.4, CH_2), 2.23 (3H, s, NCH_3), 1.87 (4H, quin, J 7.3, CH_2), 1.35 (9H, s, C(CH_3)$_3$). ^{13}C (100 MHz, $CDCl_3$); 165.7 (*C*H), 156.9 (*C*), 141.0 (*C*), 138.5 (*C*), 130.8 (*C*H), 129.5 (*C*H), 129.3 (*C*), 128.2 (*C*H),

127.3 (*C*H), 127.0 (*C*H), 118.3 (*C*), 57.3 (CH_2), 55.6 (CH_2), 49.9 (CH_3), 34.0 (*C*), 31.6 (CH_3), 28.4 (CH_2). MS(ESI^+, m/z): 618.4060 $(M + H)^+$

***t*Bu/PhMe L NMe**

(96 %). ^{1}H NMR (400 MHz, $CDCl_3$); 8.42 (2H, d, *J* 6.0, C=N*H*), 7.54 (4H, d, *J* 8.0, Ar*H*), 7.43 (2H, t, *J* 2.3, Ar*H*), 7.28-7.22 (6H, m, Ar*H*), 3.67-3.62 (4H, m, CH_2), 2.77-2.71 (4H, m, CH_2), 2.41 (3H, s, NCH_3), 2.22 (6H, s, $ArCH_3$), 1.90-1.82 (4H, m, C*H*2), 1.35 (9H, s, CCH_3), 1.34 (9H, s, CCH_3). ^{13}C (100 MHz, $CDCl_3$); 165.5 (*C*H), 156.4 (*C*), 141.0 (*C*), 140.9 (*C*H), 136.7 (*C*H), 135.4 (*C*H), 130.6 (*C*H), 129.2 (*C*H), 128.9 (*C*H), 126.9 (*C*H), 118.2 (*C*H), 57.4 (CH_2), 55.6, 50.5 (CH_3), 42.0 (CH_3), 40.6 (CH_2), 34.0 (*C*), 31.4 (CH_3), 28.4 (CH_2). MS (ESI^+, m/z): 646.4371 $(M + H)^+$, 668.4176 $(M + Na)^+$

***t*Bu/PhOMe L NMe**

(93 %). ^{1}H NMR (400 MHz, $CDCl_3$); 8.42 (2H, s, C=NH), 7.60 (4H, d, *J* 8.8, Ar*H*), 7.43 (2H, d, *J* 2.3, Ar*H*), 7.24-7.22 (2H, m, Ar*H*), 7.02-6.99 (4H, m, Ar*H*), 3.87 (6H, s, OCH_3), 3.67-3.64 (4H, m, CH_2), 2.47-2.40 (4H, m, CH_2), 2.19 (3H, s, NCH_3), 1.88-1.84 (4H, m, CH_2), 1.35 (18H, s, CH_3). ^{13}C (100 MHz, $CDCl_3$); 165.5 (CH), 158.7 (C), 156.4 (C), 141.0 (C), 130.8 (C), 130.5 (CH), 128.9 (C), 127.7 (CH), 126.7 (CH), 118.2 (C), 113.7 (CH), 57.5 (CH_2), 55.4 (CH_3), 55.3 (CH_2), 42.2 (CH_3), 34.0 (C), 31.5 (CH_3), 28.6 (CH_2). MS (ESI^+, m/z): 678.4290 $(M + H)^+$

General procedure for preparation of metal complexes

A solution of proligand (0.90 mmol) in ethanol (30.0 cm^3) was heated to 50 ºC. A solution of metal salt ($Zn(OAc)_2{\cdot}2H_2O$/$Ni(NO_3)_2{\cdot}6H_2O$/$Cu(OAc)_2{\cdot}H_2O$, 0.90 mmol) in ethanol (30.0 cm^3) was added dropwise and stirred for 2 minutes. NaOH (0.10 M aq, 2.00 cm^3) was added and the resulting solution heated to 80 ºC for 2 hours. The solution was allowed to cool to room temperature and methanol (20.0 cm^3) was added to complete precipitation. The precipitate was collected by filtration and recrystallised from dichloromethane/methanol to give the metal complexes as crystalline powders.

$Zn^{Cl}L_O^{NMe}$

(90 %). Elemental analysis: (calc. for $C_{21}H_{21}Cl_4N_3O_2Zn$): C 45.48, H 3.82, N 7.58, Zn 11.79. Found: C 45.46, H 3.76, N 7.52, Zn 12.06. ^{1}H NMR (400 MHz, CD_2Cl_2, 233 K); 8.06 (2H, s, N=C*H*), 7.29 (2H, d, J 4.8, Ar*H*), 7.01 (2H, d, J 10.5, Ar*H*), 4.49(2H, quin, J 11, CH_2), 3.56-3.47 (2H, m, CH_2), 3.16 (1H, t, J 12.1, CH_2), 2.80(1H, t, J 12.8, CH_2), 2.40 (1H, d, J 12.4, CH_2), 2.25-2.10 (2H, m, CH_2), 2.17 (3H, s, NCH_3), 2.02-1.82 (3H, m, CH_2); FTIR ν/cm^{-1} (ATR): 2868 (w), 1636 (s), 1587 (w), 1517 (w), 1347 (s), 1308 (m), 1210 (m), 1159 (s), 1105 (w), 755 (s), 699 (w). MS (ESI+, *m/z*): 551.98 (M^+ + H).

$Zn^{Br}L_O^{NMe}$

(90 %). Elemental analysis: (calc. for $C_{21}H_{21}Br_4N_3O_2Zn$): C 34.44, H 2.89, N 5.74, Zn 8.93. Found: C 34.80, H 2.98, N 5.49, Zn 9.02. ^{1}H NMR (400 MHz, CD_2Cl_2, 233 K) 8.02 (2H, s, N=C*H*), 7.57 (2H, d, J 6.5, Ar*H*), 7.17 (2H, d, J 10.1, Ar*H*), 4.63-4.48 (2H, m, CH_2), 3.55-3.48 (2H, m, CH_2), 3.14 (1H, t, J 11.9, CH_2), 2.77(1H, t, J 13.1, CH_2), 2.38 (1H, d, J 12.4, CH_2), 2.24-2.10 (2H, m, CH_2), 2.15 (3H, s, NCH_3), 1.98-1.81 (3H, m, CH_2); FTIR ν/cm^{-1} (ATR): 2921 (w), 2856 (w), 1740 (br), 1634 (s), 1577 (m), 1504 (m), 1448 (s), 1213 (m), 1134 (s), 755 (m), 697 (s). MS (MALDI, *m/z*): 733.595 (M^+ + H).

$Zn^{Nap}L_O^{NMe}$

(37 %)**.** Elemental analysis: (calc. for $C_{28}H_{26}N_3O_2Zn$): C 67.00, H 5.22, N 8.37, Zn 12.65. Found: C 66.76, H 5.63, N 7.98, Zn11.15. ^{1}H NMR (400 MHz, CD_2Cl_2, 233 K) 9.11 (2H, s, N=C*H*), 7.99 (2H, d, J 8.5, Ar*H*), 7.63 (4H, d, J 9.5, Ar*H*), 7.42 (2H, t, J 8.3, Ar*H*), 7.18 (2H, t, J 7.3, Ar*H*), 7.01 (2H, d, J 9.2, Ar*H*), 4.50 (4H, br, CH_2), 2.70 (4H, br, CH_2), 2.28 (3H, s, NCH_3), 2.05 (4H, br, CH_2); FTIR ν/cm^{-1} (ATR): 2943 (w), 2860 (w), 1616 (s), 1538 (m), 1502 (m), 1458 (s), 1409 (s), 1395 (m), 1345 (w), 1310 (m), 1254 (m), 1211 (m), 1137 (w), 1017 (m), 862 (m), 750 (m), 739 (s), 541 (m), 513 (m), 480 (m). MS (MALDI, *m/z*): 515.402 (M^+), 516.410 (M + H^+), 538.407 (M + Na^+).

$Zn^{Ph}L_o^{NMe}$

(56 %). Elemental analysis: (calc. for $C_{45}H_{41}N_3O_2Zn$): C 74.94, H 5.73, N 5.83. Found: C 74.60, H 5.70, N 5.81. ^{1}H NMR (270 MHz, $CHCl_3$); 8.18 (2H, s,

N=C*H*), 7.74-7.70 (4H, m, Ar*H*), 7.63 (2H, d, *J* 2.6, Ar*H*), 7.57-7.52 (4H, m, Ar*H*), 7.40-7.29 (11H, m, Ar*H*), 7.23-7.18 (3H, m, Ar*H*), 4.44-4.31 (4H, m, CH_2), 3.75-3.66 (4H, m, CH_2), 3.37-3.29 (4H, m, CH_2), 2.26 (3H, s, NCH_3). FTIR ν/cm^{-1} (ATR): 2858 (br, w), 1633 (s), 1602 (m), 1534 (m), 1452 (s), 1432 (s), 1406 (w), 1387 (w), 1332 (m), 1252 (w), 1115 (m), 791 (m), 752 (s), 697 (s), 598 (s). MS(MALDI$^+$, m/z): 720.4 $(M + H)^+$

Zn^{PhMe}L$_O$^{NMe}

(21 %). Elemental Analysis: (calc. for $C_{49}H_{49}N_3O_2Zn{\cdot}CH_2Cl_2$): C 70.71, H 6.06, N 5.39. Found: C 70.71, H 6.33, N 5.39. ^{1}H NMR (400 MHz, $CDCl_3$); 8.17 (2H, s, CN*H*), 7.64 (2H, s, Ar*H*), 7.61-7.59 (4H, m, Ar*H*), 7.44 (4H, d, *J* 8.1, Ar*H*), 7.27 (2H, d, *J* 2.6, Ar*H*), 7.18-7.11 (8H, m, Ar*H*), 4.47-4.38 (4H, m, CH_2), 3.39-3.32 (4H, m, CH_2), 2.43 (6H, s, ArCH_3), 2.42 (6H, s, ArCH_3), 2.26 (3H, s, NCH_3), 1.95-1.87 (4H, m, CH_2). FTIR ν/cm^{-1} (ATR): 2854 (w), 1632 (m), 1602 (w), 1533 (w), 1446 (s), 1393 (m), 1330 (w), 1284 (w), 1112 (m), 1019 (w), 801 (s), 741 (m), 718 (w). MS (ESI$^+$, m/z): 798.3041 $(M+Na)^+$.

Zn^{PhOMe}L$_O$^{NMe}

(46 %). Elemental Analysis: (calc. for $C_{49}H_{49}N_3O_6Zn{\cdot}CH_2Cl_2$): C 64.84, H 5.55, N 4.54. Found: C 65.20, H 5.47, N 4.72. ^{1}H NMR (400 MHz, $CDCl_3$); 8.16 (2H, s, CN*H*), 7.69 (4H, d, *J* 8.5, Ar*H*), 7.57 (2H, d, *J* 2.3, Ar*H*), 7.49 (4H, d, *J* 8.7, ArH), 7.23 (2H, d, *J* 2.5, Ar*H*), 6.97-6.87 (8H, m, Ar*H*), 4.40 (4H, q, *J* 7.8, CH_2), 3.86 (6H, s, OCH_3), 3.84 (6H, s, OCH_3), 3.38-3.29 (4H, m, CH_2), 2.22 (3H, s br, NCH_3), 1.87 (4H, s br, CH_2). FTIR ν/cm^{-1} (ATR): 2832 (w), 1633 (m), 1603 (w), 1506 (m), 1448 (s), 1395 (m), 1280 (m), 1249 (s), 1175 (s), 1115 (m), 1031 (s), 811 (s), 804 (s), 741 (w), 699 (w), 640 (w). MS (MALDI$^+$, m/z): 839.6 (M^+).

Zn$^{tBu/Br}$L$_o$^{NMe}

(27%). Elemental analysis: (calc. for $C_{29}H_{39}Br_2N_3O_2Zn$): C 50.71, H 5.72, N 6.12. Found: C 50.44, H 5.68, N 6.10. ^{1}H NMR (400 MHz, $CHCl_3$); 8.12 (2H, s, C=N*H*), 7.61 (2H, d, *J* 2.5, Ar*H*), 7.03 (2H, d, *J* 2.3, Ar*H*), 4.76 (2H, s br, CH_2), 3.52-3.46 (2H, m, CH_2), 3.40-2.27 (3H, m br, CH_2), 2.22 (3H, s, NCH_3), 2.17-1.64 (5H, m, CH_2), 1.28 (18H, s, C(CH_3)$_3$). FTIR ν/cm^{-1} (ATR): 2950 (br, w), 1634 (s),

1601 (w), 1454 (s), 1389 (w), 1362 (w), 1255 (w), 1151 (m), 837 (m), 758 (m), 729 (m). MS(MALDI$^+$, m/z): 708.090 $(M + Na)^+$.

$Zn^{tBu/Ph}L_o^{NMe}$

(46 %). Elemental analysis: (calc. for $C_{41}H_{49}N_3O_2Zn$): C 72.29, H 7.25, N 6.17. Found: C 72.29, H 7.35, N 5.94. ^{1}H NMR (400 MHz, $CHCl_3$); 8.15 (2H, s, C=N*H*), 7.75 (4H, d, *J* 7.2, Ar*H*), 7.46 (2H, d, *J* 2.8, Ar*H*), 7.36 (4H, t, *J* 7.4, Ar*H*), 7.26 (2H, t, *J* 7.4, Ar*H*), 7.07 (2H, d, *J* 2.6, Ar*H*), 4.40 (2H, q, *J* 8.7, CH_2), 3.36-3.30 (2H, m, CH_2), 3.18-2.38 (4H, m br, CH_2), 2.26 (3H, s, NCH_3), 2.11-2.81 (4H, m, CH_2), 1.36 (18H, s, C(CH_3)$_3$). FTIR ν/cm^{-1} (ATR): 2957 (br, w), 2863 (br, w), 1631 (s), 1597 (w), 1528 (w), 1456 (m), 1438 (m), 1408 (m), 1391 (m), 1281 (m), 1251 (m), 1225 (m), 1109 (m), 790 (s), 744 (s), 699 (s). MS (MALDI$^+$, m/z): 702.368 $(M + Na)^+$.

$Zn^{tBu/PhMe}L_O^{NMe}$

(41%). Elemental Analysis: (calc. for $C_{43}H_{53}N_3O_2Zn$): C 72.81, H 7.53, N 5.92. Found: C 71.95, H 7.42, N 5.77. ^{1}H NMR (400 MHz, $CDCl_3$); 8.16 (2H, s, N=C*H*), 7.68 (4H, d, *J* 8.0, Ar*H*), 7.46 (2H, d, *J* 2.8, Ar*H*), 7.19 (4H, d, *J* 7.9, Ar*H*), 7.06 (2H, d, *J* 2.8, Ar*H*), 4.44 (2H, m, CH_2), 3.35 (2H, m, CH_2), 2.43 (6H, s, ArCH_3), 2.26 (3H, s, NCH_3), 1.35 (18H, s, CCH_3). FTIR ν/cm^{-1} (ATR): 2948 (w), 2860 (w), 1624 (s), 1530 (m), 1395 (m), 1359 (w), 1251 (m), 1132 (m), 818 (s), 743 (m). MS (MALDI, *m/z*): 707.752 (M^+), 708.752 ($M + H^+$), 730.757 ($M + Na^+$).

$Zn^{tBu/PhOMe}L_O^{NMe}$

(56%). Elemental Analysis: (calc. for $C_{43}H_{53}N_3O_4Zn{\cdot}0.5CH_2Cl_2$): C 66.66, H 6.95, N 5.36. Found: C 66.28, H 7.68, N 5.50. ^{1}H NMR (400 MHz, $CDCl_3$); 8.15 (2H, s, N=C*H*), 7.71 (4H, d, *J* 8.8, ArH), 7.43 (2H, d, *J* 2.8, Ar*H*), 7.05 (2H, J 2.8, Ar*H*), 6.92 (4H, d, J 8.8, Ar*H*), 4.45 -4.38 (2H, m, Ar*H*), 3.89 (6H, s, OCH_3), 3.36-3.31 (2H, m, CH_2), 2.78-2.54 (4H, m, CH_2), 2.25 (3H, s, NC*H3*), 2.06-1.86 (4H, m, CH_2), 1.35 (18H, s, C(CH_3)$_3$). FTIR ν/cm^{-1} (ATR): 2950 (w), 2864 (w), 1632 (m), 1532 (w), 1469 (m), 1393 (m), 1332 (w), 1224 (m), 1057 (s), 1033 (s), 1017 (s), 782 (m). MS (ESI+, *m/z*): 762.3264 ($M + Na^+$).

$Ni^{Cl}L_O{}^{NMe}$

(80 %). Elemental analysis: (calc. for $C_{21}H_{21}Cl_4N_3O_2Ni$): C 46.03, H 3.86, N 7.67, Ni 10.71. Found: C 45.87, H 3.82, N 7.46, Ni 10.94. FTIR ν/cm^{-1} (ATR): 2861 (w, br), 1629 (s), 1586 (w), 1519 (w), 1444 (s), 1413 (m), 1309 (w), 1209 (m), 1181 (s), 1010 (w), 862 (m), 756 (s), 604 (w). MS (ESI+, *m/z*): 545.98 ($M + H^+$).

$Ni^{Br}L_O{}^{NMe}$

(75 %). Elemental analysis: (calc. for $C_{21}H_{21}Br_4N_3O_2Ni$): C 34.76, H 2.92, N 5.79, Ni 8.01. Found: C 34.77, H 2.92, N 5.64, Ni 8.70. FTIR ν/cm^{-1} (ATR): 2920 (m), 2851 (m), 1739 (br), 1631 (s), 1576 (w), 1504 (w), 1439 (s), 1408 (s), 1212 (m), 1134 (s), 865 (w), 755 (m), 699 (s). MS (ESI+, *m/z*): 721.78 ($M^+ + H$).

$Ni^{Nap}L_O{}^{NMe}$

(49 %). Elemental analysis: (calc. for $C_{28}H_{26}N_3O_2Ni$): C 67.91, H 5.29, N 8.49, Ni 11.50, Found: C 67.96, H 5.67, N 8.18, Ni 11.06. , FTIR ν/cm^{-1} (ATR): 2924 (w, Br), 1614 (s), 1538 (m), 1501 (m), 1456 (m), 1407 (m), 1346 (m), 1311 (w), 1212 (m), 974 (w), 865 (m), 744 (s), 645 (w), 620 (w). MS (ESI^+, m/z): 510.1692 $(M + H)^+$

$Ni^{Ph}L_o{}^{NMe}$

(52 %). Elemental analysis: (calc. for $C_{45}H_{41}N_3NiO_2$): C 75.64, H 5.78, N 5.88. Found: C 75.23, H 5.85, N 5.57. FTIR ν/cm^{-1} (ATR): 2923 (br, w), 1629 (s), 1597 (m), 1537 (m), 1451 (m), 1435 (m), 1405 (w), 1330 (w), 1288 (w), 1217 (w), 1116 (m), 890 (w), 882 (w), 791 (m), 752 (s), 699 (s), 599 (s). MS (ESI^+, m/z): 714.2544 $(M + H)^+$.

$Ni^{PhMe}L_O{}^{NMe}$

(76 %). Elemental Analysis: (calc. for $C_{49}H_{49}N_3O_2Ni{\cdot}CH_2Cl_2$): C 70.77, H 6.08, N 5.39. Found: C 70.77, H 6.33, N 5.39. FTIR ν/cm^{-1} (ATR): 2922 (br, w), 1629 (s), 1603 (w), 1534 (w), 1507 (m), 1439 (s), 1396 (m), 1326 (w), 1283 (w), 1241 (s), 1175 (m), 1115 (w), 1032 (m), 810 (s), 781 (w), 741 (m), 727 (w), 697 (w). MS (ESI^+, m/z): 770.3243 $(M+H)^+$.

$Ni^{PhOMe}L_O^{NMe}$

(57 %). Elemental Analysis: (calc. for $C_{49}H_{49}N_3O_6Ni \cdot 0.5CH_2Cl_2$): C 67.66, H 5.74, N 4.79. Found: C 67.81, H 5.87, N 4.78. FTIR ν/cm^{-1} (ATR): 2935 (br, w), 2360 (w), 1629 (m), 1604 (m), 1534 (w), 1507 (m), 1446 (s), 1395 (w), 1282 (w), 1241 (s), 1176 (m), 1117 (w), 1033 (s), 826 (s), 804 (s), 741 (w), 698 (w), 611 (w). MS (ESI^+, m/z): 834.3048 $(M+H)^+$.

$Ni^{tBu/Br}L_o^{NMe}$

(54 %). Elemental analysis: (calc. for $C_{29}H_{39}Br_2N_3NiO_2$ (0.5 CH_2Cl_2)): C 49.03, H 5.58, N 5.82. Found: C 49.62, H 5.57, N 5.79. FTIR ν/cm^{-1} (ATR): 2961 (br, w), 1629 (s), 1454 (s), 1389 (w), 1360 (w), 1254 (m), 1227 (w), 1153 (m), 1138 (m), 1126 (m), 837 (m), 758 (m), 728 (m). MS (ESI^+, m/z): 680.0785 $(M + H)^+$.

$Ni^{tBu/Ph}L_O^{NMe}$

(56 %). Elemental analysis: (calc. for $C_{41}H_{49}N_3NiO_2$): C 73.00, H 7.32, N 6.23. Found: C 72.77, H 7.37, N 6.23. FTIR ν/cm^{-1} (ATR): 2957 (br, w), 2865 (br, w), 1627 9s), 1596 (w), 1455 (s), 1407 (m), 1390 (m), 1282 9w), 1252 (w), 1225 (w), 1111 (w), 789 (s), 743 (s), 699 (s). MS (ESI^+, m/z): 674.3229 $(M + H)^+$.

$Ni^{tBu/PhMe}L_O^{NMe}$

(33 %). Elemental Analysis: (calc. for $C_{43}H_{53}N_3O_2Ni$): C 73.51, H 7.60, N 5.98. Found: C 72.96, H 7.55, N 6.01. FTIR ν/cm^{-1} (ATR): 2956 (w), 2859 (w), 1625 (s), 1532 (w), 1444 (m), 1359 (m), 1344 (w), 1284 (m), 1114 (m), 1051 (s), 870 (w), 814 (s), 745 (m). MS (ESI^+, m/z): 702.3576 $(M+H)^+$.

$Ni^{tBu/PhOMe}L_O^{NMe}$

(26 %). Elemental Analysis: (calc. for $C_{43}H_{53}N_3O_4Ni$): C 70.31, H 7.27, N 5.72. Found: C 69.28, H 7.21, N 5.79. FTIR ν/cm^{-1} (ATR): 2950 (br, w), 1632 (m), 1529 (w), 1509 (w), 1473 (m), 1346 (w), 1285 (w), 1253 (m), 1223 (w), 1174 (w), 1105 (w), 1032 (m), 949 (w), 871 (w), 815 (s), 792 (w), 783 (w), 743 (w), 723 (w). MS (ESI^+, m/z): 734.3482 $(M+H)^+$.

$Cu^{Cl}L_O^{NMe}$

(35 %). Elemental analysis: (calc. for $C_{21}H_{21}Cl_4N_3O_2Cu$): C 45.63, H 3.53, N 7.60, Cu 11.50. Found: C 45.48, H 3.86, N 7.47, Cu 11.43. FTIR ν/cm^{-1} (ATR): 2952

(w), 2874 (w), 1738 (w), 1632 (s), 1587 (w), 1514 (w), 1442 (s), 1414 (m), 1318 (w), 1209 (m), 1162 (m), 1144 (m), 1060 (w), 879 (w), 860 (w), 755 (s), 700 (w), 686 (w), 609 (w). MS (ESI+, m/z): 552.97 (M+ + H).

$Cu^{Br}L_O^{NMe}$

(34 %). Elemental analysis: (calc. for $C_{21}H_{21}Br_4N_3O_2Cu$): C 34.52, H 2.90, N 5.75, Cu 8.70. Found: C 34.04, H 3.01, N 5.72, Cu 8.58. FTIR ν/cm^{-1} (ATR): 2955 (w), 2874 (w), 1627 (s), 1576 (m), 1504 (w), 1447 (s), 1409 (s), 1317 (m), 1213 (w), 1138 (m), 1058 (w), 965 (w), 754 (m), 700 (s). MS (ESI+, *m/z*): 726.78 (M^+ + H).

$Cu^{Nap}L_O^{NMe}$

(59 %). Elemental analysis: (calc. for $C_{29}H_{29}CuN_3O_2$): C 67.62, H 5.67, N 8.16, Cu 12.34. Found: C 67.57, H 5.59, N 8.27, Cu 13.17. FTIR ν/cm^{-1} (ATR): 2923 (w, Br), 2359 (w), 1738 (m), 1615 (s), 1537 (m), 1502 (m), 1455 (s), 1437 (s), 1346 (m), 1216 (w), 979 (w), 834 (m), 740 (s), 653 (m). MS (ESI^+, m/z): 515.1634 $(M + H)^+$;

$Cu^{Ph}L_o^{NMe}$

(70%). Elemental analysis: (calc. for $C_{45}H_{41}CuN_3O_2$): C 75.13, H 5.74, N 5.84. Found: C 75.07, H 5.78, N 5.73. FTIR ν/cm^{-1} (ATR): 2921 (br, w), 1629 (s), 1603 (w), 1538 (m), 1452 (s), 1436 (s), 1406 (w), 1331 (w), 1217 (w), 1119 (w), 790 (m), 153 (s), 689 (s), 629 9m), 601 (m). MS (ESI^+, m/z): 719.2552 $(M + H)^+$.

$Cu^{PhMe}L_O^{NMe}$

(54%). Elemental Analysis: (calc. for $C_{49}H_{49}N_3O_2Cu$): C 75.89, H 6.37, N 5.42. Found: C 75.14, H 6.30, N 5.35. FTIR ν/cm^{-1} (ATR): 2936 (br, w), 2360 (w), 1627 (m), 1534 (w), 1507 (m), 1445 (m), 1396 (w), 1240 (w), 1174 (w), 1117 (w), 1033 (s), 974 (w), 821 (s), 804 (s), 740 (w), 724 (w), 612 (w). MS (ESI^+, m/z): 775.3114 $(M+H)^+$.

$Cu^{PhOMe}L_O^{NMe}$

(62%). Elemental Analysis: (calc. for $C_{49}H_{49}N_3O_6Cu\cdot0.5CH_2Cl_2$): C 67.41, H 5.71, N 4.76. Found: C 67.93, H 5.77, N 4.79. FTIR ν/cm^{-1} (ATR): 2929 (br, w), 2832 (w), 1628 (m), 1604 (w), 1508 (m), 1438 (s), 1396 (m), 1282 (m), 1231 (s), 1175

(m), 1031 (s), 974 (w), 826 (s), 804 (s), 742 (w), 698 (w), 611 (w). MS (ESI^+, m/z): 839.2990 $(M+H)^+$.

$Cu^{tBu/Br}L_o^{NMe}$

(50%). Elemental analysis: (calc. for $C_{29}H_{39}Br_2CuN_3O_2$): C 50.58, H 5.74, N 6.13. Found: C 50.4, H 5.67, N 5.97. FTIR ν/cm^{-1} (ATR): 2954 (br, w), 2860 (br, w), 1630 (s), 1603 (w), 1452 (s), 1392 (m), 1362 (m), 1326 (m), 1256 (m), 1155 (m), 1144 (m), 860 (m), 838 (s), 756 (s), 731 (s). MS (ESI^+, m/z): 685.0717 $(M + H)^+$.

$Cu^{tBu/Ph}L_o^{NMe}$

(85%). Elemental Analysis: (calc. for $C_{41}H_{49}N_3O_2Cu{\cdot}0.5CH_2Cl_2$): C 69.05, H 6.98, N 5.82. Found: C 69.45, H 7.07, N 5.84. FTIR ν/cm^{-1} (ATR): 2958 (br, w), 1628 (s), 1596 (w), 1530 (m), 1453 (m), 1436 (m), 1251 (m), 1226 (m), 837 (m), 787 (s), 742 (s), 697 (s), 633 (w), 604 (w). MS (ESI^+, m/z): 679.3194 $(M + H)^+$.

$Cu^{tBu/PhMe}L_O^{NMe}$

(91%). Elemental Analysis: (calc. for $C_{43}H_{53}N_3O_2Cu$): C 73.00, H 7.55, N 5.94. Found: C 72.59, H 7.49, N 5.74. FTIR ν/cm^{-1} (ATR): 2957 (w), 2861 (w), 1629 (s), 1531 (m), 1360 (w), 1225 (s), 1131 (m), 1062 (w), 817 (s), 743 (m). MS (ESI^+, m/z): 708.357318 $(M+2H)^+$.

$Cu^{tBu/PhOMe}L_O^{NMe}$

(73%). Elemental Analysis: (calc. for $C_{43}H_{53}N_3O_4Cu{\cdot}CH_2Cl_2$): C 64.11, H 6.72, N 5.10. Found: C 64.11, H 7.25, N 5.72. FTIR ν/cm^{-1} (ATR): 2950 (w), 2864 (w), 1630 (s), 1531 (m), 1439 (s), 1241 (s), 1174 (w), 825 (s), 792 (w), 743 (w). MS (ESI^+, m/z): 739.5109 $(M+H)^+$.

2.8 References

1. H. Schiff, *Liebigs Ann. Chem.*, 1864, **131**, 118-119.
2. T. T. Tidwell, *Angew. Chem. Int. Ed.*, 2008, **47**, 1016-1020.
3. W. Qin, S. Long, M. Panunzio and S. Biondi, *Molecules*, 2013, **18**.
4. P. G. Cozzi, *Chem. Soc. Rev.*, 2004, **33**, 410-421.
5. C. M. da Silva, D. L. da Silva, L. V. Modolo, R. B. Alves, M. A. de Resende, C. V. B. Martins and Â. de Fátima, *J. Adv. Res.*, 2011, **2**, 1-8.
6. A. O. d. Souza, F. C. S. Galetti, C. L. Silva, B. Bicalho, M. M. Parma, S. F. Fonseca, A. J. Marsaioli, A. C. L. B. Trindade, R. P. F. Gil, F. S. Bezerra, M. Andrade-Neto and M. C. F. d. Oliveira, *Quim. Nova*, 2007, **30**, 1563-1566.
7. M. J. Hearn and M. H. Cynamon, *J. Antimicrob. Chemother.*, 2004, **53**, 185-191.
8. H. Makio, N. Kashiwa and T. Fujita, *Adv. Synth. Catal.*, 2002, **344**, 477-493.
9. E. G. Samsel, K. Srinivasan and J. K. Kochi, *J. Am. Chem. Soc.*, 1985, **107**, 7606-7617.
10. E. N. Jacobsen, W. Zhang, A. R. Muci, J. R. Ecker and L. Deng, *J. Am. Chem. Soc.*, 1991, **113**, 7063-7064.
11. W. Zhang, J. L. Loebach, S. R. Wilson and E. N. Jacobsen, *J. Am. Chem. Soc.*, 1990, **112**, 2801-2803.
12. N. Kitajima, K. Whang, Y. Moro-oka, A. Uchida and Y. Sasada, *J. Chem. Soc., Chem. Commun.*, 1986, **0**, 1504-1505.
13. B. A. Jazdzewski and W. B. Tolman, *Coord. Chem. Rev.*, 2000, **200–202**, 633-685.
14. C. T. Lyons and T. D. P. Stack, *Coord. Chem. Rev.*, 2013, **257**, 528-540.
15. M. Franks, A. Gadzhieva, L. Ghandhi, D. Murrell, A. J. Blake, E. S. Davies, W. Lewis, F. Moro, J. McMaster and M. Schröder, *Inorg. Chem.*, 2013, **52**, 660-670.
16. N. Ito, S. E. V. Phillips, C. Stevens, Z. B. Ogel, M. J. McPherson, J. N. Keen, K. D. S. Yadav and P. F. Knowles, *Nature*, 1991, **350**, 87-90.
17. N. Ito, S. E. V. Phillips, K. D. S. Yadav and P. F. Knowles, *J. Mol. Biol.*, 1994, **238**, 704-814.
18. H. J. Krueger and R. H. Holm, *Inorg. Chem.*, 1987, **26**, 3645-3647.
19. J. Hanss and H.-J. Krüger, *Angew. Chem. Int. Ed.*, 1998, **37**, 360-363.
20. W.-Z. Lee, C.-W. Chiang, T.-H. Lin and T.-S. Kuo, *Chem. Eur. J.*, 2012, **18**, 50-53.
21. F. Thomas, *Eur. J. Inorg. Chem.*, 2007, 2379-2404.
22. Y. Wang and T. D. P. Stack, *J. Am. Chem. Soc.*, 1996, **118**, 13097-13098.
23. R. C. Pratt and T. D. P. Stack, *J. Am. Chem. Soc.*, 2003, **125**, 8716-8717.
24. R. C. Pratt and T. D. P. Stack, *Inorg. Chem.*, 2005, **44**, 2367-2375.
25. F. Thomas, O. Jarjayes, C. Duboc, C. Philouze, E. Saint-Aman and J.-L. Pierre, *Dalton Trans.*, 2004, 2662-2669.
26. P. Verma, R. C. Pratt, T. Storr, E. C. Wasinger and T. D. P. Stack, *Proc. Nat. Aca. Sci.*, 2011, **108**, 18600-18605.
27. R. C. Pratt, C. T. Lyons, E. C. Wasinger and T. D. P. Stack, *J. Am. Chem. Soc.*, 2012, **134**, 7367-7377.

28. Q. Zhao, C. Bai, W. Zhang, Y. Li, G. Zhang, F. Zhang and X. Fan, *Ind. Eng. Chem. Res.*, 2014, **53**, 4232-4238.
29. J. Cheng, X. Ma, Y. Zhang, J. Liu, X. Zhou and H. Xiang, *Inorg. Chem.*, 2014, **53**, 3210-3219.
30. Z. Abbasi, M. Behzad, A. Ghaffari, H. A. Rudbari and G. Bruno, *Inorg. Chim. Acta*, 2014, **414**, 78-84.
31. M. Orio, O. Jarjayes, H. Kanso, C. Philouze, F. Neese and F. Thomas, *Angew. Chem. Int. Ed.*, 2010, **49**, 4989-4992.
32. S. S. Mokle, B. S. Dawane, M. A. Sayyed and Y. B. Vibhute, *J. Chem. Res.*, 2006, **2006**, 101-101.
33. G. K. A Aberg, J. A. N. Chen, A. T. Maioli, G. E. Wright, US20040850868, 2004.
34. M. Sun, T. Xu, W. Gao, Y. Liu, Q. Wu, Y. Mu and L. Ye, *Dalton Transactions*, 2011, **40**, 10184-10194.
35. G. Sheldrick, *Acta Crystallogr. C*, 2015, **71**, 3-8.
36. A. Spek, *Acta Crystallogr. D*, 2009, **65**, 148-155.
37. A. W. Addison, T. N. Rao, J. Reedijk, J. van Rijn and G. C. Verschoor, *J. Che. Soc., Dalton Trans.*, 1984, **0**, 1349-1356.
38. P. Orioli, M. Di Vaira and L. Sacconi, *Inorg. Chem.*, 1971, **10**, 553-558.
39. L. Gomes, D. Pinho, C. Freire and B. de Castro, *Acta Crystallogr. C*, 1999, **55**, 1425-1427.
40. G. Rogez, J.-N. Rebilly, A.-L. Barra, L. Sorace, G. Blondin, N. Kirchner, M. Duran, J. van Slageren, S. Parsons, L. Ricard, A. Marvilliers and T. Mallah, *Angew. Chem. Int. Ed.*, 2005, **44**, 1876-1879.
41. D. Collison, M. Helliwell, V. M. Jones, F. E. Mabbs, E. J. L. McInnes, P. C. Riedi, G. M. Smith, R. G. Pritchard and W. I. Cross, *J. Chem. Soc., Faraday Trans.*, 1998, **94**, 3019-3025.
42. J. Krzystek, J.-H. Park, M. W. Meisel, M. A. Hitchman, H. Stratemeier, L.-C. Brunel and J. Telser, *Inorg. Chem.*, 2002, **41**, 4478-4487.
43. A. Sokolowski, H. Leutbecher, T. Weyhermüller, R. Schnepf, E. Bothe, E. Bill, P. Hildebrandt and K. Wieghardt, *J. Biol. Inorg. Chem.*, 1997, **2**, 444-453.
44. Y. Shimazaki, S. Huth, S. Hirota and O. Yamauchi, *Inorg. Chim. Acta*, 2002, **331**, 168-177.
45. A. Klamt and G. Schuurmann, *J. Chem. Soc., Perkin Trans. 2*, 1993, 799-805.

Chapter 3

The Oxidation of Pentacoordinate Diphenolate Zinc^{II}, Nickel^{II} and Copper^{II} complexes

3.1 Introduction

We have prepared a range of Ni^{II}, Cu^{II} and Zn^{II} complexes containing 3,5-disubstituted pentacoordinate diphenolate ligands, and have demonstrated that the change in substitution at a relatively remote position from the metal centre has little effect on the geometry about the metal centre (Chapter Two). In this Chapter we assess the effects of the 3,5-disubstitutions and the nature of the coordinated metal on the electrochemical and spectroscopic properties of each complex.

3.1.1 Previous Work

The electrochemical characterisations of pentacoordinate transition metal complexes, including the *t*butyl substituted diphenolate complexes $M^{tBu}L_o^{NMe}$ (M = Zn, Ni, Cu) (Figure 3.1.1.1), have been reported previously by the group. Each $M^{tBu}L_o^{NMe}$ possesses two redox processes at $E_{1/2}$ = 0.30 and 0.54 V, 0.13 and 0.57 V, and 0.24 and 0.57 V (*vs.* Fc^+/Fc), respectively (Figure 3.1.1.1).[1] It has been proposed that the first oxidation process of $Ni^{tBu}L_o^{NMe}$ ($E_{1/2}$ = 0.13 V) is essentially metal based such that a formal Ni^{III} species is generated on oxidation. The second process for $Ni^{tBu}L_o^{NMe}$ at 0.57 V (*vs.* Fc^+/Fc) has been assigned to a phenoxyl radical/phenolate redox couple. In contrast, both of the redox processes observed for $Zn^{tBu}L_o^{NMe}$ and $Cu^{tBu}L_o^{NMe}$ have been assigned to phenoxyl radical/phenolate couples.

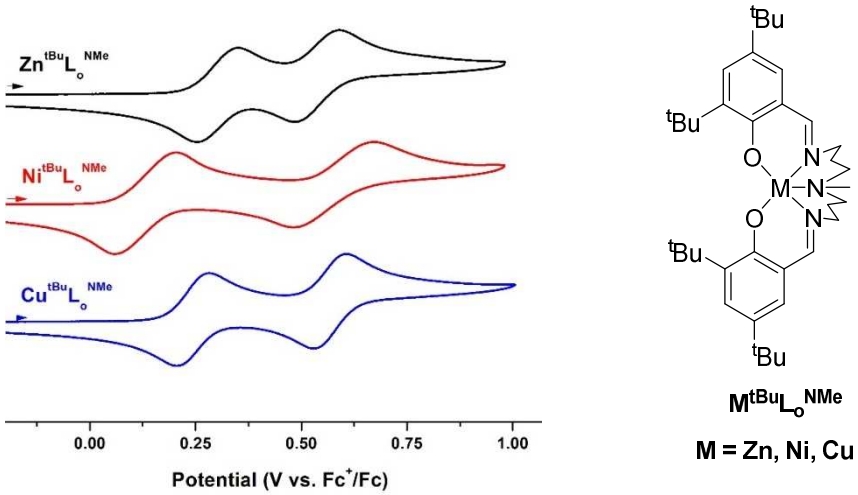
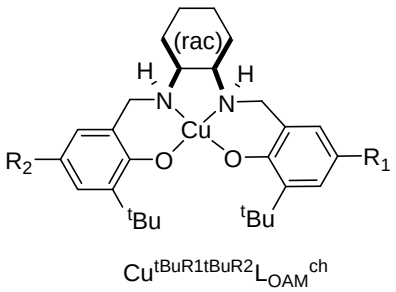


Figure 3.1.1.1: Cyclic voltammograms of $M^{tBu}L_o^{NMe}$ (M = Zn, Ni, Cu).[1]

The effect of different phenolate substituents (thioether and methoxy) on the electrochemical properties of Cu-containing diphenolate complexes ($Cu^{tBuR1tBuR2}L_{OAM}{}^{ch}$, Figure 3.1.1.2) has been investigated.[2, 3] Thioether groups have been employed to investigate the role of the thioether post translational modification at the ortho position of the tyrosinate ring at the active site of galactose oxidase.[4] EPR spectroscopic studies on $[Cu^{tBuR1tBuR2}L_{OAM}{}^{ch}]^+$ ($R_1 = R_2 =$ SMe, S^{i}Pr, S^{t}Bu) show significant delocalisation of radical character onto the thioether substituents[2] and suggest that electron donation by the thioether is key to lowering the redox potential of the tyrosine cofactor (0.45 V *vs.* 0.95 V for tyrosine *vs.* NHE)[5] (Chapter 1.4). The incorporation of OMe and ^{t}Bu groups at the 3 and 5 positions of the phenolate rings demonstrates that the potentials of the formal phenoxyl radical/phenolate redox processes can be varied over a *ca.* 200 mV range. (Table 3.1.1.1).



$Cu^{tBuR1tBuR2}L_{OAM}{}^{ch}$

R_1 = ^{t}Bu, OMe, S^{i}Pr

R_2 = ^{t}Bu, OMe, S^{i}Pr

S^{i}Pr = isopropylsulfanyl

$Cu^{tBuR1tBuR2}L_{OAM}{}^{ch}$		E_1 mV	E_2 mV
R_1	R_2		
^{t}Bu	^{t}Bu	80	210
^{t}Bu	OMe	-90	160
OMe	OMe	-120	-10
OMe	S^{i}Pr	-90	70
S^{i}Pr	S^{i}Pr	10	80
^{t}Bu	S^{i}Pr	25	150

Figure 3.1.1.2: Cu^{II} complexes incorporating a range of thioether, methoxy and isopropyl substituents and Table 3.1.1.1: Redox potentials (vs. Fc^+/Fc) for complexes incorporating different substituents. [2, 3]

3.1.2 Aims

The synthesis and characterisation of an extensive range of 5-coordinate diphenolate complexes $M^RL_O{}^{NMe}$, (M = Zn, Ni, Cu; R = Cl, Br, Nap, Ph, PhMe, PhOMe, ^{t}Bu/Br, ^{t}Bu/Ph, ^{t}Bu/PhMe, ^{t}Bu/PhOMe) (Chapter Two), enables a thorough assessment of the effects of the metal and ligand substitution on the electrochemical and spectroscopic properties of the compounds. This Chapter describes the electrochemical characterisation of each compound by cyclic voltammetry. UV/vis and EPR spectroelectrochemical studies are used to probe the electronic structures of the oxidation products.

Our initial focus is on those complexes containing identical substituents at the 3 and 5 positions of each phenolate ring $M^{R}L_{O}^{NMe}$ (M = Zn, Ni, Cu; R = Cl, Br, Nap, Ph, PhMe, PhOMe) in order to assess the effects of these substitutions at remote positions from the metal centre. We then consider the relative effects of 3 *vs.* 5 substitution on the properties of the complexes by considering $M^{R}L_{O}^{NMe}$ (M = Zn, Ni, Cu; R = ^{t}Bu/Br, ^{t}Bu/Ph, ^{t}Bu/PhMe, ^{t}Bu/PhOMe).

Our studies significantly extend the range of substituted salen-type ligands that have been investigated by electrochemistry and spectroelectrochemistry, and provide a framework for the development of new salen complexes with tailored redox properties and with coordination spheres that remain essentially unchanged as the substituents are varied.

3.2 Electrochemistry of $M^{R}L_{O}^{NMe}$ (R = Cl, Br, Nap, ^{t}Bu/Br; M = Zn, Ni, Cu).

3.2.1 Cyclic Voltammetry of $M^{R}L_{O}^{NMe}$ (M = Zn, Ni, Cu; R = Cl, Br, Nap)

The electrochemical behaviours of $M^{R}L_{O}^{NMe}$ (M = Zn, Ni, Cu; R = Cl, Br, Nap) (Figure 3.2.1.1) were investigated by cyclic voltammetry. The electrochemical experiments were undertaken in CH_2Cl_2 solution at 298 K under an inert atmosphere of argon with tetrabutylammonium tetrafluoroborate (0.4 M) as the supporting electrolyte; CH_2Cl_2 is widely used as the preferred solvent in the electrochemical investigation of compounds that possess the potential to generate phenoxyl radicals.[6-9] The electrochemical potential range (*ca.* -2.25 V – 1.15 V *vs.* Fc^{+}/Fc) and the weakly coordinating nature of CH_2Cl_2 promotes the coordination of phenoxyl radical species to metal centres in solution, despite the weaker donor ability of phenoxyl O donors when compared to their phenolate counterparts.[10] Initial studies by cyclic voltammetry show that $M^{R}L_{O}^{NMe}$ (R = Cl, Br, Nap; M = Zn, Cu) do not possess electrochemically reversible processes; oxidation processes are apparent but most do not exhibit an associated reductive process.

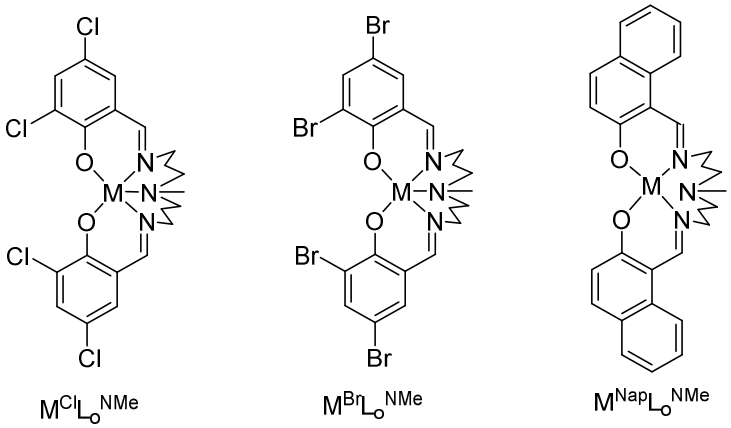


Figure 3.2.1.1: Complexes $M^{R}L_{O}^{NMe}$ (R = Cl, Br, Nap; M = Zn, Ni, Cu).

$Zn^{R}L_{O}^{NMe}$ (R = Cl, Br) possess two oxidation processes at E_p^{a} = 0.73 and 0.93 V *vs.* Fc^{+}/Fc and E_p^{a} = 0.74 and 0.83 V vs. Fc^{+}/Fc, for $Zn^{Br}L_{O}^{NMe}$ and $Zn^{Cl}L_{O}^{NMe}$, respectively (Figure 3.2.1.2 Left). $Zn^{Nap}L_{O}^{NMe}$ exhibits oxidation processes at less positive potentials at E_p^{a} = 0.49 and 0.76 V *vs.* Fc^{+}/Fc (Figure 3.2.1.2 Left). These processes all occur at more positive potentials than those previously reported for

the analogous ^{t}butyl complex $Zn^{tBu}L_o^{NMe}$, which exhibits two reversible one-electron oxidation processes at $E_{1/2}$ = 0.30 and 0.54 V (*vs*. Fc^+/Fc).[1] These processes have been assigned to ligand-based oxidations,[11] and the more positive potentials observed for $Zn^RL_O^{NMe}$ (R = Cl, Br, Nap) relative those of $Zn^{tBu}L_o^{NMe}$ are consistent with the incorporation of more electron withdrawing substituents at the 3 and 5 positions in the phenolate rings of $Zn^RL_O^{NMe}$. Furthermore, the lack of electrochemical reversibility for the redox processes in $Zn^RL_O^{NMe}$ (R = Cl, Br, Nap) relative to those in $Zn^{tBu}L_o^{NMe}$ may be attributed to the decomposition of the oxidised products of $Zn^RL_O^{NMe}$; the incorporation of sterically demanding ^{t}butyl protecting groups at 3 and 5 positions of the phenolate rings have been shown to confer stability on coordinated phenoxyl radical species,.[11-13]

$Cu^RL_O^{NMe}$ (R = Cl, Br, Nap) also exhibit two electrochemical oxidation processes that are not electrochemically reversible (E_p^a = 0.67 and 0.99 V, 0.68 and 0.92 V, and 0.62 and 0.94 V *vs.* Fc^+/Fc for Cl, Br and Nap respectively) (Figure 3.2.1.2 Right). This contrasts with the reversible electrochemical behaviour found for $Cu^{tBu}L_o^{NMe}$,[1] and for other Cu^{II} phenolate complexes containing ^{t}butyl substituted phenolate rings including the Cu^{II} complexes of 3,5-di-^{t}butyl-N-(dimethylaminoethyl) salicylideneamine, 1-ethyl-4,7-bis(3-^{t}butyl-5-methoxy-2-hydroxybenzyl)-1,4,7-triazacyclononane and 1,4,7-tris(3,5-di-^{t}butyl-2-hydroxy-benzyl)-1,4,7-triazacyclononane.[14-16]

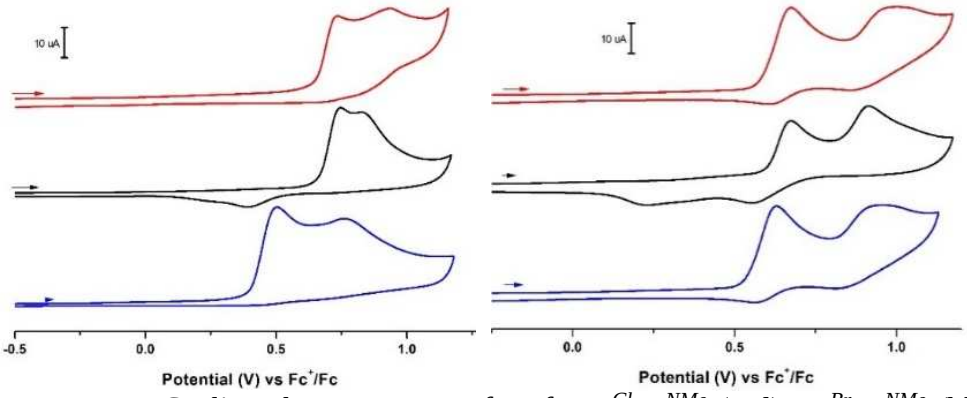


Figure 3.2.1.2: Cyclic voltammograms of: Left- $Zn^{Cl}L_O^{NMe}$ (red), $Zn^{Br}L_O^{NMe}$ (black) and $Zn^{Nap}L_O^{NMe}$ (blue); Right- $Cu^{Cl}L_O^{NMe}$ (red), $Cu^{Br}L_O^{NMe}$ (black) and $Cu^{Nap}L_O^{NMe}$ (blue). 100 mV scan rate in CH_2Cl_2 with 0.4 M $[^nBu_4N]^+[BF_4]^-$ as supporting electrolyte.

$Ni^{R}L_{O}^{NMe}$ (R = Cl, Br, Nap) exhibit processes at $E_{1/2}$ = 0.41 V, 0.41 V and 0.67 V (*vs*. Fc^{+}/Fc) for $Ni^{Cl}L_{O}^{NMe}$, $Ni^{Br}L_{O}^{NMe}$ and $Ni^{Nap}L_{O}^{NMe}$, respectively (Figure 3.2.1.3). These processes exhibit electrochemical reversibility with E_p^c and E_p^a being independent of scan rate, $|E_p^c - E_p^a|$ equivalent to that of the internal standard (Fc^{+}/Fc), $|i_p^c / i_p^a| \sim 1$, and i_p^c and i_p^a being proportional to (scan rate)$^{1/2}$ (Figure 3.2.1.4). They also show an additional oxidation process at a more positive potential (1.05 V, 1.00 V and 0.73 V *vs*. Fc^{+}/Fc for $Ni^{Cl}L_{O}^{NMe}$, $Ni^{Br}L_{O}^{NMe}$ and $Ni^{Nap}L_{O}^{NMe}$ respectively), which is not reversible although for $Ni^{Cl}L_{O}^{NMe}$ a return wave becomes apparent at higher scan rates (Figure 3.2.1.4B).

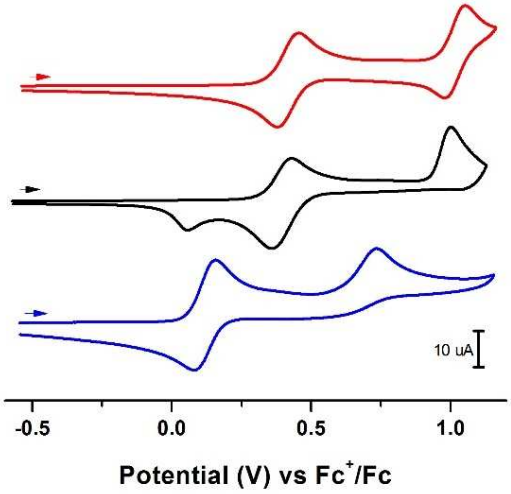
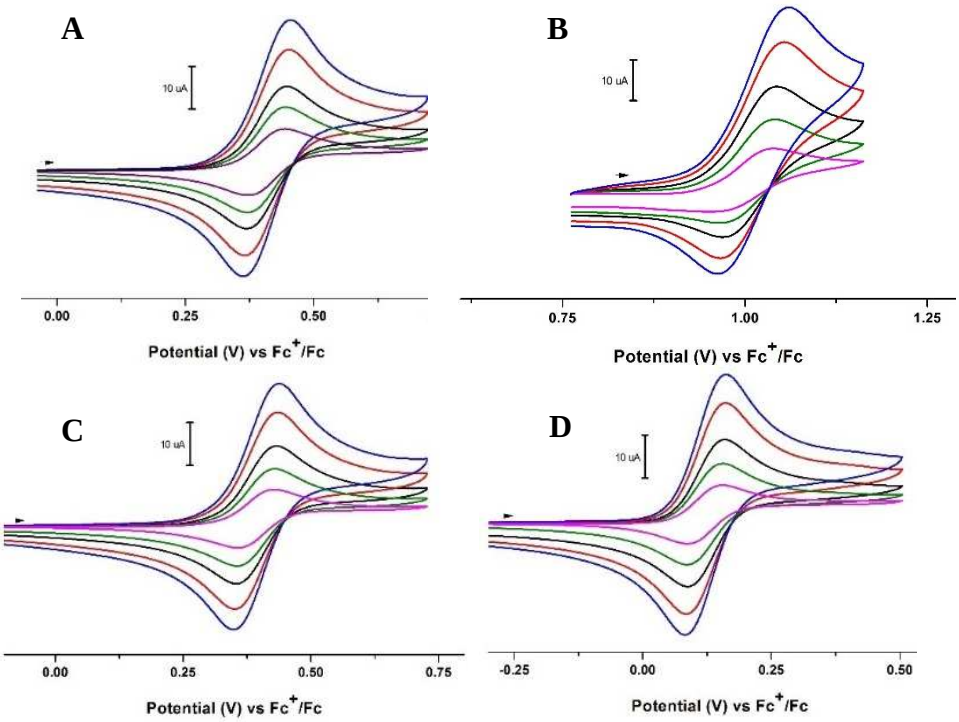


Figure 3.2.1.3*: Cyclic voltammograms of* $Ni^{Cl}L_{O}^{NMe}$ *(red),* $Ni^{Br}L_{O}^{NMe}$ *(black) and* $Ni^{Nap}L_{O}^{NMe}$ *(blue). 100 mV scan rate in* CH_2Cl_2 *with 0.4 M* $[^{n}Bu_4N]^{+}[BF_4]^{-}$ *as supporting electrolyte.*



Complex	**$E_{1/2}$ V (*vs.* Fc^+/Fc)**	**i_p^c μA (100 mV)**	**i_p^a μA (100 mV)**	**$\lvert i_p^c / i_p^a \rvert$ (100 mV)**	**$\lvert E_p^c - E_p^a \rvert$ mV**	**$\lvert E_p^c - E_p^a \rvert$ mV (Fc^+/Fc)**
[Ni($^{Cl}L_O^{NMe}$)]	0.41	19.8	-18.3	1.08	80	70
[Ni($^{Br}L_O^{NMe}$)]	0.41	18.1	-17.5	1.03	80	70
[Ni($^{Nap}L_O^{NMe}$)]	0.12	17.9	-19.6	0.91	70	70 (dmfc)

Figure 3.2.1.4*: **A** and **B**: Cyclic voltammograms of the two processes observed for $Ni^{Cl}L_O^{NMe}$ at 0.41 V (**A**) and 1.05 V (**B**) **C**: Reversible process for $Ni^{Br}L_O^{NMe}$ at 0.41 V **D**: Reversible process for $Ni^{Nap}L_O^{NMe}$ at 0.12 V. All presented at varying scan rates (300 mV blue, 200 mV red, 100 mV black, 50 mV green, 20 mV purple).*

3.2.2 UV/vis-Spectroelectrochemistry of $Ni^{Cl}L_o^{NMe}$, $Ni^{Br}L_o^{NMe}$, and $Ni^{Nap}L_o^{NMe}$

The first oxidation process for $Ni^{Cl}L_o^{NMe}$, $Ni^{Br}L_o^{NMe}$, and $Ni^{Nap}L_o^{NMe}$ at $E_{1/2}$ = 0.41, 0.41 and 0.12 V (*vs.* Fc^+/Fc), respectively were examined by UV/vis spectroelectrochemistry. This technique monitors changes in the UV/vis spectroscopic properties of species generated *in situ* during the controlled potential electrolysis of the bulk solution. Spectroelectrochemical measurements were carried out at -20 °C under an inert atmosphere of dinitrogen in CH_2Cl_2 solution with 0.4 M of supporting electrolyte ($[^nBu_4N]^+[BF_4]^-$) in an optically transparent electrochemical cell. Full experimental details are presented in Appendix 1.

The UV/vis spectra of $Ni^{Cl}L_o^{NMe}$ and $Ni^{Br}L_o^{NMe}$ are similar, with two resolved absorption bands at 239 and 371 nm (ε = 62000 and 12600 mol^{-1} dm^3 cm^{-1}) and 240 and 380 nm (ε = 65,500 and 13,800 mol^{-1} dm^3 cm^{-1}), respectively. These

absorptions may be potentially assigned to phenoxide π to π* transitions for the bands at *ca.* 240 nm and LMCT transitions for the bands at *ca.* 371 to 380 nm, as has been observed previously for other Ni^{II} diphenolate complexes including $Ni^{tBu}L_o^{NMe}$ (λ = 238, ε = 84,300 mol^{-1} dm^3 cm^{-1} and λ = 376, ε = 18,300 mol^{-1} dm^3 cm^{-1}), $Ni(L^{Py})$ (LPy = N,N′,N,N′-bis[(2-hydroxy-3,5-di^{t}butylbenzyl)(2-pyridylmethyl)]-ethylenediamine; λ = 310, ε = 13,500 mol^{-1} dm^3 cm^{-1} and λ = 369, ε = 760 mol^{-1} dm^3 cm^{-1}) and $Ni(LAmH)_2$ (LAmH =3,5-di-^{t}butyl-N-(dimethylaminoethyl)salicylideneamine); λ = 311, ε = 10,540 mol^{-1} dm^3 cm^{-1} and λ = 377, ε = 2,320 mol^{-1} dm^3 cm^{-1}).[1, 7, 14, 17, 18]

On electrochemical oxidation of $Ni^{Cl}L_o^{NMe}$ and $Ni^{Br}L$ at 253 K and 1.25 V and 1.23 V (*vs.* Ag/AgCl), respectively, the band at *ca.* 240 nm diminishes in intensity (ε = 41,800 and 38,900 mol^{-1} dm^3 cm^{-1} for $Ni^{Cl}L_o^{NMe}$ and $Ni^{Br}L_o^{NMe}$ respectively), whilst an additional shoulder grows in at 293 nm and 290 nm (ε = 22,100 and 28,200 mol^{-1} dm^3 cm^{-1}) for $Ni^{Cl}L_o^{NMe}$ and $Ni^{Br}L_o^{NMe}$ respectively. The band at *ca.* 400 nm broadens and grows in intensity (ε = 14,100 and 15,600 mol^{-1} dm^3 cm^{-1} for $Ni^{Cl}L_o^{NMe}$ and $Ni^{Br}L_o$, respectively) and the observation of an isobestic point for both species at *ca.* 262 nm indicates that the oxidation of $Ni^{R}L_o^{NMe}$ to $[Ni^{R}L_o^{NMe}]^+$ (R = Cl, Br) proceeds directly with no observable intermediates.

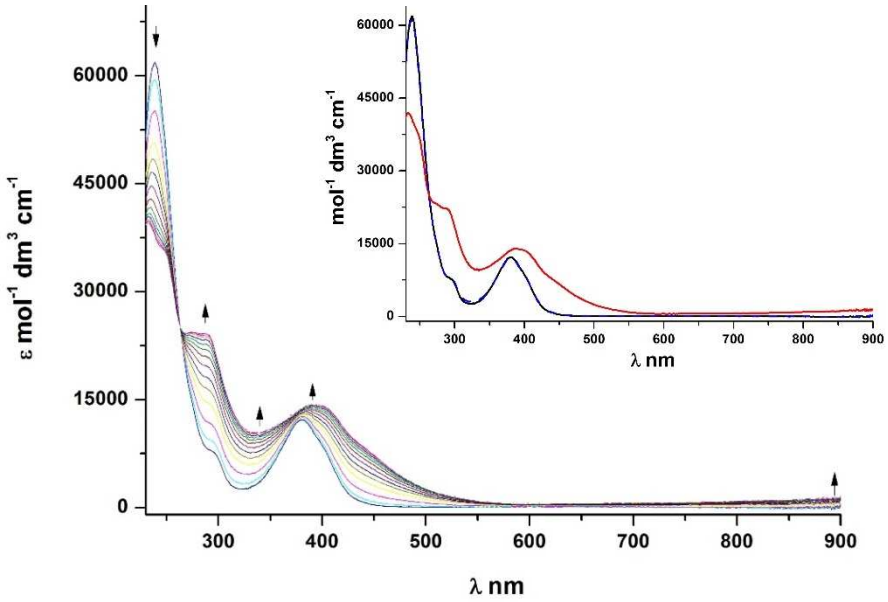


Figure 3.2.2.1: Sequential UV/vis spectra recorded during the oxidation of $^{Cl}NiL_o^{NMe}$ at 1.25 V vs. Ag/AgCl identifying the bands formed during oxidation. 0.40 mmol solution recorded at 253 K under N_2 in CH_2Cl_2 containing 0.4 M $[^nBu_4][BF_4]$ as supporting electrolyte. Inset, spectra before oxidation (black), after oxidation (red) and after re-reduction at 0.00 V vs. Ag/AgCl (blue).

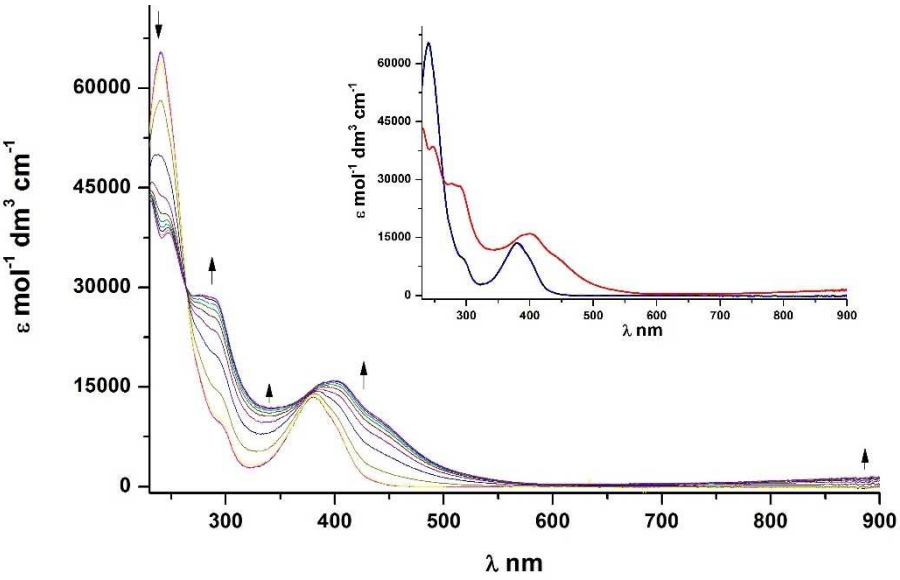


Figure 3.2.2.2: Sequential UV/vis spectra recorded during the oxidation of $^{Br}NiL_o^{NMe}$ at 1.23 V vs. Ag/AgCl identifying the bands formed during oxidation. 0.49 mmol solution recorded at 253 K under N_2 in CH_2Cl_2 containing 0.4 M $[^nBu_4][BF_4]$ as supporting electrolyte. Inset, spectra before oxidation (black), after oxidation (red) and after re-reduction at 0.00 V vs. Ag/AgCl (blue).

The UV/vis spectrum of $Ni^{Nap}L_o^{NMe}$ possesses well-resolved absorption bands at 255 nm, 314 nm and 382 nm (ε = 58,100, 20,800 and 13,000 mol^{-1} dm^3 cm^{-1}), and additional shoulders at 233 nm and 408 nm (ε = 42,800 and 9,430 mol^{-1} dm^3 cm^{-1}). On oxidation at 0.92 V (*vs.* Ag/AgCl), the bands at 314 nm and 382 nm increase in intensity (ε = 26,100 and 19,200 mol^{-1} dm^3 cm^{-1}), whilst the band at 255 nm decreases in intensity (ε = 34,000 mol^{-1} dm^3 cm^{-1}), with the shoulder at 233 nm developing into a clear band at 230 nm (ε = 53,800 mol^{-1} dm^3 cm^{-1}). The shoulder at 408 nm remains resolved but is less intense (ε = 16,100 mol^{-1} dm^3 cm^{-1}). The presence of isobestic points at 240 and 290 nm again indicates that the process occurs directly with no observable intermediates.

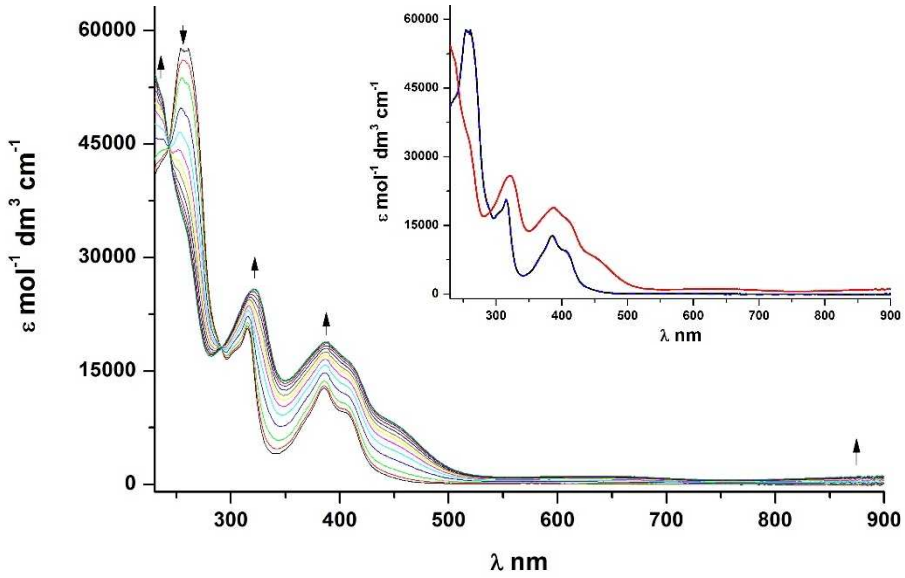


Figure 3.2.2.3: Sequential UV/vis spectra recorded during the oxidation of $^{Nap}NiL_o^{NMe}$ *at 0.92 V vs. Ag/AgCl identifying the bands formed during oxidation. 0.79 mmol solution recorded at 253 K under* N_2 *in* CH_2Cl_2 *containing 0.4 M* $[N^nBu_4][BF_4]$ *as supporting electrolyte. Inset, spectra before oxidation (black), after oxidation (red) and after re-reduction at 0.00 V vs. Ag/AgCl (blue).*

These changes observed are broadly in line with those observed for $Ni^{Cl}L_o^{NMe}$ and $Ni^{Br}L_o^{NMe}$ and the bands at *ca.* 380 nm can be assigned to a LMCT. The oxidation processes at 0.41 V, 0.41 V and 0.12 V (*vs.* Fc^+/Fc) for $Ni^{Cl}L_o^{NMe}$, $Ni^{Br}L_o^{NMe}$ and $Ni^{Nap}L_o^{NMe}$ respectively are fully chemically reversible; re-reduction generates identical spectra to those for $Ni^{Cl}L_o^{NMe}$, $Ni^{Br}L_o^{NMe}$ and $Ni^{Nap}L_o^{NMe}$ (Figures 3.2.2.1-3.2.2.3 inset).

3.2.3 Discussion

Our electrochemical results demonstrate that changes in phenolate substituents have a significant effect on the redox potentials of the oxidation processes for $Ni^{Cl}L_o^{NMe}$, $Ni^{Br}L_o^{NMe}$ and $Ni^{Nap}L_o^{NMe}$. The first oxidation process for $Ni^RL_O^{NMe}$ (R = Cl, Br, Nap) is likely to be Ni-based given its electrochemical reversibility, which is absent in the Zn^{II} and Cu^{II} analogues, and through comparisons with $Ni^{tBu}L_O^{NMe}$.[1] The additional oxidation processes at more positive potentials are considered to be ligand based. The profiles of the UV/vis spectra support the assignment of the first electrochemical process for $Ni^RL_O^{NMe}$ (R = Cl, Br, Nap) as primarily metal-based through comparisons with $[Ni^{tBu}L_o^{NMe}]^+$ (λ = 271, 303, 388, 485, and 668 nm; ε = 35,100, 37,700, 19,200, 9,500, and 2,700 mol^{-1} dm^3 cm^{-1})

and [Ni(N,N′-bis(3,5-di^{t}butylthiosalicylaldene)-1,2-phenylenediamine)]$^+$ (λ = 460 and 665 nm; ε = 1,700, and 590 mol^{-1} dm^3 cm^{-1}).[1, 12]

Complex	λ_{max} (nm)	ε (mol^{-1} dm^3 cm^{-1})	Isobestic point (nm)
$Ni^{Cl}L_O^{NMe}$	239, 296, 371	62,000, 7,700, 12,600	
$[Ni^{Cl}L_O^{NMe}]^+$	240, 293(sh), 391	41,800, 22,100, 14,100	219, 263
$Ni^{Br}L_O^{NMe}$	240, 295(sh), 380	65,500, 9,800, 13,800	
$[Ni^{Br}L_O^{NMe}]^+$	231, 247, 290(sh), 402	43,400, 38,500, 28,200, 15,600	264
$Ni^{Nap}L_O^{NMe}$	233sh, 255, 314, 382, 408(sh)	42,800, 58,100, 20,800, 13,000, 9,430	
$[Ni^{Nap}L_O^{NMe}]^+$	230, 255(sh), 314, 382, 408	53,800, 34,000, 26,100, 19,200, 16,100	244, 291

Table 3.2.3.1: Summary of UV/vis spectra of $Ni^RL_o^{NMe}$, $[Ni^RL_o^{NMe}]^+$, (R = Cl, Br, Nap).

The changes incorporated into the ligand backbone appear to modulate the redox potentials of the oxidation processes of $Ni^{Cl}L_o^{NMe}$, $Ni^{Br}L_o^{NMe}$ and $Ni^{Nap}L_o^{NMe}$. Comparison of the results for $Ni^{Cl}L_O^{NMe}$ and $Ni^{Br}L_O^{NMe}$ shows no significant change in the potential for the first oxidation ($E_{1/2}$ = 0.41 V and 0.41 V *vs.* Fc^+/Fc) but a significant perturbation in the potential of the second (E_p^a = 1.05 and 1.00 V *vs.* Fc^+/Fc, respectively). Our spectroelectrochemical results demonstrate the chemically reversible nature of the first oxidation process at 0.41 V, 0.41 V and 0.12 V (*vs.* Fc^+/Fc) for $Ni^RL_O^{NMe}$ (R = Cl, Br, Nap respectively), and are consistent with metal based oxidation processes in each case. It appears that halogen substitution at the 3 and 5 positions may contribute to the reduction in the electrochemical reversibility for the second redox process in $Ni^{Cl}L_O^{NMe}$ and $Ni^{Br}L_O^{NMe}$, and for the lack of electrochemical reversibility for $M^RL_O^{NMe}$ (M = Zn, Cu; R = Cl, Br). This is consistent with the assignment of these processes to ligand-based oxidation.

3.3 Electrochemistry of $M^{R}L_{o}^{NMe}$, (M = Zn, Ni, Cu; R = Ph, PhMe, PhOMe)

The electrochemical behaviours of $M^{R}L_{o}^{NMe}$ (M = Zn, Ni, Cu; R = Ph, PhMe, PhOMe) (Figure 3.2.1.1) were investigated by cyclic voltammetry and each complex exhibits multiple redox processes.

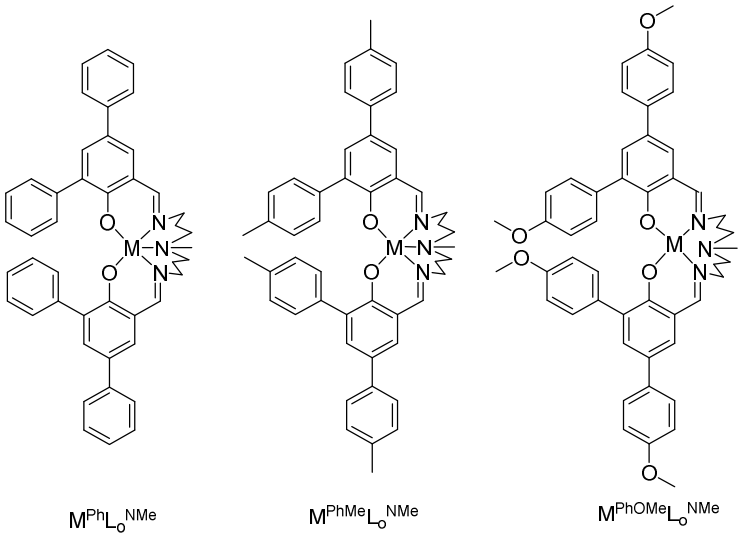


Figure 3.2.1.1: Complexes $M^{R}L_{O}^{NMe}$ (R = Ph, PhMe, PhOMe; M = Zn, Ni, Cu).

3.3.1 Cyclic Voltammetry of $Zn^{R}L_{o}^{NMe}$, (R = Ph, PhMe, PhOMe)

$Zn^{Ph}L_{o}^{NMe}$ and $Zn^{PhMe}L_{o}^{NMe}$ each exhibit three processes at E_{p}^{a} = 0.46, 0.58 and 1.06 V, and 0.39, 0.53 and 1.01 V (*vs.* Fc^{+}/Fc), respectively, whilst $Zn^{PhOMe}L_{o}^{NMe}$ possesses four processes at E_{p}^{a} = 0.31, 0.41, 0.70 and 0.78 V (*vs.* Fc^{+}/Fc) (Figure 3.3.1.1 and Table 3.3.1.1).

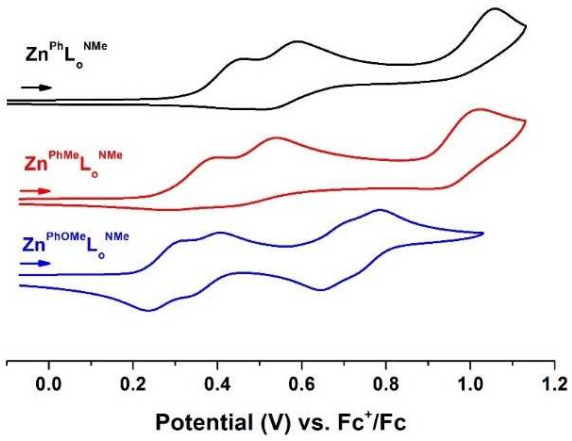


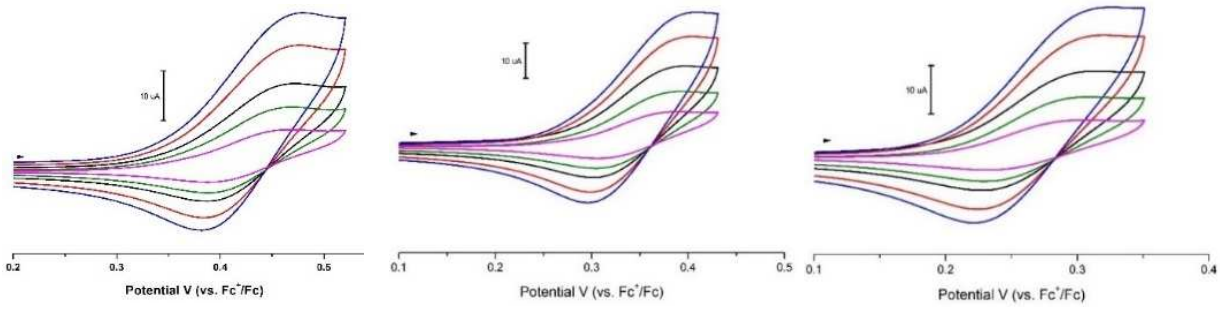
Figure 3.3.1.1: Cyclic voltammograms of $Zn^{Ph}L_o^{NMe}$ $Zn^{PhMe}L_o^{NMe}$ and $Zn^{PhOMe}L_o^{NMe}$ (100 mV scan rate).

Complex	1st Process E_p^a (V *vs.* Fc+/Fc)	2nd Process E_p^a (V *vs.* Fc+/Fc)	3rd Process E_p^a (V *vs.* Fc+/Fc)	4th Process E_p^a (V *vs.* Fc+/Fc)
$Zn^{Ph}L_o^{NMe}$	0.46	0.58	1.06	-
$Zn^{PhMe}L_o^{NMe}$	0.39	0.53	1.01	-
$Zn^{PhOMe}L_o^{NMe}$	0.31	0.41	0.70	0.78

Table 3.3.1.1: Potentials of oxidation processes observed for $Zn^{Ph}L_o^{NMe}$ $Zn^{PhM}L_o^{NMe}$ and $Zn^{PhOMe}L_o^{NMe}$.

The first two redox processes for $Zn^RL_o^{NMe}$ (R = Ph, PhMe, PhOMe) at E_p^a = 0.31-0.58 V (*vs.* Fc^+/Fc) occur at potentials similar to those of $Zn(L)_2$ (LH = bis(2'-(4',6'-di-^{t}butylhydroxyphenyl)-4,5-diphenyl imidazole; $E_{1/2}$ = 0.23 and 0.49 V *vs.* Fc^+/Fc).[19] The reversibility of the first oxidation processes for $Zn^RL_o^{NMe}$ (R = Ph, PhMe, PhOMe) is difficult to determine because of their overlap with second process in all three cases, although all three complexes demonstrate a reduction wave for this first process at faster scan rates (Figure 3.3.1.2 and Table 3.3.1.2).

The potential of the first process for $Zn^RL_o^{NMe}$ (R = Ph, PhMe, PhOMe) at E_p^a = 0.46, 0.39 and 0.31 V, respectively (Table 3.3.1.1), is more positive than that found for the ^{t}butyl substituted analogue $Zn^{tBu}L_o^{NMe}$ (0.30 V vs. Fc^+/Fc), whereas the potential for the second oxidation process of $Zn^{PhMe}L_o^{NMe}$, $Zn^{Ph}L_o^{NMe}$ and $Zn^{PhOMe}L_o^{NMe}$ is similar to that for $Zn^{tBu}L_o^{NMe}$ (0.54 V vs. Fc^+/Fc).[1] The general trend is that ligand systems incorporating more electron donating substituents lead to lower reduction potentials and this, together with the redox inactive d^{10} electronic configuration of Zn^{II} over this potential range,[11] suggests that the oxidation of $Zn^RL_o^{NMe}$ (R = Ph, PhMe, PhOMe) is associated with the formation of phenoxyl radical species.

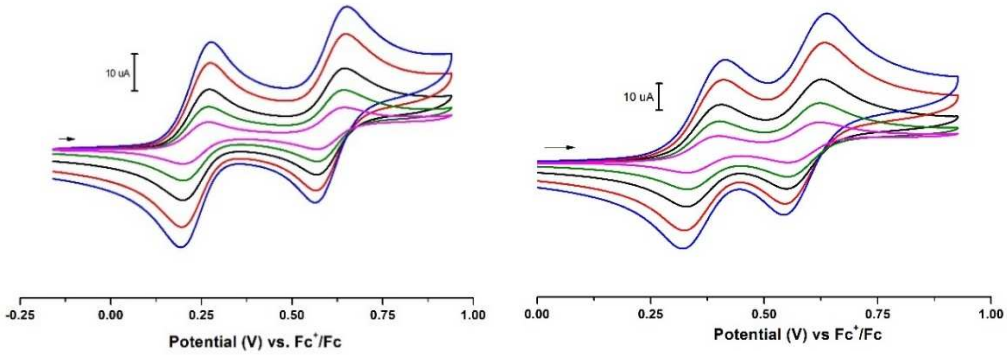


Complex	**$E_{1/2}$ V (*vs.* Fc^+/Fc)**	**i_p^c µA**	**i_p^a µA**	**$\|i_p^c/ i_p^a\|$**	**$\|E_p^c-E_p^a\|$ mV**	**$\|E_p^c-E_p^a\|$ mV (Fc^+/Fc)**
$Zn^{Ph}L_o^{NMe}$	0.43	16.1	-15.7	1.03	90	80
$Zn^{PhMe}L_o^{NMe}$	0.35	17.3	-18.1	0.96	90	80
$Zn^{PhOMe}L_o^{NMe}$	0.27	16.9	-15.3	1.10	90	80

Figure 3.3.1.2: 1st oxidation process for $Zn^{Ph}L_o^{NMe}$, $Zn^{PhMe}L_o^{NMe}$ and $Zn^{PhOMe}L_o^{NMe}$ at multiple scan rates (300 mV (blue), 200 mV (red), 100 mV (black), 50 mV (green), 20 mV (purple)).

3.3.2 Cyclic Voltammetry of $M^RL_o^{NMe}$, (M = Ni, Cu; R = Ph, PhMe, PhOMe)

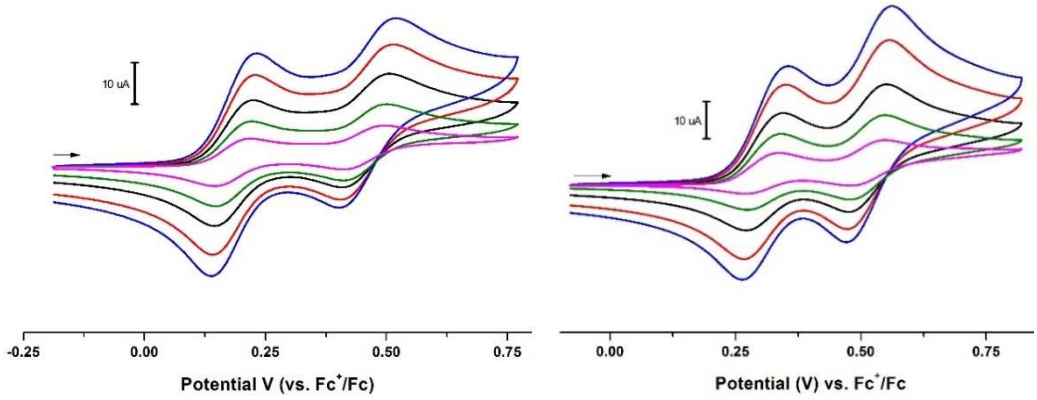
$Ni^{Ph}L_o^{NMe}$ and $Cu^{Ph}L_o^{NMe}$ each possess two reversible processes at $E_{1/2}$ = 0.24 and 0.61 and $E_{1/2}$ = 0.37 and 0.59 V (*vs.* Fc^+/Fc), respectively (Figure 3.3.1.3).



Complex	**$E_{1/2}$ V (*vs.* Fc^+/Fc)**	**i_p^c µA (100 mV)**	**i_p^a µA (100 mV)**	**$\|i_p^c/ i_p^a\|$ (100 mV)**	**$\|E_p^c-E_p^a\|$ mV**	**$\|E_p^c-E_p^a\|$ mV ($dmfc^+/dmfc$)**
$Ni^{Ph}L_o^{NMe}$	0.24	-14.3	15.0	0.95	80	80
	0.61	-14.3	15.0	0.95	90	
$Cu^{Ph}L_o^{NMe}$	0.37	-18.5	19.1	0.97	90	90
	0.59	-19.8	14.9	1.32	90	

Figure 3.3.2.1: Reversible oxidations of $Ni^{Ph}L_o^{NMe}$ (Left), and $Cu^{Ph}L_o^{NMe}$ (Right) at multiple scan rates (300 mV (blue), 200 mV (red), 100 mV (black), 50 mV (green), 20 mV (purple)).

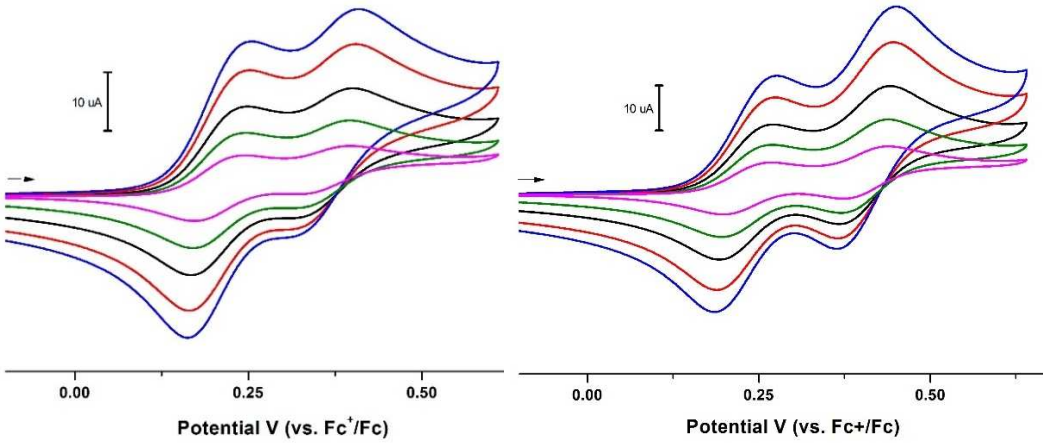
$Ni^{PhMe}L_o^{NMe}$ and $Cu^{PhMe}L_o^{NMe}$ also exhibit processes over a similar potential range to those of $Ni^{Ph}L_o^{NMe}$ and $Cu^{Ph}L_o^{NMe}$. $Ni^{PhMe}L_o^{NMe}$ exhibits one electrochemically reversible process ($E_{1/2}$ = 0.19 V *vs.* Fc^+/Fc) and a second process (E_p^a = 0.51 V *vs.* Fc^+/Fc). $Cu^{PhMe}L_o^{NMe}$ exhibits two processes ($E_{1/2}$ = 0.31 and 0.52 V *vs.* Fc^+/Fc), which are both electrochemically reversible (Figure 3.3.2.2).



Complex	**$E_{1/2}$ V (*vs.* Fc^+/Fc)**	**i_p^c μA (100 mV)**	**i_p^a μA (100 mV)**	**$\lvert i_p^c / i_p^a \rvert$ (100 mV)**	**$\lvert E_p^c - E_p^a \rvert$ mV**	**$\lvert E_p^c - E_p^a \rvert$ mV ($dmfc^+/dmfc$)**
$Ni^{PhMe}L_o^{NMe}$	0.19	15.1	-14.2	1.06	80	70
$Cu^{PhMe}L_o^{NMe}$	0.31	13.2	-14.2	0.93	70	70
	0.52	14.8	-18.0	0.82	70	

Figure 3.3.2.2: Oxidations of $Ni^{PhMe}L_o^{NMe}$ (Left), and $Cu^{PhMe}L_o^{NMe}$ (Right) at multiple scan rates (300 mV (blue), 200 mV (red), 100 mV (black), 50 mV (green), 20 mV (purple)).

The methoxy substituted complexes $Ni^{PhOMe}L_o^{NMe}$ and $Cu^{PhOMe}L_o^{NMe}$ also exhibit similar electrochemical behaviour to those of $Ni^{Ph}L_o^{NMe}$ and $Cu^{Ph}L_o^{NMe}$. The first process for $Ni^{PhOMe}L_o^{NMe}$ ($E_{1/2}$ = 0.17 V *vs.* Fc^+/Fc) is electrochemically reversible whilst the second (E_p^a = 0.40 V *vs.* Fc^+/Fc) is not reversible. Two electrochemically reversible oxidation processes are observed for $Cu^{PhOMe}L_o^{NMe}$ ($E_{1/2}$ = 0.24 and 0.40 V *vs.* Fc^+/Fc) (Figure 3.3.2.3).



Complex	$E_{1/2}$ V (*vs.* Fc^+/Fc)	i_{pc} μA (100 mV)	i_{pa} μA (100 mV)	$\lvert i_p^c / i_p^a \rvert$ (100 mV)	$\lvert E_p^c - E_p^a \rvert$ mV	$\lvert E_p^c - E_p^a \rvert$ mV ($dmfc^+/dmfc$)
$Ni^{PhOMe}L_o^{NMe}$	0.17	13.7	13.1	1.05	80	80
$Cu^{PhOMe}L_o^{NMe}$	0.24	14.3	14.0	1.02	80	80
	0.40	13.4	14.2	0.94	80	

Figure 3.3.2.3: Oxidations of $Ni^{PhOMe}L_o^{NMe}$ (Left), and $Cu^{PhOMe}L_o^{NMe}$ (Right) at multiple scan rates (300 mV (blue), 200 mV (red), 100 mV (black), 50 mV (green), 20 mV (purple)).

The first two processes of $M^RL_o^{NMe}$ (M = Ni, Cu; R = Ph, PhMe, PhOMe) may be compared to those observed for the analogous ^{t}butyl substituted complexes $M^{tBu}L_o^{NMe}$ (M = Ni, Cu), which possess two quasi reversible processes at $E_{1/2}$ = 0.13 and 0.57 V *vs.* Fc^+/Fc and two electrochemically reversible processes $E_{1/2}$ = 0.24 and 0.57 V *vs.* Fc^+/Fc, for M = Ni and Cu, respectively.[1] This redox activity is also consistent with previous results for other bis-phenolate complexes. Thus, the potentials observed for $Ni^RL_o^{NMe}$ (R = Ph, PhMe, PhOMe, ^{t}Bu)[1] are intermediate to those reported for four coordinate Ni(^{Me}L) (^{Me}L = N,N′-bis(3,5-di^{t}butylsalicylaldene)-4,5-dimethyl-1,2-phenylenediamine; $E_{1/2}$ = 0.49 V and 0.78 V *vs.* Fc^+/Fc)[20-22] and six[7] coordinate Ni(L^{tBu1}) (L^{tBu1} = 2-hydroxy-4,6-di^{t}butylbenzyl-2-(pyridylmethyl)imine); $E_{1/2}$ = −0.01 V and 0.32 V *vs.* Fc^+/Fc). The reduction potentials for $Cu^RL_o^{NMe}$, (R = Ph, PhMe, PhOMe) are similar to those of other bis-phenolate Cu^{II} species $Cu(L^{tBu2})_2$ (HL^{tBu2} = [2′-(4′,6′-di^{t}butylhydroxyphenyl)]-4,5-diphenylimidazole; $E_{1/2}$ = 0.16 and 0.50 V *vs.* Fc^+/Fc) and $Cu(L^{tBu3})_2$ [HL^{tBu3} = 2-[2′-(4′,6′-di^{t}butylhydroxyphenyl)]-4,5-bis(p-methoxyphenyl)imidazole; $E_{1/2}$= 0.11 and 0.44 V *vs.* Fc^+/Fc) which form mono- and bis- phenoxyl species.[23-26]

$M^{R}L_{o}^{NMe}$ (M = Ni, Cu, R = Ph, PhMe, PhOMe) also exhibit additional oxidation processes at more positive potentials as found for $Zn^{R}L_{o}^{NMe}$ (R = Ph, PhMe, PhOMe) (Section 3.3.1). For $M^{Ph}L_{o}^{NMe}$ and $M^{PhMe}L_{o}^{NMe}$ (M = Ni, Cu) one additional process is observed by cyclic voltammetry at >0.80 V (*vs.* Fc^{+}/Fc), whilst $Ni^{PhOMe}L_{o}^{NMe}$ and $Cu^{PhOMe}L_{o}^{NMe}$ appear to exhibit two overlapping processes at *ca.* 0.80 V (Figure 3.3.2.4).

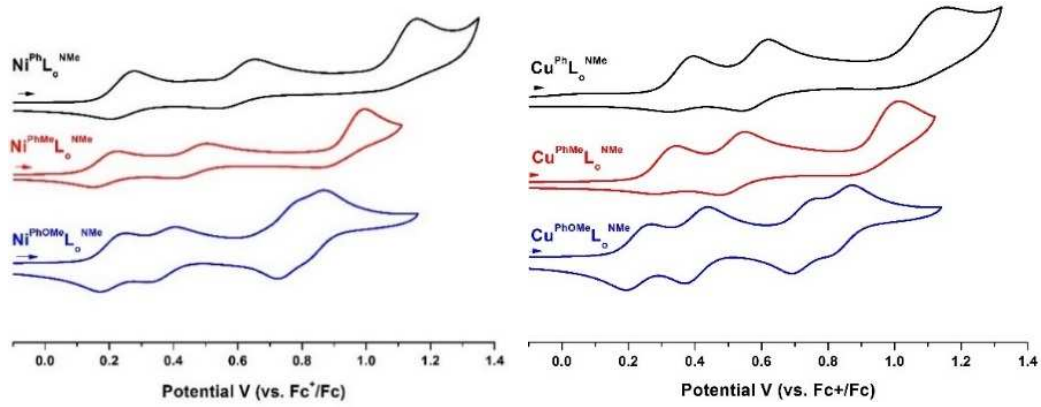


Figure 3.3.2.4: Cyclic voltammograms of $Ni^{R}L_{o}^{NMe}$ (R = Ph, PhMe, PhOMe) (Left) and $Cu^{R}L_{o}^{NMe}$ (R = Ph, PhMe, PhOMe) (Right), showing oxidation features at more positive potentials.

These processes for $M^{Ph}L_{o}^{NMe}$ and $M^{PhMe}L_{o}^{NMe}$ (M = Ni, Cu) are not reversible whereas the two closely overlapping processes for $M^{PhOMe}L_{o}^{NMe}$ (M = Ni, Cu) required further investigation by square wave voltammetry in an attempt separate these two features (Figure 3.3.2.5).

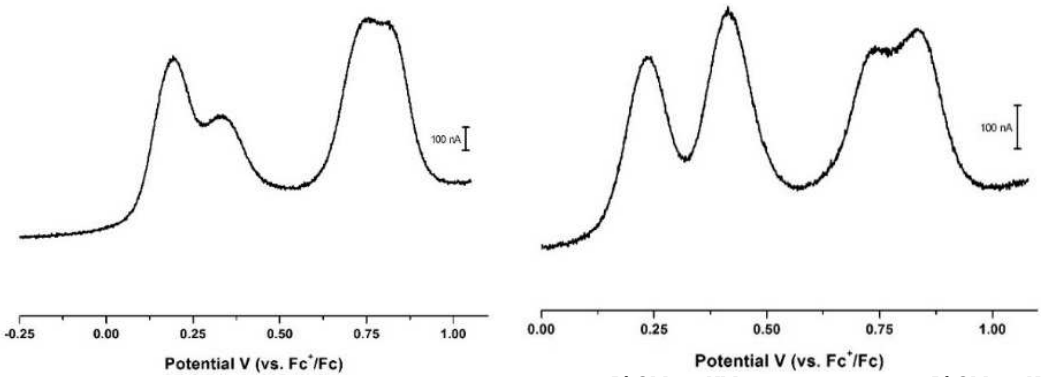


Figure 3.3.2.5: Square wave voltammetry of $Ni^{PhOMe}L_{o}^{NMe}$ (Left) and $Cu^{PhOMe}L_{o}^{NMe}$ (Right).

Exhaustive electrolysis at a potential of 0.95 V (*vs.* Fc^{+}/Fc) of a 1 mmol solution of $Ni^{PhOMe}L_{o}^{NMe}$ in CH_2Cl_2 resulted in the transfer of a total of four electrons (Figure 3.3.2.6 Left), and comparison of cyclic voltammograms recorded before and after

the electrolysis showed a fundamental change in the nature of the species after oxidation suggesting a chemical change occurs (Figure 3.3.2.6 Right).

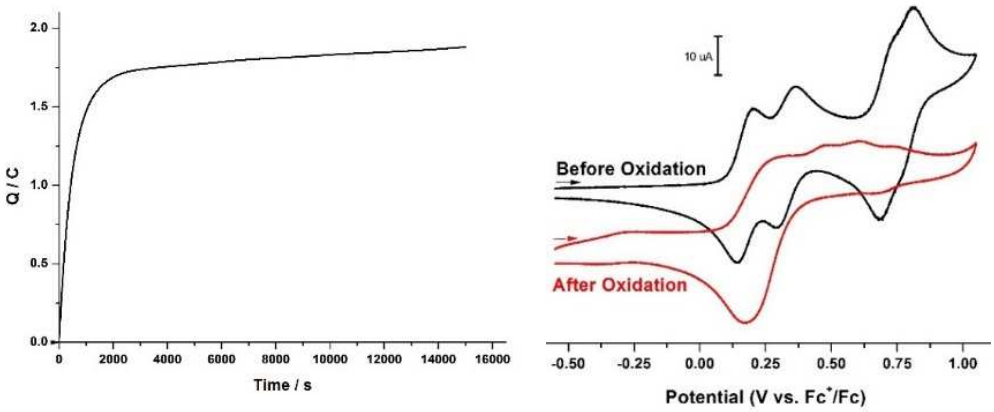


Figure 3.3.2.6: Left: Controlled potential electrolysis of $Ni^{PhOMe}L_O^{NMe}$ to $[Ni^{PhOMe}L_O^{NMe}]^{4+}$ at 0.95 V vs. Fc^+/Fc, 1 mmol solution in CH_2Cl_2 containing 0.4 M $[N^nBu_4][BF_4]$ as supporting electrolyte recorded at 253 K under Ar. Theoretical Q for a four electron process = 1.89 C; Right: Cyclic voltammograms of $Ni^{PhOMe}L_o^{NMe}$ (black) before oxidation and $[Ni^{PhOMe}L_o^{NMe}]^{4+}$ (red) after oxidation, recorded at 100 mV, 1 mmol solution in CH_2Cl_2 containing 0.4 M $[N^nBu_4][BF_4]$ as supporting electrolyte.

Analogous experiments using controlled potential electrolysis were also carried out for $Cu^{PhOMe}L_O^{NMe}$ at an applied potential of 0.98 V (*vs.* Fc^+/Fc). Similar results were obtained with significant changes observed in the redox activity of the complex after oxidation. Attempts to characterise the products of the four electron oxidation of $Ni^{PhOMe}L_O^{NMe}$ and $Cu^{PhOMe}L_O^{NMe}$ were unsuccessful.

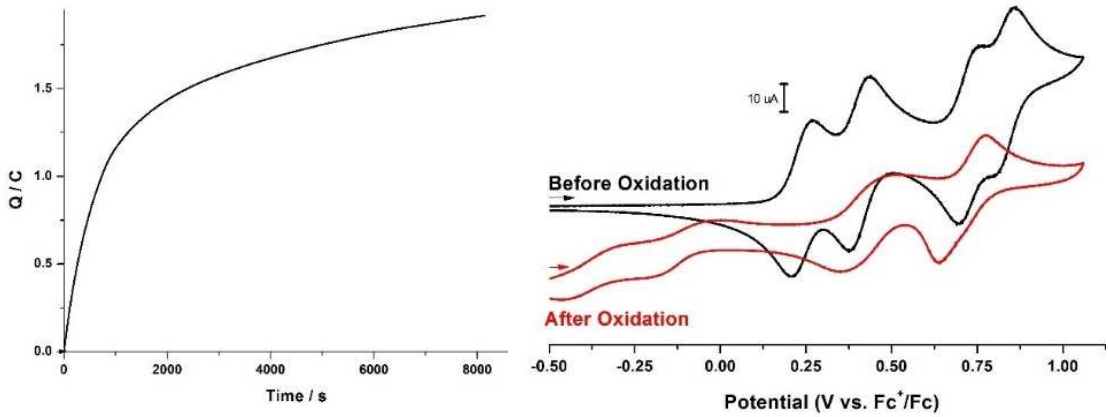


Figure 3.3.2.7: Left: Controlled potential electrolysis of $Cu^{PhOMe}L_O^{NMe}$ to $[Cu^{PhOMe}L_O^{NMe}]^{4+}$ at 0.98 V vs. Fc^+/Fc, 1 mmol solution in CH_2Cl_2 containing 0.4 M $[N^nBu_4][BF_4]$ as supporting electrolyte recorded at 253 K under Ar. Theoretical Q for a four electron process = 1.89 C; Right: Cyclic voltammograms of $Cu^{PhOMe}L_o^{NMe}$ (black) before oxidation and $[Cu^{PhOMe}L_o^{NMe}]^{4+}$ (red) after oxidation, recorded at 100 mV, 1 mmol solution in CH_2Cl_2 containing 0.4 M $[N^nBu_4][BF_4]$ as supporting electrolyte.

These results are different to those for $M^{R}L_{o}^{NMe}$ (M = Zn, Ni, Cu; R = Ph, PhMe), which exhibit only a single oxidation wave at potentials > 0.80 V. Exhaustive controlled potential electrolysis of $Ni^{PhMe}L_{o}^{NMe}$ at a potential of 1.05 V (*vs.* Fc^{+}/Fc) (Figure 3.3.2.8) is accompanied by the transfer of three electrons, demonstrating that each oxidation process at $E_{1/2}$ = 0.17 V, E_{p}^{a} = 0.40 V and E_{p}^{a} = 0.99 V (*vs.* Fc^{+}/Fc) involves one electron. Cyclic voltammetry before and after controlled potential electrolysis results in a voltammogram that does not exhibit the redox processes associated with a fresh solution of $Ni^{PhMe}L_{o}^{NMe}$. This is not surprising given that the process at E_{p}^{a} = 0.99 V (*vs.* Fc^{+}/Fc) V is not electrochemically reversible.

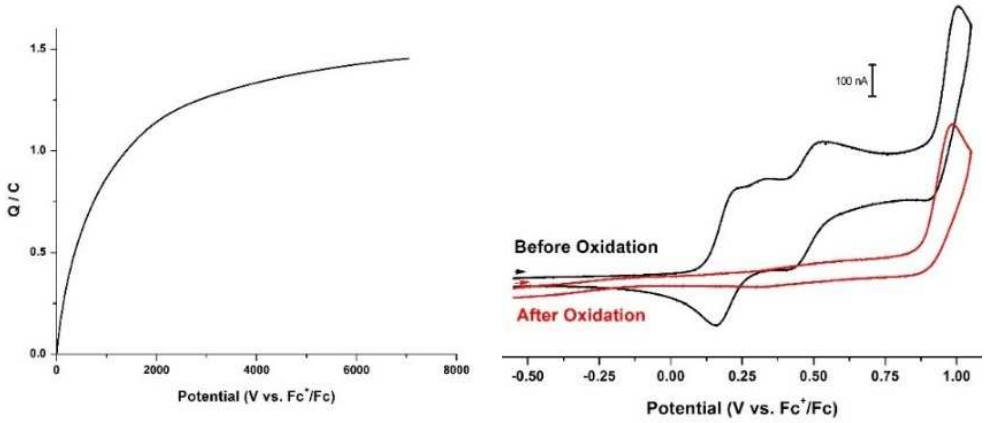


Figure 3.3.2.8: Left: Controlled potential electrolysis of $Ni^{PhMe}L_{O}^{NMe}$ to $[Ni^{PhMe}L_{O}^{NMe}]^{4+}$ at 1.05 V vs. Fc^{+}/Fc, 1 mmol solution in CH_2Cl_2 containing 0.4 M $[N^{n}Bu_4][BF_4]$ as supporting electrolyte recorded at 253 K under Ar. Theoretical Q for a three electron process = 1.43 C; Right: Cyclic voltammograms of $Ni^{PhMe}L_{o}^{NMe}$ (black) before oxidation and $[Ni^{PhMe}L_{o}^{NMe}]^{4+}$ (red) after oxidation, recorded at 100 mV, 1 mmol solution in CH_2Cl_2 containing 0.4 M $[N^{n}Bu_4][BF_4]$ as supporting electrolyte.

3.3.3 Discussion

The introduction of additional phenyl groups in the 3 and 5 positions of the phenolate rings of $M^{R}L_{o}^{NMe}$ (M = Zn, Ni, Cu; R = Ph, PhMe, PhOMe) appears to support the generation of stable products on oxidation, as observed for complexes incorporating ^{t}butyl groups in the 3 and 5 positions of the phenolate rings in $Ni^{tBu}L_{o}^{NMe}$ and $Cu^{tBu}L_{o}^{NMe}$.[1, 12, 27] The consensus view is that ^{t}butyl substitution at the 3 and 5 positions stabilise phenoxyl free radical species coordinated to metal centres by limiting decomposition pathways involving α hydrogen abstraction at the 3 and 5 positions.[11-13, 15] Our work has extended the nature of the substituents at

the 3 and 5 positions to include phenyl groups that can support coordinated phenoxyl free radical ligands. Moreover, our electrochemical characterisations of $M^{R}L_{o}^{NMe}$ (M = Zn, Ni, Cu; R = Ph, PhMe, PhOMe) demonstrate that the potentials of the oxidation processes can be tuned by substituents on the phenyl rings at the 3 and 5 positions and relatively remote from the metal centre. Thus, the introduction of electron donating groups onto the phenyl rings at the 3 and 5 positions of the phenolate rings results in a significant shift to a less positive potential for the second process in the case of $Ni^{R}L_{o}^{NMe}$ (R = Ph, PhMe, PhOMe; Figure 3.3.3.1 B), and for both the first and second processes for $M^{R}L_{o}^{NMe}$ (M = Zn, Cu; R = Ph, PhMe, PhOMe; Figure 3.3.3.1 A and C).

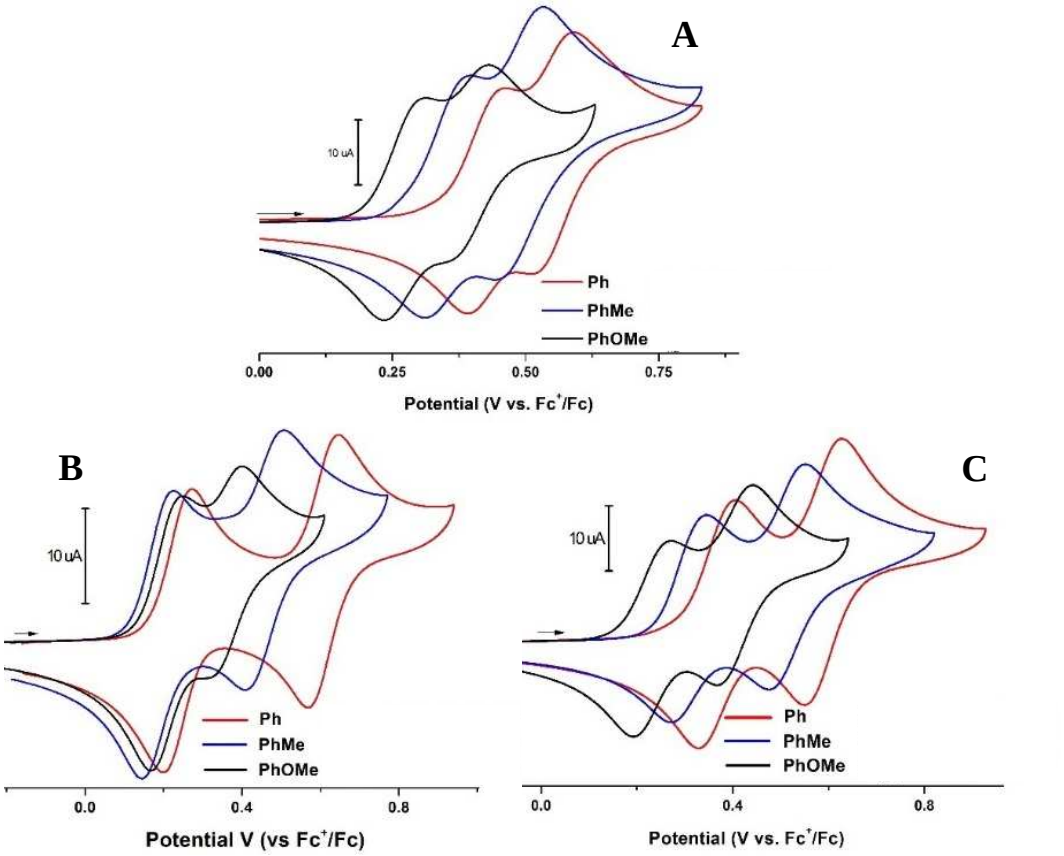


*Figure 3.3.3.1: Shift in reduction potential on introduction of electron donating substituents for **A**: $Zn^{R}L_{o}^{NMe}$ (R = Ph, PhMe, PhOMe), **B**: $Ni^{R}L_{o}^{NMe}$ (R = Ph, PhMe, PhOMe) and **C**: $Cu^{R}L_{o}^{NMe}$ (R = Ph, PhMe, PhOMe).*

The smaller shift observed for the first oxidation process of $Ni^{R}L_{o}^{NMe}$ (R = Ph, PhMe, PhOMe) relative to those of $M^{R}L_{o}^{NMe}$ (M = Zn, Cu; R = Ph, PhMe, PhOMe) as the ligand system is varied (Figures 3.3.3.1) suggests that this oxidation process is of different character in $Ni^{R}L_{o}^{NMe}$. To provide further insight into the nature of

the oxidation products of $M^{R}L_{o}^{NMe}$ (M = Zn, Ni, Cu; R = Ph, PhMe, PhOMe), UV/vis-spectroelectrochemistry was employed to monitor the oxidation of $M^{R}L_{o}^{NMe}$ (R = Ph, PhMe, PhOMe) *in situ* and controlled potential electrolysis was used to generate the oxidised materials electrochemically prior to their characterisation by EPR spectroscopy.

3.4 UV/vis and EPR Spectroscopic Studies of $Zn^{R}L_{o}^{NMe}$, (R = Ph, PhMe, PhOMe) and their Oxidation Products

3.4.1 Spectroelectrochemistry of $Zn^{R}L_{o}^{NMe}$ (R = Ph, PhMe, PhOMe)

The reversibility of the oxidation processes for $Zn^{R}L_{o}^{NMe}$, (R = Ph, PhMe, PhOMe) were difficult to determine by cyclic voltammetry (Section 3.3.1). Nevertheless we monitored the changes in UV/vis absorption that occurs on oxidation by UV/vis spectroelectrochemistry in an attempt to probe the nature of the species generated on oxidation. In addition, we were able to generate $[Zn^{PhOMe}L_{o}^{NMe}]^{+}$ *via* controlled potential electrolysis of a solution of $Zn^{PhOMe}L_{o}^{NMe}$ in CH_2Cl_2 containing 0.4 M $[N^{n}Bu_4][BF_4]$ as supporting electrolyte that allowed the nature of the oxidation product to be probed by EPR spectroscopy.

3.4.1.1 Spectroelectrochemistry of $Zn^{Ph}L_{o}^{NMe}$

The UV/vis spectrum of $Zn^{Ph}L_{o}^{NMe}$ possesses absorption bands at 268, 303 and 389 nm (ε = 98,400, 52,100 and 24,200 mol^{-1} dm^3 cm^{-1}), with an additional shoulder at 259 nm (ε = 93,700 mol^{-1} dm^3 cm^{-1}). Oxidation at 1.07 V (*vs.* Ag/AgCl) results in a loss in intensity of the bands at 268 and 303 nm and the formation of a band at 618 nm (ε = 8,560 mol^{-1} dm^3 cm^{-1}) with a shoulder at 566 nm (ε = 5,500 mol^{-1} dm^3 cm^{-1}). The band at 389 nm is replaced by a band at 375 nm (ε = 23,900 mol^{-1} dm^3 cm^{-1}) and an additional feature develops at 340 nm (ε = 12,500 mol^{-1} dm^3 cm^{-1}) (Figure 3.4.1.1.1). On re-reduction the spectrum of the original species $Zn^{Ph}L_{o}^{NMe}$ is not regenerated (Figure 3.4.1.1.1 inset). This indicates that while the redox process at $E_{1/2}$ = 0.46 V (*vs.* Fc^{+}/Fc) for $Zn^{Ph}L_{o}^{NMe}$ is electrochemically reversible over short timescales, it is not chemically reversible under the conditions of the UV/vis spectroelectrochemical experiment.

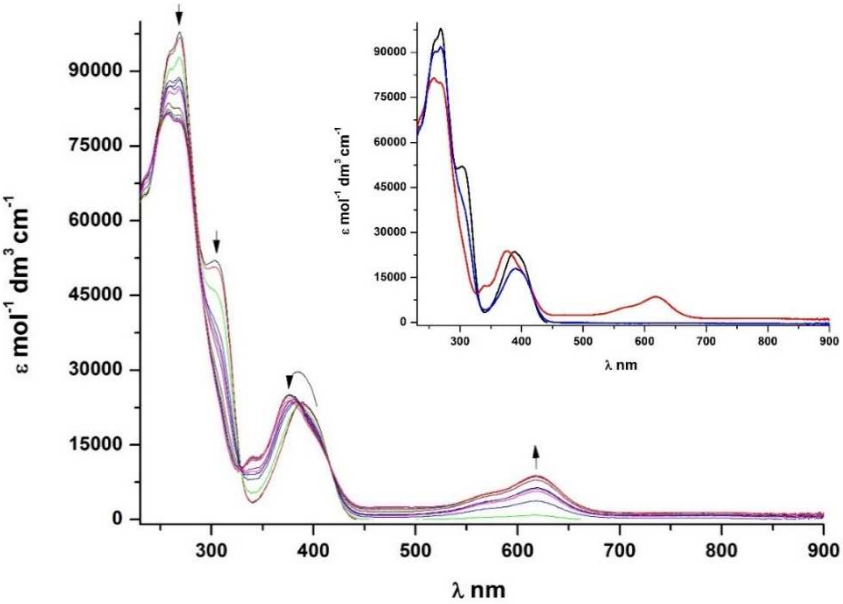


Figure 3.4.1.1.1: Sequential UV/vis spectra recorded during the oxidation of $Zn^{Ph}L_o^{NMe}$ at 1.07 V vs. Ag/AgCl identifying the bands formed during oxidation. 0.32 mmol solution recorded at 253 K under N_2 in CH_2Cl_2 containing 0.4 M $[N^nBu_4][BF_4]$ as supporting electrolyte. Inset, spectra before oxidation (black), after oxidation (red) and after re-reduction at 0.00 V vs. Ag/AgCl (blue).

3.4.1.2 Spectroelectrochemistry of $Zn^{PhMe}L_o^{NMe}$

The UV/vis spectrum of $Zn^{PhMe}L_o^{NMe}$ possesses very similar features to that of $Zn^{Ph}L_o^{NMe}$ with absorption bands at 258 and 389 nm (ε = 55,900 and 11, 800 mol^{-1} dm^3 cm^{-1}) with additional shoulders at 308 and 269 nm (ε = 28,700 and 54,000 mol^{-1} dm^3 cm^{-1}). Similar changes also occur on oxidation at 1.00 V (*vs.* Ag/AgCl) with the band at 258 nm decreasing in intensity (ε = 49,500 mol^{-1} dm^3 cm^{-1}), a band observed at 384 nm (ε = 15,200 mol^{-1} dm^3 cm^{-1}) with another band growing in at 645 nm (ε = 5,400 mol^{-1} dm^3 cm^{-1}), and additional shoulders at 347 and 592 nm (ε = 7,100 and 3,000 mol^{-1} dm^3 cm^{-1}) (Figure 3.4.1.2.1). Whilst the UV/vis spectrum of $Zn^{PhMe}L_o^{NMe}$ is not obtained on re-reduction, a similar spectral profile is observed suggesting less decomposition occurs following oxidation and re-reduction relative to the unsubstituted phenyl analogue $Zn^{Ph}L_o^{NMe}$ (Figure 3.4.1.2.1 inset).

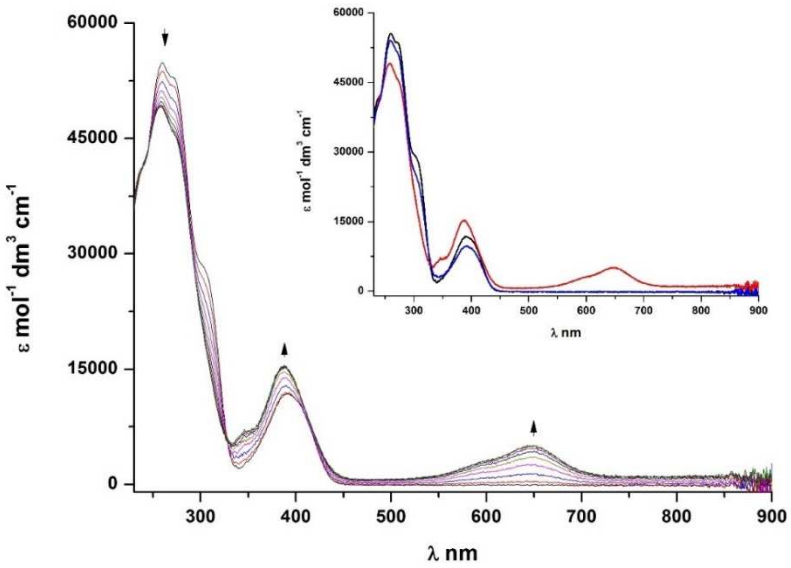


Figure 3.4.1.2.1: Sequential UV/vis spectra recorded during the oxidation of $Zn^{PhMe}L_o^{NMe}$ at 1.00 V vs. Ag/AgCl identifying the bands formed during oxidation. 0.35 mmol solution recorded at 253 K under N_2 in CH_2Cl_2 containing 0.4 M $[N^nBu_4][BF_4]$ as supporting electrolyte. Inset, spectra before oxidation (black), after oxidation (red) and after re-reduction at 0.00 V vs. Ag/AgCl (blue).

3.4.1.3 Spectroelectrochemistry of $Zn^{PhOMe}L_o^{NMe}$

The UV/vis spectrum of $Zn^{PhOMe}L_o^{NMe}$ also possesses similar features to that of $Zn^{Ph}L_o^{NMe}$ and $Zn^{PhMe}L_o^{NMe}$ with absorption bands at 260 and 396 nm (ε = 76,100 and 13,900 mol^{-1} dm^3 cm^{-1}) and additional shoulders at 244 and 279 nm (ε = 57,300 and 65,100 mol^{-1} dm^3 cm^{-1}). On oxidation at 0.92 V (*vs.* Ag/AgCl) similar changes are observed in the UV/vis spectrum of $Zn^{PhOMe}L_o^{NMe}$ to those associated with the oxidations of $Zn^{Ph}L_o^{NMe}$ and $Zn^{PhMe}L_o^{NMe}$. The band at 260 nm decreases in intensity (ε = 57,300 mol^{-1} dm^3 cm^{-1}) with shoulders at 244 and 279 nm (ε = 53,500 and 47,200 mol^{-1} dm^3 cm^{-1}). The band at 396 nm is replaced by a band at 400 nm (ε = 26,100 mol^{-1} dm^3 cm^{-1}) and a new band appears at 700 nm (ε = 12,500 mol^{-1} dm^3 cm^{-1}) with a shoulder at 633 nm (ε = 9,100 mol^{-1} dm^3 cm^{-1}) (Figure 3.4.1.3.1). On re-reduction at 0.00 V (*vs.* Ag/AgCl), the original spectral profile of $Zn^{PhOMe}L_o^{NMe}$ is obtained indicating that the first oxidation process of $Zn^{PhOMe}L_o^{NMe}$ is chemically reversible on the timescale of the spectroelectrochemical experiment (Figure 3.4.1.3.1 inset).

Given the chemical reversibility of the first oxidation process of $Zn^{PhOMe}L_o^{NMe}$ we attempted spectroelectrochemical studies on the second oxidation process for this complex. The oxidation of $Zn^{PhOMe}L_o^{NMe}$ at 1.16 V (*vs.* Ag/AgCl) is accompanied

by a decrease in intensity of the band at 260 nm to give two resolved bands at 245 and 283 nm (ε = 45,400 and 33,300 mol^{-1} dm^3 cm^{-1}). Further development of the band at 400 nm is also observed (ε = 29,300 mol^{-1} dm^3 cm^{-1}) with an additional shoulder growing in at 351 nm (ε = 17,000 mol^{-1} dm^3 cm^{-1}). The band and shoulder at 700 and 633 nm, respectively, also develop into two broad bands at 644 and 730 nm (ε = 17,700 and 17,400 mol^{-1} dm^3 cm^{-1}) (Figure 3.4.1.3.2).

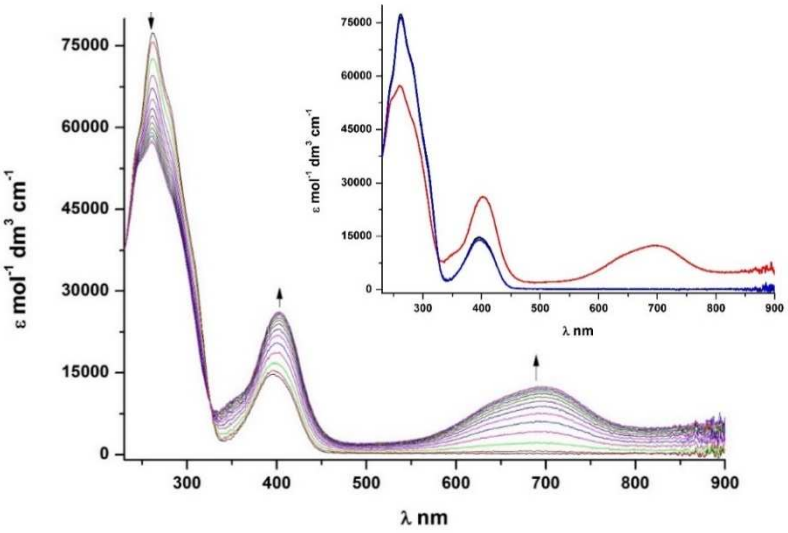


Figure 3.4.1.3.1: Sequential UV/vis spectra recorded during the oxidation of $Zn^{PhOMe}L_o^{NMe}$ at 0.92 V vs. Ag/AgCl identifying the bands formed during oxidation. 0.36 mmol solution recorded at 253 K under N_2 in CH_2Cl_2 containing 0.4 M $[N^nBu_4][BF_4]$ as supporting electrolyte. Inset, spectra before oxidation (black), after oxidation (red) and after re-reduction at 0.00 V vs. Ag/AgCl (blue).

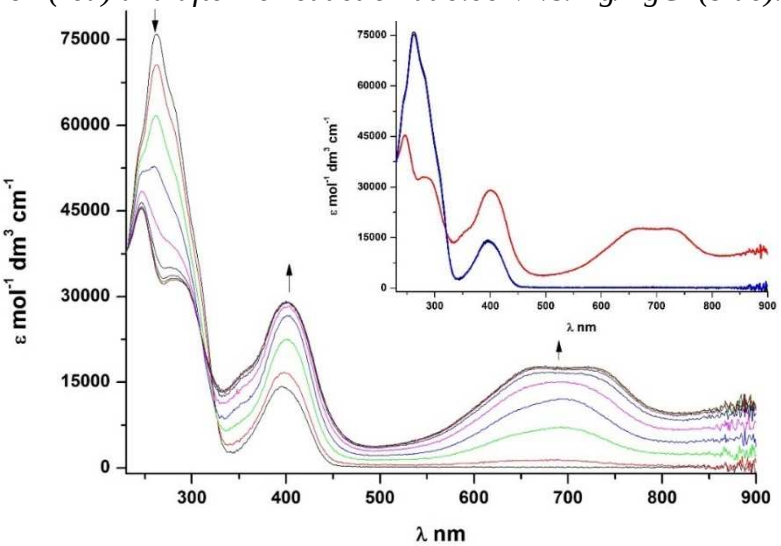


Figure 3.4.1.3.2: Sequential UV/vis spectra recorded during the oxidation of $Zn^{PhOMe}L_o^{NMe}$ at 1.16 V vs. Ag/AgCl identifying the bands formed during oxidation. 0.36 mmol solution recorded at 253 K under N_2 in CH_2Cl_2 containing 0.4 M $[N^nBu_4][BF_4]$ as supporting electrolyte. Inset, spectra before oxidation (black), after oxidation (red) and after re-reduction at 0.00 V vs. Ag/AgCl (blue).

On re-reduction, return of the spectral profile to that of $Zn^{PhOMe}L_o^{NMe}$ is observed (Figure 3.4.1.3.2 inset), indicating that both the first and second oxidation processes for $Zn^{PhOMe}L_o^{NMe}$ are chemically reversible.

3.4.2 Controlled Potential Electrolysis and EPR Spectroscopy of the Oxidation Product of $Zn^{PhOMe}L_O^{NMe}$

Within the $Zn^RL_O^{NMe}$ series of complexes, $Zn^{PhOMe}L_O^{NMe}$ exhibits the most clearly defined and reversible electrochemistry and spectroelectrochemistry (Sections 3.3.1 and 3.4.1). Therefore we selected this complex for further study by controlled potential electrolysis and characterisation of the oxidation product by EPR spectroscopy. The product of the first oxidation process observed by cyclic voltammetry at $E_{1/2}$ = 0.27 V (*vs.* Fc^+/Fc) was investigated by carrying out controlled potential electrolysis at a potential of 0.37 V (*vs.* Fc^+/Fc) until a charge equivalent to one electron had been removed (Figure 3.4.2.1 Left). Cyclic voltammetry of $[Zn^{PhOMe}L_O^{NMe}]^+$ generates a voltammogram with essentially the same profile as that for $Zn^{PhOMe}L_O^{NMe}$, confirming that $[Zn^{PhOMe}L_O^{NMe}]^+$ is stable on the timescale of the experiment (Figure 3.4.2.1 Right).

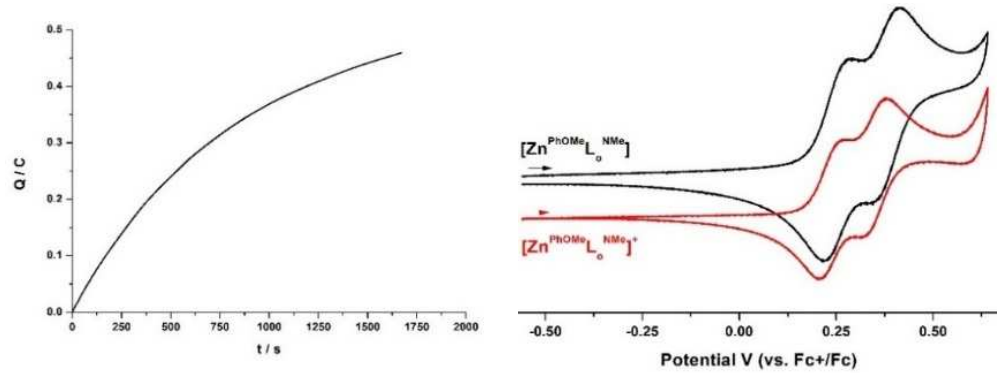


Figure 3.4.2.1: Left: Controlled potential electrolysis of $Zn^{PhOMe}L_O^{NMe}$ at 0.37 V vs. Fc^+/Fc. 243 K, 1 mmol solution in CH_2Cl_2 containing 0.4 M $[N^nBu_4][BF_4]$ as supporting electrolyte recorded at 253 K under Ar. Theoretical Q for a one electron process = 0.48 C Right: Cyclic voltammograms of $Zn^{PhOMe}L_o^{NMe}$ (black) before oxidation and $[Zn^{PhOMe}L_o^{NMe}]^+$ (red) after oxidation, recorded at 100 mV, 1 mmol solution in CH_2Cl_2 containing 0.4 M $[N^nBu_4][BF_4]$ as supporting electrolyte.

The EPR spectrum of the solution of oxidised product $[Zn^{PhOMe}L_O^{NMe}]^+$ in CH_2Cl_2 containing 0.4 M $[N^nBu_4][BF_4]$ was recorded at 293 K and as a frozen solution at 77 K. The spectra were recorded at a modulation amplitude of 1 G, and the profile

of the EPR spectrum did not change as the modulation amplitude was reduced to 0.1 G.

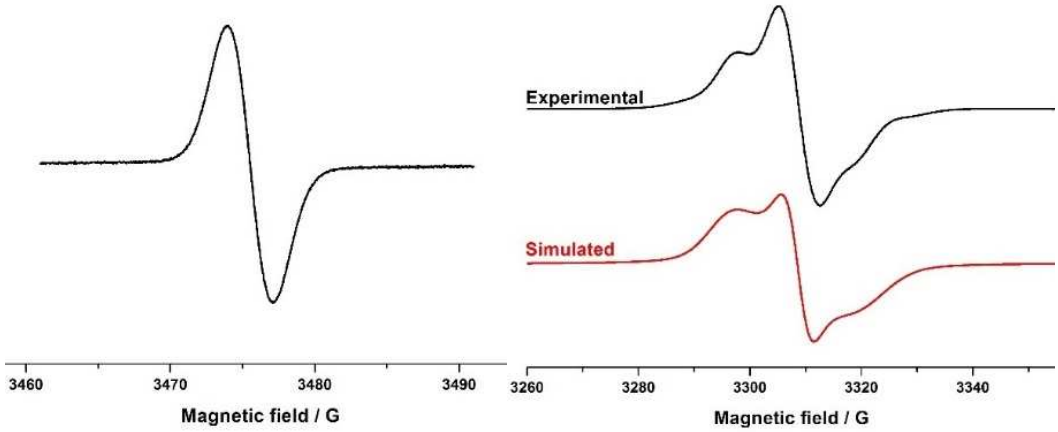


Figure 3.4.2.2: X-band CW EPR spectra of electrochemically generated $[Zn^{PhOMe}L_O{}^{NMe}]^+$ *in* CH_2Cl_2 *containing 0.4 M* $[N^nBu_4][BF_4]$ *as supporting electrolyte at 293 K– Left: Fluid solution at 293 K; Right: Frozen solution at 77 K, simulated Hamiltonian parameters:* $g_{11} = 1.99760$, $g_{22} = 2.00445$, $g_{33} = 2.01200$, *Gaussian linewidths* $W_{11} = 10$ G, $W_{22} = 4$ G, $W_{33} = 8$ G.

The fluid spectrum exhibits a single isotropic signal with g_{iso} = 2.0043, which is typical for phenoxyl-based radical $Zn^{II}(L^{\cdot})$ complexes including the one electron oxidised products of $Zn(L^5)(Cl)$ (H_2L^5 = 1,4-bis(2-methyl-ethyl)- 7- (3-^{t}butyl-5-methoxy-2-hydroxybenzyl)-1,4,7-triazacyclononane; g_{iso} = 2.00), $Zn(L^6H_2)(BF_4)$ (H_3L^6 =1,4,7- tris(3-^{t}butyl-5-methoxy-2-hydroxybenzyl)-1,4,7-triazacyclononane; g_{iso} = 2.0045), and $Zn(L^2H_2)(BF_4)$ (H_3L^2 = 1,4,7- tris(3,5-di^{t}butyl -2-hydroxybenzyl)-1,4,7-triazacyclononane; g_{iso} = 2.0045).[1, 19, 25, 28, 29] The frozen solution spectrum of $[Zn^{PhOMe}L_O{}^{NMe}]^+$ is rhombic and can be simulated with spin Hamiltonian parameters g_{11} = 1.99760, g_{22} = 2.00445, g_{33} = 2.01200 (Figure 3.5.1.2). This frozen solution spectrum contrasts with that of $[Zn^{tBu}L_O{}^{NMe}]^+$ which exhibits a single feature at g_{iso} = 2.0044; it is likely that any g-value anisotropy is contained in the line width of this spectrum (25 G). The greater g-anisotropy for $[Zn^{PhOMe}L_O{}^{NMe}]^+$ is consistent with a greater degree of delocalisation of the free radical centre across the 3 and 5-subsituents of the phenolate ring on oxidation following the introduction of more electron donating substituents in the 3 and 5 positions of the phenolate rings (see Section 3.4.3).

3.4.3 Discussion

$Zn^{Ph}L_o^{NMe}$, $Zn^{PhMe}L_o^{NMe}$, and $Zn^{PhOMe}L_o^{NMe}$ all exhibit similar UV/vis spectra with absorption bands at *ca.* 270 and 390 nm, (Table 3.4.1.4.1) which can be assigned to phenolate $\pi \rightarrow \pi^*$ transitions as previously found for other Zn^{II} phenolate complexes[11, 14] including $Zn(L^1)$ (L^1 = 1-ethyl-4,7-bis(3-^{t}butyl-5-methoxy-2-hydroxybenzyl)-1,4,7-triazacyclononane; λ = 253, 316 nm; ε = 15,000, 8,800 dm^3 mol^{-1} cm^{-1}),[16] and $[ZnL^2H_2][BF_4]$ (L^2 = 1,4,7 - tris (3,5 - di^{t}butyl – 2 - hydroxybenzyl) - 1,4,7 – triazacyclononane; λ =222, 248, 280, 300 nm; ε = 16,000, 3,400, 4,700, 1,100 dm^3 mol^{-1} cm^{-1}).[28]

Complex	λ_{max} (nm)	ε (mol^{-1} dm^3 cm^{-1})	Isobestic point (nm)
$Zn^{Ph}L_O^{NMe}$	259(sh), 268, 303, 389,	93,700, 98,400, 52,100, 24,200	
$[Zn^{Ph}L_O^{NMe}]^+$	255, 267, 340, 375, 566(sh), 618	81,700, 80,300, 12,500, 23,900, 5,500, 8,560	329
$Zn^{PhMe}L_O^{NMe}$	258, 269 (sh), 308 (sh), 389	55,900, 54,000, 28,700, 11,800	
$[Zn^{PhMe}L_O^{NMe}]^+$	258, 273(sh), 347(sh), 384, 592(sh), 645	49,500, 45,100, 7,100, 15,200, 3,000, 5,400	327
$Zn^{PhOMe}L_O^{NMe}$	260, 279(sh), 396, 244(sh)	76,100, 65,100, 13,900, 57,300	
$[Zn^{PhOMe}L_O^{NMe}]^+$	244(sh), 260, 279(sh), 400, 633(sh),700	53,500, 57,300, 47,200, 26,100, 9,100, 12500	326
$[Zn^{PhOMe}L_O^{NMe}]^{2+}$	245, 283, 351(sh), 400, 644, 730	45,400, 33,300, 17,000, 29,300, 17,700, 17,400,	

Table 3.4.3.1: Summary of UV/vis absorption bands for $Zn^RL_O^{NMe}$, $[Zn^RL_O^{NMe}]^+$ and $[Zn^{PhOMe}L_O^{NMe}]^{2+}$ (R = Ph, PhMe, PhOMe).

On oxidation, the appearance of low energy bands at *ca.* 700 nm and increase in the intensity of bands at *ca.* 410 nm (Table 3.4.3) can be attributed to phenoxyl radical $\pi \rightarrow \pi^*$ transitions as found following the one electron oxidation of $Zn(L^1)_2$ (HL^1 = 2-^{t}butyl-4-methoxy-6-[(pyridin-2-ylmethylimino)methyl]phenol; λ = 420, 605 nm; ε = 14,660, 650 mol^{-1} dm^3 cm^{-1}), $Zn(L^3)_2$ (HL^3 = 2-^{t}butyl-4-methoxy-6-(quinolin-8-yliminomethyl)phenol; λ = 410, 680 nm; ε = 15,540, 1,330 mol^{-1} dm^3 cm^{-1}), $Zn(L^4)$ (H_2L^4 = N,N',N,N'-bis[(2 – hydroxyl - 3,5 - di^{t}butylbenzyl)(2 - pyridylmethyl)] ethylenediamine; λ = 414, 700 nm; ε = 2,550, 630 mol^{-1} dm^3 cm^{-1}), and $Zn(L^7)$ (H_2L^7 = 1 - (2 – methyl - ethyl) - 4,7 - bis(3 - ^{t}butyl – 5 – methoxy – 2 - hydroxybenzyl) - 1,4,7-triazacyclononane; λ = 408, 722 nm; ε = 3,200, 400 mol^{-1} dm^3 cm^{-1}). [11, 14, 18] The increase in intensity of these bands at *ca.* 700 and *ca.* 410

nm on further oxidation to $[Zn^{R}L_{o}^{NMe}]^{2+}$ (R = Ph, PhMe, PhOMe) is consistent with the formation of a second phenoxyl radical bound to Zn^{II} as observed for the two electron oxidation of $Zn(L^{1})_2$ (HL^{1} = 2-*t*butyl-4-methoxy-6-[(pyridin-2-ylmethylimino)methyl]phenol; λ = 424, 622 nm; ε = 18,150, 1,570 mol^{-1} dm^3 cm^{-1}), $Zn(L^{3})_2$ (HL^{3} = 2-*t*butyl-4-methoxy-6-(quinolin-8-yliminomethyl)phenol; λ = 414, 700 nm; ε = 16,010, 2,300 mol^{-1} dm^3 cm^{-1}) and $Zn(L^{4})$ (H_2L^{4} = *N,N',N,N'*-bis[(2-hydroxy-3,5-di*t*butylbenzyl)(2-pyridylmethyl)] ethylenediamine; λ = 414, 700 nm; ε = 6,170, 725 mol^{-1} dm^3 cm^{-1}).[18] These UV/vis spectroscopic results, together with the 293K and 77K solution EPR spectra of $[Zn^{PhOMe}L_{o}^{NMe}]^{+}$ support the formation of phenoxyl radical ligands bound to Zn^{II} centres in the oxidation products of $Zn^{Ph}L_{o}^{NMe}$, $Zn^{PhMe}L_{o}^{NMe}$, and $Zn^{PhOMe}L_{o}^{NMe}$.

We carried out unrestricted, gas phase geometry optimisations of $[Zn^{R}L_{o}^{NMe}]^{+}$ using models based on the gas phase geometries calculated for $Zn^{R}L_{o}^{NMe}$ in Chapter 2 in order to develop models of the electronic structures of the oxidised species. The spin densities associated with each complex were then calculated for the gas phase geometries placed in a uniform dielectric medium using COSMO[30] to model the effect of the CH_2Cl_2 solvent. Isosurface plots of the spin density at 0.001 $eBohr^{-3}$ are shown in Figure 3.4.3.1 and the spin densities for the fragments in each complex are summarised in Table 3.4.3.2.

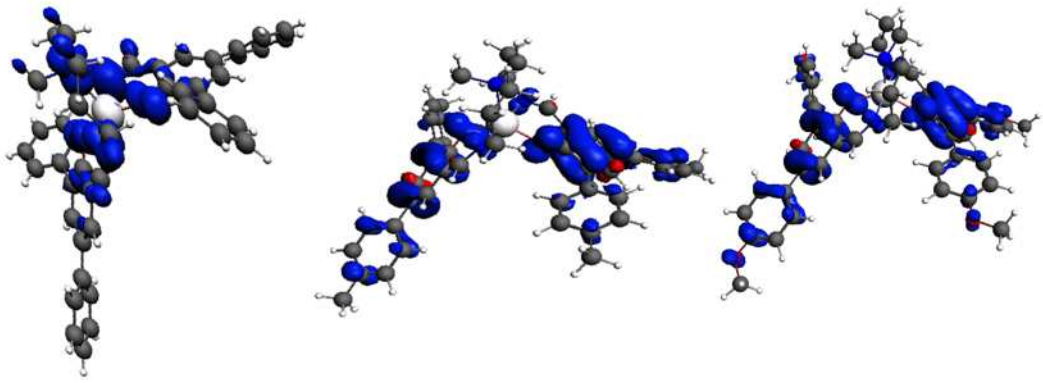


Figure 3.4.3.1: Spin density isosurfaces at the 0.001 $eBohr^{-3}$ level for $[Zn^{Ph}L_{o}^{NMe}]^{+}$ (Left), $[Zn^{PhMe}L_{o}^{NMe}]^{+}$ (centre) and $[Zn^{PhOMe}L_{o}^{NMe}]^{+}$ (Right).

	$[Zn^{Ph}L_o^{NMe}]^+$	$[Zn^{PhMe}L_o^{NMe}]^+$	$[Zn^{PhOMe}L_o^{NMe}]^+$
Zn	0.068	-0.001	-0.002
Phenolate O	0.306	0.231	0.189
Imine N	0.253	0.059	0.042
Amine N	0.118	0.000	0.000
Phenolate	0.092	0.480	0.426
3-(4-R-phenyl)	0.041	0.106	0.118
5-(4-R-phenyl)	0.009	0.118	0.247

Table 3.4.3.2: Summary of spin densities attributed to the metal carbon and heteroatom atoms which make up various fragments of $[Zn^{Ph}L_o^{NMe}]^+$, $[Zn^{PhMe}L_o^{NMe}]^+$ and $[Zn^{PhOMe}L_o^{NMe}]^+$.

For $[Zn^{R}L_o^{NMe}]^+$ there is little or no spin density associated with the Zn^{II} centre (0.068, -0.001 and -0.002 for R = Ph, PhMe and PhOMe, respectively, Table 3.4.3.2) with significant spin density associated with the phenolate O (0.189 – 0.306), imine N (0.042 – 0.253) and amine N (0.000 – 0.118) atoms. The substitution of the phenyl ring substituents with electron donating Me and OMe substituents increases the proportion of spin density on the phenolate rings from 0.092 to 0.480 and 0.426 for R = Ph, PhMe and PhOMe, respectively, and on the substituent phenyl rings from 0.041 and 0.009 in $[Zn^{Ph}L_o^{NMe}]^+$ to 0.106 and 0.118 and 0.118 and 0.247 in $[Zn^{PhMe}L_o^{NMe}]^+$ and $[Zn^{PhOMe}L_o^{NMe}]^+$, respectively, confirming that the coordinated phenoxyl radicals become more delocalised as more electron donating substituents are introduced into the 3- and 5-phenyl rings. This greater degree of delocalisation is consistent with the increased anisotropy found for the frozen solution EPR spectrum of $[Zn^{PhOMe}L_o^{NMe}]^+$ when compared to $[Zn^{tBu}L_o^{NMe}]^+$.[1] The increase in delocalisation of the spin density may also explain why $[Zn^{R}L_o^{NMe}]^+$ (R = Ph, PhMe, PhOMe) are stable in spite of spin density being localised on C atoms possessing α-H atoms in the 3- and 5-phenyl substituents.

Our electrochemical, UV/vis spectroelectrochemical, EPR spectroscopic and DFT results all support the formation of phenoxyl radical species on the oxidation of $Zn^{R}L_o^{NMe}$. We suggest that the increase in chemical reversibility and lower reduction potential (0.27 V *vs.* Fc^+/Fc) for $Zn^{PhOMe}L_o^{NMe}$ relative to $Zn^{PhMe}L_o^{NMe}$ and $Zn^{Ph}L_o^{NMe}$ (0.35 and 0.43 V *vs.* Fc^+/Fc) may be rationalised in terms of the greater electron donating nature of the OMe substitution in $Zn^{PhOMe}L_o^{NMe}$ relative to that in $Zn^{Ph}L_o^{NMe}$ and $Zn^{PhMe}L_o^{NMe}$.

3.5 UV/vis and EPR Spectroscopic Studies of $Ni^{R}L_{o}^{NMe}$, (R = Ph, PhMe, PhOMe) and their Oxidation Products

$Ni^{Ph}L_{o}^{NMe}$ $Ni^{PhMe}L_{o}^{NMe}$ and $Ni^{PhOMe}L_{o}^{NMe}$ exhibit multiple oxidation processes as revealed by cyclic voltammetry (Section 3.3). $Ni^{Ph}L_{o}^{NMe}$ possesses two electrochemically reversible processes at $E_{1/2}$ = 0.24 and 0.61 V (*vs.* Fc^{+}/Fc) with an additional process at E_{p}^{a} = 1.15 V (*vs.* Fc^{+}/Fc). $Ni^{PhMe}L_{o}^{NMe}$ exhibits one electrochemically reversible process at $E_{1/2}$ = 0.19 V (*vs.* Fc^{+}/Fc), a second process at E_{p}^{a} = 0.51 V (*vs.* Fc^{+}/Fc), which shows a return wave at faster scan rates, and a third process, which is not reversible, at E_{p}^{a} = 0.99 V (*vs.* Fc^{+}/Fc). $Ni^{PhOMe}L_{o}^{NMe}$ possesses one electrochemically reversible process at $E_{1/2}$ = 0.17 V (*vs.* Fc^{+}/Fc) and a second process, which possesses a return wave at faster scan rates at E_{p}^{a} = 0.40 V (*vs.* Fc^{+}/Fc); $Ni^{PhOMe}L_{o}^{NMe}$ also possesses two additional processes at a more anodic potentials (E_{p}^{a} = 0.78 and 0.87 V *vs.* Fc^{+}/Fc). We employed UV/vis spectroelectrochemistry and EPR spectroscopy to probe the natures of the oxidation products of $Ni^{R}L_{o}^{NMe}$ (R = Ph, PhMe and PhOMe).

3.5.1 Spectroelectrochemistry of $Ni^{R}L_{o}^{NMe}$ (R = Ph, PhMe, PhOMe)

3.5.1.1 Spectroelectrochemistry of $Ni^{Ph}L_{o}^{NMe}$

The UV/vis spectrum of $Ni^{Ph}L_{o}^{NMe}$ exhibits four bands at 255, 271, 309 and 391 nm (ε = 49,100, 48,800, 31,200 and 12,700 mol^{-1} dm^{3} cm^{-1}). On oxidation at 1.03 V (*vs.* Ag/AgCl) to $[Ni^{Ph}L_{o}^{NMe}]^{+}$ a band at 248 nm (ε = 49,800 mol^{-1} dm^{3} cm^{-1}) is observed, the band at 271 nm decreases in intensity (ε = 46,800 mol^{-1} dm^{3} cm^{-1}) and a shoulder grows in at 295 nm (ε = 38,300 mol^{-1} dm^{3} cm^{-1}). There is also a broad band centred at 401 nm (ε = 13,200 mol^{-1} dm^{3} cm^{-1}) with an additional broad shoulder at 473 nm (ε = 6,800 mol^{-1} dm^{3} cm^{-1}) (Figure 3.5.1.1.1). The spectra exhibit four isobestic points during the oxidation process, indicating that oxidation occurs directly without the formation of any observable intermediates. The process is chemically reversible with the spectrum of $Ni^{Ph}L_{o}^{NMe}$ generated on re-reduction at 0.0 V (*vs.* Ag/AgCl) (Figure 3.5.1.1.1 inset).

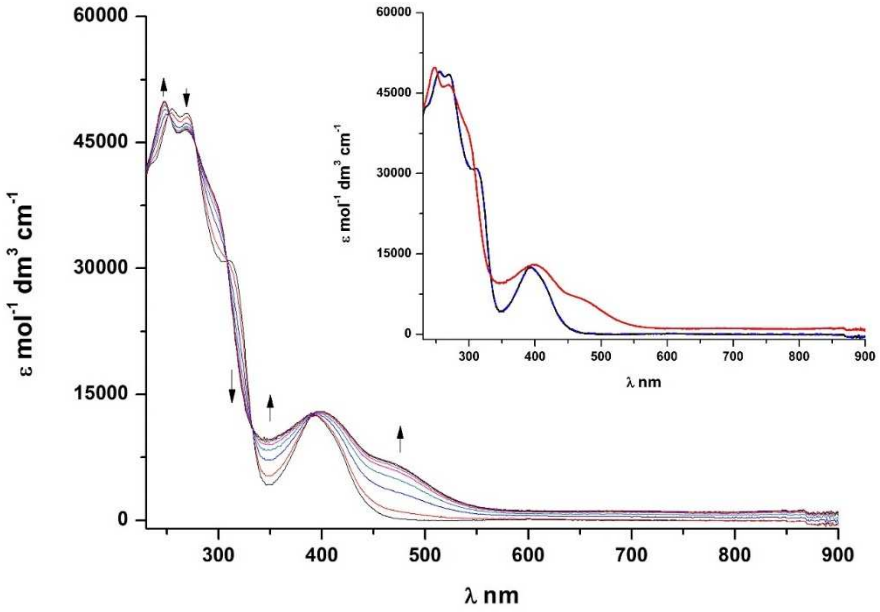


Figure 3.5.1.1.1: Sequential UV/vis spectra recorded during the oxidation of $Ni^{Ph}L_o^{NMe}$ at 1.03 V vs. Ag/AgCl identifying the bands formed during oxidation. 0.41 mmol solution recorded at 253 K under N_2 in CH_2Cl_2 containing 0.4 M $[N^nBu_4][BF_4]$ as supporting electrolyte. Inset, spectra before oxidation (black), after oxidation (red) and after re-reduction at 0.00 V vs. Ag/AgCl (blue).

The chemical reversibility exhibited by the first oxidation process of $Ni^{Ph}L_o^{NMe}$ enabled the investigation of the second oxidation of $Ni^{Ph}L_o^{NMe}$ at $E_{1/2}$ = 0.61 V (*vs* Fc^+/Fc). Significant changes were observed in the UV/vis spectrum on oxidation at 1.45 V (*vs.* Ag/AgCl), with intense bands observed at 368 and 611 nm (ε = 25,600 and 13,800 mol^{-1} dm^3 cm^{-1}), the development of a shoulder at 338 nm (ε = 19,500 mol^{-1} dm^3 cm^{-1}), a band at 233 nm (ε = 44,000 mol^{-1} dm^3 cm^{-1}) and a shoulder at *ca.* 264 nm (ε = 30,700 mol^{-1} dm^3 cm^{-1}) (Figure 3.5.1.1.2). Following oxidation, $[Ni^{Ph}L_o^{NMe}]^{2+}$ can be successfully re-reduced to $[Ni^{Ph}L_o^{NMe}]^+$ or to $Ni^{Ph}L_o^{NMe}$ (Figure 3.5.1.1.2 inset) indicating the complete chemical reversibility of the one and two electron oxidation processes.

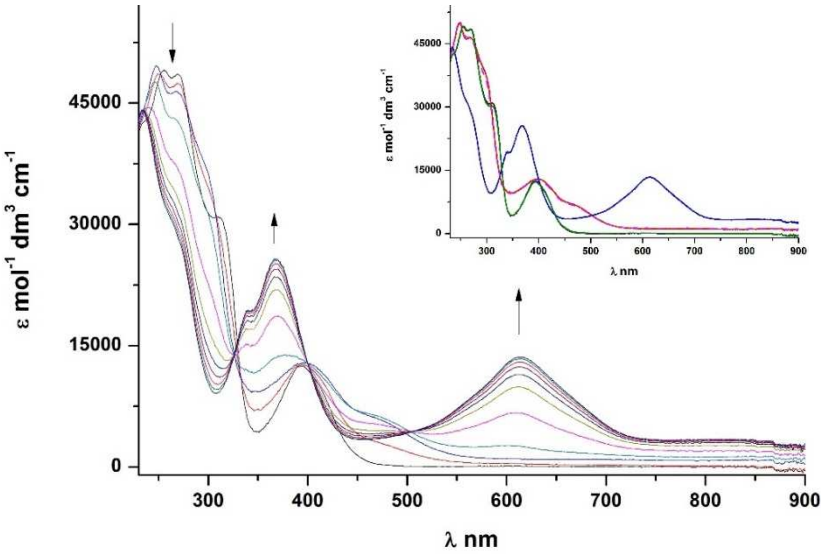


Figure 3.5.1.1.2: Sequential UV/vis spectra recorded during the oxidation of $Ni^{Ph}L_o^{NMe}$ at 1.45 V vs. Ag/AgCl identifying the bands formed during oxidation. 0.41 mmol solution recorded at 253 K under N_2 in CH_2Cl_2 containing 0.4 M $[N^nBu_4][BF_4]$ as supporting electrolyte. Inset, spectra before oxidation (black), after 1 e^- oxidation (red), after 2 e^- oxidation (blue), after re-reduction to 1 e^- oxidised species at 0.91 V vs. Ag/AgCl (magenta), and after re-reduction to original species at 0.00 V vs. Ag/AgCl (green).

3.5.1.2 Spectroelectrochemistry of $Ni^{PhMe}L_o^{NMe}$

The UV/vis spectrum of $Ni^{PhMe}L_o^{NMe}$ exhibits a similar profile to that of $Ni^{Ph}L_o^{NMe}$ with absorption bands at 253, 278 and 397 nm (ε = 65,300, 64,400 and 15,200 mol^{-1} dm^3 cm^{-1}) and shoulders at 237 and 307 nm (ε = 60,000 and 40,700 mol^{-1} dm^3 cm^{-1}). Oxidation at 0.93 V *vs.* Ag/AgCl results in an increase in intensity of the band at 253 nm (ε = 71,600 mol^{-1} dm^3 cm^{-1}), accompanied by the loss of the band at 278 nm and the development of a shoulder at 301 nm (ε = 42,500 mol^{-1} dm^3 cm^{-1}). The band at 397 nm (ε = 17,000 mol^{-1} dm^3 cm^{-1}) broadens and an additional shoulder grows in at 479 nm (ε = 7,100 mol^{-1} dm^3 cm^{-1}) (Figure 3.5.1.2.1). Overall the UV/vis spectroscopic profile for $[Ni^{PhMe}L_o^{NMe}]^+$ is similar to that of $[Ni^{Ph}L_o^{NMe}]^+$ (Figure 3.4.2.1.1). Re-reduction of $[Ni^{PhMe}L_o^{NMe}]^+$ returns the spectral profile to that of $Ni^{PhMe}L_o^{NMe}$, indicating complete chemical reversibility for this first oxidation process (Figure 3.5.1.2.1 inset).

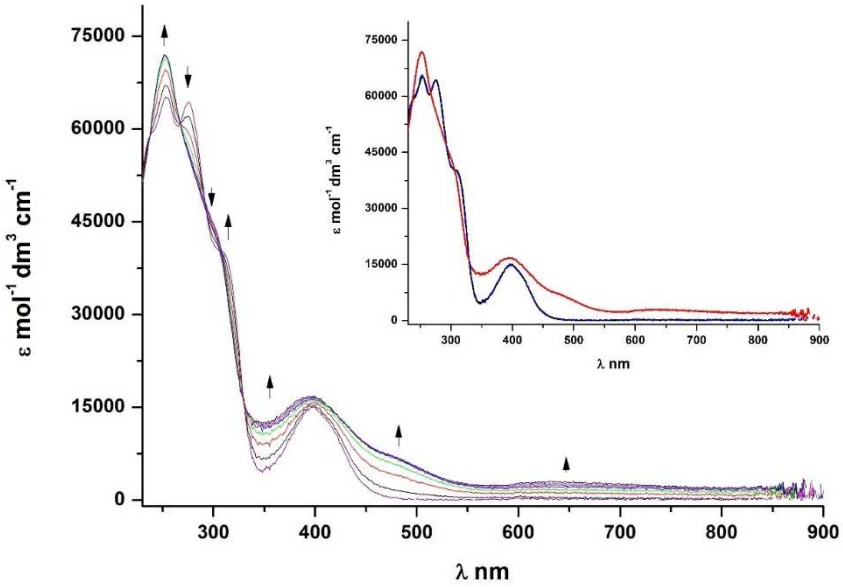


Figure 3.5.1.2.1: Sequential UV/vis spectra recorded during the oxidation of $Ni^{PhMe}L_o^{NMe}$ at 0.93 V vs. Ag/AgCl identifying the bands formed during oxidation. 0.41 mmol solution recorded at 253 K under N_2 in CH_2Cl_2 containing 0.4 M $[N^nBu_4][BF_4]$ as supporting electrolyte. Inset, spectra before oxidation (black), after oxidation (red) and after re-reduction (blue).

The two electron oxidation of $Ni^{PhMe}L_o^{NMe}$ to $[Ni^{PhMe}L_o^{NMe}]^{2+}$ (Figure 3.5.1.2.2) is accompanied by similar spectral changes to those observed for the two electron oxidation of $Ni^{Ph}L_o^{NMe}$ to $[Ni^{Ph}L_o^{NMe}]^{2+}$ (Figure 3.5.1.1.2). Thus, bands at 238, 381 and 645 nm (ε = 54,300, 33,900 and 18,200 mol^{-1} dm^3 cm^{-1}) and shoulders at 272 nm (ε = 38,100 mol^{-1} dm^3 cm^{-1}) and 347 nm (ε = 22,400 mol^{-1} dm^3 cm^{-1}) develop (Figure 3.5.1.2.2). In contrast to the two electron oxidation of $Ni^{Ph}L_o^{NMe}$, the two electron process for $Ni^{PhMe}L_o^{NMe}$ was not fully reversible and while a similar overall spectral profile to that of $Ni^{Ph}L_o^{NMe}$ was returned after re-reduction at 0.0 V (*vs.* Ag/AgCl), some decomposition was observed (Figure 3.5.1.2.2 inset).

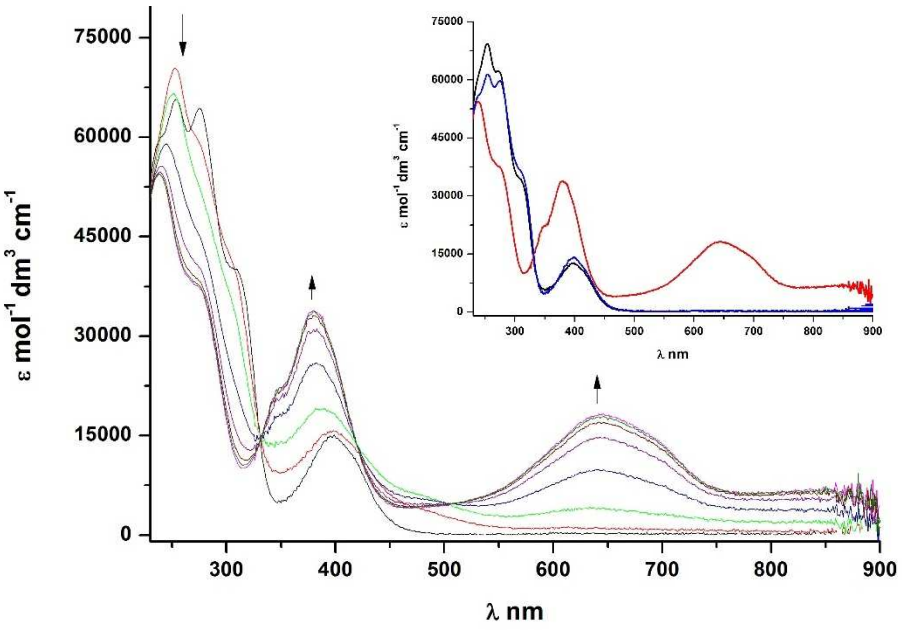


Figure 3.5.1.2.2: Sequential UV/vis spectra recorded during the two electron oxidation of $Ni^{PhMe}L_o^{NMe}$ at 1.33 V vs. Ag/AgCl identifying the bands formed during oxidation. 0.21 mmol solution recorded at 253 K under N_2 in CH_2Cl_2 containing 0.4 M $[N^nBu_4][BF_4]$ as supporting electrolyte. Inset, spectra before oxidation (black), after 2 e^- oxidation (red), after re-reduction to original species (blue).

3.5.1.3 Spectroelectrochemistry of $Ni^{PhOMe}L_o^{NMe}$

The UV/vis spectral profile of $Ni^{PhOMe}L_o^{NMe}$ shows similar features to those of $Ni^{PhMe}L_o^{NMe}$ and $Ni^{Ph}L_o^{NMe}$ with absorption bands at 257, 278 and 399 nm (ε = 85,800, 78,000 and 15,800 mol^{-1} dm^3 cm^{-1}) (Figure 3.5.1.3.1). The oxidation of $Ni^{PhOMe}L_o^{NMe}$ at 0.85 V (*vs.* Ag/AgCl) is associated with more significant changes in the UV/vis spectrum than those observed than for the analogous oxidations of $Ni^{PhMe}L_o^{NMe}$ to $[Ni^{PhMe}L_o^{NMe}]^+$ or $Ni^{Ph}L_o^{NMe}$ to $[Ni^{Ph}L_o^{NMe}]^+$. There is a greater decrease in the intensity of the high-energy features with a band and shoulder developing at 255 nm (ε = 71,900 mol^{-1} dm^3 cm^{-1}) and 280 nm (ε = 57,300 mol^{-1} dm^3 cm^{-1}), respectively, and a more significant increase in the intensity of the band around 400 nm (ε = 26,100 mol^{-1} dm^3 cm^{-1}) together with the appearance of a broad absorption band in the 700 nm region (ε = 11,700 mol^{-1} dm^3 cm^{-1}) (Figure 3.5.1.3.1). The one electron oxidation of $Ni^{PhOMe}L_o^{NMe}$ is accompanied by an isobestic point at 328 nm and re-reduction generates the UV/vis spectrum of $Ni^{PhOMe}L_o^{NMe}$, demonstrating the chemical reversibility of the process (Figure 3.5.1.3.1 inset).

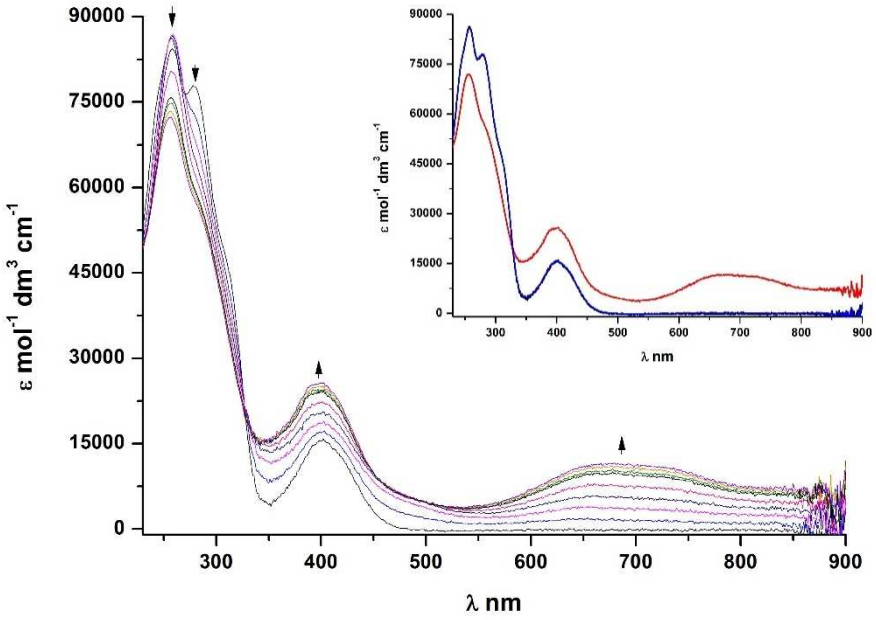


Figure 3.5.1.3.1: Sequential UV/vis spectra recorded during the oxidation of $Ni^{PhOMe}L_o^{NMe}$ at 0.85 V vs. Ag/AgCl identifying the bands formed during oxidation. 0.17 mmol solution recorded at 253 K under N_2 in CH_2Cl_2 containing 0.4 M $[N^nBu_4][BF_4]$ as supporting electrolyte. Inset, spectra before oxidation (black), after 1 e^- oxidation (red), after re-reduction to original species at 0.00 V vs. Ag/AgCl (blue).

The two electron oxidation of $Ni^{PhOMe}L_o^{NMe}$ displayed similar changes to those associated with the two-electron oxidations of $Ni^{PhMe}L_o^{NMe}$ to $[Ni^{PhMe}L_o^{NMe}]^{2+}$ and $Ni^{Ph}L_o^{NMe}$ to $[Ni^{Ph}L_o^{NMe}]^{2+}$. Two absorption bands at 243 and 282 nm (ε = 55,300 and 43,200 mol^{-1} dm^3 cm^{-1}) develop and the two-electron oxidation is accompanied by an increase in the intensity of the bands at *ca.* 400 and 700 nm (ε = 34,600 and 21,800 mol^{-1} dm^3 cm^{-1}) (Figure 3.5.1.3.2). On re-reduction of $[Ni^{PhOMe}L_o^{NMe}]^{2+}$, an identical spectrum to that previously obtained for $[Ni^{PhOMe}L_o^{NMe}]^+$ is observed, demonstrating the chemical reversibility of this second oxidation process (Figure 3.5.1.3.2).

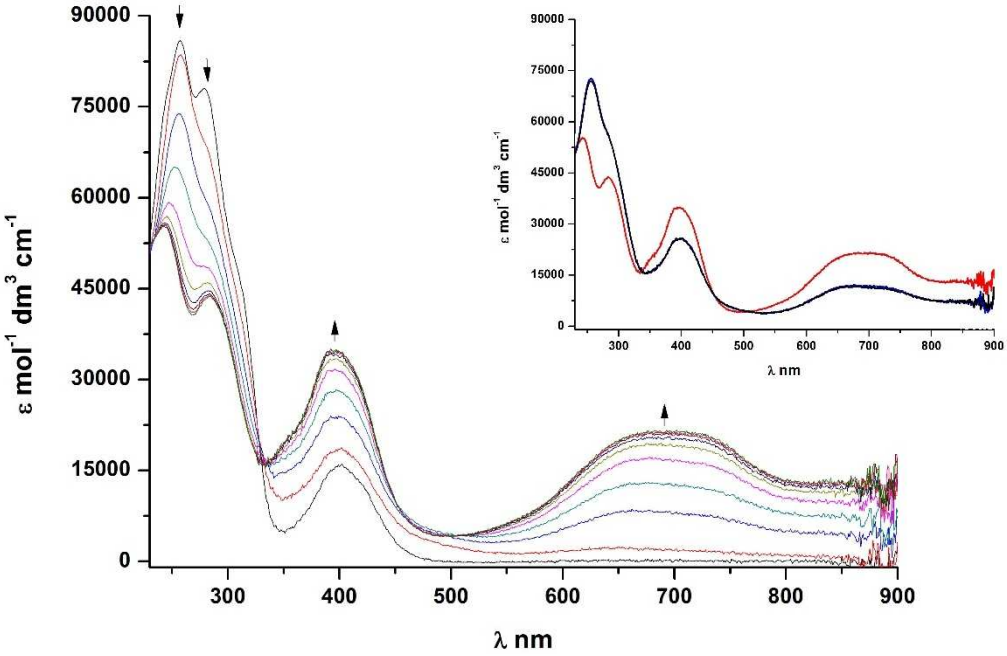


Figure 3.5.1.3.2: Sequential UV/vis spectra recorded during the oxidation of $Ni^{PhOMe}L_o^{NMe}$ at 1.13 V vs. Ag/AgCl identifying the bands formed during oxidation. 0.16 mmol solution recorded at 253 K under N_2 in CH_2Cl_2 containing 0.4 M $[N^nBu_4][BF_4]$ as supporting electrolyte. Inset, spectra of $[Ni^{PhOMe}L_o^{NMe}]^+$ (black), after 2 e^- oxidation (red), after and after re-reduction to 1 e^- oxidised species at 0.85 V vs. Ag/AgCl (blue),

The third and fourth oxidation processes for $Ni^{PhOMe}L_o^{NMe}$ at E_p^a = 0.80 and 0.87 V (*vs.* Fc^+/Fc) (Section 3.3) are more clearly defined than the third oxidation of $Ni^{PhMe}L_o^{NMe}$ or $Ni^{Ph}L_o^{NMe}$ at E_p^a = 0.99 and 1.11 V (*vs.* Fc^+/Fc), respectively. Therefore we attempted to investigate these oxidation processes for $Ni^{PhOMe}L_o^{NMe}$ by UV/vis spectroelectrochemistry. On oxidation at 1.65 V (*vs.* Ag/AgCl) significant spectral changes were observed: an intense absorption developed at 427 nm (ε = 50,300 mol^{-1} dm^3 cm^{-1}); together with bands at 236 and 282 nm (ε = 49,000 and 34,600 mol^{-1} dm^3 cm^{-1}); and a broad absorption centred around 600 nm (ε = 12,200 mol^{-1} dm^3 cm^{-1}) (Figure 3.5.1.3.3). Re-reduction at 0.00 V (*vs.* Ag/AgCl) did not generate the UV/vis spectrum of $Ni^{PhOMe}L_o^{NMe}$ (Figure 3.5.1.3.3 inset).

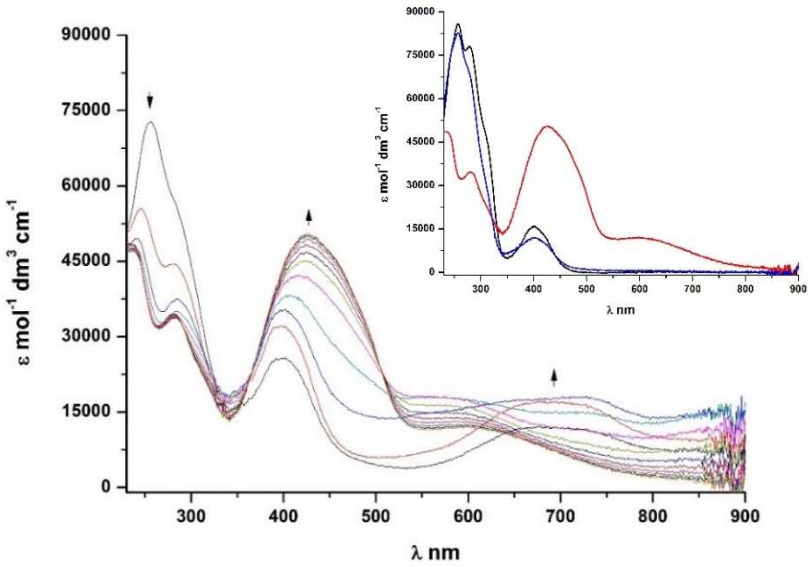


Figure 3.5.1.3.3: Sequential UV/vis spectra recorded during the oxidation of $Ni^{PhOMe}L_o^{NMe}$ at 1.65 V vs. Ag/AgCl identifying the bands formed during oxidation. 0.16 mmol solution recorded at 253 K under N_2 in CH_2Cl_2 containing 0.4 M $[N^nBu_4][BF_4]$ as supporting electrolyte. Inset, original spectra of $Ni^{PhOMe}L_o^{NMe}$ (black), after 4 e^- oxidation (red), and after re-reduction to original species at 0.00 V vs. Ag/AgCl (blue).

3.5.2 Controlled Potential Electrolysis and EPR Spectroscopy of $Ni^RL_o^{NMe}$ (R = Ph, PhMe, PhOMe)

Controlled potential electrolysis of $Ni^{Ph}L_o^{NMe}$ at 0.48 V (vs. Fc^+/Fc) confirmed that the first oxidation to $[Ni^{Ph}L_o^{NMe}]^+$ is a one electron transfer process (Figure 3.5.2.1 Left), and cyclic voltammetry carried out before and after oxidation confirmed that no significant decomposition of $[Ni^{Ph}L_o^{NMe}]^+$ occurs on the timescale of the controlled potential electrolysis experiment (Figure 3.5.2.1 Right).

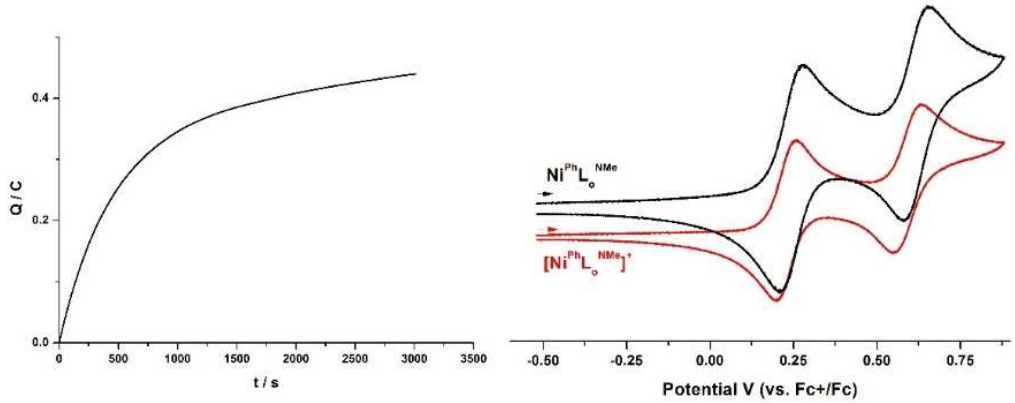


Figure 3.5.2.1: Left: Controlled potential electrolysis of $Ni^{Ph}L_O^{NMe}$ to $[Ni^{Ph}L_O^{NMe}]^+$ at 0.48 V vs. Fc^+/Fc, 1 mmol solution in CH_2Cl_2 containing 0.4 M $[N^nBu_4][BF_4]$ as supporting electrolyte recorded at 253 K under Ar. Theoretical Q for a one electron process = 0.48 C; Right: Cyclic voltammograms of $Ni^{Ph}L_o^{NMe}$ (black) before oxidation and $[Ni^{Ph}L_o^{NMe}]^+$ (red) after oxidation, recorded at 100 mV, 1 mmol solution in CH_2Cl_2 containing 0.4 M $[N^nBu_4][BF_4]$ as supporting electrolyte.

The electrolysis resulted in an olive brown solution which was EPR active as a frozen glass at 77 K (Figure 3.5.2.2 Top). The one electron oxidation of $Ni^{PhMe}L_O^{NMe}$ and $Ni^{PhOMe}L_O^{NMe}$ at 0.45 and 0.41 V (*vs.* Fc^+/Fc), respectively, generated solutions that were also EPR active at 77 K (Figure 3.5.2.2 Bottom).

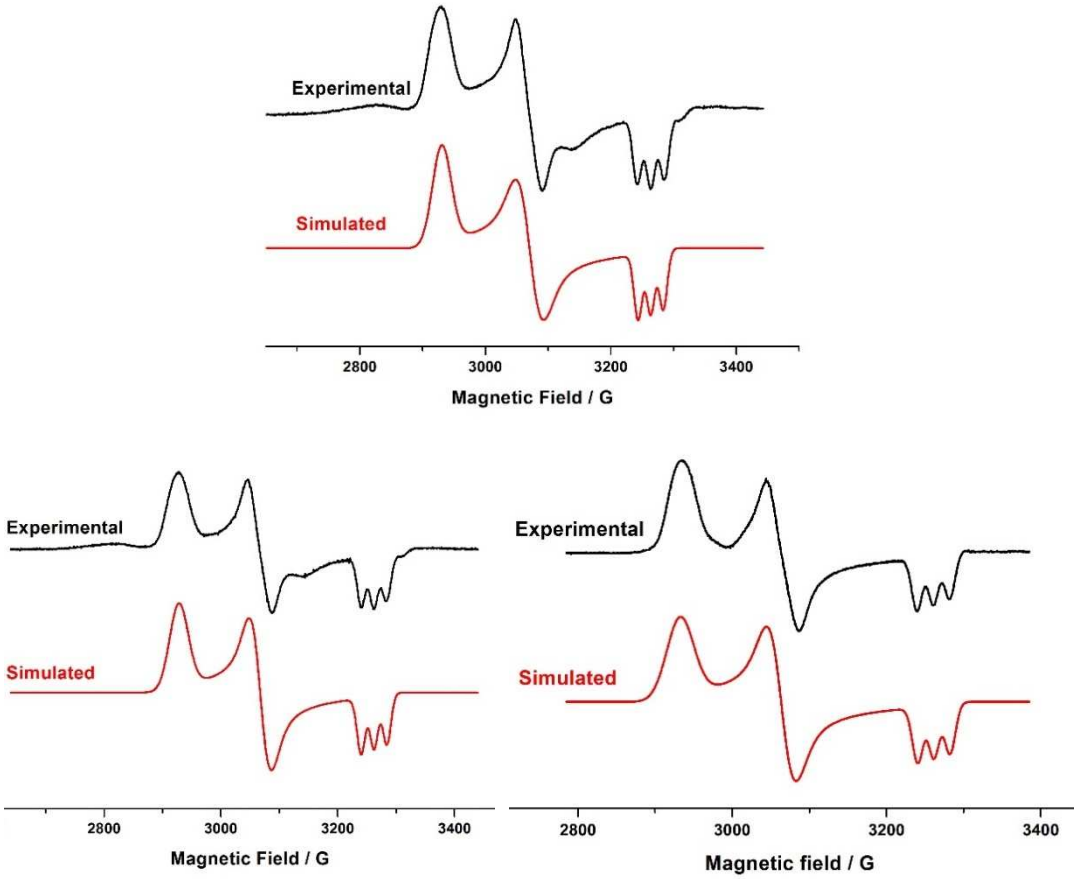


Figure 3.5.2.2: Top: (Black) X-band CW EPR spectra of electrochemically generated $[Ni^{Ph}L_O^{NMe}]^+$ in CH_2Cl_2 containing 0.4 M $[N^nBu_4][BF_4]$ as supporting electrolyte as a frozen solution at 77 K, (Red) Simulated spectra – spin Hamiltonian parameters: g_{11} = 2.2635, g_{22} = 2.1600, g_{33} = 2.0330, a_{33} = 20 G, Gaussian linewidths W_{11} = 30 G, W_{22} = 35 G, W_{33} = 13 G. Bottom Left: (Black) X-band CW EPR spectra of electrochemically generated $[Ni^{PhMe}L_O^{NMe}]^+$ in CH_2Cl_2 containing 0.4 M $[N^nBu_4][BF_4]$ as supporting electrolyte as a frozen solution at 77 K, (Red) Simulated spectra – spin Hamiltonian parameters: g_{11} = 2.2648, g_{22} = 2.1615, g_{33} = 2.0330, a_{33} = 22 G, Gaussian linewidths W_{11} = 32 G, W_{22} = 30 G, W_{33} = 14G; Bottom Right: (Black) X-band CW EPR spectra of electrochemically generated $[Ni^{PhOMe}L_O^{NMe}]^+$ in CH_2Cl_2 containing 0.4 M $[N^nBu_4][BF_4]$ as supporting electrolyte as a frozen solution at 77 K, (Red) Simulated spectra – spin Hamiltonian parameters: g_{11} = 2.2620, g_{22} = 2.1648, g_{33} = 2.0340, a_{33} = 21 G, Gaussian linewidths W_{11} = 35 G, W_{22} = 30 G, W_{33} = 14G.

The frozen solution EPR spectra of $[Ni^{Ph}L_O^{NMe}]^+$, $[Ni^{PhMe}L_O^{NMe}]^+$ and $[Ni^{PhOMe}L_O^{NMe}]^+$ at 77 K are rhombic with $g_{33} \sim 2.0$ and $g_{11}/g_{22} \sim 2.2$. An average g value ($g_{av} = 2.15$) is essentially unchanged across $[Ni^{R}L_O^{NMe}]^+$ (R = Ph, PhMe and PhOMe).

The EPR spectra of $[Ni^{Ph}L_O^{NMe}]^+$, $[Ni^{PhMe}L_O^{NMe}]^+$ and $[Ni^{PhOMe}L_O^{NMe}]^+$ possess similar principal g values to those typically observed for formal Ni^{III} species such as $[Ni(L^8)_2]^+$ (L^8H = (E)-2,4-di-*t*butyl-6-(1-(((dimethylamino) methyl) imino) ethyl) phenol; $g_{11} = 2.230$, $g_{22} = 2.146$, $g_{33} = 2.037$ in CH_2Cl_2 at 77 K)[14] and $[Ni(L^2)(DMF)_2]^+$ (L^2H_2 = N,N'-2-methylpropane-2,3-diyl-bis(salicylideneiminate); $g_{av} = 2.172$ in DMF at -140 °C),[17, 22, 31] but significantly higher than those of phenoxyl radical species (2.009-2.002)[24, 28, 32, 33] and Ni^{II}-phenoxyl radical species including $[Ni(L^9)]^+$ (L^9H_2 = *N*-(3,5-di*t*butylsalicylidene)-*N'*-(3,5-di*t*butylsalicylamine)-phenylene-1-imine-2-amine; $g_{iso} = 2.018$ in CH_2Cl_2 at 77 K) and $[Ni(L^{10})]^+$ ($L^{10}H_2$ = *N N'*-bis(3,5-di*t*butylsalicylidene)- 4,5-dimethylphenylene-1,2-diimine; $g_{iso} = 2.04$ in CH_2Cl_2 at 240-190 K and $g_{11} = 2.00$, $g_{22} = 2.02$, $g_{33} = 2.10$ in CH_2Cl_2 at 170-10 K).[1, 19, 25, 28, 29] Our EPR spectroscopic results suggests that $[Ni^{R}L_O^{NMe}]^+$ (R = Ph, PhMe and PhOMe) possess a SOMO that is predominantly metal based with a small phenoxyl radical ligand contribution (estimated as *ca.* 17 % based on Δg values).[31, 34] The high field feature in the frozen solution EPR spectra of $[Ni^{R}L_O^{NMe}]^+$ also exhibits ligand hyperfine coupling to one ^{14}N nucleus with $a_{33} = 20$, 22 and 21 G for $[Ni^{PhMe}L_O^{NMe}]^+$, $[Ni^{PhMe}L_O^{NMe}]^+$ and $[Ni^{PhOMe}L_O^{NMe}]^+$, respectively. This coupling may be assigned to nuclear hyperfine coupling involving the amine ^{14}N donor in $^{R}L_O^{NMe}$.[1, 35]

Further oxidation by controlled potential electrolysis to the two electron oxidised species $[Ni^{Ph}L_O^{NMe}]^{2+}$, $[Ni^{PhMe}L_O^{NMe}]^{2+}$ and $[Ni^{PhOMe}L_O^{NMe}]^{2+}$ generated khaki brown solutions which were EPR silent as room temperature and frozen solutions at 77 K, consistent with the two electron oxidised species possessing an S = 0 or S = 1 state as found for the *t*butyl analogue $[Ni^{tBu}L_O^{NMe}]^{2+}$.[7]

We also attempted the chemical oxidation of $Ni^{R}L_O^{NMe}$ (R = Ph, PhMe, PhOMe) in CH_2Cl_2 solution by treatment with one equivalent of $AgBF_4$. A brown solution was obtained after 10 min at room temperature, which was identified as containing

$[Ni^{R}L_{o}^{NMe}]^{+}$ by UV/vis spectroscopy. Unfortunately efforts to crystallise this species have been unsuccessful.

3.5.3 Discussion

The UV/vis spectra of $Ni^{Ph}L_{o}^{NMe}$, $Ni^{PhMe}L_{o}^{NMe}$ and $Ni^{PhOMe}L_{o}^{NMe}$ all exhibit similar features, with intense absorption bands in the 250-280 nm region (ε = 48,800-85,800 mol^{-1} dm^3 cm^{-1}) accompanied by an intense band at *ca.* 400 nm (ε = 12,700-15,800 mol^{-1} dm^3 cm^{-1}) (Table 3.5.3.1).

Complex	λ_{max} (nm)	ε (mol^{-1} dm^3 cm^{-1})	Isobestic point (nm)
$Ni^{Ph}L_{O}^{NMe}$	235(sh), 255, 271, 309, 391	42,700, 49,100, 48,800, 31,200, 12,700	
$[Ni^{Ph}L_{O}^{NMe}]^{+}$	248, 271, 295(sh), 401, 473(sh)	49,800, 46,800, 38,300, 13,200, 6,800	278, 308, 333
$[Ni^{Ph}L_{O}^{NMe}]^{2+}$	233, 264(sh), 338(sh), 368, 611,	44,000, 30,700, 19,500, 25,600, 13,800	
$Ni^{PhMe}L_{O}^{NMe}$	237(sh), 253, 278, 307(sh), 397	60,000, 65,300, 64,400, 40,700, 15,200	
$[Ni^{PhMe}L_{O}^{NMe}]^{+}$	253, 301(sh), 397, 479	71,600, 42,500, 17,000, 7,100	267, 292, 307, 328
$[Ni^{PhMe}L_{O}^{NMe}]^{2+}$	238, 272(sh), 347(sh), 381, 645	54,300, 38,100, 22,400, 33,900, 18,200	
$Ni^{PhOMe}L_{O}^{NMe}$	257, 278, 306(sh), 399	85,800, 78,000, 50,000 15,800	
$[Ni^{PhOMe}L_{O}^{NMe}]^{+}$	255, 280(sh), 400, 700	71,900, 57,300, 26,100, 11,700	328
$[Ni^{PhOMe}L_{O}^{NMe}]^{2+}$	243, 282, 400, 700	55,300, 43,200, 34,600,21,800	
$[Ni^{PhOMe}L_{O}^{NMe}]^{4+}$	236, 282, 427, 600	49,000, 34,600, 50,300, 12,200	

Table 3.5.3.1: Summary of UV/vis spectra of $Ni^{R}L_{o}^{NMe}$, $[Ni^{R}L_{o}^{NMe}]^{+}$, $[Ni^{R}L_{o}^{NMe}]^{2+}$, $[Ni^{PhOMe}L_{o}^{NMe}]^{4+}$ (R = Ph, PhMe, PhOMe).

The former are associated with phenoxide π →π* transitions,[11, 14, 18] as observed for $Zn^{Ph}L_{o}^{NMe}$, $Zn^{PhMe}L_{o}^{NMe}$ and $Zn^{PhOMe}L_{o}^{NMe}$ (Section 3.4), and the latter can be attributed to LMCT involving phenolate O-donors, as reported for similar Ni^{II} Schiff base complexes including $Ni^{tBu}L_{o}^{NMe}$ (λ = 238 nm, ε = 84,300 mol^{-1} dm^3 cm^{-1} and λ = 376 nm, ε = 18,300 mol^{-1} dm^3 cm^{-1}),[1] and the Ni^{II}-containing bis-3,5-di^{t}butylsalicyethyldimine Schiff base complexes (λ = *ca.* 310 nm, ε = *ca.* 12,000 mol^{-1} dm^3 cm^{-1} and λ = *ca.* 385 nm, ε = *ca.* 2,500 mol^{-1} dm^3 cm^{-1}).[7] The first oxidation process results in less change in the UV/vis spectra of $Ni^{Ph}L_{o}^{NMe}$ and $Ni^{PhMe}L_{o}^{NMe}$ relative to those of their Zn^{II} analogues $Zn^{Ph}L_{o}^{NMe}$ and $Zn^{PhMe}L_{o}^{NMe}$,

with no absorption bands observed at *ca.* 700 nm and no substantial increase in intensity around 410 nm. Thus, based on the UV/vis spectroscopic data $[Ni^{R}L_{o}^{NMe}]^{+}$ (R = Ph and PhMe) are likely not to be Ni^{II}-phenoxyl radical species but rather formal Ni^{III}-phenolate centres, as suggested by the frozen solution EPR spectra of $[Ni^{R}L_{o}^{NMe}]^{+}$ (R = Ph and PhMe) at 77K (Section 3.5.2). The one electron oxidation of $Ni^{PhOMe}L_{o}^{NMe}$ results in more significant changes in the UV/vis spectrum with the development of a broad band at 700 nm accompanied by a significant increase in the intensity of absorption at 400 nm. These bands are consistent with phenoxyl-radical ligand-based absorption processes, as previously observed for OMe substituted Schiff base phenolate complexes derived from 3-^{t}butyl-5-methoxysalicylaldehdye.[3] This suggests that at 253K $[Ni^{PhOMe}L_{o}^{NMe}]^{+}$ is best described as a Ni^{II}-phenoxyl radical species. In contrast, the frozen solution EPR spectrum of $[Ni^{PhOMe}L_{o}^{NMe}]^{+}$ at 77K suggests that at this temperature $[Ni^{PhOMe}L_{o}^{NMe}]^{+}$ is a Ni^{III}-phenolate species. Thus, $[Ni^{PhOMe}L_{o}^{NMe}]^{+}$ may exhibit temperature dependent redox tautomerism as has previously been observed for $[Ni(L^{11})]^{+}$ ($L^{11}H_2$ = N,N'-bis(3',5'-di^{t}butylsalicylidene)-1,2-cyclohexanediamine), which exhibits an EPR spectrum with a metal based SOMO in CH_2Cl_2 at -120 °C (g_{av} = 2.18) and a ligand based SOMO at -100 °C (g_{av} = 2.04).[31] This redox tautomerism is promoted in Ni^{II} diphenolate complexes where metal- and ligand-based redox active orbitals are close in energy.[36] Further variable temperature EPR spectroscopic studies will be required to determine the extent of redox tautomerism in $[Ni^{PhOMe}L_{o}^{NMe}]^{+}$.

We carried out unrestricted, gas phase geometry optimisations of $[Ni^{R}L_{o}^{NMe}]^{+}$ and single point COSMO[30] calculations to model the effect of the CH_2Cl_2 solvent as for $[Zn^{R}L_{o}^{NMe}]^{+}$ (Section 3.4.3). Isosurface plots of the spin density at 0.001 eBohr^{-3} are shown in Figure 3.5.3.1 and the spin densities for the fragments in each complex are summarised in Table 3.5.3.1.

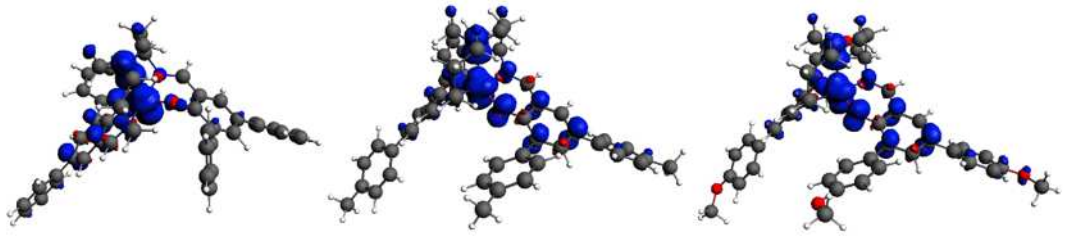


Figure 3.5.3.1: Spin density isosurfaces at the 0.001 eBohr^{-3} level for [Ni^{Ph}L$_o^{NMe}$]$^+$, [Ni^{PhMe}L$_o^{NMe}$]$^+$ and [Ni^{PhOMe}L$_o^{NMe}$]$^+$.

	[Ni^{Ph}L$_o^{NMe}$]$^+$	[Ni^{PhMe}L$_o^{NMe}$]$^+$	[Ni^{PhOMe}L$_o^{NMe}$]$^+$
Ni	0.566	0.536	0.496
Phenolate O	0.090	0.119	0.119
Imine N	0.019	0.021	0.023
Amine N	0.167	0.135	0.124
Phenolate	0.097	0.123	0.136
3-(4-R-phenyl)	0.008	0.007	0.024
5-(4-R-phenyl)	0.026	0.035	0.065

Table 3.5.3.1: Summary of spin densities attributed to the metal carbon and heteroatom atoms which make up various fragments of [Ni^{R}L$_o^{NMe}$]$^+$ (R = Ph, PhMe, PhOMe).

The spin densities of [Ni^{R}L$_o^{NMe}$]$^+$ (R = Ph, PhMe, PhOMe) are dominated by contributions from the metal centre (spin density = 0.566, 0.536, 0.496 for R = Ph, PhMe and PhOMe, respectively, Table 3.5.3.1) and support a Ni^{III}-phenolate formulation [Ni^{R}L$_o^{NMe}$]$^+$. Each [Ni^{R}L$_o^{NMe}$]$^+$ possesses a spin density contribution from the amine N-donor (0.167, 0.135, 0.124 for R = Ph, PhMe and PhOMe, respectively, Table 3.5.3.1), consistent with the assignment of the superhyperfine coupling observed in the EPR spectrum to this N-donor. The calculations also suggest a potential role for this donor in modulating the redox properties of Ni^{R}L$_o^{NMe}$, which is consistent with other studies where exogenous N donors can drive the formation of a formal Ni^{III} state on oxidation of Ni^{R}L$_o^{NMe}$.[12, 37, 38]

Further oxidation of [Ni^{R}L$_o^{NMe}$]$^+$ (R = Ph, PhMe, PhOMe) to the two electron oxidised species [Ni^{R}L$_o^{NMe}$]$^{2+}$ (R = Ph, PhMe, PhOMe) resulted in absorption spectra which were very similar for all three complexes, with intense absorptions around 400 and 700 nm. These absorptions can be assigned to phenoxyl radical $\pi \rightarrow \pi^*$ transitions,[11, 14, 18] indicating that the second oxidation for Ni^{R}L$_o^{NMe}$ (R = Ph, PhMe, PhOMe) most likely results in the formation of a ligand-based phenoxyl-radical to generate formal Ni^{III}-phenoxyl radical or Ni^{II}-diphenoxyl radical species.

In summary, UV/vis spectroelectrochemical, EPR spectroscopic and DFT theoretical results support the description of $[Ni^{Ph}L_o^{NMe}]^+$ and $[Ni^{PhMe}L_o^{NMe}]^+$ as formal Ni^{III}-phenolate species. For $[Ni^{PhOMe}L_o^{NMe}]^+$ the formulation is more ambiguous and suggests that this species may exhibit redox tautomerism involving Ni^{III}-phenolate and Ni^{II}-phenoxyl radical species over the 77K to 253K temperature range. Each complex undergoes a second oxidation process to generate Ni^{III}-phenoxyl radical or Ni^{II}-diphenoxyl radical species.

3.6 UV/vis and EPR Spectroscopic Studies of $Cu^{R}L_{o}^{NMe}$, (R = Ph, PhMe, PhOMe) and their Oxidation Products

Our electrochemical investigations by cyclic voltammetry of $Cu^{R}L_{o}^{NMe}$ (R = Ph, PhMe, PhOMe) reveal two reversible oxidation processes at $E_{1/2}$ = 0.37 and 0.59 V, 0.31 and 0.52 V and 0.24 and 0.40 V (*vs.* Fc^{+}/Fc), respectively, together with an additional oxidation process at E_{p}^{a} = 1.15 and 1.01 V (*vs.* Fc^{+}/Fc) for $Cu^{Ph}L_{o}^{NMe}$ and $Cu^{PhMe}L_{o}^{NMe}$, respectively, and two additional processes at E_{p}^{a} = 0.76 and 0.87 V (*vs.* Fc^{+}/Fc) for $Cu^{PhOMe}L_{o}^{NMe}$ (Section 3.3). The shift to lower reduction potentials upon the introduction of more electron donating substituents for all of these oxidation processes suggest ligand based redox chemistry, and UV/vis and EPR spectroscopies can be used to probe the nature of the oxidation products further.

3.6.1.1 Spectroelectrochemistry of $Cu^{Ph}L_{o}^{NMe}$

$Cu^{Ph}L_{o}^{NMe}$ exhibits a UV/vis spectrum with absorption bands at 232, 253, 274, 315 and 397 nm (ε = 52,000, 55,000, 57,500, 40,300 and 13,200 mol^{-1} dm^{3} cm^{-1}). Oxidation at 1.09 V *vs.* Ag/AgCl is accompanied by the development of bands at 314, 337, 368 and 598 nm (ε = 18,900, 16,700, 21,200 and 8,100 mol^{-1} dm^{3} cm^{-1}) (Figure 3.6.1.1.1).

The application of a potential of 0.0 V *vs.* Ag/AgCl resulted in an incomplete return of the spectral profile to that of $^{Ph}CuL_{o}^{NMe}$. However, the application of a greater over-potential (-0.4 V *vs.* Ag/AgCl) did regenerate the spectrum of $Cu^{Ph}L_{o}^{NMe}$ (Figure 3.6.1.1.1 inset) indicating that the first oxidation process of $Cu^{Ph}L_{o}^{NMe}$ is chemically reversible.

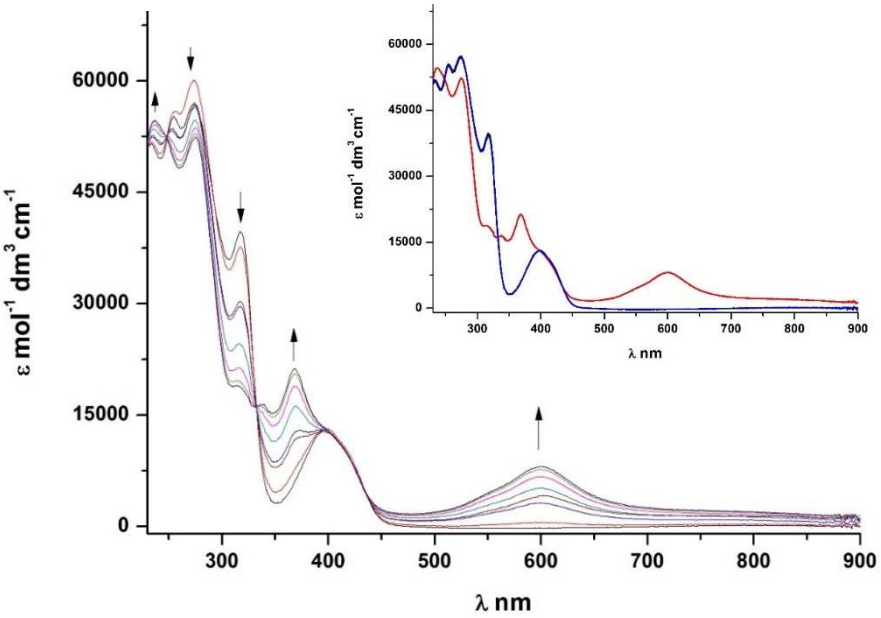


Figure 3.6.1.1.1: Sequential UV/vis spectra recorded during the oxidation of $Cu^{Ph}L_o^{NMe}$ at 1.09 V vs. Ag/AgCl identifying the bands formed during oxidation. 0.36 mmol solution recorded at 253 K under N_2 in CH_2Cl_2 containing 0.4 M $[N^nBu_4][BF_4]$ as supporting electrolyte. Inset, spectra before oxidation (black), after oxidation (red) and after re-reduction at 0.00 V 1.09 V vs. Ag/AgCl (blue).

The two electron oxidation of $Cu^{Ph}L_o^{NMe}$ led to the development of two intense bands at 373 and 626 nm (ε = 36,300 and 19,300 mol^{-1} dm^3 cm^{-1}), together with a reduction in the intensity of the bands at high energy leaving one intense band at 234 nm (ε = 54,600 mol^{-1} dm^3 cm^{-1}) with additional shoulders at 258 and 341 nm (ε = 39,700 and 24,600 mol^{-1} dm^3 cm^{-1}) (Figure 3.6.1.1.2). The chemical reversibility of this oxidation was demonstrated by the one electron re-reduction of the solution at 1.00 V *vs* Ag/AgCl to generate a UV/vis spectrum with a similar profile to that of $[^{Ph}CuL_o^{NMe}]^+$. Further re-reduction at -0.40 V *vs* Ag/AgCl essentially reproduced the spectral profile of $Cu^{Ph}L_o^{NMe}$ (Figure 3.6.1.1.2 inset).

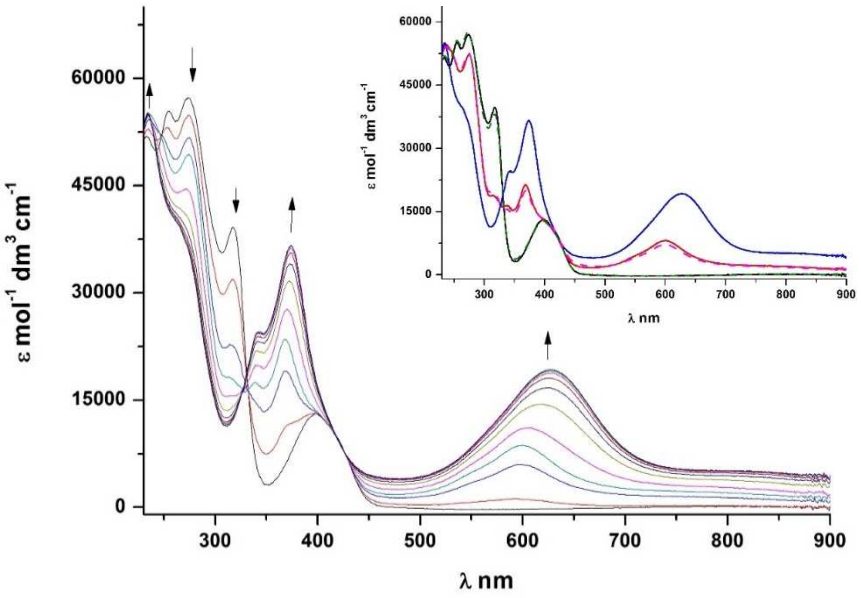


Figure 3.6.1.1.2: Sequential UV/vis spectra recorded during the oxidation of $Cu^{Ph}L_o^{NMe}$ at 1.36 V vs. Ag/AgCl identifying the bands formed during oxidation. 0.41 mmol solution recorded at 253 K under N_2 in CH_2Cl_2 containing 0.4 M $[N^nBu_4][BF_4]$ as supporting electrolyte. Inset, spectra before oxidation (black), after 1 e^- oxidation (red), after 2 e^- oxidation (blue), after re-reduction to 1 e^- oxidised species (magenta) at 1.00 V vs. Ag/AgCl, and after re-reduction to original species (green) at -0.40 V vs. Ag/AgCl.

3.6.1.2 Spectroelectrochemistry of $Cu^{PhMe}L_o^{NMe}$

$Cu^{PhMe}L_o^{NMe}$ possesses a UV/vis spectrum with absorption bands at 237, 254, 276, 314 and 401 nm (ε = 34,100, 37,000, 37,700, 24,800 and 8,200 mol^{-1} dm^3 cm^{-1}) that is similar to that for $Cu^{Ph}L_o^{NMe}$. One electron oxidation at 1.02 V *vs.* Ag/AgCl, leads to spectral changes that are similar to those observed for the oxidation of $Cu^{Ph}L_o^{NMe}$, with the development of absorption bands at 630 and 378 nm (ε = 4,380 and 12,400 mol^{-1} dm^3 cm^{-1}), a reduction in the number of bands at high energy with bands at 241 and 277 nm (ε = 35,500 and 32,000 mol^{-1} dm^3 cm^{-1}) and the development of a shoulder at *ca.* 318 nm (ε = 12,000 mol^{-1} dm^3 cm^{-1}) (Figure 3.6.1.2.1). The UV/vis spectrum of $Cu^{PhMe}L_o^{NMe}$ was not obtained on re-reduction, even after the application of a significant over-potential (-0.50 V vs. Ag/AgCl) (Figure 3.6.1.2.1 inset). Given the chemical irreversibility of this process the second oxidation process of $Cu^{PhMe}L_o^{NMe}$ observed at $E_{1/2}$ = 0.52 V (*vs.* Fc^+/Fc) by cyclic voltammetry could not be investigated by spectroelectrochemistry.

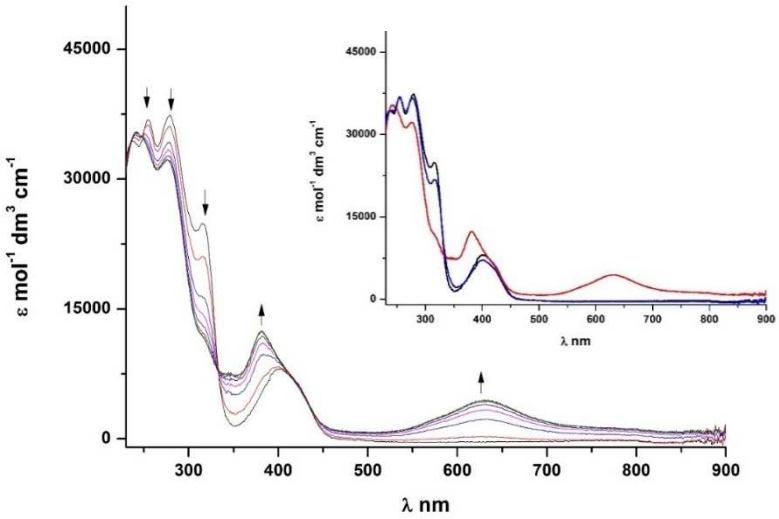


Figure 3.6.1.2.1: Sequential UV/vis spectra recorded during the oxidation of $Cu^{PhMe}L_o^{NMe}$ at 1.02 V vs. Ag/AgCl identifying the bands formed during oxidation. 0.27 mmol solution recorded at 253 K under N_2 in CH_2Cl_2 containing 0.4 M $[N^nBu_4][BF_4]$ as supporting electrolyte. Inset, spectra before oxidation (black), after oxidation (red) and after re-reduction at -0.50 V vs. Ag/AgCl (blue).

3.6.1.3 Spectroelectrochemistry of $Cu^{PhOMe}L_o^{NMe}$

$Cu^{PhOMe}L_o^{NMe}$ exhibits a similar overall profile to $Cu^{Ph}L_o^{NMe}$ and $Cu^{PhMe}L_o^{NMe}$ with absorption bands at 258, 284 and 401 nm (ε = 61,800, 58,100 and 12,200 mol^{-1} dm^3 cm^{-1}) and shoulders at 244 and 315 nm (ε = 55,600 and 38,500 mol^{-1} dm^3 cm^{-1}). One electron oxidation is associated with the appearance of absorption bands at 400 and 682 nm (ε = 22,200 and 10,200 mol^{-1} dm^3 cm^{-1}) and a reduction in the number of bands at higher energy to give three bands at 248, 259 and 274 nm (ε = 54,200, 53,600 and 51,800 mol^{-1} dm^3 cm^{-1}) (Figure 3.6.1.3 inset). On re-reduction at 0.00 V *vs* Ag/AgCl the spectral profile of $Cu^{PhOMe}L_o^{NMe}$ is obtained, demonstrating that the first oxidation process for $Cu^{PhOMe}L_o^{NMe}$ is chemically reversible (Figure 3.6.1.3.1 inset).

The two-electron oxidation of $Cu^{PhOMe}L_o^{NMe}$ at 0.92 V *vs.* Ag/AgCl results in further spectral changes, with increases in the intensities of the bands at 746 and 404 nm (ε = 22,400 and 33,000 mol^{-1} dm^3 cm^{-1}), the development of a shoulder at 686 nm (ε = 19,200 mol^{-1} dm^3 cm^{-1}) and a reduction in the intensities of the higher energy bands with two absorptions at 244 and 283 nm (ε = 44,600 and 34,000 mol^{-1} dm^3 cm^{-1}) occurring in this region (Figure 3.6.1.3.2). Re-reduction at 0.00 V *vs* Ag/AgCl generates the spectral profile of $Cu^{PhOMe}L_o^{NMe}$, demonstrating that the second oxidation process is chemically reversible (Figure 3.6.1.3.2 inset).

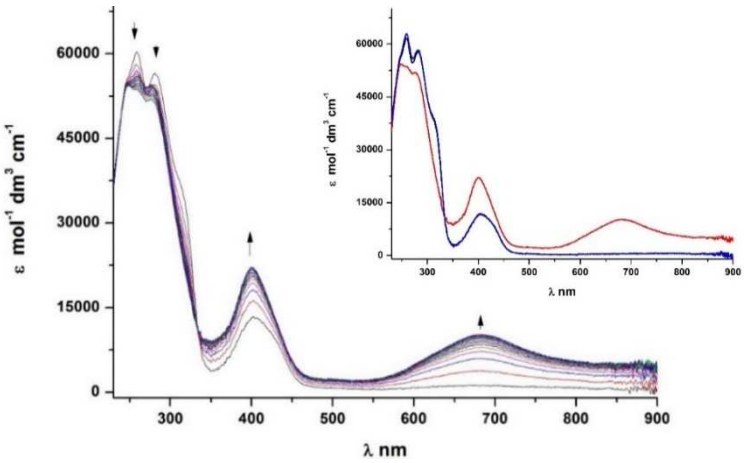


Figure 3.6.1.3.1: Sequential UV/vis spectra recorded during the oxidation of $Cu^{PhOMe}L_o^{NMe}$ at 0.90 V vs. Ag/AgCl identifying the bands formed during oxidation. 0.11 mmol solution recorded at 253 K under N_2 in CH_2Cl_2 containing 0.4 M $[N^nBu_4][BF_4]$ as supporting electrolyte. Inset, spectra before oxidation (black), after oxidation (red) and after re-reduction at 0.00 V vs. Ag/AgCl (blue).

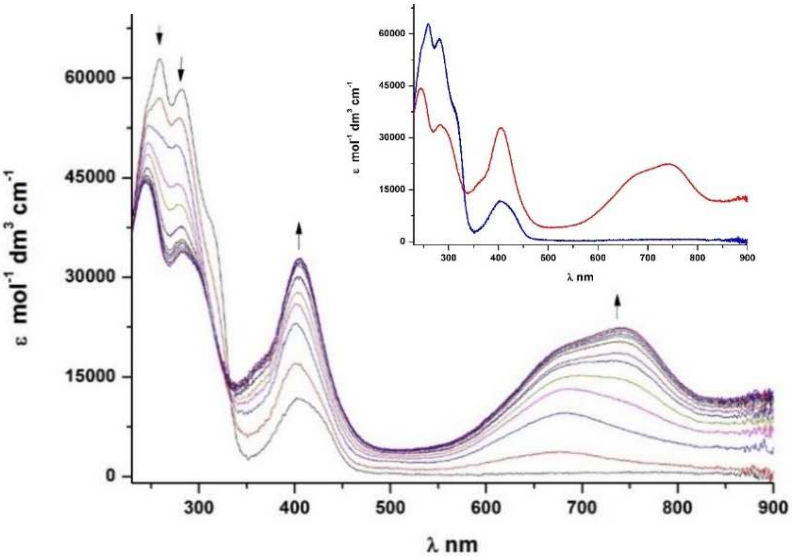


Figure 3.6.1.3.2: Sequential UV/vis spectra recorded during the oxidation of $Cu^{PhOMe}L_o^{NMe}$ at 1.18 V vs. Ag/AgCl identifying the bands formed during oxidation. 0.11 mmol solution recorded at 253 K under N_2 in CH_2Cl_2 containing 0.4 M $[N^nBu_4][BF_4]$ as supporting electrolyte. Inset, spectra before oxidation (black), after oxidation (red), after re-reduction at 0.00 V vs. Ag/AgCl (blue).

Whilst the third and fourth oxidation processes for $Cu^{PhOMe}L_o^{NMe}$ were too close to one another in potential to be investigated separately, they were studied through the application of a potential of 1.60 V *vs*. Ag/AgCl. This resulted in significant spectral changes including the growth of an intense absorption band at 435 nm (ε = 29,100 mol^{-1} dm^3 cm^{-1}) together with the development of lower intensity bands at 236 and 274 nm (ε = 40,700 and 30,600 mol^{-1} dm^3 cm^{-1}) (Figure 3.6.1.3.3). On re-

reduction, the original spectrum of $Cu^{PhOMe}L_o^{NMe}$ was not obtained, indicating that these processes are not chemically reversible (Figure 3.6.1.3.3 inset). The spectral changes observed for this oxidation are similar to those observed on the analogous oxidation of $Ni^{PhOMe}L_o^{NMe}$ (Figure 3.5.1.3.3; λ = 236, 282, 427, 600 nm, ε = 49,000, 34,600, 50,300, 12,200 mol^{-1} dm^3 cm^{-1}), suggesting similar ligand-based oxidation processes.

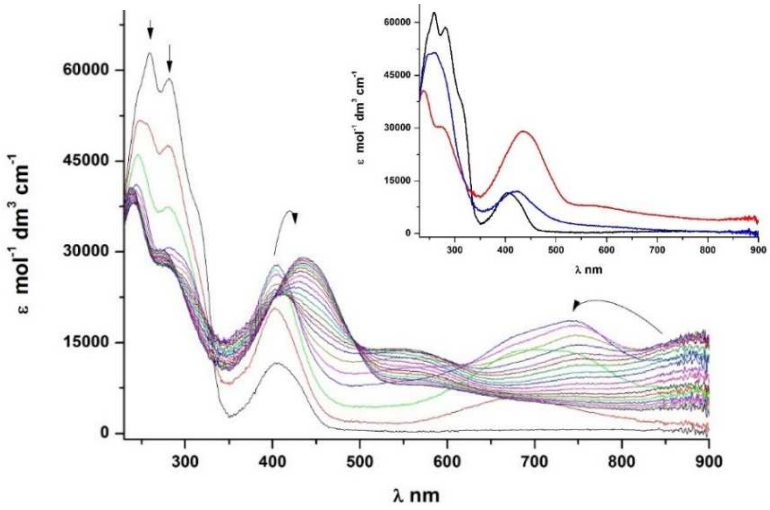


Figure 3.6.1.3.3: Sequential UV/vis spectra recorded during the oxidation of $Cu^{PhOMe}L_o^{NMe}$ at 1.60 V vs. Ag/AgCl identifying the bands formed during oxidation. 0.11 mmol solution recorded at 253 K under N_2 in CH_2Cl_2 containing 0.4 M $[N^nBu_4][BF_4]$ as supporting electrolyte. Inset, spectra before oxidation (black), after 4 e^- oxidation (red), after re-reduction at 0.00 V vs. Ag/AgCl (blue).

3.6.2 Controlled Potential Electrolysis and EPR Spectroscopy of $Cu^{Ph}L_o^{NMe}$

Given the similarities in the EPR spectroscopy (Chapter 2), electrochemistry (Section 3.3) and UV/vis spectroelectrochemistry (Section 3.6.1) of $Cu^RL_o^{NMe}$ (R = Ph, PhMe and PhOMe) we undertook controlled potential electrolytic and EPR spectroscopic studies on $Cu^{Ph}L_o^{NMe}$ as a prototypical example. Controlled potential electrolysis of a solution of $Cu^{Ph}L_o^{NMe}$ at 0.47 V *vs.* Fc^+/Fc until a charge equivalent to one electron has been removed results in the formation of a blue/green solution which is essentially EPR silent (Figure 3.6.2.1 - red trace). This is consistent with an S = 0 or 1 ground state that results from the magnetic coupling between the S = ½ Cu^{II} centre and an S = ½ coordinated radical ligand in $[^{Ph}CuL_o^{NMe}]^+$. Further electrolysis at 0.71 V (*vs.* Fc^+/Fc), to generate $[Cu^{Ph}L_o^{NMe}]^{2+}$, results in the formation of dark blue solution. The EPR spectrum of this solution at 293K exhibits a feature at g_{iso} = 2.00 (Figure 3.6.2.1 – blue trace) consistent with the generation of a second uncoupled phenoxyl radical centre in $[Cu^{Ph}L_o^{NMe}]^{2+}$. The

weak feature observed in the spectrum of $[^{Ph}CuL_o^{NMe}]^+$ can be attributed to the formation of a small quantity of the doubly oxidised species $[^{Ph}CuL_o^{NMe}]^{2+}$ under the conditions of the experiment.

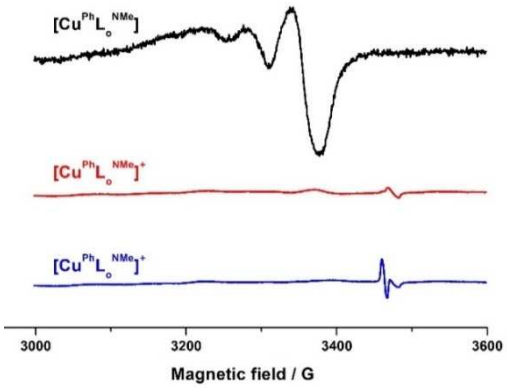


Figure 3.6.2.1: X-band CW EPR spectra of: Top- black- $Cu^{Ph}L_O^{NMe}$; Middle – red- electrochemically generated $[Cu^{Ph}L_O^{NMe}]^+$; Bottom – blue - electrochemically generated $[Cu^{Ph}L_O^{NMe}]^{2+}$; all in CH_2Cl_2 containing 0.4 M $[N^nBu_4][BF_4]$ as supporting electrolyte at 293 K.

3.6.3 Discussion

The spectral profiles for $Cu^{Ph}L_o^{NMe}$, $Cu^{PhMe}L_o^{NMe}$ and $Cu^{PhOMe}L_o^{NMe}$ are similar, and exhibit characteristic absorption bands for Cu^{II} phenolate complexes (Table 3.6.3.1).[39]

Complex	λ_{max} (nm)	ε (mol^{-1} dm^3 cm^{-1})	Isobestic point (nm)
$Cu^{Ph}L_O^{NMe}$	232, 253, 274, 315, 397	52,000, 55,000, 57,500, 40,300, 13,200	
$[Cu^{Ph}L_O^{NMe}]^+$	314, 337, 368, 598	18,900, 16,700, 21,200, 8,100	332
$[Cu^{Ph}L_O^{NMe}]^{2+}$	234, 258(sh), 341(sh), 373, 626	54,600, 39,700, 24,600, 36,300, 19,300,	
$Cu^{PhMe}L_O^{NMe}$	237, 254, 276, 314, 401	34,100, 37,000, 37,700, 24,800, 8,200	
$[Cu^{PhMe}L_O^{NMe}]^+$	241, 277, 318(sh), 378, 630	35,500, 32,000, 12,000, 12,400, 4,380	248, 334
$Cu^{PhOMe}L_O^{NMe}$	244(sh), 258, 284, 315(sh), 401	61,800, 55,600, 58,100, 38,500, 12,200	
$[Cu^{PhOMe}L_O^{NMe}]^+$	248, 259, 274 , 400, 682	54,200, 53,600, 51,800, 22,200, 10,200	332
$[Cu^{PhOMe}L_O^{NMe}]^{2+}$	244, 283, 404, 686(sh), 746	44,600, 34,000, 33,000, 19,200, 22,400	
$[Cu^{PhOMe}L_O^{NMe}]^{4+}$	236, 274, 435	40,700, 30,600, 29,100	

Table 3.6.3.1: Summary of UV/vis spectra of $Cu^RL_o^{NMe}$, $[Cu^RL_o^{NMe}]^+$, $[Cu^RL_o^{NMe}]^{2+}$, $[Cu^{PhOMe}L_o^{NMe}]^{4+}$ (R = Ph, PhMe, PhOMe).

The absorptions at *ca.* 230 and 315 nm may be attributed to phenoxide $\pi \rightarrow \pi^*$ transitions and those at *ca.* 400 nm to phenolate to Cu^{II} LMCT as found for Cu^{II}-phenolate complexes including $Cu_2(L^{12})_2$ [L^{12} = 3'-^{t}butyl-2'-hydroxybenzyl(2-pyridylmethyl)amine; λ = 223, 242, 295 nm, ε = 10,000-15,000 mol^{-1} dm^3 cm^{-1} ($\pi \rightarrow \pi^*$) and λ = 467 nm, ε = 1,820 mol^{-1} dm^3 cm^{-1} (LMCT)] and $Cu(L^{13})$ [L^{13} = N-benzyl-N',N''-di^{t}butyl-disalicyl-triaminocyclohexane; λ = 230, 258, 326 nm, ε = 6,000-17,000 mol^{-1} dm^3 cm^{-1} ($\pi \rightarrow \pi^*$) and λ = 378 nm, ε = 628 mol^{-1} dm^3 cm^{-1} (LMCT)].[11, 15, 39, 40]

On one electron oxidation to $[Cu^RL_o^{NMe}]^+$ (R = Ph, PhMe, PhOMe) similar transformations were observed for each species (Table 3.6.3.1), with the spectral changes proceeding *via* multiple isobestic points, indicative of a direct transformation with no detectable intermediates. The UV/vis spectra of $[Cu^RL_o^{NMe}]^+$ (R = Ph, PhMe, PhOMe) exhibit broad absorptions around 600-700 nm which can be attributed to the formation of phenoxyl radicals,[25, 33] consistent with a ligand based oxidation as previously inferred from our cyclic voltammetric and EPR spectroscopic results (Section 3.3 and 3.6.2). The formation of a phenoxyl radical is also associated with the development of an intense $\pi \rightarrow \pi^*$ absorption band in the 410 nm region as found for $Cu_2(L^{12})_2$ (λ = 439 nm, ε = 16,700 mol^{-1} dm^3 cm^{-1}) and $Cu(L^2)$ (λ = 390 nm, ε = 9,860 mol^{-1} dm^3 cm^{-1}),[19, 25, 33, 41] Whilst this region is partially masked by a LMCT band as has been observed for $Cu^{t\mathrm{Bu}}L_o^{NMe}$,[1] the increase in intensity in this region on the one-electron oxidation of $Cu^RL_o^{NMe}$ is consistent with the formation of a Cu^{II}-phenoxyl radical species.

The lack of chemical reversibility for the one electron oxidation of $Cu^{PhMe}L_o^{NMe}$ is somewhat surprising, especially given the apparently similar nature of this process compared to the reversible one-electron oxidation processes for $Cu^{Ph}L_o^{NMe}$ and $Cu^{PhOMe}L_o^{NMe}$. Thus, for $Cu^{PhMe}L_o^{NMe}$ the presence of a methyl group in the phenyl rings at the 3 and 5 positions of the phenolate rings may facilitate a decomposition route *via* proton abstraction.

The second oxidation processes for $Cu^{Ph}L_o^{NMe}$ and $Cu^{PhOMe}L_o^{NMe}$ are accompanied by the development of absorption bands around 400 and 700 nm of greater intensities relative to those of $[Cu^{Ph}L_o^{NMe}]^+$ and $[Cu^{PhOMe}L_o^{NMe}]^+$ (Table 3.6.1.4.1).

These changes are consistent with the formation of a bis-phenoxyl radical species as found for Zn analogues (Section 3.4) and the two electron oxidations of other Cu^{II}-diphenolate complexes including the Cu^{II} complex of 1-ethyl-4,7-bis (3-^{t}butyl-5-methoxy-2-hydroxybenzyl) -1,4,7-triazacyclononane (λ = 237, 319, 431, 485 nm, ε = 7,000, 24,000, 15,000, 3,500 mol^{-1} dm^3 cm^{-1}) and the ^{t}butyl substituted analogue $Cu^{tBu}L_o^{NMe}$ (λ = 298, 394, 430, 494, 764 nm, ε = 18,300, 8,700, 9,800, 2,400, 1,900 mol^{-1} dm^3 cm^{-1}). [1, 8, 16]

Conclusions as to the nature of the oxidation products of $Cu^{PhOMe}L^{NMe}$ following oxidation by three or four electrons remain inconclusive due to the significant level of decomposition that occurs, although the similarity in the UV/vis spectra of the oxidation products of $Ni^{PhOMe}L_o^{NMe}$ (Figure 3.5.1.3.3) and $Cu^{PhOMe}L_o^{NMe}$ (Figure 3.6.1.3.3) suggest ligand-based processes may be occurring for the three and four electron oxidation of $Ni^{PhOMe}L_O^{NMe}$ and $Cu^{PhOMe}L^{NMe}$.

We carried out unrestricted, gas phase geometry optimisations of $[Cu^{R}L_o^{NMe}]^+$, followed by single point COSMO[30] calculations to model the effect of the CH_2Cl_2 solvent as for $[M^{R}L_o^{NMe}]^+$ (M = Zn and Ni). Isosurface plots of the spin density at 0.001 $eBohr^{-3}$ are shown in Figure 3.4.4.1 and the spin densities for the fragments in each complex are summarised in Table 3.6.3.2.

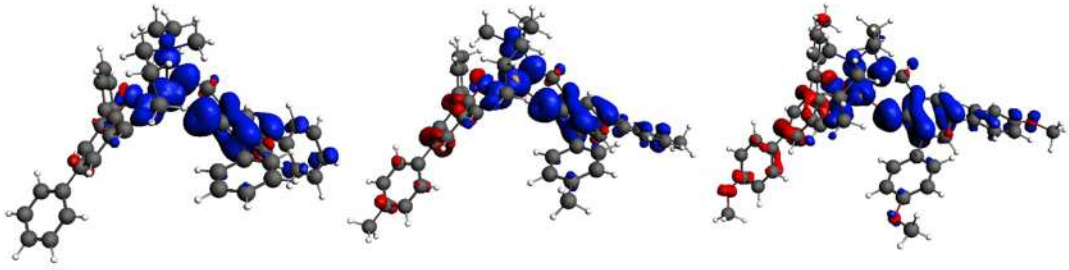


Figure 3.6.3.1: Spin density isosurfaces at the 0.001 $eBohr^{-3}$ level for $[Cu^{Ph}L_o^{NMe}]^+$, $[Cu^{PhMe}L_o^{NMe}]^+$ and $[Cu^{PhOMe}L_o^{NMe}]^+$.

	$[Cu^{Ph}L_o^{NMe}]^+$	$[Cu^{PhMe}L_o^{NMe}]^+$	$[Cu^{PhOMe}L_o^{NMe}]^+$
Cu	0.550	0.552	0.544
Phenolate O	0.435	0.399	0.382
Imine N	0.281	0.276	0.261
Amine N	0.065	0.070	0.050
Phenolate ring	0.465	0.447	0.412
3-(4-R-phenyl)	0.055	0.042	0.100
5-(4-R-phenyl)	0.124	0.145	0.216

Table 3.6.3.2: Summary of spin densities attributed to the metal carbon and heteroatom atoms which make up various fragments of $[Cu^RL_o^{NMe}]^+$ (R = Ph, PhMe, PhOMe).

Calculations for $[Cu^RL_o^{NMe}]^+$ show significant spin density localised on the metal centre (0.550, 0.552 and 0.544 for R = Ph, PhMe and PhOMe respectively). Introducing increasingly electron donating substituents is accompanied by a general decrease in the spin density localised on the coordinating imine nitrogen and phenolate oxygen donors centre (imine spin density: 0.281, 0.276 and 0.261; phenolate spin density: 0.435, 0.399 and 0.382 for R = Ph, PhMe and PhOMe respectively) (Table 3.6.3.2 and Figure 3.6.3.1).

This situation is intermediate to that seen for $[Zn^RL_o^{NMe}]^+$ and $[Ni^RL_o^{NMe}]^+$, with some contribution to the spin density from the Cu^{II} centre, but less than that seen in $[Ni^RL_o^{NMe}]^+$(R = Ph, PhMe, PhOMe). The contribution from the amine nitrogen donor, key to stabilising the Ni^{III} state of $[Ni^RL_o^{NMe}]^+$(R = Ph, PhMe, PhOMe) is significantly lower in these copper analogues than seen in their Ni^{III} counterparts, and crucially does not significantly decrease upon the introduction of more electron donating substituents, suggesting that whilst there is a not insignificant copper based contribution to the oxidative process, a different interaction may be taking place for the copper species compared to that seen in their nickel analogues, and the introduction of electron density to the phenolate substituents does not appear to result in the redox tautomerism between metal and ligand based oxidation seen in $[Ni^{PhOMe}L_o^{NMe}]^+$ (Section 3.5).

3.7 Electrochemistry of $M^{R}L_{o}^{NMe}$ (R = ^{t}Bu/Br, ^{t}Bu/Ph, ^{t}Bu/PhMe, ^{t}Bu/PhOMe; M = Zn, Ni, Cu)

We investigated the electrochemistry of the mixed substituent complexes $M^{R}L_{o}^{NMe}$ (M = Zn, Ni, Cu; R = ^{t}Bu/Br, ^{t}Bu/Ph, ^{t}Bu/PhMe, ^{t}Bu/PhOMe) (Figure 3.7.1) in order to determine the relative influence of substitution in the 3- and 5-positions of the phenolate rings in each complex. This is particularly relevant given the post translational modification found at the active site of GO at the ortho position of the tyrosine residue that has been proposed to modify the redox properties of the equatorial tyrosine residue (Tyr 272, Chapter One).[4] We have already shown that varying the substitution at the 3-position alone has limited impact on the geometry of the metal centre when compared to substitution at the 3 *and* 5 positions (Chapter Two) and we aimed to determine whether this reduction in influence translates into the electronic structures of these centres.

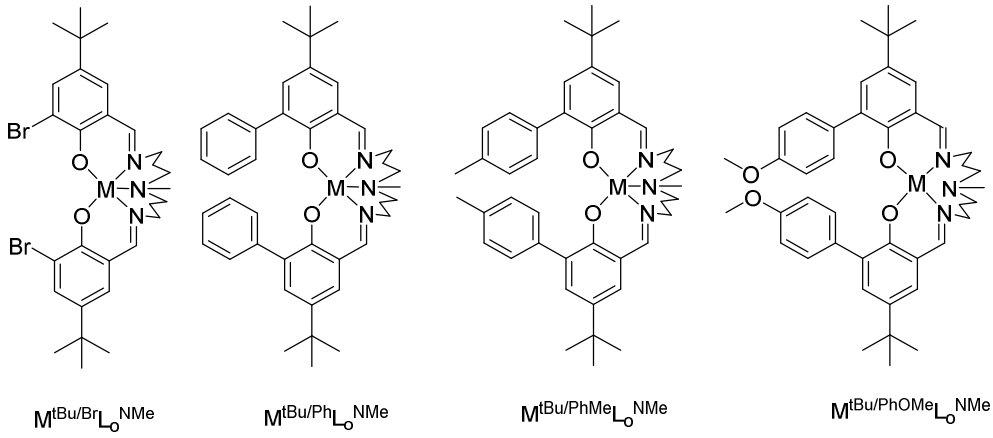


Figure 3.7.1: $M^{R}L_{o}^{NMe}$ (R = ^{t}Bu/Br, ^{t}Bu/Ph, ^{t}Bu/PhMe, ^{t}Bu/PhOMe; M = Zn, Ni, Cu).

3.7.1 Electrochemistry of $M^{tBu/Br}L_{o}^{NMe}$ (M = Zn, Ni, Cu)

$Zn^{tBu/Br}L_{o}^{NMe}$ possesses two oxidation processes at E_{p}^{a} = 0.59 and 0.84 V (*vs.* Fc^{+}/Fc) that are not electrochemically reversible (Figure 3.7.1.1). $Ni^{tBu/Br}L_{o}^{NMe}$ exhibits two oxidation processes: a reversible process at $E_{1/2}$ = 0.27 V (*vs.* Fc^{+}/Fc) and a second process at E_{p}^{a} = 0.91 V (*vs.* Fc^{+}/Fc) (Figure 3.7.1.2) that is not reversible. $Cu^{tBu/Br}L_{o}^{NMe}$ possesses two oxidation processes at E_{p}^{a} = 0.57 and 0.88 V *vs.* Fc^{+}/Fc, which are not electrochemically reversible (Figure 3.7.1.1).

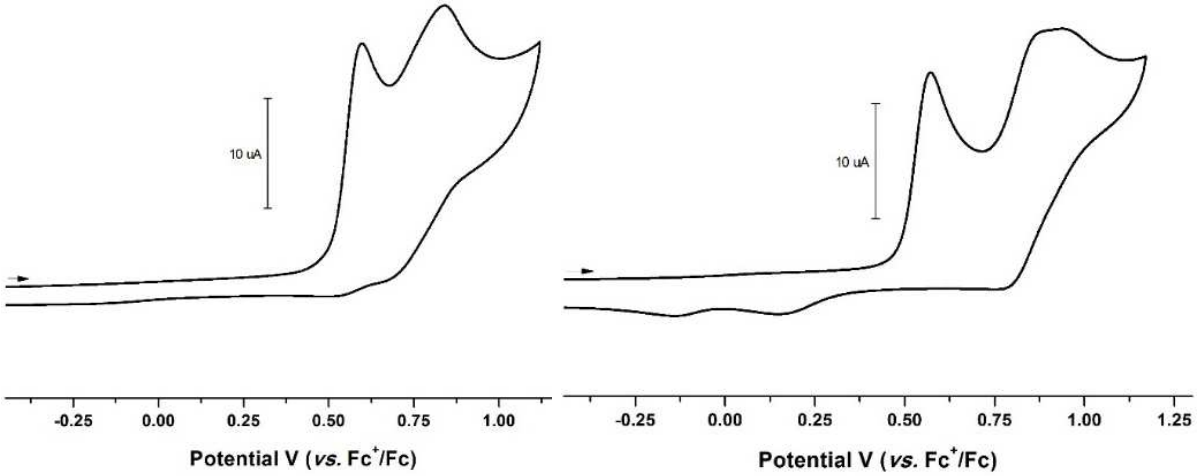
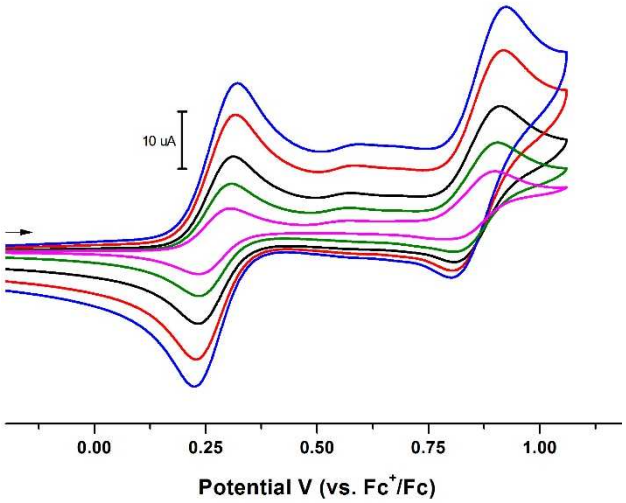


Figure 3.7.1.1: Left: Cyclic voltammogram of $Zn^{tBu/Br}L_o^{NMe}$ at 100 mV; Right: Cyclic voltammogram of $Cu^{tBu/Br}L_o^{NMe}$ at 100 mV.



Complex	**$E_{1/2}$ V (vs Fc^+/Fc)**	**i_p^c µA (100 mV)**	**i_p^a µA (100 mV)**	**$\|i_p^c/ i_p^a\|$ (100 mV)**	**$\|E_{pc}-E_{pa}\|$ mV**	**$\|E_{pc}-E_{pa}\|$ mV ($dmfc^+$/dmfc)**
$Ni^{tBu/Br}L_o^{NMe}$	0.271	-12.6	14.7	0.86	80	90

Figure 3.7.1.2: First and second oxidation processes of $Ni^{tBu/Br}L_o^{NMe}$ at multiple scan rates (300 mV (blue), 200 mV (red), 100 mV (black), 50 mV (green), 20 mV (purple)).

The electrochemically reversible process for $Ni^{tBu/Br}L_o^{NMe}$ was investigated by UV/vis spectroelectrochemistry (Figure 3.7.1.2). The UV/vis spectrum of $Ni^{tBu/Br}L_o^{NMe}$ shows absorption bands at 236 and 377 nm which can be assigned to phenoxide $\pi \rightarrow \pi^*$ and LMCT transitions respectively, [7, 14, 17, 42] with an additional shoulder at 293 nm. This is broadly consistent with the spectrum observed for $Ni^{R}L_o^{NMe}$ (R = Cl, Br) (Section 3.2) and lacks the additional bands at ~ 310 nm seen in $Ni^{R}L_o^{NMe}$ (R = Ph, PhMe, PhOMe). On oxidation at 1.06 V *vs.* Ag/AgCl the

absorption at 236 nm decreases in intensity and the shoulder at 293 nm develops into a band at 294 nm, with an additional shoulder forming at 448 nm (Figure 3.7.1.2). Unfortunately, as for $Ni^{R}L_{o}^{NMe}$ (R = Ph, PhMe, PhOMe, Section 3.5), it is not possible to unambiguously determine if a phenoxyl radical is formed due to the intense absorption bands in the 390 nm region. However, the lack of an additional low energy absorption in the 700 nm region and no significant increase in intensity around 400 nm suggest that the presence of a phenoxyl radical species is unlikely, and that the first oxidation process of $Ni^{tBu/Br}L_{o}^{NMe}$ is most likely metal-based.

As for $Ni^{R}L_{o}^{NMe}$ (R = Cl, Br, Nap, Ph, PhMe, PhOMe), the first oxidation process of $Ni^{tBu/Br}L_{o}^{NMe}$ is chemically reversible. The UV/vis spectroelectrochemical data exhibit a well-defined isobestic point during oxidation indicating a direct transition from $Ni^{tBu/Br}L_{o}^{NMe}$ to $[Ni^{tBu/Br}L_{o}^{NMe}]^{+}$ with no detectable intermediates formed. The second oxidation observed by cyclic voltammetry at E_{p}^{a} = 0.91 V (*vs.* Fc^{+}/Fc) was also investigated, however this was not reversible and significant decomposition was observed (Figure 3.7.1.3).

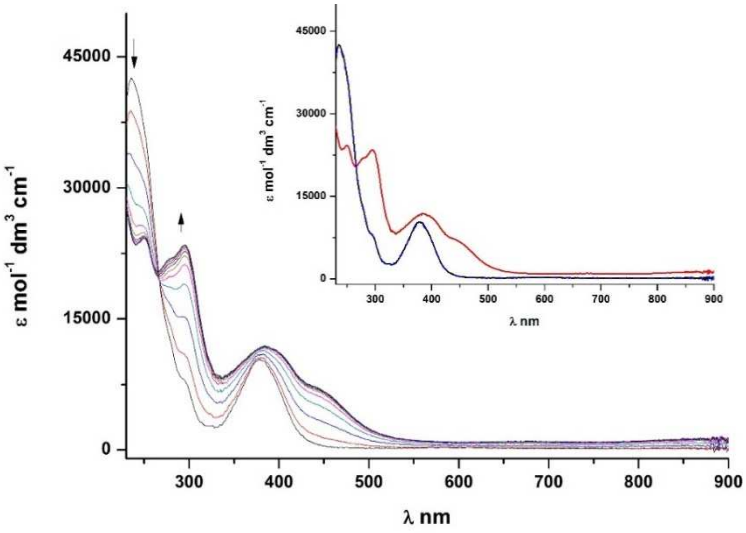


Figure 3.7.1.2: Sequential UV/vis spectra recorded during the oxidation of $Ni^{tBu/Br}L_{o}^{NMe}$ at 1.06 V vs. Ag/AgCl identifying the bands formed during oxidation. 0.36 mmol solution recorded at 253 K under N_2 in CH_2Cl_2 containing 0.4 M $[N^{n}Bu_4][BF_4]$ as supporting electrolyte. Inset, spectra before oxidation (black), after oxidation (red) and after re-reduction at 0.00 V vs. Ag/AgCl (blue).

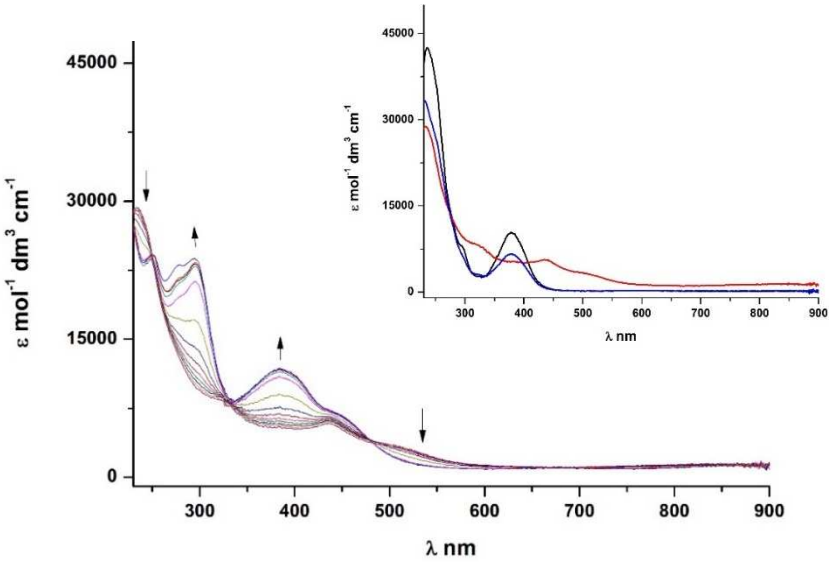
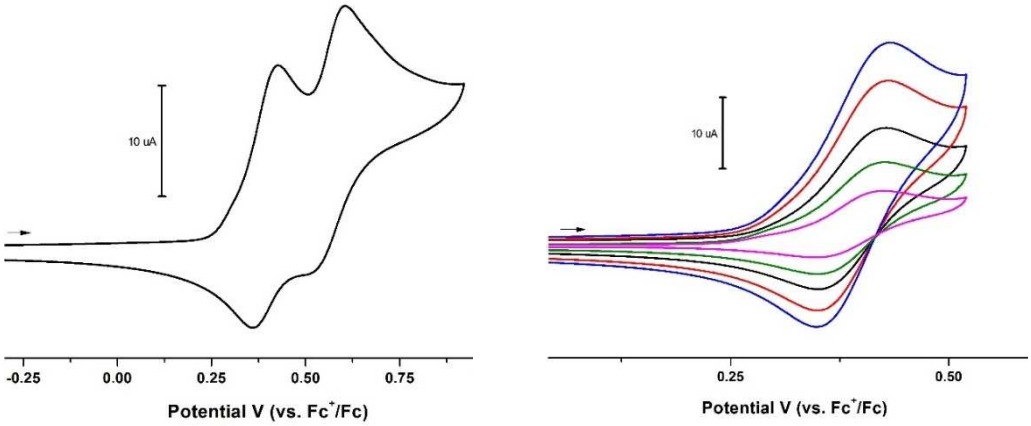


Figure 3.7.1.3: Sequential UV/vis spectra recorded during the oxidation of $Ni^{tBu/Br}L_o^{NMe}$ *at 1.66 V vs. Ag/AgCl identifying the bands formed during oxidation. 0.36 mmol solution recorded at 253 K under* N_2 *in* CH_2Cl_2 *containing 0.4 M* $[N^nBu_4][BF_4]$ *as supporting electrolyte. Inset, spectra before oxidation (black), after oxidation (red) and after re-reduction at 0.00 V vs. Ag/AgCl (blue).*

3.7.2 Cyclic Voltammetry of $M^{R}L_{o}^{NMe}$ (M = Zn, Ni, Cu; R = ^{t}Bu/Ph, ^{t}Bu/PhMe, ^{t}Bu/PhOMe)

3.7.2.1 Cyclic Voltammetry $Zn^{R}L_{o}^{NMe}$ (R = ^{t}Bu/Ph, ^{t}Bu/PhMe, ^{t}Bu/PhOMe)

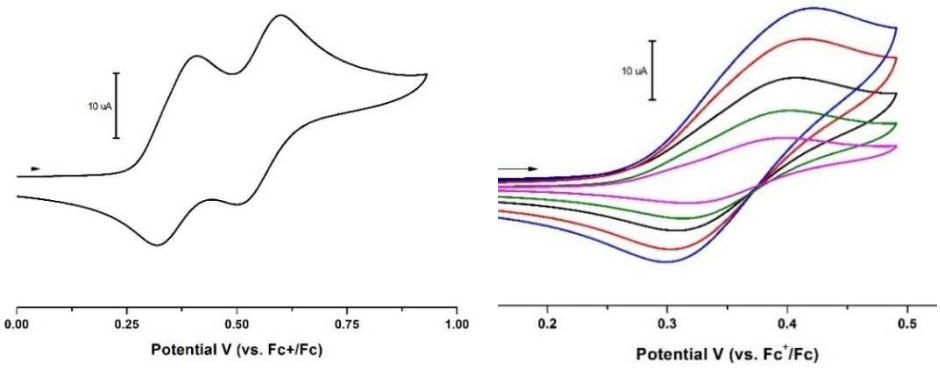
$Zn^{tBu/Ph}L_{o}^{NMe}$ exhibits a reversible oxidation process at $E_{1/2}$ = 0.39 V (*vs.* Fc^{+}/Fc), with the reversibility demonstrated *via* the application of the Nicholson equation, which was necessary owing to the closely overlapping processes that prevents the direct extraction of i_p^c and i_p^a values.[43, 44] A second oxidation process at E_p^a = 0.61 V (*vs.* Fc^{+}/Fc) is not reversible (Figure 3.7.2.1.1).



Complex	$E_{1/2}$ V (*vs.* Fc^{+}/Fc)	i_p^c µA (100 mV)	i_p^a µA (100 mV)	$\lvert i_p^c / i_p^a \rvert$ (100 mV)	$\lvert E_{pc}-E_{pa} \rvert$ mV	$\lvert E_p^c-E_p^a \rvert$ mV ($dmfc^{+}$/dmfc)
$Zn^{tBu/Ph}L_{o}^{NMe}$	0.39	-7.5	15.0	0.50	80	90

Figure 3.7.2.1.1: Two oxidation processes for $Zn^{tBu/Ph}L_{o}^{NMe}$*. at multiple scan rates (300 mV (blue), 200 mV (red), 100 mV (black), 50 mV (green), 20 mV (purple)).*

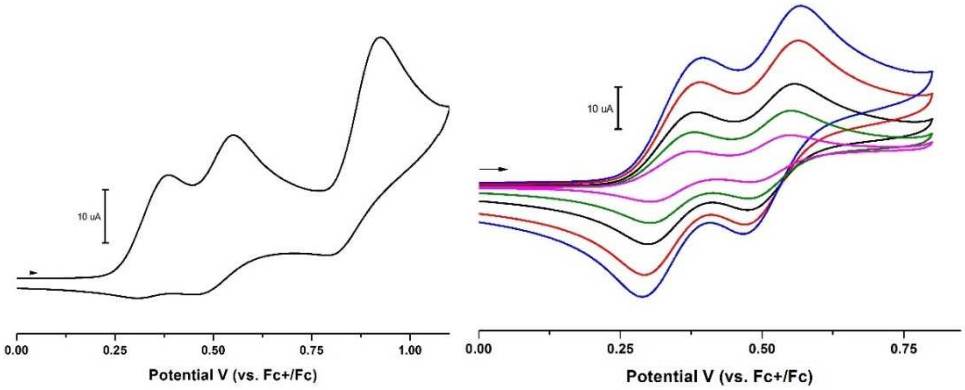
Similarly, $Zn^{tBu/PhMe}L_{o}^{NMe}$ exhibits two oxidation processes (Figure 3.7.2.1.2). The first at $E_{1/2}$ = 0.36 V (*vs.* Fc^{+}/Fc) is reversible by the application of the Nicholson equation.[43, 44] The reversibility of the second process at E_p^a = 0.61 *vs.* Fc^{+}/Fc could not be determined because of the overlap of this process with the first oxidation that precludes an accurate determination of i_p^c and i_p^a values.



Complex	$E_{1/2}$ V (*vs.* Fc^+/Fc)	i_p^c µA (100 mV)	i_p^a µA (100 mV)	$\lvert i_p^c / i_p^a \rvert$ (100 mV)	$\lvert E_{pc} - E_{pa} \rvert$ mV	$\lvert E_p^c - E_p^a \rvert$ mV ($dmfc^+/dmfc$)
$Zn^{tBu/PhMe}L_o^{NMe}$	0.36	-9.4	15.1	0.62	90	90

Figure 3.7.2.1.2: Left: Two oxidation processes for $Zn^{tBu/PhMe}L_o^{NMe}$. Right: First oxidation process of $Zn^{tBu/PhMe}L_o^{NMe}$ at multiple scan rates (300 mV (blue), 200 mV (red), 100 mV (black), 50 mV (green), 20 mV (purple)).

$Zn^{tBu/PhOMe}L_o^{NMe}$ exhibits three oxidation processes at $E_{1/2}$ = 0.34 and E_p^a = 0.55 and 0.92 V *vs.* Fc^+/Fc (Figure 3.7.2.1.3). The first process ($E_{1/2}$ = 0.34) is reversible by the Nicholson equation.[43, 44] The reversibility of the second process could not be determined and the third process is not reversible. The third process appears to be one single process in contrast to the two processes found for $Zn^{PhOMe}L_o^{NMe}$ (Section 3.3), and this conclusion is supported by square wave voltammetry (Figure 3.7.2.1.4).



Complex	$E_{1/2}$ V (*vs.* Fc^+/Fc)	i_p^c µA (100 mV)	i_p^a µA (100 mV)	$\lvert i_p^c / i_p^a \rvert$ (100 mV)	$\lvert E_{pc} - E_{pa} \rvert$ mV	$\lvert E_p^c - E_p^a \rvert$ mV ($dmfc^+/dmfc$)
$Zn^{tBu/PhOMe}L_o^{NMe}$	0.34	-15.3	17.0	0.90	80	80

Figure 3.7.2.1.3: Left: 3 oxidation processes for $Zn^{tBu/PhOMe}L_o^{NMe}$.Right: First two oxidation processes only for $Zn^{tBu/PhOMe}L_o^{NMe}$ at multiple scan rates (300 mV (blue), 200 mV (red), 100 mV (black), 50 mV (green), 20 mV (purple)).

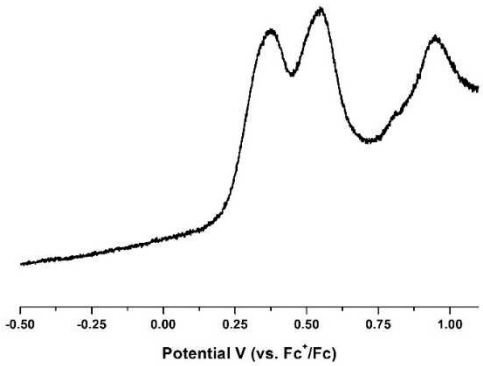
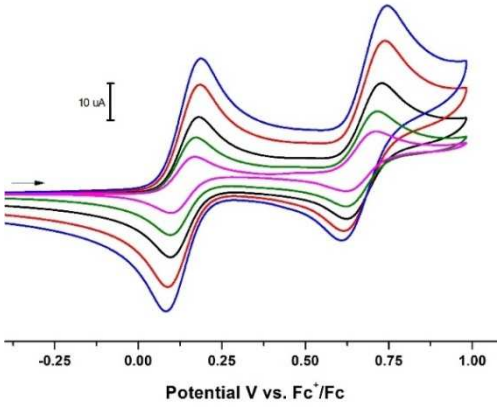


Figure 3.7.2.1.4: Square wave voltammogram of $Zn^{tBu/PhOMe}L_o^{NMe}$.

3.7.2.2 Cyclic Voltammetry of $Ni^{R}L_o^{NMe}$ (R = ^{t}Bu/Ph, ^{t}Bu/PhMe, ^{t}Bu/PhOMe)

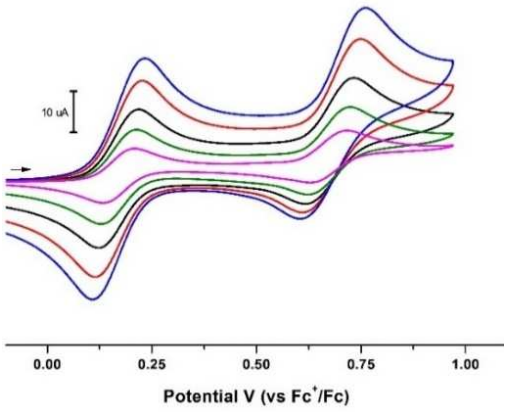
$Ni^{tBu/Ph}L_o^{NMe}$ possesses one electrochemically reversible oxidation process at $E_{1/2}$ = 0.14 V (*vs.* Fc^+/Fc), and a second process which is not reversible at E_p^a = 0.73 V (*vs.* Fc^+/Fc) (Figure 2.7.2.2.1).



Complex	**$E_{1/2}$ V (*vs.* Fc^+/Fc)**	**i_p^c μA (100 mV)**	**i_p^a μA (100 mV)**	**$\|i_p^c/ i_p^a\|$ (100 mV)**	**$\|E_p^c-E_p^a\|$ mV**	**$\|E_p^c-E_p^a\|$ mV ($dmfc^+/dmfc$)**
$Ni^{tBu/Ph}L_o^{NMe}$	0.14	-17.6	20.1	0.88	70	70

Figure 3.7.2.2.1: Two oxidation processes of $Ni^{tBu/Ph}L_o^{NMe}$ at multiple scan rates (300 mV (blue), 200 mV (red), 100 mV (black), 50 mV (green), 20 mV (purple)).

$Ni^{tBu/PhMe}L_o^{NMe}$ shows similar electrochemical behaviour with processes at $E_{1/2}$ = 0.17 V and E_p^a = 0.73 V (*vs.* Fc^+/Fc). The first process is electrochemically reversible, whilst the second oxidation process is not reversible.



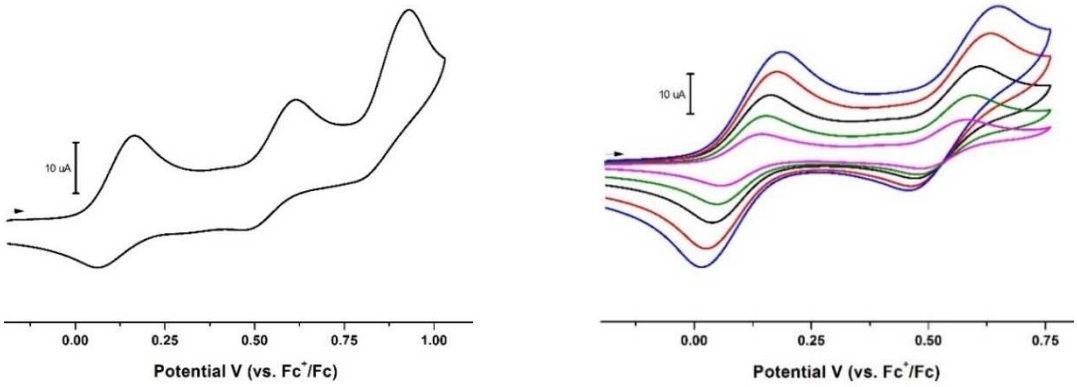
Complex	**$E_{1/2}$ V (*vs.* Fc^+/Fc)**	**i_p^c μA (100 mV)**	**i_p^a μA (100 mV)**	**$\|i_p^c/ i_p^a\|$ (100 mV)**	**$\|E_p^c-E_p^a\|$ mV**	**$\|E_p^c-E_p^a\|$ mV ($dmfc^+$/dmfc)**
$Ni^{tBu/PhMe}L_o^{NMe}$	0.17	-15.0	17.2	0.87	90	70

Figure 3.7.2.2.2: Two oxidation processes of $Ni^{tBu/PhMe}L_o^{NMe}$ at multiple scan rates (300 mV (blue), 200 mV (red), 100 mV (black), 50 mV (green), 20 mV (purple)).

$Ni^{tBu/PhOMe}L_o^{NMe}$ possesses three processes at $E_{1/2}$ = 0.10 V and E_p^a = 0.61 ad 0.93 V (*vs.* Fc^+/Fc), respectively. The first process is quasireversible; ΔE is scan rate dependant and greater than that of the internal standard ($dmfc^+$/dmfc) (Table 3.7.2.2.1) whilst the second process (E_p^a = 1.17 *vs.* Fc^+/Fc) is not reversible. The quasi-reversible nature of the first oxidation is similar to that previously reported for the *t*butyl substituted analogue $Ni^{tBu}L_o^{NMe}$.[1] $Ni^{tBu/PhOMe}L_o^{NMe}$ also exhibits a third oxidation process at more positive potential (E_p^a = 0.93 *vs.* Fc^+/Fc), which appears as a single feature as found for $Zn^{tBu/PhOMe}L_o^{NMe}$ (Section 3.7.2.1).

Scan rate	$Ni^{tBu/PhOMe}L_o^{NMe}$ 1st process ΔE	dmfc+/dmfc ΔE
20 mV	85	77
50 mV	107	80
100 mV	124	83
200 mV	153	87
300 mV	172	89

Table 3.7.2.2.1: Variation of ΔE with scan rate for first oxidation process of $Ni^{tBu/PhOMe}L_o^{NMe}$ compared to internal standard ($dmfc^+$/dmfc).

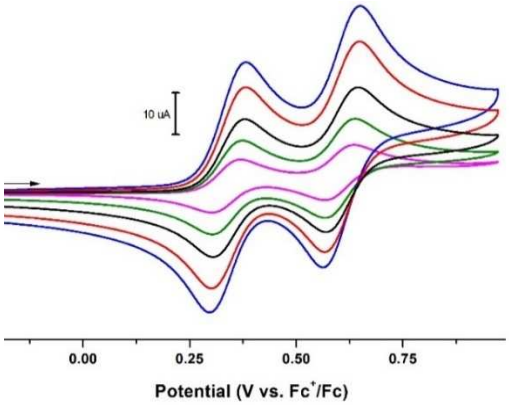


Complex	$E_{1/2}$ V (vs Fc^+/Fc)	i_p^c µA (100 mV)	i_p^a µA (100 mV)	$\lvert i_p^c / i_p^a \rvert$ (100 mV)	$\lvert E_p^c - E_p^a \rvert$ (100 mV) mV	$\lvert E_p^c - E_p^a \rvert$ mV ($dmfc^+/dmfc$)
$Ni^{tBu/PhOMe}L_o^{NMe}$	0.10	13.7	15.1	0.91	120	70

Figure 3.7.2.2.3: Left - three oxidation processes for $Ni^{tBu/PhOMe}L_o^{NMe}$; Right – First two oxidation processes of $Ni^{tBu/PhOMe}L_o^{NMe}$ at multiple scan rates (300 mV (blue), 200 mV (red), 100 mV (black), 50 mV (green), 20 mV (purple)).

3.7.2.3 Cyclic Voltammetry of $Cu^RL_o^{NMe}$ (R = ^{t}Bu/Ph, ^{t}Bu/PhMe, ^{t}Bu/PhOMe)

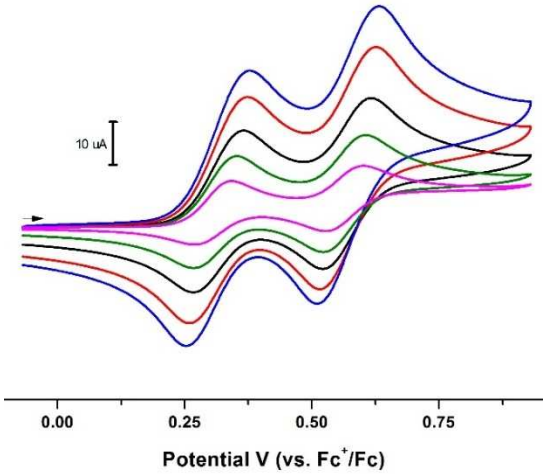
$Cu^{tBu/Ph}L_o^{NMe}$ exhibits two reversible oxidation processes at $E_{1/2}$ = 0.34 V and 0.61 V (*vs.* Fc^+/Fc) (Figure 3.7.2.3.1).



Complex	$E_{1/2}$ V (vs Fc^+/Fc)	i_p^c µA (100 mV)	i_p^a µA (100 mV)	$\lvert i_p^c / i_p^a \rvert$ (100 mV)	$\lvert E_p^c - E_p^a \rvert$ mV	$\lvert E_p^c - E_p^a \rvert$ mV (Fc^+/Fc)
$Cu^{tBu/Ph}L_o^{NMe}$	0.34	-14.5	16.5	0.88	70	80
	0.61	-16.0	17.2	0.93	70	

Figure 3.7.2.3.1: Two oxidation processes of $Cu^{tBu/Ph}L_o^{NMe}$ at multiple scan rates (300 mV (blue), 200 mV (red), 100 mV (black), 50 mV (green), 20 mV (purple)).

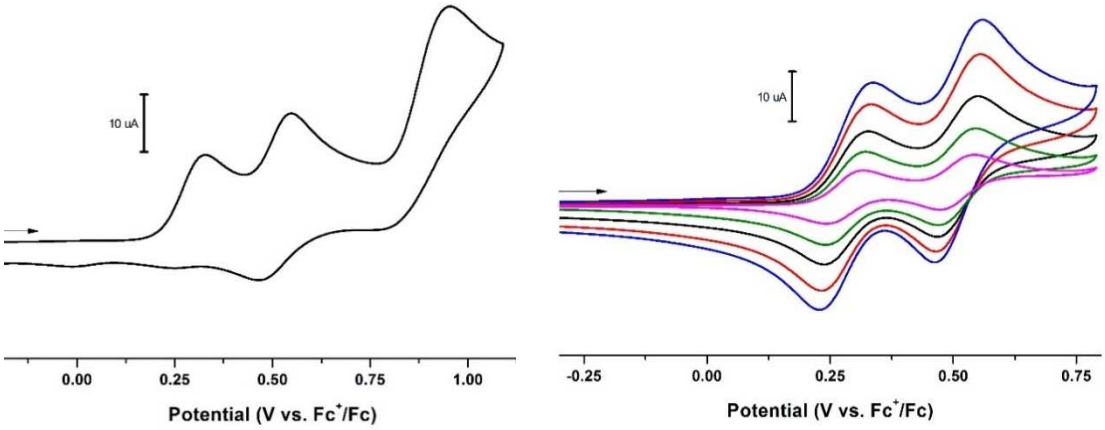
Cu$^{t\text{Bu/PhMe}}$L$_o^{\text{NMe}}$ also exhibits two reversible oxidation processes at less positive reduction potentials than Cu$^{t\text{Bu/Ph}}$L$_o^{\text{NMe}}$ ($E_{1/2}$ = 0.31 and 0.57 V *vs.* Fc$^+$/Fc, Figure 3.7.2.3.2).



Complex	**$E_{1/2}$ V (vs Fc$^+$/Fc)**	**i_p^c μA (100 mV)**	**i_p^a μA (100 mV)**	**$\lvert i_p^c / i_p^a \rvert$ (100 mV)**	**$\lvert E_p^c - E_p^a \rvert$ mV**	**$\lvert E_p^c - E_p^a \rvert$ mV (Fc$^+$/Fc)**
Cu$^{t\text{Bu/PhMe}}$L$_o^{\text{NMe}}$	0.28	-14.4	20.5	0.70	90	90
	0.57	-16.6	14.4	1.15	90	

Figure 3.7.2.3.2: Two oxidation processes of Cu$^{t\text{Bu/PhMe}}$L$_o^{\text{NMe}}$ *at multiple scan rates (300 mV (blue), 200 mV (red), 100 mV (black), 50 mV (green), 20 mV (purple)).*

Cu$^{t\text{Bu/PhOMe}}$L$_o^{\text{NMe}}$ exhibits two oxidation processes at a less positive potentials than those of Cu$^{t\text{Bu/PhMe}}$L$_o^{\text{NMe}}$ and Cu$^{t\text{Bu/Ph}}$L$_o^{\text{NMe}}$. As for M$^{t\text{Bu/PhOMe}}$L$_o^{\text{NMe}}$ (M = Zn, Ni), Cu$^{t\text{Bu/PhOMe}}$L$_o^{\text{NMe}}$ possesses an additional oxidation process at E_p^a = 0.95 V *vs.* (*vs.* Fc$^+$/Fc) (Figure 3.7.2.3.3). The Nicholson equation[43, 44] demonstrates that the first process at $E_{1/2}$ = 0.28 V (*vs.* Fc$^+$/Fc) is electrochemically reversible; the reversibility of the second process at E_p^a = 0.55 V (*vs.* Fc$^+$/Fc) is difficult to determine owing to the overlapping potentials and the third process at E_p^a = 0.95 V (*vs.* Fc$^+$/Fc) is not electrochemically reversible. The third process at E_p^a = 0.95 V (*vs.* Fc$^+$/Fc) appears as a single feature as observed for Zn$^{t\text{Bu/PhOMe}}$L$_o^{\text{NMe}}$ and Ni$^{t\text{Bu/PhOMe}}$L$_o^{\text{NMe}}$.



Complex	**$E_{1/2}$ V (vs Fc^+/Fc)**	**i_p^c μA (100 mV)**	**i_p^a μA (100 mV)**	**$\|i_p^c/ i_p^a\|$ (100 mV)**	**$\|E_p^c-E_p^a\|$ mV**	**$\|E_p^c-E_p^a\|$ mV (Fc^+/Fc)**
$Cu^{tBu/PhOMe}L_o^{NMe}$	0.28	-12.6	13.8	0.91	90	90

Figure 3.7.2.3.3: Two oxidation processes of $Cu^{tBu/PhOMe}L_o^{NMe}$ *at multiple scan rates (300 mV (blue), 200 mV (red), 100 mV (black), 50 mV (green), 20 mV (purple)).*

3.7.2.4 Discussion

For $M^RL_o^{NMe}$ (M = Zn, Cu; R = ^{t}Bu/Ph, ^{t}Bu/PhMe, ^{t}Bu/PhOMe) there is a decrease in potential for the first oxidation process with R = ^{t}Bu/Ph>^{t}Bu/PhMe>^{t}Bu/PhOMe (0.39 → 0.36 → 0.34 V and 0.34 → 0.32 → 0.28 V *vs.* Fc^+/Fc for $Zn^RL_o^{NMe}$ and $Cu^RL_o^{NMe}$ respectively) (Figure 3.7.2.4.1). These changes are significantly less than the changes observed for $M^RL_o^{NMe}$ (R = Ph, PhMe, PhOMe, Section 3.3) where the decreases in potential for the first oxidation process as R is varied from Ph to PhMe to PhOMe is greater (0.43 > 0.35 > 0.27 V and 0.37 > 0.30 > 0.21 V *vs.* Fc^+/Fc for $Zn^RL_o^{NMe}$ and $Cu^RL_o^{NMe}$, respectively). For $Ni^RL_o^{NMe}$ (R = ^{t}Bu/Ph, ^{t}Bu/PhMe, ^{t}Bu/PhOMe) there is no consistent trend in the potential of the first oxidation, consistent with a metal-based oxidation process that is less dependent on the nature of the ligand substituents.

There is little change in the potential of the second oxidation process for $M^{tBu/Ph}L_o^{NMe}$ and $M^{tBu/PhMe}L_o^{NMe}$ (E_p^a = 0.61, 0.73 and 0.64 V and 0.61, 0.73 and 0.61 V *vs.* Fc^+/Fc for M = Zn, Ni and Cu and $M^{tBu/Ph}L_o^{NMe}$ and $M^{tBu/PhMe}L_o^{NMe}$, respectively) whereas the second oxidation process for $M^{tBu/PhOMe}L_o^{NMe}$ occurs at lower potential (E_p^a = 0.55, 0.61 and 0.55 V *vs.* Fc^+/Fc for M = Zn, Ni and Cu, respectively). This behaviour is markedly different to the trends found for

$M^{R}L_{o}^{NMe}$ (M = Zn, Ni, Cu; R = Ph, PhMe, PhOMe), where a consistent, approximately equal reduction in potential of the second oxidation process is found as the substituents varied from Ph>PhMe>PhOMe (Section 3.3).

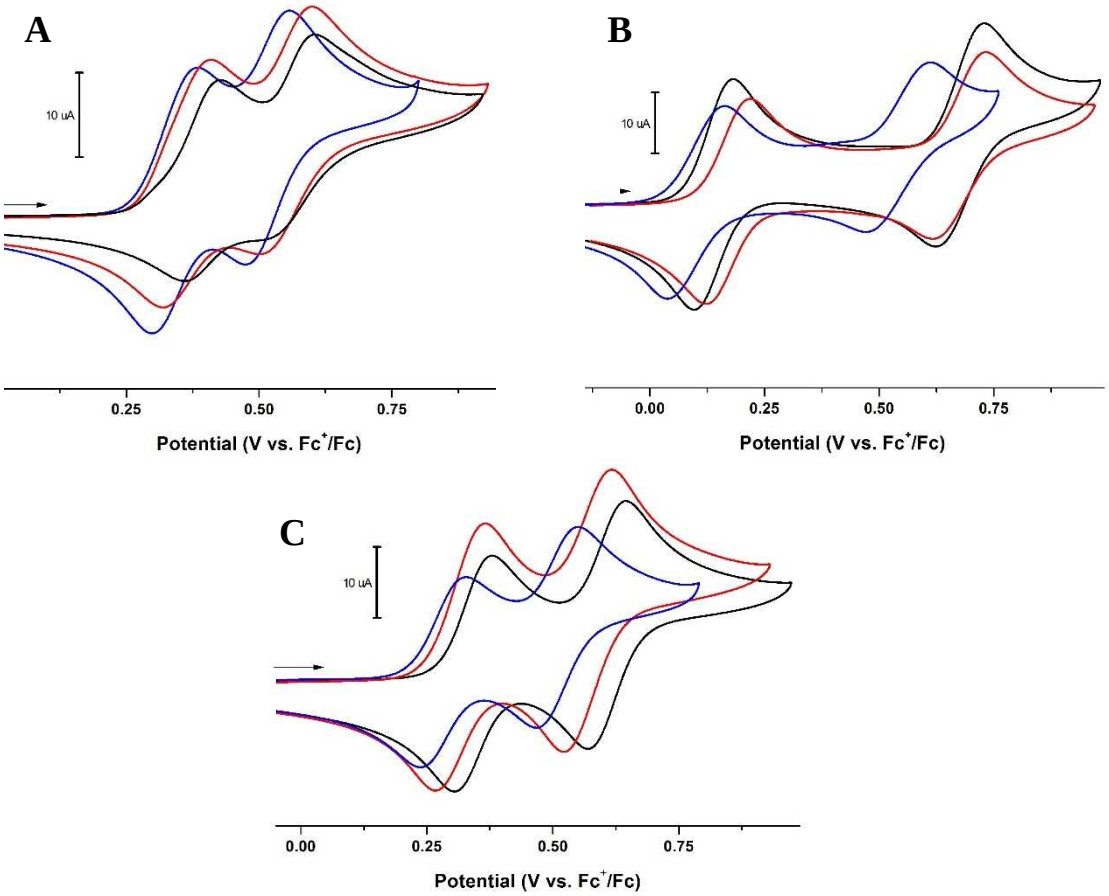


*Figure 2.7.2.4.1: Cyclic voltammograms of $M^{R}L_{o}^{NMe}$ (R = ^{t}Bu/Ph (black), ^{t}Bu/PhMe (red), ^{t}Bu/PhOMe (blue)); **A** - M = Zn; **B** – M = Ni; **C** – M = Cu.*

The irreversible electrochemical behaviours of $Zn^{tBu/R}L_{o}^{NMe}$ precluded their study by UV/vis spectroelectrochemistry and by controlled potential electrolysis. We attempted UV/vis spectroelectrochemical and controlled potential electrolytic studies of $M^{tBu/R}L_{o}^{NMe}$ (M = Ni, Cu) in order to characterise the oxidation products.

3.7.3 UV/vis and EPR spectroscopy of the Oxidation Products of $Ni^{R}L_{o}^{NMe}$ (R = ^{t}Bu/Ph, ^{t}Bu/PhMe, ^{t}Bu/PhOMe)

3.7.3.1 Spectroelectrochemistry of $Ni^{R}L_{o}^{NMe}$ (R = ^{t}Bu/Ph, ^{t}Bu/PhMe, ^{t}Bu/PhOMe)

The first oxidation process for $Ni^{tBu/Ph}L_{o}^{NMe}$ and $Ni^{tBu/PhMe}L_{o}^{NMe}$ is electrochemically reversible by cyclic voltammetry ($E_{1/2}$ = 0.14 and 0.17 V *vs.* Fc^{+}/Fc respectively), whilst the second process at (E_{p}^{a} = 0.73 and 0.73 V *vs.* Fc^{+}/Fc respectively) is not electrochemically reversible. $Ni^{tBu/PhOMe}L_{o}^{NMe}$ possesses one quasi-reversible process at $E_{1/2}$ = 0.10 V *vs.* Fc^{+}/Fc, together with two further processes at E_{p}^{a} = 0.61 and 0.93 V *vs.* Fc^{+}/Fc. These processes were investigated by UV/vis spectroelectrochemistry.

3.7.3.1.1 Spectroelectrochemistry of $Ni^{tBu/Ph}L_{o}^{NMe}$

The UV/vis spectrum of $Ni^{tBu/Ph}L_{o}^{NMe}$ displays similar features to those of $Ni^{R}L_{o}^{NMe}$ (R = Ph, PhMe and PhOMe, Section 3.5), with an intense absorption at 236 nm (ε = 60,500 mol^{-1} dm^{3} cm^{-1}), shoulders around 268 and 297 nm (ε = 28,900 and 11,600 mol^{-1} dm^{3} cm^{-1}) and an intense absorption band at 387 nm (ε = 14,000 mol^{-1} dm^{3} cm^{-1}). On oxidation at 1.10 V *vs.* Ag/AgCl similar changes in the UV/vis spectrum to those observed for $Ni^{Ph}L_{o}^{NMe}$ (Section 3.5) are found, with a reduction in intensity of the high energy bands to give a shoulder which tends towards 230 nm (ε = 46,500 mol^{-1} dm^{3} cm^{-1} at 230 nm) and additional less intense absorptions at 272 and 300 nm (ε = 24,600 and 25,000 mol^{-1} dm^{3} cm^{-1}). There is also a broadening of the band at 387 nm (ε = 13,300 mol^{-1} dm^{3} cm^{-1}) and an additional shoulder develops at *ca.* 470 nm (ε = 6,000 mol^{-1} dm^{3} cm^{-1}). This oxidation also proceeds *via* three isobestic points (271, 379 and 407 nm) indicating a direct transformation with no observable intermediates (Figure 3.7.3.1.1.1). On re-reduction at 0.00 V (*vs.* Ag/AgCl) the original spectral profile of $Ni^{tBu/Ph}L_{o}^{NMe}$ is obtained, indicating that this oxidation process is chemically reversible over the timescale of the experiment (Figure 3.7.3.1.1.1 inset).

Subsequent oxidation at 1.60 V *vs.* Ag/AgCl is accompanied by the loss of the absorption band at 300 nm and a reduction in intensity of the band at 387 nm (ε = 8,500 mol^{-1} dm^{3} cm^{-1}). Further reduction in the intensity of the high energy band at

234 nm (ε = 41,000 mol^{-1} dm^3 cm^{-1}) is accompanied by the growth of a new band at 485 nm (ε = 4,160 mol^{-1} dm^3 cm^{-1}) (Figure 3.8.3.1.1.2). On re-reduction some decomposition is observed such that the original spectrum of $Ni^{tBu/Ph}L_o^{NMe}$ is not regenerated (Figure 3.7.3.1.1.2 inset).

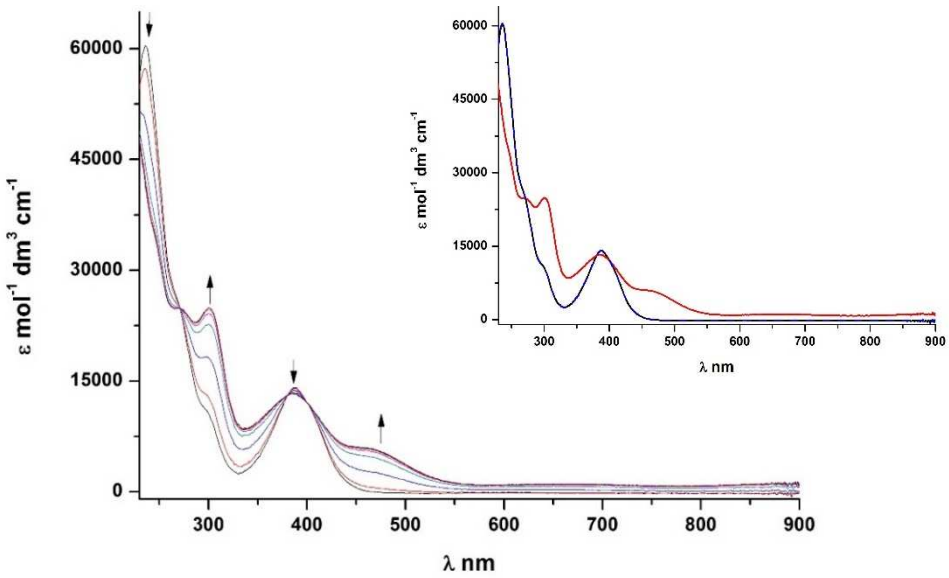


Figure 3.7.3.1.1.1: Sequential UV/vis spectra recorded during the oxidation of $Ni^{tBu/Ph}L_o^{NMe}$ 1.10 V vs. Ag/AgCl identifying the bands formed during oxidation. 0.49 mmol solution recorded at 253 K under N_2 in CH_2Cl_2 containing 0.4 M $[N^nBu_4][BF_4]$ as supporting electrolyte. Inset, spectra before oxidation (black), after oxidation (red) and after re-reduction at 0.00 V vs. Ag/AgCl (blue).

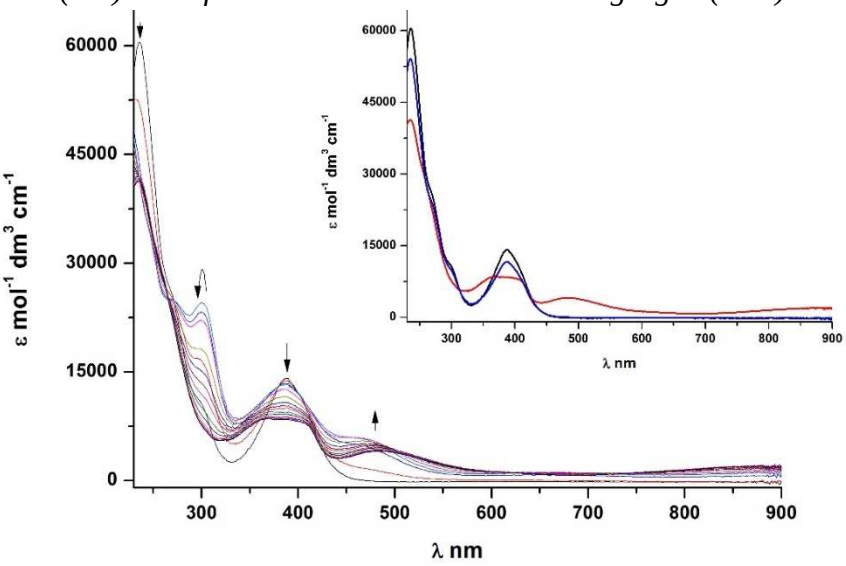


Figure 3.7.3.1.1.2: Sequential UV/vis spectra recorded during the two electron oxidation of $Ni^{tBu/Ph}L_o^{NMe}$ at 1.60 V vs. Ag/AgCl identifying the bands formed during oxidation. 0.49 mmol solution recorded at 253 K under N_2 in CH_2Cl_2 containing 0.4 M $[N^nBu_4][BF_4]$ as supporting electrolyte. Inset, spectra before oxidation (black), after oxidation (red) and after re-reduction at 0.00 V vs. Ag/AgCl (blue).

3.7.3.1.2 Spectroelectrochemistry of Ni$^{tBu/PhMe}L_o^{NMe}$

The UV/vis spectrum of Ni$^{tBu/PhMe}L_o^{NMe}$ exhibits a similar spectrum to that of Ni$^{tBu/Ph}L_o^{NMe}$ with intense absorptions at 237 and 388 nm (ε = 49,300 and 11,300 mol^{-1} dm^3 cm^{-1}) and shoulders at *ca.* 270 and 300 nm (ε = 20,500 and 9,700 mol^{-1} dm^3 cm^{-1}). On oxidation at 1.00 V *vs.* Ag/AgCl there is a reduction in intensity of the high energy absorptions, which is accompanied by the formation of a distinct band at 303 nm (ε = 20,000 mol^{-1} dm^3 cm^{-1}) and a broadening of the absorption at 388 nm (ε = 10,700 mol^{-1} dm^3 cm^{-1}) with a shoulder at *ca.* 470 nm (ε = 4,140 mol^{-1} dm^3 cm^{-1}). The oxidation process proceeds *via* three isobestic points, suggesting no intermediate species are involved (Figure 3.7.3.1.2.1). Re-reduction at 0.00 V *vs.* Ag/AgCl regenerates the original spectral profile of Ni$^{tBu/PhMe}L_o^{NMe}$ that indicates this first oxidation process is chemically reversible (Figure 3.7.3.1.2.1 inset).

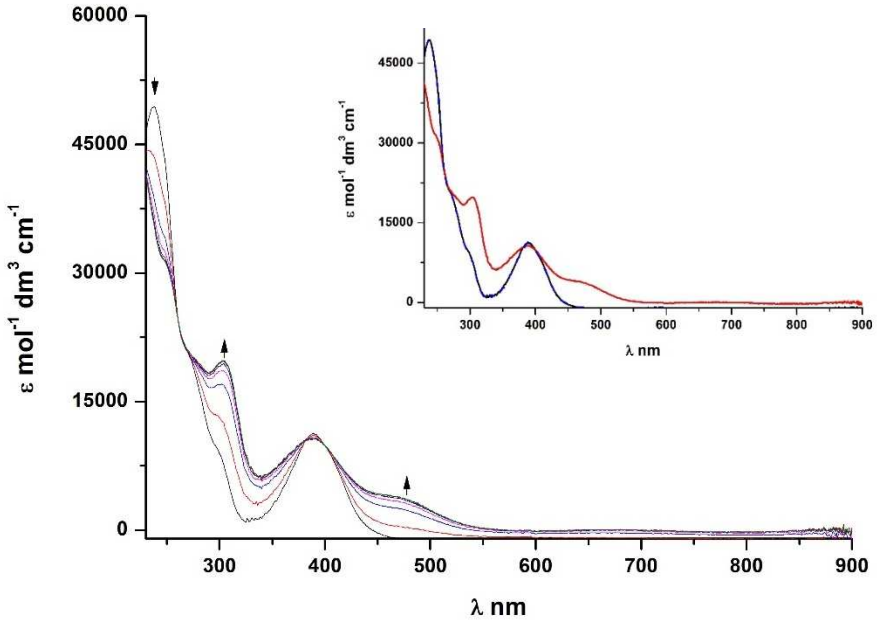


Figure 3.7.3.1.2.1: Sequential UV/vis spectra recorded during the oxidation of Ni$^{tBu/PhMe}L_o^{NMe}$ at 1.00 V vs. Ag/AgCl identifying the bands formed during oxidation. 0.28 mmol solution recorded at 253 K under N_2 in CH_2Cl_2 containing 0.4 M [N^nBu_4][BF_4] as supporting electrolyte. Inset, spectra before oxidation (black), after oxidation (red) and after re-reduction at 0.00 V vs. Ag/AgCl (blue).

The second oxidation process for Ni$^{tBu/PhMe}L_o^{NMe}$ was also investigated by UV/vis spectroelectrochemistry at 1.50 V *vs.* Ag/AgCl. Similar spectral changes are observed to those found for the analogous oxidation of Ni$^{tBu/Ph}L_o^{NMe}$. The UV/vis spectrum possesses less intense absorptions at 239 nm and *ca.* 390 nm (ε = 31,500

and 6,520 mol^{-1} dm^3 cm^{-1}), a broad absorption at 508 nm (ε = 1,950 mol^{-1} dm^3 cm^{-1}) and a broad lower energy band at *ca.* 880 nm (ε = 768 mol^{-1} dm^3 cm^{-1}). On re-reduction at 0.00 V *vs.* Ag/AgCl some decomposition was observed with the UV/vis spectrum of the original species, $Ni^{tBu/PhMe}L_o^{NMe}$, not being fully regenerated (Figure 3.7.3.1.2.2 inset).

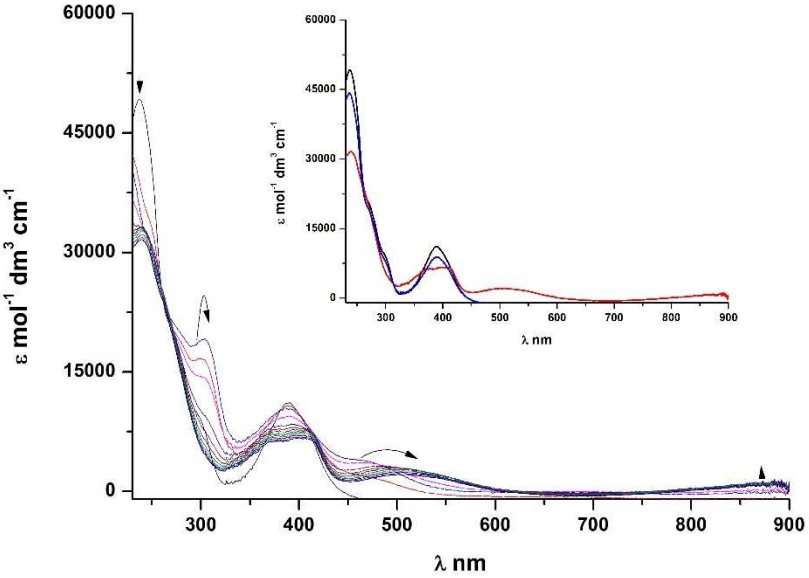


Figure 3.7.3.1.2.2: Sequential UV/vis spectra recorded during the oxidation of $Ni^{tBu/PhMe}L_o^{NMe}$ at 1.50 V vs. Ag/AgCl identifying the bands formed during oxidation. 0.28 mmol solution recorded at 253 K under N_2 in CH_2Cl_2 containing 0.4 M $[N^nBu_4][BF_4]$ as supporting electrolyte. Inset, spectra before oxidation (black), after oxidation (red) and after re-reduction at 0.00 V vs. Ag/AgCl (blue).

3.7.3.1.3 Spectroelectrochemistry of $Ni^{tBu/PhOMe}L_o^{NMe}$

$Ni^{tBu/PhOMe}L_o^{NMe}$ exhibits a similar UV/vis spectrum to those of $Ni^{tBu/PhMe}L_o^{NMe}$ and $Ni^{tBu/Ph}L_o^{NMe}$ with intense absorption bands at 247 and 388 nm (ε = 51,300 and 14,100 mol^{-1} dm^3 cm^{-1}) with an additional band at 230 nm (ε = 56,500 mol^{-1} dm^3 cm^{-1} at 230 nm) and additional shoulders around 270 and 300 nm (ε = 24,500 and 16,400 mol^{-1} dm^3 cm^{-1}). Oxidation at 0.95 V *vs.* Ag/AgCl is accompanied by a decrease in intensity of the higher energy bands with the development of a band at 309 nm (ε = 22,000 mol^{-1} dm^3 cm^{-1}), a broadening of the band at 388 nm (ε = 13,100 mol^{-1} dm^3 cm^{-1}) and the formation of a shoulder at 480 nm (ε = 5,300 mol^{-1} dm^3 cm^{-1}). On re-reduction at 0.00 V (*vs.* Ag/AgCl) the original spectral profile of $Ni^{tBu/PhOMe}L_o^{NMe}$ was generated demonstrating the chemical reversibility of this first oxidation process.

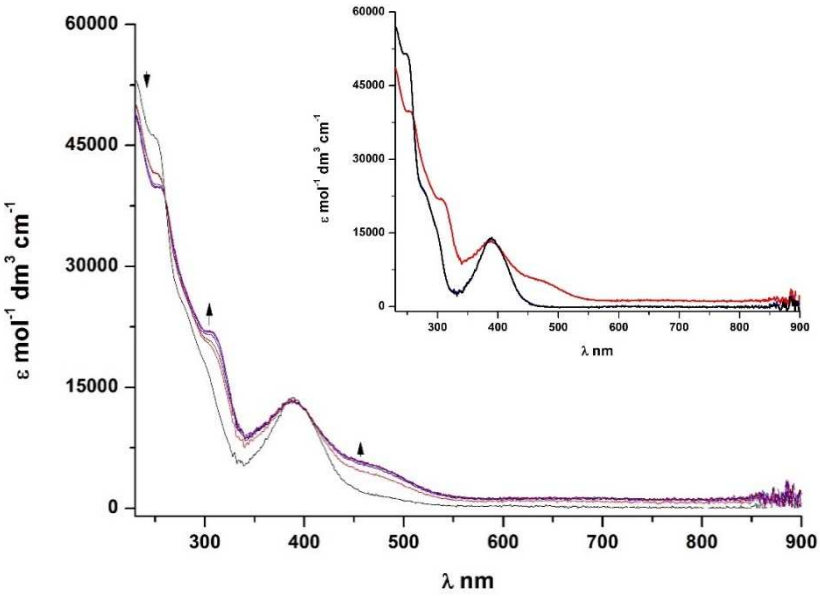


Figure 3.7.3.1.3.1: Sequential UV/vis spectra recorded during the oxidation of $Ni^{tBu/PhOMe}L_o^{NMe}$ at 0.95 V vs. Ag/AgCl identifying the bands formed during oxidation. 0.26 mmol solution recorded at 253 K under N_2 in CH_2Cl_2 containing 0.4 M $[N^nBu_4][BF_4]$ as supporting electrolyte. Inset, spectra before oxidation (black), after oxidation (red) and after re-reduction at 0.00 V vs. Ag/AgCl (blue).

The second oxidation of $Ni^{tBu/PhOMe}L_o^{NMe}$ was also investigated by UV/vis spectroelectrochemistry at 1.32 V *vs.* Ag/AgCl and demonstrated very similar spectral changes to those observed on the two electron oxidation of $Ni^{tBu/PhMe}L_o^{NMe}$ and $Ni^{tBu/Ph}L_o^{NMe}$. Oxidation is accompanied by a further reduction in the intensity of high energy bands and the appearance of a broad band around 560 nm (ε = 4,140 mol^{-1} dm^3 cm^{-1}). There is a loss of intensity for the band at 388 nm and separate bands develop at 378 and 417 nm (ε = 10,100 and 9,600 mol^{-1} dm^3 cm^{-1}). On re-reduction at 0.00 V *vs.* Ag/AgCl the original spectral profile of $Ni^{tBu/PhOMe}L_o^{NMe}$ is not obtained; this demonstrates that the second oxidation process of $Ni^{tBu/PhOMe}L_o^{NMe}$ is not chemically reversible.

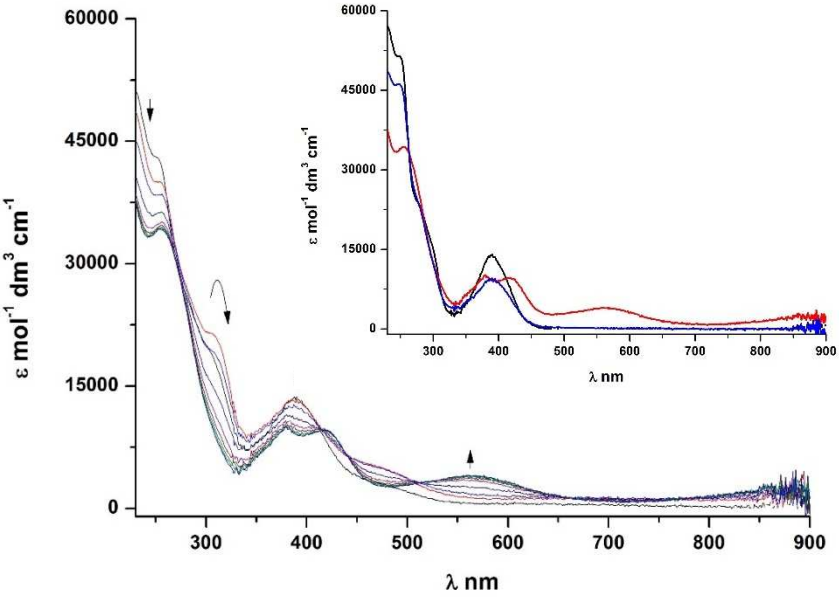


Figure 3.7.3.1.3.2: Sequential UV/vis spectra recorded during the oxidation of $Ni^{tBu/PhOMe}L_o^{NMe}$ at 1.32 V vs. Ag/AgCl identifying the bands formed during oxidation. 0.26 mmol solution recorded at 253 K under N_2 in CH_2Cl_2 containing 0.4 M $[N^nBu_4][BF_4]$ as supporting electrolyte. Inset, spectra before oxidation (black), after oxidation (red) and after re-reduction at 0.00 V vs. Ag/AgCl (blue).

3.7.3.2 Controlled Potential Electrolysis and EPR Spectroscopy of the Oxidation Products of $Ni^{tBu/Ph}L_o^{NMe}$

$Ni^{tBu/Ph}L_O^{NMe}$ was studied by controlled potential electrolysis and by EPR spectroscopy as a prototypical example of $Ni^RL_O^{NMe}$ (R = ^{t}Bu/Ph, ^{t}Bu/PhMe, ^{t}Bu/PhOMe). Exhaustive controlled potential electrolysis of $Ni^{tBu/Ph}L_O^{NMe}$ at a potential of 0.75 V (*vs.* Fc^+/Fc) resulted in a charge equivalent to in excess of two electrons being removed (Figure 3.7.3.2.1 Left). Cyclic voltammetry following the electrolysis of $Ni^{tBu/Ph}L_O^{NMe}$ showed small changes in the cyclic voltammogram indicating some decomposition of $[Ni^{tBu/Ph}L_O^{NMe}]^{2+}$ (Figure 3.7.3.2.1 Right). Further exhaustive electrolysis at a potential of 1.05 V (*vs.* Fc^+/Fc) resulted in a charge equivalent to a further three electrons being removed from the system (Figure 3.7.3.3.5.7 Left). Cyclic voltammetry following this electrolysis showed complete decomposition with no oxidation processes observed (Figure 3.7.3.2.2 Right).

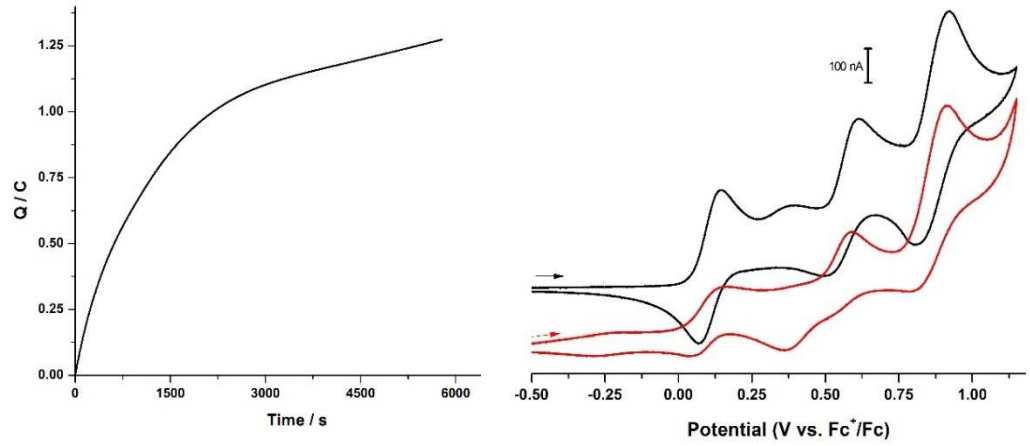


Figure 3.7.3.2.1: Left: Controlled potential electrolysis of $Ni^{tBu/PhOMe}L_O^{NMe}$ at 0.75 V vs. Fc^+/Fc, 1 mmol solution in CH_2Cl_2 containing 0.4 M $[N^nBu_4][BF_4]$ as supporting electrolyte recorded at 253 K under Ar. Theoretical Q for a two electron process = 0.95 C; Right: Cyclic voltammograms before oxidation (black) and after oxidation (red), recorded at 100 mV, 1 mmol solution in CH_2Cl_2 containing 0.4 M $[N^nBu_4][BF_4]$ as supporting electrolyte.

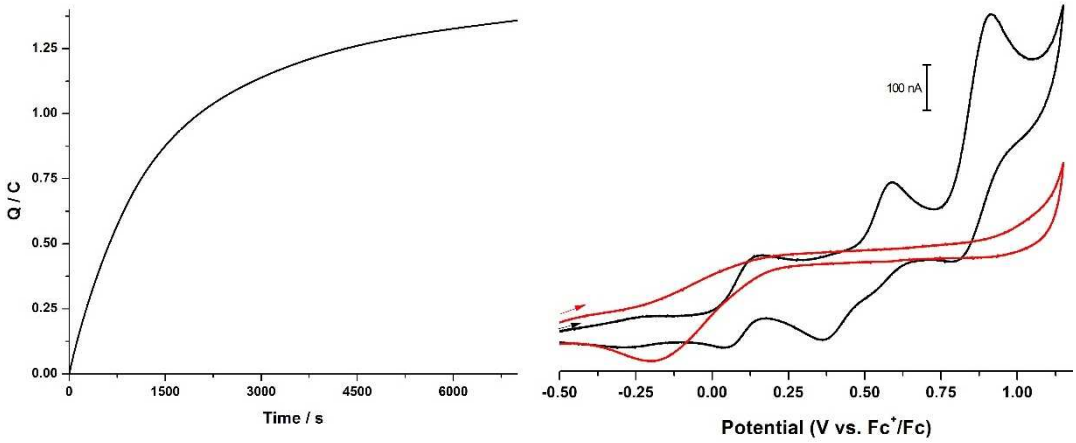


Figure 3.7.3.2.2: Left: Controlled potential electrolysis of $[Ni^{tBu/PhOMe}L_O^{NMe}]^{2+}$ at 1.05 V vs. Fc^+/Fc, 1 mmol solution in CH_2Cl_2 containing 0.4 M $[N^nBu_4][BF_4]$ as supporting electrolyte recorded at 253 K under Ar. Theoretical Q for a three electron process = 1.42 C; Right: Cyclic voltammograms before oxidation (black) and after oxidation (red), recorded at 100 mV, 1 mmol solution in CH_2Cl_2 containing 0.4 M $[N^nBu_4][BF_4]$ as supporting electrolyte.

Further investigations into the nature of the oxidised species following controlled potential electrolysis were undertaken using EPR spectroscopy in order to investigate the oxidation products of $Ni^{tBu/Ph}L_o^{NMe}$. Controlled potential electrolysis of a fresh solution of $Ni^{tBu/Ph}L_o^{NMe}$ at 0.24 V *vs.* Fc^+/Fc until a charge equivalent to one electron had been removed resulted in the generation of a khaki brown solution of $[Ni^{tBu/Ph}L_o^{NMe}]^+$ that was examined by EPR spectroscopy at 77 K (Figure 3.7.3.2.3). The EPR spectrum possesses features that are similar to those of

$Ni^{Ph}L_o^{NMe}$, $Ni^{PhMe}L_o^{NMe}$, and $Ni^{PhOMe}L_o^{NMe}$ together with additional features at g = 1.912, 2.114, 2.217 and 2.364; similar additional features have been reported for $Ni^{tBu}L_o^{NMe}$.[1] The frozen solution EPR spectrum of $[Ni^{tBu/Ph}L_o^{NMe}]^+$could not be fully simulated as a single species, however the most prominent features could be simulated (Figure 3.7.3.2.1) with spin Hamiltonian parameters g_{11} = 2.267, g_{22} = 2.163, g_{33} = 2.032, a_{33} = 22 G that are similar to those for $Ni^{tBu}L_o^{NMe}$ and $Ni^{R}L_o^{NMe}$ (R = Ph, PhMe, PhOMe) (Section 3.5.2).[1]

The average g-value (g_{av} = 2.15) for $[Ni^{tBu/Ph}L_o^{NMe}]^+$ is identical to that found for $[Ni^{tBu/Ph}L_O^{NMe}]^+$, $[Ni^{tBu/Ph}L_O^{NMe}]^+$ and $[Ni^{tBu/Ph}L_O^{NMe}]^+$ and is consistent with a small phenoxyl radical contribution to the SOMO of *ca.* 17%.[31, 34]

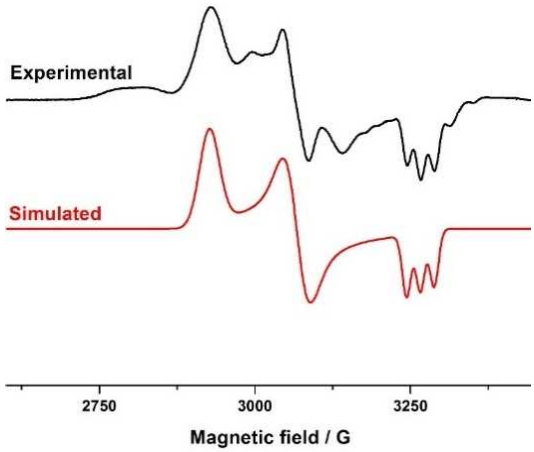


Figure 3.7.3.2.3: (Black) X-band CW EPR spectra of electrochemically generated $[Ni^{tBu/Ph}L_O^{NMe}]^+$ in CH_2Cl_2 containing 0.4 M $[N^nBu_4][BF_4]$ as supporting electrolyte as a frozen solution at 77 K, (Red) Simulated spectra – spin Hamiltonian parameters: g_{11} = 2.267, g_{22} = 2.163, g_{33} = 2.032, a_{33} = 22 G, Gaussian linewidths W_{11} = 32 G, W_{22} = 35 G, W_{33} = 14 G.

3.7.3.2.1 Discussion

$Ni^{tBu/Ph}L_o^{NMe}$, $Ni^{tBu/PhMe}L_o^{NMe}$, and $Ni^{tBu/PhOMe}L_o^{NMe}$ possess similar UV/vis spectra which undergo similar changes on one-electron oxidation (Table 3.7.3.2.1.1).

Complex	λ_{max} (nm)	ε (mol^{-1} dm^3 cm^{-1})	Isobestic point (nm)
$Ni^{tBu/Ph}L_O^{NMe}$	236, 268(sh), 297(sh), 387	60,500, 28,900, 11,600, 14,000	
$[Ni^{tBu/Ph}L_O^{NMe}]^+$	230, 272, 287, 300, 385, 470(sh)	46,500, 24,600, 13,300, 25,000, 13,300, 6,000	271, 379, 407
$[Ni^{tBu/Ph}L_O^{NMe}]^{2+}$	234, 387, 485	41,000, 8,500, 4,160	
$Ni^{tBu/PhMe}L_O^{NMe}$	237, 270(sh), 300(sh), 388	49,300 20,500, 9,700 11,300	
$[Ni^{tBu/PhMe}L_O^{NMe}]^+$	230, 303, 388, 470, 468(sh)	41,200, 20,000, 10,700, 4,140, 3,850	261, 383, 401
$[Ni^{tBu/PhMe}L_O^{NMe}]^{2+}$	239, 390, 508	31,500 6,520, 1,950	
$Ni^{tBu/PhOMe}L_O^{NMe}$	230, 247, 270(sh), 300(sh), 388	56,500, 51,300, 24,500, 16,400, 14,100	
$[Ni^{tBu/PhOMe}L_O^{NMe}]^+$	230, 256, 309, 388, 480(sh)	48,500, 39,900, 22,000, 13,100, 5,300	260, 380, 404
$[Ni^{tBu/PhOMe}L_O^{NMe}]^{2+}$	230, 256, 378, 417, 560	37,800, 34,200, 10,100, 9,600, 4,140	

Table 3.7.3.3.1: Summary of UV/vis spectra of $Ni^RL_o^{NMe}$, $[Ni^RL_o^{NMe}]^+$, $[Ni^RL_o^{NMe}]^{2+}$, (R = ^{t}Bu/Ph, ^{t}Bu/PhMe, ^{t}Bu/PhOMe).

The first oxidation of each complex is accompanied by a decrease in the intensity of high energy absorption bands and a broadening of the absorption at *ca.* 400 nm. This first process is chemically reversible. EPR spectroscopy on a frozen solution of $[Ni^{tBu/Ph}L_o^{NMe}]^+$ reveals a metal component in the SOMO of $[Ni^{tBu/Ph}L_o^{NMe}]^+$, however additional features at g = 2.36, 2.21 and 2.11 that may be associated with a phenoxyl radical species are also present. This suggests that Ni^{III}-phenolate and Ni^{II}-phenoxyl radical redox tautomers may be present in solution as proposed for $[Ni^{PhOMe}L_o^{NMe}]^+$ (Section 3.5) and $[Ni(L^{11})]^+$ ($L^{11}H_2$ = N,N'-bis(3',5'-di^{t}butylsalicylidene)-1,2-cyclohexanediamine) (Section 3.5.3).[31] The results of our controlled potential electrolysis and EPR experiments on $Ni^{tBu/Ph}L_o^{NMe}$ suggests that the nature of the oxidative processes of $Ni^{tBu/Ph}L_o^{NMe}$ and of $[Ni^{tBu/Ph}L_o^{NMe}]^+$ is ambiguous and that further study by variable temperature UV/vis and EPR spectroscopies are required to characterise these species fully. The oxidations of $Ni^RL_o^{NMe}$ (R = ^{t}Bu/Ph, ^{t}Bu/PhMe, ^{t}Bu/PhOMe) by more than one electron are not chemically reversible.

3.7.3.3 UV/vis and EPR Spectroscopies of $Cu^{R}L_{o}^{NMe}$ (R = ^{t}Bu/Ph, ^{t}Bu/PhMe, ^{t}Bu/PhOMe)

$Cu^{R}L_{o}^{NMe}$ (R = ^{t}Bu/Ph, ^{t}Bu/PhMe) exhibit two reversible oxidation processes by cyclic voltammetry at $E_{1/2}$ = 0.34 and 0.61 V, and 0.32 and 0.57 V (*vs.* Fc^{+}/Fc) respectively. $Cu^{tBu/PhOMe}L_{o}^{NMe}$ exhibits one reversible process at $E_{1/2}$ = 0.28 (*vs.* Fc^{+}/Fc) and two further processes at E_{p}^{a} = 0.90 and 0.51 V (*vs.* Fc^{+}/Fc).

3.7.3.3.1 Spectroelectrochemistry of $Cu^{tBu/Ph}L_{o}^{NMe}$

$Cu^{tBu/Ph}L_{o}^{NMe}$ exhibits a UV/vis spectrum broadly similar to those found for $Cu^{R}L_{o}^{NMe}$ (R = Ph, PhMe, PhOMe) (Section 3.6), although the absorption bands of $Cu^{tBu/Ph}L_{o}^{NMe}$ are generally shifted to higher energy; an intense absorption band tends towards the limit of the spectroscopic window of CH_2Cl_2 at 230 nm (ε = 68,800 mol^{-1} dm^3 cm^{-1} at 230 nm). This band is accompanied by a feature at 270 nm (ε = 28,500 mol^{-1} dm^3 cm^{-1}) with a shoulder around 310 nm (ε = 12,900 mol^{-1} dm^3 cm^{-1}) and a further intense absorption at 388 nm (ε = 15,900 mol^{-1} dm^3 cm^{-1}).

On oxidation at 1.11 V *vs.* Ag/AgCl small spectral changes are observed with a reduction in intensity of the high energy absorption at 230 nm (ε = 55,200 mol^{-1} dm^3 cm^{-1}) that is accompanied by a reduction in intensity for the bands at *ca.* 400 nm (ε = 12,500 mol^{-1} dm^3 cm^{-1}) and some growth in intensity at *ca.* 350 and 500 nm (ε = 8,100 and 2,630 mol^{-1} dm^3 cm^{-1}). Re-reduction at 0.00 V *vs.* Ag/AgCl generates the original spectral profile of $Cu^{tBu/Ph}L_{o}^{NMe}$ demonstrating the chemical reversibility of the first oxidation process.

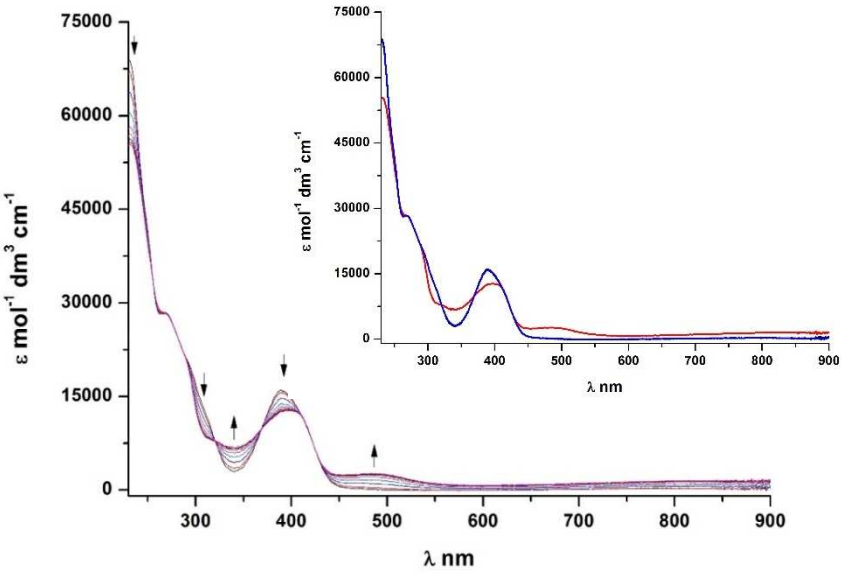


Figure 3.7.3.3.1.1: Sequential UV/vis spectra recorded during the oxidation of $Cu^{tBu/Ph}L_o^{NMe}$ *at 1.11 V vs. Ag/AgCl identifying the bands formed during oxidation. 0.37 mmol solution recorded at 253 K under* N_2 *in* CH_2Cl_2 *containing 0.4 M* $[N^nBu_4][BF_4]$ *as supporting electrolyte. Inset, spectra before oxidation (black), after oxidation (red) and after re-reduction at 0.00 V vs. Ag/AgCl (blue).*

The subsequent oxidation of $Cu^{tBu/Ph}L_o^{NMe}$ at 1.45 V *vs.* Ag/AgCl resulted in further changes to the UV/vis spectrum with an additional growth of the bands at *ca.* 350, 500 and 870 nm (ε = 12,100, 6,410 and 3,270 mol^{-1} dm^3 cm^{-1}) and the development of a band at 234 nm (ε = 48,600 mol^{-1} dm^3 cm^{-1}). These changes are smaller than those found for the second oxidation process of $Cu^{Ph}L_o^{NMe}$, and do not result in the formation of the characteristic bands that would indicate the formation of a phenoxyl radical species. On re-reduction at 0.00 V (*vs.* Ag/AgCl) a spectral profile very similar to that originally observed for $Cu^{tBu/Ph}L_o^{NMe}$ is obtained with only very little decomposition, indicating that both of these oxidation processes are essentially chemically reversible.

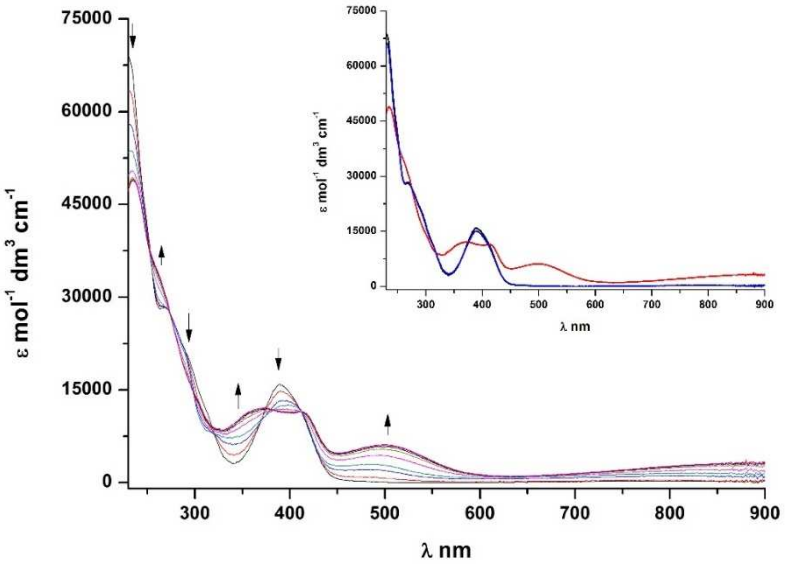


Figure 3.7.3.3.1.2: Sequential UV/vis spectra recorded during the oxidation of $Cu^{tBu/Ph}L_o^{NMe}$ at 1.45 V vs. Ag/AgCl identifying the bands formed during oxidation. 0.37 mmol solution recorded at 253 K under N_2 in CH_2Cl_2 containing 0.4 M $[N^nBu_4][BF_4]$ as supporting electrolyte. Inset, spectra before oxidation (black), after oxidation (red) and after re-reduction at 0.00 V vs. Ag/AgCl (blue).

3.7.3.3.2 Spectroelectrochemistry of $Cu^{tBu/PhMe}L_o^{NMe}$

The spectrum of $Cu^{tBu/PhMe}L_o^{NMe}$ exhibited a very similar profile to that of $Cu^{tBu/Ph}L_o^{NMe}$ with intense absorptions at high energy (230 and 274 nm, ε = 84,000 and 31,900 mol^{-1} dm^3 cm^{-1}) and an additional intense band at 391 nm (ε = 18,800 mol^{-1} dm^3 cm^{-1}). On oxidation very similar spectral changes are observed to those found for the analogous oxidation of $Cu^{tBu/Ph}L_o^{NMe}$ with the UV/vis spectrum possessing a band at 404 nm (ε = 15,300 mol^{-1} dm^3 cm^{-1}), a weak band around 510 nm (ε = 2,650 mol^{-1} dm^3 cm^{-1}) and a reduction in intensity of the higher energy bands to give two bands at 233 and 275 nm (ε = 67,900 and 34,100 mol^{-1} dm^3 cm^{-1}). Subsequent oxidation at 1.50 V *vs.* Ag/AgCl is accompanied by a further reduction in the intensity of the bands at 236 and 267 nm (ε = 59,600 and 39,900 mol^{-1} dm^3 cm^{-1}), together with an increase in the number of bands at lower energy to give four bands at 376, 421, 528 and 880 nm (ε = 14,700, 15,000, 6,900 and 4,200 mol^{-1} dm^3 cm^{-1}). Both oxidation processes are chemically reversible with the original spectral profile of $Cu^{tBu/PhMe}L_o^{NMe}$ generated on re-reduction at 0.00 V *vs.* Ag/AgCl in each case (Figures 3.7.3.3.2.1 inset and 3.7.3.3.2.2 inset).

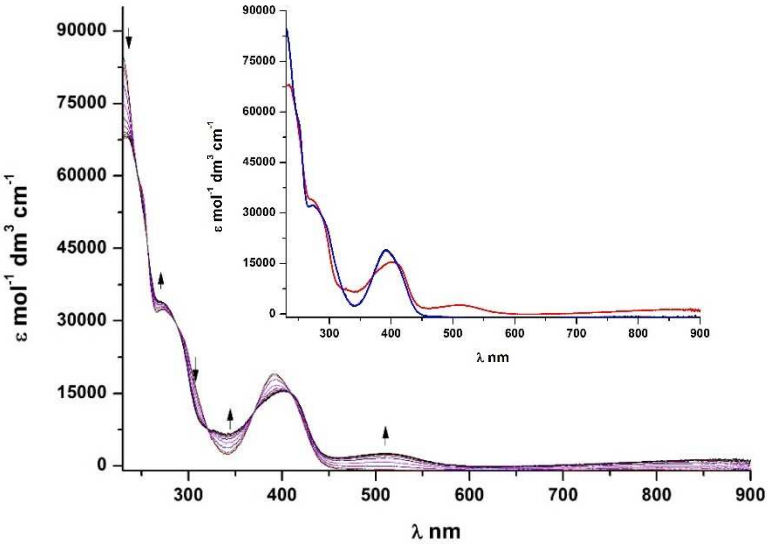


Figure 3.7.3.3.2.1: Sequential UV/vis spectra recorded during the oxidation of $Cu^{tBu/PhMe}L_o^{NMe}$ *at 1.05 V vs. Ag/AgCl identifying the bands formed during oxidation. 0.31 mmol solution recorded at 253 K under* N_2 *in* CH_2Cl_2 *containing 0.4 M* $[N^nBu_4][BF_4]$ *as supporting electrolyte. Inset, spectra before oxidation (black), after oxidation (red) and after re-reduction at 0.00 V vs. Ag/AgCl (blue).*

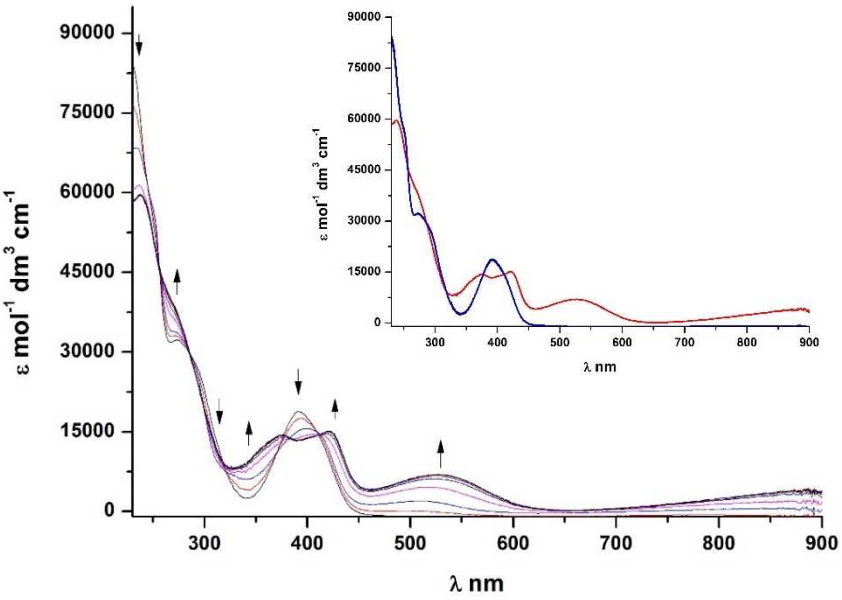


Figure 3.7.3.3.2.2: Sequential UV/vis spectra recorded during the oxidation of $Cu^{tBu/PhMe}L_o^{NMe}$ *at 1.50 V vs. Ag/AgCl identifying the bands formed during oxidation. 0.31 mmol solution recorded at 253 K under* N_2 *in* CH_2Cl_2 *containing 0.4 M* $[N^nBu_4][BF_4]$ *as supporting electrolyte. Inset, spectra before oxidation (black), after oxidation (red) and after re-reduction at 0.00 V vs. Ag/AgCl (blue).*

3.7.3.3.3 Spectroelectrochemistry of $Cu^{tBu/PhOMe}L_o^{NMe}$

The spectrum of $Cu^{tBu/PhOMe}L_o^{NMe}$ is broadly similar to those of $Cu^{tBu/PhMe}L_o^{NMe}$ and $Cu^{tBu/Ph}L_o^{NMe}$. $Cu^{tBu/PhOMe}L_o^{NMe}$ possesses more distinct high energy absorption bands with a feature at 230 nm (ε = 66,600 mol^{-1} dm^3 cm^{-1}) in addition to bands at 253, 282 and 391 nm (ε = 49,200, 27,900 and 15,600 mol^{-1} dm^3 cm^{-1}). Oxidation at 0.98 V *vs.* Ag/AgCl is accompanied by similar changes to those found for the analogous oxidations of $Cu^{tBu/PhMe}L_o^{NMe}$ and $Cu^{tBu/Ph}L_o^{NMe}$ with a decrease in the intensity of the band at 391 nm and the growth of bands at 397 nm (ε = 9,610 mol^{-1} dm^3 cm^{-1}) and 233 nm (ε = 54,400 mol^{-1} dm^3 cm^{-1}), and shoulders at 247 and 280 nm (ε = 51,300 and 29,300 mol^{-1} dm^3 cm^{-1}). More significant changes are observed on oxidation at 1.29 V *vs.* Ag/AgCl with a further reduction in the intensity of the highest energy band (230 nm, ε = 48,100 mol^{-1} dm^3 cm^{-1}), and the growth of bands at 378, 433, 574 and 880 nm (ε = 11,500, 11,200, 5,430 and 3,360 mol^{-1} dm^3 cm^{-1}). Re-reduction generated the UV/vis spectrum of $Cu^{tBu/PhOMe}L_o^{NMe}$ demonstrating that both of these oxidation processes are chemically reversible.

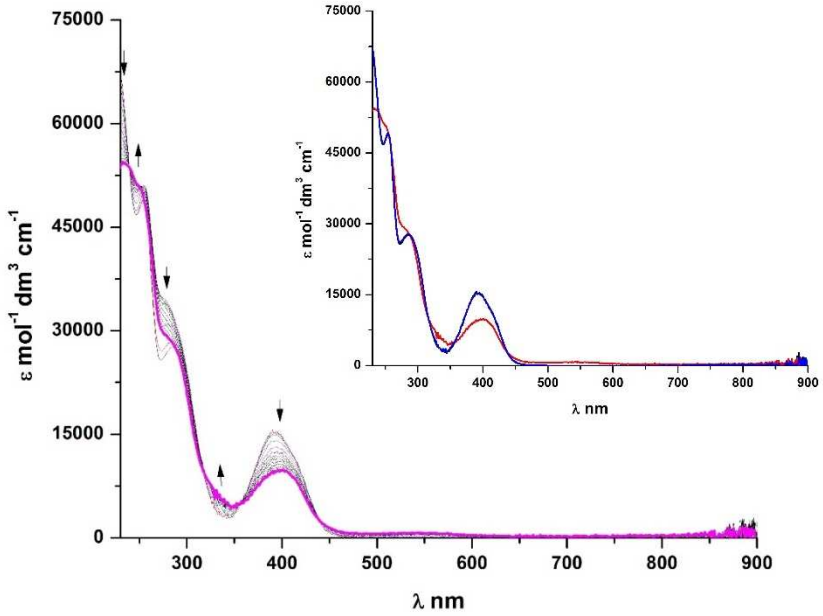


Figure 3.7.3.3.3.1: Sequential UV/vis spectra recorded during the oxidation of $Cu^{tBu/PhOMe}L_o^{NMe}$ at 0.98 V vs. Ag/AgCl identifying the bands formed during oxidation. 0.27 mmol solution recorded at 253 K under N_2 in CH_2Cl_2 containing 0.4 M $[N^nBu_4][BF_4]$ as supporting electrolyte. Inset, spectra before oxidation (black), after oxidation (red) and after re-reduction (blue) at -0.50 V vs. Ag/AgCl.

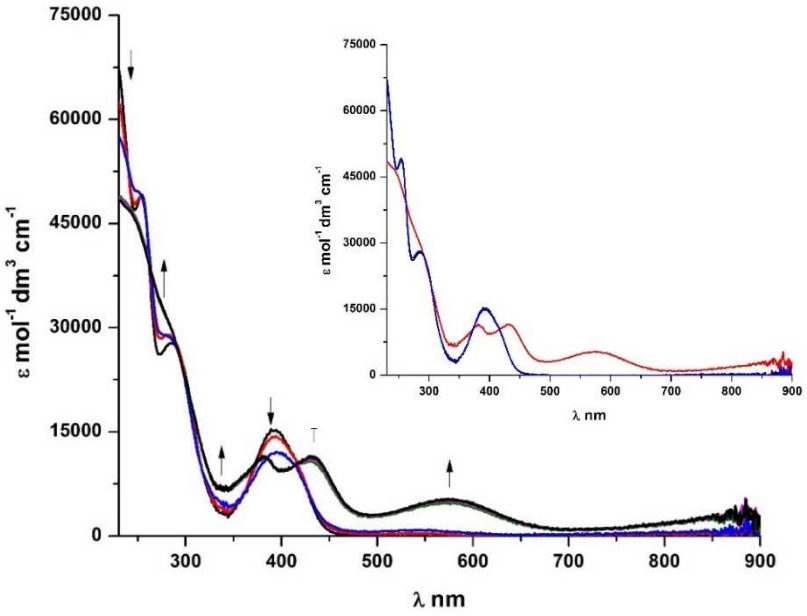


Figure 3.7.3.3.3.2: Sequential UV/vis spectra recorded during the oxidation of $Cu^{tBu/PhOMe}L_o^{NMe}$ at 1.29 V vs. Ag/AgCl identifying the bands formed during oxidation. 0.27 mmol solution recorded at 253 K under N_2 in CH_2Cl_2 containing 0.4 M $[N^nBu_4][BF_4]$ as supporting electrolyte. Inset, spectra before oxidation (black), after oxidation (red) and after re-reduction (blue) at 0.00 V vs. Ag/AgCl.

3.7.3.3.4 Discussion

The changes observed in the UV/vis spectra of the mixed substituent complexes $M^RL_o^{NMe}$ (M = Ni, Cu; R = ^{t}Bu/Ph, ^{t}Bu/PhMe, ^{t}Bu/PhOMe) are much more similar to those seen in $Ni^{tBu}L_o^{NMe}$ and $Cu^{tBu}L_o^{NMe}$ than the doubly aromatic substituted complexes $M^RL_o^{NMe}$ (M = Ni, Cu; R = Ph, PhMe, PhOMe, Sections 3.4-3.6), with less intense bands observed at lower energy in the oxidised species (Table 3.7.3.3.4.1). $Cu^RL_o^{NMe}$ (R = ^{t}Bu/Ph, ^{t}Bu/PhMe, ^{t}Bu/PhOMe) all exhibit two reversible oxidation processes; this behaviour is different to the doubly aromatic substituted complexes where $Cu^RL_o^{NMe}$ (R = Ph, PhOMe) show two reversible processes but $Cu^{PhMe}L_o^{NMe}$ only shows one reversible oxidation process. Further insight into the processes observed and the differences between these complexes can be gained through further study of the oxidised species by EPR spectroscopy.

Complex	λ_{max} (nm)	ε (mol^{-1} dm^3 cm^{-1})	Isobestic point (nm)
Cu$^{t\text{Bu/Ph}}$L$_O^{\text{NMe}}$	230, 270, 310(sh), 388	68,800, 28,500, 12,900, 15,900	
[Cu$^{t\text{Bu/Ph}}$L$_O^{\text{NMe}}$]$^+$	230, 270, 388, 500	55,200, 28,300, 12,500, 2,630	256, 280, 320, 359, 421
[Cu$^{t\text{Bu/Ph}}$L$_O^{\text{NMe}}$]$^{2+}$	234, 350, 410, 500, 870	48,600, 12,100, 11,400, 6,410, 3,270	
Cu$^{t\text{Bu/PhMe}}$L$_O^{\text{NMe}}$	230, 274, 391	84,000, 31,900, 18,800	
[Cu$^{t\text{Bu/PhMe}}$L$_O^{\text{NMe}}$]$^+$	233, 275, 404, 510	67,900, 34,100, 15,300, 2,650	245, 255, 288, 320, 369, 409
[Cu$^{t\text{Bu/PhMe}}$L$_O^{\text{NMe}}$]$^{2+}$	236, 267(sh), 376, 421, 528, 880	59,600, 39,900, 14,700, 15,000, 6,900, 4,200	
Cu$^{t\text{Bu/PhOMe}}$L$_O^{\text{NMe}}$	230, 253, 282, 391	66,600, 49,200, 27,900, 15,600	
[Cu$^{t\text{Bu/PhOMe}}$L$_O^{\text{NMe}}$]$^+$	233, 247(sh), 280(sh), 397	54,400, 51,300, 29,300, 9,610	240, 315, 356, 439
[Cu$^{t\text{Bu/PhOMe}}$L$_O^{\text{NMe}}$]$^{2+}$	230, 378, 433, 574, 880	48,100, 11,500, 11,200, 5,430, 3,360	

Table 3.7.3.3.4.1: Summary of UV/vis spectra of Cu^{R}L$_o^{NMe}$, [Cu^{R}L$_o^{NMe}$]$^+$, [Cu^{R}L$_o^{NMe}$]$^{2+}$, (R = ^{t}Bu/Ph, ^{t}Bu/PhMe, ^{t}Bu/PhOMe).

3.7.3.4 Controlled Potential Electrolysis and EPR Spectroscopy of Cu$^{t\text{Bu/Ph}}$L$_O^{\text{NMe}}$ and Cu$^{t\text{Bu/PhOMe}}$L$_O^{\text{NMe}}$

The oxidation products of Cu$^{t\text{Bu/Ph}}$L$_O^{\text{NMe}}$ and Cu$^{t\text{Bu/PhOMe}}$L$_O^{\text{NMe}}$ were generated by controlled potential electrolysis and examined by EPR spectroscopy. Controlled potential electrolysis of Cu$^{t\text{Bu/PhOMe}}$L$_O^{\text{NMe}}$ at a potential of 0.69 V (*vs.* Fc$^+$/Fc) proceeded rapidly (Figure 3.7.3.4.1 Left). This electrolysis was terminated when a charge equivalent to two electrons had been removed. The cyclic voltammogram of the solution of [Cu$^{t\text{Bu/PhOMe}}$L$_O^{\text{NMe}}$]$^{2+}$ was similar to that for Cu$^{t\text{Bu/PhOMe}}$L$_O^{\text{NMe}}$ prior to electrolysis (Figure 3.7.3.4.1 Right).

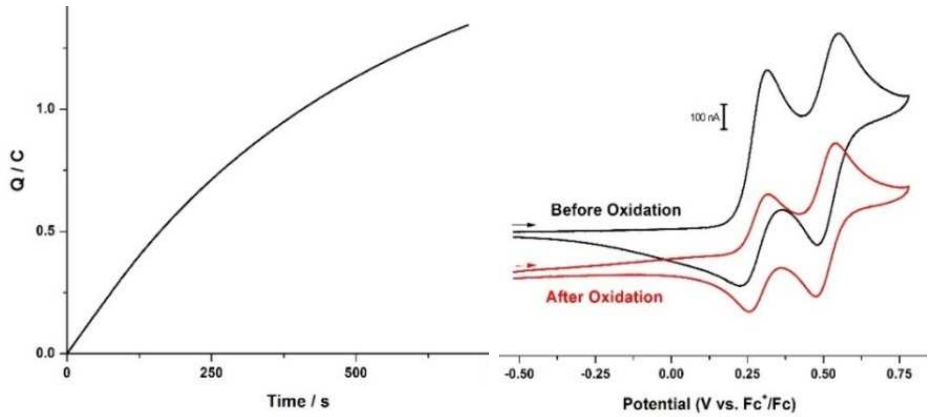


Figure 3.7.3.4.1: Left: Controlled potential electrolysis of $Cu^{tBu/PhOMe}L_O^{NMe}$ to $[Cu^{tBu/PhOMe}L_O^{NMe}]^{2+}$ at 0.69 V vs. Fc^+/Fc, 1 mmol solution in CH_2Cl_2 containing 0.4 M $[N^nBu_4][BF_4]$ as supporting electrolyte recorded at 253 K under Ar. Theoretical Q for a two electron process = 0.48 C; Right: Cyclic voltammograms of $Cu^{tBu/PhOMe}L_O^{NMe}$ (black) before oxidation and $[Cu^{tBu/PhOMe}L_O^{NMe}]^{2+}$ (red) after oxidation, recorded at 100 mV, 1 mmol solution in CH_2Cl_2 containing 0.4 M $[N^nBu_4][BF_4]$ as supporting electrolyte.

The frozen solution EPR spectrum of $[Cu^{tBu/PhOMe}L_O^{NMe}]^{2+}$ is of low intensity and possesses a four-line hyperfine splitting and high g anisotropy, which can be attributed to a Cu^{II} species (Figure 3.7.3.4.2). The frozen solution EPR spectrum of $[Cu^{tBu/PhOMe}L_O^{NMe}]^{2+}$ is markedly different to that of $[Cu^{Ph}L_O^{NMe}]^{2+}$ where a spectrum consistent with a phenoxyl radical species was observed (Section 3.6).

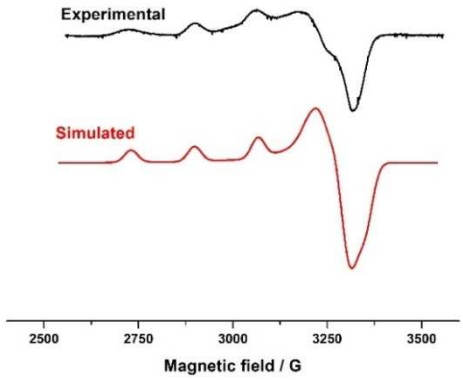


Figure 3.7.3.4.2: (Black) X-band CW EPR spectra of electrochemically generated $[Cu^{tBu/PhOMe}L_O^{NMe}]^{2+}$ in CH_2Cl_2 containing 0.4 M $[N^nBu_4][BF_4]$ as supporting electrolyte as a frozen solution at 77 K, (Red) Simulated spectra – spin Hamiltonian parameters: g_{11} = 2.050, g_{22} = 2.005, g_{33} = 2.220, A_{11} = 13 G, A_{33} = 170 G Gaussian linewidths W_{11} = 35 G, W_{22} = 28 G, W_{33} = 35 G.

Similar experiments on $Cu^{tBu/Ph}L_O^{NMe}$ following controlled potential electrolysis at a potential of 0.76 V (*vs.* Fc^+/Fc) led to rapid oxidation (Figure 3.7.3.4.3 Left) and significant differences were observed in the cyclic voltammogram of $[Cu^{tBu/Ph}L_O^{NMe}]^{2+}$ compared to the cyclic voltammogram of $Cu^{tBu/Ph}L_O^{NMe}$ (Figure 3.7.3.4.3 Right). The frozen solution EPR spectrum of the electrochemically generated species is similar that for $[Cu^{tBu/PhOMe}L_O^{NMe}]^{2+}$ and is consistent with a Cu^{II} species present in solution (Figure 3.7.3.4.4).

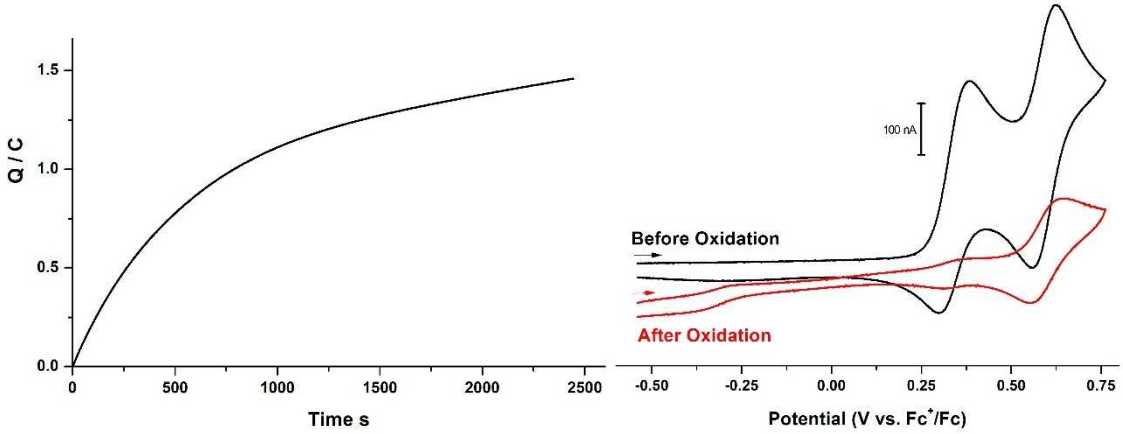


Figure 3.7.3.4.3: Left: Controlled potential electrolysis of $Cu^{tBu/Ph}L_O^{NMe}$ at 0.76 V vs. Fc^+/Fc, 1 mmol solution in CH_2Cl_2 containing 0.4 M $[N^nBu_4][BF_4]$ as supporting electrolyte recorded at 253 K under Ar. Theoretical Q for a two electron process = 1.33 C; Right: Cyclic voltammograms before oxidation (black) and after oxidation (red), recorded at 100 mV, 1 mmol solution in CH_2Cl_2 containing 0.4 M $[N^nBu_4][BF_4]$ as supporting electrolyte.

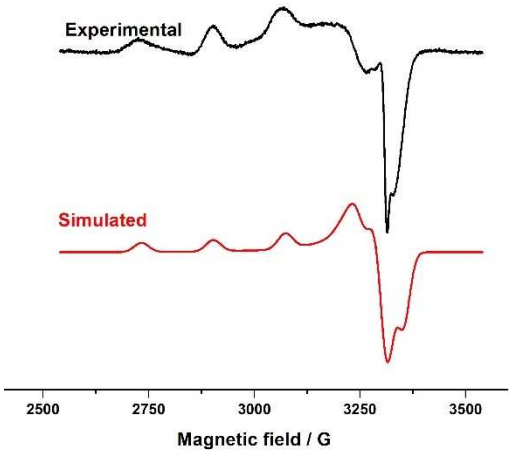


Figure 3.7.3.4.4: (Black) X-band CW EPR spectra of electrochemically generated $[Cu^{tBu/Ph}L_O^{NMe}]^{2+}$ in CH_2Cl_2 containing 0.4 M $[N^nBu_4][BF_4]$ as supporting electrolyte as a frozen solution at 77 K, (Red) Simulated spectra – spin Hamiltonian parameters: g_{11} = 2.060, g_{22} = 2.005, g_{33} = 2.224, A_{11} = 5 G, A_{33} = 168 G Gaussian linewidths W_{11} = 45 G, W_{22} = 40 G, W_{33} = 35 G.

Given the significant change in profile of the cyclic voltammogram of $Cu^{tBu/Ph}L_O^{NMe}$ before and after oxidation by two electrons and the observation of a Cu^{II} signal in the EPR spectra for frozen solutions of $Cu^{tBu/PhoMe}L_O^{NMe}$ and $Cu^{tBu/Ph}L_O^{NMe}$ after oxidation by two electrons, we suspect that the oxidation products $[Cu^{tBu/PhoMe}L_O^{NMe}]^{2+}$ and $[Cu^{tBu/Ph}L_O^{NMe}]^{2+}$ observed by UV/vis spectroelectrochemistry are unstable over the timescale of the controlled potential electrolysis experiment. It is likely that these oxidation products decompose to generate Cu^{II} species.

3.7.4 Discussion

$M^RL_o^{NMe}$ (M = Zn, Ni, Cu; R = ^{t}Bu/Ph, ^{t}Bu/PhMe, ^{t}Bu/PhOMe) exhibit multiple oxidation processes as for $M^RL_o^{NMe}$ (M = Zn, Ni, Cu; R = Ph, PhMe, PhOMe) (Sections 3.3-3.5). However, electro- and spectrochemical evidence for the assignment of these oxidation processes to metal and/or ligand-based events is less conclusive. Thus, the characteristic features associated with the formation of phenoxyl radicals are not resolved in UV/vis spectra of $[Cu^RL_o^{NMe}]^+$ (R = ^{t}Bu/Ph, ^{t}Bu/PhMe, ^{t}Bu/PhOMe). In addition, EPR spectroscopic studies on frozen solutions of $[Ni^{tBu/Ph}L_o^{NMe}]^+$ suggest that $[Ni^{tBu/Ph}L_o^{NMe}]^+$ may exhibt redox tautomerism[31] involving formal Ni^{III}-phenolate and Ni^{II}-phenoxyl radical centres. Controlled potential electrolysis experiments on solutions of $Ni^{tBu/PhOMe}L_o^{NMe}$, $Cu^{tBu/Ph}L_O^{NMe}$ and $Cu^{tBu/PhOMe}L_O^{NMe}$ also suggest that the oxidation products of these species are significantly less stable than their $[M^RL_o^{NMe}]^+$ (M = Zn, Ni, Cu; R = Ph, PhMe, PhOMe) counterparts. This decrease in stability over the timescale of the controlled potential electrolysis experiment may be associated with a reduced delocalisation of radical character across the ligand framework in $[M^RL_o^{NMe}]^+$ (M = Zn, Ni, Cu; R = ^{t}Bu/Ph, ^{t}Bu/PhMe, ^{t}Bu/PhOMe) relative to $[M^RL_o^{NMe}]^+$ (M = Zn, Ni, Cu; R = Ph, PhMe, PhOMe); the former series possesses one phenyl ring substiuent at the 3-position of the phenolate ring whereas the latter possess phenyl substituents at the 3- and 5-positions.

3.8 Conclusions

$M^{R}L_{o}^{NMe}$ (M = Zn, Ni, Cu; R = Cl, Br, Nap, Ph, PhMe, PhOMe, ^{t}Bu/Br, ^{t}Bu/Ph, ^{t}Bu/PhMe, ^{t}Bu/PhOMe), synthesised and characterised in Chapter 2, have been investigated by electrochemistry, UV/vis spectroelectrochemistry and by EPR spectroscopy. Whilst all $M^{R}L_{o}^{NMe}$ exhibit some redox activity, significant differences are found for the redox properties of each complex as R is varied.

$M^{R}L_{o}^{NMe}$ (M = Zn, Ni, Cu; R = Cl, Br, Nap, ^{t}Bu/Br) possess oxidation processes that are typically not reversible. This may most likely be attributed to decomposition following the generation of phenoxyl radical character that may delocalise to reactive positions that are insufficiently protected by the halogen or napthyl substituents. This conclusion is supported by the increase in reversibility demonstrated for the first oxidation process of $Ni^{R}L_{o}^{NMe}$ (R = Cl, Br, Nap, ^{t}Bu/Br) relative to their Cu and Zn counterparts. The UV/vis spectroscopic studies of the oxidation products $Ni^{R}L_{o}^{NMe}$ (R = Cl, Br, Nap, ^{t}Bu/Br) suggest that the first process is metal centred and is associated with the formation of a species which possesses a formal Ni^{III} centre. Thus, the reduced phenoxyl radical character of such Ni^{III} species renders these complexes less susceptible to decomposition irrespective of the nature of the substitutions within the ligand framework.

The trends in potential for the oxidation proceses of $M^{R}L_{o}^{NMe}$ (M = Zn, Ni, Cu; R = Ph, PhMe, PhOMe, ^{t}Bu/Ph, ^{t}Bu/PhMe, ^{t}Bu/PhOMe) are summarised in Figure 3.8.1. For $M^{R}L_{o}^{NMe}$ (M = Cu or Zn, R = Ph, PhMe, PhOMe) there is a shift to a less positive potential on the introduction of more electron donating substituents (Ph<PhMe<PhOMe) for each process. For the M = Ni case the first redox process remains largely unaffected by the nature of the substituents pendant to the phenolate rings; the trends in potential for the second and subsequent processes revert to the trends observed for M = Cu or Zn (Figure 3.8.1).

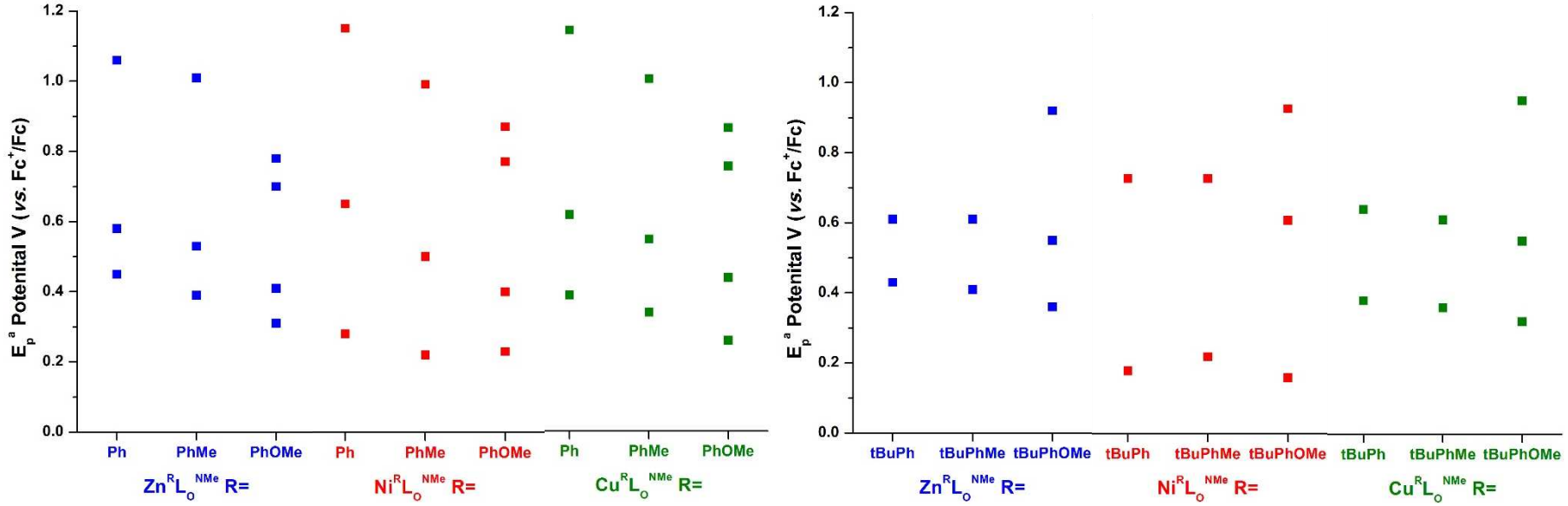


Figure 3.8.1: Summary of E_p^a values for oxidation processes of $M^RL_o^{NMe}$ (M = Zn (blue), Ni (red), Cu (green); Left: (R = Ph, PhMe, PhOMe), demonstrating less positive reduction potentials with increasingly electron donating substituents for $Zn^RL_o^{NMe}$ and $Cu^RL_o^{NMe}$, together with unchanged reduction potential for the first metal centred oxidation process for $Ni^RL_o^{NMe}$ (E_p^a = 0.21 – 0.28 V), and less positive reduction potentials for the subsequent oxidation processes for $Ni^RL_o^{NMe}$; Right: (R = ^{t}Bu/Ph, ^{t}Bu/PhMe, ^{t}Bu/PhOMe,), demonstrating less positive reduction potentials with increasingly electron donating substituents for $Zn^RL_o^{NMe}$ and $Cu^RL_o^{NMe}$, together with unchanged reduction potential for the first metal centred oxidation process for $Ni^RL_o^{NMe}$ (E_p^a = 0.21 – 0.28 V), and less positive reduction potentials for the subsequent oxidation processes for $Ni^RL_o^{NMe}$.

The variation of substituents at the 3 position of the phenolate rings only in $M^{R}L_{o}^{NMe}$ (M = Zn, Ni, Cu; R = ^{t}Bu/Ph, ^{t}Bu/PhMe, ^{t}Bu/PhOMe) results in less variation in the reduction potentials of each oxidation process relative to their R = Ph, PhMe, and PhOMe counterparts (Figure 3.8.2). A third oxidation process is only observed for $M^{tBu/PhOMe}L_{o}^{NMe}$ with only two processes observed for $M^{tBu/Ph}L_{o}^{NMe}$ and $M^{tBu/PhMe}L_{o}^{NMe}$.

UV/vis spectroelectrochemical and EPR spectroscopic studies on the oxidation products confirm the formation of a phenoxyl radical species on the first and second oxidations of $M^{R}L_{o}^{NMe}$ (M = Zn, Cu; R = Ph, PhMe, PhOMe). EPR spectroscopy unambiguously confirmed the formation of a formal Ni^{III} species $[Ni^{R}L_{o}^{NMe}]^{+}$ as the one electron oxidation product of $Ni^{R}L_{o}^{NMe}$ (R = Ph, PhMe, PhOMe) at 77 K, with evidence of phenoxyl radical formation observed by UV/vis spectroscopy on further oxidation to $[M^{R}L_{o}^{NMe}]^{2+}$ (R = Ph, PhMe, PhOMe). UV/vis spectrolectrochemistry of $[Ni^{PhOMe}L_{o}^{NMe}]^{+}$ at 253 K supports a formulation with significant Ni^{II}-phenoxyl radical character and together with the EPR spectroscopic results suggests that $[Ni^{PhOMe}L_{o}^{NMe}]^{+}$ may demonstrate redox tautomersim involving formal Ni^{III}-phenolate and Ni^{II}-phenoxyl radical centres. Further variable temperature spectroscopic measurements are required in order to further investigate the extent of redox tautomerism in $[Ni^{PhOMe}L_{o}^{NMe}]^{+}$. DFT calculations supported these conclusions and also highlight a potential role of the amine nitrogen donor in stabilising a formal Ni^{III} state, with significant spin density (0.167, 0.135 and 0.124 for $[Ni^{R}L_{o}^{NMe}]^{+}$; R = Ph, PhMe and PhOMe respectively) localised on this amine N-donor.

Investigations into the oxidation products of $M^{R}L_{o}^{NMe}$ (M = Zn, Ni, Cu; R = ^{t}Bu/Ph, ^{t}Bu/PhMe, ^{t}Bu/PhOMe) remain less conclusive. EPR spectroscopic studies on $[Ni^{tBu/Ph}L_{O}^{NMe}]^{+}$ at 77 K provide evidence for the formation of a formal Ni^{III} species, however, a Ni^{II}-phenoxyl radical component may be present in frozen solution at this temperature. UV/vis spectroscopy provides some evidence for the production of phenoxyl radical species on oxidation for $Cu^{R}L_{o}^{NMe}$ (R = ^{t}Bu/Ph, ^{t}Bu/PhMe, ^{t}Bu/PhOMe), however, controlled potential electrolysis and EPR spectroscopic studies suggest that these oxidation products are not stable for prolonged periods in solution. Thus, $M^{R}L_{o}^{NMe}$ (M = Zn, Ni, Cu; R = ^{t}Bu/Ph,

^{t}Bu/PhMe, ^{t}Bu/PhOMe)) remain as candidates for further study in order to fully understand the nature of the oxidation processes in these compounds.

In summary, we have significantly extended the range of phenolate substitution patterns that can support metal-phenoxyl radical species in salen-type complexes beyond the common 3,5-^{t}butyl subsitutions. Furthermore these alternate 3,5-subsitutions can tune the reduction potentials for these centres for potential catalytic applications, particularly as oxidation catalysts[45-47]. In addition, our approach could also facilitate the incorporation of redox active salen-type complexes into solid supported materials or metal-organic frameworks to develop new materials with tailored redox activities or magnetic properties for use in catalysis.

3.9 References

1. M. Franks, A. Gadzhieva, L. Ghandhi, D. Murrell, A. J. Blake, E. S. Davies, W. Lewis, F. Moro, J. McMaster and M. Schröder, *Inorg. Chem.*, 2013, **52**, 660-670.
2. P. Verma, R. C. Pratt, T. Storr, E. C. Wasinger and T. D. P. Stack, *Proc. Nat. Acad. Sci. USA*, 2011, **108**, 18600-18605.
3. R. C. Pratt, C. T. Lyons, E. C. Wasinger and T. D. P. Stack, *J. Am. Chem. Soc.*, 2012, **134**, 7367-7377.
4. N. Ito, S. E. V. Phillips, C. Stevens, Z. B. Ogel, M. J. McPherson, J. N. Keen, K. D. S. Yadav and P. F. Knowles, *Nature*, 1991, **350**, 87-90.
5. C. Wright and A. G. Sykes, *J. Inorg. Biochem.*, 2001, **85**, 237-243.
6. T. Kurahashi and H. Fujii, *J. Am. Chem. Soc.*, 2011, **133**, 8307-8316.
7. O. Rotthaus, F. Thomas, O. Jarjayes, C. Philouze, E. Saint-Aman and J.-L. Pierre, *Chem. Eur. J.*, 2006, **12**, 6953-6962.
8. F. Thomas, O. Jarjayes, C. Duboc, C. Philouze, E. Saint-Aman and J.-L. Pierre, *Dalton Trans.*, 2004, **0**, 2662-2669.
9. E. Saint-Aman, S. Menage, J.-L. Pierre, E. Defrancq and G. Gellon, *New J. Chem.*, 1998, **22**, 393-394.
10. C. T. Lyons and T. D. P. Stack, *Coord. Chem. Rev.*, 2013, **257**, 528-540.
11. J. A. Halfen, B. A. Jazdzewski, S. Mahapatra, L. M. Berreau, E. C. Wilkinson, L. Que and W. B. Tolman, *J. Am. Chem. Soc.*, 1997, **119**, 8217-8227.
12. P. A. Stenson, A. Board, A. Marin-Becerra, A. J. Blake, E. S. Davies, C. Wilson, J. McMaster and M. Schröder, *Chem. Eur. J.*, 2008, **14**, 2564-2576.
13. S. E. J. Rigby, J. H. A. Nugent and P. J. O'Malley, *Biochem.*, 1994, **33**, 1734-1742.
14. D. Parker, E. Stephen Davies, C. Wilson and J. McMaster, *Inorg. Chim. Acta*, 2007, **360**, 203-211.
15. A. Sokolowski, H. Leutbecher, T. Weyhermüller, R. Schnepf, E. Bothe, E. Bill, P. Hildebrandt and K. Wieghardt, *J. Biol. Inorg. Chem.*, 1997, **2**, 444-453.
16. E. Bill, J. Müller, T. Weyhermüller and K. Wieghardt, *Inorg. Chem.*, 1999, **38**, 5795-5802.
17. C. Freire and B. de Castro, *Polyhedron*, 1998, **17**, 4227-4235.
18. M. Orio, C. Philouze, O. Jarjayes, F. Neese and F. Thomas, *Inorg. Chem.*, 2010, **49**, 646-658.
19. L. Benisvy, A. J. Blake, D. Collison, E. S. Davies, C. D. Garner, E. J. L. McInnes, J. McMaster, G. Whittaker and C. Wilson, *Dalton Trans.*, 2003, 1975-1985.
20. L. Benisvy, R. Kannappan, Y.-F. Song, S. Milikisyants, M. Huber, I. Mutikainen, U. Turpeinen, P. Gamez, L. Bernasconi, E. J. Baerends, F. Hartl and J. Reedijk, *Eur. J. Inorg. Chem.* , 2007, 637-642.
21. C. Freire and B. de Castro, *J. Chem. Soc., Dalton Trans.*, 1998, 1491-1498.
22. I. C. Santos, M. Vilas-Boas, M. F. M. Piedade, C. Freire, M. T. Duarte and B. de Castro, *Polyhedron*, 2000, **19**, 655-664.

23. L. Benisvy, E. Bill, A. J. Blake, D. Collison, E. S. Davies, C. D. Garner, C. I. Guindy, E. J. L. McInnes, G. McArdle, J. McMaster, C. Wilson and J. Wolowska, *Dalton Trans.*, 2004, 3647-3653.
24. L. Benisvy, R. Bittl, E. Bothe, C. D. Garner, J. McMaster, S. Ross, C. Teutloff and F. Neese, *Angew. Chem. Int. Ed.*, 2005, **44**, 5314-5317.
25. L. Benisvy, E. Bill, A. J. Blake, D. Collison, E. S. Davies, C. D. Garner, G. McArdle, E. J. L. McInnes, J. McMaster, S. H. K. Ross and C. Wilson, *Dalton Trans.*, 2006, 258-267.
26. Y. Wang and T. D. P. Stack, *J. Am. Chem. Soc.*, 1996, **118**, 13097-13098.
27. D. Sellmann, H. Binder, D. Häußinger, F. W. Heinemann and J. Sutter, *Inorg. Chim. Acta*, 2000, **300–302**, 829-836.
28. A. Sokolowski, J. Müller, T. Weyhermüller, R. Schnepf, P. Hildebrandt, K. Hildenbrand, E. Bothe and K. Wieghardt, *J. Am. Chem. Soc*, 1997, **119**, 8889-8900.
29. B. A. Jazdzewski and W. B. Tolman, *Coord. Chem. Rev.*, 2000, **200–202**, 633-685.
30. A. Klamt and G. Schuurmann, *J. Chem. Soc. , Perkin Trans. 2*, 1993, 799-805.
31. Y. Shimazaki, F. Tani, K. Fukui, Y. Naruta and O. Yamauchi, *J. Am. Chem. Soc.*, 2003, **125**, 10512-10513.
32. Y. Wang, J. L. DuBois, B. Hedman, K. O. Hodgson and T. D. P. Stack, *Science*, 1998, **279**, 537-540.
33. T. Maki, Y. Araki, Y. Ishida, O. Onomura and Y. Matsumura, *J. Am. Chem. Soc.*, 2001, **123**, 3371-3372.
34. T. Storr, E. C. Wasinger, R. C. Pratt and T. D. P. Stack, *Angew. Chem. Int. Ed.*, 2007, **46**, 5198-5201.
35. H. J. Krueger and R. H. Holm, *Inorg. Chem.*, 1987, **26**, 3645-3647.
36. O. Rotthaus, O. Jarjayes, C. Perez Del Valle, C. Philouze and F. Thomas, *Chem. Commun.*, 2007, 4462-4464.
37. M. Gennari, M. Orio, J. Pécaut, F. Neese, M.-N. Collomb and C. Duboc, *Inorg. Chem.*, 2010, **49**, 6399-6401.
38. D. Nakane, Y. Wasada-Tsutsui, Y. Funahashi, T. Hatanaka, T. Ozawa and H. Masuda, *Inorg. Chem.*, 2014, **53**, 6512-6523.
39. A. K. Nairn, S. J. Archibald, R. Bhalla, B. C. Gilbert, E. J. MacLean, S. J. Teat and P. H. Walton, *Dalton Trans.*, 2006, 172-176.
40. B. Adam, E. Bill, E. Bothe, B. Goerdt, G. Haselhorst, K. Hildenbrand, A. Sokolowski, S. Steenken, T. Weyhermüller and K. Wieghardt, *Chem. Eur. J.*, 1997, **3**, 308-319.
41. E. R. Altwicker, *Chem. Rev.*, 1967, **67**, 475-531.
42. M. Orio, C. Philouze, O. Jarjayes, F. Neese and F. Thomas, *Inorg. Chem.*, 2009, **49**, 646-658.
43. R. S. Nicholson and I. Shain, *Anal. Chem.*, 1964, **36**, 706-723.
44. R. S. Nicholson, *Anal. Chem.*, 1966, **38**, 1406-1406.
45. N. S. Venkataramanan, G. Kuppuraj and S. Rajagopal, *Coord. Chem. Rev.*, 2005, **249**, 1249-1268.
46. W. Zhang, J. L. Loebach, S. R. Wilson and E. N. Jacobsen, *J. Am. Chem. Soc.*, 1990, **112**, 2801-2803.
47. E. N. Jacobsen, W. Zhang, A. R. Muci, J. R. Ecker and L. Deng, *J. Am. Chem. Soc.*, 1991, **113**, 7063-7064.

Chapter 4

Diphenolate and Dithiophenolate Zn^{II}, Ni^{II} and Cu^{II} Complexes as Analogues of the Active Site of Nickel Superoxide Dismutase

4.1 Introduction

A number of synthetic analogues of the active site of nickel superoxide dismutase (NiSOD) have been prepared following the elucidation of the X-ray crystal structure in 2004 (Chapter 1).[1] Recent work within the McMaster group has demonstrated that transition metal containing dithiophenolate complexes incorporating a tethered nitrogen containing bridge, Ni^{t}BuLs^{Py} (Figure 4.1.2.1),[2] can be synthesised as analogues of the active site of NiSOD. Ni^{t}BuLs^{Py} possesses a reversible oxidation process at $E_{1/2}$ = 0.05 V *vs.* Fc^{+}/Fc that is associated with the formation of [Ni^{t}BuLs^{Py}]$^{+}$. Preliminary investigations into the electronic structure of this species have been carried out and the CH_2Cl_2 solution EPR spectrum of [Ni^{t}BuLs^{Py}]$^{+}$ at 77K can be simulated with spin Hamiltonian parameters (g_{11} = 2.282, g_{22} = 2.200, g_{33} = 2.016, A_{33} = 20.9 G)[2] that are similar to those of the oxidised form of NiSOD isolated from *S. seoulensis* (g_{11} = 2.30, g_{22} = 2.24, g_{33} = 2.01, A_{33} = 24.9 G) (Figure 4.1.1).[3, 4] However, a detailed description of the electronic structure of [Ni^{t}BuLs^{Py}]$^{+}$, an understanding of the role of the coordination sphere in controlling the chemistry of Ni^{t}BuLs^{Py} and an assessment of the potential of Ni^{t}BuLs^{Py} as a catalyst for superoxide dismutation have not emerged.

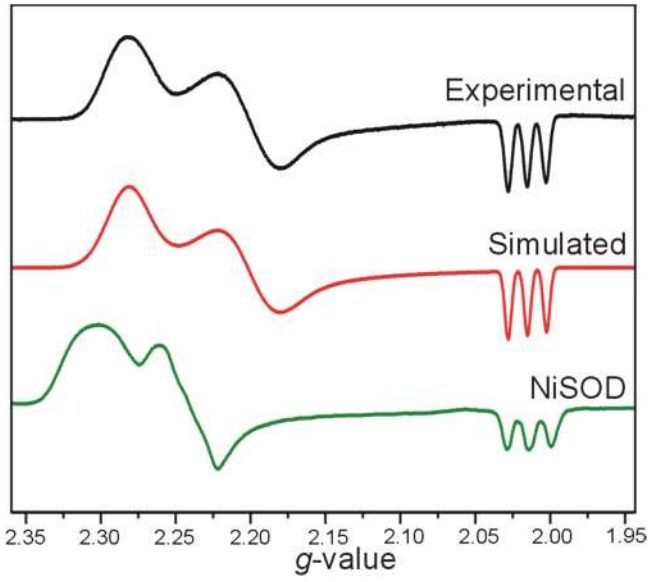


Figure 4.1.1: X-band EPR spectrum at 77 K of [Ni^{t}BuLs^{Py}]$^{+}$ in frozen CH_2Cl_2 solution (black), simulation (red). Spin Hamiltonian parameters: g_{11} = 2.282, g_{22} = 2.200, g_{33} = 2.016, A_{33} = 20.9 G, Gaussian linewidths W_{11} = 32 G, W_{22} = 44 G, W_{33} = 8 G.[2] X-band EPR spectrum at 77 K of native oxidised S. seoulensis NiSOD (green) (g = 2.30, 2.24 and 2.01, A_{33} = 24.9 G). [3,4]

4.1.2 Aims

The aims of the research described in this Chapter are to extend the range of transition metal complexes containing pendant N-donor groups capable of acting as a fifth ligand to the metal centre M^{t}BuL$_{X}^{R}$ (M = Zn, Ni, Cu; X = S, O; R = Ph, Py, PyOMe) (Figure 4.1.2.1) in order to provide further insight into the chemistry of the active site of NiSOD. In this study we will:

- Study M^{t}BuL$_{X}^{R}$ as their dithiophenolate (X = S; M = Ni) and diphenolate (X = O; M = Zn, Ni, Cu) counterparts to provide insight into the role of the S-ligation in controlling the electronic structure of the active site of NiSOD;
- Vary the nature of the N-donor to assess its role controlling the electronic structures of M^{t}BuL$_{X}^{R}$ and [M^{t}BuL$_{X}^{R}$]$^{+}$ (X = O, S, R = Py, PyOMe, Ph)
- Examine the electronic structure of Ni^{t}BuL$_{S}^{Py}$ by pulsed ESEEM and HYSCORE EPR spectroscopic studies, supported by DFT calculations.

The electronic structure of each M$^{t\mathrm{Bu}}$L$_{X}^{R}$ (M = Zn, Ni, Cu; X = S, O; R = Ph, Py, PyOMe) (Figure 4.1.2.1) will be probed by electrochemistry, UV/vis spectroelectrochemistry and by EPR spectroscopy as appropriate.

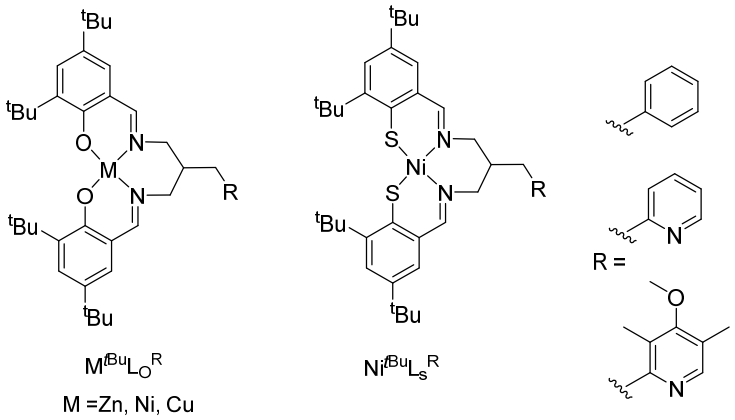


Figure 4.1.2.1: M$^{t\mathrm{Bu}}$L$_{X}^{R}$ (M = Zn, Ni, Cu; X = S, O; R = Ph, Py, PyOMe) examined in this chapter.

4.2 Investigations into the Role of Pendant Pyridine Donors in Controlling the Properties of Ni-containing Diphenolate Complexes

Complexes incorporating a N_3O_2 coordination sphere have been developed as analogues for the active site of NiSOD. Thus, [Ni(DBPP)] (DBPP = 2,6-bis{[(S)-2-(diphenyl-hydroxymethyl)-1-pyrrolidinyl]methyl}pyridine) is a Ni^{II} N_3O_2 complex that on oxidation generates a solution that exhibits a rhombic EPR signal (g_{11} = 2.30, g_{22} = 2.24, g_{33} = 2.01, a_{33} = 24.9 G), which is typical for a Ni^{III} centre with an axial ^{14}N interaction,[5] and which is similar to that observed for the oxidised form of NiSOD.[6] $Ni^{tBu}L_O^{Py}$ has previously been synthesised within the group (Scheme 4.2.1.1) and also possesses a Ni^{II} N_3O_2 coordination sphere. The one-electron oxidation of a solution of this complex in CH_2Cl_2 generates a rhombic EPR signal (g_{11} = 2.50, g_{22} = 2.204, g_{33} = 2.033) with a three line hyperfine splitting in the g_{33} region corresponding to an interaction with a single ^{14}N donor (a_{33} = 22 G).[2]

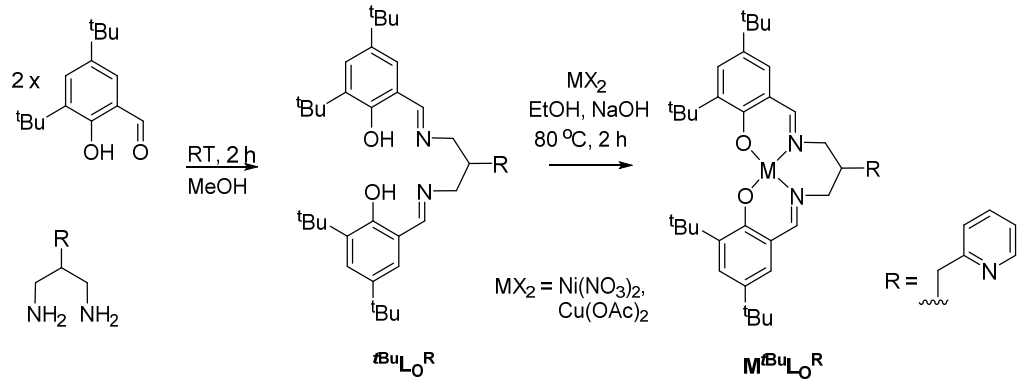
The development of complexes incorporating N_3O_2 chelating ligands also provides a route to assess candidate N-donor containing bridges before their introduction into ligand frameworks containing dithiophenolate donors; diphenolate donors are usually less susceptible to oxidative decomposition when compared to their dithiophenolate counterparts.[7]

4.2.1 The Syntheses and Characterisation of Ni^{II} Complexes with Ligands Incorporating Diphenolate Donors

$M^{tBu}L_O^R$ (M = Ni, Cu; R = Py) have been prepared previously within the group according to a similar synthetic procedure used for the syntheses of $M^RL_O^{NMe}$ (M = Zn, Ni, Cu; R = Cl, Br, Nap, Ph, PhMe, PhOMe, ^{t}Bu/Br, ^{t}Bu/Ph, ^{t}Bu/PhMe, ^{t}Bu/PhOMe) in Chapter 2 (Scheme 4.2.1.1).

In this section, we describe the syntheses and characterisation of $M^{tBu}L_O^{Ph}$ (M = Zn, Ni, Cu), which incorporate a non N-donor containing phenyl group within the bridge. A comparison of the electrochemical and spectroelectrochemical properties of $M^{tBu}L_O^{Ph}$ (M = Zn, Ni, Cu) and $M^{tBu}L_O^{Py}$ (M = Ni, Cu) may provide insight into

the role of the pendant pyridyl group as a potential N-donor in controlling the

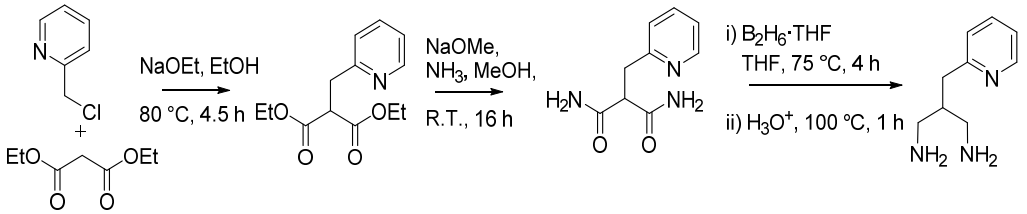


chemistry of $M^{tBu}L_O^{Py}$.

Scheme 4.2.1.1: Synthesis of diphenolate compounds incorporating a pendant bridge $M^{tBu}L_O^R$ (where M = Zn, Ni, Cu; R = Py).[2]

We also describe the syntheses and characterisations of $M^{tBu}L_O^{PyOMe}$ (M = Zn, Ni, Cu) that contain 2,4-dimethyl-5-methoxypyridine as a potential N-donor. We selected this group since 2,4-dimethyl-5-methoxypyridine has previously been shown to coordinate to and stabilise highly oxidised Fe centres employed in C-H bond activation.[8] Previous attempts to isolate $[Ni^{tBu}L_S^{Py}]^+$ as a stable salt have been unsuccessful and we reasoned that a more basic N-donor may provide a route for the isolation of $[Ni^{tBu}L_S^{PyOMe}]^+$ in the solid state.

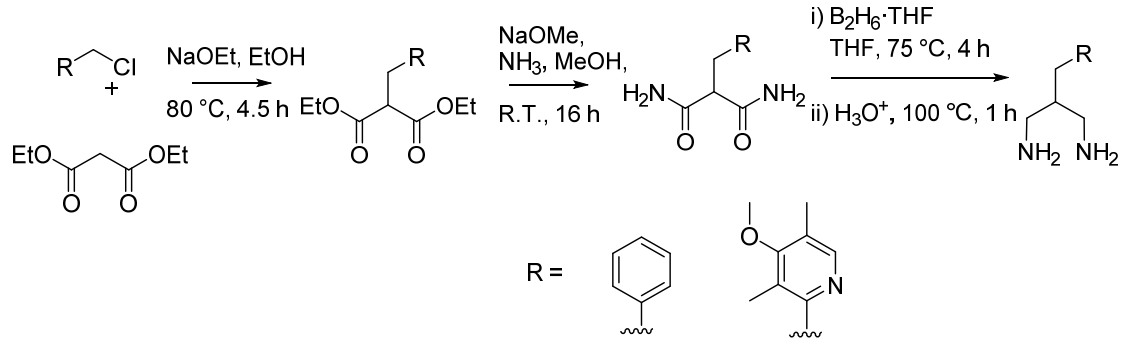
2-(2-Pyridylmethyl)-1,3-propanediamine is synthesised from 2-picolyl chloride, which is coupled to diethylmalonate under basic conditions. The product reacts with ammonia to give (2-pyridylmethyl)-1,3-propanediamide. Reduction of (2-pyridylmethyl)-1,3-propanediamide with borane yields the desired 2-(2-pyridylmethyl)-1,3-propanediamine in overall 27 % yield over three steps (Scheme 4.2.1.2).



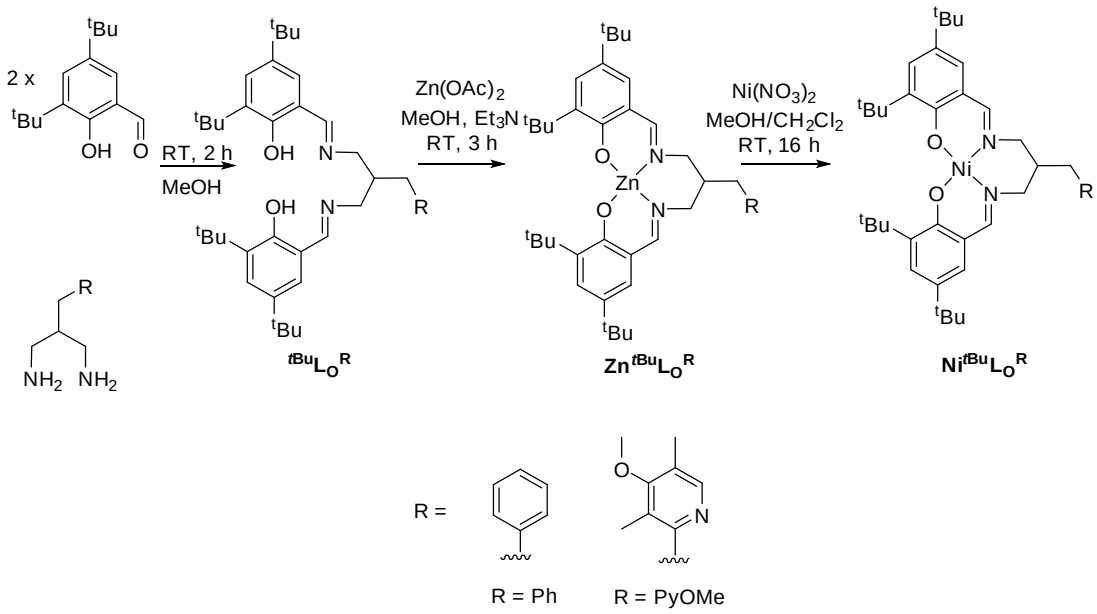
Scheme 4.2.1.2: Synthesis of 2-(2-pyridylmethyl)-1,3-propanediamine precursor.

The substituted pyridyl containing diamine, 2-((4-methoxy-3,5-dimethylpyridin-2-yl)methyl)propane-1,3-diamine, may be synthesised from 2-(chloromethyl)-3,5-dimethyl-4-methoxypyridine using analogous procedures to those used for the unsubstituted analogue, 2-(2-pyridylmethyl)-1,3-propanediamine (Scheme 4.2.1.3). The precursor to $^{t\text{Bu}}L_O^{Ph}$, 2-benzylpropane-1,3-diamine, may be synthesised from benzyl chloride and diethylmalonate (Scheme 4.2.1.3) using the same synthetic methodology employed for 2-(2-pyridylmethyl)-1,3-propanediamine (Scheme 4.2.1.3).[2, 9, 10]

$M^{tBu}L_O^{PyOMe}$ and $M^{tBu}L_O^{Ph}$ (M = Zn, Ni, Cu) may be prepared *via* the formation of the proligands $^{t\text{Bu}}L_O^{PyOMe}$ and $^{t\text{Bu}}L_O^{Ph}$ followed by direct metal complexation (Scheme 4.2.1.4). The synthesis of each proligand proceeded quantitatively to give a yellow oil which was characterised by ^1H and ^{13}C NMR spectroscopies and by mass spectrometry. The proligands were used without further purification and treated with one equivalent of metal salt [$Zn(OAc)_2$/$Ni(NO_3)_2$/$Cu(OAc)_2$] and NaOH in ethanol to give $M^{tBu}L_O^{PyOMe}$ and $M^{tBu}L_O^{Ph}$ (M = Zn, Ni, Cu; Scheme 4.2.1.4).



Scheme 4.2.1.3: Synthesis of 2-((4-methoxy-3,5-dimethylpyridin-2-yl)methyl)propane-1,3-diamine and 2-benzylpropane-1,3-diamine.



Scheme 4.2.1.4: Synthesis of $M^{tBu}L_O^R$ (M = Zn, Ni, Cu; R = Ph, PyOMe).

$Ni^{tBu}L_O^{PyOMe}$ and $Cu^{tBu}L_O^{PyOMe}$ were structurally characterised by X-ray crystallography. Suitable crystals were grown by layering methanol onto a solution of each complex in CH_2Cl_2. $Ni^{tBu}L_O^{PyOMe}$, and $Cu^{tBu}L_O^{PyOMe}$ crystallise in the triclinic space group P-1 with Z' = 1. The structure of $Ni^{tBu}L_O^{PyOMe}$ was treated with the Platon SQUEEZE procedure[11] in order to remove the scattering contribution of several disordered CH_2Cl_2 solvent molecules. The structure of $Cu^{tBu}L_O^{PyOMe}$ exhibits disorder in the region of the substituted pyridine over two orientations (C34-C43, O3, N3; C34A-C43A, O3A, N3A; Figure 4.2.1.2); the occupancies of these orientations were refined competitively converging at a ratio of 0.52:0.48. Further crystallographic experimental details are given in Appendix 2.

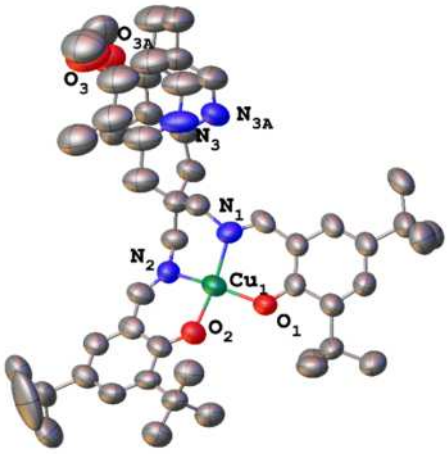


Figure 4.2.2.1: Structure of $Cu^{tBu}L_O^{PyOMe}$ showing disordered pyridine bridge.

The structures of Ni$^{t\text{Bu}}$L$_{O}^{\text{PyOMe}}$ and Cu$^{t\text{Bu}}$L$_{O}^{\text{PyOMe}}$ exhibit distorted square planar geometries around the metal centres, with Cu$^{t\text{Bu}}$L$_{O}^{\text{PyOMe}}$ (with the dihedral angle between N1-Cu-O1 plane and the N2-Cu-O2 plane = 32.7(4) °) possessing a more distorted geometry than Ni$^{t\text{Bu}}$L$_{O}^{\text{PyOMe}}$ (where the dihedral angle between N1-Ni-O1 plane and the N2-Ni-O2 plane =19.9(2) °). The pyridyl N3 nitrogen shows no interaction with the M$^{\text{II}}$ centre in Ni$^{t\text{Bu}}$L$_{O}^{\text{PyOMe}}$, or Cu$^{t\text{Bu}}$L$_{O}^{\text{PyOMe}}$ with the M$^{\text{II}}$ centre and pyridyl N(3) atom being located *ca.* 6 Å from one another in each case.

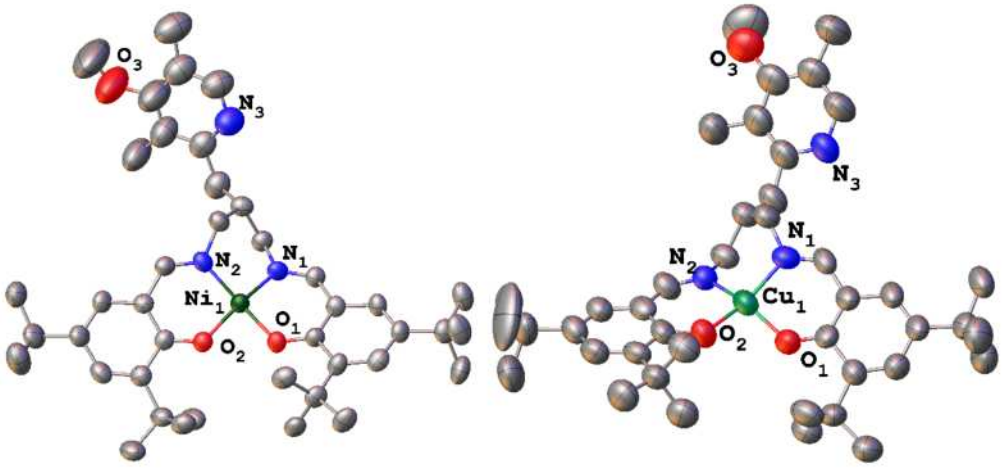


Figure 4.2.1.2: Geometric structures of Ni$^{t\text{Bu}}$L$_{O}^{\text{PyOMe}}$ (left) and Cu$^{t\text{Bu}}$L$_{O}^{\text{PyOMe}}$ (right). H atoms and the disordered component of Cu$^{t\text{Bu}}$L$_{O}^{\text{PyOMe}}$ are omitted for clarity.

	Ni$^{t\text{Bu}}$L$_{O}^{\text{PyOMe}}$	Cu$^{t\text{Bu}}$L$_{O}^{\text{PyOMe}}$
Ni1—O1	1.857(5)	1.931(8)
Ni1—O2	1.845(5)	1.900(6)
Ni1—N1	1.865(6)	1.952(7)
Ni1—N2	1.870(7)	1.998(9)
O1-M-O2	84.5(2)	90.5(3)
N1-M-N2	91.3(3)	92.3(4)
O1-M-N1	93.8(2)	93.6(3)
O1-M-N2	165.2(3)	155.9(4)
O2-M-N1	165.0(3)	156.7(4)
O2-M-N2	94.0(3)	93.2(3)

Table 4.2.1.1: Key bond lengths (Å) and angles (°) for Ni$^{t\text{Bu}}$L$_{O}^{\text{PyOMe}}$ and Cu$^{t\text{Bu}}$L$_{O}^{\text{PyOMe}}$.

These structures can be compared to the structure of Ni(N,N'-bis(3,5-di-$^{t\text{Bu}}$salicylidene)-1,3-propanediamine) which does not incorporate a pendant bridge (bond distances Ni-O1 = Ni-O2 = 1.857(2) Å, Ni-N1 = Ni-N2 = 1.867(2) Å, O1-Ni-N1 = 93.90(9)°, O1-Ni-N2 = 164.07(9)°, O1-Ni-O2 = 84.88(9)°, N1-Ni-N2 = 91.53(11)°),[12] and to the structures of Ni$^{t\text{Bu}}$L$_{O}^{\text{Py}}$ and Cu$^{t\text{Bu}}$L$_{O}^{\text{PyOMe}}$ (Ni$^{t\text{Bu}}$L$_{O}^{\text{Py}}$: Ni-

O1 = Ni-O2 = 1.842(3) Å, Ni-N1 = Ni-N2 = 1.848(4) Å; O1-Ni-N1 = 93.99(17)°, O1-Ni-N2 = 165.46(17)°, O1-Ni-O2 = 84.1(2)°, N1-Ni-N2 = 91.4(3)°; Cu$^{t\text{Bu}}$L$_{\text{O}}^{\text{PyOMe}}$: Cu-O1 = 1.907(4) Å, Cu-O2 = 1.896(4) Å, Cu-N1 = 1.945(5) Å, Cu-N2 = 1.952(5) Å; O1-Cu-N1 93.74(19)°, O2-Cu-N2 93.4(2) °, O1-Cu-N2 156.2(2)°, N1-Cu-O2 156.5(2)°, O1-Cu-O2 90.43(18)°, N1-Cu-N2 92.1(2)°)[2] incorporating a unsubstituted pendant pyridine bridge.

The similarity in the bond lengths and coordination geometries observed between Ni$^{t\text{Bu}}$L$_{\text{O}}^{\text{Py}}$ and Ni$^{t\text{Bu}}$L$_{\text{O}}^{\text{PyOMe}}$ (Ni-O$_{\text{av}}$ = 1.842(3) Å, Ni-N$_{\text{av}}$ = 1.848(4) Å and N1-Ni-O1 plane to N2-Ni-O2 plane angle = 19.6(4)° for Ni$^{t\text{Bu}}$L$_{\text{O}}^{\text{Py}}$; Ni-O$_{\text{av}}$ = 1.851(7); Ni-N$_{\text{av}}$ = 1.868(9) and N1-Ni-O1 plane to N2-Ni-O2 plane angle = 19.9(2)° for Ni$^{t\text{Bu}}$L$_{\text{O}}^{\text{PyOMe}}$) and between Cu$^{t\text{Bu}}L_{\text{O}}^{\text{Py}}$ and Cu$^{t\text{Bu}}$L$_{\text{O}}^{\text{PyOMe}}$ (Cu-O$_{\text{av}}$ = 1.902(6) Å, Cu-N$_{\text{av}}$ = 1.949(7) and N1-Cu-O1 plane to N2-Cu-O2 plane angle = 32.659(6)° for Cu$^{t\text{Bu}}$L$_{\text{O}}^{\text{Py}}$; Cu-O$_{\text{av}}$ = 1.916(10) Cu-N$_{\text{av}}$ = 1.975(11) and Å and N1-Cu-O1 plane to N2-Cu-O2 plane angle = 32.7(4)° for Cu$^{t\text{Bu}}$L$_{\text{O}}^{\text{PyOMe}}$) suggests that the more sterically demanding substituted pyridine does not significantly perturb the coordination geometry of the metal centre.

The solution and frozen solution EPR spectra of Cu$^{t\text{Bu}}$L$_{\text{O}}^{\text{PyOMe}}$ and Cu$^{t\text{Bu}}$L$_{\text{O}}^{\text{Ph}}$ were recorded in CH_2Cl_2/toluene (10:1) and the spectra at 77 K can be simulated with spin Hamiltonian parameters g_{11} = 2.020, g_{22} = 2.052, g_{33} = 2.210, A_{11} = 19 G, A_{22} = 30 G, A_{33} = 193 G for Cu$^{t\text{Bu}}$L$_{\text{O}}^{\text{PyOMe}}$ and g_{11} = 2.020, g_{22} = 2.052, g_{33} = 2.210, a_{11} = 19 G, a_{22} = 30 G, a_{33} = 193 G for Cu$^{t\text{Bu}}$L$_{\text{O}}^{\text{Ph}}$ (Figure 4.3.2.3). These parameters are similar to those for Cu$^{t\text{Bu}}$L$_{\text{O}}^{\text{Py}}$ (g_{11} = 2.038, g_{22} = 2.050, g_{33} = 2.210, a_{xx} = 20 G, a_{yy} = 32 G, a_{zz} = 193 G),[4] and are consistent with four lines arising from a d^9 Cu$^{\text{II}}$ S= ½ complex in a square planar coordination environment with additional superhyperfine splitting observed as a result of an interaction with two ^{14}N (I = 1) donors in the immediate coordination sphere.

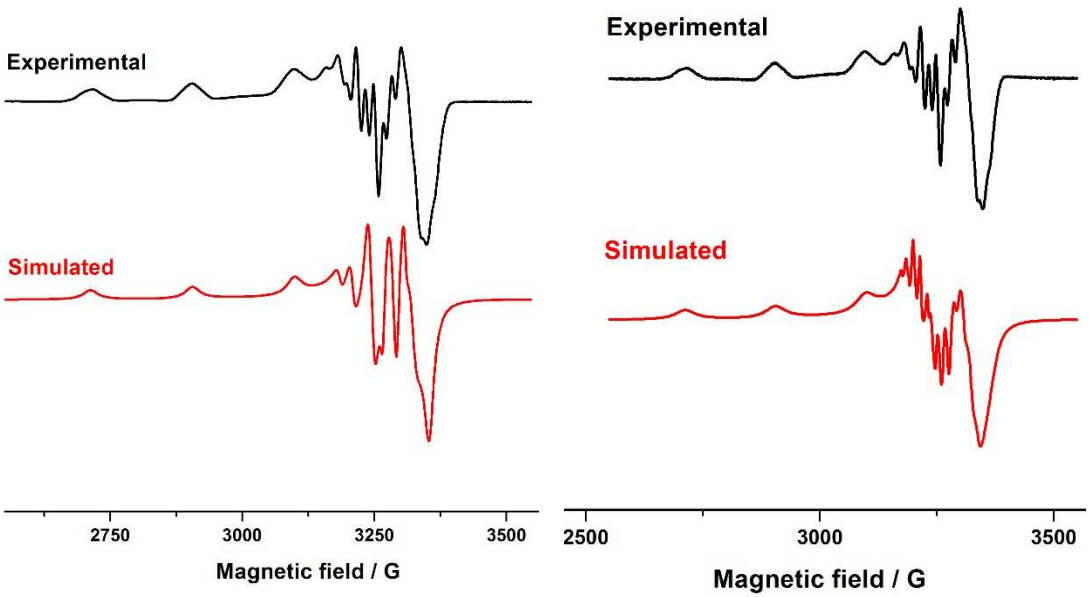
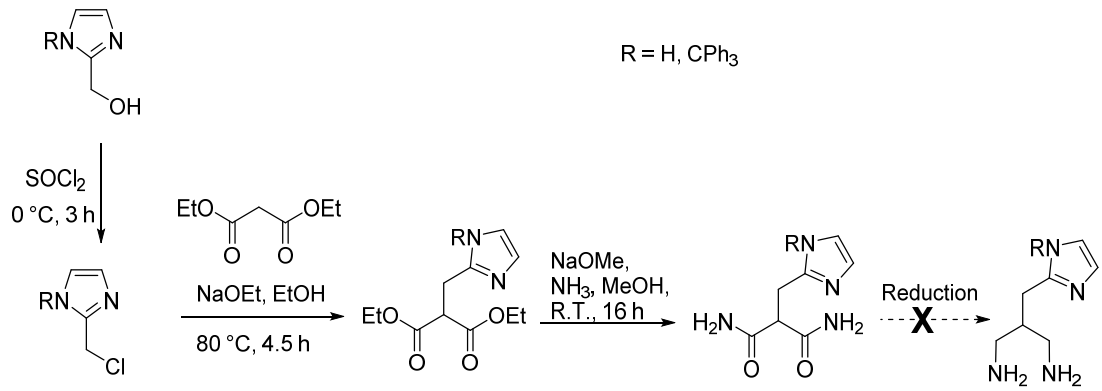


Figure 4.2.1.3: Experimental (black) and simulated (red) fluid (top) and frozen (bottom) X-band EPR spectra of $Cu^{tBu}Lo^{PyOMe}$ (left) and $Cu^{tBu}Lo^{Ph}$ (right). Hamiltonian parameters: $Cu^{tBu}Lo^{PyOMe}$: g_{11} = 2.030, g_{22} = 2.052, g_{33} = 2.210, A_{11} = 32 G, A_{22} = 15 G, A_{33} = 193 G, a_{11} = 15 G, a_{22} = 15 G (2 x ^{14}N =, I = 1), Gaussian linewidths W_{11} = 7 G, W_{22} = 10 G, W_{33} = 20 G; $Cu^{tBu}Lo^{Ph}$: g_{11} = 2.030, g_{22} = 2.052, g_{33} = 2.210, A_{11} = 30 G, A_{22} = 15 G, A_{33} = 193 G, a_{11} = 15 G, a_{22} = 15 G (2 x ^{14}N =, I = 1), Gaussian linewidths W_{11} = 7 G, W_{22} = 5 G, W_{33} = 30 G.

We also attempted to incorporate an imidazole N-donor within the ligand framework in order to more closely replicate the axial histidine N-donor found at the active site of NiSOD. 4(5)-(Hydroxymethyl)imidazole can be converted to chloro methyl imidazole by reaction with thionyl chloride, which allows a similar synthetic strategy to that used for the pyridine containing bridge (Scheme 4.2.1.5) to be investigated. Whilst an imidazole containing diamide can be readily synthesised in an analogous manner to the previous phenyl and pyridyl derivatives, attempts to reduce the diamide to the corresponding diamine proved unsuccessful. We investigated a variety of reaction conditions, with only intractable products found for attempted reduction with B_2H_6, NaH and $LiAlH_4$ as the reducing agent and no reaction with $NaBH_4$ as the reducing agent.



Scheme 4.2.1.5: Attempted syntheses of imidazole containing diamines.

The protection of the imidazole N atom with a trityl group (R = CPh_3) allowed access to the corresponding methanol-tritylimidazole, which could be converted to the chloro species and subsequently the diester and diamide. However, reduction to the corresponding diamine remained unsuccessful.

4.2.2 Electrochemistry of $M^{tBu}L_O^R$ (M = Zn, Ni, Cu; R = Py, Ph, PyOMe)

4.2.2.1 Introduction

The electrochemistries of $M^{tBu}L_O^{Py}$ (M = Ni, Cu) have been investigated previously.[2] $Ni^{tBu}L_O^{Py}$ and $Cu^{tBu}L_O^{Py}$ possess two overlapping oxidation processes at $E_{1/2}$ = 0.37 and 0.44 V, and $E_{1/2}$ = 0.47 and E_p^a = 0.69 V *vs.* Fc^+/Fc, respectively. The overlapping nature of these processes for $Ni^{tBu}L_O^{Py}$ precluded a comprehensive determination of their electrochemical reversibility. In contrast, the increase in separation in potential between the two oxidation processes for $Cu^{tBu}L_O^{Py}$ allowed each process to be investigated separately. The first oxidation process of $Cu^{tBu}L_O^{Py}$ at $E_{1/2}$ = 0.47 V is electrochemically reversible, whilst the second process exhibits an increasing ΔE with scan rate suggesting that this oxidation is not a wholly diffusion controlled process.[2]

UV/vis spectroelectrochemistry demonstrates that the oxidation processes for $Ni^{tBu}L_O^{Py}$ are chemically reversible but those of $Cu^{tBu}L_O^{Py}$ are chemically irreversible.[2] The UV/vis spectrum of $[Ni^{tBu}L_O^{Py}]^{2+}$ suggests the presence of a phenoxyl radical following the two-electron oxidation of $Ni^{tBu}L_O^{Py}$, and EPR spectroscopy of $[Ni^{tBu}L_O^{Py}]^+$ at room temperature reveals a signal with g_{iso} = 2.047, intermediate to that seen for a coordinated phenoxyl radical (g_{av} = 2.005) and a formal Ni^{III} species (g_{av} = 2.13 - 2.17). On cooling, the EPR spectrum at 77 K results in a complex spectrum where the principal features may be simulated with spin Hamiltonian parameters g_{11} = 2.250, g_{22} = 2.204, g_{33} = 2.033, together with splitting in the a_{33} region consistent with an interaction with a ^{14}N (I = 1) donor.[13] These results suggest that $[Ni^{tBu}L_O^{Py}]^+$ may exhibit redox tautomerism with this species shifting towards a more metal centred radical with the coordination of the pyridyl N donor at low temperature.[2]

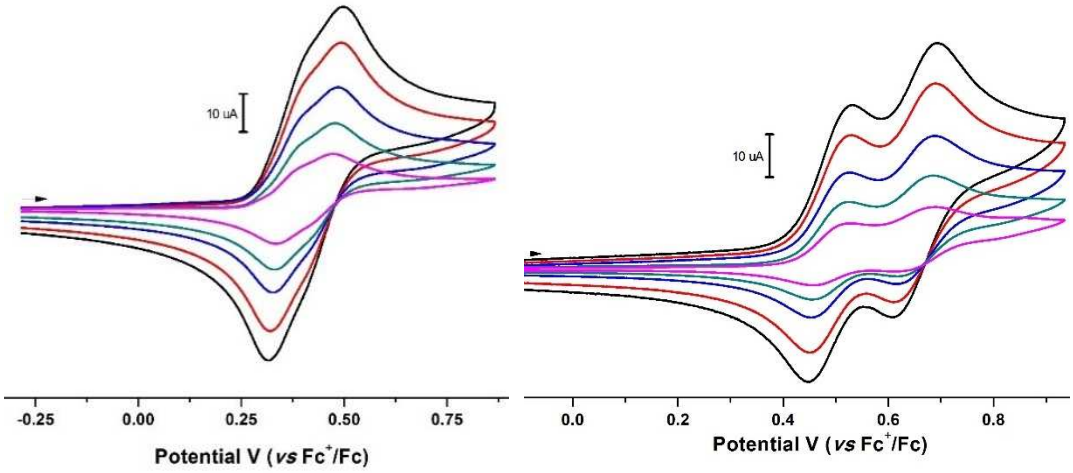


Figure 4.3.2.1.1: Cyclic voltammograms of Ni$^{t\text{Bu}}$LO^{Py} (left) and Cu$^{t\text{Bu}}$LO^{Py} (right).[2]

Electrochemical investigation of M$^{t\text{Bu}}$L$_O^R$ (M = Zn, Ni, Cu; R = Ph, PyOMe) will allow comparison to the results obtained for Ni$^{t\text{Bu}}$L$_O^{Py}$ and Cu$^{t\text{Bu}}$L$_O^{Py}$ to provide further insight into the role of the pendant arm in such complexes.

4.2.2.2 Cyclic Voltammetry of M$^{t\text{Bu}}$L$_O^R$ (M = Zn, Ni, Cu; R = Ph, PyOMe)

The cyclic voltammogram of Zn$^{t\text{Bu}}$L$_O^{Ph}$ exhibits an oxidation process at E_p^a = 0.74 V (*vs.* Fc$^+$/Fc) (Figure 4.2.2.2.1*)*. On close inspection the return wave appears to exhibit two features. The scan rate dependency of the shape of this return wave is consistent with the process being described as an electrochemical oxidation followed by a chemical reaction. Based on this data it is not possible to determine fully the nature of this oxidation process.

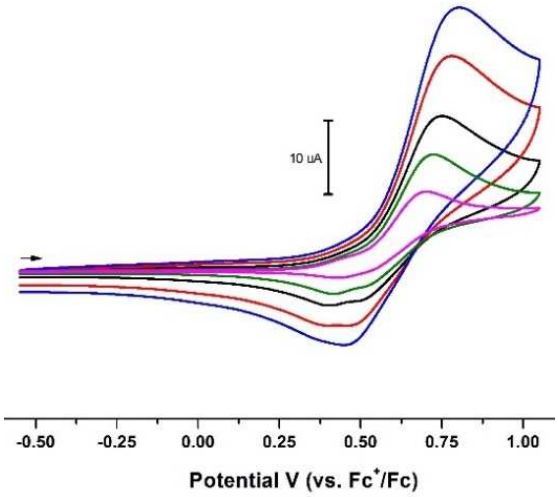
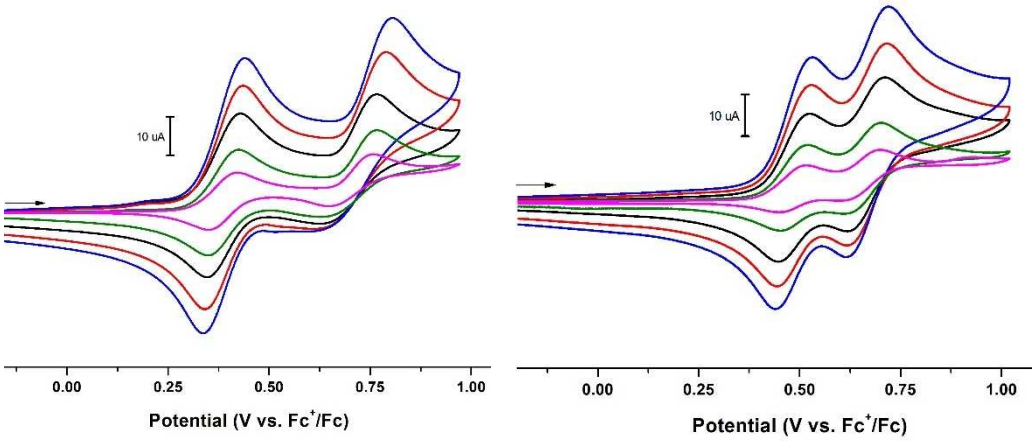


Figure 4.2.2.2.1: Cyclic voltammogram of oxidation processes of Zn$^{t\text{Bu}}$LO^{Ph} at multiple scan rates (300 mV (blue), 200 mV (red), 100 mV (black), 50 mV (green), 20 mV (purple)).

Ni$^{t\text{Bu}}$L$_O$$^{\text{Ph}}$ and Cu$^{t\text{Bu}}$L$_O$$^{\text{Ph}}$ possess two clearly separated oxidation processes (Figure 4.2.2.2.2). The first process at $E_{1/2}$ = 0.39 V (*vs.* Fc^+/Fc) for Ni$^{t\text{Bu}}$L$_O$$^{\text{Ph}}$ is electrochemically reversible over the range of scan rates investigated (20- 300 mVs^{-1}), whilst the second oxidation at E_p^a = 0.76 V (*vs.* Fc^+/Fc) is not reversible. Cu$^{t\text{Bu}}$L$_O$$^{\text{Ph}}$ also exhibits an electrochemically reversible oxidation process at $E_{1/2}$ = 0.48 V (*vs.* Fc^+/Fc), together with an additional process at E_p^a = 0.71 V (*vs.* Fc^+/Fc) for which a return wave develops at faster scan rates.



Complex	$E_{1/2}$ V (vs Fc^+/Fc)	i_p^c µA (100 mV)	i_p^a µA (100 mV)	$\lvert E_p^c - E_p^a \rvert$ mV	$\lvert E_p^c - E_p^a \rvert$ mV (Fc^+/Fc)
Ni$^{t\text{Bu}}$L$_O$$^{\text{Ph}}$	0.39	-16.9	22.9	80	80
Cu$^{t\text{Bu}}$L$_O$$^{\text{Ph}}$	0.48	-19.8	19.7	70	70

Figure 4.2.2.2.2: Cyclic voltammogram of first oxidation process of Ni$^{t\text{Bu}}$L$_O$$^{\text{Ph}}$ (left) and Cu$^{t\text{Bu}}$L$_O$$^{\text{Ph}}$ (right) at multiple scan rates (300 mV (blue), 200 mV (red), 100 mV (black), 50 mV (green), 20 mV (purple)).

Zn$^{t\text{Bu}}$L$_O$$^{\text{PyOMe}}$ possesses an oxidation process at *ca.* 0.5 V (*vs.* Fc^+/Fc) (Figure 4.2.2.2.3). Two return reduction waves (E_p^c = 0.25 and 0.46 V *vs.* Fc^+/Fc) are observed in the cyclic voltammogram.

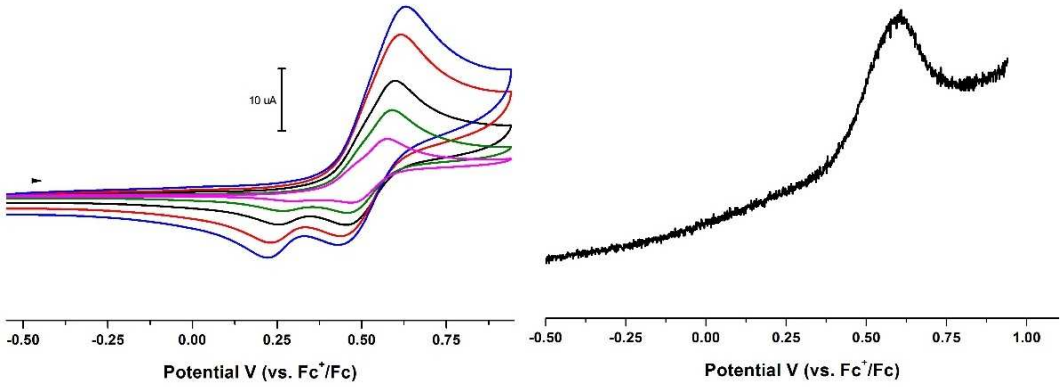


Figure 4.2.2.2.3: Left: Cyclic voltammogram of oxidation processes of $Zn^{tBu}L_O^{PyOMe}$ at multiple scan rates (300 mV (blue), 200 mV (red), 100 mV (black), 50 mV (green), 20 mV (purple)); Right: Square wave voltammogram of $Zn^{tBu}L_O^{PyOMe}$.

Two overlapping oxidation processes are observed for $Ni^{tBu}L_O^{PyOMe}$ and $Cu^{tBu}L_O^{PyOMe}$ at E_p^a = 0.42 and 0.53 V and 0.52 and 0.69 V *vs.* Fc^+/Fc, for $Ni^{tBu}L_O^{PyOMe}$ and $Cu^{tBu}L_O^{PyOMe}$, respectively. The overlapping nature of these processes preludes an accurate determination of i_p^a and i_p^c values, and attempts were made to resolve these processes by square wave voltammetry (Figures 4.2.2.2.4 and 4.2.2.2.5).

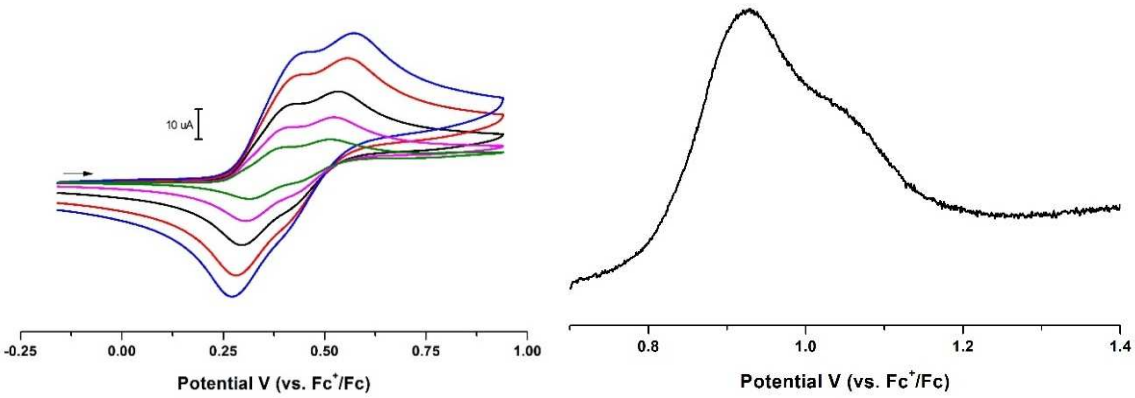


Figure 4.2.2.2.4: Left: Cyclic voltammogram of oxidation processes of $Ni^{tBu}L_O^{PyOMe}$ at multiple scan rates (300 mV (blue), 200 mV (red), 100 mV (black), 50 mV (green), 20 mV (purple)); Right: Square wave voltammogram of $Ni^{tBu}L_O^{PyOMe}$.

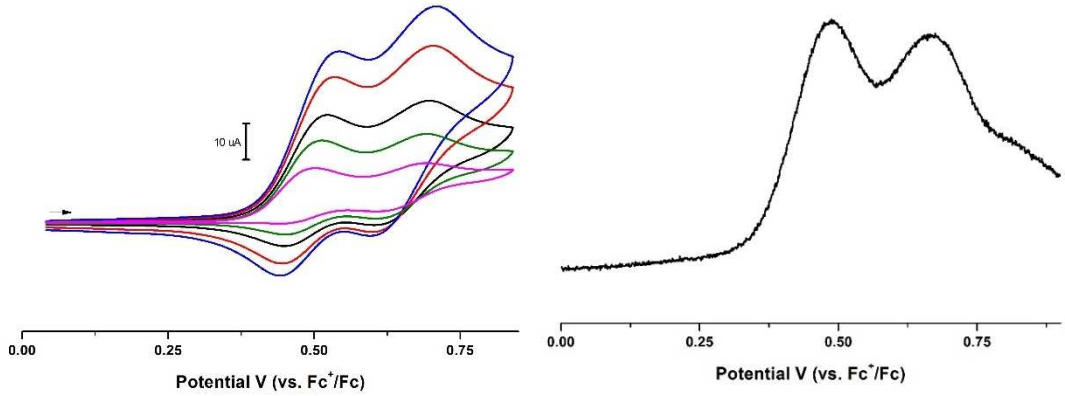


Figure 4.2.2.2.5: Left: Cyclic voltammogram of oxidation processes of $Cu^{tBu}L_O^{PyOMe}$ *at multiple scan rates (300 mV (blue), 200 mV (red), 100 mV (black), 50 mV (green), 20 mV (purple)); Right: Square wave voltammogram of* $Cu^{tBu}L_O^{PyOMe}$.

4.2.2.3 Spectroelectrochemistry of $Ni^{tBu}L_O^{Ph}$

The UV/Vis spectrum of $Ni^{tBu}L_O^{Ph}$ exhibits an intense absorption band at 271 nm (ε = 55,646 mol^{-1} dm^3 cm^{-1}) with a shoulder at 253 nm (ε = 45,078 mol^{-1} dm^3 cm^{-1}) and weaker absorption bands at 357 and 427 nm (ε = 8,090 and 6,717 mol^{-1} dm^3 cm^{-1}). Oxidation at 1.20 V *vs.* Ag/AgCl is accompanied by an increase in the intensity of the band at 271 nm (ε = 68,900 mol^{-1} dm^3 cm^{-1}) and as the oxidation process proceeds this band decreases in intensity (ε = 29,900 mol^{-1} dm^3 cm^{-1}). The bands at 357 and 427 nm also decrease in intensity to leave a single band centred at 394 nm (ε = 5,100 mol^{-1} dm^3 cm^{-1}). This multi-component change suggests that multiple processes may be involved in the oxidation process. Re-reduction of the solution did not regenerate the UV/vis spectrum of $Ni^{tBu}L_O^{Ph}$, even after the application of a significant over-potential (-0.5 V *vs.* Ag/AgCl) (Figure 4.2.2.3.1 inset).

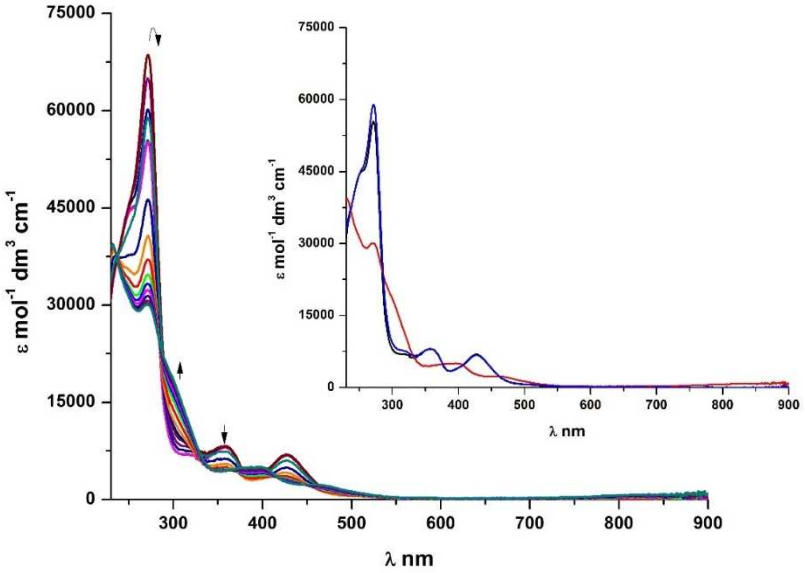


Figure 4.2.2.3.1: Sequential UV/vis spectra recorded during the oxidation of $Ni^{tBu}L_O^{Ph}$ at 1.20 V vs. Ag/AgCl identifying the bands formed during oxidation. 0.38 mmol solution recorded at 253 K under N_2 in CH_2Cl_2 containing 0.4 M $[N^nBu_4][BF_4]$ as supporting electrolyte. Inset, spectra before oxidation (black), after oxidation (red) and after re-reduction (blue).

4.2.2.2 Controlled Potential Electrolysis of $Ni^{tBu}L_O^{Ph}$

The nature of the species generated by controlled potential electrolysis of a solution of $Ni^{tBu}L_O^{Ph}$ at 0.33 V (*vs.* Fc^+/Fc) after a charge equivalent to one electron had been removed (Figure 4.2.2.4.1) was studied by EPR spectroscopy.

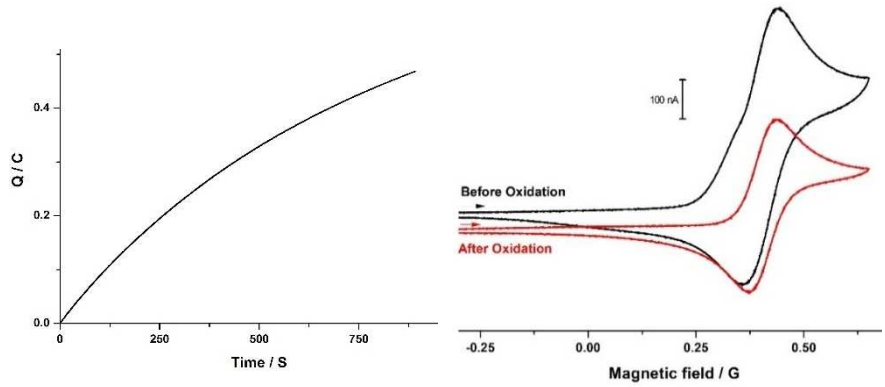


Figure 4.2.2.4.1: Left: Controlled potential electrolysis of $Ni^{tBu}L_O^{Ph}$ to $[Ni^{tBu}L_O^{Ph}]^+$ at 0.33 V vs. Fc^+/Fc, 1 mmol solution in CH_2Cl_2 containing 0.4 M $[N^nBu_4][BF_4]$ as supporting electrolyte recorded at 253 K under Ar. Theoretical Q for a one electron process = 0.48 C; Right: Cyclic voltammograms of $Ni^{tBu}L_O^{Ph}$ (black) before oxidation and $[Ni^{tBu}L_O^{Ph}]^+$ (red) after oxidation, recorded at 100 mV, 1 mmol solution in CH_2Cl_2 containing 0.4 M $[N^nBu_4][BF_4]$ as supporting electrolyte.

The fluid solution EPR spectrum at 298 K of the one electron oxidised product possesses an isotropic signal with g_{iso} = 2.047 (Figure 4.2.2.4.2 left). The spectrum of the frozen solution at 77 K can be simulated with Hamiltonian parameters g_{11} = 2.1520, g_{22} = 2.0175, g_{33} = 1.9985 (Figure 4.2.2.4.2 right). The high g-anisotropy associated with this spectrum is consistent with the generation of a species with significant Ni^{III} character.

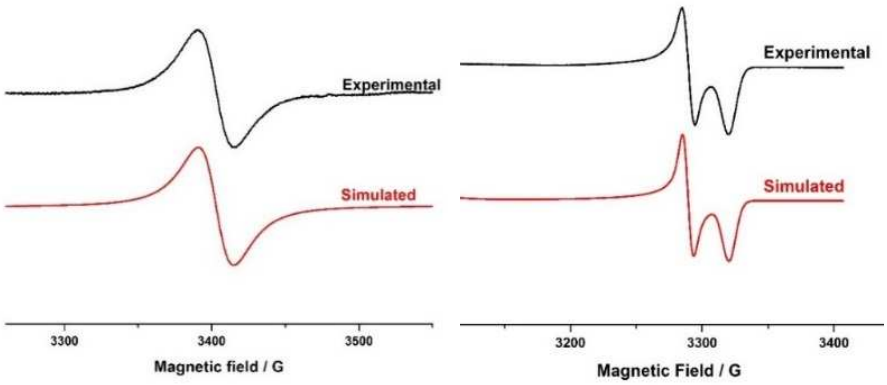


Figure 4.2.2.4.2: Left: (Black) X-band CW EPR spectra of electrochemically generated $[Ni^{tBu}L_O^{Ph}]^+$ in CH_2Cl_2 containing 0.4 M $[N^nBu_4][BF_4]$ as supporting electrolyte as a fluid solution at room temperature, (Red) Simulated spectra – spin Hamiltonian parameters: g = 2.047 Lorentzian linewidth W = 23 G; Right: (Black) X-band CW EPR spectra of electrochemically generated $[Ni^{tBu}L_O^{Ph}]^+$ in CH_2Cl_2 containing 0.4 M $[N^nBu_4][BF_4]$ as supporting electrolyte as a frozen solution at 77 K, (Red) Simulated spectra – spin Hamiltonian parameters: g_{11} = 2.1520, g_{22} = 2.0175, g_{33} = 1.9985, Gaussian linewidths W_{11} = 55 G, W_{22} = 6.5 G, W_{33} = 10 G.

4.2.2.5 Spectroelectrochemistry of $Cu^{tBu}L_O^{Ph}$

$Cu^{tBu}L_O^{Ph}$ possesses UV/vis absorption bands at 240 nm (ε = 45,900 mol^{-1} dm^3 cm^{-1}), 278 nm (ε = 28,000 mol^{-1} dm^3 cm^{-1}), and 382 nm (ε = 11,800 mol^{-1} dm^3 cm^{-1}) with additional shoulders at 249 nm (ε = 42,800 mol^{-1} dm^3 cm^{-1}) and 310 nm (ε = 10,600 mol^{-1} dm^3 cm^{-1}). Oxidation at 1.17 V *vs* Ag/AgCl is accompanied by similar changes in the UV/vis spectrum to those seen for the oxidation of $Ni^{tBu}L_O^{Ph}$ (Section 4.2.3.1) with an initial increase in intensity of the high energy bands at 240 and 278 nm to ε = 46,500 and 46,100 mol^{-1} dm^3 cm^{-1}, respectively. This is followed by a decrease in the intensity of these bands to ε = 42,100 and 32,500 mol^{-1} dm^3 cm^{-1} respectively, and a decrease in the intensity of the band at 382 nm (ε = 6,600 mol^{-1} dm^3 cm^{-1}). The multi-component nature of the changes observed again suggests that two processes may accompany the oxidation of $Cu^{tBu}L_O^{Ph}$. The

re-reduction of the oxidised species did not regenerate the UV/vis spectrum of Cu$^{t\text{Bu}}$L$_O^{\text{Ph}}$ (Figure 4.2.2.5.1 inset), indicating that this oxidation process is not chemically reversible.

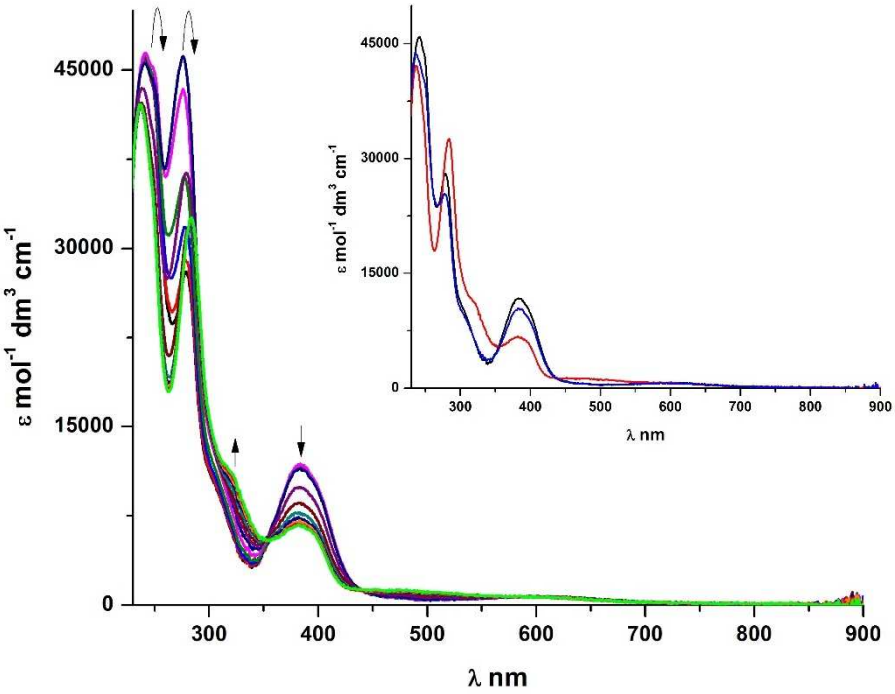


Figure 4.2.2.5.1: Sequential UV/vis spectra recorded during the oxidation of Cu$^{t\text{Bu}}$L$_O^{\text{Ph}}$ identifying the bands formed during oxidation. 0.25 mmol solution recorded at 253 K under N_2 in CH_2Cl_2 containing 0.4 M [N^nBu_4][BF_4] as supporting electrolyte. Inset, spectra before oxidation (black), after oxidation (red) and after re-reduction (blue).

4.2.2.6 Spectroelectrochemistry of Ni$^{t\text{Bu}}$L$_O^{\text{PyOMe}}$

The UV/vis spectrum of Ni$^{t\text{Bu}}$L$_O^{\text{PyOMe}}$ possesses three absorption bands at 272, 358 and 428 nm (ε = 23,500, 3,400 and 2,900 mol^{-1} dm^3 cm^{-1}) with an additional shoulder at 253 nm (ε = 19,300 mol^{-1} dm^3 cm^{-1}). On oxidation at 1.40 V *vs.* Ag/AgCl the development of two new bands is observed at 391 and 422 nm (ε = 3,147 and 3,991 mol^{-1} dm^3 cm^{-1}), together with a shift of the highest energy band to 236 nm (ε = 21,233 mol^{-1} dm^3 cm^{-1}). Re-reduction essentially regenerates the UV/vis spectrum of Ni$^{t\text{Bu}}$L$_O^{\text{PyOMe}}$ suggesting that the oxidation of Ni$^{t\text{Bu}}$L$_O^{\text{PyOMe}}$ at 1.40 V *vs.* Ag/AgCL is essentially chemically reversible.

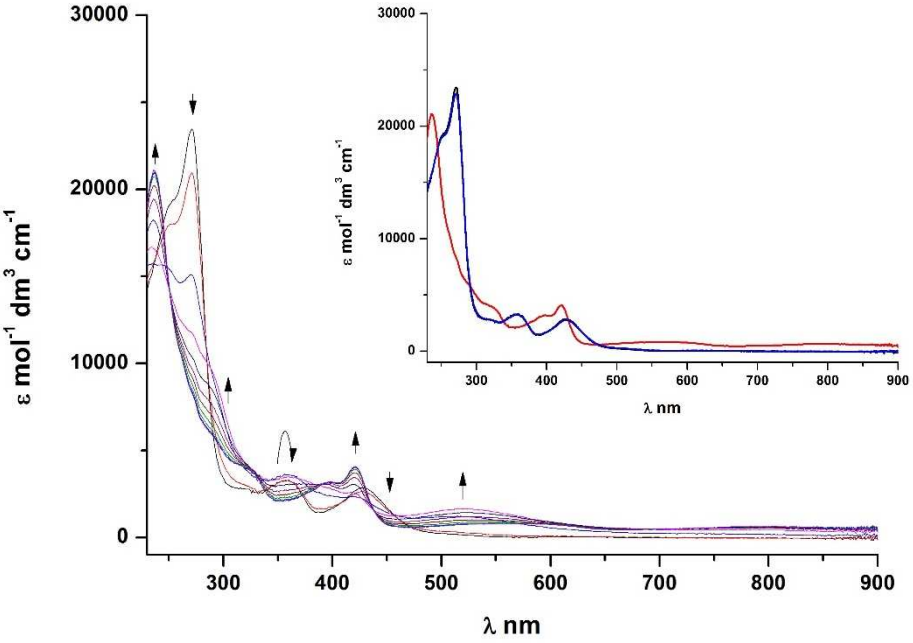


Figure 4.2.2.6.1: Sequential UV/vis spectra recorded during the oxidation of $Ni^{tBu}L_O^{PyOMe}$ at 1.40 V vs. Ag/AgCl identifying the bands formed during oxidation. 0.82 mmol solution recorded at 253 K under N_2 in CH_2Cl_2 containing 0.4 M $[N^nBu_4][BF_4]$ as supporting electrolyte. Inset, spectra before oxidation (black), after oxidation (red) and after re-reduction (blue).

4.2.2.7 Controlled Potential Electrolysis of $Ni^{tBu}L_O^{PyOMe}$

Given the reversible nature of the spectroelectrochemical experiments on $Ni^{tBu}L_O^{PyOMe}$ we attempted to oxidise a solution of $Ni^{tBu}L_O^{PyOMe}$ by one electron using controlled potential electrolysis at 0.68 V *vs.* Fc^+/Fc until a total charge equivalent to one electron had been removed (Q = 0.66). There is little change in the cyclic voltammograms recorded using a platinum wire working electrode before and after electrolysis (Figure 4.2.2.7.1), consistent with the cyclic voltammetric (Section 4.2.2) and spectroelectrochemical (Section 4.2.3.4) experiments which suggest that the product of the oxidation of $Ni^{tBu}L_O^{PyOMe}$ is stable on the timescale of the experiments.

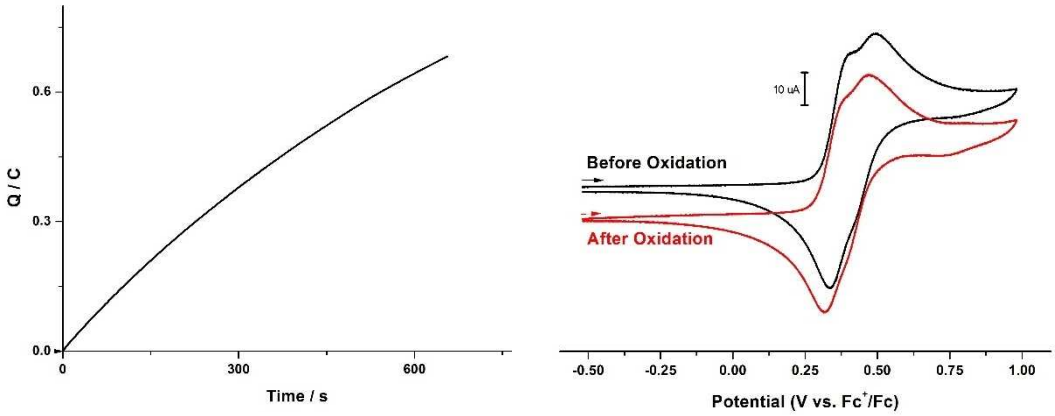


Figure 4.2.2.7.1: Left: Controlled potential electrolysis of $Ni^{tBu}L_O^{PyOMe}$ to $[Ni^{tBu}L_O^{PyOMe}]^+$ at 0.48 V vs. Fc^+/Fc, 1 mmol solution in CH_2Cl_2 containing 0.4 M $[N^nBu_4][BF_4]$ as supporting electrolyte recorded at 253 K under Ar. Theoretical Q for a one electron process = 0.66 C; Right: Cyclic voltammograms of $Ni^{tBu}L_O^{PyOMe}$ (black) before oxidation and $[Ni^{tBu}L_O^{PyOMe}]^+$ (red) after oxidation, recorded at 100 mV, 1 mmol solution in CH_2Cl_2 containing 0.4 M $[N^nBu_4][BF_4]$ as supporting electrolyte.

The product of the one electron oxidation of a solution of $Ni^{tBu}L_O^{PyOMe}$ was investigated using EPR spectroscopy. The frozen solution EPR spectrum at 77 K is rhombic with high g anisotropy (Figure 4.2.2.7.2) and can be simulated with the spin Hamiltonian parameters g_{11} = 2.2490, g_{22} = 2.2020, g_{33} = 2.0325, a_{22} = 17 G, a_{33} = 24 G. These parameters are consistent with the spin density being principally localised on the metal centre as a formal Ni^{III}-phenolate species. Superhyperfine splitting is observed consistent with the binding of the substituted pyridyl N-donor to the Ni^{III} centre. The frozen solution EPR spectrum of $[Ni^{tBu}L_O^{PyOMe}]^+$ spectrum is similar to that of the spectrum of $[Ni^{tBu}L_O^{Py}]^+$ (g_{11} = 2.250, g_{22} = 2.204, g_{33} = 2.033) and suggests that the introduction of dimethylmethoxypyridine does not significantly perturb the electronic structure of the oxidation product when compared to that resulting from the oxidation of $Ni^{tBu}L_O^{Py}$.[2]

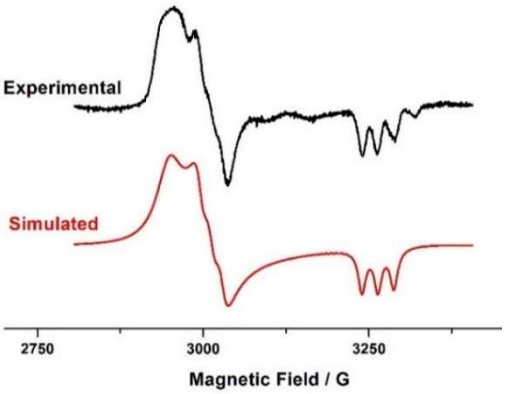


Figure 4.2.2.7.2: (Black) X-band CW EPR spectra of electrochemically generated $[Ni^{tBu}L_O^{PyOMe}]^+$ in CH_2Cl_2 containing 0.4 M $[N^nBu_4][BF_4]$ as supporting electrolyte as a frozen solution at 77 K, (Red) Simulated spectra – spin Hamiltonian parameters: g_{11} = 2.2490, g_{22} = 2.2020, g_{33} = 2.0325, a_{22} = 17 G, a_{33} = 24 G, Gaussian linewidths W_{11} = 28 G, W_{22} = 13 G, W_{33} = 8 G.

4.2.2.8 Spectroelectrochemistry of $Cu^{tBu}L_O^{PyOMe}$

The UV/Vis spectrum of $Cu^{tBu}L_O^{PyOMe}$ exhibits absorption bands at 241, 278 and 384 nm (ε = 48,000, 28,500 and 12,100 mol^{-1} dm^3 cm^{-1}). Oxidation at 1.40 V *vs.* Ag/AgCl results in a loss of the higher energy bands at 278 and 384 nm and the appearance of new absorption bands at 297 and 442 nm (ε = 19,300 and 8,300 mol^{-1} dm^3 cm^{-1}). Re-reduction does not regenerate the original UV/vis spectral profile of $Cu^{tBu}L_O^{PyOMe}$.

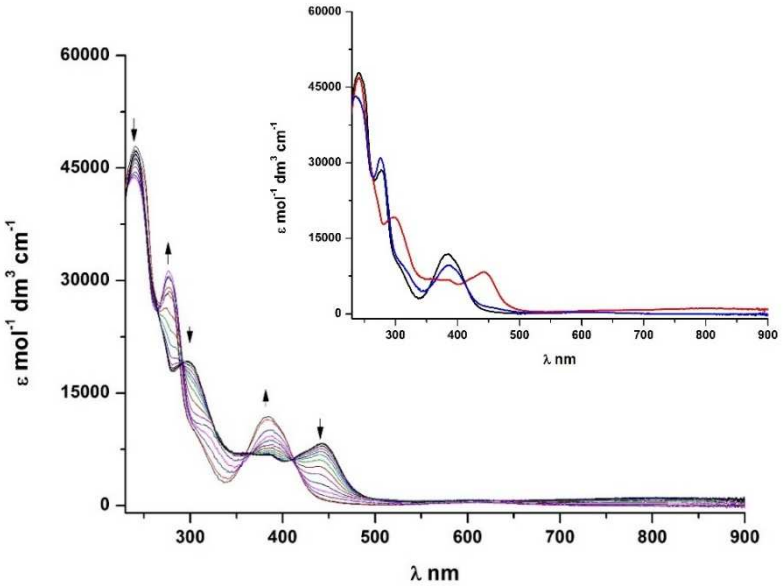


Figure 4.2.2.8.1: Sequential UV/vis spectra recorded during the oxidation of $Cu^{tBu}L_O^{PyOMe}$ at 1.40 V vs. Ag/AgCl identifying the bands formed during oxidation. 0.37 mmol solution recorded at 253 K under N_2 in CH_2Cl_2 containing 0.4 M $[N^nBu_4][BF_4]$ as supporting electrolyte. Inset, spectra before oxidation (black), after oxidation (red) and after re-reduction (blue).

4.2.3 Discussion

The cyclic voltammograms of $M^{tBu}L_O^R$ (M = Ni, Cu; R = Py, PyOMe, Ph) are compared in Figure 4.2.3.1 and reveal the influence of the nature of the pendant group attached to the backbone of the salen-type ligand framework on the electrochemical properties of $M^{tBu}L_O^R$ (M = Ni, Cu; R = Py, PyOMe, Ph). For $Ni^{tBu}L_O^R$ (R = Py, PyOMe, Ph) while there is little change in reduction potential for the first oxidation process between $Ni^{tBu}L_O^{PyOMe}$ and $Ni^{tBu}L_O^{Py}$ (0.01 V), there is a larger shift (0.03 V) to more positive potential for $Ni^{tBu}L_O^{Ph}$. This suggests that ligands incorporating a pendant pyridyl substituent stabilise the products of oxidation of $Ni^{tBu}L_O^{PyOMe}$ and $Ni^{tBu}L_O^{Py}$. There are no significant shifts in potential for the first and second oxidation processes of $Cu^{tBu}L_O^{PyOMe}$, $Cu^{tBu}L_O^{PyOMe}$ and $Cu^{tBu}L_O^{Ph}$.

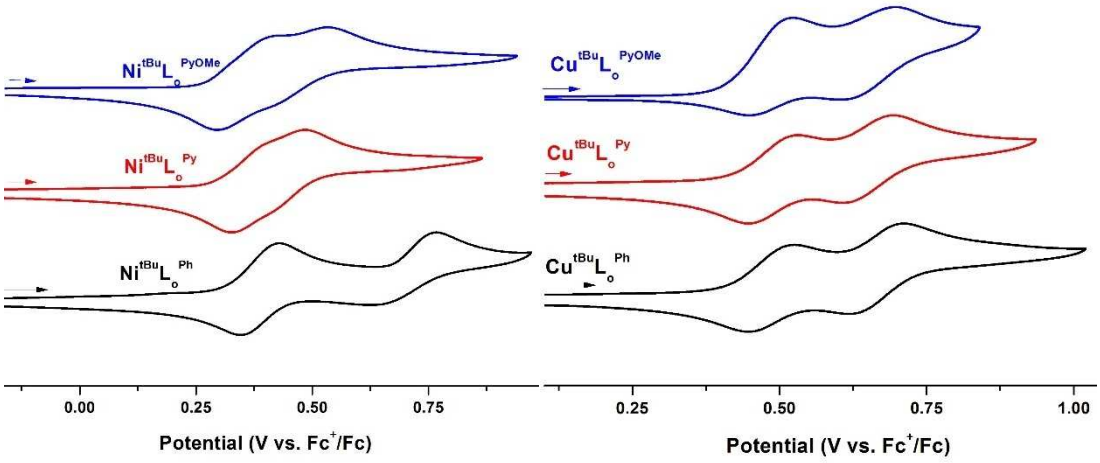


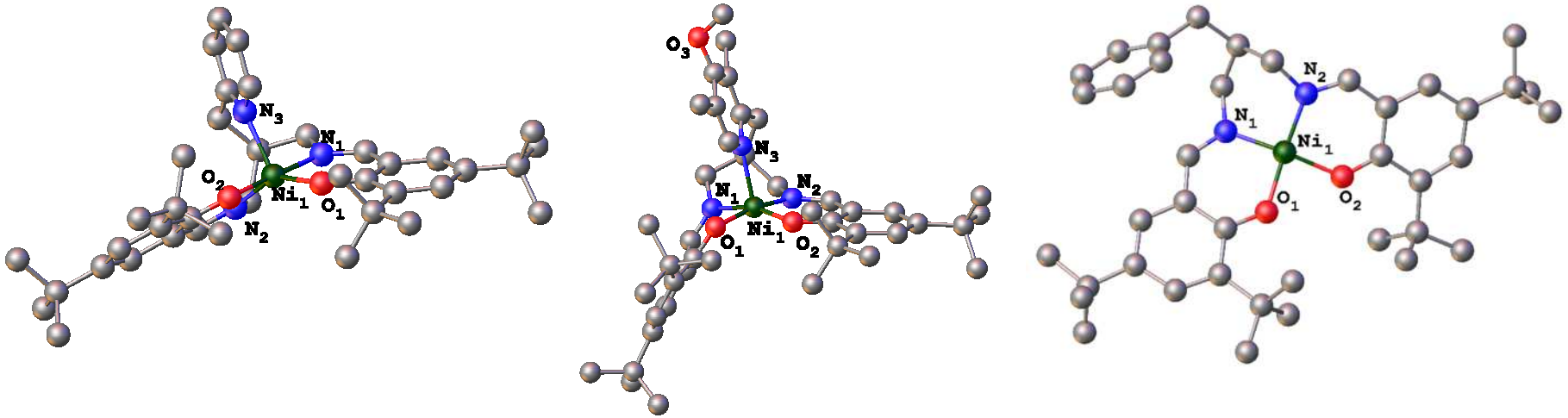
Figure 4.2.3.1: Left: Comparison of oxidation processes for $Ni^{tBu}L_O^{PyOMe}$, $Ni^{tBu}L_O^{Py}$ and $Ni^{tBu}L_O^{Ph}$; Right: Comparison of oxidation processes for $Cu^{tBu}L_O^{PyOMe}$, $Cu^{tBu}L_O^{PyOMe}$ and $Cu^{tBu}L_O^{Ph}$; All recorded at 100 mV.

$M^{tBu}L_O^R$ (M = Ni, Cu; R = Ph, PyOMe) exhibit broadly similar UV/Vis spectra with intense absorptions at high energy (*ca.* 270 nm for M = Ni and 240 and 280 nm for M = Cu) which may be assigned to phenoxide $\pi \rightarrow \pi^*$ transitions as found for $M^{tBu}L_O^{NMe}$ (M = Zn, Ni, Cu; Chapter 3), together with lower energy bands which are assigned to LMCT transitions similar to those reported for other Ni(N_2O_2) complexes including Ni(salpd) (salpd = bis-(salicyaldehyde)-ethylenediimine.[2, 14, 15] The appearance of a new absorption band at 422 nm

following the oxidation of Ni$^{t\text{Bu}}$L$_{\text{O}}^{\text{PyOMe}}$ is consistent with the formation of phenoxyl radical species as found for M$^{t\text{Bu}}$L$_{\text{O}}^{\text{NMe}}$ (M = Zn, Ni, Cu; Chapter 3), and in Ni(L$^{\text{BZ}}$) (L$^{\text{BZ}}$ = 1,2-bis(3,5-di^{t}butyl-2-hydroxybenzimino)benzene; λ = 375, 417, 445, 544 and 918 nm, ε = 9,620, 9,900, 10,000, 3,060, 2,900 mol^{-1} dm^{3} cm^{-1}).[15] However, the absence of chemical reversibility for the oxidation and re-reduction of Cu$^{t\text{Bu}}$L$_{\text{O}}^{\text{PyOMe}}$ precludes any definitive conclusion about the nature of this oxidation process being made.

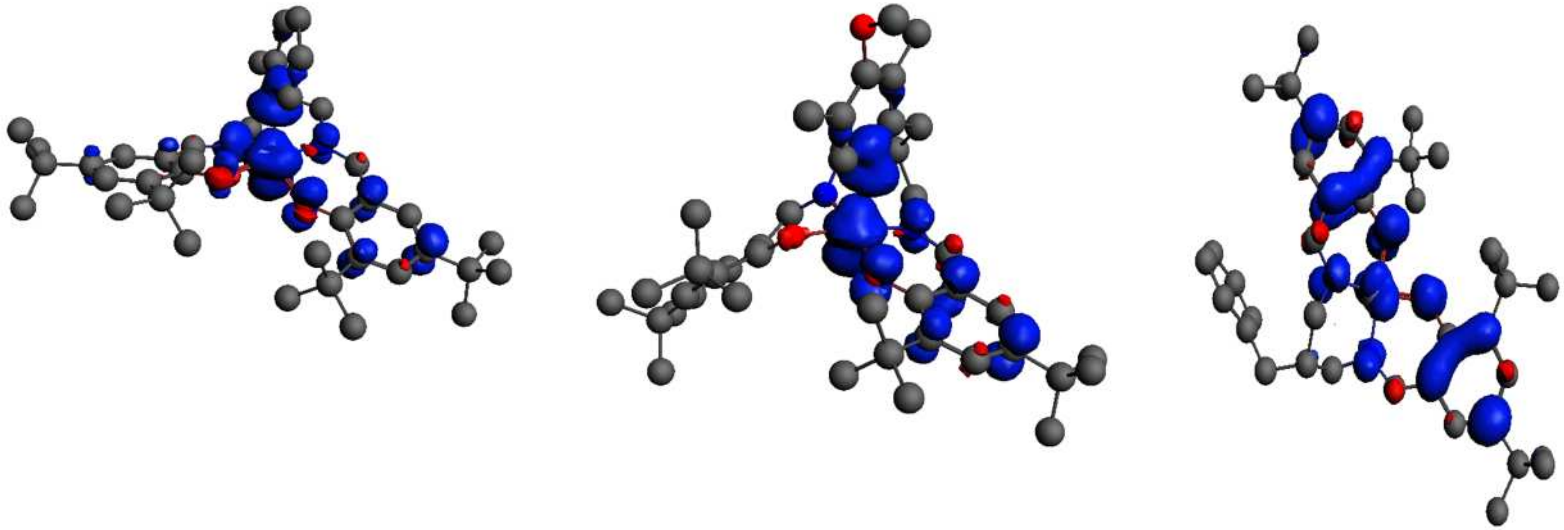
The results for Ni$^{t\text{Bu}}$L$_{\text{O}}^{\text{Ph}}$ and Cu$^{t\text{Bu}}$L$_{\text{O}}^{\text{Ph}}$ are also less conclusive and clear evidence for the formation of a phenoxyl radical is not seen. The apparent multicomponent nature of the spectral change suggests intermediates are present for the oxidation processes, and this combined with the absence of chemical reversibility precludes any significant conclusions being drawn based on this data.

We have employed DFT calculations to provide insight into the electronic structures of [Ni$^{t\text{Bu}}$L$_{\text{O}}^{\text{Ph}}$]$^{+}$, [Ni$^{t\text{Bu}}$L$_{\text{O}}^{\text{PyOMe}}$]$^{+}$ and [Ni$^{t\text{Bu}}$L$_{\text{O}}^{\text{Py}}$]$^{+}$. Models derived from the X-ray crystal structures of Ni$^{t\text{Bu}}$L$_{\text{O}}^{\text{PyOMe}}$ and Ni$^{t\text{Bu}}$L$_{\text{O}}^{\text{Py}}$ were used in the gas phase geometry optimisations, and in the absence of an X-ray crystal structure of Ni$^{t\text{Bu}}$L$_{\text{O}}^{\text{Ph}}$, a model for [Ni$^{t\text{Bu}}$L$_{\text{O}}^{\text{Ph}}$]$^{+}$was constructed based on the model of [Ni$^{t\text{Bu}}$L$_{\text{O}}^{\text{Py}}$]$^{+}$. Calculations of the vibrational frequencies were used as a tool to verify that an energy minimum was reached in the unrestricted gas-phase geometry optimisations [Ni$^{t\text{Bu}}$L$_{\text{O}}^{\text{Ph}}$]$^{+}$, [Ni$^{t\text{Bu}}$L$_{\text{O}}^{\text{PyOMe}}$]$^{+}$ and [Ni$^{t\text{Bu}}$L$_{\text{O}}^{\text{Py}}$]$^{+}$. The gas-phase structures were used as models in single point calculations where the effects of solvation by CH_2Cl_2 on the electronic structure were modelled using the COSMO conductor-like screening model.[16]



	$[Ni^{tBu}L_O^{Py}]^+$	$[Ni^{tBu}L_O^{PyOMe}]^+$	$[Ni^{tBu}L_O^{Ph}]^+$		$[Ni^{tBu}L_O^{Py}]^+$	$[Ni^{tBu}L_O^{PyOMe}]^+$	$[Ni^{tBu}L_O^{Ph}]^+$
Ni_1-N_1	1.979	1.899	1.850	Ni_1-O_1	2.043	1.933	1.848
Ni_1-N_2	2.031	1.899	1.858	Ni_1-O_2	1.980	1.875	1.849
Ni_1-N_3	2.047	2.158	---				
O_1-Ni_1-O_2	84.60	86.02	85.66	O_2-Ni_1-N_2	89.92	93.39	94.27
O_1-Ni_1-N_1	90.19	86.48	94.30	O_2-Ni_1-N_3	114.98	103.25	---
O_1-Ni_1-N_2	174.50	168.77	159.77	N_1-Ni_1-N_2	94.53	91.05	92.81
O_1-Ni_1-N_3	93.87	92.19	---	N_1-Ni_1-N_3	99.41	92.02	---
O_2-Ni_1-N_1	145.46	163.22	159.22	N_2-Ni_1-N_3	88.14	98.85	---

Figure 4.2.3.2 and Table 4.2.3.1: Gas phase geometry optimised DFT derived structures of $[Ni^{tBu}L_O^{Py}]^+$ (left), $[Ni^{tBu}L_O^{PyOMe}]^+$ (centre) and $[Ni^{tBu}L_O^{Ph}]^+$ (right).



Atom	$[Ni^{tBu}L_O^{Py}]^+$ Spin Density (%)	$[Ni^{tBu}L_O^{PyOMe}]^+$ Spin Density (%)	$[Ni^{tBu}L_O^{Ph}]^+$ Spin Density (%)
Ni	0.680	0.630	0.282
O1	0.041	0.076	0.117
O2	-0.014	-0.007	0.121
$N1_{(imine)}$	0.020	0.032	0.040
$N2_{(imine)}$	0.041	0.032	0.045
$N3_{(pyridyl)}$	0.125	0.144	--

Figure 4.2.3.3 and Table 4.2.3.2: Spin density isosurfaces at the 0.001 eBohr^{-3} level of $[Ni^{tBu}L_O^{Py}]^+$ (left) and $[Ni^{tBu}L_O^{PyOMe}]^+$ (centre) and $[Ni^{tBu}L_O^{Ph}]^+$ (right).

The gas-phase DFT-derived geometries show that the pendant pyridyl N-donor coordinates to the Ni^{III} centre in $[Ni^{tBu}L_O^{PyOMe}]^+$ and $[Ni^{tBu}L_O^{Py}]^+$ (Figure 4.2.3.2). The gas-phase geometries of these species are significantly different; $[Ni^{tBu}L_O^{PyOMe}]^+$ adopts an essentially square based pyramidal geometry ($\tau = 0.09$) whilst $[Ni^{tBu}L_O^{Py}]^+$ adopts a more distorted conformation towards a trigonal bipyramidal geometry ($\tau = 0.48$). In spite of this difference in geometry the electronic structures, as reported by the spin density, are remarkably similar. Thus, the spin density in both $[Ni^{tBu}L_O^{PyOMe}]^+$ and $[Ni^{tBu}L_O^{Py}]^+$ is predominantly localised on the Ni centre (0.680 and 0.630 respectively), as would be expected for a formal Ni^{III} species with significant spin density localised on the pyridyl N-donor atom (Table 4.2.3.2).

The gas phase geometry optimised structure of $[Ni^{tBu}L_O^{Ph}]^+$ possesses a distorted square planar geometry (Figure 4.2.3.2). In addition, the spin density distribution for $[Ni^{tBu}L_O^{Ph}]^+$ is markedly different to that in $[Ni^{tBu}L_O^{PyOMe}]^+$ and $[Ni^{tBu}L_O^{Py}]^+$ with a spin density of 0.282 localised on the Ni centre and significantly more spin localised on the phenolate O donors (0.17 and 0.121) (Figure 4.2.3.3). These results suggest that, whilst the oxidation of $Ni^{tBu}L_O^{Ph}$ possesses some metal character, it is significantly less than that found for $[Ni^{tBu}L_O^{PyOMe}]^+$ and $[Ni^{tBu}L_O^{Py}]^+$. This is consistent with the EPR spectrum of $[Ni^{tBu}L_O^{Ph}]^+$ which although exhibiting high g anisotropy typical of a Ni^{III} species, does have an average g value ($g_{av} = 2.06$) which is significantly lower than those observed for $[Ni^{tBu}L_O^{PyOMe}]^+$ and $[Ni^{tBu}L_O^{Py}]^+$ ($g_{av} = 2.16$ and 2.16),[2] consistent with $[Ni^{tBu}L_O^{Ph}]^+$ possessing a higher degree of ligand radical character.

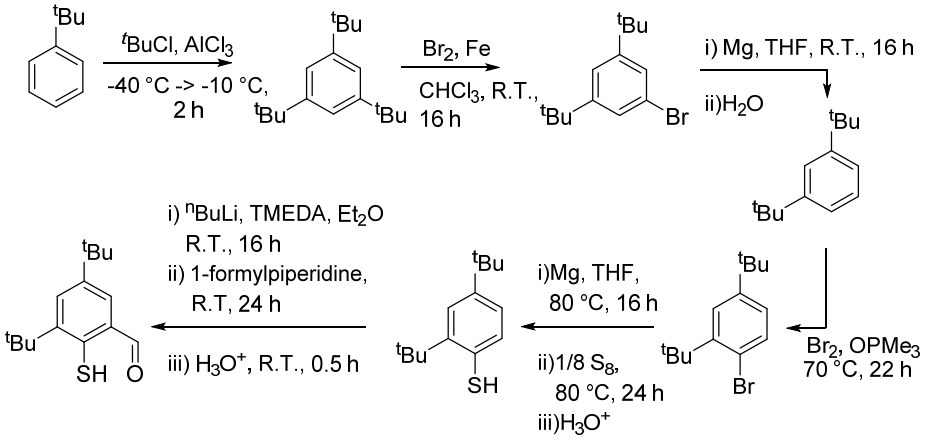
In conclusion, our EPR spectroscopic investigations and DFT calculations of the oxidised species $[Ni^{tBu}L_O^{R}]^+$ R = Ph, Py, PyOMe) are consistent with an oxidation process that is largely metal based. This is markedly different to the results reported for the analogous dithiophenolate complexes where the N_2S_2 coordination environment in $Ni^{tBu}L_S^{Ph}$ does not support the formation of a Ni^{III} species on the oxidation of $Ni^{tBu}L_S^{Ph}$; a N_3S_2 environment, as found in $Ni^{tBu}L_S^{Py}$, is required to promote the formation of a Ni^{III}-thiophenolate centre.[2, 17] In contrast, the harder O donors in $Ni^{tBu}L_O^{R}$ appear to stabilise a Ni^{III}-phenolate species even in the absence of an additional pyridyl N donor and thus, while the pyridyl N-donor does appear

to bind to the metal centre in $[Ni^{tBu}L_O^{PyOMe}]^+$ and $[Ni^{tBu}L_O^{Py}]^+$, it is not a requirement for the generation of oxidised products with Ni^{III} character.

4.3 Preparation and Characterisation of $Ni^{tBu}L_S^{Py}$ and $Ni^{tBu}L_S^{PyOMe}$

4.3.1 Syntheses of the Ni^{II}-dithiophenolate Complexes $Ni^{tBu}L_SPy$ and $Ni^{tBu}L_S^{PyOMe}$

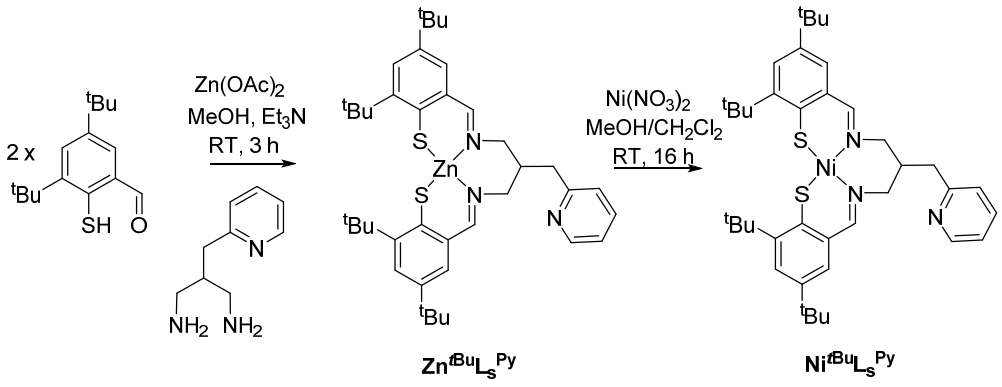
$Ni^{tBu}L_S^{Py}$ is synthesised *via* a Schiff base condensation reaction between 3,5-di^{t}butylthiosalicyaldehyde (Scheme 4.3.1.1) and 2-(2-pyridylmethyl)-1,3-propanediamine (Section 4.2.1).



Scheme. 4.3.1.1: Synthesis of the 3,5-di^{t}butylthiosalicyaldehyde precursor.

The synthesis of 3,5-di^{t}butylthiosalicylaldehyde from ^{t}butyl benzene *via* a 6 step procedure is capricious and low yielding (Scheme 4.2.1.1).[17-19] However, sufficient quantities of 3,5-di^{t}butylthiosalicyaldehyde can be purified by column chromatography and obtained in a 58 % yield from 2,4-di^{t}butylbenzenethiol as a light yellow solid suitable for further synthetic use.

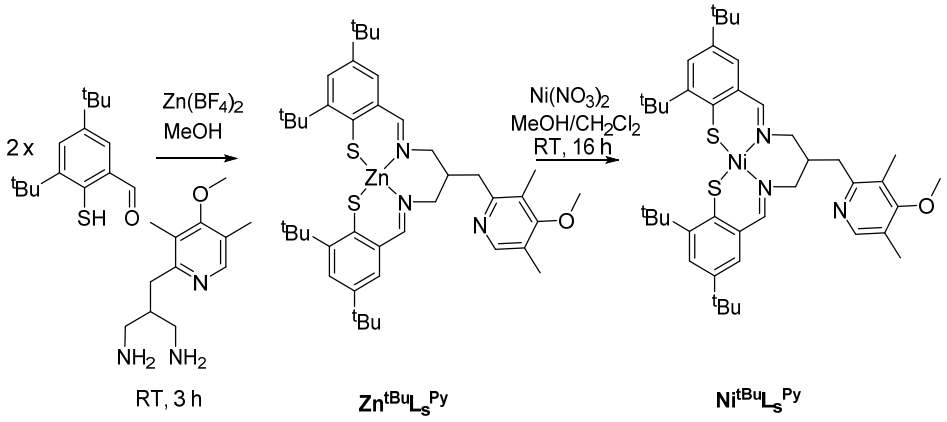
The synthesis of $Zn^{tBu}L_S^{Py}$ can be performed in one pot from 2-(2-pyridylmethyl)-1,3-propanediamine (Previously synthesised in Section 4.2.1) and 3,5-di^{t}butylthiosalicylaldehyde under basic conditions with triethylamine in methanol. We found that synthesis of $Ni^{tBu}L_S^{Py}$ *via* transmetalation of $Zn^{tBu}L_S^{Py}$ with $Ni(NO_3)_2{\cdot}6H_2O$ (Scheme 4.3.1.2)[2] was more reliable than the direct metalation of the proligand $^{tBu}L_S^{Py}$ with $Ni(NO_3)_2{\cdot}6H_2O$. The complete transmetalation of $Zn^{tBu}L_S^{Py}$ to $Ni^{tBu}L_S^{Py}$ was verified by inductively coupled plasma optical emission spectroscopy (ICP-OES); no residual zinc was found in preparations of $Ni^{tBu}L_S^{Py}$.



Scheme 4.3.1.2: Synthesis of Ni$^{tBu}L_S^{Py}$.

4.3.2 Synthesis of Ni^{tBu}L$_S^{PyOMe}$

Following the synthesis of Ni^{tBu}L$_O^{PyOMe}$ (Section 4.2), the dithiophenolate analogue Ni^{tBu}L$_S^{PyOMe}$ was prepared from 2,4-di^{t}butylthiobenzaldehyde and 2-[(4-methoxy-3,5-dimethylpyridin-2-yl)methyl]propane-1,3-diamine *via* Zn^{tBu}L$_S^{PyOMe}$. Initial attempts to isolate Zn^{tBu}L$_S^{PyOMe}$ under the same conditions employed in the synthesis of Zn^{tBu}L$_S^{Py}$ led to the isolation of a mixture of products that could not be characterised. Modification of the synthetic procedure, by the use of $Zn(BF_4)_2$ as the source of Zn^{II}, led to the successful isolation of Zn^{tBu}L$_S^{PyOMe}$. Transmetalation with $Ni(NO_3)_2$ gave Ni^{tBu}L$_S^{PyOMe}$ (Scheme 4.3.2.1).

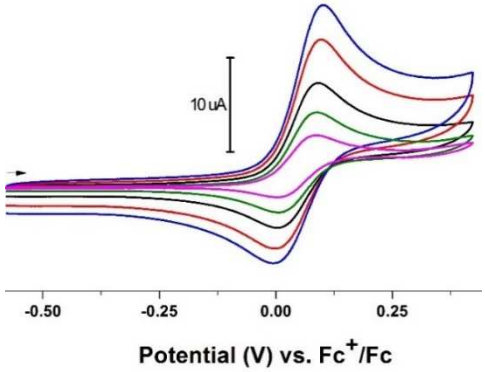


Scheme 4.3.2.1: Synthesis of Ni$^{tBu}L_S^{PyOMe}$.

4.3.3 Electrochemistry of Ni^{tBu}L$_S^{Py}$ and Ni^{tBu}L$_S^{PyOMe}$

Cyclic voltammetry of a solution of Ni^{tBu}L$_S^{Py}$ at 298 K in CH_2Cl_2 containing 0.4 M $[N^nBu_4][BF_4]$ under Ar confirms the presence of an oxidation process at E_p^a = 0.05 V (*vs.* Fc^+/Fc) with an unusually large peak separation of 100 mV (Figure 4.2.2.1)

that is greater than that of the internal standard ($dmfc^+$/dmfc, 70 mV). This is identical to the voltammogram previously observed for $Ni^{tBu}L_S^{Py}$, with the large peak separation assigned to the structural rearrangement upon oxidation that may be associated with the binding of the pyridyl N-donor to the Ni centre.[2]



Complex	$E_{1/2}$ V (vs Fc^+/Fc)	i_p^c µA (100 mV)	i_p^a µA (100 mV)	$\|E_p^c-E_p^a\|$ mV	$\|E_p^c-E_p^a\|$ mV ($dmfc^+$/dmfc)
$Ni^{tBu}L_S^{Py}$	0.05	14.5	17.6	100	70

Fig 4.3.2.1: Reversible oxidations of $Ni^{tBu}L_S^{Py}$ *at multiple scan rates (300 mV (blue), 200 mV (red), 100 mV (black), 50 mV (green), 20 mV (purple)).*

The electrochemical properties of $Ni^{tBu}L_S^{PyOMe}$ were also investigated by cyclic voltammetry in CH_2Cl_2. An oxidation was observed at E_p^a = 0.09 V *vs.* Fc^+/Fc, however this process does not exhibit electrochemical reversibility over the range of scan rates investigated (Figure 4.3.2.2). This redox potential is close to the oxidation potential observed for $Ni^{tBu}L_S^{Py}$ (E_p^a = 0.10 V *vs*. Fc+/Fc).

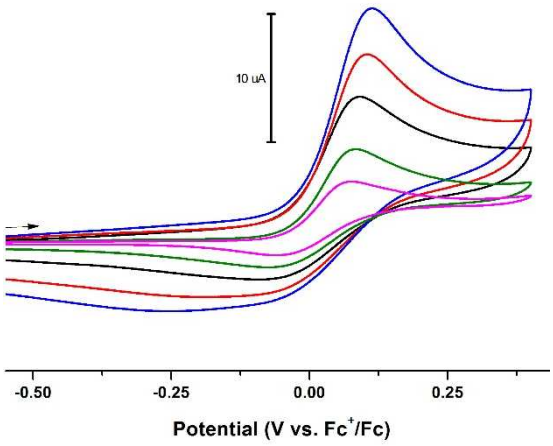


Figure 4.3.2.2: Cyclic voltammogram of $Ni^{tBu}L_S^{PyOMe}$ *at multiple scan rates (300 mV (blue), 200 mV (red), 100 mV (black), 50 mV (green), 20 mV (purple)).*

The ability of a sterically bulky group to bind to the nickel centre in this ligand set was verified through the addition of exogenous bulky pyridines to a solution of $Ni^{tBu}L_S^{Ph}$. These experiments showed a loss of the return wave of the cyclic voltammogram on the addition of 4-*t*butyl pyridine, suggesting an irreversible interaction of the sterically bulky pyridine with the nickel centre. This, together with our results for $Ni^{tBu}L_O^{PyOMe}$ (Section 4.2) suggests that the increased steric bulk of the pyridyl bridge in $Ni^{tBu}L_S^{PyOMe}$ does not prevent the pyridyl nitrogen interacting with the Ni centre on oxidation.

4.4 EPR spectroscopy of $Ni^{tBu}L_S^{Py}$

4.4.1 Continuous Wave (CW) EPR Spectroscopy of $[Ni^{tBu}L_S^{Py}]^+$

$[Ni^{tBu}L_S^{Py}]^+$ was generated by controlled potential electrolysis at 0.38 V *vs.* Fc^+/Fc in a CH_2Cl_2 solution at room temperature containing 0.4 M of $[NBu_4][BF_4]$ as supporting electrolyte. It is essential to carry out this oxidation at room temperature in order to avoid the formation of disulfide dimers as has been previously observed on oxidation of Ni Schiff base dithiophenolate complexes at low temperatures.[17] On oxidation a colour change from orange/brown to a deep red/brown is observed and the presence of $[Ni^{tBu}L_S^{Py}]^+$ was confirmed by continuous wave (CW) EPR spectroscopy (Figure 4.4.1.1), with a three line hyperfine splitting observed, consistent with the coordination of the pyridyl N-donor to the Ni centre.

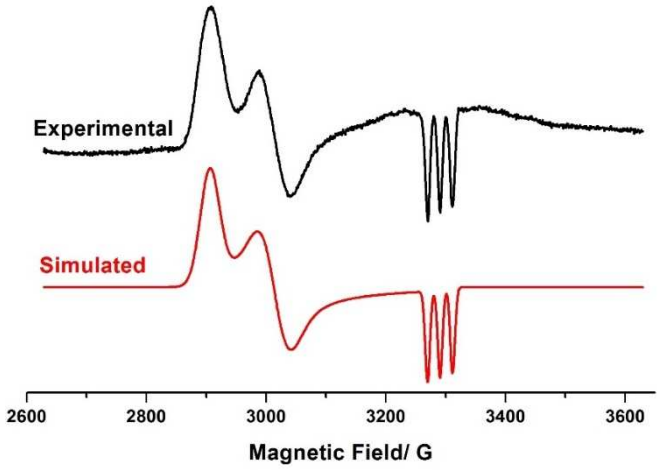


Figure 4.4.1.1: X-band EPR spectrum of $[Ni^{tBu}L_S^{Py}]^+$ (top) and simulated spectrum (bottom). Spin Hamiltonian parameters: g_{11} = 2.282, g_{22} = 2.200, g_{33} = 2.016, A_{33} = 20.9 G, Gaussian linewidths W_{11} = 32 G, W_{22} = 44 G, W_{33} = 8 G.

4.4.2 ESEEM and HYSCORE EPR Spectroscopy and DFT Calculations on $Ni^{tBu}L_S^{Py}$

4.4.2.1 Introduction

In order to investigate the nature of the oxidised species $[Ni^{tBu}L_S^{Py}]^+$ in greater detail we employed a combination of DFT calculations and pulsed EPR techniques to probe the electronic structure of this species. Whilst extensive computational work has been carried out on synthetic analogues of NiSOD,[20-22] comparatively little work has been carried out using advanced EPR spectroscopic methods to reveal details of the electronic structures of these centres, despite the native

enzyme being extensively characterised by EPR spectroscopy through ^{61}Ni, ^{15}N and ^{33}S isotopic labelling studies (Chapter 1).[1, 23]

Our preliminary continuous wave X-band frozen solution EPR spectroscopic studies on $[Ni^{tBu}L_S^{Py}]^+$ have resolved a three line splitting in the g_{33} region, which we have assigned to the coupling of the axial N-donor derived from the pendant pyridine group (Section 4.4.1).[2] The linewidth of the EPR spectrum precludes the extraction of hyperfine coupling constants in the g_{11}/g_{22} region. In order to explore further the electronic structure of $[Ni^{tBu}L_S^{Py}]^+$ we employed pulsed electron spin echo envelope modulation (ESEEM)[24, 25] and a three pulse 2D hyperfine sub level correlation spectroscopic (HYSCORE) experiment. The experiments were carried out in collaboration with the EPSRC EPR Service at The University of Manchester by Dr Amgalanbaatar Baldansuren.

Standard one dimensional ESEEM experiments use two or three microwave pulse sequences (separated by time τ for two pulse methods or times τ and T for three pulse), after which the intensity of the echo (observed after time τ or τ + T for two and three pulse methods respectively) is recorded, giving an overall sequence which can be described as $\pi/2 - \tau - \pi/2$ - τ - echo for 2 pulse methods or $\pi/2 - \tau - \pi/2 - T - \pi/2 - \tau$ - echo for 3 pulse (Figure 4.4.2.1.1). The echo envelope is modulated by the NMR frequencies of the nuclei coupled with the electron spin. Three pulse methods generally give spectra that are easier to interpret due to a reduction in interference from combination frequencies.[26]

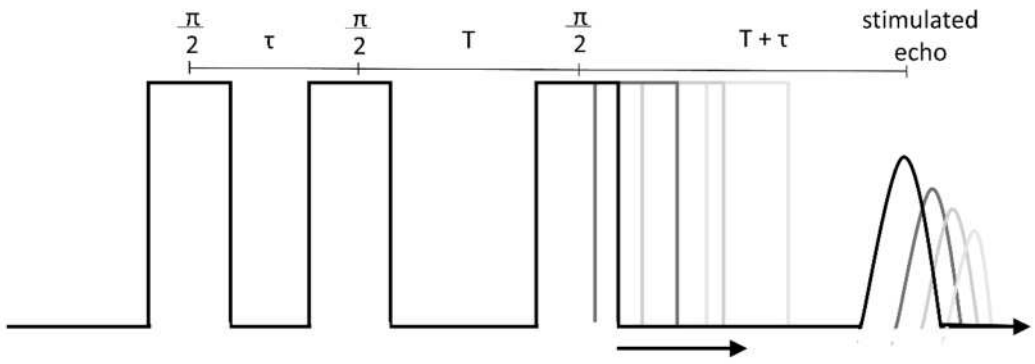


Figure 4.4.2.1.1: Three pulse ESEEM sequence. Two pulses separated by time τ are applied followed by a third pulse after further time T. The stimulated echo is observed time τ after the final pulse. T is incremented in order to obtain the echo envelope.

HYSCORE utilises a three pulse ESEEM sequence with an additional pulse between the second and third pulses in order to transfer populations from one M_s state to the other with an overall pulse sequence which may be described as $\pi/2 - \tau - \pi/2 - T_1 - \pi - T_2$ - $\pi/2 - \tau$ - echo (Figure 4.4.2.1.2).[27] The echo intensity is recorded as a function of the time between the second and third and third and fourth pulses (T_1 and T_2).

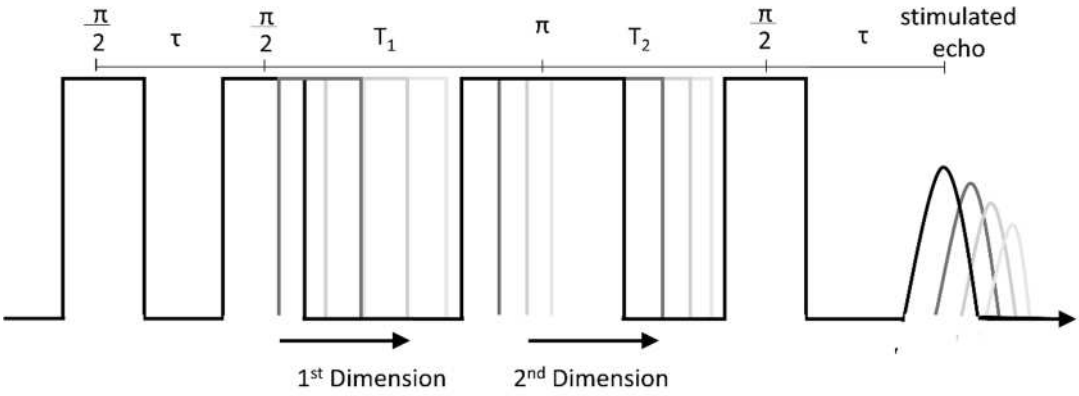


Figure 4.4.3.1.2: HYSCORE pulse sequence, based on a three pulse ESEEM sequence (Figure 4.5.2.1.1) with an additional pulse π between the second and third pulses.

4.4.2.2 ESEEM and HYSCORE of $[Ni^{tBu}L_S^{Py}]^+$

ESEEM EPR spectroscopy of a frozen solution of $[Ni^{tBu}L_S^{Py}]^+$ in CH_2Cl_2 containing 0.4 M $[^nBu_4N][BF_4]$ at 20 K was used to investigate hyperfine interactions with ^{14}N donors within the ligand framework. The X-band three pulse ESEEM spectra are shown in Figure 4.4.2.2.1. The dominant peaks at ~14.6 MHz in these spectra correspond to strongly coupled matrix proton nuclei. The broadened ridge at lower frequency suggests multiple ^{14}N environments interacting with the unpaired electron and possessing differing nuclear Zeeman and isotropic coupling scales as the cancellation condition for a single ^{14}N nucleus, where the nuclear Zeeman and hyperfine interaction cancel each other out, is not satisfied.[28]

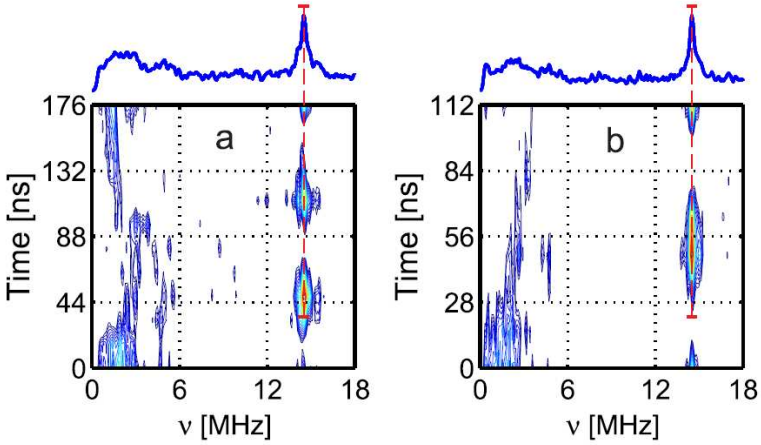


Figure 4.4.2.2.1: X-band 14N three pulse ESEEM spectra of [Ni^{tBu}L$_S^{Py}$]$^+$ recorded at 342 mT, ~9.7 GHz, 20 K.

In order to probe these ^{14}N interactions further, the corresponding HYSCORE experiment was carried out (Figure 4.4.2.2.2). An intense cross peak is observed in the HYSCORE spectrum in the (-,+) quadrant, which is symmetrically resolved in the (+,-) quadrant of the full plot (Figure 4.4.2.2.2 right). This peak exhibits a maximum at (±6.1, ∓2.3) MHz which is assigned to the double quantum transition (m_I = -1 → m_I = +1) ν_{dq}. The frequency of the double quantum transition can be described by the equation $\nu_{dq} = 2[\nu_{eff}^2{}_{\pm} + K]^{½}$ where $\nu_{eff} = |^{14}\nu_N \pm a_{iso}^N/2|^2$ and $K = k^2(3+\eta^2)$ (where $^{14}\nu_N$ is the nuclear Zeeman frequency *ca.* 1.05 MHz at X-band; a_{iso}^N is the isotropic hyperfine constant *ca.* 0.1-5.0 MHz; k and η are quadrupole parameters). Using the frequency values from our experiment and estimating a_{iso}^N as 3.8 MHz and K as 0.6 MHz^2 results in the value of the quadrupolar coupling constant κ *ca.* 0.39-0.45 as η varies between 0 and 1. These parameters allow the HYSCORE spectrum to be simulated,[29] with good correlation in the position of the cross peaks observed between the simulated and experimental spectra (Figure 4.4.2.2.3).

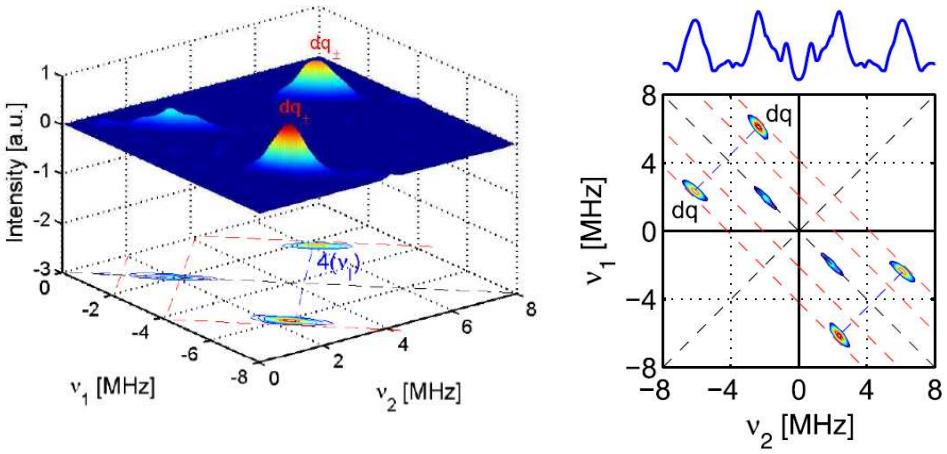


Figure 4.4.2.2.2: HYSCORE spectrum of $[Ni^{tBu}L_S^{Py}]^+$ recorded using τ = 136 ns at 339.7 mT, ~9.7 GHz, 15 K. Left: 3 D plot of (-,+) quadrant. Right: Full spectrum showing all four quadrants which reveals the symmetrical cross peaks in the (-,+) and (+,-) quadrants.

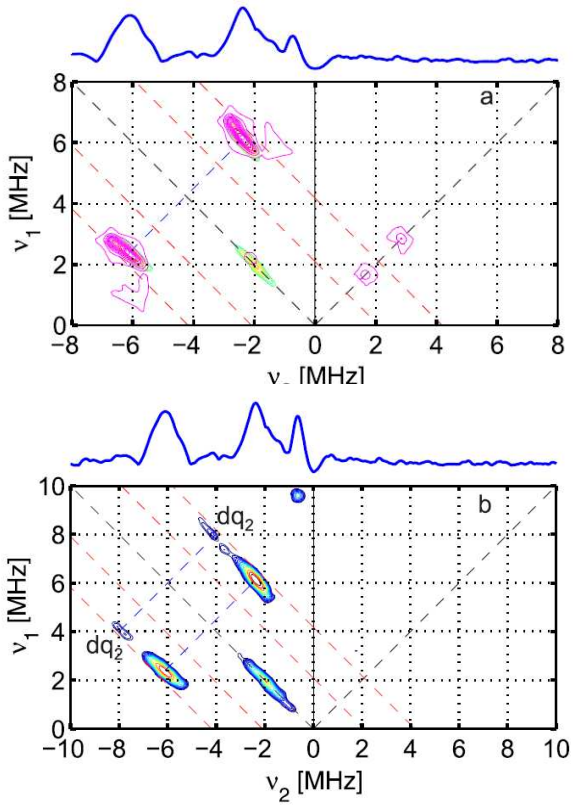


Figure 4.4.2.2.3: Contour presentation of the numerical simulation of the X-band ^{14}N HYSCORE spectrum of $[Ni^{tBu}L_S^{Py}]^+$ in the (+,−) and (+,+) quadrants using EasySpin[29]. Top: The cross-peak was well reproduced, based on k = 0.42 MHz, η ~ 0.5, a_{iso}^N ~3.8 MHz; Bottom: The weak cross peak is assigned to the double quantum transition of the nitrogen with a_{iso}^N ~5.8 MHz, labelled dq2.

The HYSCORE spectrum of $[Ni^{tBu}L_S^{Py}]^+$ also exhibits an additional cross peak at (±8.1, ∓4.1) which is assigned to a second ^{14}N atom with a_{iso}^N *ca.* 5.8 MHz and K *ca.* 0.8 MHz^2 leading to κ *ca.* 0.44 – 0.51 MHz when η varies between 0 and 1. The values found for these two nitrogen environments are summarised in Table 4.3.2.2.1.

Nucleus	$^{14}\nu_N$ (MHz)	a_{iso}^N (MHz)	K (MHz^2)	κ	η
$^{14}N(1)$	1.05	3.8	0.6	0.39-0.45	0-1
$^{14}N(2)$	1.05	5.8	0.8	0.44-0.51	0-1

Table 4.4.3.2.1: Summary of nuclear hyperfine and quadrupole coupling constants of ^{14}N environments observed by HYSCORE spectroscopy in $[Ni^{tBu}L_S^{Py}]^+$.

This result shows the presence of two coupled ^{14}N centres in different environments in the immediate coordination sphere of the formal Ni^{III} centre of $[Ni^{tBu}L_S^{Py}]^+$, in addition to the coupling assigned to the axial pyridyl ^{14}N in the frozen solution CW EPR spectrum of $[Ni^{tBu}L_S^{Py}]^+$ with a_{33} = 20.9 G.

4.4.2.3. DFT Calculations on $[Ni^{tBu}L_S^{Py}]^+$

We have employed DFT calculations to provide a qualitative description of the electronic structure of $[Ni^{tBu}L_S^{Py}]^+$ which can then be compared to the results obtained from the EPR, ESEEM and HYSCORE spectroscopic studies. We carried out gas-phase DFT geometry optimisations of $[Ni^{tBu}L_S^{Py}]^+$ using a model derived from the crystal structure of $Ni^{tBu}L_S^{Py}$.[2] The calculation of vibrational frequencies verified that an energy minimum has been reached in the geometry optimisation process. This gas-phase geometry optimised structure was then used as a model in single point calculations to model the effects of solvation using COSMO.[16] The geometry optimised structure of $[Ni^{tBu}L_S^{Py}]^+$ is presented in Figure 4.4.2.3.1 and Table 4.4.2.3.1 and compared to that previously obtained for the diphenolate analogue, $[Ni^{tBu}L_O^{Py}]^+$ (Section 4.2).

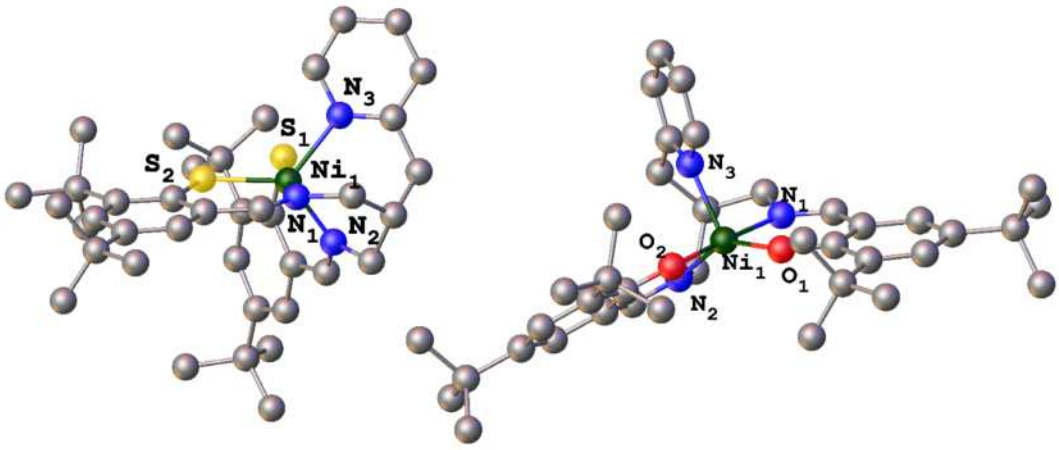


Figure 4.4.2.3.1: DFT derived structures of [Ni^{tBu}L$_S$^{Py}]$^+$ (left) and [Ni^{tBu}L$_O$^{Py}]$^+$ (right).

	[Ni^{tBu}L$_S$^{Py}]$^+$	[Ni^{tBu}L$_O$^{Py}]$^+$		[Ni^{tBu}L$_S$^{Py}]$^+$	[Ni^{tBu}L$_O$^{Py}]$^+$
Ni1-N1	1.913	1.979	Ni1-X1	2.234	2.043
Ni1-N2	1.982	2.031	Ni1-X2	2.156	1.980
Ni1-N3	2.117	2.047			
X1-Ni1-X2	86.43	84.60	X2-Ni1-N2	126.46	89.92
X1-Ni1-N1	175.16	90.19	X2-Ni1-N3	126.35	114.98
X1-Ni1-N2	89.07	174.50	N1-Ni1-N2	91.99	94.53
X1-Ni1-N3	85.60	93.87	N1-Ni1-N3	89.58	99.41
X2-Ni1-N1	96.71	145.46	N2-Ni1-N3	106.36	88.14

Table 4.4.2.3.1: Key bond lengths (Å) and angles (°) of DFT derived structures of [Ni^{tBu}L$_S$^{Py}]$^+$ and [Ni^{tBu}L$_O$^{Py}]$^+$. X = S/O.

The geometry optimised structure of [Ni^{tBu}L$_S$^{Py}]$^+$ possess a distorted trigonal bipyrimidal geometry (τ = 0.81) in which the imine N-donor N2 lies out of the NiS_2 plane. The second imine N donor N1 is essentially co-planar with the NiS_2 unit. Gas phase geometry optimisations suggest that [Ni^{tBu}L$_O$^{Py}]$^+$ possesses a structure that is more distorted towards a square-based pyramidal geometry (τ = 0.48; Section 4.2).

Whilst the majority of the spin density in $[Ni^{tBu}L_S^{Py}]^+$ is localised on the Ni and S centres (Table 4.4.2.3.2), significant differences are found for the distribution of spin density across the remaining nuclei. Thus, the imine N1 that is essentially co-planar with the NiS_2 plane possesses significantly less spin density (0.028) than its imine N2 counterpart (0.066), the spin density of which is similar to that associated with the pyridyl N-donor (0.050). The electronic structure computed for $[Ni^{tBu}L_S^{Py}]^+$ can be compared to that calculated for $[Ni^{tBu}L_O^{Py}]^+$. The distributions in spin densities are broadly similar but with more electron spin localised on the Ni centre (0.680 *vs.* 0.578 for $[Ni^{tBu}L_O^{Py}]^+$ and $[Ni^{tBu}L_S^{Py}]^+$, respectively, Table 4.4.2.3.2) and on the axial pyridyl N-donor (0.125 *vs.* 0.050 for $[Ni^{tBu}L_O^{Py}]^+$ and $[Ni^{tBu}L_S^{Py}]^+$ respectively).

Atom	$[Ni^{tBu}L_S^{Py}]^+$ Spin Density (%)	$[Ni^{tBu}L_O^{Py}]^+$ Spin Density (%)
Ni	0.578	0.680
X1	-0.030	0.041
X2	0.227	-0.014
$N1_{(imine)}$	0.028	0.020
$N2_{(imine)}$	0.066	0.041
$N3_{(pyridyl)}$	0.050	0.125

Table 4.4.2.3.2: Spin density of $[Ni^{tBu}L_S^{Py}]^+$ and $[Ni^{tBu}L_O^{PyOMe}]^+$derived from DFT calculations X = S/O

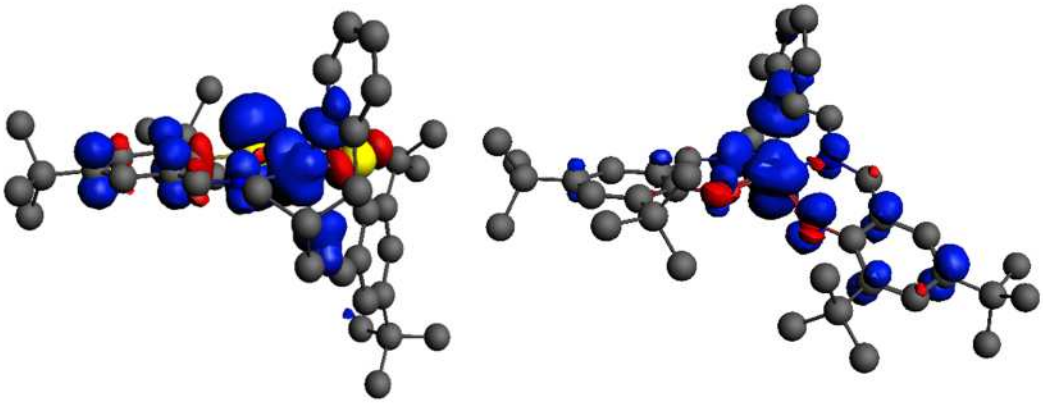


Figure 4.4.2.3.2: Spin density of $[Ni^{tBu}L_S^{Py}]^+$ and $[Ni^{tBu}L_O^{PyOMe}]^+$.

The two different imine N atom environments in $[Ni^{tBu}L_S^{Py}]^+$ (spin density 0.028 and 0.066, for N1 and N2, respectively) can be matched with the two different a_{iso}^N values, 3.8 and 5.8 MHz, derived from the ESEEM and HYSCORE spectroscopic experiments on $[Ni^{tBu}L_S^{Py}]^+$ (Section 4.4.2.2), which provides some validation of

the electronic structure, and hence geometry, for $[Ni^{tBu}Ls^{Py}]^{+}$ derived from DFT calculations.

4.4 Conclusions

We have synthesised and characterised diphenolate ($M^{tBu}L_O^{Py}$, $M^{tBu}L_O^{PyOMe}$, and $M^{tBu}L_O^{Ph}$; M = Zn, Ni, Cu) and dithiophenolate ($Ni^{tBu}L_S^{Py}$, and $Ni^{tBu}L_S^{PyOMe}$) complexes as analogues for the active site of NiSOD. These complexes represent the first examples of analogues that incorporate a pendant aromatic N-donor to a ligand framework incorporating imine N and phenolate-O or thiophenolate-S donors which exhibit reversible electrochemistry and a Ni-N interaction in the oxidised state. EPR spectroscopic studies on $[Ni^{tBu}L_O^{R}]^+$ (R = Py, PyOMe, Ph) show that these complexes possess a Ni-based SOMO such that they are formally Ni^{III} centres. In contrast $[Ni^{tBu}L_S^{Ph}]^+$ appears to require an additional N-donor to drive a metal-based oxidation process.[2] Thus, the calculated electronic structure of $[Ni^{tBu}L_S^{R}]^+$, derived from DFT calculations and supported by EPR, ESEEM and HYSCORE spectroscopic studies of $[Ni^{tBu}L_S^{Py}]^+$ support a metal-based SOMO in this complex and show spin densities across the imine-N and pyridyl N-donors.

The importance of additional axial N donors to support the Ni^{III} state in thiolate complexes has been suggested previously (Chapter One)[13, 17, 22, 30-34] However, the complexes $M^{tBu}L_X^{R}$ (M = Ni, Cu, X = S, O, R = Py, PyOMe) presented in this Chapter represent the first examples where an additional N-donor is incorporated into the N_2X_2 ligand that supports the formation of $[M^{tBu}L_X^{R}]^+$ that, in the case of $[Ni^{tBu}L_S^{Py}]^+$, possess EPR spectroscopic properties that are remarkably similar to those of the oxidised form of NiSOD.

4.5 Experimental

Synthesis of diethyl (2-pyridylmethyl)-1,3-propanedioate

Diethyl malonate (43.3 ml, 256 mmol) was added to sodium ethoxide (15.4 g, 227 mmol) in ethanol (175 cm^3). 2-Picolyl chloride hydrochloride (15.0 g, 91.0 mmol) was added to give a pink solution. The mixture was heated under reflux for 4.5 hours before removal of the solvent *in vacuo*. The residue was cooled to 0 ^oC and acidified with 4 M HCl (75.0 cm^3). Treatment of the aqueous phase with 6M NaOH (45.0 cm^3) at 0 ^oC precipitated an oil, which was extracted with Et_2O. The combined ether extracts were dried over Na_2SO_4, filtered and concentrated *in vacuo* to produce yellow oil. Excess diethyl malonate was removed by distillation under reduced pressure to leave the product as a yellow oil (16.0 g, 54 %).

^1H (400 MHz) $CDCl_3$; 8.50 (1H, d, *J* 4.4, Ar*H*), 7.58 (1H, td, *J* 7.7 1.7, Ar*H*), 7.20 (1H, d, *J* 7.7, Ar*H*), 7.15-7.08 (1H, m, Ar*H*), 4.24-4.14 (4H, dq, *J* 7.2, 2.1, C*H*$_2$CH$_3$), 4.10 (1H, t, *J* 7.7, EtOOCC*H*CO), 3.41-3.36 (2H, d, *J* 7.7, CHC*H*$_2$), 1.23 (6H, t, *J* 7.2, C*H*$_3$); ^{13}C (100 MHz) $CDCl_3$; 169.0 (*C*), 157.6 (*C*), 148.9 (*C*H), 136.7 (*C*H), 123.7 (*C*H), 121.8 (*C*H), 61.4 (*C*H$_2$), 51.3 (*C*H), 36.2 (*C*H$_2$), 13.9 (*C*H$_3$). MS (ESI^+, m/z): 252.1227 $(M + H)^+$

Synthesis of (2-pyridylmethyl)-1,3-propanediamide

A solution of methanol (20.0 cm^3) and sodium methoxide (0.37 g, 6.90 mmol) was saturated with gaseous ammonia at 0 ^oC. This was added to a solution of diethyl (2-pyridylmethyl)-1,3-propanedioate (16.0 g, 64.0 mmol) in methanol (40.0 cm^3). The mixture was stirred for 16 hours at room temperature, and stored at -20 °C for a further 24 hours before the product collected as a white solid by vacuum filtration (9.40 g, 76 %).

^1H (400 MHz) $(CD_3)_2SO$; 8.46 (1H, d, *J* 4.8, Ar*H*), 7.67 (1H, td, *J* 7.7 1.8, Ar*H*), 7.29 (2H, s, N*H*$_2$), 7.24-7.16 (2H, m, Ar*H*), 7.01 (2H, s, N*H*$_2$), 3.68 (1H, t, *J* 3.7, H$_2$NOCC*H*), 3.11 (2H, d, *J* 7.4, C*H*$_2$CH), ^{13}C (100 MHz) $(CD_3)_2SO$; 176.0 (*C*), 164.2 (*C*), 154.0 (*C*H), 141.5 (*C*H), 128.6 (*C*H), 126.6 (*C*H), 57.4 (*C*H), 41.9 (*C*H$_2$); MS (ESI^+, m/z): 194.0928 $(M + H)^+$

Synthesis of 2-(2-pyridylmethyl)-1,3-propanediamine

A 1 M solution of B_2H_6.THF (226 cm^3, 226 mmol) was added to a suspension of (2-pyridylmethyl)-1,3-propanediamide (9.40 g, 49.0 mmol) in THF (50.0 cm^3) over 30 minutes at 0 ^oC. The reaction mixture was then heated to reflux for 3 hours, after which it was cooled to 0 ^oC and the excess diborane destroyed by cautious drop-wise addition of distilled water (40.0 cm^3). The solvent was removed *in vacuo* to give a white solid, which was dissolved in 6 M HCl (100 cm^3). This was heated at reflux for 1 hour and the solvent subsequently removed *in vacuo*. The residue was re-dissolved in water (100 cm^3) and treated with 6 M NaOH (70.0 cm^3). The solution was extracted with $CHCl_3$ (4 x 200 cm^3), dried over $MgSO_4$, and the solvent removed *in vacuo* to yield a colourless oil (5.35 g, 66 %).

^{1}H (400 MHz) $CDCl_3$; 8.41 (1H, s, Ar*H*), 7.51-7.44 (1H, m, Ar*H*), 7.08-7.02 (1H, m, Ar*H*), 7.02-6.96 (1H, m, Ar*H*), 2.73-2.68 (2H, m, ArCH_2), 2.63-2.56 (4H, m, NH_2), 1.88-1.78 (1H, m, CH_2CHCH_2), 1.19 (4H, s, NH_2CH_2); ^{13}C (100 MHz) $CDCl_3$; 160.8 (C), 149.2 (CH), 136.1 (CH), 123.4 (CH), 121.0 (CH), 44.9 (CH), 43.4 (CH_2), 38.6 (CH_2). MS (ESI^+, m/z): 166.1320 $(M + H)^+$

Synthesis of diethyl 2-((4-methoxy-3,5-dimethylpyridin-2-yl)methyl)malonate

Prepared as diethyl (2-pyridylmethyl)-1,3-propanedioate using 4-methoxy-3,5-dimethylpyridine (5.00 g, 22.5 mmol), diethyl malonate (9.00 g, 56.0 mmol), and sodium ethoxide (1.15 g, 50.0 mmol sodium in ethanol (50.0 cm^3)) to give diethyl 2-((4-methoxy-3,5-dimethylpyridin-2-yl)methyl)malonate (4.29 g, 61 %).

^{1}H (400 MHz) $CDCl_3$; 8.32 (1H, s, Ar*H*), 4.55 (1H, t, *J* 8.2, EtOOCC*H*CO), 4.21-4.10 (4H, m, *J* 7.2, 2.1, CH_2CH_3), 3.98 (3H, s, OCH_3), 3.57 (2H, d, *J* 8.2, CHCH_2), 2.37 (3H, s, ArCH_3), 2.36 (3H, s, ArCH_3), 1.21 (6H, t, *J* 7.0, CH_3); ^{13}C (100 MHz) $CDCl_3$; 181.3 (*C*), 168.0 (*C*), 167.1 (*C*), 144.5 (*C*), 127.1 (*C*H), 125.1 (*C*H), 120.2 (*C*), 62.9 (CH_2), 50.1 (*C*H), 46.3 (CH_3), 26.2 (CH_2), 14.1 (CH_3), 14.0 (CH_3), 10.1 (*C*H3). FTIR ν/cm^{-1} (ATR): 3468 (w, br), 2992 (w0, 2462 (w, br), 1747 (s), 1730 (s), 1609 (w), 1467 (m), 1445 (m), 1370 (m), 1325 (m), 1304 (m), 1260 (s), 1149 (s), 1106 (m), 1032 (m), 1013 (m), 924 (w), 862 (m), 758 (m). MS (ESI^+, m/z): 310.1638 $(M + H)^+$.

Synthesis of 2-((4-methoxy-3,5-dimethylpyridin-2-yl)methyl)malonamide

Prepared as (2-pyridylmethyl)-1,3-propanediamide using diethyl 2-((4-methoxy-3,5-dimethylpyridin-2-yl)methyl)malonate (3.10 g, 10.0 mmol), sodium methoxide (0.03 g, 0.56 mmol), methanol (200 cm^3) and gaseous ammonia to give 2-((4-methoxy-3,5-dimethylpyridin-2-yl)methyl)malonamide (2.10 g, 84 %).

^{1}H (400 MHz) $(CD_3)_2SO$; 8.10 (1H, s, Ar*H*), 7.27 (2H, s, N*H*$_2$), 6.96 (2H, s, N*H*$_2$), 3.85 (1H, t, *J* 7.3, C*H*), 3.70 (3H, s, OC*H*$_3$), 3.04 (2H, d, *J* 7.2, C*H*$_2$), 2.19 (3H, s, C*H*$_3$), 2.17 (3H, s, C*H*$_3$). ^{13}C (100 MHz) $(CD_3)_2SO$; 171.6 (*C*), 163.3 (*C*), 157.8 (*C*), 148.4 (*C*H), 124.4 (*C*), 123.8 (*C*), 60.1 (*C*H), 51.5 (*C*H$_3$), 33.5 (*C*H$_2$), 13.3 (*C*H$_3$), 11.2 (*C*H$_3$). FTIR ν/cm^{-1} (ATR): 3376 (m), 3194 (m), 1669 (s), 1625 (m), 1592 (w), 1562 (w), 1415 (m), 1380 (m), 1065 (m), 1003 (m), MS (ESI$^+$, m/z): 252.1337 $(M + H)^+$

Synthesis of 2-((4-methoxy-3,5-dimethylpyridin-2-yl)methyl)propane-1,3-diamine

A 1 M solution of B_2H_6.THF (40.0 cm^3, 40.0 mmol) was added to a suspension of 2-((4-methoxy-3,5-dimethylpyridin-2-yl)methyl)malonamide (2.00 g, 7.97 mmol) in THF (10.0 cm^3) over 10 minutes at 0 ^{o}C. The reaction mixture was then heated to reflux for 3 hours, after which it was cooled to 0 ^{o}C and the excess diborane destroyed by cautious drop-wise addition of distilled water (20.0 cm^3). The solvent was removed *in vacuo* to give a white solid, which was dissolved in 6 M HCl (50 cm^3). This was heated at reflux for 1 h and the solvent subsequently removed *in vacuo*. The residue was re-dissolved in water (50 cm^3) and treated with 6 M NaOH (20.0 cm^3). The solution was extracted with $CHCl_3$/MeOH (19:1, 6 x 50 cm^3), dried over $MgSO_4$, and the solvent removed *in vacuo* to give a colourless oil. (1.2 g, 68 %)

^{1}H (400 MHz) $CDCl_3$; 8.18 (1H, s, Ar*H*), 3.77 (3H, s, OC*H*$_3$), 2.81-2.75 (6H, m NC*H*$_2$, CHC*H*$_2$), 2.26 (3H, s, C*H*$_3$), 2.25 (3H, s, C*H*$_3$), 1.94 (1H, quin, *J* 5.5, C*H*), 1.40 (4H, s br, N*H*$_2$). ^{13}C (100 MHz) $CDCl_3$; 163.9 (*C*), 159.2 (*C*), 148.9 (*C*H), 124.5 (*C*), 123.8 (*C*), 59.8 (*C*H$_3$), 43.8 (*C*H$_2$), 43.8 (*C*H), 36.2 (*C*H$_2$), 13.2 (*C*H$_3$), 11.4 (*C*H$_3$). MS (ESI$^+$, m/z): 224.1755 $(M + H)^+$

Synthesis of diethyl 2-benzylmalonate

Prepared as diethyl (2-pyridylmethyl)-1,3-propanedioate using benzyl chloride (19 g, 150 mmol), diethyl malonate (76.1 ml 452 mmol), and sodium ethoxide (9.50 g, 413 mmol of sodium in ethanol (170 cm^3)) to give diethyl 2-benzylmalonate as a yellow oil (23.3 g, 62 %).

^{1}H (400 MHz) $CDCl_3$; 7.32-7.27 (2H, m, Ar*H*), 7.25-7.20 (3H, m, Ar*H*), 4.18 (4H, qd, *J* 7.1, 2.3, C*H*$_2$CH$_3$), 3.67 (1H, t, *J* 7.9, C*H*), 3.24 (2H, d, *J* 7.9, CHC*H*$_2$), 1.23 (6H, t, *J* 7.1, C*H*$_3$). ^{13}C (100 MHz) $CDCl_3$; 167.8 (*C*), 132.5 (*C*), 131.0 (*C*H), 128.9 (*C*H), 128.8 (*C*H), 68.2 (*C*H$_2$), 38.7 (*C*H), 30.4 (*C*H$_2$), 14.1 (*C*H$_3$). MS (ESI$^+$, m/z): 273.1107 $(M + Na)^+$

Synthesis of 2-benzylmalonamide

Prepared as (2-pyridylmethyl)-1,3-propanediamide using diethyl 2-benzylmalonate (23.1 g, 92.4 mmol), sodium methoxide (0.54 g, 10.8 mmol), methanol (150 cm^3) and gaseous ammonia to give 2-benzylmalonamide (5.21 g, 30 %).

^{1}H (400 MHz) $CDCl_3$; MeOD; 7.10-6.98 (5H, m, Ar*H*), 3.63 (4H, s, N*H*$_2$), 2.90 (2H, t, C*H*$_2$N), 2.75 (2H, t, C*H*$_2$N), 2.58 (2H, d, C*H*$_2$Ar), 1.98 (1H, t, C*H*). ^{13}C (100 MHz) $CDCl_3$; 139.5 (*C*), 129.0 (*C*H), 128.4 (*C*H), 126.2 (*C*H), 44.3(*C*H$_2$), 42.3 (*C*H$_2$), 36.9 (*C*H). FTIR ν/cm^{-1} (ATR): 3444 (w), 3371 (m), 3188 (m), 3027 (w), 1730 (m), 1667 (s), 1646 (s), 1600 (m), 1429 (w), 1442 (m), 1414 (m), 1381 (m), 1280 (m), 1195 (m), 1166 (m), 1154 (m), 1114 (m), 752 (s), 695 (s), 653 (s), 548 (s), 518 (s). MS (ESI) 193.0973 (M + H), 215.0792 $(M + Na)^+$.

Synthesis of 2-benzylpropane-1,3-diamine

Prepared as 2-((4-methoxy-3,5-dimethylpyridin-2-yl)methyl)propane-1,3-diamine using 2-benzylmalonamide (3.75 g, 19.5 mmol), B_2H_6.THF (100 cm^3, 100 mmol), in THF (25.0 cm^3), followed by refluxing in 6 M HCl (100 cm^3) before neutralisation with 6 M NaOH (35.0 cm^3) and extraction with $CHCl_3$/MeOH (19:1, 6 x 50 cm^3) to give 2-benzylpropane-1,3-diamine (2.40 g, 75 %)

^{1}H (400 MHz) $CDCl_3$; 7.26-7.20 (2H, m, Ar*H*), 7.17-7.11 (3H, m, Ar*H*), 2.69-2.59 (4H, m, NC*H*$_2$), 2.54 (2H, d, *J* 7.3, ArC*H*$_2$), 2.07 (4H, s (br), N*H*$_2$), 1.69 (1H, quin,

J 6.4, C*H*). ^{13}C (100 MHz) $CDCl_3$; 140.5 (*C*), 129.0 (*C*H), 128.4 (*C*H), 125.9 (*C*H), 45.4 (*C*H), 43.3 (CH_2), 36.7 (CH_2). MS (ESI) 165.1390 (M + H).

Typical procedure for synthesis of $^{tBu}L_O^R$ (R = PyOMe, Ph)

A solution of diamine (2.25 mmol) in methanol (5.00 cm^3) was slowly added to a stirred solution of 3,5-di^{t}butylsalicyaldehyde (1.03 g, 4.40 mmol) in methanol (30.0 cm^3) at room temperature. The bright yellow solution was stirred at room temperature for 2 hours before the solvent was removed *in vacuo* to give a yellow oil which was used without further purification.

$^{tBu}L_O^{PyOMe}$

(98 %). ^{1}H (400 MHz) $CDCl_3$; 8.38 (2H, s, N=C*H*), 8.21 (1H, s, Ar*H*), 7.40 (2H, d, *J* 2.4, Ar*H*), 7.09 (2H, d, *J* 2.4, Ar*H*), 3.75-3.72 (4H, m, NCH_2), 3.72 (3H, s, OCH_3), 2.96 (2H, d, *J* 7.3, ArCH_2), 2.79 (1H, quin, J 6.3, C*H*), 2.25 (3H, s, ArCH_3), 2.23 (3H, s, ArCH_3), 1.47 (18H, s, C(CH_3)$_3$), 1.32 (18H, s, C(CH_3)$_3$). ^{13}C (100 MHz) $CDCl_3$; 167.1 (*C*H), 164.0 (*C*), 158.2 (*C*), 148.8 (*C*H) 140.0 (*C*), 136.7 (*C*), 131.9 (*C*), 127.9 (*C*), 126.9 (*C*H), 125.9 (*C*H), 124.1 (*C*), 117.9 (*C*), 61.0 (CH_2), 59.8 (CH_3), 40.0 (*C*H), 36.4 (CH_2), 35.0 (*C*), 34.1 (*C*), 31.5 (CH_3), 29.5 (CH_3), 13.2 (CH_3), 11.3 (CH_3). MS (ESI) 656.4777 $(M + H)^+$.

$^{tBu}L_O^{Ph}$

(99 %). ^{1}H (400 MHz) $CDCl_3$; 13.85 (2H, s, O*H*), 8.39 (2H, s, N=C*H*), 7.42 (2H, d, *J* 2.4, Ar*H*), 7.37-7.31 (2H, m, Ar*H*), 7.27-7.24 (3H, m, Ar*H*), 7.11 (2H, d, *J* 2.5, Ar*H*), 3.66 (4H, ddd, *J* 33.1, 13.0, 5.0, NCH_2), 2.83 (2H, d, *J* 7.5, ArCH_2), 2.52 (1H, quin, *J* 6.3, CH_2C*H*), 1.58 (18H, s, CH_3), 1.33 (18H, s, CH_3). ^{13}C (100 MHz) $CDCl_3$; 167.1 (*C*H), 158.2 (*C*), 140.1 (*C*), 139.8 (*C*), 136.7 (*C*), 129.2 (*C*H), 128.5 (*C*H), 127.0 (*C*H), 126.2 (*C*H), 125.9 (*C*H), 117.9 (*C*), 60.4 (CH_2), 42.1 (*C*H), 37.0 (CH_2), 35.1 (*C*), 34.1 (*C*), 31.5 (CH_3), 29.5 (CH_3). MS (ESI) 597.4436 $(M + H)^+$.

Typical procedure for preparation of $M^{tBu}L_O^R$ (M = Zn, Ni, Cu, R = PyOMe, Ph)

A solution of proligand (0.50 g, 0.76 mmol) in ethanol (80.0 cm^3) was heated to 50 ºC. A solution of metal salt ($Zn(OAc)_2 \cdot 2H_2O$/$Ni(NO_3)_2 \cdot 6H_2O$/$Cu(OAc)_2 \cdot H_2O$, 0.76 mmol) in ethanol (20.0 cm^3) was added dropwise and stirred for 2 minutes.

NaOH (0.1 M aq, 3.00 cm^3) was added and the resulting solution heated to 80 ºC for 2 h. The solution was allowed to cool to room temperature and methanol (20 cm^3) was added to complete precipitation. The precipitate was collected by filtration and recrystallised from CH_2Cl_2/methanol to give the metal complexes as crystalline powders.

$Zn^{tBu}L_O^{PyOMe}$

(0.27 g, 36 %). ^{1}H (400 MHz) $CDCl_3$; 8.10 (1H, s, Ar*H*), 7.47-7.43 (4H, m, Ar*H*, N=C*H*), 6.86 (2H, m, Ar*H*), 3.77 (3H, s, OCH_3), 3.30 (4H, d, *J* 14.4, NCH_2), 2.31-2.25 (3H, m, CH_2CHCH_2, CHCH_2), 2.24 (3H, s, ArCH_3), 2.20 (3H, s, ArCH_3), 1.46 (18H, s, C(CH_3)$_3$), 1.36 (18H, s, C(CH_3)$_3$). FTIR ν/cm^{-1} (ATR): 2953 (m), 2906 (w), 2867 (w), 1616 (s), 1530 (m), 1438 (s), 1411 (m), 1392 (m), 1361 (m), 1326 m, 1252 s, 1165 (s), 1109 (m), 1062 (m), 1024 (m), 771 (s).

$Ni^{tBu}L_O^{PyOMe}$

(0.27 g, 50 %) Elemental Analysis: (calc. for $C_{42}H_{59}N_3NiO_3$): C 70.79, H 8.35, N 5.90. Found: C 70.55, H 8.36, N 5.94. ^{1}H (400 MHz) $CDCl_3$; 8.26 (1H, s, Ar*H*), 7.35-7.31 (4H, m, Ar*H*, N=C*H*), 6.89 (2H, d, *J* 2.5, Ar*H*), 3.80 (3H, s, OCH_3), 3.71 (2H, dd, *J* 12.6, 6.9, NCH_2), 3.43 (2H, dd, *J* 12.6, 5.7, NCH_2), 2.66-2.57 (3H, m, CH_2CHCH_2, CHCH_2), 2.28 (3H, s, ArCH_3), 2.24 (3H, s, ArCH_3), 1.44 (18H, s, C(CH_3)$_3$), 1.29 (18H, s, C(CH_3)$_3$). ^{13}C (100 MHz) $CDCl_3$;164.7 (*C*H), 164.0 (*C*), 162.3 (*C*), 156.5 (*C*), 149.0 (*C*H), 140.9 (*C*), 135.9 (*C*), 129.0 (*C*H), 125.5 (*C*H), 124.9 (*C*), 120.0 (*C*), 59.9 (*C*H_3), 59.7 (*C*H_2), 36.8 (*C*H2), 35.8 (*C*), 35.4 (*C*H), 33.8 (*C*), 31.3 (*C*H_3), 29.6 (*C*H_3), 13.3 (*C*H_3), 11.4 (*C*H_3). FTIR ν/cm^{-1} (ATR):2946 (m), 2901 (w), 2866 (w), 1614 (s), 1532 (m), 1545 (m), 1449 (m), 1436 (s), 1410 (m), 1389 (m), 1360 (m), 1318 (s), 1204 (s), 1173 (s), 836 (s), 784 (s), 773 (s). MS (ESI) 712.3983 $(M + H)^+$, 734.3802 $(M + Na)^+$.

$Cu^{tBu}L_O^{PyOMe}$

(0.44 g, 80 %) Elemental Analysis: (calc. for $C_{42}H_{59}CuN_3O_3$): C 70.31, H 8.29, N 5.86. Found: C 69.80, H 8.15, N 5.69. FTIR ν/cm^{-1} (ATR): 2947 (m), 2902 (w), 2864 (w), 1620 (s), 1529 (m), 1450 (m), 1433 (m), 1321 (m), 1268 (m), 1254 (m), 1237 (m), 1097 (m), 876 (w), 835 (m), 788 (m), 772 (s). MS (ESI) 717.3903 $(M + H)^+$, 739.3717 $(M + Na)^+$.

Zn$^{t\mathrm{Bu}}$L$_{\mathrm{O}}^{\mathrm{Ph}}$

(0.53 g, 48 %)^{1}H (400 MHz) $CDCl_3$; 8.44 (2H, s, N=C*H*), 7.49 (2H, d, *J* 1.4, Ar*H*), 7.41-7.36 (2H, m, Ar*H*), 7.33.28 (2H, m, Ar*H*), 7.17 (2H, d, *J* 1.4, Ar*H*), 3.77 (4H, ddd, *J* 33.8, 21.3, 4.6, NCH_2), 2.89 (2H, d, *J* 7.4, ArCH_2), 2.57 (1H, quin, *J* 5.7, CH_2C*H*), 1.56 (18H, s, CH_3), 1.40 (18H, s, CH_3). ^{13}C (100 MHz) $CDCl_3$; 167.2 (*C*H), 158.2 (*C*), 140.2 (*C*), 139.8 (*C*), 136.7 (*C*), 129.3 (*C*H), 128.6 (*C*H), 127.0 (*C*H), 126.3 (*C*H), 126.0 (*C*H), 118.0 (*C*), 60.4 (CH_2), 42.2 (*C*H), 37.1 (CH_2), 35.2 (*C*), 34.2 (*C*), 31.6 (CH_3), 29.5 (CH_3). FTIR ν/cm^{-1} (ATR):2954 (s), 2901 (w), 2871 (m), 1631 (s), 1594 (s), 1469 (s), 1438 (s), 1391 (m), 1360 (m), 1335 (m), 1277 (m), 1250 (m), 1188 (s), 1023 (m), 742 (s), 705 (s).

Ni$^{t\mathrm{Bu}}$L$_{\mathrm{O}}^{\mathrm{Ph}}$

(0.54 g, 50 %) Elemental Analysis: (calc. for $C_{40}H_{54}N_2NiO_2$): C 73.51, H 8.33, N 4.29. Found: C 73.50, H 8.66, N 4.27. ^{1}H (400 MHz) $CDCl_3$; 7.40-7.36 (2H, m, Ar*H*), 7.33-7.31 (3H, m, Ar*H*), 7.18 (2H, d, *J* 7.2, Ar*H*), 7.14 (2H, s, N=CH), 6.88 (2H, d, *J* 2.4, Ar*H*), 3.62 (2H, dd, *J* 12.8, 7.5, NCH_2), 3.33 (2H, dd, *J* 12.8, 5.7, NCH_2), 2.57 (2H, d, *J* 7.7, CHCH_2), 2.29 (1H, quin, *J* 7.0, CH_2C*H*), 1.44 (18H, s, C(CH_3)$_3$), 1.30 (18H, s, C(CH_3)$_3$). ^{13}C (100 MHz) $CDCl_3$; 164.4 (*C*H), 162.4 (*C*), 140.4 (*C*), 138.1 (*C*), 135.9 (*C*), 129.2 (*C*H), 128.9 (*C*H), 128.8 (*C*H), 126.8 (*C*H), 125.4 (*C*H), 119.9 (*C*), 59.8 (CH_2), 38.4 (CH_2), 37.9 (*C*H), 35.9 (*C*), 33.8 (*C*), 31.3 (CH_3), 29.6 (CH_3). FTIR ν/cm^{-1} (ATR): 2949 (m), 2902 (w), 2867 (w), 1617 (s), 1532 (w), 1453 (s), 1437 (s), 1409 (m), 1591 (m), 1315 (m), 1248 (m), 1203 (w), 1173 (s), 874 (w), 835 (w), 772 (m), 743 (m), 697 (m). MS (ESI) 653.3611 (M + H)$^+$, 675.3431 (M + Na)$^+$.

Cu$^{t\mathrm{Bu}}$L$_{\mathrm{O}}^{\mathrm{Ph}}$

(0.82 g, 75 %) Elemental Analysis: (calc. for $C_{40}H_{54}CuN_2O_2$): C 72.97, H 8.27, N 4.25. Found: C 72.81, H 8.46, N 4.21. FTIR ν/cm^{-1} (ATR): 2946 (m), 2906 (w), 2866 (w), 1622 (s), 1530 (m), 1451 (m), 1434 (m), 1321 (m), 1269 (w), 1252 (m), 1236 (w), 1169 (s), 788 (m), 772 (s), 743 (m), 679 (m). MS (ESI) 658.3554 (M + H)$^+$, 680.3373 (M + Na)$^+$.

Synthesis of 1,3,5-tri^{t}butylbenzene

To a mixture of ^{t}butylbenzene (77.5 cm^3, 0.50 mol) and ^{t}butyl chloride (500 cm^3, 4.60 mol) at -40 °C was added anhydrous aluminium chloride (33.0 g, 0.25 mol) in ca. 2 g portions over a 10 minute period. The temperature was allowed to rise to -10 °C and the reaction stirred for 2 hours to give a light orange solution. This was poured onto iced water (2.00 L) and stirred for 15 minutes to obtain a colourless solution which was extracted with diethyl ether (3 x 200 cm^3). The organic phase was dried over $MgSO_4$ and the solvent removed *in vacuo*. The partially crystalline product was recrystallised from MeOH to give white crystals (83.6 g, 68 %).

Elemental analysis: (Calc. for $C_{18}H_{30}$): C 87.73, H 12.27. Found: C 87.41, H 12.16. ^{1}H (400 MHz) $CDCl_3$; 7.36 (3H, s, Ar*H*), 1.43 (27H, s, CC*H*$_3$). ^{13}C (100 MHz) $CDCl_3$; 149.6 (*C*), 119.2 (*C*H), 34.7 (*C*), 31.3 (*C*H$_3$). MS (EI$^+$, m/z): 269.2232 (M + Na)$^+$

1-bromo-3,5-di^{t}butylbenzene

A solution of bromine (30.9 cm^3, 604 mmol) in chloroform (100 cm^3) was added dropwise to a cooled (0 ^{o}C) mixture of 1,3,5-tri^{t}butylbenzene (71.0 g, 288 mmol) and iron powder (16.9 g, 302 mmol) in chloroform (145 cm^3). The addition was controlled in such a way as to ensure that the temperature did not exceed 5 ^{o}C, and the reaction mixture was then stirred at room temperature for 16 hours. The reaction mixture was poured onto ice water and the organic layer separated, washed with NaOH (10 %, 3 x 200 cm^3) and the solvent removed *in vacuo* to give an orange residue which was distilled under reduced pressure (93-95 ^{o}C) to give 1-bromo-3,5-di*tert*butylbenzene as a white crystalline solid (52.8 g, 88 %).

^{1}H (400 MHz) $CDCl_3$; 7.35 (3H, s, Ar*H*), 1.33 (18H, s, C(C*H*$_3$)$_3$); ^{13}C (100 MHz) $CDCl_3$; 153.0 (*C*), 125.7 (*C*H), 122.2 (*C*H), 121.0 (*C*), 35.0 (*C*), 31.3 (*C*H$_3$). MS (ESI$^+$, m/z): 291.0724 (M + Na)$^+$

Synthesis of 1,3-di^{t}butlybenzene

A solution of 1-bromo-3,5-di^{t}butylbenzene (52.8 g, 197 mmol in dry THF was added dropwise to a mixture of magnesium (10.0 g, 423 mmol) and anhydrous THF (300 cm^3) under N_2 at 0 ^{o}C. The addition of 2 grains of iodine and 2 drops of

1,2-dibromoethane initiated the reaction which was then heated to reflux for 16 hours. After cooling to 0 ^{o}C the reaction was hydrolysed with water (20.0 cm^3) and the mixture filtered through kieselguhr. The solvent was removed in vacuo to give a cloudy orange residue which was extracted with diethyl ether (3 x 100 cm^3) and dried over $MgSO_4$. The solvent was removed *in vacuo* and the yellow residue distilled under reduced pressure (48 ^{o}C) to give a clear oil. (21.6 g, 58 %).

Elemental analysis: (Calc. for $C_{14}H_{22}$): C 88.35, H 11.65. Found: C 87.27, H 11.62. ^{1}H (400 MHz) $CDCl_3$; 7.51 (1H, s, ArH), 7.31-7.27 (3H, m, ArH), 1.40 (18H, s $C(CH_3)_3$); ^{13}C (100 MHz) $CDCl_3$; 150.6 (*C*), 127.6 (*C*H), 122.4 (*C*H), 122.2 (*C*H), 34.8 (*C*), 31.5 (*C*H_3). MS (ESI^+, m/z): 191.1755 $(M + H)^+$

Synthesis of 1-bromo-2,4-di^{t}butyl-benzene

A solution of bromine (7.37 cm^3, 148 mmol) in trimethylphosphate (50.0 cm^3) was added dropwise to a hot (70 ^{o}C) solution of 1,3-di^{t}butylbenzene (21.6 g, 114 mmol) in trimethylphosphate (250 cm^3). The reaction was stirred at 70 ^{o}C for 6 hours before the addition of further bromine (1.00 cm^3, 19.2 mmol) in trimethylphospate (5.00 cm^3). The reaction was then stirred at 70 ^{o}C for a further 16 hours. The reaction was extracted with petroleum ether (40-60), washed with saturated Na_2SO_3 solution until the organic layer decolourised, washed with brine and dried over $MgSO_4$. The solvent was removed *in vacuo* and the residual yellow oil distilled under reduced pressure (79 °C) to give 1-bromo-2,4-di^{t}butylbenzene as a colourless oil (22.1g, 73 %).

^{1}H (400 MHz) $CDCl_3$; 7.56-7.51 (2H, m, Ar*H*), 7.10 (1H, dd, Ar*H*), 1.57 (9H, s, $C(CH_3)_3$), 1.35 (9H, s, $C(CH_3)_3$) ; ^{13}C (100 MHz) $CDCl_3$; 150.0 (*C*), 146.9 (*C*), 135.2 (*C*H), 125.2 (*C*H), 124.5 (*C*H), 119.4 (*C*H), 36.8 (*C*), 34.7 (*C*), 31.3 (*C*H_3), 29.8 (*C*H_3). MS (ESI^+, m/z): 270.0809 $(M + H)^+$

Synthesis of 2,4-di^{t}butyl-benzenethiol

A solution of 1-bromo-2,4-di^{t}butyl-benzene (8.00 g, 29.7 mmol) in THF (20.0 cm^3) was added dropwise to a mixture of magnesium (1.40 g, 57.6 mmol) and THF (100 cm^3) at 0 °C. The reaction was initiated with 2 grains of iodine and 2 drops of dibromoethane, and heated to reflux for 3 hours. The mixture was cooled to room temperature and sulfur (0.96 g) added, before being refluxed for a further 18 hours.

The mixture was cooled to room temperature and quickly decanted before being hydrolysed with excess hydrochloric acid (5 %, 20.0 cm^3). The THF was removed in vacuo and the residue extracted with chloroform (3 x 100 cm^3), washed with brine (100 cm^3) and dried over $MgSO_4$. The solvent was removed *in vacuo* and the residual yellow oil distilled using short path kugelruhr apparatus to give 2,4-di-^{t}butylbenzenethiol (0.90 g, 14 %).

^{1}H (400 MHz) $CDCl_3$; 7.50 (1H, s, Ar*H*), 7.23 (1H, d, *J* 8.0, Ar*H*), 7.13 (1H, d, *J* 8.2, Ar*H*), 3.60 (1H, s, S*H*), 1.57 (9H, s, CH_3), 1.38 (9H, s, CH_3); MS 223.1524 $(M + H)^+$

Synthesis of 2,4-di^{t}butylthiobenzaldehyde

A solution of 2,4-di^{t}butylbenzenethiol (0.90 g, 4.05 mmol) in ether (5.00 cm^3) was added dropwise to a mixture of ether (10.0 cm^3), ^{n}BuLi (5.13 cm^3, 1.60 M in hexanes) and TMEDA (1.26 cm^3, 8.40 mmol) at 0 °C. The solution was allowed to warm to room temperature and stirred for 16 hours. The mixture was cooled to 0 °C and 1-formylpiperidine (0.93 g, 8.20 mmol) cautiously added dropwise. The solution was allowed to warm to room temperature and stirred for a further 22 hours. The solution was cooled to 0 °C and quenched by the addition of hydrochloric acid (20.0 cm^3) and stirred for 30 minutes. The mixture was extracted with ether (3 x 20.0 cm^3), dried over $MgSO_4$, and the solvent removed *in vacuo* to give a yellow oil which was purified by column chromatography (silica gel, petroleum ether: CH_2Cl_2 1:0 to 1:1) to yield a yellow solid which was used without further purification (0.58 g, 58 %).

Elemental analysis: (Calc. for $C_{15}H_{22}OS$): C 71.95, H 8.86. Found: C 71.39, H 8.97. ^{1}H (400 MHz) $CDCl_3$;10.10 (1H, s, S*H*), 8.23 (1H, s, Ar*H*), 7.68 (1H, d, J 2.2, Ar*H*), 7.52 (1H, d, J 2.2, Ar*H*), 1.58 (9H, s, CH_3), 1.35 (9H, s, CH_3); ^{13}C (100 MHz) $CDCl_3$; 195.7 (*C*H), 148.7 (*C*), 147.1 (*C*), 134.9 (*C*), 133.4 (*C*H), 130.9 (*C*), 129.6 (*C*H), 36.9 (*C*), 34.5 (*C*), 31.1 (*C*H_3), 29.7 (*C*H_3); FTIR ν/cm^{-1} (ATR): 3436 (w), 2945 (s), 2905 (m), 2869 (m), 1670 (w), 1596 (w), 1477 (m), 1462 (m), 1431 (m), 1395 (m), 1361 (s), 1265 (m), 1229 (s), 1199 (m), 1156 (m), 1086 (m), 1051 (s), 1021 (s), 964 (s), 882 (s). MS (ESI^+, m/z) 251.1458 (M + H), 273.1276 (M + Na).

Synthesis of $Zn^{tBu}L_S^{Py}$

A solution of 2,4-di^{t}butylthiobenzaldehyde (900 mg, 3.60 mmol) in methanol (10.0 cm^3) was added to a solution of $Zn(OAc)_2 \cdot 2H_2O$ (0.41 g, 1.87 mmol) in methanol (10.0 cm^3) and stirred for 15 minutes at room temperature. A solution of 2-(2-pyridylmethyl)-1,3-propanediamine (300 mg, 1.80 mmol) in methanol (5.00 cm^3) and triethylamine (1.70 cm^3, 3.60 mmol) were added dropwise and the mixture stirred at room temperature for 16 hours. A yellow powder was isolated by filtration and dried *in vacuo* (930 mg, 93 %).

Elemental analysis: (Calc. for $C_{39}H_{53}N_3S_2Zn$): C 67.56, H 7.70 N 6.06. Found: C 66.29, H 7.73, N 5.91 ^{1}H (400 MHz) $CDCl_3$; 8.63 (1H, d, *J* 4.8, Ar*H*), 8.40 (2H, s, N=C*H*), 7.67 (1H, td, *J* 7.7, 1.8, Ar*H*), 7.59 (2H, d, *J* 2.1, Ar*H*), 7.23-7.17 (2H, m, Ar*H*), 7.09 (2H, d, *J* 1.7, Ar*H*), 4.57 (2H, s, NCH_2), 3.72 (2H, s, NCH_2), 2.94 (2H, s, CHCH_2), 2.94 (1H, s, C*H*), 1.70 (18H, s, C(CH_3)$_3$), 1.34 (18H, s, C(CH_3)$_3$). FTIR ν/cm^{-1} (ATR): 2959 (m), 2905 (w), 2868 (w), 1672 (m), 1636 (m), 1603 (m), 1479 (m), 1458 (m), 1422 (m), 1391 (m), 1361 (m), 1260 (m), 1227 (m), 1154 (m), 1088 (m), 1048 (m), 1022 (m), 773 (s). MS (MALDI$^+$, m/z): 692.3 $(M + H)^+$.

Synthesis of $Ni^{tBu}L_S^{Py}$

A solution of $Ni(NO_3)_2 \cdot 6H_2O$ (155 mg, 0.53 mmol) in methanol (10.0 cm^3) was added dropwise to a solution of $Zn^{tBu}L_S^{Py}$ (370 mg, 0.53 mmol) in CH_2Cl_2 (15.0 cm^3) and the mixture stirred at room temperature for 16 hours. Excess methanol (20.0 cm^3) was added to complete precipitation and a brown powder was isolated by filtration, washed with methanol (10.0 cm^3) and dried *in vacuo* (125 mg, 35 %).

Elemental analysis: (Calc. for $C_{39}H_{53}N_3NiS_2$): C 68.22, H 7.78 N 6.12, Ni 8.55. Found: C 65.55, H 7.65, N 5.75, Ni 8.64, Zn 0.0. ^{1}H (400 MHz) $CDCl_3$; 8.64 (1H, d, *J* 4.5, Ar*H*), 7.86 (2H, s, N=C*H*), 7.71 (1H, t, *J* 7.5, Ar*H*), 7.46-49 (2H, m, Ar*H*), 7.26-7.21 (2H, m, Ar*H*), 7.09 (2H, d, *J* 1.7, Ar*H*), 3.99 (2H, dd, J 12.1 7.2, NCH_2), 3.74 (2H, dd, J 12.2, 5.7, NCH_2), 2.92 (2H, d, J 6.5, CHCH_2), 2.88-2.80 (1H, m, C*H*), 1.68 (18H, s, C(CH_3)$_3$), 1.34 (18H, s, C(CH_3)$_3$). FTIR ν/cm^{-1} (ATR): 2947(m), 2902 (m), 1617 (s), 1570 (w), 1451 (m), 1390 (m), 1360 (m), 1264 (m), 1163 (m), 1057 (s), 744 (s), 639 (m). MS (MALDI$^+$, m/z): 686.3128 $(M)^+$.

Synthesis of $Zn^{tBu}L_S^{PyOMe}$

Zinc tetrafluoroborate hydrate (190 mg, 1.25 mmol) was added to a solution of 3,5-ditbutylthiosalicylaldehyde (400 mg, 1.60 mmol) in methanol (20.0 cm^3). 2-((4-methoxy-3,5-dimethylpyridin-2-yl)methyl)propane-1,3-diamine (178 mg, 1.00 mmol) was added and the resulting solution was stirred at room temperature overnight. A yellow solid was isolated by filtration and recrystallised from CH_2Cl_2/methanol to give $Zn^{tBu}L_S^{Py}$ as a yellow crystalline solid. (500 mg, 85 %).

^1H (400 MHz) $CDCl_3$; 8.63 (1H, d, *J* 4.8, Ar*H*), 8.23 (2H, s, N=C*H*), 7.53 (2H, s, Ar*H*), 7.46 (2H, s, Ar*H*), 6.63 (1H, s, Ar*H*), 5.60 (3H, s, OCH_3), 5.35-5.30 (4H., m, NCH_2), 3.40 (6H, br, s, CH_3), 3.22 (2H, s, CHCH_2), 2.58 (1H, s, C*H*), 1.56 (18H, s, C(CH_3)$_3$), 1.33 (18H, s, C(CH_3)$_3$). FTIR ν/cm^{-1} (ATR): 2954 (m), 2868 (w), 1226 (w), 1600 (w), 1560 (w), 1475 (m), 1394 (m), 1361 (m), 1297 (w), 1260 (m), 1219 (w), 1047 (s), 878 (w), 816 (w), 772 (s), 686 (w). MS (ESI^+, m/z): 750.3414 $(M + H)^+$

Synthesis of $Ni^{tBu}L_S^{PyOMe}$

Prepared as $Ni^{tBu}L_S^{Py}$ using $Zn^{tBu}L_S^{PyOMe}$ (500 mg, 0.66 mmol) in methanol (10 cm^3) and $Ni(NO_3)_2{\cdot}6H_2O$ (192 mg, 0.66 mmol) in methanol (10 cm^3) to give $Ni^{tBu}L_S^{PyOMe}$ (100 mg, 20 %).

FTIR ν/cm^{-1} (ATR): 2955 (m), 2906 (w), 2869 (w), 1625 (m), 1599 (w), 1458 (m), 1424 (m), 1394 (w), 1361 (m), 1301 (m), 1261 (m), 1219 (w), 1090 (s), 1040 (s), 879 (w), 816 (w), 772 (s), 773 (w), 688 (w). MS (ESI^+, m/z): 744.3511 $(M + H)^+$

Synthesis of 4-(chloromethyl)-1H-imidazole

Thionyl chloride (30.0 cm^3, 42.4 mmol) was cooled to 0 °C and (1H-imidazol-4-yl)methanol (5.00 g, 51.0 mmol) was added portionwise over 5 minutes. This was stirred at 0 °C for 3 hours and a cream precipitate was formed. This was collected by filtration and washed with chloroform (30.0 cm^3) (4.56 g, 77 %).

^1H (400 MHz) DMSO; 14.79 (1H, s br, N*H*), 9.12 (1H, s, C*H*), 7.75 (1H, s, C*H*), 4.89 (2H, s, CH_2): ^{13}C (100 MHz) DMSO; 135.9 (*C*H), 129.9 (*C*), 119.0 (*C*H), 34.9 (*C*H_2). FTIR ν/cm^{-1} (ATR): 3138 (m), 2678 (m), 2586 (m), 1613 (m), 1465

(w), 1432 (m), 1288 (m), 1143 (m), 914 (m), 809 (m), 710 (s), 618 (s). MS (ESI) 117.0217 $(M + H)^+$.

Synthesis of Diethyl 2-((1H-imidazol-4-yl)methyl)malonate

Prepared as diethyl (2-pyridylmethyl)-1,3-propanedioate using 4-(chloromethyl)-1H-imidazole (3.00 g, 25.7 mmol), diethyl malonate (12.7 cm^3, 75.0 mmol), and sodium ethoxide (1.50 g, 65.0 mmol of sodium in 50 cm^3 of ethanol) to give diethyl 2-((1H-imidazol-4-yl)methyl)malonate as a pale yellow oil (5.10 g, 83%).

^{1}H (400 MHz) $CDCl_3$; 8.77 (1H, s br, N*H*), 7.65 (1H, s, Ar*H*), 6.87 (1H, s, Ar*H*), 4.25-4.12 (4H, m, $CH_3C\mathit{H_2}$), 3.77 (1H, t, *J* 7.4, C*H*), 3.22 (2H, d, *J* 7.4, $CHC\mathit{H_2}$), 1.23 (6H, t, *J* 7.2, $C\mathit{H_3}$). ^{13}C (100 MHz) $CDCl_3$; 169.1 (*C*), 134.7 (*C*H), 133.0 (*C*), 118.0 (*C*H), 61.7 ($C\mathit{H_2}$), 52.1 (*C*H), 25.9 ($C\mathit{H_2}$), 14.0 ($C\mathit{H_3}$). FTIR ν/cm^{-1} (ATR): 3466 (m, br), 3059 (w), 2984 (w), 1731 (m), 1489 (w), 1444 (m), 1329 (w), 1149 (m), 1031 (m), 1010 (m), 889 (w), 755 (s), 694 (s), 637 (s). MS (ESI) 241.1194 $(M + H)^+$.

Synthesis of 2-((1H-imidazol-4-yl)methyl)malonamide

Prepared as (2-pyridylmethyl)-1,3-propanediamide using diethyl 2-((1H-imidazol-4-yl)methyl)malonate (5.10 g, 21.3 mmol), sodium methoxide (0.15 g, 2.80 mmol), methanol (200 cm^3) and gaseous ammonia to give 2-((1H-imidazol-4-yl)methyl)malonamide (3.60 g, 93 %).

^{1}H (400 MHz) $(CD_3)_2SO$; 7.48 (1H, s, ArH), 7.25 (2H, s, $N\mathit{H_2}$), 7.01 (2H, s, $N\mathit{H_2}$), 6.68 (1H, s, Ar*H*), 3.37 (1H, t, *J* 7.5, C*H*), 2.88 (2H, d, *J* 7.3, $C\mathit{H_2}$). ^{13}C (100 MHz) $(CD_3)_2SO$; 171.4 (*C*), 134.9 (*C*H), 134.8 (*C*H), 53.4 (*C*H), 49.0 ($C\mathit{H_2}$). FTIR ν/cm^{-1} (ATR): 3372 (w), 3282 (w), 3190 (w), 3131 (w), 2973 (w), 2900 (w), 1662 (s), 1606 (m), 1455 (m), 1370 (s), 1162 (m), 1084 (m), 838 (m), 755 (m), 660 (m), 623 (s), 593 (s), 512 (s), 420 (s). MS (ESI) 205.0723 $(M + Na)^+$.

Synthesis of (1-trityl-1H-imidazol-4-yl)methanol

A solution of 4(5)-hydroxymethylimidazole (4.00 g, 40.8 mmol) in dimethylforamide (130 cm^3) and trimethylamine (9.90 cm^3) was stirred at room temperature. Trityl chloride (13.9 g, 50 mmol) was added portionwise and the

solution stirred overnight. A white solid was separated by filtration and washed with ether (12.5 g, 90 %).

FTIR ν/cm^{-1} (ATR): 3174 (w), 3063 (w), 2978 (w), 2603 (w), 2496 (w), 1891 (m), 1481 (m), 1443 (m), 1397 (m), 1132 (s), 1036 (s), 991 (s), 763 (s), 750 (s), 699 (s), 654 (m). MS (ESI) 341.1639 (M + H), 363.1467 (M + Na)$^{+}$.

Synthesis of 4-(chloromethyl)-1-trityl-1H-imidazole

Prepared as 4-(chloromethyl)-1H-imidazole using thionyl chloride (40.0 cm^3, 207 mmol) and (1-trityl-1H-imidazol-4-yl)methanol (15.0 g, 44.1 mmol) to give 4-(chloromethyl)-1-trityl-1H-imidazole as a white solid (5.50 g, 35 %)

^{1}H (400 MHz) $CDCl_3$; 7.37-7.28 (17H, m, Ar*H*), 2.82 (2H, s, C*H*$_2$). FTIR ν/cm^{-1} (ATR): 3463 (w, br), 3138 (w), 3060 (w), 3023 (w), 1489 (m), 1444 (m), 1329 (w), 1290 (w), 1154 (m), 1030 (w), 1009 (m), 889 (m), 756 (s), 694 (s), 637 (s). MS (ESI) 359.1868 (M + H)$^{+}$.

Synthesis of Diethyl 2-((1-trityl-1H-imidazol-4-yl)methyl)malonate

Prepared as diethyl (2-pyridylmethyl)-1,3-propanedioate using 4-(chloromethyl)-1-trityl-1H-imidazole (2.50 g, 7.00 mmol), diethyl malonate (2.60 cm^3 15.5 mmol), and sodium ethoxide (0.32 g, 13.9 mmol of sodium in ethanol (10.0 cm^3)) to give diethyl 2-((1-trityl-1H-imidazol-4-yl)methyl)malonate as a yellow oil (3.35 g, 99 %).

^{1}H (400 MHz) $CDCl_3$; 7.37-7.28 (17H, m, Ar*H*), 4.24 (4H, q, *J* 7.2, CH_3CH_2), 3.38 (2H, s, $CHCH_2$), 3.14 (1H, s, CH_2CH), 1.32 (6H, t, *J* 7.2, CH_2CH_3). ^{13}C (100 MHz) $CDCl_3$; 166.7 (*C*), 147.0 (*C*), 128.0 (*C*H, br), 127.9 (*C*, br), 127.3 (*C*), 82.0 (*C*H), 61.7 (*C*H2), 41.7 (CH_2), 14.1 (CH_3). FTIR ν/cm^{-1} (ATR): 3463 (m, br), 3063 (w), 3024 (w), 2984 (w), 1732 (s), 1597 (w), 1489 (m), 1444 (s), 1370 (w), 1329 (m), 1272 (m), 1031 (m), 1010 (s), 889 (m), 756 (s), 695 (s), 637 (s).

Synthesis of 2-((1-trityl-1H-imidazol-4-yl)methyl)malonamide

Prepared as (2-pyridylmethyl)-1,3-propanediamide using diethyl 2-((1-trityl-1H-imidazol-4-yl)methyl)malonate (2.00 g, 4.15 mmol), sodium methoxide (0.025 g,

0.46 mmol), methanol (20.0 cm^3) and gaseous ammonia to give 2-((1-trityl-1H-imidazol-4-yl)methyl)malonamide as a white solid (0.98 g, 56 %).

^{1}H (400 MHz) $(CD_3)_2SO$: 7.44 (2H, br, s, N*H*$_2$), 7.32 (1H, t, J 1.5, Ar*H*), 7.31-7.28 (6H, m, Ar*H*), 7.26-7.20 (10H, m, Ar*H*), 7.02 (2H, s, br, N*H*$_2$), 6.45 (1H, s, C*H*), 2.97 (2H, s, C*H*$_2$). ^{13}C (100 MHz) $(CD_3)_2SO$: 169.6 (*C*), 148.2 (*C*), 128.2 (*C*H), 128.0 (*C*H), 127.1 (*C*H), 81.0 (*C*H), 43.5 (*C*H$_2$). FTIR ν/cm^{-1} (ATR): 3464 (w, br), 3140 (w), 2798 (w), 2698 (w), 2627 (w), 2590 (w), 1615 (w), 1489 (w), 1444 (m), 1148 (m), 929 (w), 890 (w), 756 (s), 695 (s), 636 (s).

4.6 References

1. J. Wuerges, J.-W. Lee, Y.-I. Yim, H.-S. Yim, S.-O. Kang and K. D. Carugo, *Proc. Nat. Acad. Sci. USA*, 2004, **101**, 8569-8574.
2. M. Franks, PhD, The University of Nottingham, 2011.
3. P. A. Bryngelson, S. E. Arobo, J. L. Pinkham, D. E. Cabelli and M. J. Maroney, *J. Am. Chem. Soc.*, 2004, **126**, 460-461.
4. D. P. Barondeau, C. J. Kassmann, C. K. Bruns, J. A. Tainer and E. D. Getzoff, *Biochem.*, 2004, **43**, 8038-8047.
5. W.-Z. Lee, C.-W. Chiang, T.-H. Lin and T.-S. Kuo, *Chem. Eur. J.,* 2012, **18**, 50-53.
6. S. B. Choudhury, J.-W. Lee, G. Davidson, Y.-I. Yim, K. Bose, M. L. Sharma, S.-O. Kang, D. E. Cabelli and M. J. Maroney, *Biochem.*, 1999, **38**, 3744-3752.
7. J. Hioe and H. Zipse, *Org. Biomol. Chem.*, 2010, **8**, 3609-3617.
8. G. Xue, R. De Hont, E. Münck and L. Que, *Nat. Chem.*, 2010, **2**, 400-405.
9. P. S. Walker, P. M. Bergin, M. C. Grossel and P. N. Horton, *Inorg. Chem.*, 2004, **43**, 4145-4153.
10. P. B. Russell, *J. Am. Chem. Soc.*, 1950, **72**, 1853-1854.
11. A. Spek, *Acta Crystallogra. D*, 2009, **65**, 148-155.
12. Y. Shimazaki, N. Arai, T. J. Dunn, T. Yajima, F. Tani, C. F. Ramogida and T. Storr, *Dalton Trans.*, 2011, **40**, 2469-2479.
13. H. J. Krueger and R. H. Holm, *Inorg. Chem.*, 1987, **26**, 3645-3647.
14. W.-K. Dong, Y.-X. Sun, C.-Y. Zhao, X.-Y. Dong and L. Xu, *Polyhedron*, 2010, **29**, 2087-2097.
15. O. Rotthaus, F. Thomas, O. Jarjayes, C. Philouze, E. Saint-Aman and J.-L. Pierre, *Chem. Eur. J.*, 2006, **12**, 6953-6962.
16. A. Klamt and G. Schuurmann, *J. Chem. Soc., Perkin Trans. 2*, 1993, 799-805.
17. P. A. Stenson, A. Board, A. Marin-Becerra, A. J. Blake, E. S. Davies, C. Wilson, J. McMaster and M. Schröder, *Chem. Eur. J.*, 2008, **14**, 2564-2576.
18. P. C. Myhre, T. Rieger and J. T. Stone, *J. Org. Chem.*, 1966, **31**, 3425-3426.
19. C. M. D. Komen and F. Bickelhaupt, *Synth. Commun.*, 1996, **26**, 1693-1697.
20. C. S. Mullins, C. A. Grapperhaus and P. M. Kozlowski, *J. Biol. Inorg. Chem.*, 2006, **11**, 617-625.
21. J. Shearer and N. Zhao, *Inorg. Chem.*, 2006, **45**, 9637-9639.
22. M. Gennari, M. Orio, J. Pécaut, F. Neese, M.-N. Collomb and C. Duboc, *Inorg. Chem.*, 2010, **49**, 6399-6401.
23. H.-I. Lee, J.-W. Lee, T.-C. Yang, S.-O. Kang and B. Hoffman, *J. Biol. Inorg. Chem.*, 2010, **15**, 175-182.
24. S. A. Dikanov and Y. D. Tsevtkov, *Electron Spin Echo Envelope Modulation (ESEEM) Spectroscopy.*, CRC Press, Boca Raton, 1992.
25. L. G. Rowan, E. L. Hahn and W. B. Mims, *Phys. Rev.*, 1965, **137**, A61-A71.
26. Y. Deligiannakis, M. Louloudi and N. Hadjiliadis, *Coord. Chem. Rev.*, 2000, **204**, 1-112.
27. P. Höfer, A. Grupp, H. Nebenführ and M. Mehring, *Chem. Phys. Lett.*, 1986, **132**, 279-282.
28. S. A. Dikanov, Y. D. Tsvetkov, M. K. Bowman and A. V. Astashkin, *Chem. Phys. Lett.*, 1982, **90**, 149-153.
29. S. Stoll and A. Schweiger, *J. Mag. Reson.*, 2006, **178**, 42-55.
30. J. Shearer, *Acc. Chem. Res.*, 2014, **47**, 2332-2341.
31. H. J. Kruger, G. Peng and R. H. Holm, *Inorg. Chem.*, 1991, **30**, 734-742.

32. D. Nakane, Y. Wasada-Tsutsui, Y. Funahashi, T. Hatanaka, T. Ozawa and H. Masuda, *Inorg. Chem.*, 2014, **53**, 6512-6523.
33. M. T. Kieber-Emmons, J. Annaraj, M. S. Seo, K. M. Van Heuvelen, T. Tosha, T. Kitagawa, T. C. Brunold, W. Nam and C. G. Riordan, *J. Am. Chem. Soc.*, 2006, **128**, 14230-14231.
34. E. M. Gale, A. C. Simmonett, J. Telser, H. F. Schaefer and T. C. Harrop, *Inorg. Chem.*, 2011, **50**, 9216-9218.

Chapter 5

Conclusions

We have synthesised and characterised a series of Zn^{II}, Ni^{II} and Cu^{II} diphenolate complexes $M^{R}L_{O}^{NMe}$ (M = Zn, Ni, Cu; R = Cl, Br, Nap, Ph, PhMe, PhOMe, ^{t}Bu/Br, ^{t}Bu/Ph, ^{t}Bu/PhMe, ^{t}Bu/PhOMe), and a series of four coordinate diphenolate and dithiophenolate complexes $M^{tBu}L_{O}^{Py}$, $M^{tBu}L_{O}^{PyOMe}$, $M^{tBu}L_{O}^{Ph}$, $Ni^{tBu}L_{S}^{PyOMe}$ and $Ni^{tBu}L_{S}^{Py}$ as analogues of the active sites of GO[1-3] and NiSOD.[4, 5] The majority of these complexes have been characterised by X-ray crystallography. $M^{tBu}L_{O}^{Py}$, $M^{tBu}L_{O}^{PyOMe}$, $Ni^{tBu}L_{S}^{PyOMe}$ and $Ni^{tBu}L_{S}^{Py}$ possess pendant pyridyl N-donors that have the potential to adopt pentacoordinate geometries. This is particularly relevant to the active site of NiSOD, which has been proposed to adopt a four coordinate geometry in its reduced state and a five coordinate geometry in its oxidised form.[6]

We have significantly extended the range of 3,5-functionalised salicylaldehydes that can be incorporated within salen-type ligands; the majority of these functionalised salicyaldehydes were accessed *via* Suzuki coupling. Thus, $M^{R}L_{O}^{NMe}$ (M = Zn, Ni, Cu; R = Cl, Br, Nap, Ph, PhMe, PhOMe, ^{t}Bu/Br, ^{t}Bu/Ph, ^{t}Bu/PhMe, ^{t}Bu/PhOMe) (Figure 5.1) have been prepared and characterised. Aromatic and ^{t}butyl substituents in $M^{R}L_{O}^{NMe}$ (M = Zn, Ni, Cu; R = Ph, PhMe, PhOMe, ^{t}Bu/Ph, ^{t}Bu/PhMe, ^{t}Bu/PhOMe) promote electrochemical reversibility with two, three or four oxidation processes observed for each complex. Within each series M = Zn, Ni or Cu there is a shift to less positive potential for these processes as the electron donating nature of the substituents is varied with R = Ph < PhMe < PhOMe.

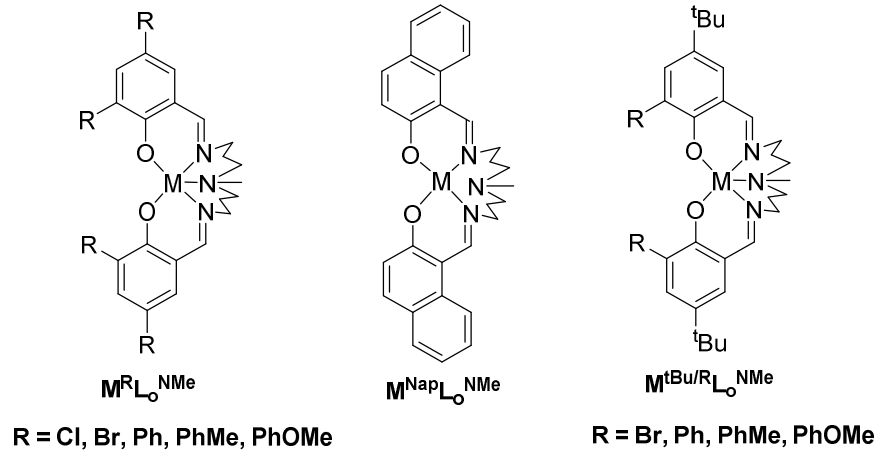


Figure 5.1: Complexes synthesised in chapter 2, M = Zn, Ni, Cu.

We investigated the nature of the oxidised species $[M^{R}L_{O}^{NMe}]^{+}$ and $[M^{R}L_{O}^{NMe}]^{2+}$ (M = Zn, Ni, Cu; R = Cl, Br, Nap, Ph, PhMe, PhOMe, ^{t}Bu/Br, ^{t}Bu/Ph, ^{t}Bu/PhMe, ^{t}Bu/PhOMe) by UV/vis spectroelectrochemistry and EPR spectroscopy (as appropriate) to provide insight into the nature of the oxidation processes in each complex. For M = Zn or Cu, the oxidation processes are assigned as ligand-based that generate one or two phenoxyl radical centres bound to a Zn^{II} or Cu^{II} centre. These phenoxyl radical complexes are particularly relevant to the chemistry of the active site of GO in its oxidised form that possesses a phenoxyl radical (as Tyr272$^{\bullet}$) bound to a Cu^{II} centre. A peculiar feature of the active site of GO is that Tyr272 possesses a thioether substitution at the 3-position of the phenyl ring of Tyr272 formed by a post-translational modification involving Cys228.[2] Our results show that the variation of the 3- and 5-subsituents about the phenolate rings in $M^{R}L_{O}^{NMe}$ can influence the potential of the oxidation processes in these complexes, with a variation at the 5-position having the greater effect. Thus, our results lend support to the role of the thioether substitution at the 3-position of the phenyl ring of Tyr272 in tuning the reduction potential of the phenoxyl/phenolate couple at the active site to optimise the catalytic function of GO.[7]

Our UV/vis, EPR and DFT studies show that the first oxidation process for the majority of $Ni^{R}L_{O}^{NMe}$ (R = Cl, Br, Nap, Ph, PhMe, PhOMe, ^{t}Bu/Br, ^{t}Bu/Ph, ^{t}Bu/PhMe, ^{t}Bu/PhOMe) are metal-based and are associated with the generation of formal Ni^{III} species, $[Ni^{R}L_{O}^{NMe}]^{+}$. We also suggest that $[Ni^{PhOMe}L_{O}^{NMe}]^{+}$ displays temperature dependent redox tautomerism involving Ni^{II}-phenoxyl (observed at 253 K) and Ni^{III}-phenolate species (observed at 77 K). The precise natures of the oxidation products of $M^{R}L_{O}^{NMe}$ (M = Zn, Ni, Cu; R = ^{t}Bu/Ph, ^{t}Bu/PhMe, ^{t}Bu/PhOMe) remain ambiguous and our initial studies on $[Ni^{R}L_{O}^{NMe}]^{+}$ (R = ^{t}Bu/Ph, ^{t}Bu/PhMe, ^{t}Bu/PhOMe) suggest that the electronic structures in these complexes are finely balanced between Ni^{II}-phenoxyl and Ni^{III}-phenolate descriptions. The full characterisation of $[M^{R}L_{O}^{NMe}]^{+}$ and $[M^{R}L_{O}^{NMe}]^{2+}$ (M = Zn, Ni, Cu; R = ^{t}Bu/Ph, ^{t}Bu/PhMe, ^{t}Bu/PhOMe) could form the basis for further research together with investigations into complexes in which substituents at the 5-postion only are varied.

The second theme of research described in this thesis focusses on the properties of $Ni^{tBu}L_{S}^{Py}$ (Figure 5.2) as an analogue for the active site of NiSOD. Previous

preliminary studies had shown that this complex possesses a reversible oxidation process at 0.05 V (*vs.* Fc^+/Fc), and that $[Ni^{tBu}L_S^{Py}]^+$ exhibits an EPR spectrum similar to that found for the oxidised form of NiSOD.[8] We have built upon these results by probing the electronic structure of $[Ni^{tBu}L_S^{Py}]^+$ using ESEEM and HYSCORE spectroscopies. We attempted to stabilise the formal Ni^{III} centre through the incorporation of the electron donating 2,4-dimethyl-5-methoxypyridine as the pendant N-donor. We found little effect; $Ni^{tBu}L_S^{PyOMe}$ possesses a similar reduction potential (E_p^a = 0.09 V *vs.* Fc^+/Fc) to $Ni^{tBu}L_S^{Py}$ (E_p^a = 0.10 *vs.* Fc^+/Fc). The syntheses and characterisations of the analogous diphenolate complexes $Ni^{tBu}L_O^{Py}$,[8] $Ni^{tBu}L_O^{PyOMe}$ and $Ni^{tBu}L_O^{Ph}$ (Figure 5.2) provided a route to assess the role of phenolate-O *vs.* thiophenolate-S coordination in controlling the electronic properties of these complexes.

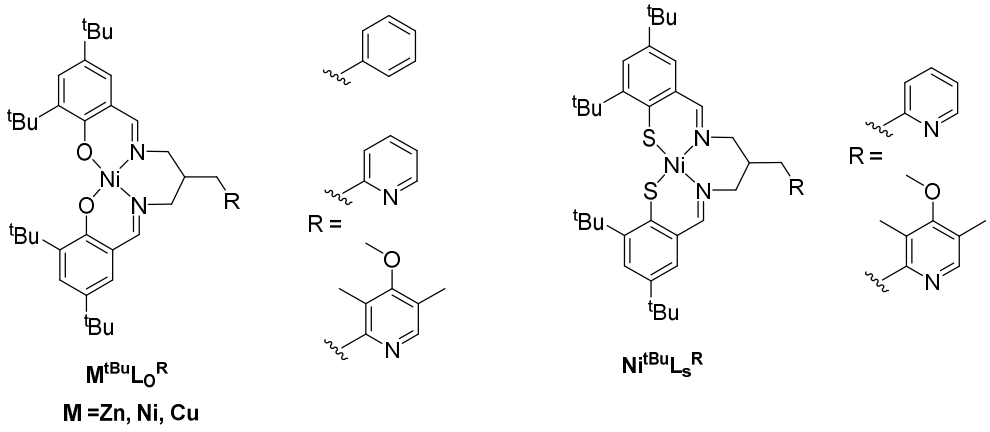


Figure 5.2: Complexes synthesised in chapter 4.

Our ESEEM and HYSCORE spectroscopic studies of $[Ni^{tBu}L_S^{Py}]^+$ revealed details of small ^{14}N hyperfine couplings (a_{iso}^N= 3.8 MHz and a_{iso}^N= 5.8 MHz) that are not resolved in the continuous wave X-band frozen solution EPR spectrum of $[Ni^{tBu}L_S^{Py}]^+$. We assign these additional hyperfine couplings to the two imine N donors in $[Ni^{tBu}L_S^{Py}]^+$. One of these imine ^{14}N isotropic hyperfine couplings is significantly larger than the other and DFT calculations reveal an unequal distribution of the spin density across the imine N-donors. This distribution may result from the coordination geometry about the formal Ni^{III} centre in which one imine N-donor moves out of the NiS_2 plane to give an overall trigonal bipyramidal geometry (Figure 5.3). We assign the larger isotropic hyperfine coupling to this imine N-donor on the basis of the relative spin densities for the imine N donors. We

observe a similar distribution in spin density for the diphenolate analogue $[Ni^{tBu}L_O^{Py}]^+$ although the spin density is significantly more localised on the Ni centre than in $[Ni^{tBu}L_S^{Py}]^+$.

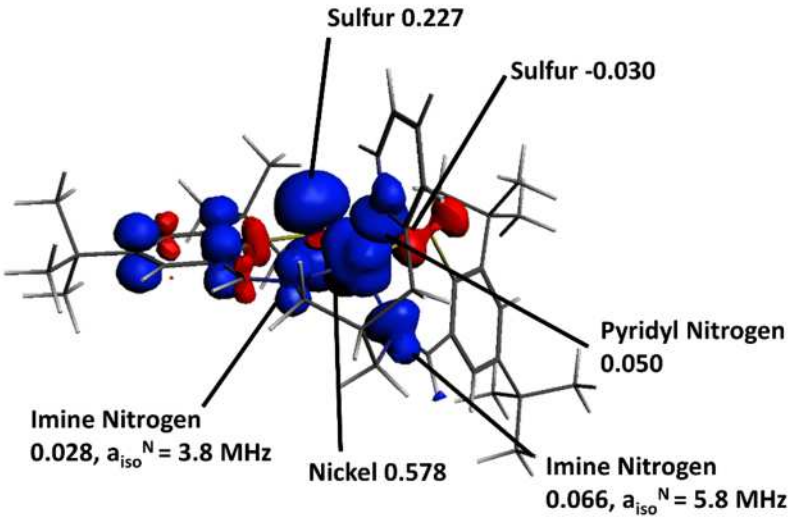


Figure 5.3: The DFT-derived geometry optimised structure and spin densities of $[Ni^{tBu}L_S^{Py}]^+$ and isotropic hyperfine coupling constants for the imine N donors derived from HYSCORE spectroscopic experiments.

We demonstrated that the first oxidation process for $Ni^{tBu}L_O^{Py}$,[8] $Ni^{tBu}L_O^{PyOMe}$ and $Ni^{tBu}L_O^{Ph}$ is metal based irrespective of the presence of a third N donor in $Ni^{tBu}L_O^{Py}$ and $Ni^{tBu}L_O^{PyOMe}$ or its absence in $Ni^{tBu}L_O^{Ph}$. This behaviour contrasts with that found for $Ni^{tBu}L_S^{Py}$ and $Ni^{tBu}L_S^{Ph}$ [8] where the oxidation processes are metal and ligand-based, respectively. Thus, the third N-donor in $Ni^{tBu}L_S^{Py}$ appears to drive a metal-based oxidation process whilst the harder phenolate-O donors in $Ni^{tBu}L_O^{Py}$,[8] $Ni^{tBu}L_O^{PyOMe}$ and $Ni^{tBu}L_O^{Ph}$ are sufficient to support a metal-based process. This points to the clear role for the axial His1 ligation in the oxidised form of NiSOD in ensuring a metal-based oxidation process with little thiyl radical character thereby limiting potentially damaging free radical side-reactions that might otherwise be initiated by coordinated thiyl radical centres.

The work described in this thesis reveals several opportunities for further study. Thus, variable temperature spectroscopic measurements are required on the one electron oxidation product of $Ni^{PhOMe}L_O^{NMe}$ in order to fully elucidate the nature of the potential temperature dependent redox tautomerism, revealed by the EPR and UV/vis spectroscopic studies reported in Chapter Three. The wide range of

molecules presented in Chapters Two and Three provides opportunities for a comprehensive screening of catalytic activity to be undertaken, particularly with respect to the potential applications of $M^{R}L_{O}^{NMe}$ (M = Zn, Ni, Cu; R = Cl, Br, Nap, Ph, PhMe, PhOMe, ^{t}Bu/Br, ^{t}Bu/Ph, ^{t}Bu/PhMe, ^{t}Bu/PhOMe) towards the oxidation of small molecules.

$Ni^{tBu}L_{S}^{Py}$ (Chapter Four) may also possess the potential as a catalyst for the disproportionation of superoxide as an analogue of the active site of NiSOD. Initial investigations with KO_2 have suggested that $Ni^{tBu}L_{S}^{Py}$ displays some reactivity towards $O_2^{\cdot-}$, with the loss of the EPR signal associated with $O_2^{\cdot-}$ following the addition of $Ni^{tBu}L_{S}^{Py}$ to a solution of KO_2 in CH_2Cl_2 with 18-crown-6; more extensive investigations employing $Ni^{tBu}L_{S}^{Py}$ and $[Ni^{tBu}L_{S}^{Py}]^{+}$ are required in order to probe this reaction further.

References

1. M. M. Whittaker and J. W. Whittaker, *J. Biolog. Chem.*, 1988, **263**, 6074-6080.
2. N. Ito, S. E. V. Phillips, C. Stevens, Z. B. Ogel, M. J. McPherson, J. N. Keen, K. D. S. Yadav and P. F. Knowles, *Nature*, 1991, **350**, 87-90.
3. A. J. Baron, C. Stevens, C. Wilmot, K. D. Seneviratne, V. Blakeley, D. M. Dooley, S. E. Phillips, P. F. Knowles and M. J. McPherson, *J. Biolog. Chem.*, 1994, **269**, 25095-25105.
4. D. P. Barondeau, C. J. Kassmann, C. K. Bruns, J. A. Tainer and E. D. Getzoff, *Biochem.*, 2004, **43**, 8038-8047.
5. J. Wuerges, J.-W. Lee, Y.-I. Yim, H.-S. Yim, S.-O. Kang and K. D. Carugo, *Proc. Nat. Acad. Sci. USA*, 2004, **101**, 8569-8574.
6. A. T. Fiedler, P. A. Bryngelson, M. J. Maroney and T. C. Brunold, *J. Am. Chem. Soc.*, 2005, **127**, 5449-5462.
7. C. Wright and A. G. Sykes, *J. Inorg. Biochem.*, 2001, **85**, 237-243.
8. M. Franks, PhD, The University of Nottingham, 2011.

Appendices

Appendix 1 – **General Synthetic Experimental Procedures and Physical Measurements**

Appendix 2 - **X-ray Crystallographic Experimental Details and Additional Information and Figures**

Appendix 3 - **Computational Methods**

Appendix 1

General Synthetic Experimental Procedures and Physical Measurements

All manipulations were carried out using standard Schlenk techniques under an atmosphere of argon or nitrogen unless otherwise stated. Dichloromethane and methanol were purchased as anhydrous solvents and tetrahydrofuran and diethyl ether were dried by passage through activated alumina towers and degassed before use.

The ^{1}H and ^{13}C NMR spectra were recorded variously on a Bruker AV(III)500 operating at 500 MHz and 125 MHz respectively, a Bruker AV(III)400, Bruker AV400, Bruker DPX400 or Bruker AV(III)400 HD spectrometers all operating at 400.2 and 100.6 MHz, respectively, or a JEOL EX270 spectrometer operating at 270 and 68 MHz respectively; chemical shifts are quoted in parts per million and are relative to tetramethylsilane. FTIR spectra were recorded using a Thermo Scientific Nicolet iS5 FTIR spectrometer with an iD5 ATR accessory attachment or a Bruker Alpha FTIR with a 'Platinum' ATR attachment.

ICP-OES data were recorded on a Perkin Elmer Optima 2000 Optical Emission Spectrometer. Elemental microanalyses were carried out variously using an Exeter Analytica CE-440 Elemental Analyzer by Tong Liu at The University of Nottingham and a Carlo Erba CE1108 Elemental Analyzer by Stephen Boyer at the Microanalysis Service, London Metropolitan University, U.K. Mass spectrometery was carried out using a Bruker Daltonics microTOF electrospray mass spectrometer, a Bruker Ultraflex III equipped with a matrix-assisted laser desorption ionisation (MALDI) source or a Waters AutoSpec in EI mode.

Continuous wave X band EPR spectra were recorded using a Bruker EMX spectrometer. Frozen solution spectra were collected using a Wilmad quartz EPR dewar with liquid N_2. The simulations of CW EPR spectra were performed using the Bruker WINEPR SimFonia package.

The X-band pulsed EPR measurements were performed on a Bruker ElexSys E580 spectrometer at 15 − 20 K at the EPSRC EPR Service at The University of Manchester by Dr Amgalanbaatar Baldansuren. A standard dielectric ring Bruker EPR cavity (ER4118XM-D5) was used, which was equipped with an Oxford CF 935 helium flow cryostat. The 2D three-pulse ESEEM experiments were performed using the pulse sequence $\pi/2 - \tau - \pi/2 - T - \pi/2 - \tau -$ echo, and the intensity of the stimulated echo signal was recorded as a function of T at different, constant τ.[1] After 1D fast Fourier transformation along the time T axis absolute value spectra were obtained. The 2D ESEEM spectra, so-called hyperfine sublevel correlation spectra (HYSCORE),[2] were recorded employing the sequence $\pi/2 - \tau - \pi/2 - t1 - \pi - t2 - \pi/2 - \tau -$ echo with mw pulses of length $t\pi/2$ = 16 ns and $t\pi$ = 32 ns, τ = 136 ns, starting times t1,2 = 180−200 ns, and time increments Δt1,2 = 20 ns. The intensity of the inverted echo following the fourth pulse is measured with t2 and t1 varied and constant τ. Unwanted features from the experimental echo envelopes were removed by using a four-step phase cycle.[3] In both dimensions 256 data points were collected. The relaxation decay was subtracted by baseline corrections (fitting by polynomials of 3-6 degree) in both time domains, subsequently applying apodisation (Hamming window) and zero-filling to 1024 data points in both dimensions. After 2D fast Fourier transformation absolute value spectra were calculated. The sensitivity of the HYSCORE experiment has been monitored by replacing the second and the third $\pi/2$- pulses with matched pulses of length 14 ns. To monitor suppression effects, values of τ were also varied from 180 to 300 ns.

Cyclic voltammetric measurements were made using an Autolab PGSTAT302N potentiostat and performed in a single-compartment cell using a three-electrode system consisting of a glassy carbon working electrode, a glassy carbon or Pt wire secondary electrode, and a saturated calomel (SCE) or Ag/AgCl reference electrode. Experiments were carried out at 293 K, in dichloromethane containing 1 mM of test sample and 0.4 M $[N^nBu_4][BF_4]$ as supporting electrolyte under an atmosphere of Ar. All cyclic voltammograms were recorded at a series of scan-rates (ν) (typically ν = 0.02, 0.05, 0.1, 0.2, 0.3 V s^{-1}), and the potentials of these measurements were referenced to the Fc^+/Fc couple by internal calibration. Where

necessary, the $FeCp^*_2{}^+/FeCp^*_2$ couple was used as the internal standard to avoid overlapping redox couples, and the $FeCp^*_2{}^+/FeCp^*_2$ couple was referenced to the Fc^+/Fc couple.[4] Assessments of electrochemical reversibility were made based on comparison of the magnitude of ΔE_p to that of the internal standard (Fc^+/Fc or $FeCp^*_2{}^+/FeCp^*_2$), the independence of $E_p{}^a$ and $E_p{}^c$ to scan rate, the ratio of $i_p{}^a$ to $i_p{}^c$ and the proportionality of $i_p{}^a$ and $i_p{}^c$ to scan rate. Where appropriate the Nicholson equation (**1**)[5, 6] was employed to account for the sloping baseline of the voltammogram.

$$\frac{ipc}{ipa} = \frac{(ipc)0}{ipa} + \frac{(i\lambda)0 \times 0.485}{ipa} + 0.086$$

Equation 1: Nicholson Equation[5, 6]

Coulometric measurements were performed with a two compartment H-cell at 293 K in CH_2Cl_2 containing 0.4 M $[N^nBu_4][BF_4]$ as supporting electrolyte. The cell consisted of a Pt/Rh gauze basket working electrode that was separated from the Pt/Rh gauze secondary electrode by a glass frit. The working electrode compartment was fitted with a magnetic stirrer bar and the test solution was stirred rapidly during electrolysis and the reference electrode was also placed in the centre of this compartment.

All UV/vis spectra were recorded on a Perkin Elmer Lambda 16 spectrometer in an optically transparent electrochemical (OTE) cell. Potentials at the working electrode were controlled by a Sycopel Scientific Ltd. DD10M potentiostat. The OTE cell consisted of a modified quartz cuvette (pathlength 0.05 mm) fitted with an optically transparent Rh/Pt gauze working electrode, a Pt wire secondary electrode in a fritted PTFE sleeve, and a SCE reference electrode. Both reference and secondary electrodes were connected to the cell *via* salt bridge tubes. The temperature of the experiment (253 K) was controlled by purging a stream of cooled N_2 gas over the cell surface.

Appendix 2

X-ray Crystallographic Experimental Details

Crystal data is given in the tables below, and selected bond lengths and angles are listed in the main text. Crystals were examined variously on a Bruker APEX CCD or Bruker AXS SMART 1000 area detector diffractometers using graphite-monochromated Mo Kα radiation (λ = 0.71073 Å), or on an Agilent Technologies SuperNova Atlas CCD, an Agilent technologies Atlas GV1000 CCD or a Rigaku XtalLAB PRO MM007 equipped with a PILATUS3 R 200K Hybrid Pixel Array detector diffractometer using mirror-monochromated CuKα radiation (λ = 1.5418 Å) or at beamline I19 of Diamond Light Source using synchotorn radiation and a Rigaku Saturn 724+ area detector diffractometer. Intensities were integrated from data recorded on 0.3 (APEX and SMART) or 1° (SuperNova, GV1000, MM007, DLS) frames by ω rotation. Cell parameters were refined from the observed positions of all strong reflections in each data set. Semi empirical absorption corrections based on symmetry equivalent and repeat reflections (APEX and SMART), Gaussian grid face-indexed absorption correction with a beam profile correction (Supernova, GV1000 and MM007) or Gaussian grid spherical based absorption correction (DLS) were applied.

The structures were solved variously by direct, iterative and heavy atom methods and were refined by full-matrix least-squares on all unique F^2 values, with anisotropic displacement parameters for all non-hydrogen atoms (except for some partially occupied disordered atoms - detailed in the enclosed .cif files- which could not be refined anisotropically and were therefore refined isotopically), and with constrained riding hydrogen geometries, unless otherwise stated. The largest features in final difference syntheses were close to heavy atoms or along chemical bonds and were of no chemical significance.

Full details of refinements are given in the 'Refine_Special_Details' section of the enclosed .cif files. Where necessary ($Zn^{Ph}L_o^{NMe}$, $Cu^{tBu/Br}L_o^{NMe}$, $Ni^{tBu}L_o^{PyOMe}$) Platon SQUEEZE[7] was used to account for the scattering from highly disordered

solvent molecules and details of this procedure are also given in the enclosed .cif files.

Programs used were Bruker AXS SMART,[8] (control, APEX and SMART) CrysAlisPro[9] (control and integration Supernova, GV1000 and MM007 and integration DLS), Bruker AXS SAINT[8] (integration, APEX and SMART), Superflip[10] (structure solution) SHELXTL[11, 12] (structure solution and refinement) and OLEX2[13] (structure solution, refinement and molecular graphics), and Platon[7] (SQUEEZE). Cif files were checked using checkCIF[14] and *via* the University of Nottingham School of Chemistry Crystal Structure Service's internal validation and archiving procedure.

Structures in Chapter Two

	$\mathbf{Zn^{Cl}L_o^{NMe}}$ (GJJMSA)	$\mathbf{Ni^{Cl}L_o^{NMe}}$ (GJJMSB)	$\mathbf{Cu^{Cl}L_o^{NMe}}$ (GJJMSD)
Crystal data			
Chemical formula	$C_{21}H_{21}Cl_4N_3O_2Zn{\cdot}CH_2Cl_2$	$C_{21}H_{21}Cl_4N_3NiO_2$	$C_{21}H_{21}Cl_4CuN_3O_2$
M_r	639.50	547.92	552.75
Crystal system, space group	monoclinic, $P2_1/c$	monoclinic, $P2_1/c$	monoclinic, $P2_1/c$
Temperature (K)	90	120	90
a, *b*, *c* (Å)	9.5714 (7), 13.5473 (10), 20.0487 (14)	16.9253 (9), 13.7416 (9), 19.6430 (12)	19.442 (4), 12.849 (3), 20.178 (5)
β (°)	97.131 (1)	98.069 (6)	115.231 (3)
V (Å^3)	2579.5 (3)	4523.3 (5)	4559.8 (18)
Z	4	8	8
Radiation type	Mo *K*α	Cu *K*α	Mo *K*α
μ (mm^{-1})	1.60	5.79	1.45
Crystal size (mm)	0.53 × 0.41 × 0.23	0.45 × 0.28 × 0.21	0.49 × 0.36 × 0.20
Data collection			
Diffractometer	Bruker *SMART APEX* CCD area detector diffractometer	SuperNova, Single source at offset, Atlas diffractometer	Bruker *SMART APEX* CCD area detector diffractometer
Absorption correction	Multi-scan *SADABS2007*/2 (Bruker,2007) was used for absorption correction. wR2(int) was 0.0412 before and 0.0267 after correction. The Ratio of min to max transmission is 0.8863. The λ/2 correction factor is 0.0015.	Gaussian *CrysAlis PRO*, Agilent Technologies, Version 1.171.36.28 (release 01-02-2013 CrysAlis171 .NET) (compiled Feb 1 2013,16:14:44) Numerical absorption correction based on gaussian integration over a multifaceted crystal model	Multi-scan *SADABS2007*/2 (Bruker,2007) was used for absorption correction. wR2(int) was 0.0582 before and 0.0469 after correction. The Ratio of min to max transmission is 0.8495. The λ/2 correction factor is 0.0015.
T_{min}, T_{max}	0.661, 0.746	0.276, 0.638	0.633, 0.746
No. of measured, independent and observed reflections	15826, 5937, 5368 [$I > 2\sigma(I)$]	20474, 9007, 8174 [$I \geq 2u(I)$]	36891, 10200, 8719 [$I > 2\sigma(I)$]
R_{int}	0.016	0.022	0.036
$(\sin\theta/\lambda)_{max}$ (Å^{-1})	0.653	0.625	0.655
Refinement			
$R[F^2 > 2\sigma(F^2)]$, $wR(F^2)$, *S*	0.030, 0.081, 1.04	0.029, 0.070, 1.05	0.029, 0.071, 1.08
No. of reflections	5937	9007	10200
No. of parameters	347	589	590
No. of restraints	0	0	0
H-atom treatment	H-atom parameters were constrained	H-atom parameters were constrained	H-atom parameters were constrained
Weighting Scheme	$w = 1/[\sigma^2(F_o^2) + (0.0518P)^2 + 1.018P]$ where $P = (F_o^2 + 2F_c^2)/3$	$w = 1/[\sigma^2(F_o^2) + (0.0273P)^2 + 2.9758P]$ where $P = (F_o^2 + 2F_c^2)/3$	$w = 1/[\sigma^2(F_o^2) + (0.0189P)^2 + 5.1982P]$ where $P = (F_o^2 + 2F_c^2)/3$
$\Delta\rangle_{max}$, $\Delta\rangle_{min}$ (e Å^{-3})	0.80, -0.33	0.87, -0.51	0.56, -0.53

	Zn^{Br}L$_o^{NMe}$ (ZNGMLJ)	**Ni^{Br}L$_o^{NMe}$** (NIGMLM)	**Cu^{Br}L$_o^{NMe}$** (CUGMLO)
Crystal data			
Chemical formula	$C_{21}H_{21}Br_4N_3O_2Zn$	$C_{21}H_{21}Br_4N_3NiO_2$	$C_{21}H_{21}Br_4CuN_3O_2$
M_r	732.42	725.76	730.59
Crystal system, space group	monoclinic, $P2_1/c$	monoclinic, $P2_1/c$	monoclinic, $P2_1/c$
Temperature (K)	120	120	120
a, b, c (Å)	20.0543 (3), 13.11710 (14), 20.2785 (3)	20.3204 (6), 12.8347 (3), 20.6356 (6)	20.0822 (11), 12.9216 (5), 20.4827 (11)
β (°)	114.7829 (16)	117.653 (4)	115.909 (7)
V (Å^3)	4843.05 (12)	4767.1 (3)	4780.9 (5)
Z	8	8	8
Radiation type	Cu $K\alpha$	Cu $K\alpha$	Cu $K\alpha$
μ (mm^{-1})	9.34	9.23	9.32
Crystal size (mm)	0.41 × 0.21 × 0.17	0.21 × 0.20 × 0.16	0.24 × 0.20 × 0.11
Data collection			
Diffractometer	GV1000, Atlas diffractometer	GV1000, Atlas diffractometer	GV1000, Atlas diffractometer
Absorption correction	Gaussian *CrysAlis PRO*, Agilent Technologies, Version 1.171.36.32 (release 02-08- 2013 CrysAlis171 .NET) (compiled Aug 2 2013, 16:46:58) Numerical absorption correction based on gaussian integration over a multifaceted crystal model	Gaussian *CrysAlis PRO*, Agilent Technologies, Version 1.171.37.34 (release 22-05- 2014 CrysAlis171 .NET) (compiled May 22 2014, 16:03:01) Numerical absorption correction based on gaussian integration over a multifaceted crystal model	Gaussian *CrysAlis PRO*, Agilent Technologies, Version 1.171.37.34 (release 22-05- 2014 CrysAlis171 .NET) (compiled May 22 2014, 16:03:01) Numerical absorption correction based on gaussian integration over a multifaceted crystal model.
T_{min}, T_{max}	0.172, 0.492	0.289, 0.437	0.255, 0.539
No. of measured, independent and observed reflections	20047, 9553, 9225 [$I > 2\sigma(I)$]	20173, 9380, 8914 [$I > 2\sigma(I)$]	55138, 9604, 8902 [$I > 2\sigma(I)$]
R_{int}	0.023	0.020	0.088
$(\sin\theta/\lambda)_{max}$ (Å^{-1})	0.625	0.625	0.627
Refinement			
$R[F^2 > 2\sigma(F^2)]$, $wR(F^2)$, S	0.036, 0.089, 1.11	0.032, 0.076, 1.10	0.101, 0.203, 1.18
No. of reflections	9553	9380	9604
No. of parameters	590	619	590
No. of restraints	0	54	0
H-atom treatment	H-atom parameters were constrained	H-atom parameters were constrained	H-atom parameters were constrained
Weighting Scheme	$w = 1/[\sigma^2(F_o^2) + (0.0389P)^2 + 11.0353P]$ where $P = (F_o^2 + 2F_c^2)/3$	$w = 1/[\sigma^2(F_o^2) + (0.0261P)^2 + 9.6892P]$ where $P = (F_o^2 + 2F_c^2)/3$	$w = 1/[\sigma^2(F_o^2) + (0.0001P)^2 + 134.5484P]$ where $P = (F_o^2 + 2F_c^2)/3$
$\Delta\rangle_{max}$, $\Delta\rangle_{min}$ (e Å^{-3})	1.38, -1.21	1.08, -1.07	2.68, -1.93

	Zn^{Nap}L$_o^{NMe}$ (ZNGMMA)	**Ni^{Nap}L$_o^{NMe}$** (NIGMLA)	**Cu^{Nap}L$_o^{NMe}$** (CUGMLA)
Crystal data			
Chemical formula	$C_{29}H_{29}N_3O_2Zn\cdot CH_2Cl_2$	$C_{29}H_{29}N_3NiO_2\cdot 0.5(CH_2Cl_2)$	$C_{29}H_{29}CuN_3O_2\cdot CH_2Cl_2$
M_r	601.85	552.72	600.02
Crystal system, space group	monoclinic, $P2_1/c$	monoclinic, $P2_1/c$	monoclinic, $P2_1/c$
Temperature (K)	120	120	120
a, b, c (Å)	6.4587 (2), 29.0723 (12), 14.5741 (5)	6.6007 (5), 28.023 (2), 14.5488 (11)	6.56059 (9), 28.4809 (4), 14.6164 (3)
β (°)	95.131 (3)	94.988 (7)	95.1042 (14)
V (Å^3)	2725.61 (18)	2680.9 (4)	2720.27 (7)
Z	4	4	4
Radiation type	Cu $K\alpha$	Cu $K\alpha$	Cu $K\alpha$
μ (mm^{-1})	3.32	2.21	3.21
Crystal size (mm)	0.30 × 0.13 × 0.06	0.13 × 0.11 × 0.06	0.28 × 0.06 × 0.05
Data collection			
Diffractometer	SuperNova, Dual, Cu at zero, Atlas diffractometer	SuperNova, Dual, Cu at zero, Atlas diffractometer	GV1000, Atlas diffractometer
Absorption correction	Gaussian *CrysAlis PRO*, Agilent Technologies, Version 1.171.36.28 (release 01-02-2013 CrysAlis171 .NET) (compiled Feb 1 2013,16:14:44) Numerical absorption correction based on gaussian integration over a multifaceted crystal model	Gaussian *CrysAlis PRO*, Agilent Technologies, Version 1.171.36.28 (release 01-02-2013 CrysAlis171 .NET) (compiled Feb 1 2013,16:14:44) Numerical absorption correction based on gaussian integration over a multifaceted crystal model	Gaussian *CrysAlis PRO*, Agilent Technologies, Version 1.171.36.28a (release 18-03-2013 CrysAlis171 .NET) (compiled Mar 18 2013,11:47:30) Numerical absorption correction based on gaussian integration over a multifaceted crystal model
T_{min}, T_{max}	0.832, 1.166	0.916, 0.992	0.664, 1.062
No. of measured, independent and observed reflections	10520, 5291, 4568 [$I > 2\sigma(I)$]	10965, 5308, 3658 [$I > 2\sigma(I)$]	23843, 5470, 4926 [$I > 2\sigma(I)$]
R_{int}	0.033	0.064	0.035
$(\sin\theta/\lambda)_{max}$ (Å^{-1})	0.625	0.627	0.627
Refinement			
$R[F^2 > 2\sigma(F^2)]$, $wR(F^2)$, S	0.059, 0.165, 1.03	0.079, 0.238, 1.05	0.052, 0.138, 1.07
No. of reflections	5291	5308	5470
No. of parameters	373	373	373
No. of restraints	0	1	0
H-atom treatment	H-atom parameters constrained	H-atom parameters constrained	H-atom parameters constrained
	$w = 1/[\sigma^2(F_o^2) + (0.0811P)^2 + 7.4098P]$ where $P = (F_o^2 + 2F_c^2)/3$	$w = 1/[\sigma^2(F_o^2) + (0.1315P)^2 + 1.3421P]$ where $P = (F_o^2 + 2F_c^2)/3$	$w = 1/[\sigma^2(F_o^2) + (0.0649P)^2 + 4.526P]$ where $P = (F_o^2 + 2F_c^2)/3$
$\Delta\rangle_{max}$, $\Delta\rangle_{min}$ (e Å^{-3})	0.58, -1.09	1.04, -0.65	0.80, -0.72

	$\mathbf{Zn^{Ph}L_o^{NMe}}$ DJEJMA	$\mathbf{Ni^{Ph}L_o^{NMe}}$ NIGMLQ	$\mathbf{Cu^{Ph}L_o^{NMe}}$ CUGMLD
Crystal data			
Chemical formula	$C_{45}H_{41}N_3O_2Zn$	$2(C_{45}H_{41}N_3NiO_2)\cdot 2(C_4H_{10}O)$	$C_{45}H_{41}CuN_3O_2\cdot CH_2Cl_2$
M_r	721.24	1577.27	804.27
Crystal system, space group	Orthorhombic, *Fdd*2	Monoclinic, *C*2/*c*	Monoclinic, *C*2/*c*
Temperature (K)	120	100	120
a, *b*, *c* (Å)	70.527 (4), 18.0267 (5), 13.0246 (4)	17.9517 (5), 13.1830 (3), 35.4629 (8)	17.8580 (4), 13.1236 (3), 32.7901 (8)
α, β, γ (°)	90, 90, 90	90, 104.298 (3), 90	90, 96.321 (2), 90
V (Å^3)	16559.1 (12)	8132.6 (3)	7638.0 (3)
Z	16	4	8
Radiation type	Cu *K*α	Synchrotron, λ = 0.6889 Å	Cu *K*α
μ (mm^{-1})	1.11	0.48	2.43
Crystal size (mm)	0.20 × 0.15 × 0.05	0.07 × 0.05 × 0.02	0.42 × 0.24 × 0.13
Data collection			
Diffractometer	GV1000, Atlas	Kappa Rigaku Saturn724+	GV1000, Atlas
Absorption correction	Gaussian *CrysAlis PRO*, Agilent Technologies, Version 1.171.37.34 (release 22-05-2014 CrysAlis171 .NET) (compiled May 22 2014,16:03:01) Numerical absorption correction based on gaussian integration over a multifaceted crystal model	Multi-scan *CrysAlis PRO*, Agilent Technologies, Version 1.171.37.33 (release 27-03-2014 CrysAlis171 .NET) (compiled Mar 27 2014,17:12:48) Empirical absorption correction using spherical harmonics, implemented in SCALE3 ABSPACK scaling algorithm.	Gaussian *CrysAlis PRO*, Agilent Technologies, Version 1.171.36.32 (release 02-08-2013 CrysAlis171 .NET) (compiled Aug 2 2013,16:46:58) Numerical absorption correction based on gaussian integration over a multifaceted crystal model
T_{min}, T_{max}	0.842, 0.953	0.827, 1.000	0.540, 1.000
No. of measured, independent and observed reflections	61440, 8305, 7016 [$I \geq 2u(I)$]	51955, 13489, 10320 [$I > 2\sigma(I)$]	15745, 7544, 6416 [$I > 2\sigma(I)$]
R_{int}	0.126	0.056	0.035
$(\sin\theta/\lambda)_{max}$ (Å^{-1})	0.625	0.762	0.625
Refinement			
$R[F^2 > 2\sigma(F^2)]$, $wR(F^2)$, S	0.156, 0.456, 1.98	0.059, 0.125, 1.10	0.048, 0.131, 1.04
No. of reflections	8305	13489	7544
No. of parameters	489	547	536
No. of restraints	0	30	6
H-atom treatment	H-atom parameters constrained	H-atom parameters constrained	H-atom parameters constrained
	$w = 1/[\sigma^2(F_o^2) + (0.2P)^2]$ where $P = (F_o^2 + 2F_c^2)/3$	$w = 1/[\sigma^2(F_o^2) + (0.0186P)^2 + 26.1835P]$ where $P=(F_o^2+2F_c^2)/3$	$w = 1/[\sigma^2(F_o^2) + (0.0652P)^2 + 9.6375P]$ where $P=(F_o^2+2F_c^2)/3$
$\Delta\rangle_{max}$, $\Delta\rangle_{min}$ (e Å^{-3})	3.29, -1.30	0.72, -0.56	0.76, -0.78
Absolute structure	Flack, H. D. (1983). Acta Cryst. A39, 876-881.	–	–
Absolute structure parameter	0.18 (9)	–	–

	$Zn^{PhMe}L_o^{NMe}$ ZNGMLX	$Ni^{PhMe}L_o^{NMe}$ NIGMLU	$Cu^{PhMe}L_o^{NMe}$ CUGMLU
Crystal data			
Chemical formula	$C_{49}H_{49}N_3O_2Zn \cdot 1.63(CH_2Cl_2)$	$C_{49}H_{49}N_3NiO_2$	$C_{49}H_{49}CuN_3O_2$
M_r	915.28	770.62	775.45
Crystal system, space group	Monoclinic, $P2_1/c$	Triclinic, $P\bar{1}$	Monoclinic, $P2_1/n$
Temperature (K)	120	120	120
a, b, c (Å)	12.3652 (3), 18.0539 (4), 47.6046 (13)	12.4998 (6), 17.6305 (9), 18.7247 (10)	12.0694 (4), 17.8015 (5), 19.0382 (7)
α, β, γ (°)	90, 110.685 (3), 90	88.407 (4), 82.138 (4), 89.044 (4)	90, 105.898 (4), 90
V (Å^3)	9942.2 (5)	4085.8 (4)	3934.0 (2)
Z	8	4	4
Radiation type	Cu $K\alpha$	Synchrotron, λ = 0.6889 Å	Cu $K\alpha$
μ (mm^{-1})	2.60	0.48	1.12
Crystal size (mm)	0.64 × 0.13 × 0.06	150.0 × 25.0 × 5.0	0.13 × 0.05 × 0.04
Data collection			
Diffractometer	XtalLAB PRO MM007, PILATUS3 R 200K	Kappa Rigaku Saturn724+	GV1000, AtlasS2
Absorption correction	Gaussian *CrysAlis PRO* 1.171.38.41n (Rigaku Oxford Diffraction, 2015) Numerical absorption correction based on gaussian integration over a multifaceted crystal model	Multi-scan *CrysAlis PRO*, Agilent Technologies, Version 1.171.37.35 (release 13-08-2014 CrysAlis171 .NET) (compiled Aug 13 2014,18:06:01) Empirical absorption correction using spherical harmonics, implemented in SCALE3 ABSPACK scaling algorithm.	Gaussian *CrysAlis PRO*, Agilent Technologies, Version 1.171.37.34 (release 22-05-2014 CrysAlis171 .NET) (compiled May 22 2014,16:03:01) Numerical absorption correction based on gaussian integration over a multifaceted crystal model
T_{min}, T_{max}	0.561, 0.902	0.612, 1.000	0.913, 0.969
No. of measured, independent and observed reflections	139422, 20736, 18179 [$I > 2\sigma(I)$]	43773, 25766, 13702 [$I > 2\sigma(I)$]	25409, 7742, 5915 [$I > 2\sigma(I)$]
R_{int}	0.071	0.087	0.057
$(\sin\theta/\lambda)_{max}$ (Å^{-1})	0.634	0.760	0.622
Refinement			
$R[F^2 > 2\sigma(F^2)]$, $wR(F^2)$, S	0.076, 0.206, 1.06	0.110, 0.344, 1.11	0.049, 0.128, 1.06
No. of reflections	20736	25766	7742
No. of parameters	1184	1067	525
No. of restraints	101	0	30
H-atom treatment	H-atom parameters constrained	H-atom parameters constrained	H-atom parameters constrained
	$w = 1/[\sigma^2(F_o^2) + (0.0897P)^2 + 24.9323P]$ where $P = (F_o^2 + 2F_c^2)/3$	$w = 1/[\sigma^2(F_o^2) + (0.1278P)^2 + 12.4457P]$ where $P = (F_o^2 + 2F_c^2)/3$	$w = 1/[\sigma^2(F_o^2) + (0.0549P)^2 + 1.6547P]$ where $P = (F_o^2 + 2F_c^2)/3$
$\Delta\rangle_{max}$, $\Delta\rangle_{min}$ (e Å^{-3})	1.08, -0.93	1.53, -1.16	

	$\mathbf{Zn^{PhOMe}L_o^{NMe}}$ DJEJME	$\mathbf{Ni^{PhOMe}L_o^{NMe}}$ NIGMMC	$\mathbf{Cu^{PhOMe}L_o^{NMe}}$ CUGMLZ
Crystal data			
Chemical formula	$C_{49}H_{49}N_3O_6Zn{\cdot}2(CH_2Cl_2)$	$1(C_{49}H_{49}N_3NiO_6){\cdot}CH_2Cl_2$	$C_{49}H_{49}CuN_3O_6{\cdot}CH_2Cl_2$
M_r	1011.13	919.54	924.37
Crystal system, space group	Monoclinic, $P2_1/n$	Monoclinic, $P2_1/c$	Monoclinic, $P2_1/n$
Temperature (K)	120	120	120
a, b, c (Å)	13.5675 (6), 13.6877 (7), 25.8979 (14)	11.4656 (7), 63.2428 (17), 24.9235 (14)	11.4772 (4), 63.3598 (18), 19.0467 (7)
α, β, γ (°)	90, 97.368 (5), 90	90, 133.219 (10), 90	107.070 (4)
V (Å^3)	4769.7 (4)	13170 (2)	13240.5 (8)
Z	4	12	12
Radiation type	Cu $K\alpha$	Cu $K\alpha$	Cu $K\alpha$
μ (mm^{-1})	3.21	2.20	2.25
Crystal size (mm)	0.30 × 0.06 × 0.04	0.22 × 0.12 × 0.04	0.22 × 0.17 × 0.05
Data collection			
Diffractometer	GV1000, Atlas	XtalLAB PRO MM007, PILATUS3 R 200K	XtalLAB PRO MM007, PILATUS3 R 200K
Absorption correction	Gaussian *CrysAlis PRO*, Agilent Technologies, Version 1.171.36.32 (release 02-08-2013 CrysAlis171 .NET) (compiled Aug 2 2013,16:46:58) Numerical absorption correction based on gaussian integration over a multifaceted crystal model	Gaussian *CrysAlis PRO* 1.171.38.41n (Rigaku Oxford Diffraction, 2015) Numerical absorption correction based on gaussian integration over a multifaceted crystal model	Gaussian *CrysAlis PRO* 1.171.38.41n (Rigaku Oxford Diffraction, 2015) Numerical absorption correction based on gaussian integration over a multifaceted crystal model Empirical absorption correction using spherical harmonics, implemented in SCALE3 ABSPACK scaling algorithm
T_{min}, T_{max}	0.691, 1.000	0.725, 0.927	0.826, 0.952
No. of measured, independent and observed reflections	20352, 9300, 5583 [$I > 2\sigma(I)$]	140410, 27326, 19214 [$I > 2\sigma(I)$]	116463, 23180, 16728
R_{int}	0.061	0.108	0.12
$(\sin\theta/\lambda)_{max}$ (Å^{-1})	0.625	0.635	0.595
Refinement			
$R[F^2 > 2\sigma(F^2)]$, $wR(F^2)$, S	0.078, 0.222, 1.01	0.130, 0.339, 1.06	0.156, 0.397, 1.06
No. of reflections	9300	27326	23180
No. of parameters	630	1793	1799
No. of restraints	82	1717	3180
H-atom treatment	H-atom parameters constrained	H-atom parameters constrained	H-atom parameters constrained
	$w = 1/[\sigma^2(F_o^2) + (0.0956P)^2 + 7.6542P]$ where $P = (F_o^2 + 2F_c^2)/3$	$w = 1/[\sigma^2(F_o^2) + (0.1185P)^2 + 109.0767P]$ where $P = (F_o^2 + 2F_c^2)/3$	$w = 1/[\sigma^2(F_o^2) + (0.1238P)^2 + 247.7982P]$ where $P = (F_o^2 + 2F_c^2)/3$
$\Delta\rangle_{max}$, $\Delta\rangle_{min}$ (e Å^{-3})	0.74, -0.86	0.99, -1.61	1.35, −1.40

	Zn$^{tBu/Br}$L$_o^{NMe}$ ZNGMLI	**Ni$^{tBu/Br}$L$_o^{NMe}$** NIGMLP	**Cu$^{tBu/Br}$L$_o^{NMe}$** CUGMLV
Crystal data			
Chemical formula	$C_{29}H_{39}Br_2N_3O_2Zn\cdot0.5(C_4H_{10}O)$	$C_{29}H_{39}Br_2N_3NiO_2\cdot C_{0.25}Cl_{0.5}$	$(C_{29}H_{39}Br_2CuN_3O_2)1.5(CH_2Cl_2)$
M_r	723.88	700.89	812.38
Crystal system, space group	Monoclinic, *I*2/*a*	Monoclinic, $P2_1/c$	Triclinic, $P\bar{1}$
Temperature (K)	120	100	120
a, *b*, *c* (Å)	20.1979 (4), 10.97291 (19), 30.1639 (7)	19.062 (2), 13.6788 (12), 12.564 (2)	10.9570 (7), 17.1928 (10), 19.7601 (12)
α, β, γ (°)	90, 102.242 (2), 90	90, 108.719 (16), 90	96.175 (5), 100.181 (5), 108.304 (5)
V (Å^3)	6533.2 (2)	3102.7 (8)	3425.1 (4)
Z	8	4	4
Radiation type	Cu *K*α	Synchrotron, λ = 0.6889 Å	Cu *K*α
μ (mm^{-1})	4.16	3.01	6.04
Crystal size (mm)	0.16 × 0.04 × 0.03	0.2 × 0.02 × 0.01	0.40 × 0.06 × 0.06
Data collection			
Diffractometer	GV1000, Atlas	Kappa Rigaku Saturn724+	GV1000, TitanS2
Absorption correction	Gaussian *CrysAlis PRO*, Agilent Technologies, Version 1.171.36.32 (release 02-08-2013 CrysAlis171 .NET) (compiled Aug 2 2013,16:46:58) Numerical absorption correction based on gaussian integration over a multifaceted crystal model	Multi-scan *CrysAlis PRO*, Agilent Technologies, Version 1.171.37.33 (release 27-03-2014 CrysAlis171 .NET) (compiled Mar 27 2014,17:12:48) Empirical absorption correction using spherical harmonics, implemented in SCALE3 ABSPACK scaling algorithm.	Gaussian *CrysAlis PRO*, Agilent Technologies, Version 1.171.37.35 (release 13-08-2014 CrysAlis171 .NET) (compiled Aug 13 2014,18:06:01) Numerical absorption correction based on gaussian integration over a multifaceted crystal model
T_{min}, T_{max}	0.736, 0.950	0.372, 1.000	0.520, 0.850
No. of measured, independent and observed [$I > 2\sigma(I)$] reflections	30349, 6550, 5756	15394, 8082, 5705	23964, 13147, 8603
R_{int}	0.052	0.110	0.077
$(\sin\theta/\lambda)_{max}$ (Å^{-1})	0.626	0.766	0.622
Refinement			
$R[F^2 > 2\sigma(F^2)]$, $wR(F^2)$, *S*	0.034, 0.088, 1.04	0.121, 0.333, 1.06	0.072, 0.200, 1.03
No. of reflections	6550	8082	13147
No. of parameters	402	390	710
No. of restraints	74	60	67
H-atom treatment	H-atom parameters constrained	H-atom parameters constrained	H-atom parameters constrained
	$w = 1/[\sigma^2(F_o^2) + (0.040P)^2 + 11.7855P]$ where $P = (F_o^2 + 2F_c^2)/3$	$w = 1/[\sigma^2(F_o^2) + (0.1306P)^2 + 18.0765P]$ where $P = (F_o^2 + 2F_c^2)/3$	$w = 1/[\sigma^2(F_o^2) + (0.0699P)^2 + 6.2963P]$ where $P = (F_o^2 + 2F_c^2)/3$
$\Delta\rangle_{max}$, $\Delta\rangle_{min}$ (e Å^{-3})	0.81, -0.76	1.71, -1.73	1.14, -0.85

	$Zn^{tBu/Ph}L_o^{NMe}$ ZNGMLP	$Ni^{tBu/Ph}L_o^{NMe}$ NIGMLI	$Cu^{tBu/Ph}L_o^{NMe}$ CUGMLJ
Crystal data			
Chemical formula	$C_{41}H_{49}N_3O_2Zn$	$C_{41}H_{49}N_3NiO_2$	$C_{41}H_{49}CuN_3O_2$
M_r	681.20	674.54	679.37
Crystal system, space group	Monoclinic, $P2_1/c$	Monoclinic, $P2_1/c$	Monoclinic, $P2_1/c$
Temperature (K)	120	120	120
a, b, c (Å)	18.4862 (4), 15.8981 (3), 12.7350 (3)	18.4880 (4), 15.9370 (3), 12.6056 (2)	18.4440 (3), 15.9223 (3), 12.6519 (2)
α, β, γ (°)	90, 107.191 (2), 90	90, 106.856 (2), 90	90, 106.8093 (19), 90
V (Å^3)	3575.56 (14)	3554.57 (12)	3556.75 (11)
Z	4	4	4
Radiation type	Cu $K\alpha$	Cu $K\alpha$	Cu $K\alpha$
μ (mm^{-1})	1.25	1.08	1.16
Crystal size (mm)	0.24 × 0.05 × 0.03	0.39 × 0.14 × 0.09	0.52 × 0.07 × 0.04
Data collection			
Diffractometer	GV1000, TitanS2	GV1000, Atlas	SuperNova, Dual, Cu at zero, Atlas
Absorption correction	Gaussian *CrysAlis PRO*, Agilent Technologies, Version 1.171.37.35 (release 13-08-2014 CrysAlis171 .NET) (compiled Aug 13 2014,18:06:01) Numerical absorption correction based on gaussian integration over a multifaceted crystal model	Gaussian *CrysAlis PRO*, Agilent Technologies, Version 1.171.37.31 (release 14-01-2014 CrysAlis171 .NET) (compiled Jan 14 2014,18:38:05) Numerical absorption correction based on gaussian integration over a multifaceted crystal model	Gaussian *CrysAlis PRO*, Agilent Technologies, Version 1.171.37.34 (release 22-05-2014 CrysAlis171 .NET) (compiled May 22 2014,16:03:01) Numerical absorption correction based on gaussian integration over a multifaceted crystal model.
T_{min}, T_{max}	0.815, 0.966	0.732, 0.931	0.805, 0.966
No. of measured, independent and observed [$I > 2\sigma(I)$] reflections	20473, 6934, 5679	56659, 7194, 6468	28475, 7117, 6427
R_{int}	0.053	0.041	0.032
$(\sin\theta/\lambda)_{max}$ (Å^{-1})	0.623	0.624	0.625
Refinement			
$R[F^2 > 2\sigma(F^2)]$, $wR(F^2)$, S	0.045, 0.120, 1.04	0.033, 0.091, 1.04	0.034, 0.095, 1.03
No. of reflections	6934	7194	7117
No. of parameters	460	460	460
No. of restraints	0	0	0
H-atom treatment	H-atom parameters constrained	H-atom parameters constrained	H-atom parameters constrained
	$w = 1/[\sigma^2(F_o^2) + (0.0561P)^2 + 1.9636P]$ where $P = (F_o^2 + 2F_c^2)/3$	$w = 1/[\sigma^2(F_o^2) + (0.0489P)^2 + 1.2953P]$ where $P = (F_o^2 + 2F_c^2)/3$	$w = 1/[\sigma^2(F_o^2) + (0.0533P)^2 + 1.8567P]$ where $P = (F_o^2 + 2F_c^2)/3$
$\Delta\rangle_{max}$, $\Delta\rangle_{min}$ (e Å^{-3})	0.50, -0.35	0.26, -0.43	0.33, -0.44

	$\mathbf{Zn}^{\mathbf{tBu/PhMe}}\mathbf{L_o}^{\mathbf{NMe}}$ ZNGMLV	$\mathbf{Ni}^{\mathbf{tBu/PhMe}}\mathbf{L_o}^{\mathbf{NMe}}$ NIGMLT	$\mathbf{Zn}^{\mathbf{tBu/PhOMe}}\mathbf{L_o}^{\mathbf{NMe}}$ ZNGMLT
Crystal data			
Chemical formula	$C_{43}H_{53}N_3O_2Zn$	$C_{43}H_{53}N_3NiO_2$	$C_{43}H_{53}N_3O_4Zn$
M_r	709.25	702.59	741.25
Crystal system, space group	Orthorhombic, *Pbca*	Orthorhombic, *Pcca*	Orthorhombic, *Fdd*2
Temperature (K)	120	120	120
a, *b*, *c* (Å)	11.9393 (3), 68.446 (3), 18.7860 (9)	19.0760 (13), 15.4438 (9), 12.8772 (7)	42.759 (2), 25.5160 (15), 7.1350 (3)
α, β, γ (°)	90, 90, 90	90, 90, 90	90, 90, 90
V (Å^3)	15351.8 (11)	3793.7 (4)	7784.5 (7)
Z	16	4	8
Radiation type	Cu *K*α	Cu *K*α	Cu *K*α
μ (mm^{-1})	1.18	1.03	1.23
Crystal size (mm)	0.24 × 0.07 × 0.04	0.11 × 0.05 × 0.05	0.22 × 0.06 × 0.04
Data collection			
Diffractometer	XXtalLAB PRO MM007, PILATUS3 R 200K	GV1000, TitanS2	GV1000, AtlasS2
Absorption correction	Gaussian *CrysAlis PRO* 1.171.38.41 (Rigaku Oxford Diffraction, 2015) Numerical absorption correction based on gaussian integration over a multifaceted crystal model	Gaussian *CrysAlis PRO*, Agilent Technologies, Version 1.171.37.35 (release 13-08-2014 CrysAlis171 .NET) (compiled Aug 13 2014,18:06:01) Numerical absorption correction based on gaussian integration over a multifaceted crystal model	Gaussian *CrysAlis PRO*, Agilent Technologies, Version 1.171.37.34 (release 22-05-2014 CrysAlis171 .NET) (compiled May 22 2014,16:03:01) Numerical absorption correction based on gaussian integration over a multifaceted crystal model
T_{min}, T_{max}	0.381, 0.964	0.931, 0.963	0.851, 0.961
No. of measured, independent and observed [$I > 2\sigma(I)$] reflections	48006, 15543, 11803	17273, 3654, 2661	13501, 3178, 3093
R_{int}	0.074	0.079	0.031
$(\sin\theta/\lambda)_{max}$ (Å^{-1})	0.637	0.624	0.623
Refinement			
$R[F^2 > 2\sigma(F^2)]$, $wR(F^2)$, S	0.163, 0.360, 1.17	0.066, 0.155, 1.11	0.024, 0.061, 1.06
No. of reflections	15543	3654	3178
No. of parameters	986	298	250
No. of restraints	1086	129	1
H-atom treatment	H-atom parameters constrained	H atoms treated by a mixture of independent and constrained refinement	H-atom parameters constrained
	$w = 1/[\sigma^2(F_o^2) + (0.0001P)^2 + 368.2047P]$ where $P = (F_o^2 + 2F_c^2)/3$	$w = 1/[\sigma^2(F_o^2) + (0.0411P)^2 + 4.1671P]$ where $P = (F_o^2 + 2F_c^2)/3$	$w = 1/[\sigma^2(F_o^2) + (0.0346P)^2 + 4.4488P]$ where $P = (F_o^2 + 2F_c^2)/3$
$\Delta\rangle_{max}$, $\Delta\rangle_{min}$ (e Å^{-3})	1.46, -2.14	0.40, -0.47	0.21, -0.17
Absolute structure	–	–	Flack x determined using 1001 quotients [(I+)-(I-)]/[(I+)+(I-)]
Absolute structure parameter	–	–	0.020 (17)

	Ni$^{tBu/PhOMe}$L$_o^{NMe}$ NIGMLS	**Cu$^{tBu/PhOMe}$L$_o^{NMe}$** CUGMLP
Crystal data		
Chemical formula	$C_{43}H_{53}N_3NiO_4$	$C_{43}H_{53}CuN_3O_4$
M_r	734.59	739.42
Crystal system, space group	Monoclinic, *C*2/*c*	Triclinic, $P\bar{1}$
Temperature (K)	120	120
a, *b*, *c* (Å)	25.7944 (11), 6.9695 (2), 22.2964 (9)	12.9106 (7), 13.1211 (6), 13.7129 (7)
α, β, γ (°)	90, 109.422 (5), 90	71.379 (4), 63.226 (5), 72.881 (4)
V (Å^3)	3780.2 (3)	1934.0 (2)
Z	4	2
Radiation type	Cu *K*α	Cu *K*α
μ (mm^{-1})	1.10	1.15
Crystal size (mm)	0.37 × 0.20 × 0.13	0.25 × 0.22 × 0.10
Data collection		
Diffractometer	SuperNova, Dual, Cu at zero, Atlas	SuperNova, Dual, Cu at zero, Atlas
Absorption correction	Gaussian *.CrysAlis PRO*, Agilent Technologies, Version 1.171.37.35 (release 13-08-2014 CrysAlis171 .NET) (compiled Aug 13 2014,18:06:01) Numerical absorption correction based on gaussian integration over a multifaceted crystal model	Gaussian *CrysAlis PRO*, Agilent Technologies, Version 1.171.37.35 (release 13-08-2014 CrysAlis171 .NET) (compiled Aug 13 2014,18:06:01) Numerical absorption correction based on gaussian integration over a multifaceted crystal model
T_{min}, T_{max}	0.772, 0.875	0.809, 0.910
No. of measured, independent and observed [$I > 2\sigma(I)$] reflections	7232, 3725, 3418	13973, 7554, 7080
R_{int}	0.029	0.028
$(\sin\theta/\lambda)_{max}$ (Å^{-1})	0.623	0.624
Refinement		
$R[F^2 > 2\sigma(F^2)]$, $wR(F^2)$, S	0.040, 0.108, 1.03	0.038, 0.103, 1.03
No. of reflections	3725	7554
No. of parameters	274	498
No. of restraints	78	0
H-atom treatment	H atoms treated by a mixture of independent and constrained refinement	H-atom parameters constrained
	$w = 1/[\sigma^2(F_o^2) + (0.0681P)^2 + 1.4898P]$ where $P = (F_o^2 + 2F_c^2)/3$	$w = 1/[\sigma^2(F_o^2) + (0.0604P)^2 + 0.8744P]$ where $P = (F_o^2 + 2F_c^2)/3$
$\Delta\rangle_{max}$, $\Delta\rangle_{min}$ (e Å^{-3})	0.61, -0.48	0.50, -0.38

Additional figures showing the full contents of the asymmetric unit including multiple molecules where Z'>1 and disordered components of the structures discussed in Chapter Two are detailed below. π-π interactions between neighbouring molecules (where present) are also detailed. H atoms and lattice solvent molecules are omitted for clarity in all cases. Full structural information is available in the enclosed .cif files.

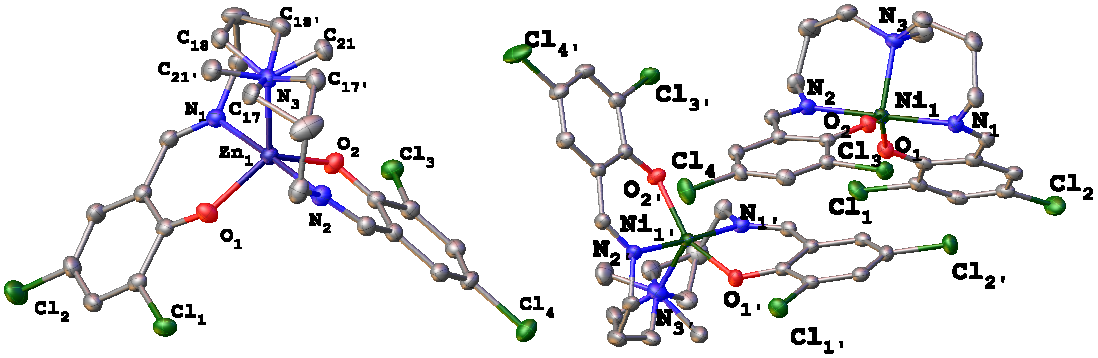


Figure A2.1: Left: $Zn^{Cl}L_o^{NMe}$- Z' = 1; Right: $Ni^{Cl}L_o^{NMe}$- Z' = 2. π-π interactions between neighbouring molecules: Face-Face Centroid-centroid separation 3.5553(11) Å, plane-plane angle 176.61(6), plane-plane shift 1.140(3) Å; Edge-Face Centroid-centroid separation 5.5608(11) Å, plane-plane angle 66.31(6) º, plane-plane shift 2.945(4) Å.

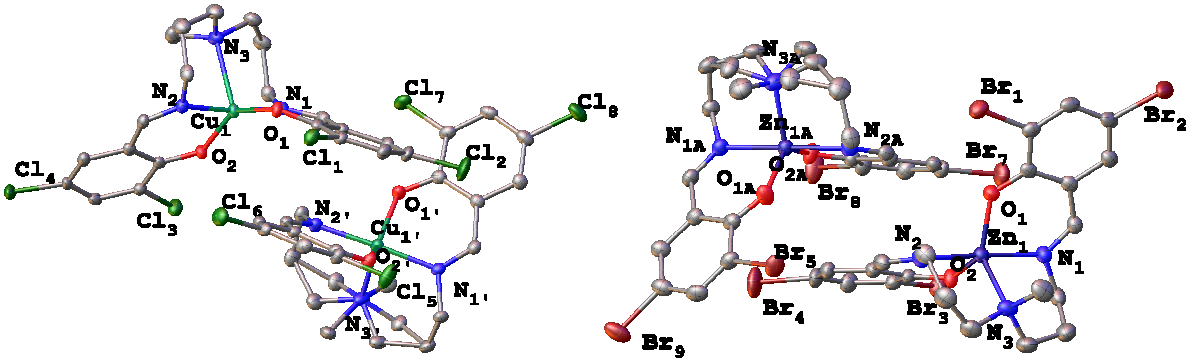


Figure A2.2: Left: $Cu^{Cl}L_o^{NMe}$ Z' = 2. π-π interactions between neighbouring molecules: Face-Face Centroid-centroid separation 3.5408(13) Å, plane-plane angle 3.36(7) º, plane-plane shift 0.840(3) Å; Edge-Face Centroid-centroid separation 5.6982(14) Å, plane-plane angle 70.14(7) º, plane-plane shift 2.976(4) Å.; Right: $Zn^{Br}L_o^{NMe}$- Z' = 2. π-π interactions between neighbouring molecules: Face-Face Centroid-centroid separation 3.59221(3) Å, plane-plane angle 3.87192(6) º, plane-plane shift 1.04528(6) Å. Edge-Face Centroid-centroid separation 5.76038(5) Å, plane-plane angle 68.1016(8) º, plane-plane shift 2.95091(6) Å.

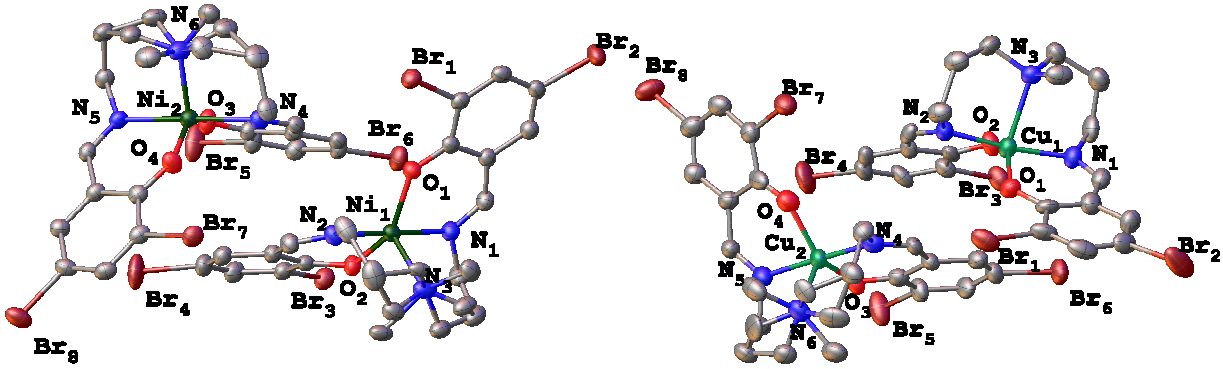


Figure A2.3: Left: $Ni^{Br}L_o^{NMe}$ Z' = 2 π-π interactions between neighbouring molecules: Face-Face Centroid-centroid separation 3.66328(7) Å, plane-plane angle 6.20923(14) º, plane-plane shift 1.13849(15) Å. Edge-Face Centroid-centroid separation 5.69715(11) Å, plane-plane angle 68.8413(17) º, plane-plane shift 2.42989(12) Å.; Right: $Cu^{Br}L_o^{NMe}$- Z' = 2 π-π interactions between neighbouring molecules: Face-Face Centroid-centroid separation 5.6834(2) Å, plane-plane angle 69.410(3) º, plane-plane shift 2.6738(2) Å. Edge-Face Centroid-centroid separation 5.6834(2) Å, plane-plane angle 69.410(3) º, plane-plane shift 2.6738(2) Å.

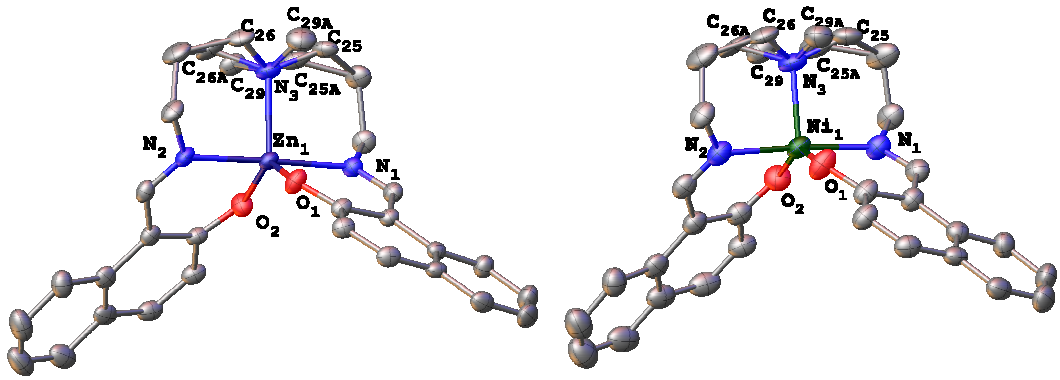


Figure A2.4: Left: $Zn^{Nap}L_o^{NMe}$- Z' = 1 ; Right: $Ni^{Nap}L_o^{NMe}$- Z' = 1

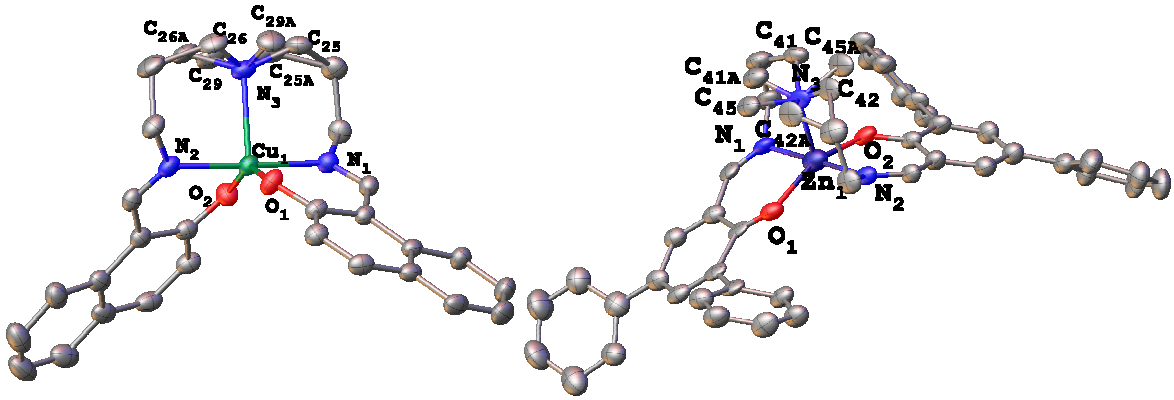


Figure A2.5: Left: $Cu^{Nap}L_o^{NMe}$- Z' = 1; Right: $Zn^{Ph}L_o^{NMe}$- Z' = 1 . π-π interactions between neighbouring molecules: Face-Face Centroid-centroid separation 4.351(11) Å, plane-plane angle 17.1(6) º, plane-plane shift 1.76(2) Å. Edge-Face Centroid-centroid separation 5.741(9) Å, plane-plane angle 118.4(5) º, plane-plane shift 3.29(3) Å.

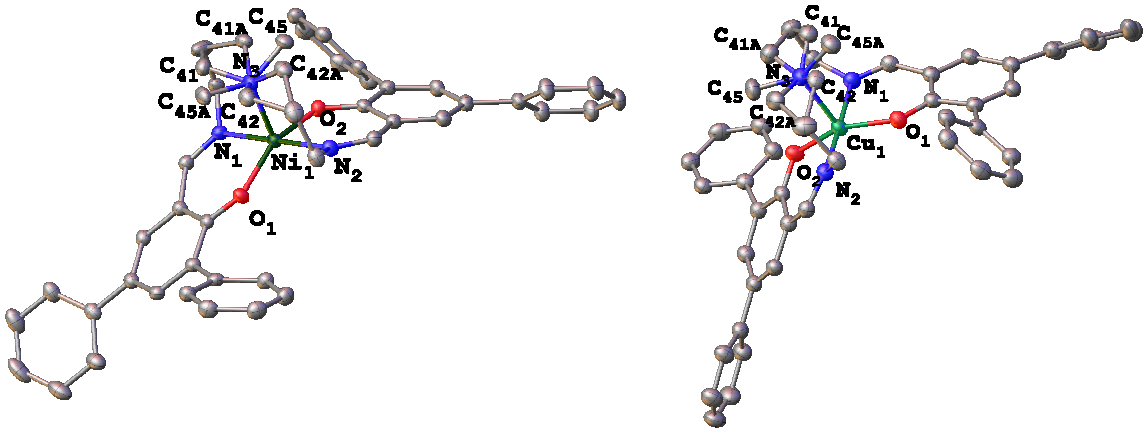


Figure A2.6: Left: $Ni^{Ph}L_o^{NMe}$- Z' = 1 π-π interactions between neighbouring molecules: Face-Face Centroid-centroid separation 4.4104(18) Å, plane-plane angle 17.35(10) º, *plane-plane shift 1.971(4) Å. Edge-Face Centroid-centroid separation 5.7253(12) Å, plane-plane angle 119.02(7) º, plane-plane shift 3.293(4) Å.; Right: $Cu^{Ph}L_o^{NMe}$- Z' = 1 π-π interactions between neighbouring molecules: Face-Face Centroid-centroid separation* 4.18696(10) Å, *plane-plane angle* 16.9011(6) º, *plane-plane shift* 1.33142(14) Å. *E-F Centroid-centroid separation 5.63902(10) Å, plane-plane angle 110.3190(15) º, plane-plane shift 2.88812(14) Å.*

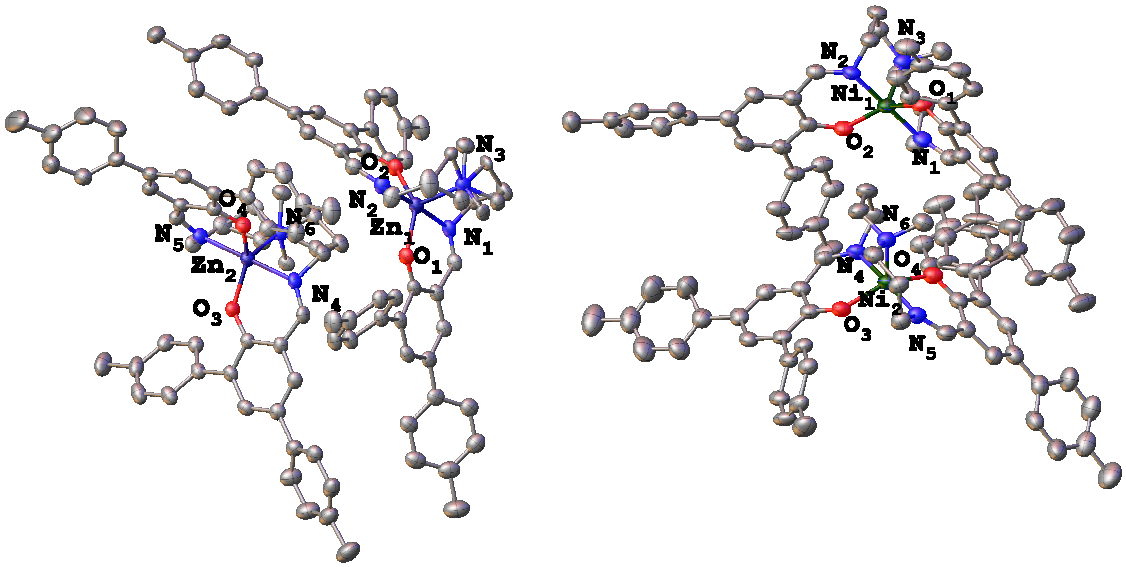


Figure A2.7: Left: $Zn^{PhMe}L_o^{NMe}$- Z' = 2 π-π interactions between neighbouring molecules: Edge-Face (Phenolate-methylphenyl) Centroid-centroid separation 4.907(2) Å, plane-plane angle 101.96(12) º, plane-plane shift 0.091(7) Å; Edge-Face (methylphenyl-methylphenyl) Centroid-centroid separation 5.200(3) Å, plane-plane angle 76.41(13) º, plane-plane shift 1.575(9) Å. ; Right: $Ni^{PhMe}L_o^{NMe}$- Z' = 2 π-π interactions between neighbouring molecules: Edge-Face (Phenolate-methylphenyl) Centroid-centroid separation 5.058(3) Å, plane-plane angle 98.1(3) º, plane-plane shift 1.746(11) Å; Edge-Face (methylphenyl-methylphenyl) Centroid-centroid separation 5.269(5) Å, plane-plane angle 80.7(3) º, plane-plane shift 1.142(13) Å.

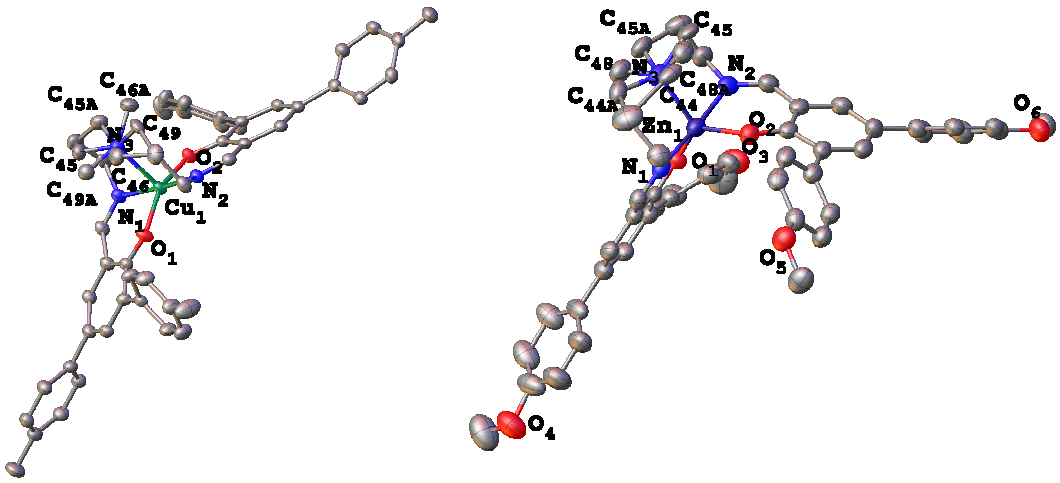


Figure A2.8: Left: $Cu^{PhMe}L_o^{NMe}$- Z' = 1 π-π interactions between neighbouring molecules: Edge-Face (Phenolate-methylphenyl) Centroid-centroid separation 5.0966(16) Å, plane-plane angle 82.19(9) º, plane-plane shift 1.830(5) Å; Edge-Face (methylphenyl-methylphenyl) Centroid-centroid separation 4.9790(16) Å, plane-plane angle 1.385(6) º, plane-plane shift 1.385(6) Å.; Right: $Zn^{PhOMe}L_o^{NMe}$- Z' = 1 π-π interactions between neighbouring molecules: Edge-Face (methoxyphenyl-methoxyphenyl) Centroid-centroid separation 4.798(4) Å, plane-plane angle 29.4(2) º, plane-plane shift 2.277(10) Å. Edge-Face (phenolate-methoxyphenyl) Centroid-centroid separation 4.622(3) Å, plane-plane angle 32.92(17) º, plane-plane shift 2.203(10) Å.

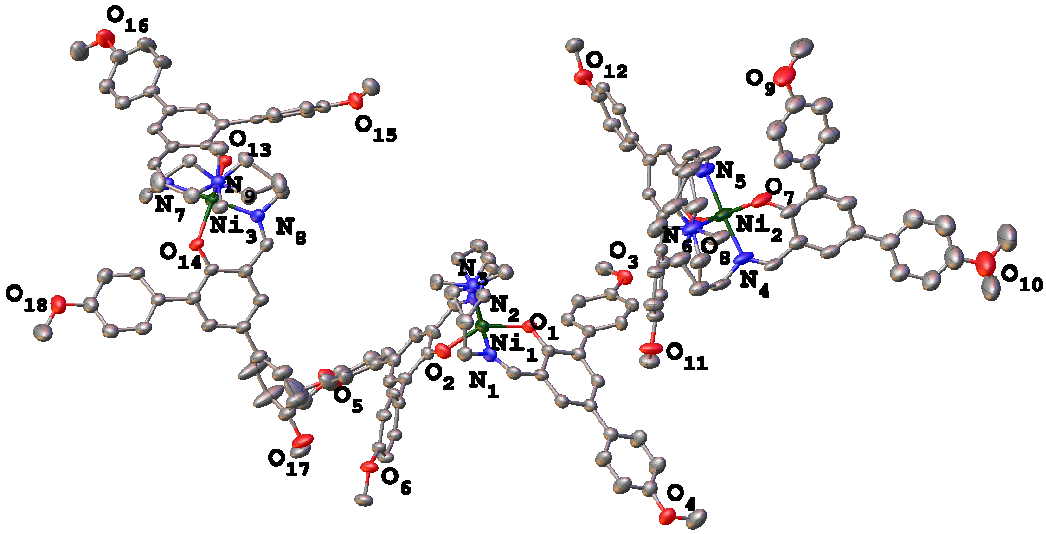


Figure A2.9: $Ni^{PhOMe}L_o^{NMe}$- Z' = 1

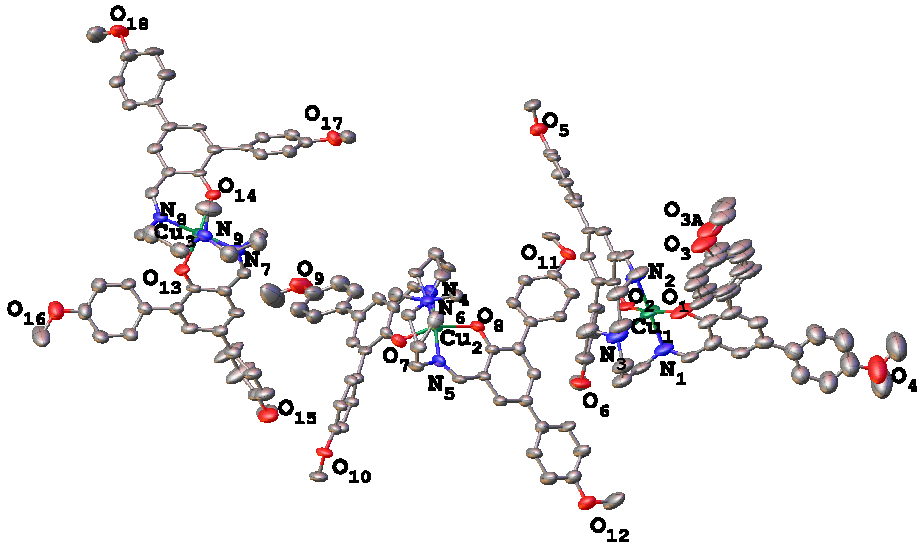


Figure A2.10: $Cu^{PhOMe}L_o^{NMe}$- Z' = 1 π-π interactions between neighbouring molecules: Face-Face (phenolate-phenolate) Centroid-centroid separation 3.917(6), plane-plane angle 11.6(4), plane-plane shift 1.07(2). Edge-Face (methoxyphenyl-methoxyphenyl) Centroid-centroid separation 4.71(2), plane-plane angle 88.7(11), plane-plane shift 0.84(9).

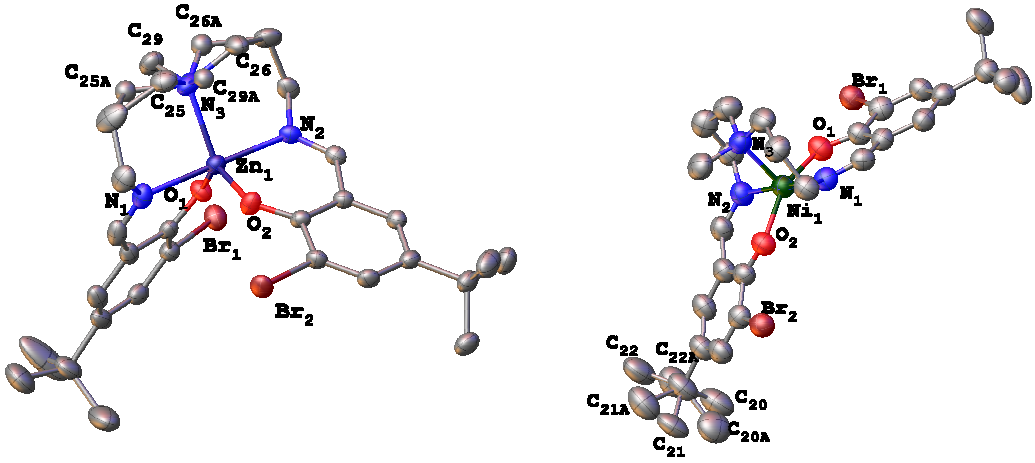


Figure A2.11: Left: $Zn^{tBu/Br}L_o^{NMe}$- Z' = 1; Right: $Ni^{tBu/Br}L_o^{NMe}$- Z' = 1

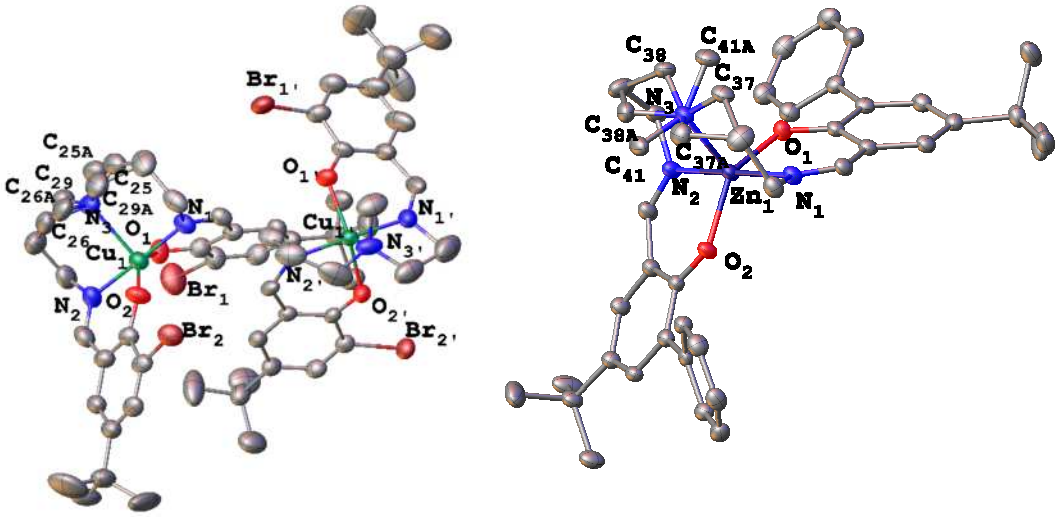


Figure A2.12: Left: $Cu^{tBu/Br}L_o^{NMe}$- Z' = 2 π-π interactions between neighbouring molecules: Face-Face Centroid-centroid separation 3.825(6) Å, plane-plane angle 24.2(2) º, plane-plane shift 1.378(12) Å; Right: $Zn^{tBu/Ph}L_o^{NMe}$- Z' = 1 π-π interactions between neighbouring molecules: Face-Face Centroid-centroid separation 5.4882(14) Å, plane-plane angle 74.02(8) º, plane-plane shift 1.202(6) Å.

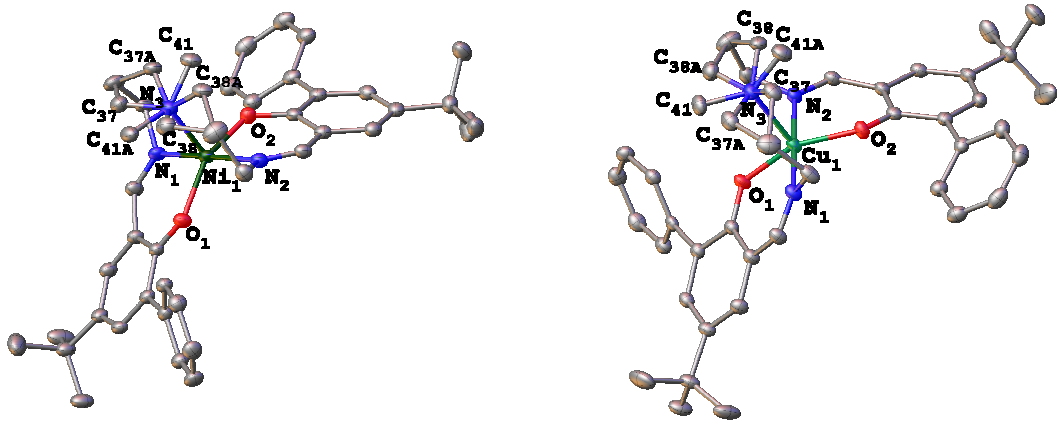


Figure A2.13: Left: $Ni^{tBu/Ph}L_o^{NMe}$- Z' = 1 π-π interactions between neighbouring molecules: Face-Face Centroid-centroid separation 5.5252(8) Å, plane-plane angle 75.50(5) º, plane-plane shift 1.437(3) Å.; Right: $Cu^{tBu/Ph}L_o^{NMe}$- Z' = 1 π-π interactions between neighbouring molecules: Face-Face Centroid-centroid separation 5.51201(7) Å, plane-plane angle 75.8993(14) º, plane-plane shift 1.37113(12) Å.

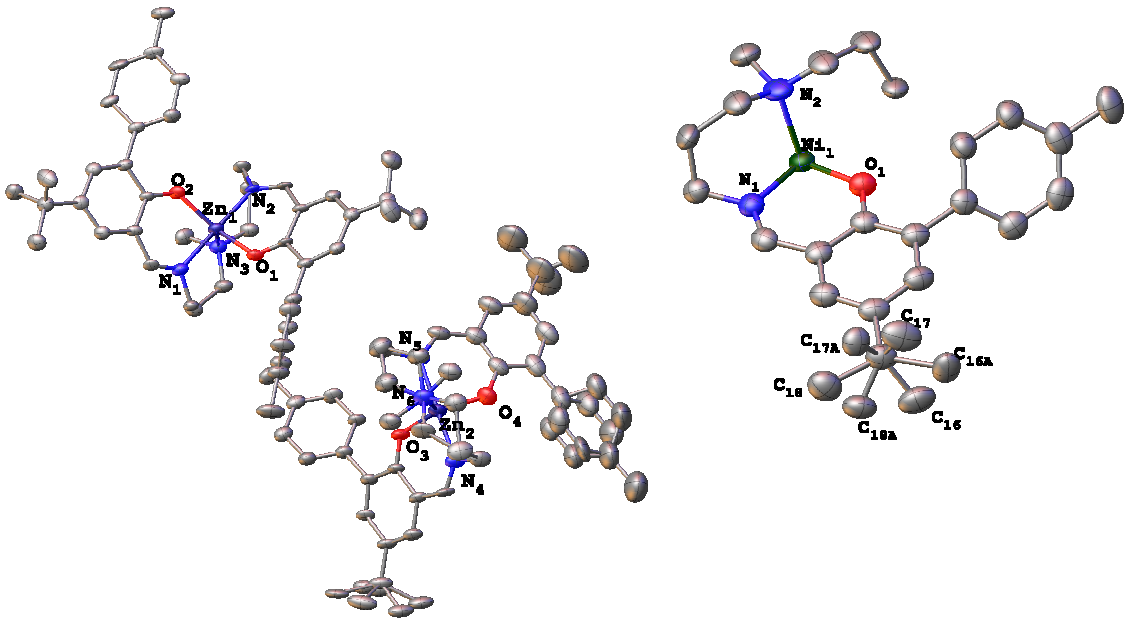


Figure A2.14: Left: Zn$^{tBu/PhMe}L_o^{NMe}$- Z' = 2 π-π interactions between neighbouring molecules: Edge-Face (phenolate-methylphenyl) Centroid-centroid separation 4.823(6) Å, plane-plane angle 69.2(3) º, plane-plane shift 0.61(2) Å. Edge-Face (methylphenyl-methylphenyl) Centroid-centroid separation 5.127(6) Å, plane-plane angle 100.1(4) º, plane-plane shift 1.42(2) Å; Right: Ni$^{tBu/PhMe}L_o^{NMe}$- Z' = 0.5

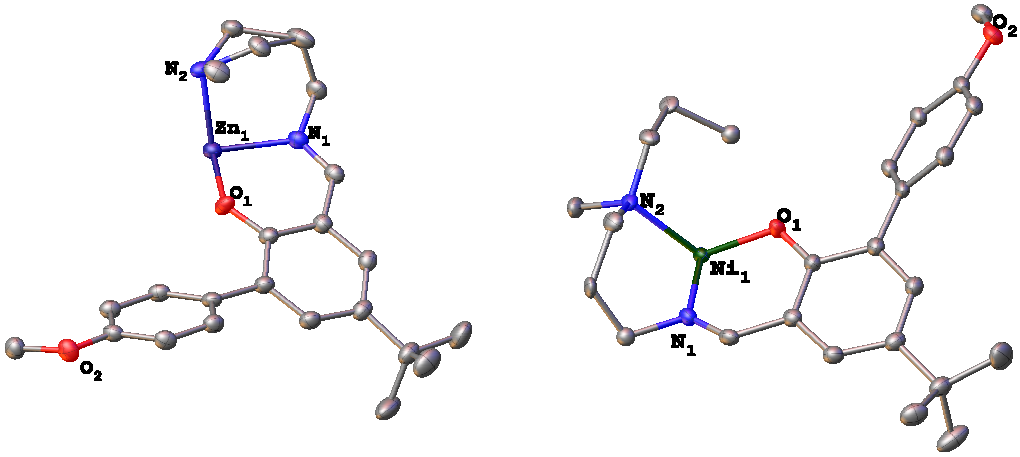


Figure A2.15: Left: Zn$^{tBu/PhOMe}L_o^{NMe}$- Z' = 0.5; Right: Ni$^{tBu/PhOMe}L_o^{NMe}$- Z' = 0.5

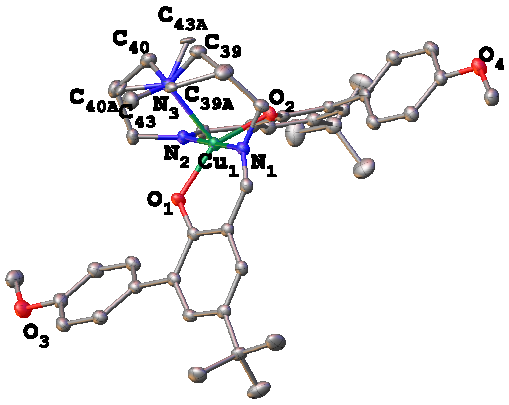


Figure A2.16: $Cu^{tBu/PhOMe}L_o^{NMe}$- Z' = 1

Structures in Chapter Four

	Ni^{tBu}L$_o^{PyOMe}$ NIGMLR	**Cu^{tBu}L$_o^{PyOMe}$** CUGMMB
Crystal data		
Chemical formula	$C_{42}H_{59}N_3NiO_3$	$C_{42}H_{59}CuN_3O_3$
M_r	841.03	717.46
Crystal system, space group	Triclinic, $P\bar{1}$	Triclinic, $P\bar{1}$
Temperature (K)	120	120
a, *b*, *c* (Å)	11.4009 (17), 14.2445 (17), 14.7044 (18)	11.0585 (18), 13.6897 (17), 14.6561 (15)
α, β, γ (°)	108.655 (11), 92.666 (11), 103.349 (11)	103.426 (10), 101.892 (12), 96.292 (12)
V (Å^3)	2182.5 (5)	2082.7 (5)
Z	2	2
Radiation type	Cu *K*α	Cu *K*α
μ (mm^{-1})	2.65	1.03
Crystal size (mm)	0.22 × 0.05 × 0.04	0.47 × 0.06 × 0.04
Data collection		
Diffractometer	SuperNova, Dual, Cu at zero, Atlas	XXtalLAB PRO MM007, PILATUS3 R 200K
Absorption correction	Gaussian *CrysAlis PRO*, Agilent Technologies, Version 1.171.37.35 (release 13-08-2014 CrysAlis171 .NET) (compiled Aug 13 2014,18:06:01) Numerical absorption correction based on gaussian integration over a multifaceted crystal model.	Gaussian *CrysAlis PRO* 1.171.38.41n (Rigaku Oxford Diffraction, 2015) Numerical absorption correction based on gaussian integration over a multifaceted crystal model.
T_{min}, T_{max}	0.874, 0.973	0.792, 0.967
No. of measured, independent and observed [$I > 2\sigma(I)$] reflections	15646, 8443, 4149	23873, 8250, 3011
R_{int}	0.091	0.158
$(\sin\theta/\lambda)_{max}$ (Å^{-1})	0.627	0.644
Refinement		
$R[F^2 > 2\sigma(F^2)]$, $wR(F^2)$, *S*	0.133, 0.411, 1.12	0.158, 0.512, 1.38
No. of reflections	8443	8250
No. of parameters	457	548
No. of restraints	112	243
H-atom treatment	H-atom parameters constrained	H-atom parameters constrained
$\Delta\rangle_{max}$, $\Delta\rangle_{min}$ (e Å^{-3})	1.04, -1.09	1.28, -0.66

Appendix 3

Computational Methods

DFT calculations, including geometry optimisations and spectroscopic calculations, were performed using the Amsterdam Density Functional (ADF) suite of programs, version 2014.01.[15] Models derived from crystallographically obtained structures were used for geometry optimisations and no constraints were placed on these optimisations.

Slater type orbitals triple plus polarisation basis sets using the ZORA/TZP database of the ADF suite were employed, with scalar relativistic approaches used within the ZORA Hamiltonian for the inclusion of relativistic effects. The functionals of Becke[16] and Perdew[17] were used. COSMO[18] solvation functions were employed.

Molecular models were manipulated using the program ArgusLab, optimised structures were visualised using Mercury[19] and plots of calculated electronic structures were produced using Molekel[20] and ADF.[15]

Appendices References

1. A. Schweiger and G. Jeschke, *Principles of Pules Electron Paramagnetic Resonance*, Oxford University Press, Oxford, 2001.
2. P. Höfer, A. Grupp, H. Nebenführ and M. Mehring, *Chem. Phys. Lett.*, 1986, **132**, 279-282.
3. C. Gemperie, G. Aebli, A. Schweiger and R. R. Ernst, *J. Mag. Reson.*, 1990, **24**, 279.
4. I. Noviandri, K. N. Brown, D. S. Fleming, P. T. Gulyas, P. A. Lay, A. F. Masters and L. Phillips, *J. Phys. Chem. B*, 1999, **103**, 6713-6722.
5. R. S. Nicholson and I. Shain, *Anal. Chem.*, 1964, **36**, 706-723.
6. R. S. Nicholson, *Anal. Chem.*, 1966, **38**, 1406-1406.
7. A. Spek, *Acta Crystallogr. D*, 2009, **65**, 148-155.
8. SMART and SAINT, *Bruker AXS Inc.: Madison, WI*, 2001.
9. CrysAlisPRO, *Agilent Technologies: Yarnton, England*, 2010.
10. L. Palatinus and G. Chapuis, *J. Appl. Crystallogr.*, 2007, **40**, 786-790.
11. G. Sheldrick, *Acta Crystallogr. A*, 2008, **64**, 112-122.
12. G. Sheldrick, *Acta Crystallogr. C*, 2015, **71**, 3-8.
13. O. V. Dolomanov, L. J. Bourhis, R. J. Gildea, J. A. K. Howard and H. Puschmann, *J. Appl. Crystallogr.*, 2009, **42**, 339-341.
14. checkcif.iucr.org.
15. G. te Velde, F. M. Bickelhaupt, E. J. Baerends, C. Fonseca Guerra, S. J. A. van Gisbergen, J. G. Snijders and T. Ziegler, *J. Comput. Chem.*, 2001, **22**, 931-967.
16. A. D. Becke, *Phys. Rev. A*, 1988, **38**, 3098-3100.
17. J. P. Perdew, *Phys. Rev. B*, 1986, **33**, 8822-8824.
18. A. Klamt and G. Schuurmann, *J. Chem. Soc., Perkin Trans. 2*, 1993, 799-805.
19. C. F. Macrae, P. R. Edgington, P. McCabe, E. Pidcock, G. P. Shields, R. Taylor, M. Towler and J. van de Streek, *J. Appl. Crystallogr.*, 2006, **39**, 453-457.
20. S. Portmann and H. P. Lüthi, *CHIMIA Int. J. Chem.*, 2000, **54**, 766-770.